OCTOBER 2017

AJNR

VOLUME 38 • PP 1849–2031

AJNR

AMERICAN JOURNAL OF NEURORADIOLOGY

OCTOBER 2017
VOLUME 38
NUMBER 10
WWW.AJNR.ORG

THE JOURNAL OF DIAGNOSTIC AND INTERVENTIONAL NEURORADIOLOGY

ASL imaging in preoperative evaluation of gliomas
Multinodular and vacuolating neuronal tumor of the cerebrum
Localizing the L5 vertebra using nerve morphology on MRI

Official Journal ASNR • ASFNR • ASHNR • ASPNR • ASSR

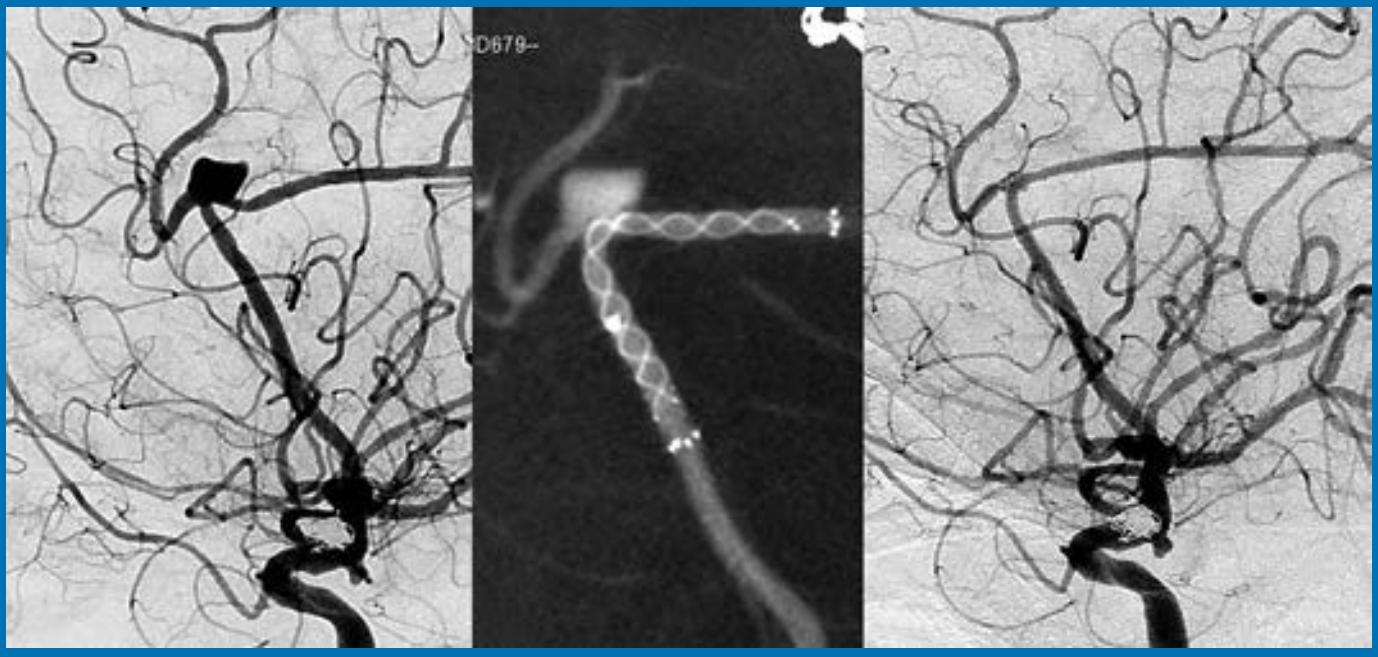

MicroVention® TERUMO

Access Product Solutions

Sofia® Plus

Distal Access Catheter

Soft Torqueable Catheter Optimized for Intracranial Access with Excellent Navigation and Trackability

Neurovascular Malformation Solutions

Scepter® XC

Occlusion Balloon Catheter

Clinical Applications in Four Key Areas: Balloon Remodeling, Stent Delivery, Liquid Embolic Injection, and Balloon-Test Occlusion

INDICATIONS FOR USE:

The SOFIA® Catheter is indicated for general intravascular use, including the neuro and peripheral vasculature. The SOFIA® Catheter can be used to facilitate introduction of diagnostic or therapeutic agents. The SOFIA® Catheter is not intended for use in coronary arteries.

The Scepter C® and Scepter XC® Occlusion Balloon Catheters are intended for use in the peripheral and neuro vasculature where temporary occlusion is desired. The balloon catheters provide temporary vascular occlusion which is useful in selectively stopping or controlling blood flow. The balloon catheters also offer balloon assisted embolization of intracranial aneurysms. For use in the peripheral vasculature for the infusion of diagnostic agents, such as contrast media, and therapeutic agents such as embolization materials. For neurovascular use for the infusion of diagnostic agents such as contrast media, and therapeutic agents, such as embolization materials, that have been approved or cleared for use in the neurovasculature and are compatible with the inner diameter of the Scepter C/XC Balloon Catheter.

The LVIS® Device is intended for use with bare platinum embolic coils for the treatment of unruptured, wide neck (neck ≥ 4 mm or dome to neck ratio < 2), intracranial, saccular aneurysms arising from a parent vessel with a diameter ≥ 2.5 mm and ≤ 4.5 mm.

The Headway® Duo Microcatheter is intended for general intravascular use, including the peripheral and coronary vasculature for the infusion of diagnostic agents, such as contrast media, and therapeutic agents, such as embolization materials. The Headway® Duo Microcatheter is intended for neurovascular use, for the infusion of diagnostic agents, such as contrast media, and therapeutic agents that have been cleared or approved for use in the neurovasculature and are compatible with the inner diameter of the Headway® Duo Microcatheter.

A 360-Degree Approach to Neuroendovascular Therapy

Aneurysm Therapy Solutions

LVIS® | LVIS® Jr.
Intraluminal Support Device

Braided Coil Assist Stents with High Neck Coverage, Excellent Opening, and Improved Radial Force*

**Humanitarian Device: Authorized by Federal Law for use with bare platinum embolic coils for the treatment of unruptured, wide neck (neck ≥ 4 mm or dome to neck ratio < 2), intracranial, saccular aneurysms arising from a parent vessel with a diameter ≥ 2.5 mm and ≤ 4.5 mm. The effectiveness of this device for this use has not been demonstrated.*

Access Product Solutions

Headway® DUO
Microcatheter

Innovative Catheter Technology and Construction in a Complete Range of Sizes and Softness

For more information or a product demonstration, contact your local MicroVention representative:

MicroVention® TERUMO

MicroVention, Inc.
Worldwide Headquarters PH +1.714.247.8000
35 Enterprise
Aliso Viejo, CA 92656 USA
MicroVention UK Limited PH +44 (0) 191 258 6777
MicroVention Europe, S.A.R.L. PH +33 (1) 39 21 77 46
MicroVention Deutschland GmbH PH +49 211 210 798-0
microvention.com

MICROVENTION, Scepter C, Scepter XC, Sofia, LVIS and Headway are registered trademarks of MicroVention, Inc. • Refer to Instructions for Use, contraindications and warnings for additional information. Federal (USA) law restricts this device for sale by or on the order of a physician. ©2017 MicroVention, Inc. Aug. 2017

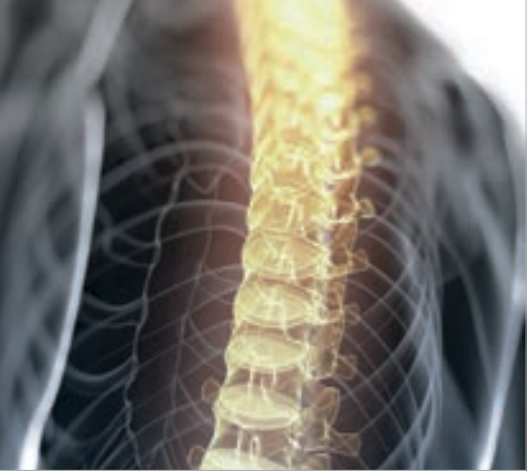

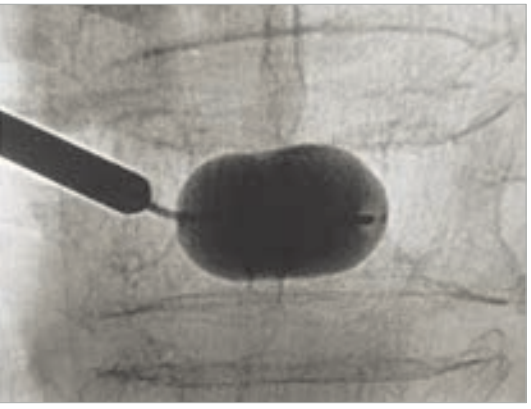

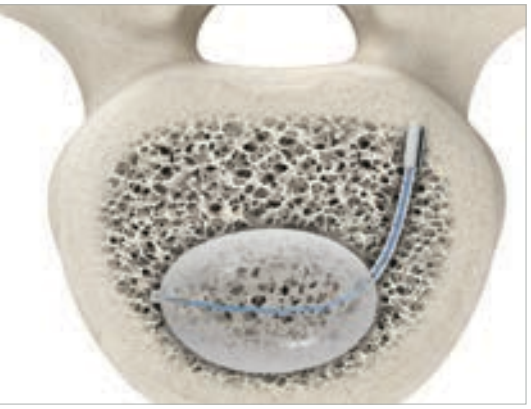

stryker

Unipedicular approach.

Bipedicular results.*

AVAflex® Balloon System

Simplify your approach in treating vertebral compression fractures (VCFs) and create larger voids with a single incision. The AVAflex system's flexible, curved balloon is available up to 30mm, the longest balloon on the market today.† Our curved, coaxial needle achieves targeted cement placement. It's more than a minimally invasive approach with the potential for less risk of patient trauma. It's a powerful reminder that we're in this together.

Achieve precision with a single incision.

strykerIVS.com/avaflex

* Based on fill volume
† As of March 2017

1000-025-577 Rev None

Unleash Your Tiger

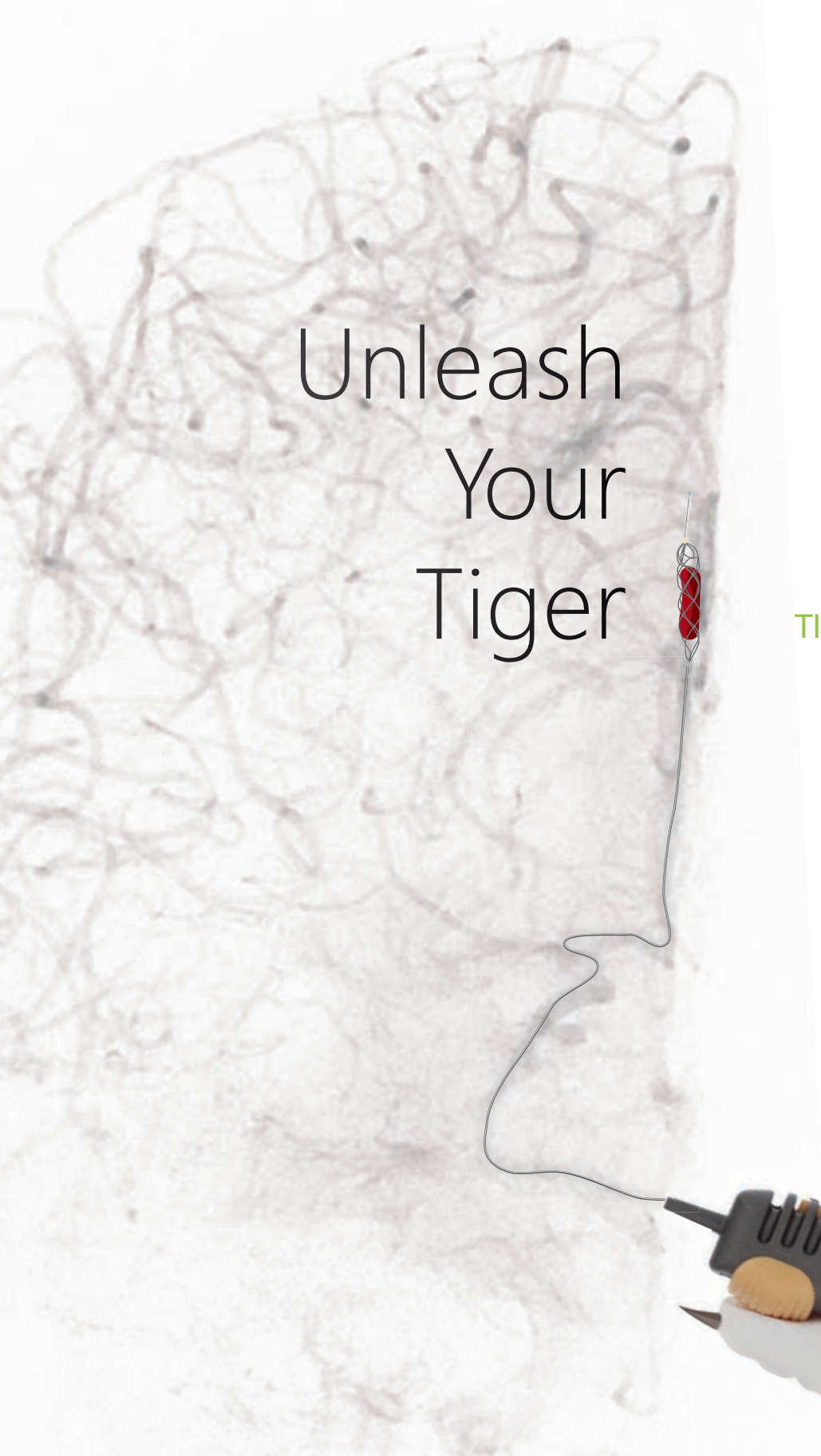

TIGERTRIEVER

RAPIDMEDICAL
The brain at your fingertips

//www.rapid-medical.com

Magic®

balt

FLOW-DEPENDENT MICROCATHETER SERIES

Now available through Balt USA

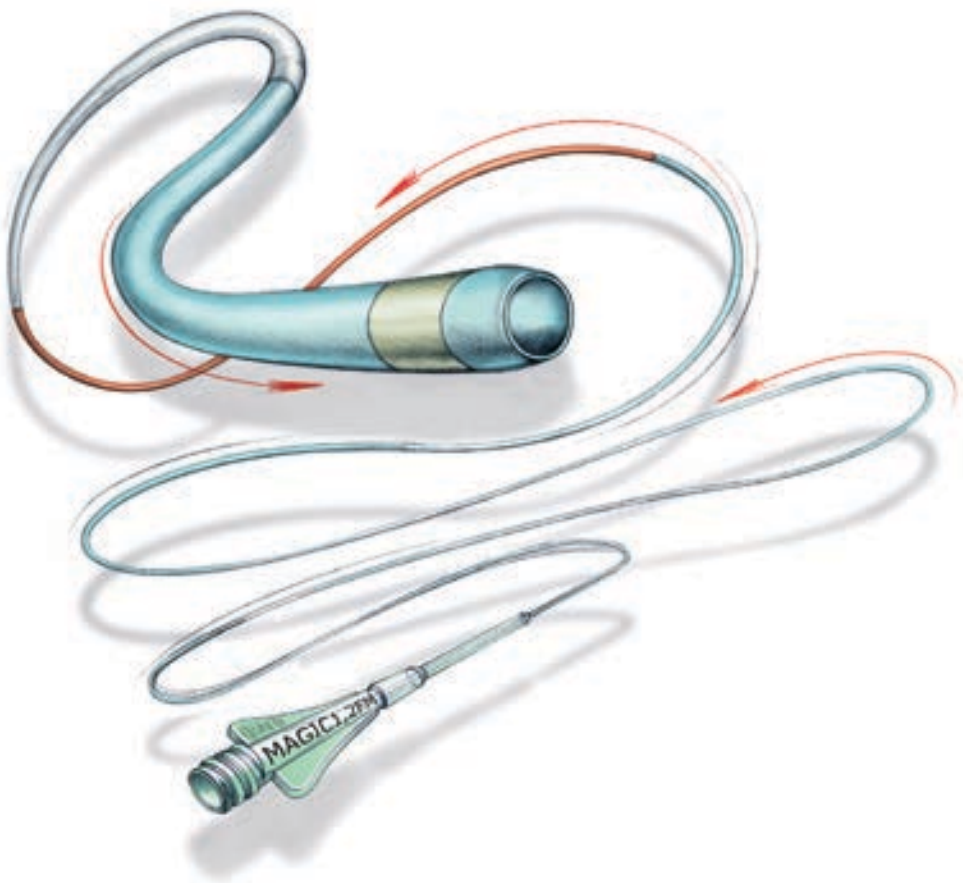

ordermagics@balt-usa.com

MAGIC catheters are designed for general intravascular use. They may be used for the controlled, selective regional infusion of therapeutic agents or embolic materials into vessels.[1]

Federal (USA) law restricts this device to sale, distribution by or on the order of a physician. Indications, contraindications, warnings and instructions for use can be found in the product labeling supplied with each device.

1. Magic Catheters IFU – Ind 19

balt
inspiring innovation

BALT USA
18 Technology Drive #169, Irvine, CA 92618
P 949.788.1443 **F** 949.788.1444

© 2017 BALT USA MKTG-068 Rev. B

ASNR 56th Annual Meeting & The Foundation of the ASNR Symposium 2018

June 2 - 7, 2018 | Vancouver, B.C., CANADA

The Vancouver Convention Centre East
© 2013 Vancouver Convention Centre

Welcome and Greetings

Please join us in Vancouver, CANADA for the **56th Annual Meeting of the American Society of Neuroradiology** on June 2–7, 2018 at the Vancouver Convention Centre East. Surrounded by the coastal mountains and located on the waterfront, you can enjoy these spectacular views in the heart of downtown Vancouver. With its undeniable charm and friendly atmosphere, Vancouver is known around the world as both a popular tourist attraction and one of the best places to live.

ASNR enthusiastically presents **Neuroradiology: Adding Value and Improving Healthcare** at the Symposium of the Foundation of the ASNR, as well as the common thread throughout the Annual Meeting. Implementing a value-based strategy in imaging has grasped the attention of nearly every healthcare provider; in particular with Radiologists understanding that the future will demand their imaging practices deliver better value. Value in healthcare is typically defined as those imaging strategies that yield improved outcomes, lower costs, or both. As payment transitions from a fee-for-service to a value-based system, thus creating a fundamentally different marketplace dynamic, measuring good outcomes are at the center of this changeover. At this time of uncertainty what little remains clear is that without a well-defined knowledge of their outcomes, no medical specialty will be able to succeed in the future value-based system. The Symposium will feature how Neuroradiology, in its many subspecialty areas, adds value to clinical care pathways by directing healthcare practice towards better outcomes. The annual meeting programming will continue on this theme emphasizing imaging that improves health outcomes, while considering costs, thus adding value. Our discussions will incorporate many innovative approaches to how neuroimaging currently does and will continue to improve overall healthcare performance.

As the Program Chair for ASNR 2018, it is my pleasure and honor to welcome you to Vancouver, CANADA for our annual meeting! Vancouver is known for being a very walkable city with a compact downtown core hosting many places to enjoy. So pack your comfortable walking shoes and let's tour together with our colleagues and friends!

Pina Sanelli

Pina C. Sanelli, MD, MPH, FACR
ASNR 2018 Program Chair/President-Elect

NEURORADIOLOGY
Adding Value & Improving Healthcare

ASNR 2018 ▪ VANCOUVER

ASFNR ASHNR ASPNR ASSR SNIS

THE FOUNDATION OF THE ASNR

Pina C. Sanelli, MD, MPH, FACR
ASNR 2018 Program Chair/President-Elect

Programming developed in cooperation with the…

American Society of Functional Neuroradiology (ASFNR)
Max Wintermark, MD

American Society of Head and Neck Radiology (ASHNR)
Deborah R. Shatzkes, MD

American Society of Pediatric Neuroradiology (ASPNR)
Ashok Panigrahy, MD

American Society of Spine Radiology (ASSR)
John D. Barr, MD, FACR, FSIR, FAHA

Society of NeuroInterventional Surgery (SNIS)
Mahesh V. Jayaraman, MD

ASNR Health Policy (HPC) Committee
William D. Donovan, MD, MPH, FACR,
Gregory N. Nicola, MD, FACR

ASNR Computer Sciences & Informatics (CSI) Committee
John L. Go, MD, FACR

ASNR Research Scientist Programming Committee
Dikoma C. Shungu, PhD, Timothy P.L. Roberts, PhD

The International Hydrocephalus Imaging Working Group (IHIWG) / CSF Flow Group
William G. Bradley, Jr., MD, PhD, FACR, Harold L. Rekate, MD and Bryn A. Martin, PhD

Abstract Deadline: Friday, December 15, 2017
Please visit 2018.asnr.org for more information

Fairmont Waterfront
© Copyright 2017 FRHI

Pan Pacific Vancouver
© 2017 Pan Pacific Hotels and Resorts

ASNR 56th Annual Meeting
c/o American Society of Neuroradiology
800 Enterprise Drive, Suite 205
Oak Brook, Illinois 60523-4216
Phone: 630-574-0220 + Fax: 630 574-0661
2018.asnr.org

AJNR

AMERICAN JOURNAL OF NEURORADIOLOGY

Publication Preview at www.ajnr.org features articles released in advance of print. Visit www.ajnrblog.org to comment on AJNR content and chat with colleagues and AJNR's News Digest at http://ajnrdigest.org to read the stories behind the latest research in neuroimaging.

OCTOBER 2017 • VOLUME 38 • NUMBER 10 • WWW.AJNR.ORG

Official Journal:
American Society of Neuroradiology
American Society of Functional Neuroradiology
American Society of Head and Neck Radiology
American Society of Pediatric Neuroradiology
American Society of Spine Radiology

EDITOR-IN-CHIEF

Jeffrey S. Ross, MD
Professor of Radiology, Department of Radiology, Mayo Clinic College of Medicine, Phoenix, AZ

SENIOR EDITORS

Harry J. Cloft, MD, PhD
Professor of Radiology and Neurosurgery, Department of Radiology, Mayo Clinic College of Medicine, Rochester, MN

Thierry A.G.M. Huisman, MD
Professor of Radiology, Pediatrics, Neurology, and Neurosurgery, Chairman, Department of Imaging and Imaging Science, Johns Hopkins Bayview, Director, Pediatric Radiology and Pediatric Neuroradiology, Johns Hopkins Hospital, Baltimore, MD

Yvonne W. Lui, MD
Associate Professor of Radiology, Chief of Neuroradiology, New York University School of Medicine, New York, NY

C.D. Phillips, MD, FACR
Professor of Radiology, Weill Cornell Medical College, Director of Head and Neck Imaging, New York-Presbyterian Hospital, New York, NY

Pamela W. Schaefer, MD
Clinical Director of MRI and Associate Director of Neuroradiology, Massachusetts General Hospital, Boston, Massachusetts, Associate Professor, Radiology, Harvard Medical School, Cambridge, MA

Charles M. Strother, MD
Professor of Radiology, Emeritus, University of Wisconsin, Madison, WI

STATISTICAL SENIOR EDITOR

Bryan A. Comstock, MS
Senior Biostatistician, Department of Biostatistics, University of Washington, Seattle, WA

EDITORIAL BOARD
Ashley H. Aiken, *Atlanta, GA*
Lea M. Alhilali, *Phoenix, AZ*
John D. Barr, *Dallas, TX*
Ari Blitz, *Baltimore, MD*
Barton F. Branstetter IV, *Pittsburgh, PA*
Jonathan L. Brisman, *Lake Success, NY*
Julie Bykowski, *San Diego, CA*
Keith Cauley, *Danville, PA*
Asim F. Choudhri, *Memphis, TN*
Alessandro Cianfoni, *Lugano, Switzerland*
J. Matthew Debnam, *Houston, TX*
Seena Dehkharghani, *New York, NY*
Colin Derdeyn, *Iowa City, IA*
Rahul S. Desikan, *San Francisco, CA*
Yonghong Ding, *Rochester, MN*
Clifford J. Eskey, *Hanover, NH*
Saeed Fakhran, *Phoenix, AZ*
Massimo Filippi, *Milan, Italy*
Allan J. Fox, *Toronto, Ontario, Canada*
Wende N. Gibbs, *Los Angeles, CA*
Christine M. Glastonbury, *San Francisco, CA*
John L. Go, *Los Angeles, CA*
Allison Grayev, *Madison, WI*
Brent Griffith, *Detroit, MI*
Wan-Yuo Guo, *Taipei, Taiwan*
Ajay Gupta, *New York, NY*
Rakesh K. Gupta, *Lucknow, India*
Lotfi Hacein-Bey, *Sacramento, CA*
Christopher P. Hess, *San Francisco, CA*
Andrei Holodny, *New York, NY*
Benjamin Huang, *Chapel Hill, NC*
George J. Hunter, *Boston, MA*
Mahesh V. Jayaraman, *Providence, RI*
Valerie Jewells, *Chapel Hill, NC*
Christof Karmonik, *Houston, TX*
Timothy J. Kaufmann, *Rochester, MN*
Hillary R. Kelly, *Boston, MA*
Toshibumi Kinoshita, *Akita, Japan*
Kennith F. Layton, *Dallas, TX*
Michael M. Lell, *Nürnberg, Germany*
Michael Lev, *Boston, MA*
Karl-Olof Lovblad, *Geneva, Switzerland*
Franklin A. Marden, *Chicago, IL*
M. Gisele Matheus, *Charleston, SC*
Joseph C. McGowan, *Merion Station, PA*
Stephan Meckel, *Freiburg, Germany*
Christopher J. Moran, *St. Louis, MO*
Takahisa Mori, *Kamakura City, Japan*
Suresh Mukherji, *Ann Arbor, MI*
Amanda Murphy, *Toronto, Ontario, Canada*
Alexander J. Nemeth, *Chicago, IL*
Sasan Partovi, *Cleveland, OH*
Laurent Pierot, *Reims, France*
Jay J. Pillai, *Baltimore, MD*
Whitney B. Pope, *Los Angeles, CA*
M. Judith Donovan Post, *Miami, FL*
Tina Young Poussaint, *Boston, MA*
Joana Ramalho, *Lisbon, Portugal*
Otto Rapalino, *Boston, MA*
Álex Rovira-Cañellas, *Barcelona, Spain*
Paul M. Ruggieri, *Cleveland, OH*
Zoran Rumboldt, *Rovinj-Rovigno, Croatia*
Amit M. Saindane, *Atlanta, GA*
Erin Simon Schwartz, *Philadelphia, PA*
Lubdha M. Shah, *Salt Lake City, UT*
Aseem Sharma, *St. Louis, MO*
J. Keith Smith, *Chapel Hill, NC*
Maria Vittoria Spampinato, *Charleston, SC*
Gordon K. Sze, *New Haven, CT*
Krishnamoorthy Thamburaj, *Hershey, PA*
Cheng Hong Toh, *Taipei, Taiwan*
Thomas A. Tomsick, *Cincinnati, OH*
Aquilla S. Turk, *Charleston, SC*
Willem Jan van Rooij, *Tilburg, Netherlands*
Arastoo Vossough, *Philadelphia, PA*
Elysa Widjaja, *Toronto, Ontario, Canada*
Max Wintermark, *Stanford, CA*
Ronald L. Wolf, *Philadelphia, PA*
Kei Yamada, *Kyoto, Japan*
Carlos Zamora, *Chapel Hill, NC*

EDITORIAL FELLOW
Vahe Zohrabian, *New Haven, CT*

SPECIAL CONSULTANTS TO THE EDITOR
AJNR Blog Editor
Neil Lall, *Denver, CO*
Case of the Month Editor
Nicholas Stence, *Aurora, CO*
Case of the Week Editors
Juan Pablo Cruz, *Santiago, Chile*
Sapna Rawal, *Toronto, Ontario, Canada*
Classic Case Editor
Sandy Cheng-Yu Chen, *Taipei, Taiwan*
Facebook Editor
Peter Yi Shen, *Sacramento, CA*
Health Care and Socioeconomics Editor
Pina C. Sanelli, *New York, NY*
Physics Editor
Greg Zaharchuk, *Stanford, CA*
Podcast Editor
Wende N. Gibbs, *Los Angeles, CA*
Twitter Editor
Jennifer McCarty, *Atlanta, Georgia*

YOUNG PROFESSIONALS ADVISORY COMMITTEE
Asim K. Bag, *Birmingham, AL*
Anna E. Nidecker, *Sacramento, CA*
Peter Yi Shen, *Sacramento, CA*

Founding Editor
Juan M. Taveras
Editors Emeriti
Mauricio Castillo, Robert I. Grossman, Michael S. Huckman, Robert M. Quencer

Managing Editor
Karen Halm
Assistant Managing Editor
Laura Wilhelm
Digital Publications and Social Media Coordinator
Kylie Mason
Executive Director, ASNR
Mary Beth Hepp
Director of Communications, ASNR
Angelo Artemakis

stryker®
Neurovascular

Purposeful innovation in mind.

Smooth and stable.

Target Detachable Coils deliver consistently smooth deployment and exceptional microcatheter stability. Designed to work seamlessly together for framing, filling and finishing. Target Coils deliver the high performance you demand.

For more information, please visit www.strykerneurovascular.com/Target or contact your local Stryker Neurovascular sales representative.

Target®
DETACHABLE COILS

Copyright © 2016 Stryker
NV00018669.AA

We're Inside Every Great Neuroradiologist!

ASNR MEMBERS RECEIVE

American Journal of Neuroradiology (AJNR)
The leading neuroradiology research journal, published monthly

Neurographics
Bimonthly educational journal with CME for members

ASNR Annual Meeting
Discounts for members on the field's premier conference

eCME
Online collection of lectures and articles with SA-CME and Category 1 credit

Advocacy
Coding/reimbursement, quality standards and practice guidelines; demonstrating neuroradiology's value!

Networking
Access to 5,000 peers

... And More!

Join the leaders in neuroradiology today!
Learn more at www.asnr.org/join

ASNR
American Society of Neuroradiology
800 Enterprise Dr., Suite 205, Oak Brook, IL 60523 • (630)574-0220 • membership@asnr.org • www.asnr.org

Strengthen ASNR's representation at the national level.

Your membership in the American Medical Association strengthens ASNR's representation in the AMA House of Delegates—the policymaking body of the AMA that brings forth the views and interests of all physicians to establish national policy on health, medical, professional and governance matters.

Please activate your 2017 AMA membership, visit ama-assn.org or call AMA Member Relations at (800) 262-3211. If you are currently a member, thank you.

AMA member benefits and resources include:

- Unlimited access to **The JAMA Network®** which brings together *JAMA* and all 11 specialty journals with CME.
  jamanetwork.com
- **STEPS Forward™**, the AMA's new practice transformation series designed to help physicians achieve the Quadruple Aim: better patient experience, better population health and lower overall costs with improved professional satisfaction.
  stepsforward.org
- Free 18-month trial of ***DynaMed Plus®***, an evidence-based, clinical support tool that features thousands of images and provides immediate answers to clinical questions.
  offers.jamanetwork.com

AMA
AMERICAN MEDICAL ASSOCIATION

ASNR
American Society of Neuroradiology

© 2016 American Medical Association. All rights reserved. 16-1648

Trevo® XP ProVue Retrievers

See package insert for complete indications, complications, warnings, and instructions for use.

INDICATIONS FOR USE

1. The Trevo Retriever is indicated for use to restore blood flow in the neurovasculature by removing thrombus for the treatment of acute ischemic stroke to reduce disability in patients with a persistent, proximal anterior circulation, large vessel occlusion, and smaller core infarcts who have first received intravenous tissue plasminogen activator (IV t-PA). Endovascular therapy with the device should start within 6 hours of symptom onset.
2. The Trevo Retriever is intended to restore blood flow in the neurovasculature by removing thrombus in patients experiencing ischemic stroke within 8 hours of symptom onset. Patients who are ineligible for intravenous tissue plasminogen activator (IV t-PA) or who fail IV t-PA therapy are candidates for treatment.

COMPLICATIONS

Procedures requiring percutaneous catheter introduction should not be attempted by physicians unfamiliar with possible complications which may occur during or after the procedure. Possible complications include, but are not limited to, the following: air embolism; hematoma or hemorrhage at puncture site; infection; distal embolization; pain/headache; vessel spasm, thrombosis, dissection, or perforation; emboli; acute occlusion; ischemia; intracranial hemorrhage; false aneurysm formation; neurological deficits including stroke; and death.

COMPATIBILITY

3x20mm retrievers are compatible with Trevo® Pro 14 Microcatheters (REF 90231) and Trevo® Pro 18 Microcatheters (REF 90238). 4x20mm retrievers are compatible with Trevo® Pro 18 Microcatheters (REF 90238). 4x30mm retrievers are compatible with Excelsior® XT-27® Microcatheters (150cm x 6cm straight REF 275081) and Trevo® Pro 18 Microcatheters (REF 90238). 6x25mm Retrievers are compatible with Excelsior® XT-27® Microcatheters (150cm x 6cm straight REF 275081). Compatibility of the Retriever with other microcatheters has not been established. Performance of the Retriever device may be impacted if a different microcatheter is used.

Balloon Guide Catheters (such as Merci® Balloon Guide Catheter and FlowGate® Balloon Guide Catheter) are recommended for use during thrombus removal procedures.

Retrievers are compatible with the Abbott Vascular DOC® Guide Wire Extension (REF 22260).

Retrievers are compatible with Boston Scientific RHV (Ref 421242).

SPECIFIC WARNINGS FOR INDICATION 1

- The safety and effectiveness of the Trevo Retrievers in reducing disability has not been established in patients with large core infarcts (i.e., ASPECTS ≤ 7). There may be increased risks, such as intracerebral hemorrhage, in these patients.
- The safety and effectiveness of the Trevo Retrievers in reducing disability has not been established or evaluated in patients with occlusions in the posterior circulation (e.g., basilar or vertebral arteries) or for more distal occlusions in the anterior circulation.

WARNINGS APPLIED TO BOTH INDICATIONS

- Administration of IV t-PA should be within the FDA-approved window (within 3 hours of stroke symptom onset).
- Contents supplied STERILE, using an ethylene oxide (EO) process. Nonpyrogenic.
- To reduce risk of vessel damage, adhere to the following recommendations:
  - Take care to appropriately size Retriever to vessel diameter at intended site of deployment.
  - Do not perform more than six (6) retrieval attempts in same vessel using Retriever devices.
  - Maintain Retriever position in vessel when removing or exchanging Microcatheter.
- To reduce risk of kinking/fracture, adhere to the following recommendations:
  - Immediately after unsheathing Retriever, position Microcatheter tip marker just proximal to shaped section. Maintain Microcatheter tip marker just proximal to shaped section of Retriever during manipulation and withdrawal.
  - Do not rotate or torque Retriever.
  - Use caution when passing Retriever through stented arteries.
- Do not resterilize and reuse. Structural integrity and/or function may be impaired by reuse or cleaning.
- The Retriever is a delicate instrument and should be handled carefully. Before use and when possible during procedure, inspect device carefully for damage. Do not use a device that shows signs of damage. Damage may prevent device from functioning and may cause complications.
- Do not advance or withdraw Retriever against resistance or significant vasospasm. Moving or torquing device against resistance or significant vasospasm may result in damage to vessel or device. Assess cause of resistance using fluoroscopy and if needed resheath the device to withdraw.
- If Retriever is difficult to withdraw from the vessel, do not torque Retriever. Advance Microcatheter distally, gently pull Retriever back into Microcatheter, and remove Retriever and Microcatheter as a unit. If undue resistance is met when withdrawing the Retriever into the Microcatheter, consider extending the Retriever using the Abbott Vascular DOC guidewire extension (REF 22260) so that the Microcatheter can be exchanged for a larger diameter catheter such as a DAC® catheter. Gently withdraw the Retriever into the larger diameter catheter.
- Administer anti-coagulation and anti-platelet medications per standard institutional guidelines.

PRECAUTIONS

- Prescription only – device restricted to use by or on order of a physician.
- Store in cool, dry, dark place.
- Do not use open or damaged packages.
- Use by "Use By" date.
- Exposure to temperatures above 54°C (130°F) may damage device and accessories. Do not autoclave.
- Do not expose Retriever to solvents.
- Use Retriever in conjunction with fluoroscopic visualization and proper anti-coagulation agents.
- To prevent thrombus formation and contrast media crystal formation, maintain a constant infusion of appropriate flush solution between guide catheter and Microcatheter and between Microcatheter and Retriever or guidewire.
- Do not attach a torque device to the shaped proximal end of DOC® Compatible Retriever. Damage may occur, preventing ability to attach DOC® Guide Wire Extension.

Concentric Medical
301 East Evelyn Avenue
Mountain View, CA 94041

Stryker Neurovascular
47900 Bayside Parkway
Fremont, CA 94538

strykerneurovascular.com

Date of Release: SEP/2016

EX_EN_US

Copyright © 2016 Stryker
NV00018973.AB

Target® Detachable Coil

See package insert for complete indications, contraindications, warnings and instructions for use.

INTENDED USE / INDICATIONS FOR USE

Target Detachable Coils are intended to endovascularly obstruct or occlude blood flow in vascular abnormalities of the neurovascular and peripheral vessels.

Target Detachable Coils are indicated for endovascular embolization of:

- Intracranial aneurysms
- Other neurovascular abnormalities such as arteriovenous malformations and arteriovenous fistulae
- Arterial and venous embolizations in the peripheral vasculature

CONTRAINDICATIONS

None known.

POTENTIAL ADVERSE EVENTS

Potential complications include, but are not limited to: allergic reaction, aneurysm perforation and rupture, arrhythmia, death, edema, embolus, headache, hemorrhage, infection, ischemia, neurological/intracranial sequelae, post-embolization syndrome (fever, increased white blood cell count, discomfort), TIA/stroke, vasospasm, vessel occlusion or closure, vessel perforation, dissection, trauma or damage, vessel rupture, vessel thrombosis. Other procedural complications including but not limited to: anesthetic and contrast media risks, hypotension, hypertension, access site complications.

WARNINGS

- Contents supplied STERILE using an ethylene oxide (EO) process. Do not use if sterile barrier is damaged. If damage is found, call your Stryker Neurovascular representative.
- For single use only. Do not reuse, reprocess or resterilize. Reuse, reprocessing or resterilization may compromise the structural integrity of the device and/or lead to device failure which, in turn, may result in patient injury, illness or death. Reuse, reprocessing or resterilization may also create a risk of contamination of the device and/or cause patient infection or cross-infection, including, but not limited to, the transmission of infectious disease(s) from one patient to another. Contamination of the device may lead to injury, illness or death of the patient.
- After use, dispose of product and packaging in accordance with hospital, administrative and/or local government policy.
- **This device should only be used by physicians who have received appropriate training in interventional neuroradiology or interventional radiology and preclinical training on the use of this device as established by Stryker Neurovascular.**
- Patients with hypersensitivity to 316LVM stainless steel may suffer an allergic reaction to this implant.
- MR temperature testing was not conducted in peripheral vasculature, arteriovenous malformations or fistulae models.
- The safety and performance characteristics of the Target Detachable Coil System (Target Detachable Coils, InZone Detachment Systems, delivery systems and accessories) have not been demonstrated with other manufacturer's devices (whether coils, coil delivery devices, coil detachment systems, catheters, guidewires, and/or other accessories). Due to the potential incompatibility of non Stryker Neurovascular devices with the Target Detachable Coil System, the use of other manufacturer's device(s) with the Target Detachable Coil System is not recommended.
- To reduce risk of coil migration, the diameter of the first and second coil should never be less than the width of the ostium.
- In order to achieve optimal performance of the Target Detachable Coil System and to reduce the risk of thromboembolic complications, it is critical that a continuous infusion of appropriate flush solution be maintained between a) the femoral sheath and guiding catheter, b) the 2-tip microcatheter and guiding catheters, and c) the 2-tip microcatheter and Stryker Neurovascular guidewire and delivery wire. Continuous flush also reduces the potential for thrombus formation on, and crystallization of infusate around, the detachment zone of the Target Detachable Coil.
- Do not use the product after the "Use By" date specified on the package.
- Reuse of the flush port/dispenser coil or use with any coil other than the original coil may result in contamination of, or damage to, the coil.
- Utilization of damaged coils may affect coil delivery to, and stability inside, the vessel or aneurysm, possibly resulting in coil migration and/or stretching.
- The fluoro-saver marker is designed for use with a Rotating Hemostatic Valve (RHV). If used without an RHV, the distal end of the coil may be beyond the alignment marker when the fluoro-saver marker reaches the microcatheter hub.
- If the fluoro-saver marker is not visible, do not advance the coil without fluoroscopy.
- Do not rotate delivery wire during or after delivery of the coil. Rotating the Target Detachable Coil delivery wire may result in a stretched coil or premature detachment of the coil from the delivery wire, which could result in coil migration.
- Verify there is no coil loop protrusion into the parent vessel after coil placement and prior to coil detachment. Coil loop protrusion after coil placement may result in thromboembolic events if the coil is detached.
- Verify there is no movement of the coil after coil placement and prior to coil detachment. Movement of the coil after coil placement may indicate that the coil could migrate once it is detached.
- Failure to properly close the RHV compression fitting over the delivery wire before attaching the InZone® Detachment System could result in coil movement, aneurysm rupture or vessel perforation.
- Verify repeatedly that the distal shaft of the catheter is not under stress before detaching the Target Detachable Coil. Axial compression or tension forces could be stored in the 2-tip microcatheter causing the tip to move during coil delivery. Microcatheter tip movement could cause the aneurysm or vessel to rupture.
- Advancing the delivery wire beyond the microcatheter tip once the coil has been detached involves risk of aneurysm or vessel perforation.
- The long term effect of this product on extravascular tissues has not been established so care should be taken to retain this device in the intravascular space.

Damaged delivery wires may cause detachment failures, vessel injury or unpredictable distal tip response during coil deployment. If a delivery wire is damaged at any point during the procedure, do not attempt to straighten or otherwise repair it. Do not proceed with deployment or detachment. Remove the entire coil and replace with undamaged product.

- After use, dispose of product and packaging in accordance with hospital, administrative and/or local government policy.

CAUTIONS / PRECAUTIONS

- Federal Law (USA) restricts this device to sale by or on the order of a physician.
- Besides the number of InZone Detachment System units needed to complete the case, there must be an extra InZone Detachment System unit as back up.
- Removing the delivery wire without grasping the introducer sheath and delivery wire together may result in the detachable coil sliding out of the introducer sheath.
- Failure to remove the introducer sheath after inserting the delivery wire into the RHV of the microcatheter will interrupt normal infusion of flush solution and allow back flow of blood into the microcatheter.
- Some low level overhead light near or adjacent to the patient is required to visualize the fluoro-saver marker; monitor light alone will not allow sufficient visualization of the fluoro-saver marker.
- Advance and retract the Target Detachable Coil carefully and smoothly without excessive force. If unusual friction is noticed, slowly withdraw the Target Detachable Coil and examine for damage. If damage is present, remove and use a new Target Detachable Coil. If friction or resistance is still noted, carefully remove the Target Detachable Coil and microcatheter and examine the microcatheter for damage.
- If it is necessary to reposition the Target Detachable Coil, verify under fluoroscopy that the coil moves with a one-to-one motion. If the coil does not move with a one-to-one motion or movement is difficult, the coil may have stretched and could possibly migrate or break. Gently remove both the coil and microcatheter and replace with new devices.
- Increased detachment times may occur when:
  - Other embolic agents are present.
  - Delivery wire and microcatheter markers are not properly aligned.
  - Thrombus is present on the coil detachment zone.
- Do not use detachment systems other than the InZone Detachment System.
- Increased detachment times may occur when delivery wire and microcatheter markers are not properly aligned.
- Do not use detachment systems other than the InZone Detachment System.

Stryker Neurovascular
47900 Bayside Parkway
Fremont, CA 94538

strykerneurovascular.com

Date of Release: MAR/2016

EX_EN_US

Copyright © 2016 Stryker
NV00018669.AB

AJNR

AMERICAN JOURNAL OF NEURORADIOLOGY

OCTOBER 2017
VOLUME 38
NUMBER 10
WWW.AJNR.ORG

Publication Preview at www.ajnr.org features articles released in advance of print. Visit www.ajnrblog.org to comment on AJNR content and chat with colleagues and AJNR's News Digest at http://ajnrdigest.org to read the stories behind the latest research in neuroimaging.

1849 **PERSPECTIVES** *M.I. Vargas*

REVIEW ARTICLES

1850 **Neuroimaging Changes in Menkes Disease, Part 1** *R. Manara, et al.* PEDIATRICS

1858 **Neuroimaging Changes in Menkes Disease, Part 2** *R. Manara, et al.* PEDIATRICS

SOCIAL MEDIA

1866 **Maximizing the Tweet Engagement Rate in Academia: Analysis of the AJNR Twitter Feed** *V. Wadhwa, et al.*

RESEARCH PERSPECTIVES

1869 **Spinal and Paraspinal Plexiform Neurofibromas in Patients with Neurofibromatosis Type 1: A Novel Scoring System for Radiological-Clinical Correlation** *M. Mauda-Havakuk, et al.* SPINE

GENERAL CONTENTS

1876 **3D Pseudocontinuous Arterial Spin-Labeling MR Imaging in the Preoperative Evaluation of Gliomas** *Q. Zeng, et al.* ADULT BRAIN

1884 **Diagnostic Accuracy of Neuroimaging to Delineate Diffuse Gliomas within the Brain: A Meta-Analysis** *N. Verburg, et al.* ADULT BRAIN

1892 **Imaging Biomarkers for Adult Medulloblastomas: Genetic Entities May Be Identified by Their MR Imaging Radiophenotype** *V.C. Keil, et al.* ADULT BRAIN

1899 **Multinodular and Vacuolating Neuronal Tumor of the Cerebrum: A New "Leave Me Alone" Lesion with a Characteristic Imaging Pattern** *R.H. Nunes, et al.* ADULT BRAIN

1905 **Age, Sex, and Racial Differences in Neuroimaging Use in Acute Stroke: A Population-Based Study** *A. Vagal, et al.* ADULT BRAIN

1911 **Improved Detection of Anterior Circulation Occlusions: The "Delayed Vessel Sign" on Multiphase CT Angiography** *D. Byrne, et al.* ADULT BRAIN

1917 **Concordance of Time-of-Flight MRA and Digital Subtraction Angiography in Adult Primary Central Nervous System Vasculitis** *H. de Boysson, et al.* ADULT BRAIN

1923 **In Vivo Imaging of Venous Side Cerebral Small-Vessel Disease in Older Adults: An MRI Method at 7T** *C.E. Shaaban, et al.* ADULT BRAIN

AJNR (Am J Neuroradiol ISSN 0195–6108) is a journal published monthly, owned and published by the American Society of Neuroradiology (ASNR), 800 Enterprise Drive, Suite 205, Oak Brook, IL 60523. Annual dues for the ASNR include $170.00 for journal subscription. The journal is printed by Cadmus Journal Services, 5457 Twin Knolls Road, Suite 200, Columbia, MD 21045; Periodicals postage paid at Oak Brook, IL and additional mailing offices. Printed in the U.S.A. POSTMASTER: Please send address changes to American Journal of Neuroradiology, P.O. Box 3000, Denville, NJ 07834, U.S.A. Subscription rates: nonmember $390 ($460 foreign) print and online, $310 online only; institutions $450 ($520 foreign) print and basic online, $895 ($960 foreign) print and extended online, $370 online only (basic), extended online $805; single copies are $35 each ($40 foreign). Indexed by PubMed/Medline, BIOSIS Previews, Current Contents (Clinical Medicine and Life Sciences), EMBASE, Google Scholar, HighWire Press, Q-Sensei, RefSeek, Science Citation Index, and SCI Expanded. Copyright © American Society of Neuroradiology.

1929 **Basal Ganglia T1 Hyperintensity in Hereditary Hemorrhagic Telangiectasia** *A. Parvinian, et al.* — ADULT BRAIN

1934 **Analysis of White Matter Damage in Patients with Multiple Sclerosis via a Novel In Vivo MR Method for Measuring Myelin, Axons, and G-Ratio** *A. Hagiwara, et al.* — ADULT BRAIN

1941 **Pre- and Postcontrast 3D Double Inversion Recovery Sequence in Multiple Sclerosis: A Simple and Effective MR Imaging Protocol** *P. Eichinger, et al.* — ADULT BRAIN

1946 **Dual-Energy CT in Enhancing Subdural Effusions that Masquerade as Subdural Hematomas: Diagnosis with Virtual High-Monochromatic (190-keV) Images** *U.K. Bodanapally, et al.* — ADULT BRAIN

1953 **Assessment of Iron Deposition in the Brain in Frontotemporal Dementia and Its Correlation with Behavioral Traits** *R. Sheelakumari, et al.* — ADULT BRAIN

1959 **Multicenter Experience with FRED Jr Flow Re-Direction Endoluminal Device for Intracranial Aneurysms in Small Arteries** *M.A. Möhlenbruch, et al.* — INTERVENTIONAL

1966 **Clinical Impact of Flat Panel Volume CT Angiography in Evaluating the Accurate Intraoperative Deployment of Flow-Diverter Stents** *F. Clarençon, et al.* — INTERVENTIONAL

1973 **Packing Density Necessary to Reach a High Complete Occlusion Rate in Circumferential Unruptured Intracranial Aneurysms Treated with Stent-Assisted Coil Embolization** *R.T. Tosello, et al.* — INTERVENTIONAL

1978 **The Use and Utility of Aspiration Thrombectomy in Acute Ischemic Stroke: A Systematic Review and Meta-Analysis** *D. Wei, et al.* — INTERVENTIONAL

1984 **Endovascular Treatment of Dural Arteriovenous Fistulas of the Transverse and Sigmoid Sinuses Using Transarterial Balloon-Assisted Embolization Combined with Transvenous Balloon Protection of the Venous Sinus** *E. Piechowiak, et al.* — INTERVENTIONAL

1990 **Anatomic Location of Tumor Predicts the Accuracy of Motor Function Localization in Diffuse Lower-Grade Gliomas Involving the Hand Knob Area** *S. Fang, et al.* — FUNCTIONAL

1998 **Flat Panel Angiography in the Cross-Sectional Imaging of the Temporal Bone: Assessment of Image Quality and Radiation Dose Compared with a 64-Section Multisection CT Scanner** *G. Conte, et al.* — HEAD & NECK

2003 **Measurement for Detection of Incomplete Partition Type II Anomalies on MR Imaging** *K.L. Reinshagen, et al.* — HEAD & NECK, PEDIATRICS

2008 **Localizing the L5 Vertebra Using Nerve Morphology on MRI: An Accurate and Reliable Technique** *M.E. Peckham, et al.* — SPINE

2015 **Test-Retest and Interreader Reproducibility of Semiautomated Atlas-Based Analysis of Diffusion Tensor Imaging Data in Acute Cervical Spine Trauma in Adult Patients** *D.J. Peterson, et al.* — SPINE

2021 **Yield of Image-Guided Needle Biopsy for Infectious Discitis: A Systematic Review and Meta-Analysis** *A.L. McNamara, et al.* — SPINE

2028 **[^{18}F]-Sodium Fluoride PET MR–Based Localization and Quantification of Bone Turnover as a Biomarker for Facet Joint–Induced Disability** *N.W. Jenkins, et al.* — SPINE

ONLINE FEATURES

WHITE PAPER

E65 **American Society of Functional Neuroradiology–Recommended fMRI Paradigm Algorithms for Presurgical Language Assessment** *D.F. Black, et al.* — FUNCTIONAL

MEMORIAL

E74 **Torgny Greitz, MD, PhD, FACR, Professor of Neuroradiology, Emeritus** *T. Hindmarsh, et al.*

LETTERS

E77 **Spinal Cord, Spinal Root, and Brain MRI Abnormalities in Congenital Zika Syndrome** *B. Joob, et al.*

E78 **High-Resolution Hybrid Imaging Could Improve Cordotomy Lesions and Outcomes** *M.I. Vargas, et al.*

E79 **The Concept of "Number Needed to Image"** *S. Haller*

E81 **Coregistration and Fusion: An Easy and Reliable Method for Identifying Cranial Nerve IV on MRI** *A. Lecler, et al.*

E83 ***Reply*** *P. Bunch, et al.*

E84 **Minor Stroke and Thrombolysis: What Is in the Pipeline?** *S. Gallerini, et al.*

E86 ***Reply*** *M. Messer, et al.*

E87 ERRATUM

BOOK REVIEWS *R.M. Quencer, Section Editor*
Please visit www.ajnrblog.org to read and comment on Book Reviews.

A2/A3 aneurysm before (left) and after (center) deployment of FRED Jr endoluminal device. Six-month follow-up (right) shows complete occlusion of the aneurysm.

Indicates Editor's Choices selection
Indicates Fellows' Journal Club selection
Indicates open access to non-subscribers at www.ajnr.org
Indicates article with supplemental on-line table
Indicates article with supplemental on-line photo
Indicates article with supplemental on-line video
Evidence-Based Medicine Level 1
Evidence-Based Medicine Level 2

Title: Spring in Geneva. This picture was taken at the botanical garden of Geneva.

Maria Isabel Vargas, MD, Geneva University Hospitals, Division of Neuroradiology, Geneva, Switzerland

Neuroimaging Changes in Menkes Disease, Part 1

R. Manara, L. D'Agata, M.C. Rocco, R. Cusmai, E. Freri, L. Pinelli, F. Darra, E. Procopio, R. Mardari, C. Zanus, G. Di Rosa, C. Soddu, M. Severino, M. Ermani, D. Longo, S. Sartori, and the Menkes Working Group in the Italian Neuroimaging Network for Rare Diseases

ABSTRACT

SUMMARY: Menkes disease is a rare multisystem X-linked disorder of copper metabolism. Despite an early, severe, and progressive neurologic involvement, our knowledge of brain involvement remains unsatisfactory. The first part of this retrospective and review MR imaging study aims to define the frequency rate, timing, imaging features, and evolution of intracranial vascular and white matter changes. According to our analysis, striking but also poorly evolutive vascular abnormalities characterize the very early phases of disease. After the first months, myelination delay becomes evident, often in association with protean focal white matter lesions, some of which reveal an age-specific brain vulnerability. In later phases of the disease, concomitant progressive neurodegeneration might hinder the myelination progression. The currently enriched knowledge of neuroradiologic finding evolution provides valuable clues for early diagnosis, identifies possible MR imaging biomarkers of new treatment efficacy, and improves our comprehension of possible mechanisms of brain injury in Menkes disease.

ABBREVIATION: MD = Menkes disease

Menkes disease (MD) is a rare X-linked recessive disorder (Online Mendelian Inheritance in Man No. 309400; http://omim.org/)[1] due to mutations in the *ATP7A* gene (Xq13.2-q13.3), causing impaired absorption and cellular metabolism of copper. The overall incidence of MD in Europe is reported to be 1 in 300,000 births.[2] Although the disease shows great clinical heterogeneity, most affected children present with early growth failure, hypothermia, failure to thrive, cutis laxa, and sparse, kinky hair (pili torti).[3]

The central nervous system is primarily involved, with severe cognitive and sensorimotor impairment, poor quality of life, and reduction in life expectancy. The spectrum of neurologic manifestations is strikingly wide; drug-resistant epilepsy appears in the first trimester of life, followed by regression of developmental milestones and progression to death in early childhood. Despite the wide phenotypic spectrum, some of the clinical features seem to present a recurrent age-related course, suggesting a possible concomitant role of brain maturation and age-related vulnerability to copper dysmetabolism. For example, epilepsy typically shows a 3-stage course: 1) focal seizures progressing to status epilepticus (<3 months), 2) epileptic spasms (6–11 months), and 3) multifocal seizures, tonic spasms, and myoclonus (20–25 months).[4]

The scarce neuropathologic data refer to the late phases of MD and point to diffuse cerebral and cerebellar atrophy, neuronal loss, gliosis within cortical and deep gray matter, loss of Purkinje cells, and cerebral white matter spongy changes along with loss of myelin sheaths and axons. Intracranial arteries appear thin-walled and strikingly tortuous.[5,6]

In the past decades, MR imaging investigations have been routinely applied to in vivo intracranial changes in children with MD.

From the Neuroradiology (R. Manara, M.C.R.), Sezione di Neuroscienze, Medicine and Surgery Department, University of Salerno, Salerno, Italy; Department of Neuroscience (L.D.), University of Padova, Padova, Italy; Neurology Unit (R.C., D.L.), Department of Imaging, Bambino Gesù Children's Hospital IRCCS, Roma, Italy; Department of Pediatric Neuroscience (E.F.), Foundation I.R.C.C.S., Neurological Institute "C. Besta," Milano, Italy; Neuroradiology (L.P.), Section of Pediatric Neuroradiology, Department of Diagnostic Imaging ASST Spedali Civili, Brescia, Italy; Child Neuropsychiatry Unit (F.D.), Department of Life and Reproduction Sciences, University of Verona, Verona, Italy; Metabolic and Neuromuscular Unit (E.P.), Department of Neuroscience, Meyer Children Hospital, Firenze, Italy; Department of Neuroscience (R. Mardari, M.E.) and Pediatric Neurology and Neurophysiology Unit, Department of Woman and Child Health (S.S.), University Hospital of Padova, Padova, Italy; Institute for Maternal and Child Health (C.Z.), IRCCS "Burlo Garofolo," Trieste, Italy; Unit of Child Neurology and Psychiatry (G.D.R.), Department of Human Pathology of the Adult and Developmental Age, University Hospital of Messina, Messina, Italy; Ospedale Pediatrico Microcitemico "A. Cao" (C.S.), AOB Cagliari, Italy; and Neuroradiology Unit (M.S.), Istituto Giannina Gaslini, Genova, Italy.

Renzo Manara and Lauracarmen D'Agata contributed equally to the study and should be considered "first coauthors." Daniela Longo and Stefano Sartori should both be considered "senior coauthors."

Please address correspondence to Renzo Manara, MD, Neuroradiology, Sezione di Neuroscienze, Dept of Medicine and Surgery, University of Salerno, via S. Allende 1, Baronissi (SA), 84081 Italy; e-mail: rmanara@unisa.it

Indicates open access to non-subscribers at www.ajnr.org

Indicates article with supplemental on-line appendix and table.

Indicates article with supplemental on-line photos.

http://dx.doi.org/10.3174/ajnr.A5186

Table 1: Main data on intracranial vessel abnormalities in our MD sample and in 29 controls

	Children with MD	Controls
Sample size (No.)	26 Children	29 Children
Sex	25 M, 1 F	19 M, 10 F
Age at MRA (mean) (range) (mo)	14 ± 19 (2.2–86.7)[a]	11.5 ± 15 (0.2–82.3)
Tortuosity index (mean) (range)	0.41 ± 0.30 (0.07–1.08)[a]	0.07 ± 0.08 (0.01–0.31)[b]
Smoker score (mean) (range)	6.0 ± 1.3 (1–6)[c]	1.7 ± 0.7 (1–3)[b]

[a] Calculated at first MRA in 15 children with MD.
[b] $P < .0001$.
[c] Calculated at first MRI in 26 children with MD.

Nonetheless, due to the rarity of the disease, imaging findings are also scarce, and our knowledge is based on scattered case reports and small case series. Increased intracranial vessel tortuosity, protean white matter signal abnormalities, transient temporal lobe changes, cerebral and cerebellar atrophy, basal ganglia anomalies, and subdural collections have been variably reported and associated with the clinical phenotype, leading to several and sometimes conflicting pathogenic hypotheses. So far, the frequency rate, precise characterization, timing, evolution, and likely pathogenesis of these neuroradiologic abnormalities remain unsatisfactorily understood.

The present large retrospective and review MR imaging study aimed to improve our knowledge of the intracranial involvement in Menkes disease to provide possible neuroradiologic biomarkers useful for diagnosis and follow-up. In particular, this first Part will address the intracranial vascular and white matter changes that might be observed during the course of MD.

MATERIALS AND METHODS

MR imaging and MRA findings of children with MD were retrospectively evaluated. Children were enrolled if they had a biochemically or genetically confirmed MD diagnosis and at least 1 MR imaging. All images were evaluated by 2 neuroradiologists with >15 years of experience in pediatric neuroradiology (R. Manara and D.L.), who were aware of the diagnosis but blinded to the clinical findings; discordant findings were discussed until consensus was reached.

The study included 40 MRIs (25 MRAs, all with the time-of-flight technique) of 26 children with MD (mean age at first MR image, 7.5 ± 5.9 months; range, 0.3–32.2 months; 1 female). Most studies were performed on 1.5T scanners (37/40) and included at least T2/FLAIR and T1-weighted images; DWI was available in 25/40 MRIs.

Intracranial Blood Vessel Evaluation

The qualitative evaluation of increased artery tortuosity was obtained from MRA or parenchymal T2-weighted images whenever angiography studies were not available. A semiquantitative evaluation of basilar artery dolichoectasia (Smoker score, see the On-line Appendix) was performed on axial T2 imaging. A quantitative evaluation of the basilar artery tortuosity was performed with commercially available software (syngo MultiModality Workplace; Siemens, Erlangen, Germany; see the On-line Appendix) in children with MD, who had time-of-flight 3D-MRA in a DICOM format (15 children; mean age, 14 ± 19 months; range, 2.2–86.7 months). Briefly, after recognizing the proximal and the distal end of the basilar artery, the software allowed the measurement in millimeters of the effective length of the whole vessel (curved length) and the linear distance between the 2 extremes. A tortuosity index was subsequently calculated according to the formula: (Curved Length/Linear Length) − 1. The index is supposed to be zero if the 2 lengths are equal.

Basilar artery semiquantitative and quantitative evaluations were compared with those of 29 children without MD (Table 1) who underwent brain MR imaging and MRA for other indications.

The presence of stenosis or ectasia of the intracranial arteries was also evaluated on MRA studies, while the presence of venous sinus ectasia was assessed on parenchymal imaging.

White Matter Change Evaluation

Qualitative parenchymal evaluation was performed on all MRIs. Tumefactive lesions, centrum semiovale DWI hyperintense lesions, focal nontumefactive white matter lesions, and abnormal myelination, identified in previous publications, were recorded.

Literature Review

An extensive search was performed in all major data bases (Embase, Scopus, PubMed, Cochrane, and also www.google.com) with the following terms: "Menkes" and "brain MR imaging." We included all articles reporting MR neuroimaging findings and age at MR imaging examination. From case descriptions or direct inspection of the published images, we investigated the presence/absence of abnormal findings on MR imaging/MRA. The lack of description combined with the impossibility of defining their presence/absence with the available published images was recorded as "not mentioned." We also recorded any available information about the size, distribution, signal pattern, evolution, and proposed pathogenic hypothesis of white matter abnormalities described in children with MD.

Our literature review included 47 articles published between 1989 and August 2016 that are listed in the On-line Appendix.

Statistical Analysis

The variables with normal distribution were analyzed by using the Student t test, while for ordinal variables, the Mann-Whitney U test was used. Categoric variables were analyzed by using the χ^2 of the Pearson or the Fisher Exact test when required. The significance level was $P < .05$.

RESULTS

Table 2 summarizes the main features of our sample and of the literature data regarding children with MD who underwent brain MR imaging.

In our sample, 15 children with MD were alive at the time of the study; for the remaining 11 children, death occurred at 6.3 ± 4.6 years of age (range, 9 months to 17.5 years). All children showed severe early-onset neurodevelopmental impairment; most patients presented with epilepsy during the early phases of MD.

The On-line Table and Fig 1 summarize the main neuroradiologic findings of children with MD included in the study and in our literature review.

Intracranial Vessel Abnormalities

Literature Review. At the first MR imaging, increased artery tortuosity was present in 45/62 children with MD (73%), absent in 2, and not mentioned in 15. At follow-up, increased artery tortuosity was described in 14/23 (61%; in 4, the finding was not mentioned at the first examination), while in 9, it was not mentioned; no case of tortuosity evolution was reported.

Our Sample. Increased artery tortuosity was detected in all children at any age. The finding was evident both on T2 parenchymal imaging and MRA (On-line Fig 1). Both semiquantitative and quantitative basilar artery evaluation showed significantly increased tortuosity compared with age-matched controls ($P < .0001$; Table 1 and Fig 2) and no correlation with age. Children with MD with neuroradiologic follow-up showed no significant evolution of the basilar artery changes (Table 3).

Stenosis and ectasia of the intracranial arteries, though repeatedly mentioned in the literature as possible pathogenic mechanisms of parenchymal lesions,[7,8] were never detected in any of the present children with MD or in those reported in the literature.

Widening of the venous sinuses, recently reported in 1 child with MD,[7] was detected in 1/26 children in the present sample (On-line Fig 2*A*).

Table 2: Demographics and main clinical data of our children with MD and of children with MD in the literature who underwent brain MRI

Demographics	Present Sample	Literature Review (On-line Appendix)
Sample size	26 Children	62 Children
Sex	25 M; 1 F	57 M; 5 F
Age at clinical onset (mean) (range) (mo)	3.7 ± 2.5 (1–8)[a]	4.5 ± 3.3 (0.1–14)[b]
Age at first MRI (mean) (range) (mo)	7.5 ± 5.9 (0.3–32.2)	7.1 ± 5.6 (0.6–34.0)
Follow-up MRI	8/26 Children	23/62 Children
Age at last follow-up (mean) (range) (mo)	25.3 ± 19.4 (3.6–86.7)	10.2 ± 6.28 (1.5–30)
Follow-up duration (mean) (range) (mo)	22.8 ± 23.1 (1.4–78.5)	6.1 ± 5.9 (0.3–26)
Epilepsy	23/26	37/62
Age at epilepsy onset (mean) (range) (mo)	6.5 ± 3.4 (2.2–15.0)	4.6 ± 3.3 (0.1–14)[c]

[a] Calculated from 25/26 MD children.
[b] Calculated from 31/62 MD children.
[c] Calculated 19/37 MD children with epilepsy.

White Matter Changes: Tumefactive Lesions

Literature Review. At first MR imaging, white matter tumefactive lesions were detected in 21/62 children with MD (33%; mean age, 4.8 ± 1.9 months; range, 1.2–10 months); in 3/62 (5%), the lesions were absent (mean age, 4.5 months; range, 3.5–6 months), whereas in the remaining 38/62, this finding was not mentioned. In 5/21 cases, tumefactive lesions were not restricted to the temporal regions. At follow-up MR im-

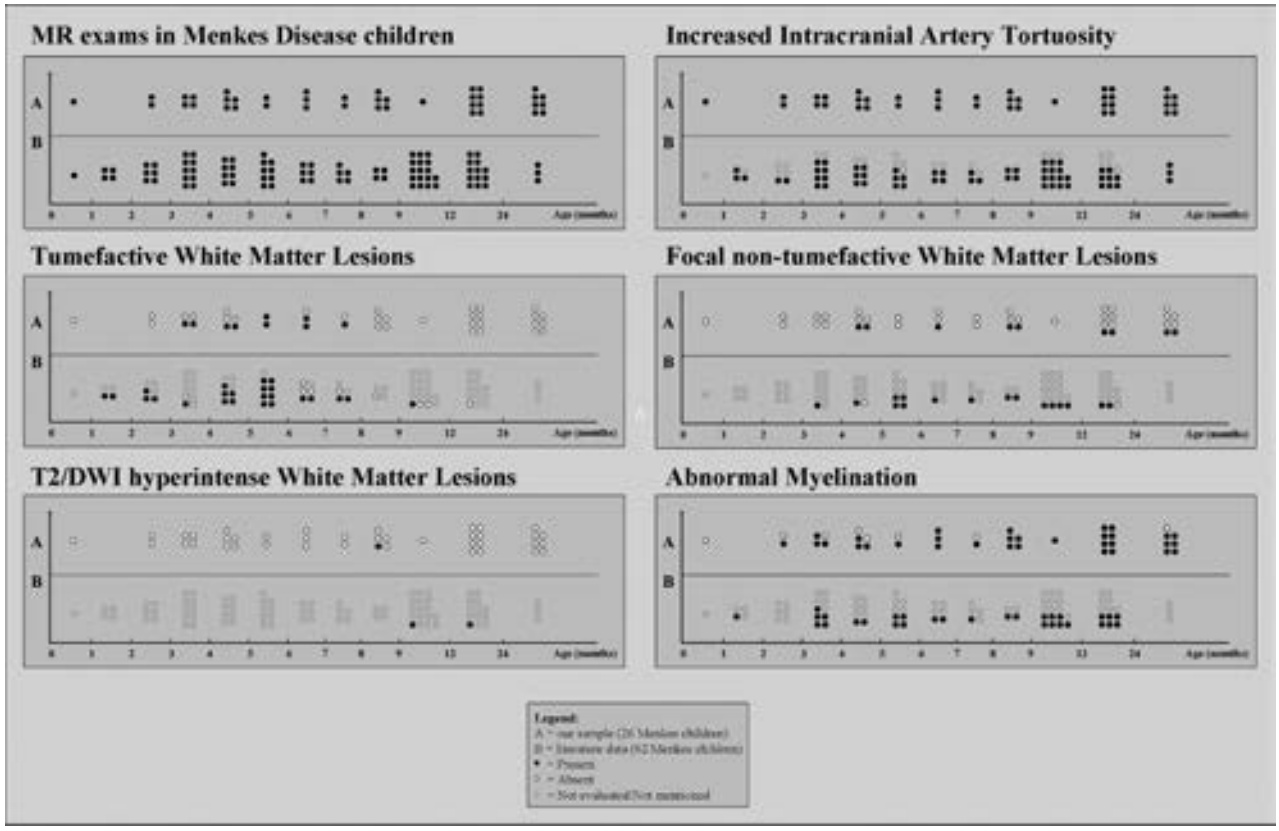

FIG 1. MR imaging findings in Menkes disease according to age at examination: *A*, Our sample (26 children, 40 examinations). *B*, Literature review (62 children, 86 examinations).

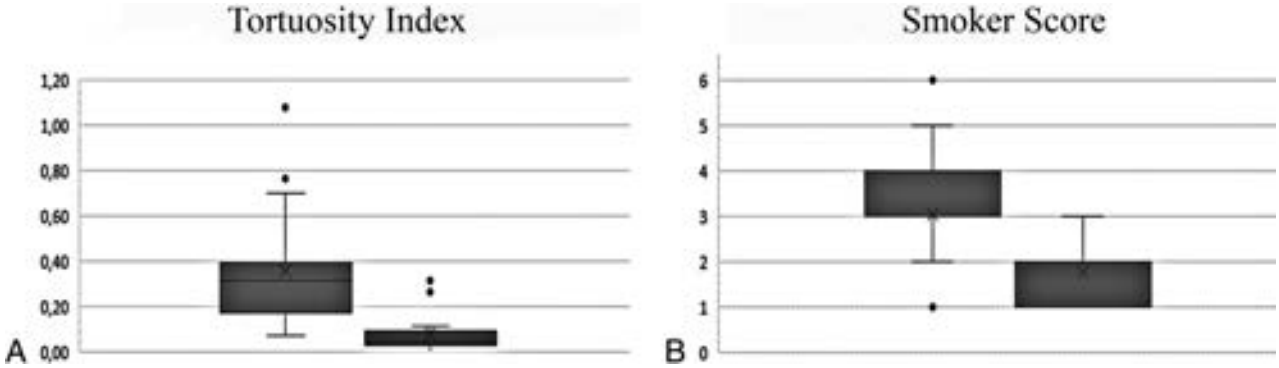

FIG 2. Tortuosity index (*A*) and Smoker score values (*B*) in children with MD (*box on the left*) and age-matched controls (*box on the right*). The difference was highly significant ($P < .0001$).

Table 3: Tortuosity index and Smoker score evolution among our MD children with MR follow-up

	First MR Exam	Last MR Exam
Tortuosity index	0.29 ± 0.11 (0.14–0.39)	0.26 ± 0.10 (0.14–0.32)[a]
Smoker score	3 ± 1.3 (1–6)	3.3 ± 0.7 (2–4)[b]

[a] Obtained from 3 MD children with MRA follow-up (follow-up duration: 46.3 ± 30.3 months).
[b] Obtained from 7 MD children with MRI follow-up (follow-up duration: 25.5 ± 25.3 months).

aging, tumefactive lesions were detected in 3/23 children (13%; mean age, 2.7 months; range, 1.5–4 months; in one child, the lesions were absent at first examination), were absent in 7/23 (30%) (mean age, 8.6 ± 2.9 months; range, 6–15 months; all had tumefactive lesions at first MR imaging), and were not mentioned in the remaining 13/23.

Our Sample. Tumefactive lesions were detected at first MR imaging in 7/26 (27%; mean age, 5.8 ± 1.3 months; range, 4.6–7.7 months; On-line Fig 3) and in 2 additional children with MD at follow-up MR imaging (both at 3.6 months of age). Among children with MD examined in the time window of 3–8 months, the detection rate was 9/16 (56%). In addition, among the 9 children with MD with tumefactive lesions, 2 had follow-up MR imaging and both showed full regression of the lesions. The presence of recurrent seizures or status epilepticus in the month preceding MR imaging was not associated with the detection of tumefactive lesions (6/9 versus 18/31 MRIs, nonsignificant, Fisher exact test). Temporal involvement was detected in all children with MD with tumefactive lesions (unilaterally in 1/9) and spread toward other lobes in 6/9 children (patients 5, 7, 9, 10, 16, and 26); the extratemporal involvement was more frequent than that reported in the literature in children with MD (67% versus 23%, $P = .04$, Fisher exact test). Tumefactive lesions were distinctly asymmetric in 3/9.

All tumefactive lesions had strikingly T2-hyperintense subcortical white matter that appeared iso-hypointense on DWI with increased apparent diffusion coefficient values; the cortical ribbon did not appear involved despite sulcal effacement.

WM Changes: Centrum Semiovale DWI Hyperintense Lesions

Literature Review. Bilateral drop-shaped centrum semiovale lesions have been reported in 1/62 children with MD (1.6%) at 10 months of age; the lesions, hyperintense in DWI with restriction of water molecule movement, showed a size increase at 13-month follow-up.

Our Sample. Bilateral centrum semiovale lesions with identical signal features were detected in an 8-month-old child (3.9%, patient 6, On-line Fig 2*B*).

WM Changes: Focal Nontumefactive White Matter Lesions

Literature Review. Focal white matter lesions other than the tumefactive and DWI-hyperintense ones described above were detected at first MR imaging in 14/62 children with MD (23%; mean age, 7.2 ± 3.6 months; range 3–17 months) and were not mentioned in the remaining 48/62 children. At follow-up MR imaging, white matter focal lesions were present in 3/23 children with MD (13% not mentioned in previous examinations), absent in 2/23 (absent and not mentioned in previous examinations in 1 case each), and not mentioned in 18/23 (notably, 3 of them had lesions at first MR imaging, while in 15, the finding had not been mentioned).

Our Sample. Focal white matter lesions were detected in 9/26 children with MD (35%; mean age, 14.1 ± 11.0 months; range 4.6–32.7 months). Among the 8 patients with MR follow-up, 5 still had no lesions, 1 showed lesion regression, and 2 presented with new lesions.

Abnormal Myelination

Literature Review. Abnormal myelination was reported at first MR imaging in 20/62 children with MD (32%; mean age, 6.6 ± 3.9 months) and was not mentioned in the remaining 42/62 children. At follow-up, this finding was detected in 9/23 (39%) (in 4/9, it was not mentioned at previous MR imaging) and was not described in the remaining cases.

Our Sample. Abnormal myelination was found in 19/26 (73%; mean age, 8.7 ± 6.5 months; On-line Fig 4). Normal myelination was more frequently detected among earlier MRIs (especially younger than 6 months of age). In 1 child, the abnormal myelination appeared at follow-up at 15.6 months of age (the first MR imaging performed at 4.8 months showed normal myelination for age). Cases with longer follow-up MR imaging showed a progres-

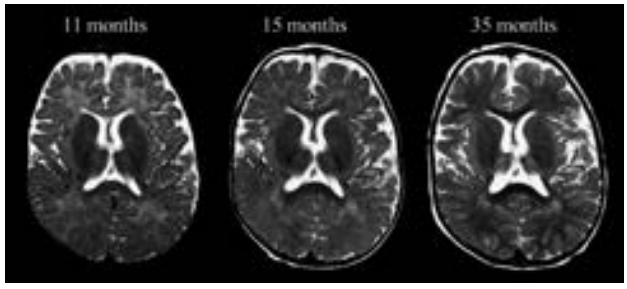

FIG 3. Axial T2-weighted images at the level of the genu/splenium of the corpus callosum in a boy (patient 8) affected by Menkes disease, showing the progressive-though-delayed supratentorial myelination.

sion of the myelination during the disease course (Fig 3). In the girl with MD, the myelination became normal at the last MR imaging (86.7 months of age).

Further Statistical Analyses

Possible associations among clinical data and parenchymal or vascular abnormalities were investigated, revealing a weak association between increased basilar artery tortuosity and white matter lesions, different from tumefactive lesions (0.56 ± 0.35 versus 0.24 ± 0.12, $P = .02$), and a trend toward an association between earlier epilepsy onset and tumefactive lesions (4.9 ± 2.5 versus 7.6 ± 3.7, $P = .07$) and between later clinical onset and white matter lesions, different from tumefactive lesions (4.9 ± 2.3 versus 3.2 ± 2.5 months, $P = .09$). No further significant associations were found among clinical and neuroradiologic findings (eg, tumefactive lesions versus status epilepticus or refractory seizures in the month preceding MR imaging examination, tumefactive lesions versus basal ganglia abnormalities, increased vascular tortuosity severity versus inguinal hernia, a marker of connective tissue laxity, or basal ganglia lesions; $P > .1$ in all cases).

DISCUSSION

The present retrospective cross-sectional multicenter study analyzed the neuroradiologic MR imaging abnormalities in children affected by Menkes disease, providing a detailed description of intracranial vascular and parenchymal changes in this rare disease. In this Part, we will address the most remarkable intracranial vessel and white matter MR imaging findings in our sample (26 children with MD) and the available literature (62 children with MD).

Intracranial Vascular Changes

Increased artery tortuosity is considered a typical diagnostic feature of Menkes disease, being reported in nearly 75% of cases and absent in <4% of cases. Nonetheless, it is still unclear whether this feature is progressive, eventually leading to blood supply abnormalities; stable since birth; or detectable even at a fetal stage, thus representing a useful prenatal diagnostic disease marker. Indeed, in the MD literature, abnormal intracranial artery tortuosity has sometimes been described only on follow-up examinations, thus suggesting a possible progression of artery changes. However, these case reports lacked a careful description of the anatomic conformation of the intracranial arteries at disease onset, leaving some uncertainty as to whether the tortuosity had truly appeared at follow-up or had been overlooked at disease onset. In our sample, an increased tortuosity was a constant age-independent MD marker, thus confirming its important diagnostic role in the very first months of life. The youngest child with MD (patient 26), scanned in the neonatal period (20 days of life) for cutis laxa before neurologic onset, already showed the typical vessel changes. On the contrary, the lack of intracranial increased arterial tortuosity seems to make MD rather unlikely and should prompt reconsidering other diagnoses.

An increased tortuosity of the intracranial arteries was confirmed in our sample by both semiquantitative and quantitative basilar artery evaluations, which showed significant changes compared with age-matched subjects. Considering that the control group included children undergoing MR imaging/MRA for the suspicion of intracranial vascular problems, the difference is even more meaningful and confirms the major role of intracranial artery evaluation in the diagnostic work-up of MD. Regarding the evolution of the intracranial artery changes, the lack of association between age and both the tortuosity index and Smoker score at the cross-sectional evaluation and the lack of significant changes in children with MD undergoing MR imaging follow-up provide some evidence of early, most likely late-fetal or early-postnatal, vessel wall damage that remains relatively stable during the subsequent disease course. Intracranial artery elongation has been related to decreased activity of the copper-dependent lysyl oxidase, which is involved in elastin and collagen cross-linking, resulting in structural impairment of the blood vessel wall.[9-15] Because during the whole intrauterine life, the circulating copper is provided by the mother, early vascular wall impairment points to a key role of *ATP7A* for lysyl oxidase function within the cell.[16]

The absence of intracranial artery ectasia and stenosis, either at onset or at follow-up, is another important result. Previous studies have reported possible ectasia or distal narrowing of intracranial arteries.[7,8] Even though no imaging study directly has yet shown significant vessel lumen abnormalities, artery narrowing has been repeatedly advocated as a likely cause of ischemia and encephalomalacia. Actually, according to our experience (Online Fig 1*C*), the apparent distal artery caliper change was the result of artifacts related to the acquisition sequence used for investigating intracranial arteries. In fact, the commonly used MRA sequence (TOF) applies a saturation band just above the acquisition slab, aiming to cancel the cranial-caudal (venous) blood flow. The increased tortuosity of intracranial arteries can easily result in artery segments with downward-directed blood flow; the consequent artifactual signal loss might eventually lead to the false detection of stenosis and subsequent ectasia as the blood flow becomes again caudal-cranial. Indeed, the rare pathologic studies seem to confirm our neuroimaging findings, showing mild intima hypertrophy without significant abnormalities of vessel caliper and patency.[6]

Recently, dural sinus ectasia has been reported in a child with MD and has been suggested as a potentially interesting new disease marker.[8] Indeed, this feature has also been detected in 1 child of our sample. Nonetheless, its low detection rate (1/26, 4%) raises some doubts about the real impact of venous changes and the utility of a dedicated evaluation of the intracranial venous system in the suspicion of MD.

Parenchymal Abnormalities

White Matter Tumefactive Lesions. In previous publications,[17-19] tumefactive white matter lesions have been variably named "white matter cystic changes,"[19] "leukoencephalopathy,"[20] and "transient edema of the temporal lobes."[21] All these lesions shared the following MR imaging features: The affected white matter presented striking T2-hyperintensity and increased ADC values consistent with vasogenic edema, the cortical ribbon was relatively spared, and the lesions had mild/moderate mass effect. Because data were derived almost exclusively from case reports, the frequency rate of tumefactive lesions in MD has not yet been defined. The present literature analysis points to a frequency rate slightly above one-third of children with MD, similar to that observed in our sample (37% versus 34%, respectively), thus suggesting that tumefactive lesions are usually not overlooked in routine conventional MRIs.

Tumefactive lesions may be uni- or bilateral, symmetric or asymmetric; most lesions are localized in the temporal lobes, disclosing the high vulnerability of these regions, especially the anterior portion (temporal pole). Nonetheless, involvement of other cerebral lobes is not uncommon: An extratemporal involvement was reported in nearly one-quarter of the children with MD with tumefactive lesions in the literature. In our sample, the detection of extratemporal lesions rose to two-thirds, most probably not because of differences between the 2 study populations but because of the different, more systematic approach at imaging evaluation.

One of the most interesting results of the present study is the identification of a specific age window for the appearance of tumefactive lesions. According to the literature review, children with MD presented with tumefactive lesions solely within the age range of 1.2–10 months (3–8 months in our sample). The recognition of a specific age window for tumefactive lesions implies the existence of an age-dependent brain vulnerability in MD that does not include the very early postnatal period and does not persist beyond the tenth month of life. Besides, the lack of detection of tumefactive lesions in children with MD undergoing MR imaging after 10 months of age suggests an evolution of those lesions that were detected in >50% of MRIs during the age window of 3–8 months. Indeed, the literature review,[18,21] as well as 2 children with MD in our sample (patients 22 and 23), showed the reversibility of tumefactive lesions at follow-up MR imaging, raising some questions about their nature and pathogenesis.

In the past, some authors[4,17,20,22] hypothesized for tumefactive lesions an ischemic pathogenesis that is not consistent with the currently available neuroradiologic findings because of the following: 1) Tumefactive lesions involve almost exclusively the white matter, sparing the contiguous cortex, while the latter is usually more vulnerable to ischemia; 2) DWI does not reveal cytotoxic edema, which, instead, characterizes ischemia; 3) tumefactive lesions do not respect vascular territories; and 4) tumefactive lesions seem to be reversible, while ischemic lesions are mostly irreversible and typically result in focal encephalomalacia.

Other authors suggested the existence of a pathogenic relationship between tumefactive lesions and refractory seizures or status epilepticus.[17,18,20] A protracted epileptic activity might result in severe parenchymal edema, both vasogenic and cytotoxic.[17] Vasogenic edema primarily derives from the persistent and severe brain acidosis associated with status epilepticus, eventually leading to blood-brain barrier alteration, parenchymal swelling, and sulcal effacement, while cytotoxic edema is likely due to the excessive neuronal stimulation with alteration of cell membrane permeability and neuronal/glial swelling. Postcritical cytotoxic edema usually prevails in the cortex,[17] might spread to ipsilateral pulvinar and hippocampal formation, and has no or mild mass effect. Actually, tumefactive lesions did not show cytotoxic-like features in any children in the literature or our sample children with MD. In addition, in our relatively large sample, we were not able to replicate the hypothesized association between tumefactive lesions and the presence of status epilepticus or refractory seizures in the few days before MR imaging, even while restricting the analysis to within the temporal window in which tumefactive lesions have been detected (3–8 months). Taken together, these data do not support the hypothesis of a causal relationship between tumefactive lesions and excessive seizure activity. Most likely, tumefactive lesions and status epilepticus are simply independent epiphenomena of the same copper-related metabolic dysfunction.

DWI Hyperintense Centrum Semiovale Lesions. Although found in only 2 children with MD, considering both the literature and our sample, white matter cytotoxic-like lesions merit discussion due to their very peculiar MR imaging features. In both children with MD, these lesions had an oval or drop-like shape (On-line Fig 2*B*), were well recognizable on T2 images, but different from tumefactive lesions; they were located in the deep white matter and were strikingly DWI hyperintense with decreased ADC values. In the sole child with MD with follow-up MR imaging after 3 months, the lesions increased in size, maintaining a prevalent cytotoxic edema-like appearance. The pathogenesis of these lesions is still uncertain; the prolonged persistence of cytotoxic edema is not consistent with a brain infarct because the latter loses DWI hyperintensity within 1 month, evolving into focal encephalomalacia; in addition, the affected regions, both at onset and follow-up, did not correspond to a specific vascular territory. Most likely, centrum semiovale lesions are due to copper-dependent metabolic processes,[22] leading to compromised mitochondrial function and eventually to a metabolic, not ischemic, stroke.

The very low frequency of DWI hyperintense lesions of the centrum semiovale in children with MD suggests the coexistence of environmental or genetic pathogenic factors, but it also hinders their identification. One of the 2 children with centrum semiovale lesions, for example, had a rare deletion of the exon 21, while in the other child, the genetics were not specified.

Focal Nontumefactive White Matter Lesions. According to our literature review, focal nontumefactive white matter lesions are reported in about one-fourth of children with MD, while the analysis of our sample showed a frequency rate slightly above 40%. Once again, the difference rate is most likely due to a more systematic search in our sample rather than to a true lower rate of focal nontumefactive white matter lesions in the literature data. These white matter lesions appear as T2/FLAIR-hyperintense/DWI-isointense regions, do not show a precise or restricted temporal occurrence, and present no specific morphologic pattern

(all lobes were variably involved in our sample). From the literature review, it was not possible to gain useful information about lesion evolution because follow-up data were lacking. In our sample, focal nontumefactive white matter lesions had a heterogeneous and unpredictable course, with lesions progressing during the disease course in most cases but also with 1 child who showed lesion regression at follow-up. According to some authors, focal white matter lesions stem from the progressive and diffuse cortical neurodegeneration and represent a secondary white matter degeneration.[23] However, this hypothesis does not explain why the lesions are focal, while neurodegeneration is more often a global phenomenon and focal cortical lesions are absent or present with regional inconsistency. In addition, our study did not reveal any association between these lesions and the presence or the severity of brain atrophy. According to other authors, these lesions would result from ischemic phenomena caused by vascular anomalies.[1,4,7,8,19,22,24] The association between intracranial artery tortuosity and nontumefactive white matter lesions found in the present study seems to support a possible link between the processes leading to vascular wall abnormalities and white matter involvement. Nonetheless, because tortuosity changes do not seem to be associated with artery lumen changes, the ischemic hypothesis remains aleatory; moreover, focal white matter lesions do not cluster in specific vascular territories, and both the literature review and our sample analysis did not detect any lesion with DWI features of acute ischemia.

An alternative hypothesis suggested a relationship between white matter changes and the metabolic energetic failure due to copper-dependent enzymes.[17] Similar white matter abnormalities have been observed in mitochondriopathies caused by deficiency of the cytochrome C oxidase enzyme,[17] which is also impaired in MD and might result in brain cell death and demyelination. The present study was not powered for addressing this issue properly, but the extreme phenotypic variability of white matter lesions suggests that several pathogenic mechanisms are likely involved, leading to progressive white matter deterioration.

Abnormal Myelination. Abnormal myelination of the supratentorial white matter is a well-known finding in MD. It is present in about one-third of the literature MRIs and in more than two-thirds of our sample. Discrepancies in the detection rate most likely reside in the challenging discrimination between abnormal myelination both in early and in late phases of the disease course. In fact, brain myelination is physiologically incomplete in the first years of life, and its evaluation requires some expertise in pediatric neuroradiology. On the other hand, advanced phases of MD might present with superimposing neurodegenerative processes that imply diffuse gliosis/Wallerian degeneration with concomitant white matter signal abnormalities.

Notably, most children with MD have normal myelination at birth, suggesting that the lack of *ATP7A* function does not significantly influence myelin formation during fetal development, in contrast to what happens regarding vascular tortuosity that is abnormal even despite maternal-mediated copper absorption. Abnormal myelination is therefore diagnosed when the expected myelination milestones are not reached (eg, the anterior limb of the internal capsule at 6 months of age) and might become more evident with increasing age. Whether myelination abnormalities were due to a halt or a delay in the myelination process, it appears unequivocally disentangled by the longitudinal MR imaging evaluation that, in our sample, repeatedly showed myelination progression (Fig 3) or even myelin full maturation at 7 years of age, though the latter child with MD was the female subject (patient 13), likely with a milder form of MD.

CONCLUSIONS

Intracranial vascular and white matter findings appear strikingly heterogeneous in Menkes disease. According to our data and literature review, a significantly increased arterial tortuosity seems to represent an early and reliable diagnostic biomarker of Menkes disease. On the other hand, there is no evidence of significant vessel wall change evolution during the disease course, and the role of artery changes in the pathogenesis of brain injury appears to be very weak, if present at all. Regarding the white matter involvement, myelin abnormalities seem to result from different, sometimes concomitant pathogenic mechanisms. Besides a delayed-but-improving postnatal myelination process, neurodegenerative phenomena implying gliosis and Wallerian degeneration might variably influence myelin signal. In addition, several heterogeneous focal lesions might occur, some of which seem to reveal a temporally selective white matter vulnerability during the course of Menkes disease.

ACKNOWLEDGMENTS

We thank the association "Angeli per la vita" and the Società Italiana di Neurologia Pediatrica, which strongly supported this spontaneous large Italian study.

The Menkes Working Group in the Italian Neuroimaging Network for Rare Disease includes the following memebers: Irene Toldo, Cinzia Peruzzi, Roberta Vittorini, Alberto Spalice, Carlo Fusco, Margherita Nosadini, Laura Farina, Alessandro Stecco, Gabriele Polonara, Maria Alice Donati, Lucio Giordano, Carlo Dionisi-Vici, Diego Martinelli, Aba Tocchet, Giuseppe Fariello, Francesco Nicita, Daniele Frattini, Paola Martelli, and Gaetano Cantalupo.

The following are collaborators in this work: I. Toldo, Pediatric Neurology and Neurophysiology Unit, Department of Woman and Child Health, University Hospital of Padova, Padova, Italy; C. Peruzzi, Child Neuropsychiatry, Ospedale Maggiore, Novara, Italy; R. Vittorini, Child Neurology and Psychiatry, Department of Pediatrics and Pediatric Specialties, AOU Città della Salute e della Scienza, Torino, Italy; A. Spalice, Children Neurology Division, University La Sapienza Roma, Italy; C. Fusco, Child Neurology and Psychiatry Unit, Department of Pediatrics, ASMN-IRCCS, Reggio Emilia, Italy; M. Nosadini, Pediatric Neurology and Neurophysiology Unit, Department of Woman and Child Health, University Hospital of Padova, Padova, Italy; L. Farina, Department of Neuroradiology, Foundation IRCCS Neurological Institute "C. Besta," Milano, Italy; A. Stecco, Unit of Neuroradiology, Institute of Radiology, Department of Diagnosis, Health Services and Therapy, "Maggiore della Carità" University Hospital-Novara, Novara, Italy; G. Polonara, Clinica di Neuroradiologia, Dipartimento di Scienze Cliniche Specialistiche ed Odontostomatologiche; Universita Politecnica delle Marche, Ancona, Italy; M.A. Donati, Metabolic Unit, A. Meyer Children's Hospital, Firenze, Italy;

L. Giordano, Child Neuropsychiatry Unit, "Spedali Civili," Brescia, Italy; C. Dionisi-Vici, Division of Metabolism, Bambino Gesù Children's Hospital, IRCCS, Roma, Italy; D. Martinelli, Division of Metabolism, Bambino Gesù Children's Hospital, IRCCS, Roma, Italy; A. Tocchet, Child Neurology and Psychiatry, Department of Pediatrics and Pediatric Specialties, AOU Città della Salute e della Scienza, Torino, Italy; G. Fariello, Ospedale Fatebenefratelli, Villa San Pietro, Dipartimento Immagini, Roma, Italy; F. Nicita, Department of Pediatrics and Child Neuropsychiatry, Child Neurology Division, Umberto I Hospital, Sapienza University of Roma, Roma, Italy; D. Frattini, Child Neurology and Psychiatry Unit, Department of Pediatrics, ASMN-IRCCS, Reggio Emilia, Italy; P. Martelli, Child Neuropsychiatry Unit, "Spedali Civili," Brescia, Italy; G. Cantalupo, Child Neuropsychiatry Unit, Department of Surgical Sciences, Dentistry, Gynecology and Pediatrics, University of Verona, Verona, Italy; F. Zennaro, Institute for Maternal and Child Health-IRCCS "Burlo Garofolo," Trieste, Italy.

Disclosures: Renzo Manara—*UNRELATED*: *Payment for Lectures Including Service on Speakers Bureaus*: Shire, *Comments:* about €1000.

REFERENCES

1. Rizk T, Mahmoud A, Jamali T, et al. **Menkes disease presenting with epilepsia partialis continua.** *Case Rep Neurol Med* 2014;2014:525784 CrossRef Medline
2. Tümer Z, Møller LB. **Menkes disease.** *European J Hum Genet* 2010; 18:511–18 CrossRef
3. Nassogne MC, Sharrard M, Hertz-Pannier L, et al. **Massive subdural haematomas in Menkes disease mimicking shaken baby syndrome.** *Childs Nerv Syst* 2002;18:729–31 CrossRef Medline
4. Bahi-Buisson N, Kaminska A, Nabbout R, et al. **Epilepsy in Menkes disease: analysis of clinical stages.** *Epilepsia* 2006;47:380–86 CrossRef Medline
5. Van der Knaap MS, Valk J. *Magnetic Resonance of Myelination and Myelin Disorders Disorders*. Berlin: Springer; 2005
6. Vuia O, Heye D. **Neuropathologic aspects in Menkes' kinky hair disease (trichopoliodystrophy): Menkes' kinky hair disease.** *Neuropaediatrie* 1974;5:329–39 CrossRef Medline
7. Bernhard MK, Merkenschlager A, Mayer T, et al. **The spectrum of neuroradiological features in Menkes disease: widening of the cerebral venous sinuses.** *J Pediatr Neuroradiol* 2012;1:121–25
8. Gandhi R, Kakkar R, Rajan S, et al. **Menkes kinky hair syndrome: a rare neurodegenerative disease.** *Case Rep Radiol* 2012;2012:684309 CrossRef Medline
9. Kaler SG, Holmes CS, Goldstein DS, et al. **Neonatal diagnosis and treatment of Menkes disease.** *N Engl J Med* 2008;358:605–14 CrossRef Medline
10. Kaler SG. **ATP7A-related copper transport disease: emerging concepts and future trends.** *Nat Rev Neurol* 2011;7:15–29 CrossRef Medline
11. Tang J, Donsante A, Desai V, et al. **Clinical outcomes in Menkes disease patients with a copper-responsive ATP7A mutation, G727R.** *Mol Genet Metab* 2008;95:174–81 CrossRef
12. Danks DM, Campbell PE, Walker-Smith J, et al. **Menkes' kinky-hair syndrome.** *Lancet* 1972;1:1100–02 Medline
13. Danks DM, Cartwright E, Stevens BJ, et al. **Kinky hair disease: further definition of the defect in copper transport.** *Science* 1973;179: 1140–42 Medline
14. Cosimo QC, Daniela L, Elsa B, et al. **Kinky hair, kinky vessels, and bladder diverticula in Menkes disease.** *J Neuroimaging* 2011;21: e114–16 CrossRef Medline
15. Gu YH, Kodama H, Shiga K, et al. **A survey of Japanese patients with Menkes disease from 1990 to 2003: incidence and early signs before typical symptomatic onset, pointing the way to earlier diagnosis.** *J Inherit Metab Dis* 2005;28:473–78 Medline
16. Royce PM, Camakaris J, Danks DM. **Reduced lysyl oxidase activity in skin fibroblasts from patients with Menkes' syndrome.** *Biochem J* 1980;192:579–86 Medline
17. Barnerias C, Boddaert N, Guiraud P, et al. **Unusual magnetic resonance imaging features in Menkes disease.** *Brain Dev* 2008;30: 489–92 CrossRef Medline
18. Ito H, Mori K, Sakata M, et al. **Pathophysiology of the transient temporal lobe lesion in a patient with Menkes disease.** *Pediatr Int* 2008;50:825–27 CrossRef Medline
19. Jain P, Sharma S, Sankhyan N, et al. **Macrocephaly with diffuse white matter changes simulating a leukodystrophy in Menkes disease.** *Indian J Pediatr* 2013;80:160–62 CrossRef Medline
20. Bindu PS, Taly AB, Kothari S, et al. **Electro-clinical features and magnetic resonance imaging correlates in Menkes disease.** *Brain Dev* 2013;35:398–405 CrossRef Medline
21. Ekici B, Çaliskan M. Tatli B. **Reversible temporal lobe edema: an early MRI finding in Menkes disease.** *J Pediatr Neurosci* 2012;7: 160–61 CrossRef Medline
22. Johnsen DE, Coleman L, Poe L. **MR of progressive neurodegenerative change in treated Menkes' kinky hair disease.** *Neuroradiology* 1991;33:181–82 CrossRef Medline
23. Lee ES, Ryoo JW, Choi DS, et al. **Diffusion-weighted MR imaging of unusual white matter lesion in a patient with Menkes disease.** *Korean J Radiol* 2007;8:82–85 CrossRef Medline
24. Lee J, Peña MM, Nose Y, et al. **Biochemical characterization of the human copper transporter Ctr1.** *J Biol Chem* 2002;277:4380–87 Medline

Neuroimaging Changes in Menkes Disease, Part 2

R. Manara, M.C. Rocco, L. D'agata, R. Cusmai, E. Freri, L. Giordano, F. Darra, E. Procopio, I. Toldo, C. Peruzzi, R. Vittorini, A. Spalice, C. Fusco, M. Nosadini, D. Longo, S. Sartori, and the Menkes Working Group in the Italian Neuroimaging Network for Rare Diseases

ABSTRACT

SUMMARY: This is the second part of a retrospective and review MR imaging study aiming to define the frequency rate, timing, imaging features, and evolution of gray matter changes in Menkes disease, a rare multisystem X-linked disorder of copper metabolism characterized by early, severe, and progressive neurologic involvement. According to our analysis, neurodegenerative changes and focal basal ganglia lesions already appear in the early phases of the disease. Subdural collections are less common than generally thought; however, their presence remains important because they might challenge the differential diagnosis with child abuse and might precipitate the clinical deterioration. Anecdotal findings in our large sample seem to provide interesting clues about the protean mechanisms of brain injury in this rare disease and further highlight the broad spectrum of MR imaging findings that might be expected while imaging a child with the suspicion of or a known diagnosis of Menkes disease.

ABBREVIATION: MD = Menkes disease

Menkes disease (MD; Online Mendelian Inheritance in Man No. 309400; http://omim.org/)[1,2] is a rare metabolic disorder due to mutations in the *ATP7A* gene (Xq13.2-q13.3) encoding for the trans-Golgi copper-transporter P-type adenosine triphosphatase. Its dysfunction causes an impaired absorption and cellular metabolism of copper and results in an early, severe multisystem disease usually progressing to death in early childhood.[3,4] Affected infants might exhibit a sagging facial appearance, micrognathia, arched palate, laxity of the skin (cutis laxa), supernumerary wormian bones, reduced bone density, bladder diverticula, increased vascular tortuosity, and sparse "peculiar white hair" (pili torti).[5,6] Failure to thrive, hypothermia, hypotonia, impaired cognitive development, and relentless regression of developmental milestones highlight and reflect the primary involvement of the central nervous system. The scarce neuropathologic findings, both at gross and histology examination, are overtly dominated by neurodegeneration. At postmortem examination, MD typically presents with diffuse neuronal loss, gliosis, and cerebral white matter spongiosis, which result in cerebral and cerebellar atrophy.[7] Consistently, in vivo brain MRIs disclose protean findings at disease onset or during the follow-up that encompass focal white and gray matter lesions and extracerebral changes but also cerebral and cerebellar atrophy, revealing that neurodegenerative changes might appear long before death. However, even though case reports and small case series can outline the mutable involvement of the brain and allow formulating possible pathogenic hypotheses of brain damage, the available literature fails to provide adequate information about the frequency, severity, and the evolution of the reported cerebral and extracerebral lesions. In addition, often the "case report" approach does not provide sufficient evidence for confirming or refuting the numerous hypothesized pathogenic mechanisms of brain involvement.

This article is the second part of an extensive retrospective and review study that investigated the neuroimaging involvement of

From the Neuroradiology (R.M., M.C.R.), Sezione di Neuroscienze, Medicine and Surgery Department, University of Salerno, Salerno, Italy; Department of Neuroscience (L.D.), University of Padova, Padova, Italy; Neurology Unit (R.C., D.L.), Bambino Gesù Children's Hospital IRCCS, Roma, Italy; Department of Pediatric Neuroscience (E.F.), Foundation IRCCS, Neurological Institute "C. Besta," Milano, Italy; Child Neuropsychiatry Unit (L.G.), "Spedali Civili," Brescia, Italy; Child Neuropsychiatry Unit (F.D.), Department of Life and Reproduction Sciences, University of Verona, Verona, Italy; Metabolic and Neuromuscular Unit (E.P.), Department of Neuroscience, Meyer Children Hospital, Firenze, Italy; Pediatric Neurology and Neurophysiology Unit (I.T., M.N., S.S.), Department of Woman and Child Health, University Hospital of Padova, Padova, Italy; Child Neuropsychiatry (C.P.), Ospedale Maggiore, Novara, Italy; Child Neurology and Psychiatry (R.V.), Department of Pediatrics and Pediatric Specialties, AOU Città della Salute e della Scienza, Torino, Italy; Children Neurology Division (A.S.), University La Sapienza Roma, Roma, Italy; and Child Neurology and Psychiatry Unit, (C.F.), Department of Pediatrics, ASMN-IRCCS, Reggio Emilia, Italy.

Renzo Manara and Maria Chiara Rocco contributed equally to the study and should be considered "first coauthors"; Daniela Longo and Stefano Sartori should be both considered "senior coauthors."

Please address correspondence to Renzo Manara, MD, Neuroradiology, Sezione di Neuroscienze, Department of Medicine and Surgery, University of Salerno, via S. Allende 1, Baronissi (SA), 84081, Italy; e-mail: rmanara@unisa.it

Indicates open access to non-subscribers at www.ajnr.org

Indicates article with supplemental on-line appendix and table.

Indicates article with supplemental on-line photos.

http://dx.doi.org/10.3174/ajnr.A5192

Main neuroradiologic findings from literature review and in our sample

	Literature Review				Our Sample			
	First MRI		Follow-Up MRI		First MRI		Follow-Up MRI	
	62 Children with MD		23 Children with MD		26 Children with MD		8 Children with MD	
Brain Parenchyma	No.	%	No.	%	No.	%	No.	%
Basal ganglia abnormalities								
Yes	11	(18%)	1	(4%)	11	(44%)	6	(75%)
No	1	(2%)	3	(13%)	15	(56%)	2	(25%)
NR	50	(81%)	19	(83%)				
Cerebral atrophy								
Yes	41	(66%)	21	(91%)	21	(81%)	7	(88%)
No	5	(8%)	0	(9%)	5	(19%)	1	(12%)
NR	16	(26%)	2					
Cerebellar atrophy								
Yes	19	(31%)	9	(39%)	18	(70%)	8	(100%)
No	1	(2%)	0	(61%)	7	(30%)	0	
NR	42	(68%)	14					
Subdural collections								
Yes	15	(24%)	15	(65%)	7	(27%)	2	(25%)
No	7	(11%)	2	(9%)	19	(73%)	6	(75%)
NR	40	(65%)	6	(26%)				

Note:—NR indicates not reported/mentioned.

MD. Intracranial vascular and white matter changes at onset and during the disease course have been presented in the first part. The present part will focus primarily on the neurodegenerative processes (cerebral and cerebellar atrophy), focal lesions involving the basal ganglia, and subdural collections that might be detected in these children. In addition, we will present other neuroradiologic findings that have not been reported previously, expanding the spectrum of neuroimaging findings in MD and providing additional interesting clues on the still-elusive pathogenic mechanisms leading to brain damage in this rare disease.

MATERIALS AND METHODS

This section has been extensively reported in Part I.[8] Briefly, MR imaging and MRA findings of 26 children with MD (mean age at first MR imaging, 7.5 ± 5.9 months; range, 0.3–32.2 months; 1 female) were retrospectively evaluated. Children were enrolled if they had a biochemically or genetically confirmed MD diagnosis and at least 1 MR imaging. Two neuroradiologists (R.M. and L.D.) with >15 years of experience in pediatric neuroradiology evaluated all MR imaging examinations (40 MRIs and 25 MRAs), aware of the diagnosis but blinded to the clinical findings; discordant findings were discussed until consensus was reached.

Parenchymal Evaluation

Qualitative parenchymal evaluation was performed in all MRIs. Cerebral atrophy was considered if there was an increase of supratentorial CSF spaces in children with normal or decreased head circumference (all our children with MD were normo- or microcephalic except patients 7 and 21). The third ventricle laterolateral diameter was measured on axial images at the level of the foramen of Monro. Cerebellar atrophy was considered when a definite enlargement of cerebellar CSF spaces was noted. Signal abnormalities of the basal ganglia, subdural collections, and any other brain signal or morphologic abnormality were also recorded.

Literature Review

Our literature review included 47 articles published between 1989 and August 2016 that reported MR neuroimaging findings in children with MD and age at MR imaging examination (On-line Appendix). As already explained in Part 1, these articles were retrieved by searching in the major databases (Embase, Scopus, PubMed, Cochrane, and also www.google.com) with the following terms: "Menkes" and "brain MR imaging." The presence or absence of the above-mentioned MR imaging abnormalities were evaluated considering both the descriptions and available images of the selected articles. We considered as "not mentioned" any feature that could not be unequivocally defined as present or absent. We also recorded any available information about size, distribution, signal pattern, evolution, and proposed pathogenic hypothesis of MD-related brain lesions.

Statistical Analysis

The variables with normal distribution were analyzed by using the Student *t* test, while for ordinal variables, the Mann-Whitney *U* test was used. A second-order model correlation was used for fitting the third ventricle enlargement versus the age at MR imaging examination. Significance was set at $P < .05$.

RESULTS

Clinical features of our sample and children in the literature with MD are summarized in the On-line Table 1, also published in Part 1. Among the 26 children with MD, 11 had died before our MR imaging evaluation (mean age, 6.3 ± 4.6 years; range, 9 months to 17.5 years). All 26 children showed early onset of severe psychomotor delay, and most of them presented with epilepsy during the early phases of MD.

The Table and Fig 1 summarize the main neuroradiologic findings of children with MD included in the study and in our literature review.

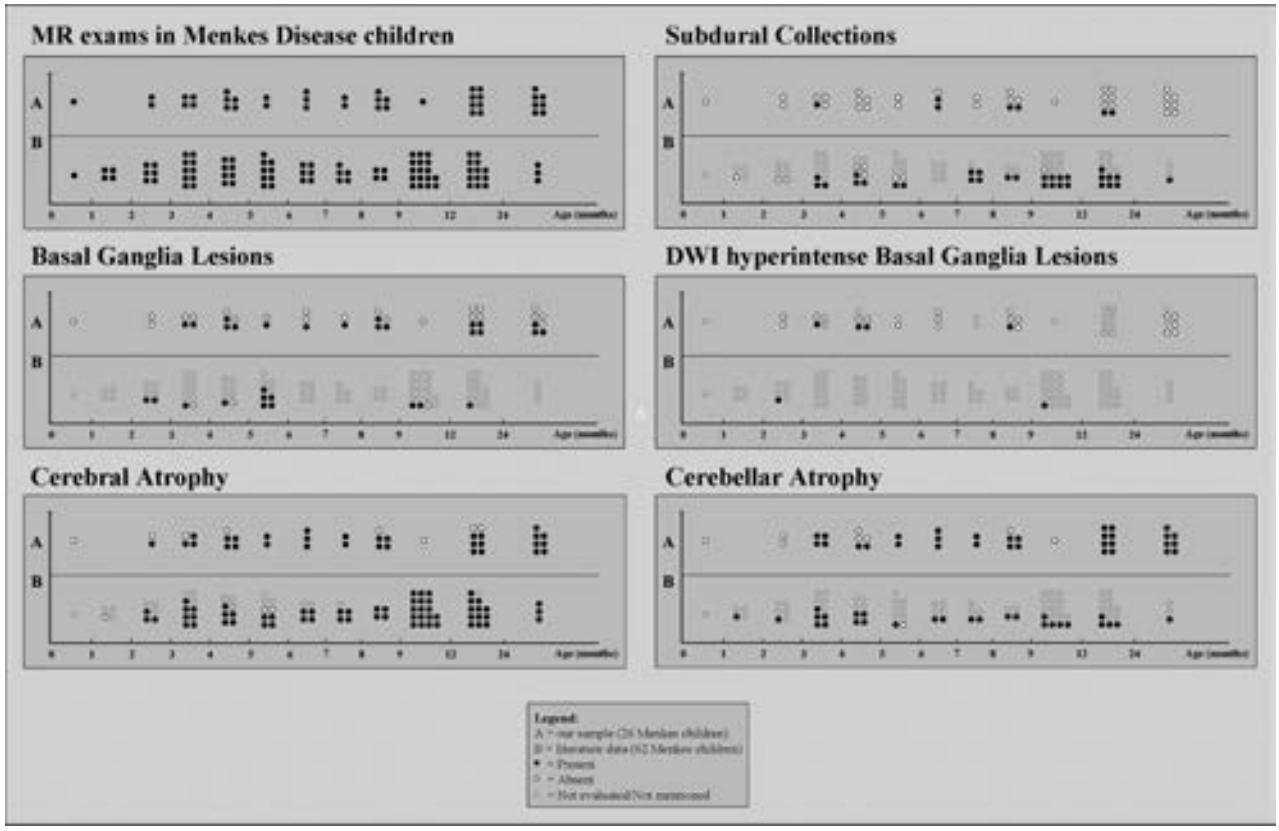

FIG 1. MR imaging findings in Menkes disease according to age at examination. *A*, Our sample (26 children, 40 examinations). *B*. Literature review (62 children, 86 examinations).

Basal Ganglia Abnormalities

Literature Review. Basal ganglia abnormalities were detected in 11/62 children with MD (18%; mean age, 6.2 ± 4.1 months; range, 2–17 months); 1 child did not present with basal ganglia abnormalities, while the finding was not mentioned in 50/62 children. Five children with basal ganglia abnormalities had follow-up MR imaging; lesion regression or persistence was reported in 1 case each, while in 3 cases, the finding was not mentioned.

Our Sample. Basal ganglia abnormalities were present in 15/26 children with MD (58%; mean age, 15.7 ± 19.5 months; range, 3.6–86.7 months; Fig 2 and On-line Fig 1); in 11/15 children, the lesions were present at first MR imaging. The lesions were typically asymmetric and involved the caudate head and anterior putamen. Among children with basal ganglia abnormalities, 3 had no DWI, while in 4/12 (all younger than 1 year of age), the lesions were DWI-hyperintense with decreased ADC values. DWI ischemic-like features disappeared in 1 child, while the remaining 3/4 children had no follow-up MR imaging.

None of the 4 children with basal ganglia abnormalities and subsequent follow-up MR imaging showed lesion regression. Considering both the literature and our sample findings, new basal ganglia lesions were detected in the timeframe between 2 and 16 months.

Cerebral Atrophy

Literature Review. Cerebral atrophy was detected at the first MR imaging in 41/62 children with MD (66%; mean age, 12.4 ± 21.9 months; range, 2 months to 12 years); it was absent in 5/62 and not mentioned in the remaining 16/62. At follow-up MR imaging, cerebral atrophy was reported in 21/23 children with MD (91%; mean age, 10.9 ± 6.0 months; range, 3–30 months), and it was already present, absent, or not mentioned at the previous examination in 13/21, 2/21, and 6/21 cases, respectively.

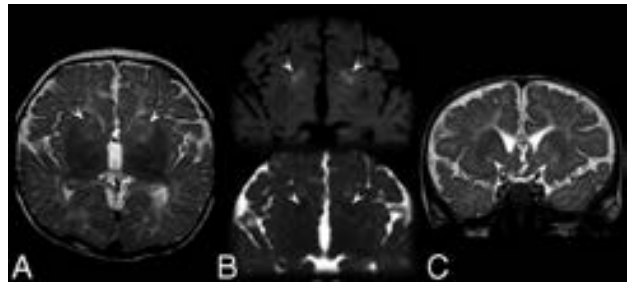

FIG 2. Brain MR imaging in a 5-month-old boy (patient 17) affected by Menkes disease. *A*, Axial T2-weighted image shows inhomogeneous hyperintensity in the anterior portion of the neostriatum more evident on the left side. *B*, Axial diffusion-weighted imaging (upper image) and apparent diffusion coefficient map (lower image) show small bilateral regions of restriction of the water molecule motion (*arrowheads*). *C*, Coronal T2-weighted image at the level of the anterior portion of the basal ganglia discloses the bilateral-though-asymmetric involvement of the caudate head, nucleus accumbens, and anterior putamen (*arrowheads*).

Our Sample. Cerebral atrophy was detected at first examination in 21/26 children with MD (81%; mean age, 8.0 ± 6.2 months; range, 2.2–32.2 months) and persisted among those with available follow-up MR imaging. Regarding the 5 children with MD with

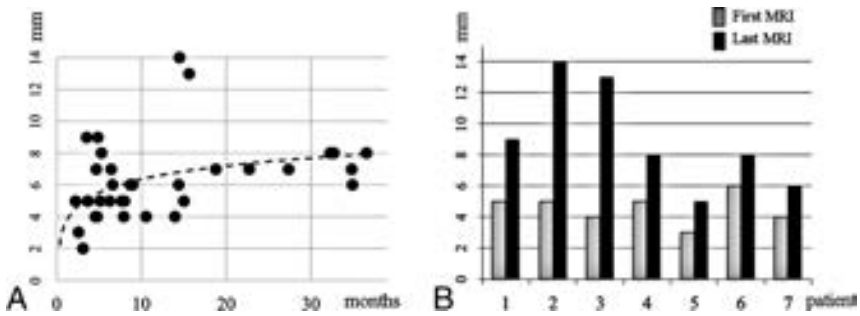

FIG 3. Diameter of the third ventricle. *A*, Cross-sectional MR imaging findings in the 25 male children with Menkes disease show the significant correlation between ventricle dilation and age at examination ($r = 0.4$, $P < .001$). *B*, MR imaging findings in children with Menkes disease with neuroradiologic follow-up show significant ventricular enlargement despite a relatively short follow-up (median follow-up, 10.8 months; $P = .01$, paired *t* test).

no atrophy at the first examination, 2 developed it at follow-up, 2 had no follow-up, and 1 did not present with cerebral atrophy at follow-up MR imaging but the imaging was performed very early, at 3.6 months of age. Cerebral atrophy was always present in children examined after 17 months of age.

The quantitative evaluation of ventricular dilation showed a significant correlation between third ventricle diameter and age at MR imaging in male children with MD ($r = 0.4$, $P < .001$, Fig 3*A*). Notably, ventricle enlargement seemed to increase rapidly during the first year of life and become thereafter relatively stable. All our children with MD showed a variable increase of third ventricle diameter at follow-up (median increase, 3 mm; range, 2–9 mm; median follow-up, 10.8 months; Fig 3*B*).

Cerebellar Atrophy

Literature Review. Cerebellar atrophy at first MR imaging was present in 19/62 children with MD (31%; mean age, 6.4 ± 4.5 months; range, 1.2–18 years), absent in 1/62 (5 months of age), and not mentioned in 42/62. At MR imaging follow-up, cerebellar atrophy was found in 9/23 children with MD (39%; mean age, 11.9 ± 7.5 months; range, 3–30 months), while it was not mentioned in the remaining cases; in 3/9 children with MD, the atrophy was not reported at the first examination.

Our Sample. Cerebellar atrophy was detected at first MR imaging in 18/26 children with MD (69%; mean age, 8.7 ± 6.6 months; range, 3.1–32.2 months). In 4 children with MD, cerebellar atrophy appeared during follow-up MR imaging. All children with MD investigated after 1 year of age had cerebellar atrophy.

Subdural Collections

Literature Review. Hematomas or hygromas at first MR imaging were present in 15/62 (24%; mean age, 7.1 ± 4.1 months; range, 3–17 months), absent in 7/62, and not mentioned in the remaining 40/62 children with MD. At follow-up MR imaging, subdural collections were present in 15/23 (65%; mean age, 12 ± 5.9 months; range, 4.5–30 months; and absent or not mentioned in the previous MR imaging in 3/15 and 7/15, respectively), absent in 2/23, and not mentioned in 6/23.

Our Sample. Subdural collections were detected in 5/26 children with MD (18%; mean age, 9.1 ± 4 months; range, 3.6–15.6 months; On-line Fig 2). At follow-up MR imaging, subdural collections appeared in 2 further children with MD at 3.6 and 15.6 months of age and disappeared in 1 child.

Other Neuroradiologic Findings

Besides the above-mentioned findings, the thorough evaluation of the MRIs of our sample revealed several miscellaneous parenchymal abnormalities that could not be set among the known classic neuroradiologic findings of MD.

T2-Pulvinar Sign. T2/FLAIR-hyperintensity of the posterior thalamus (Fig 4) was detected bilaterally in 4/26 children with MD, especially in advanced phases of the disease (ie, at 13.9, 14.4, 16.9, and 18.7 months of age); in 2 further children, bilateral pulvinar signal abnormalities were rather mild (8.9 and 6.6 months).

Focal Cortical-Subcortical Lesions. The MR imaging of a 2-month-old child with MD (patient 3) presenting with repetitive seizures showed a large left DWI hyperintense cortical-subcortical parieto-occipital lesion; ADC values were decreased with the disappearance of the cortical ribbon on T1 and T2 images (Fig 5). The lesion was not recognizable at 1-month follow-up MR imaging. The MR imaging of a 4-month-old boy (patient 25) presenting with status epilepticus showed the disappearance of the cortical ribbon on T1 and T2 images in a large left parieto-occipital region that did not correspond to any vascular territory; the study protocol did not include DWI. The follow-up MR imaging performed 11 months later showed evolution into encephalomalacia of the lesion; concomitant bilateral temporal encephalomalacia was also noted.

A 32-month-old boy (patient 20) showed left temporal encephalomalacia.

A 3-month-old boy (patient 21) presented with bilateral occipital cortical-subcortical T2*-hypointense lesions (posthemorrhagic encephalomalacia with hemosiderin deposits, On-line Fig 3*A*); the tentorium was also T2*-hypointense.

Postictal MR Imaging Changes. The MR imaging of a 5-month-old boy (patient 17) presenting with status epilepticus revealed signal abnormalities and swelling of the left hippocampal formation (On-line Fig 3*B*).

A 4-month-old boy (patient 26) presenting with a status epilepticus had corpus callosum DWI hyperintensity, most likely consistent with a reversible splenium lesion (the boy had no further follow-up MR imaging to confirm this hypothesis).

Incidental MR Imaging Changes Not Directly Related to Menkes Disease

A 37-month-old boy (patient 9) underwent MR imaging a few days after cardiopulmonary resuscitation; the examination showed diffuse and severe brain ischemia with Wallerian degeneration of the corticospinal tract and trans-synaptic degeneration of the substantia nigra and the subthalamic nucleus; concomitant cortical laminar necrosis was also noted on T1 images.

A child (patient 14) presented with an iatrogenic cortical

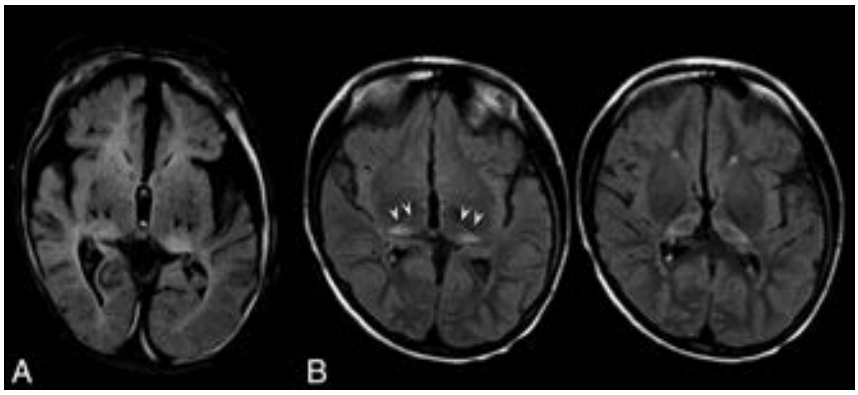

FIG 4. Axial FLAIR images at the level of the thalami. *A*, A 14-month-old boy (patient 14) shows bilateral hyperintensity of the pulvinar (*arrowheads*); bilateral subdural collections, brain atrophy, and abnormal myelination are also evident. *B*, An 87-month-old girl (patient 13) shows bilateral hyperintensity of the pulvinar. Note the severe symmetric volume loss of the thalami.

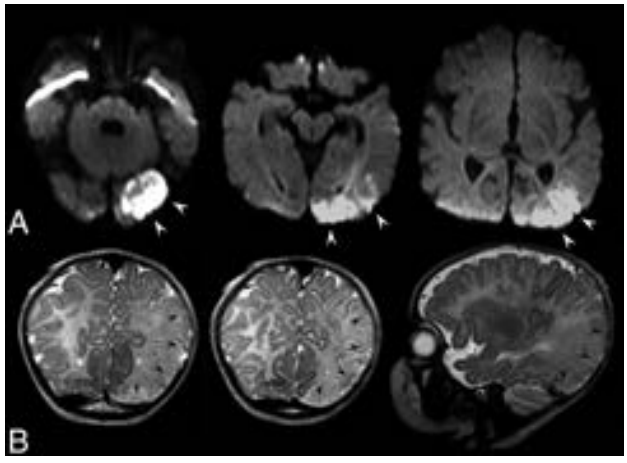

FIG 5. Brain MR imaging of a 2-month-old boy (patient 3) disclosing a left cortical-subcortical occipital-temporal-parietal lesion. *A*, Axial diffusion-weighted images show that the lesion is markedly hyperintense (*white arrowheads*), mimicking an acute cerebral ischemia. ADC values were decreased (not shown). *B*, Coronal and sagittal T2-weighted images show the disappearance of the cortical ribbon (*black arrowheads*). The lesion was fully recovered at follow-up MR imaging 1 month later (not shown).

blood clot close to an intrathecal drainage set for subdural collections.

Finally, a 9-month-old boy (patient 4) had focal white matter lesions without mass effect, which were more evident in the subcortical temporal-polar regions (possible intermediate stage of transient tumefactive lesions); unfortunately, no previous or follow-up examinations were available to confirm this pathogenic hypothesis.

Further Statistical Analyses

No significant association was found between neurodegenerative changes, focal gray matter lesions, or subdural collections and clinical, vascular, or white matter findings. In particular, there was no association between basal ganglia abnormalities and tumefactive lesions and prolonged jaundice at birth or the presence or severity of intracranial artery tortuosity ($P > .1$ for all associations).

DISCUSSION

The present retrospective cross-sectional multicenter study analyzed the neuroradiologic MR imaging abnormalities in a large sample of Italian children affected by Menkes disease and reviewed the pertinent literature up to August 2016. Because several children had >1 MR imaging evaluation, the study also provided interesting information on the evolution of disease-related MR imaging abnormalities. In this second section, we address the issues of neurodegeneration and basal ganglia focal lesions, comparing neuroimaging findings of our sample (26 children with MD) with those reported in the literature (62 children with MD). In addition, we discussed other previously unreported peculiar findings that widened the spectrum of MR imaging abnormalities in MD, providing interesting clues on the possible pathogenesis of brain injury.

Basal Ganglia Abnormalities

Basal ganglia involvement was common among children with MD, though the frequency rate was significantly higher in our sample than in the literature (58% versus 18%). Indeed, according to our experience, these T2/FLAIR hyperintense lesions may be easily overlooked, especially when the myelination of the surrounding white matter is impaired. Basal ganglia involvement was typically bilateral but asymmetric; the head of the caudate nucleus and anterior putamen seemed to be especially vulnerable, followed, in our sample, by the globus pallidus. According to both our cohort and literature data, the involvement of the basal ganglia was scarcely or not reversible. When the sequence was available, basal ganglia abnormalities were frequently (transiently) hyperintense in DWI; this finding implies cytotoxic edema as the main lesion mechanism for deep gray matter involvement in MD.

The detection at pathology of cystic-necrotic ischemic-like changes in the past led to hypothesizing an ischemic pathogenesis for basal ganglia lesions.[7] Increased tortuosity of the main cerebral arteries could effectively result in distortion and occlusion of small perforating arteries, even in the absence of overt artery stenosis. Nonetheless, the concomitant involvement of the caudate head and anterior putamen, which are supplied by different groups of perforating arteries (originating from the anterior and middle cerebral arteries, respectively), and the lack of involvement of the interposed anterior limb of the internal capsule, which shares the same vascular supply of the head of the caudate, point to a metabolic rather than an ischemic mechanism. The resulting cytotoxic edema due to intracellular copper-related energetic failure might eventually evolve into the cystic-necrotic changes observed at pathology.

Regarding lesion timing, even though previous reports suggested a late involvement of the basal ganglia in MD,[9] we found deep gray matter signal abnormalities already in the first months of life. Actually, new focal lesions were never observed after 16 months of age, pointing to early damage of these highly metabolic

regions. Different from the hypotheses in previous case reports or small series,[3] no significant association was found between basal ganglia abnormalities and seizures or tumefactive white matter lesions.

Cerebral Atrophy

In MD, cerebral atrophy appeared rather early during the disease course because it was recognizable in most children at first MR imaging and progressed rapidly with time, reaching a sort of "plateau" in later phases of the disease. Cerebral atrophy likely results from the combined effects of metabolic impairment, concomitant infection distress (common in children with MD), prolonged status epilepticus, increased susceptibility to oxidative stress (due to superoxide-dismutase enzyme deficiency), and energetic deficit (due to respiratory chain impairment) acting on a developing brain and resulting in severe cell death and neuronal loss.[3,10-13] Cerebral atrophy became a constant feature at 1.5 years of age, reflecting well the strikingly dramatic neurocognitive impairment of these children. In addition, cerebral atrophy was poorly or not reversible despite the introduction, soon after disease clinical onset, of copper histidine treatment in almost all patients of our sample. Taken together, MR imaging and clinical findings confirm that neurodegenerative phenomena are of primary importance because they occur early and progress rapidly in MD. Any attempt to treat this disease should therefore take into consideration that a late treatment beginning would likely result in a poor neurocognitive outcome.

Cerebellar Atrophy

Severe depletion of cerebellar neurons (about 50% of Purkinje cells) with morphologic degenerative changes in the remaining cells[14] and degeneration of all 3 cerebellar cortical layers and the deep nuclei with white matter gliosis[7,10] are likely the pathologic underpinnings of MR imaging findings recorded in the present study. Indeed, the strikingly high rate of cerebellar atrophy (>80% in our sample) is consistent with the typical MD pathologic features and with the well-known clinical picture (hypotonia and cerebellar deficits are very common in children with MD). According to our experience, cerebellar atrophy was progressive, irreversible, and diffuse, with symmetric involvement of both the vermis and hemispheres. Cerebellar atrophy in MD may be easily overlooked due to the presence of other overwhelming supratentorial findings, thus explaining the difference in the detection rate between our sample and literature data. Notably, the present study showed that cerebellar atrophy was an early feature in both the literature and in our sample (1.2 versus 3 months), commonly associated with cerebral atrophy, thus highlighting the global neurodegenerative involvement of the central nervous system. Cerebellar atrophy most likely shares with cerebral atrophy its multifactorial pathogenesis and its poor response to medical treatment when started after clinical onset.

Subdural Collections

Among children with MD, subdural collections are relatively common because they might be observed in about one-fourth of cases. As repeatedly addressed in the literature, their detection at first MR imaging might raise considerable problems in the differential diagnosis with head trauma and, above all, nonaccidental head trauma.[13,15-18] A child abuse misdiagnosis might be favored by the increased susceptibility to spontaneous fractures due to osteoporosis in MD and by the presence of supernumerary wormian bones that might mimic cranial vault fractures (On-line Fig 4). The presence of suggestive clinical (eg, "kinky hair") or imaging features (eg, increased intracranial artery tortuosity) and specific laboratory findings (low serum copper and ceruloplasmin levels) should aid in addressing the correct diagnosis. The pathogenic mechanism leading to subdural collections is thought to depend on increased vessel wall fragility in MD,[19,20] with rupture and hemorrhagic extravasation eased by the presence of brain atrophy.[21] In our sample, all children with subdural collections had concomitant brain atrophy as reported in the literature, even though there was no significant association with both qualitative and quantitative evaluation of brain atrophy severity. In addition, subdural collections did not appear to be more frequent in older children with MD, when cerebral atrophy was more pronounced. Most likely, other concomitant factors such as trivial head trauma, infections, or the rapidity of atrophy progression, might have a role. From an imaging point of view, in our sample, subdural collections were extremely protean, included both hematomas and hygromas, were most frequently localized in the frontal regions, but could be hemispheric, thin, or exerting a severe mass effect on the brain structures, single or multiple, symmetric or asymmetric. Only 1 child required decompressive surgery, and the outcome was very poor.

Other Neuroradiologic Findings

Within this Part are included a few MR imaging findings that have not been clearly mentioned in previous literature but that might help in defining the whole phenotypic variability of brain damage in MD. The bilateral T2/FLAIR hyperintensity of the posterior thalamus ("pulvinar sign") was a relatively frequent finding of MD (15%), especially in older children. Actually, subtle pulvinar involvement was also recognizable in previous studies[3] and should not be unexpected because the pulvinar is a key target of prolonged seizure activity. Pulvinar cytotoxic edema is commonly detected in children with status epilepticus.[22] Repetitive episodes of refractory seizures and status epilepticus characterize the clinical history of children with MD and might therefore lead to irreversible degeneration of this region. Besides, both direct and secondary trans-synaptic neurodegenerative changes might have a role, especially in the late phases of disease.[23]

DWI hyperintensity of the corpus callosum and swelling of the hippocampal formation found in 2 children with MD were also likely related to prolonged seizure activity. Similarly, 2 further children with MD investigated for status epilepticus had ischemic-like lesions on conventional MR imaging sequences, with large and severe cortical-subcortical involvement; one of them also had DWI that showed confirmatory cytotoxic-like features. However, 1 child showed full regression of the lesion in all sequences (including DWI), while the other, though the condition was evolving into encephalomalacia, had a nonvascular territorial involvement. Both cases therefore appeared as ischemic stroke mimics, probably related to the recent severe and prolonged seizure activity. Further evidence of a nonvascular pathogenesis is

provided by the location of cortical brain injury in our sample: Two of 3 children with MD with focal encephalomalacia had lesions close to the temporal poles (1 bilaterally) (ie, in regions that are relatively protected from ischemia).

Finally, bilateral occipital cortical hemorrhagic lesions and anoxic-ischemic lesions secondary to a cardiac arrest were each identified in 1 child with MD. These findings cannot be included in the classic MR imaging abnormalities of MD. Nonetheless, they further highlight the extreme heterogeneity of brain damage among children with MD and support the hypothesis that its pathogenesis is most likely multifactorial and only partially understood.

CONCLUSIONS

Brain involvement in Menkes disease appears to be strikingly severe and heterogeneous. Besides early and poorly evolutive vascular abnormalities and delayed myelination, signs of progressive neurodegeneration are typically found. In addition, during the disease course, several cerebral and extracerebral lesions might occur, some of which are restricted within specific age windows, revealing selective age-dependent brain vulnerability during disease progression. The present detailed description of neuroradiologic findings at onset and during the disease course provides valuable clues for an early diagnosis and paves the way for the identification of reliable MR imaging biomarkers for monitoring the efficacy of new treatments. In addition, the careful analysis of lesion imaging features and evolution on a relatively large sample of patients allows dismissing pathogenic hypotheses proposed on the basis of anecdotal observations, leading to an improved definition of the possible mechanisms of brain damage in children affected by Menkes disease.

ACKNOWLEDGMENTS

We thank the association "Angeli per la vita" and the Società Italiana di Neurologia Pediatrica, which strongly supported this spontaneous large Italian study.

The Menkes Working Group in the Italian Neuroimaging Network for Rare Diseases includes the following members: Rodica Mardari, Caterina Zanus, Gabriella Di Rosa, Consolata Soddu, Mariasavina Severino, Mario Ermani, Laura Farina, Allesandro Stecco, Gabriele Polonara, Maria Alice Donati, Lorenzo Pinelli, Carlo Dionisi-Vici, Diego Martinelli, Aba Tocchet, Giuseppe Fariello, Francesco Nicita, Daniele Frattini, Paola Martelli, and Gaetano Cantalupo.

The following are collaborators in this work: R. Mardari, Department of Neuroscience, University Hospital of Padova, Padova, Italy; C. Zanus, Institute for Maternal and Child Health, IRCCS "Burlo Garofolo," Trieste, Italy; G. Di Rosa, Unit of Child Neurology and Psychiatry, Department of Human Pathology of the Adult and Developmental Age, University Hospital of Messina, Messina, Italy; C. Soddu, Ospedale Pediatrico Microcitemico "A. Cao," AOB Cagliari, Italy; M. Severino, Neuroradiology Unit, Istituto Giannina Gaslini, Genova, Italy; M. Ermani, Department of Neuroscience, University Hospital of Padova, Padova, Italy; L. Farina, Department of Neuroradiology, Foundation IRCCS, Neurological Institute "C. Besta," Milano, Italy; A. Stecco, Unit of Neuroradiology, Institute of Radiology, Department of Diagnosis, Health Services and Therapy "Maggiore della Carità," University Hospital—Novara, Novara, Italy; G. Polonara, Clinica di Neuroradiologia, Dipartimento di Scienze Cliniche Specialistiche ed Odontostomatologiche, Universita' Politecnica delle March, Ancona, Italy; M.A. Donati, Metabolic Unit, A. Meyer Children's Hospital, Firenze, Italy; L. Pinelli, Neuroradiology, Section of Pediatric Neuroradiology, Department of Diagnostic Imaging, ASST Spedali Civili, Brescia; C. Dionisi-Vici, Division of Metabolism, Bambino Gesù Children's Hospital, IRCCS, Roma, Italy; D. Martinelli, Division of Metabolism, Bambino Gesù Children's Hospital, IRCCS, Roma, Italy; A. Tocchet, Child Neurology and Psychiatry, Department of Pediatrics and Pediatric Specialties, AOU Città della Salute e della Scienza, Torino, Italy; G. Fariello, Ospedale Fatebenefratelli, Villa San Pietro Dipartimento Immagini, Roma, Italy; F. Nicita, Department of Pediatrics and Child Neuropsychiatry, Child Neurology Division, Umberto I Hospital, Sapienza, University of Roma, Roma, Italy; D. Frattini, Child Neurology and Psychiatry Unit, Department of Pediatrics, ASMN-IRCCS, Reggio Emilia, Italy; P. Martelli, Child Neuropsychiatry Unit, "Spedali Civili," Brescia, Italy; G. Cantalupo, Child Neuropsychiatry Unit, Department of Surgical Sciences, Dentistry, Gynecology and Pediatrics, University of Verona, Verona, Italy; F. Zennara, Institute for Maternal and Child Health-IRCCS "Burlo Garofolo," Trieste, Italy.

Disclosures: Renzo Manara—*UNRELATED: Payment for Lectures Including Service on Speakers Bureaus*: Shire, *Comments:* about €1000.

REFERENCES

1. Rizk T, Mahmoud A, Jamali T, et al. **Menkes disease presenting with epilepsia partialis continua.** *Case Rep Neurol Med* 2014;2014:525784 CrossRef Medline
2. Park HD, Moon HK, Lee J, et al. **A novel ATP7A gross deletion mutation in a Korean patient with Menkes disease.** *Ann Clin Lab Sci* 2009;39:188–91 Medline
3. Bindu PS, Taly AB, Kothari S, et al. **Electro-clinical features and magnetic resonance imaging correlates in Menkes disease.** *Brain Dev* 2013;35:398–405 CrossRef Medline
4. Tümer Z, Møller LB. **Menkes disease.** *European J Hum Genet* 2010; 18:511–18 CrossRef
5. Menkes JH, Alter M, Steigleder GK, et al. **A sex-linked recessive disorder with retardation of growth, peculiar hair, and focal cerebral and cerebellar degeneration.** *Pediatrics* 1962;29:764–79 Medline
6. Zlatic S, Comstra HS, Gokhale A, et al. **Molecular basis of neurodegeneration and neurodevelopmental defects in Menkes disease.** *Neurobiol Dis* 2015;81:154–61 CrossRef Medline
7. Vuia O, Heye D. **Neuropathologic aspects in Menkes' kinky hair disease (trichopoliodystrophy): Menkes' kinky hair disease.** *Neuropaediatrie* 1974;5:329–39 CrossRef Medline
8. Manara R, D'agata L, Rocco MC, et al. **Neuroimaging changes in Menkes disease, part 1.** *AJNR Am J Neuroradiol* 2017 May 11. [Epub ahead of print] CrossRef Medline
9. Koprivsek K, Lucic M, Kozic D, et al. **Basal ganglia lesions in the early stage of Menkes disease.** *J Inherit Metabol Dis* 2010;33:301–02 CrossRef Medline
10. Matsubara O, Takaoka H, Nasu M, et al. **An autopsy case of Menkes kinky hair disease.** *Pathol Int* 1978;28:585–94
11. Moon HR, Chi JG, Yeon KM, et al. **Menkes disease: an autopsy case with metal analysis of hair.** *J Korean Med Sci* 1987;2:75–83 CrossRef Medline
12. Leventer RJ, Kornberg AJ, Phelan EM, et al. **Early magnetic resonance imaging findings in Menkes' disease.** *J Child Neurol* 1997;12: 222–24 CrossRef Medline

13. Rennert J, Doelken R, Doelken M, et al. **Menkes disease: MRI appearance of a rare neurodegenerative disorder.** *J Pediatr Neurol* 2009; 7:317–20
14. Yokoyama A, Ohno K, Hirano A, et al. **Cerebellar expression of copper chaperone for superoxide, cytosolic Cu/Zn-superoxide dismutase, 4-hydroxy-2-nonenal, acrolein and heat shock protein 32 in patients with Menkes kinky hair disease: immunohistochemical study.** *Yonago Acta Med* 2014;57:23–35 Medline
15. Gandhi R, Kakkar R, Rajan S, et al. **Menkes kinky hair syndrome: a rare neurodegenerative disease.** *Case Rep Radiol* 2012;2012: 684309 CrossRef Medline
16. Lubbe E. **From the coalface of clinical paediatric peurology: Menkes disease-a lesson not to be forgotten.** *S Afr J Child Health* 2012;6: 56–59
17. Fister P, Raku J, Primec RZ, et al. **Menkes kinky hair disease (Menkes syndrome): a case report.** *Acta Dermatovenerol Alp Pannonica Adriat* 2006;15:126–30 Medline
18. Nassogne MC, Sharrard M, Hertz-Pannier L, et al. **Massive subdural haematomas in Menkes disease mimicking shaken baby syndrome.** *Childs Nerv Syst* 2002;18:729–31 CrossRef Medline
19. Ozawa H, Kodama H, Murata Y, et al. **Transient temporal lobe changes and a novel mutation in a patient with Menkes disease.** *Pediatr Int* 2001;43:437–40 CrossRef Medline
20. Jacobs DS, Smith AS, Finelli DA, et al. **Menkes kinky hair disease: characteristic MR angiographic findings.** *AJNR Am J Neuroradiol* 1993;14:1160–63 Medline
21. Jain P, Sharma S, Sankhyan N, et al. **Macrocephaly with diffuse white matter changes simulating a leukodystrophy in Menkes disease.** *Indian J Pediatr* 2013;80:160–62 CrossRef Medline
22. Ohe Y, Hayashi T, Deguchi I, et al. **MRI abnormality of the pulvinar in patients with status epilepticus.** *J Neuroradiology* 2014;41:220–26 CrossRef
23. Martin JJ, Leroy JG. **Thalamic lesions in a patient with Menkes kinky-hair disease.** *Clin Neuropathol* 1984;5:206–09

Maximizing the Tweet Engagement Rate in Academia: Analysis of the AJNR Twitter Feed

V. Wadhwa, E. Latimer, K. Chatterjee, J. McCarty, and R.T. Fitzgerald

ABSTRACT

SUMMARY: The use of social media by medical professionals and organizations is increasing, with Twitter receiving the most attention. User engagement is an important goal of social media activity, and engagement metrics represent a viable gauge of value in social media. No thorough analysis of tweet characteristics that increase academic user engagement has yet been published. In this study, the authors analyzed the *American Journal of Neuroradiology* Twitter feed to determine the tweet characteristics that were associated with higher engagement rates.

Twitter (Twitter Inc, San Francisco, California), which is primarily based on status updates ("tweets") consisting of 140 characters or fewer, with an optional 6 pictures or fewer, is one of the largest social media platforms. Twitter is increasingly being adopted by radiologists, as is evident at various national meetings.[1] Many of the widely circulated general and subspecialty radiology journals, including *Radiology*, *RadioGraphics*, and the *American Journal of Neuroradiology* (AJNR), use social media to increase readership and interact with readers and authors, providing a dynamic platform for scientific discussion.[2] User engagement is the key outcome of tweeting for individual users and organizations alike, and irrespective of content, some tweets may be more engaging than others. However, the tweet characteristics associated with a high engagement rate have not yet been studied for radiology journals. The objective of this study was to identify the characteristics of AJNR tweets associated with high user engagement rate.

MATERIALS AND METHODS

Data Source

The AJNR Twitter account (@TheAJNR) has been active since January 2013 and has more than 4000 tweets and 2500 followers as of February 2017. Twitter analytics, which include impressions, engagements, and engagement rate for each tweet, were obtained from the AJNR Twitter account for tweets published from August 2015–July 2016. Impressions refer the number of times a Twitter user is served a tweet within their timeline or as part of a search result. Engagements are defined by the total number of times a user interacted with a tweet. Clicks anywhere on the tweet, including retweets, replies, follows, likes, links, cards, hashtags, embedded media, username, profile photo, or tweet expansion, result in engagement. The engagement score for each tweet was calculated as the number of engagements divided by impressions.

Tweet Characteristics

For this study, tweets with an engagement score above the 75th percentile were considered as "high engagement tweets," and tweets below the 25th percentile were considered as "low engagement tweets." Each tweet was further characterized by the month, time of day (morning, afternoon, evening, and night), weekend versus weekday, presence or absence of an imbedded image or hashtag, and type of tweet. The time of day in Central Standard Time (CST) was divided as morning (06:00–11:59 hours), afternoon (12:00–16:59 hours), evening (17:00–20:59 hours) and night (21:00–05:59 hours). The type of tweet was divided into the following subtypes: Fellows' Journal Club, Editor's Choice Article, Tweet Chat, Case, Article, Blog, and Miscellaneous.

Statistical Analysis

All data were stored in Excel 2013 (Microsoft, Redmond, Washington) and analyzed by using SPSS version 23 (IBM, Armonk, New York). A multivariate logistic regression model was constructed to identify the tweet characteristics associated with a high engagement rate. A 2-sided P value $< .05$ was considered statistically significant.

Received April 6, 2017; accepted after revision May 4.

From the Departments of Radiology (V.W., E.L., R.T.F.) and Internal Medicine (K.C.), University of Arkansas for Medical Sciences, Little Rock, Arkansas; and Department of Radiology and Imaging Sciences (J.M.), Emory University, Atlanta, Georgia.

Please address correspondence to Vibhor Wadhwa, MD, Department of Radiology, University of Arkansas for Medical Sciences, 4301 W Markham St, Little Rock, AR 72205; e-mail: vibhorwadhwa90@gmail.com; @wadhwa_rad

Indicates article with supplemental on-line appendix.

http://dx.doi.org/10.3174/ajnr.A5283

Table 1: Frequency distribution of tweet characteristics

Characteristic	Frequency	High ER Tweets	% High ER	Odds Ratio[a]	95% CI[a]	*P* Value[a]
Picture						
Yes	405	235	58.02%	28.749	17.654–46.816	.000
No	627	23	3.67%	#		
Hashtag						
Yes	751	242	32.22%	3.266	1.747–6.108	.000
No	281	16	5.69%	#		
Weekday	910	231	25.38%	0.613	0.348–1.081	.91
Weekend	122	27	22.13%	#		
Time of day						
Morning	606	200	33.00%	#	0.298–0.730	.001
Afternoon	318	47	14.78%	0.467	0.249–1.842	.445
Evening	66	7	10.60%	0.677	0.115–1.773	.254
Night	42	4	9.52%	0.452		

Note:—# indicates reference category; ER, engagement rate.
[a] From the logistic regression model. The "Month of Tweet" (Fig 1) was also part of the logistic model and did not show any independent statistical significance.

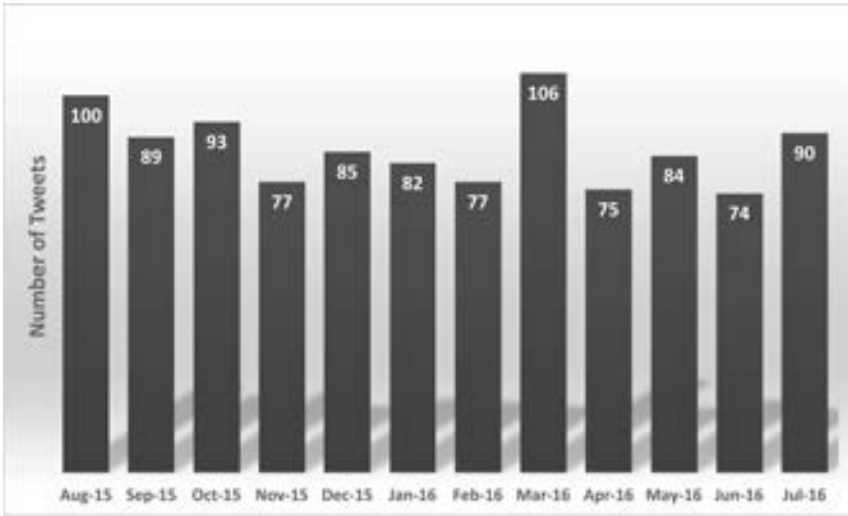

FIG 1. Tweet frequency per month over the study period.

Table 2: Distribution by tweet types

Type of Tweet	Frequency
Fellows' Journal Club	19
Editor's Choice	11
Tweet Chat	122
Case	200[a]
Article	384
Blog	159
Other	137

[a] 186/200 "Case" tweets had a high engagement rate. χ^2 analysis of "Case" (200) versus remaining Tweet types (832) showed a significantly higher engagement rate ($P < .001$; odds ratio, 140.238 [95% CI, 77.387–254.133]).

RESULTS

A total of 1032 tweets were published during the study period. Of these, 405 (39.2%) tweets included an image, and 751 (72.8%) tweets had a hashtag. There were 122 (11.8%) tweets were posted on a weekend. Most tweets were posted in the morning (606; 58.7%) and afternoon (318; 30.8%) hours (Table 1). The months of March (106 tweets) and August (100 tweets) had the highest AJNR Twitter activity (Fig 1). Overall, 258/1032 tweets were included in the "high engagement" category (75th percentile). The engagement rate of these tweets was 6.57% and above. The mean engagement rate of all tweets was 4.75%, and the median engagement rate was 3.4%.

Using the logistic regression model, the presence of an image independently increased the tweet engagement rate by 28.75 times ($P < .001$), and the presence of a hashtag increased the rate by 3.27 times ($P < .001$). Tweets published in the morning hours were twice as likely to have a high engagement rate compared with those published in the afternoon hours ($P = .001$). No significant difference was found in tweets published on weekends compared with weekdays, evening or night compared with morning or afternoon, or according to the month (Table 1). In an independent χ^2 analysis, the "Case" tweet type was 140-fold more engaging compared with all other tweet types because of the presence of a combination of engaging factors (Table 2). The 10 tweets with the highest engagement rate during the study period are shown in the On-line Appendix.

DISCUSSION

Our study examined the impact of tweet characteristics on user engagement and demonstrated that tweets including an image or hashtag and those published in the morning hours had the highest engagement rate.

Kelly et al[2] showed that AJNR had the second highest number of tweets in the year 2015 (3274) among all radiology journals with an official Twitter presence, second only to the *Journal of Vascular and Interventional Radiology*. AJNR also had the greatest number of favorites (a form of engagement) per 100 followers. They also showed that radiology journals with Twitter profiles have higher Impact Factors than those without profiles, as well as a positive association between Impact Factor and the number of followers of a journal's Twitter profile. Cosco[3] has also shown a strong association of Impact Factors and citations of general medical journals with a journal's Twitter following. Radiology articles published in journals have been disseminated through Twitter and have been shown to be effective in increasing readership. Hoang et al[4] showed increased readership of an AJNR article after promotion of the article on social media. Private practice radiology groups are adopting social media platforms (Facebook and Twitter) earlier than academic radiology departments, indicating the use of social media extending beyond research and academics.[5]

Twitter has been used to increase user engagement at various national scientific meetings. Hawkins et al[1] showed increased use of Twitter at the 2011 and 2012 Radiological Society of North America (RSNA) annual meetings. The recent annual meeting of

the American Society of Regional Anesthesia and Pain Medicine showed increased user engagement on Twitter, with Twitter content being scientific and created by meeting attendees, which also engaged nonattendees as evidenced by "retweeting," mostly of picture-containing tweets.[6] Similarly, the Irish Society of Urology Annual Meeting 2014 demonstrated that Twitter use facilitated interaction between delegates and significant participation of virtual followers.[7]

In the present study, we found that the presence of an image independently increased the engagement rate by nearly 29 times. This may be related to radiology images being more engaging than text tweets. It has been suggested by some Twitter experts to use photos to drive engagement.[8] We also found that tweets containing a hashtag have a 3-fold increased engagement rate compared with those without a hashtag. A hashtag refers to a word or phrase preceded by a hash or pound sign (#) and is used to identify messages on a specific topic. The use of hashtags gives more visibility to the tweet because users can search for common topics of interest, such as #ASNR17, #RadRes, and #NeuroRad, which in turn may contribute to increased engagement. Tracking hashtag use over time is possible by using third-party Web sites. Symplur (Upland, California), a health care social media analytics organization, was used by Hawkins et al[1] for their study to track the hashtags #RSNA11 and #RSNA12. Symplur was also used by Gouda et al[9] to track hashtags associated with heart failure.

Our study also analyzed the impact of the time of day on tweet engagement. The highest Twitter activity for @TheAJNR was during the morning hours, which also had twice higher engagement compared with afternoon tweets. No significant difference was found between morning and afternoon tweets compared with evening and night tweets, possibly because of the small number of later-hour tweets.

One limitation of this study was the inclusion of only 1 year of tweets. In addition, the high engagement rate of image-containing tweets may be related to the inherent nature of radiology as an imaging-based medical specialty, and further research is necessary to identify the engaging factors for other specialties and organizations.

CONCLUSIONS

Tweets including an image and/or a hashtag and those published in the morning hours had the highest user engagement rate for the AJNR Twitter feed. Our data may allow other organizations and individual Twitter users to maximize the potential impact of their social media efforts. Further research is required to identify if this high engagement on Twitter leads to meaningful engagement with the journal itself.

REFERENCES

1. Hawkins CM, Duszak R, Rawson JV. **Social media in radiology: early trends in Twitter microblogging at radiology's largest international meeting.** *J Am Coll Radiol* 2014;11:387–90 CrossRef Medline
2. Kelly BS, Redmond CE, Nason GJ, et al. **The use of Twitter by radiology journals: an analysis of Twitter activity and Impact Factor.** *J Am Coll Radiol* 2016;13:1391–96 CrossRef Medline
3. Cosco TD. **Medical journals, impact and social media: an ecological study of the Twittersphere.** *CMAJ* 2015;187:1353–57 CrossRef Medline
4. Hoang JK, McCall J, Dixon AF, et al. **Using social media to share your radiology research: how effective is a blog post?** *J Am Coll Radiol* 2015;12:760–65 CrossRef Medline
5. Glover M, Choy G, Boland GW, et al. **Radiology and social media: are private practice radiology groups more social than academic radiology departments?** *J Am Coll Radiol* 2015;12:513–18 CrossRef Medline
6. Schwenk ES, Jaremko KM, Gupta RK, et al. **Upgrading a social media strategy to increase Twitter engagement during the spring annual meeting of the American Society of Regional Anesthesia and Pain Medicine**. *Reg Anesth Pain Med* 2017;42:283–88 CrossRef Medline
7. Nason GJ, O'Kelly F, Bouchier-Hayes D, et al. **Twitter expands the reach and engagement of a national scientific meeting: the Irish Society of Urology.** *Ir J Med Sci* 2015;184:685–89 CrossRef Medline
8. Stecyk J. #TweetTip: use photos to drive engagement. https://blog.twitter.com/2015/tweettip-use-photos-to-drive-engagement. Accessed April 2, 2017
9. Gouda P, Das D, Clark A, et al. **The impact and implications of Twitter for cardiovascular medicine.** *J Card Fail* 2017;23:266–67 CrossRef Medline

Spinal and Paraspinal Plexiform Neurofibromas in Patients with Neurofibromatosis Type 1: A Novel Scoring System for Radiological-Clinical Correlation

M. Mauda-Havakuk, B. Shofty, S. Ben-Shachar, L. Ben-Sira, S. Constantini, and F. Bokstein

ABSTRACT

BACKGROUND AND PURPOSE: Neurofibromatosis type 1 is a common tumor predisposition syndrome. The aim of this study was to characterize the radiologic presentation of patients with neurofibromatosis type 1 with widespread spinal disease and to correlate it to clinical presentation and outcome.

MATERIALS AND METHODS: We conducted a historical cohort study of adult patients with neurofibromatosis type 1 with spinal involvement. Longitudinal clinical evaluation included pain and neurologic deficits. Radiologically, spinal involvement was classified according to a novel classification system, and a radiologic risk score was calculated.

RESULTS: Two hundred fifty-seven adult patients with neurofibromatosis type 1 are followed in our center. Thirty-four of these patients qualified for inclusion in this study. Three independent factors were found to be associated with increased risk for neurologic deficit: 1) bilateral tumors at the same level in the cervical region that approximated each other, 2) paraspinal tumors at the lumbar region, and 3) intradural lesions. On the basis of these factors, we calculated a combined risk score for neurologic deficits for each patient. We found a clear correlation between patient status and the calculated radiologic risk score. Patients with neurologic deficits were found to have a higher risk score (9 ± 8.3) than patients without neurologic deficits (2.5 ± 2.9, $P < .05$). Patients who progressed during the follow-up period had significantly higher scores at presentation than patients with stable conditions (9.9 ± 8.73 versus 3.9 ± 5.3, respectively; $P < .05$).

CONCLUSIONS: In this series, neurologic deficit is correlated with tumor burden and subtype. We found no direct correlation with tumor burden and pain. Our novel radiologic classification scoring system may be used to predict increased risk for neurologic morbidity.

ABBREVIATIONS: NF1 = neurofibromatosis type 1; PN = plexiform neurofibromas

Neurofibromatosis type 1 (NF1; Online Mendelian Inheritance in Man #162200) is a common genetic autosomal dominant syndrome. NF1 effects approximately 1:2000 individuals worldwide.[1,2] The syndrome is characterized by a combination of clinical traits: café au lait macules, Lisch nodules (iris hamartomas), neurofibromas (cutaneous, subcutaneous, plexiform), optic pathway gliomas, and bone dysplasia.[1,3]

Spinal manifestations of NF1 include bone changes such as acute kyphoscoliosis at the cervical-thoracic junction and vertebral body anomalies, soft-tissue abnormalities such as dural ectasia and lateral meningocele, and various spinal tumors.[1,4] Neoplastic spinal involvement in NF1 varies widely; patients may be affected by nerve sheath tumors such as neurofibromas, plexiform neurofibromas (PN), and intramedullary glial tumors. Figure 1 demonstrates a typical case of a complex spinal involvement in a patient with NF1. To date, no association has been found between spinal tumor burden and clinical outcome.

Generally, an operation is reserved for tumors associated with progressive neurologic deficits.[5] Patients with NF1 with massive spinal involvement present a major clinical challenge. Often the burden of the disease is overwhelming. Thus, it is extremely difficult to follow up, even using innovative volumetric assessment methods. It may also be difficult to identify the culprit tumor responsible for specific clinical symptoms. Malignant transformation, though rare, poses a significant problem and usually also necessitates surgical resection when feasible.[6]

Many biologically targeted therapies have been used in the clinical and preclinical setting. A few examples are RAS (receptor associated) targeted therapy, mTOR (mechanistic target of rapa-

Received April 17, 2017; accepted after revision June 2.

From the Gilbert Israeli NF Center (M.M.-H., B.S., S.B.-S., L.B.-S., S.C., F.B.), Pediatric Radiology Unit (M.M.-H., L.B.-S.), Pediatric Neurosurgery (B.S., S.C.), and Neuro-Oncology Service (F.B.), Dana Children's Hospital, Tel-Aviv Medical Center, and Tel-Aviv University, Tel-Aviv, Israel.

M. Mauda-Havakuk and B. Shoftly contributed equally to this article.

Please address correspondence to Ben Shofty, MD, Department of Neurosurgery, Tel-Aviv Medical Center, 6th Weizmann St, Tel-Aviv, Israel, 64239; e-mail: shoftyben@gmail.com

http://dx.doi.org/10.3174/ajnr.A5338

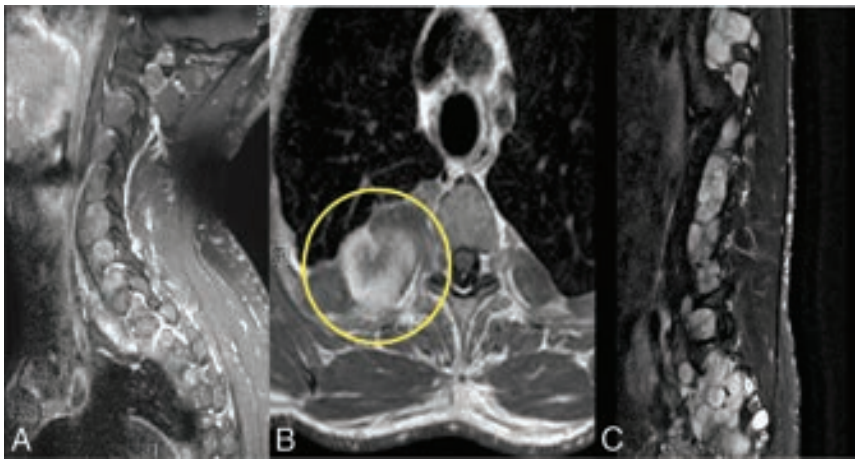

FIG 1. Complex spinal manifestation in a patient with NF1. Spinal MR imaging study of a 36-year-old asymptomatic patient with NF1. Note that the tumors involve all the neuroforamina in the cervical and lumbar segments (*A* and *C*). Axial T1 with gadolinium demonstrates massive paraspinal involvement of the thoracic region (*B*). Sagittal T2 with fat saturation of the lumbar region demonstrates multiple tumors in the neuroforamina and in the lumbar spine (*C*).

mycin) inhibitors,[7] interferon,[8] or multi kinase inhibitors.[9] Recently, promising preliminary results were published[10] demonstrating a response to treatment with mitogen-activated protein kinase inhibitor in a phase 1 study. The possibility of medical treatment for PN further highlights the need to accurately prognosticate patients with spinal NF1.

There is a clinical subtype of NF1, "spinal-NF1," that is associated with a unique phenotype and genotype and should be differentiated from regular NF1-associated spinal involvement. These patients (spinal-NF1) characteristically display massive neoplastic enlargement of most of the spinal roots and multiple paraspinal tumors, with very few of the dermal manifestations typical of NF1.[11] Molecularly, in patients with spinal-NF1, a large deletion encompassing the *NF1* gene can be found.

Our study focuses on spinal involvement in patients with NF1 in general, rather than the spinal-NF1 subtype. Included were both patients with spinal-NF and those with NF who presented with spinal manifestations.

The aim of this study was to characterize the variety of spinal radiologic presentations of patients with NF1. In addition, we propose a novel classification and radiologic scoring system for patients with spinal involvement. We intended to demonstrate a correlation between our scoring system and symptoms such as pain and neurologic deficits.

MATERIALS AND METHODS

This study was approved by the institutional review board of Tel-Aviv Medical Center. Records of all 257 adult patients with NF1 treated at the Gilbert Israeli NF1 Center between 2008 and 2014 were retrospectively reviewed. Thirty-four patients with documented NF1-associated neoplastic spinal involvement, including MR imaging studies of the spine (at least 2 MR imaging studies) and sufficient clinical follow-up data (>2 years of clinical follow-up) were included in the analysis. Each patient's imaging studies were evaluated and classified with our classification method by a radiology resident (M.M.-H.), under the supervision of a senior neuroradiologist (L.B.-S.); both were blinded to the clinical condition of the patients.

Patients were initially grouped according to their clinical presentation: asymptomatic and symptomatic (with pain or neurologic deficits); then, we analyzed specifically the groups of patients with pain or neurologic deficits related to their spinal manifestations.

We tried to develop a new radiologic classification that would allow risk stratification of spinal patients with NF. We therefore classified the tumors into 4 groups:

1. Foraminal tumor: a tumor involving the nerve roots and the neuroforamen.
2. "Kissing" tumors: bilateral-foraminal tumors that approximated each other at the same level, to <2 mm, with significant compression of the cord or thecal sac (See Fig 2*B* for an example).
3. Paraspinal tumor: a tumor epicentered lateral to the neuroforamina, having a large soft-tissue component outside the spinal canal.
4. Intradural tumor: a tumor epicentered inside the thecal sac.

See Fig 1 for an example of our radiologic classification system.

Tumors were counted and scored independently for each subtype. For example, a patient with a paraspinal tumor in the cervical segment received 1 point for this region and 0 points for the thoracic and lumbar regions. For tumors in group 1 (foraminal), the number of spinal levels (nerves) involved was counted for each spinal segment on each side. For example, a patient with bilateral cervical foraminal tumors in 3 different levels was given a score of 6 for cervical foraminal tumor. For tumors in group 2 (kissing), 1 point was given for each level involved. Tumors in group 4 (intradural) were rare, usually involving a single lesion per segment; their presence or absence was also documented for each segment. Because tumors in group 3 (paraspinal) are manifested as bulky, massive, paraspinal, soft-tissue masses that cannot be counted for multiplicity, we decided to take into account the presence or absence of the paraspinal tumor in each spinal segment (cervical, thoracic, lumbosacral). See Fig 2*A* for a schematic representation of our classification system. The overall clinical course was determined on the basis of the clinical documentation and then correlated with radiologic data.

For statistical analysis, we used SPSS, Version 21 (IBM, Armonk, New York). Differences in the mean distribution of the tumors between groups of patients at presentation (symptomatic versus asymptomatic, pain versus no pain, neurologic deficit versus no neurologic deficit) were evaluated with the Student independent samples *t* test, with significance set at $P < .05$. Tumor subgroups that demonstrated a significant difference ($P < .05$) or a trend difference in prevalence ($P < .1$) among the clinical groups were further analyzed. The effect of each tumor subtype on the outcome measures (pain, neurologic deficit, neurologic deterioration), as indicated by the previous analysis, was evaluated with a logistic regression, and the

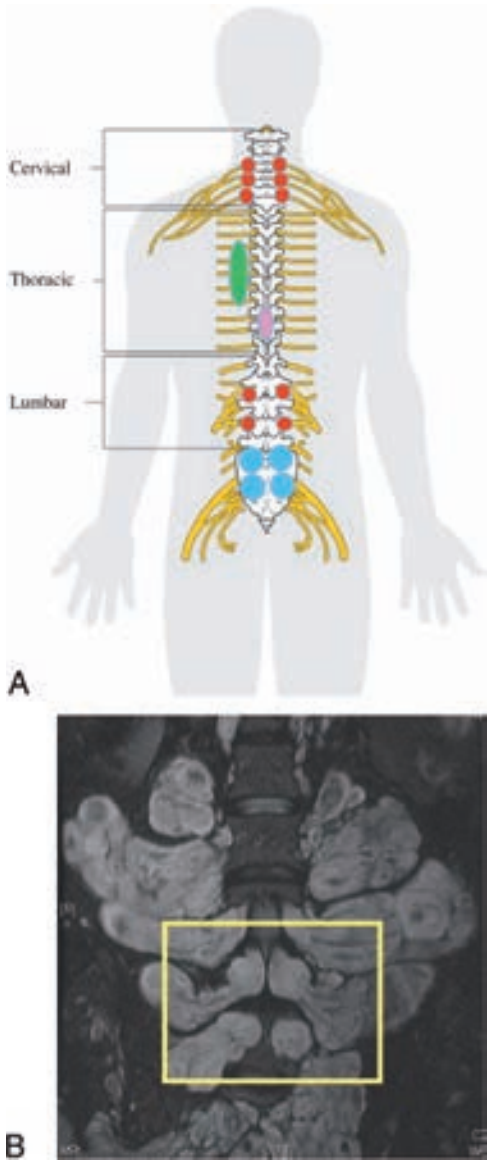

FIG 2. Schematic representation of our classification of spinal involvement in NF1 (*A*). A *red circle* represents tumors within the neuroforamina (group 1). *Blue circles* represent bilateral tumors within the neuroforamina with sac compression (kissing neurofibromas, group 2). The *green ellipse* represents paraspinal involvement (group 3). The *purple ellipse* represents an intradural lesion (group 4). A patient with this imaging result would have received a score of 6 for cervical foraminal, 2 for thoracic, 2 for lumbar foraminal, 1 for thoracic paraspinal, 1 for intradural thoracic, and 2 for 2 pairs of lumbar kissing tumors. The spinal cord schema image has been released as part of an open knowledge project by Cancer Research UK and attributed to Cancer Research UK/Wikimedia Commons. *B*, T2 with fat saturation coronal MR imaging study of the lumbar region of a patient with NF1. In the *yellow rectangle*, we see an example of 2 pairs of bilateral tumors approximating each other at the same level to <1–2 mm, with significant compression of the thecal sac (kissing PN). Note the large paraspinal component of the tumors (group 1).

odds ratio for outcome was calculated. A radiologic risk score was computed on the basis of the ORs of the significant categories for each patient and was correlated with neurologic and radiologic outcome. The complete risk score calculation would be the following:

$$OR_1 \times n\ tumors_1 + OR_2 \times n\ tumors_2 \ldots OR_n \times n\ tumors_n.$$

RESULTS

Of 257 adult patients with NF1 followed in our institution, 41 (15.9%) had documented spinal involvement based on spinal imaging. Thirty-four (83%) had sufficient clinical follow-up data to be included in this study. Seventeen of the patients (50%) were females; the median age at first spinal imaging was 31 years (range, 14–55 years). The mean follow-up time was 3.5 ± 2.9 years. Seventeen patients (50%) had a positive family history of NF1. Fifteen patients (44%) underwent an operation due to progressive symptomatic spinal disease.

Follow-up data were available for 30 patients. Four patients were excluded from the outcome analysis due to either surgeries at presentation ($n = 3$) or insufficient follow-up data ($n = 1$). At the last follow-up, 7/30 (23%) patients available for evaluation demonstrated radiologic progression. Tumor distribution varied widely; see the Table for detailed description of the entire group.

We analyzed tumor distribution according to the following factors:

- Symptomatic: Only 22 of 34 patients (64%) were symptomatic at presentation due to their spinal disease. The spinal distribution of the tumors did not differ between symptomatic and asymptomatic patients for all tumor types. The only exception was group 2, kissing neurofibromas in the cervical region. Those were more abundant in the symptomatic group compared with the asymptomatic group (1.1 ± 2.3 versus 0.3 ± 0.78, respectively; $P < .05$). (See Fig 3 for a detailed distribution of symptomatic and asymptomatic tumors by group.)
- Pain: Fifteen of 34 patients (44%) had pain associated with their spinal disease. The spinal distribution of the tumors did not differ between patients in either group (Fig 4).
- Neurologic deficit: Thirteen of 34 patients (38%) presented with neurologic deficits related to their spinal disease; 21/34 (62%) were neurologically intact. These patients had significantly more tumors in the cervical and lumbosacral regions (Fig 5). Kissing cervical neurofibromas were more common in patients with neurologic deficits than in intact patients, with an average of 1.7 ± 0.7 versus 0.2 ± 0.6, respectively ($P < .05$). A similar difference in the amount of kissing neurofibromas was found for the lumbosacral area, with an average of 2.83 ± 1.4 versus 0.95 ± 2.2, respectively ($P < .05$). In addition, a difference between the groups was observed in the number of patients with cervical paraspinal tumors. In the neurologically impaired group, more patients had cervical paraspinal tumors (0.46 ± 0.15 patients) in comparison with the neurologically intact group (0.2 ± 0.4 patients, $P < .05$).
- We tried to quantify the impact of differences in tumor distribution at different levels on clinical status (as manifested by pain and neurologic impairment). Thus, we used a series of logistic regressions examining the increase in associated risk of neurologic deficit or pain with each type of tumor (stratified by group and location). Three independent factors were found to be associated (either statistically significant or with a trend toward significance) with an increased risk for neurologic deficits: The first was the presence of kissing neurofibromas (group 3) in the cervical region, the second was associated with paraspinal tumors (group 1) in the lumbar region, and the third was related to intradural disease (group 4) (Fig 5), with respective ORs of 1.7 ($P = .07$), 3.7 ($P = .08$), and 4.2 ($P =$

.03). On the basis of these data, we calculated a risk score for neurologic deficits for each patient. The risk score was calculated as follows: the number of kissing neurofibromas was multiple by 1.7, if lumbar paraspinal tumors were present we added 3.7 and if an intradural disease was present we added 4.2.

Calculation of Radiologic Risk Score

Risk score = 1.7× n (of cervical kissing neurofibromas) + 3.7 (if lumbar paraspinal tumors were present) + 4.2 (if an intradural disease was present).

For pain, no risk factors were found to be significant. In addition, no difference related to pain was found in the risk score. Patients with neurologic deficits were found to have a significantly higher risk score, with an average of 9 ± 8.3, compared with 2.5 ± 2.9 in neurologically intact patients ($P < .05$, Fig 6).

While a total of 34 patients were included in this study, we only had long-term follow-up data for 30 patients. During the follow-up period, 24/30 (80%) remained neurologically stable, while the conditions of 6/30 (20%) deteriorated. The mean risk score calculated according to the proposed method was significantly higher for patients with deteriorating conditions (10 ± 8.7) compared with those with stable conditions (3.9 ± 5.3, $P < .05$).

Detailed tumor distribution for the entire cohort (n = 34)

	Group 1: Neuroforaminal[a]	Group 2: Kissing Neurofibromas[a]	Group 3: Paraspinal[b]	Group 4: Intradural[b]
Cervical	7.3 ± 6 (0–14)	0.8 ± 1.9 (0–6)	10 (29%)	3 (8%)
Thoracic	4.9 ±7.5 (0–24)	0	13 (38%)	3 (8%)
Lumbo-sacral	8.8 ± 7.7 (0–20)	1.6 ± 3.5 (0–16)	15 (44%)	5 (14%)

[a] The average number ± SD of involved levels in each spinal region for each tumor type for the entire cohort (n = 34). Numbers in parentheses represent the range of affected levels.
[b] Number of patients (%). Note that for intradural and paraspinal tumors, the number represents the total number of patients, regardless of how many levels are affected.

DISCUSSION

The main findings of this article are based on a novel radiologic classification system that correlates well with clinical presentation and outcome, producing a potentially useful radiologic risk scoring method.

Patients with NF1 with spinal involvement present the treating multidisciplinary team with unique difficulties. High tumor burden poses a significant radiologic challenge when attempting to assess anatomic progression. Clinically, it is often difficult to distinguish the culprit tumor responsible for the symptoms. Due to the complexity and associated morbidity of plexiform neurofibroma operations, they are often kept as a last resort when all other conservative therapeutic measures have failed and the tumor responsible for neurologic deterioration is identified beyond all doubt. In light of the novel treatment options for PN currently being developed (at least among patients with NF1), a means of evaluating these tumors and their course of progression is essential for treatment decision-making.[10]

In a series of 149 patients with spinal neurofibromas, spinal involvement was classified into several types according to the anatomic location of the tumors in the spinal canal and foramina.[12] Despite the large number of patients in the cohort, only 12 had NF1, and only a minority of the patients had multiple spinal tumors. We found 3 other studies that looked into the incidence and variety of spinal tumors in patients with NF1 more specifically. Recently, a large series of spinal findings in patients with NF1 was published, describing 97 patients with baseline imaging of the spine.[13] In this series, 78 patients had spinal neurofibromas, but only 26 patients had clinical

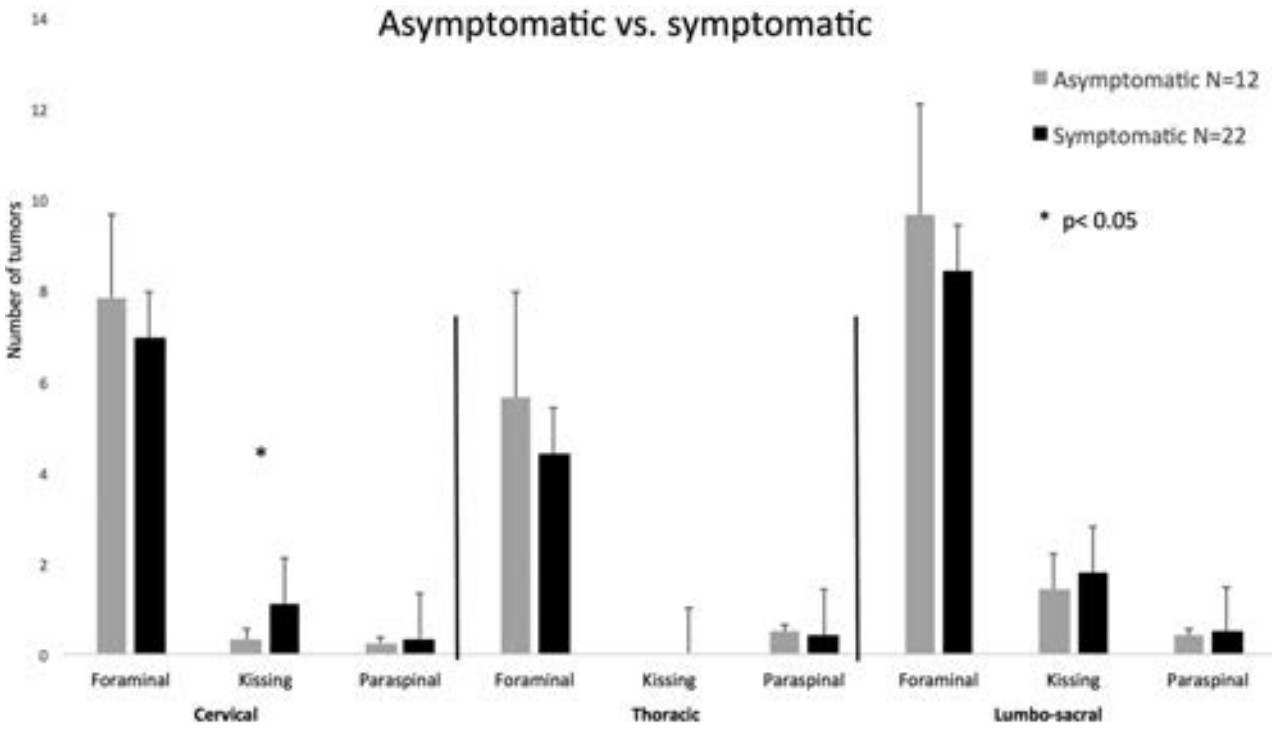

FIG 3. Spinal tumor distribution in asymptomatic and symptomatic patients. *Error bars* represent the standard error of the mean.

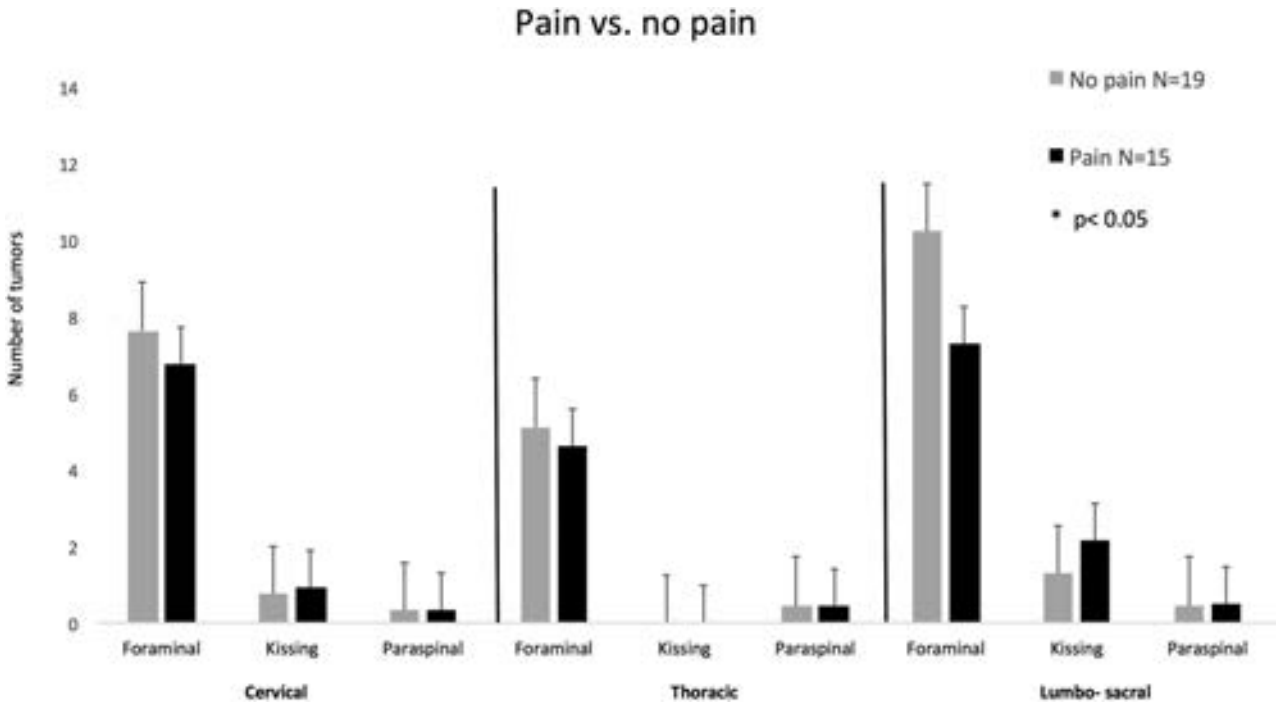

FIG 4. Spinal tumor distribution in patients with and without pain. *Error bars* represent the standard error of the mean.

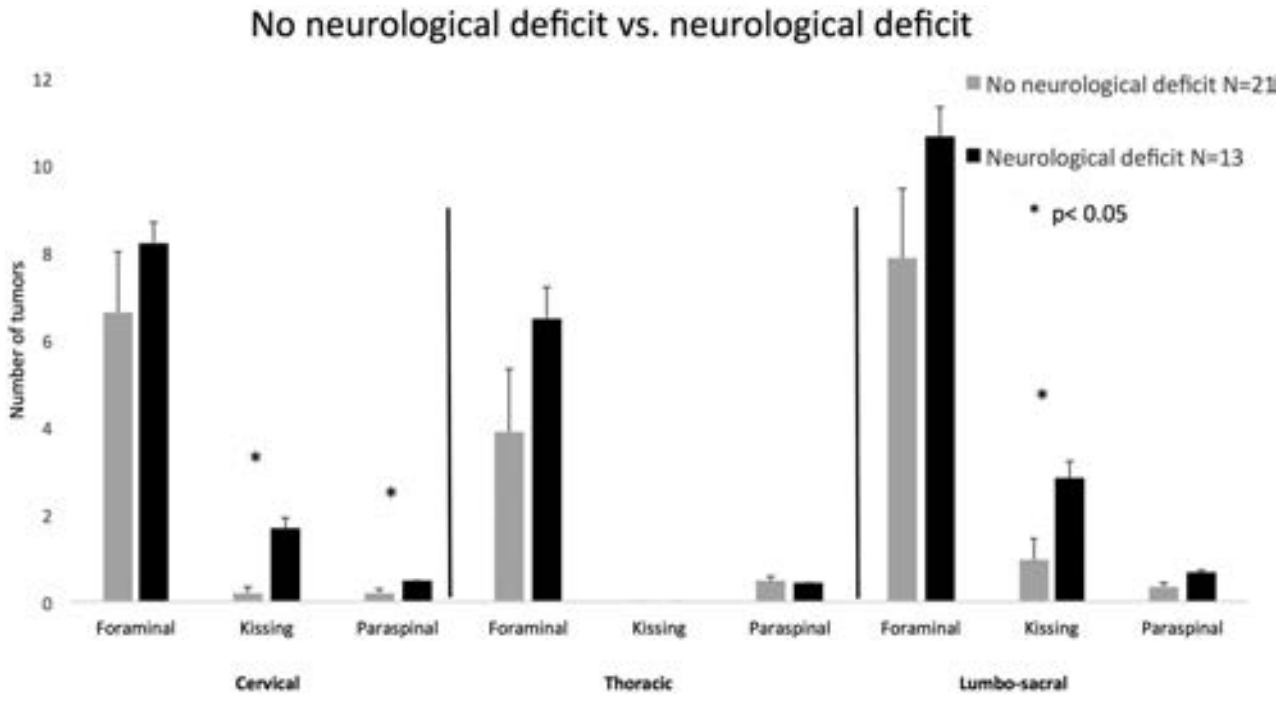

FIG 5. Spinal tumor distribution in patients with neurologic deficits and in neurologically intact patients. Patients with neurologic deficits had more paraspinal tumors in the cervical region (group 1) and more kissing NF (group 3) in the cervical and the lumbar regions. *Error bars* represent the standard error of the mean.

and radiologic follow-up. The authors did not provide radiologic correlation to neurologic deficits or to any other symptoms. The only prognostic finding in that series was an increased risk of spinal curvature abnormalities associated with paraspinal PN.[13] In 2 other studies of patients with NF1 with spinal involvement, correlation between imaging and clinical outcome was found only in the cervical region[5] or specifically for intradural involvement.[14]

Most of the patients in our series demonstrated a severe burden of spinal disease presenting with multilevel disease. This finding probably represents a selection bias because usually the more severe cases are referred to tertiary NF1 centers such as ours, with a strong neuro-oncologic and neurosurgical orientation. The follow-up period in our series is relatively long (3.5 years) with a good follow-up adherence by patients (~90%), allowing us to better evaluate the clinical and radiologic outcome.

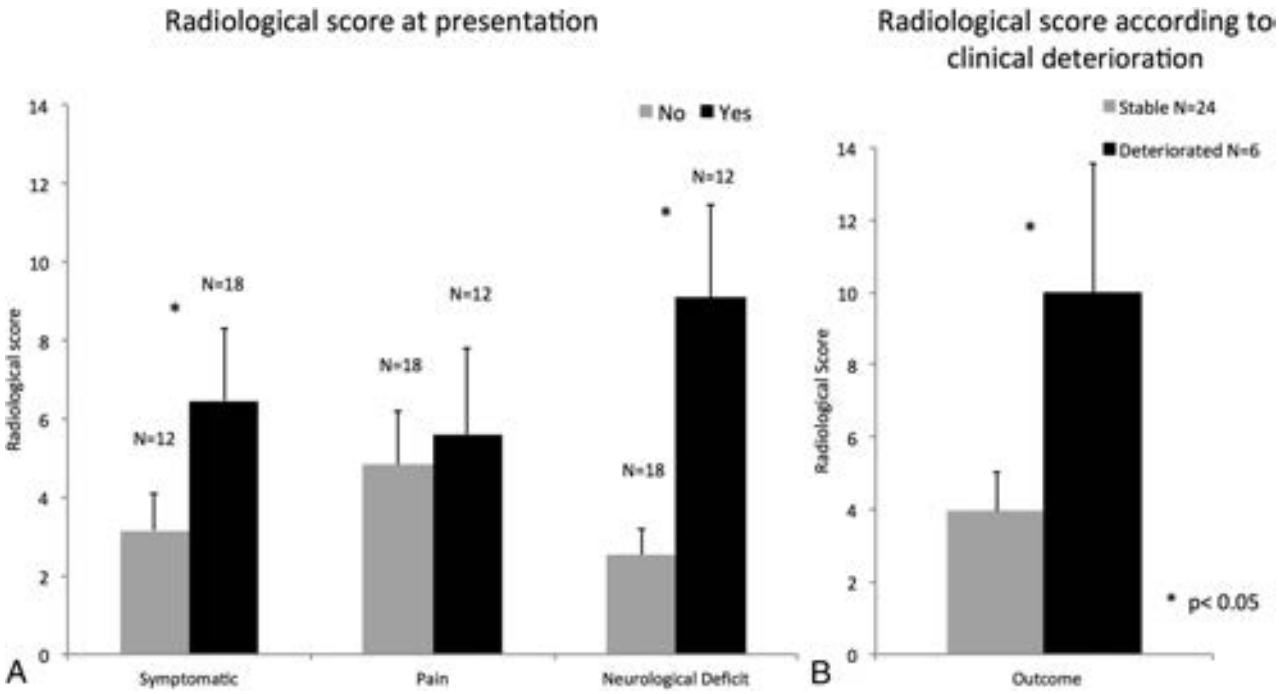

FIG 6. Radiologic risk scores for different patient groups. Symptomatic patients (with neurologic deficits and/or pain) had higher scores compared with asymptomatic patients (*A*). Patients showing neurologic deterioration had higher scores compared with patients with stable conditions (*B*).

Sixty-four percent of our patients were symptomatic at presentation; 24% had both pain and neurologic disability. In our series, only 20% of patients demonstrated clinical progression. We saw no difference in overall tumor burden at presentation between patients with progressive or stable neurologic conditions. This illustrates the lack of a simple correlation between MR imaging tumor burden and clinical outcome. We found that in general, the correlation among radiologic manifestations, clinical presentation, and outcome is limited when using traditional radiologic evaluation. This limitation motivated us to develop a radiologic risk score aimed at predicting long-term neurologic outcome.

From our data, 2 factors emerge as having a significant influence on a patient's neurologic outcome: kissing neurofibromas in the cervical spine and paraspinal lumbar tumors. In addition, intradural tumors, as expected, tend to cause significant neurologic morbidity as well. We incorporated all of these cardinal radiologic risk factors into a simple, easy-to-use radiologic risk score. This score has shown a good correlation with the clinical condition at presentation, with significantly higher scores in symptomatic patients with disease-associated neurologic deficits (Fig 6*A*). In addition, individual patient scores were highly predictive of clinical progression. Patients with neurologic deterioration had an average score of ~10 compared with an average score of ~4 in patients with clinically stable conditions (Fig 6*B*).

This new scoring system, though requiring further validation in prospective, long-term follow-up studies, may aid in risk stratification of a patient with complex spinal NF1, assist in determining radiologic and clinical follow-up intervals, and help clarify the need for medical treatment. In addition, these risk factors should be taken into account when presented independently, in cases in which the risk score is unusable.

This work has a few methodologic limitations. First, the historical cohort design has the shortcomings of any retrospective study. In addition, the numbers in our series are limited; this feature necessitated minimally reduced statistical significance levels in some of the analysis. Another shortcoming is the design of our radiologic risk score, which was built for patients with high disease burden and probably will not serve to predict neurologic deterioration or indicate the need for surgical intervention in patients with a single spinal tumor or a limited disease burden.

We believe that our study helps to characterize and classify the challenging population of patients with NF1 with spinal involvement.

CONCLUSIONS

In this limited series, 3 factors were found to be highly correlated with neurologic deficit: paraspinal tumors in the cervical region, kissing neurofibromas in the cervical region, and intradural lesions. Pain was not correlated with tumor burden in any of the spinal segments. Our innovative radiologic classification and scoring system produces a risk score that is significantly associated with the neurologic impairment and clinical progression. This score may aid in identifying patients who have an increased risk of neurologic deterioration and the need for a future operation, based on their imaging at presentation.

REFERENCES

1. Restrepo CS, Riascos RF, Hatta AA, et al. **Neurofibromatosis type 1: spinal manifestations of a systemic disease.** *J Comput Assist Tomogr* 2005;29:532–39 CrossRef Medline
2. Uusitalo E, Leppävirta J, Koffert A, et al. **Incidence and mortality of neurofibromatosis: a total population study in Finland.** *J Invest Dermatol* 2015;135:904–06 CrossRef Medline

3. **Neurofibromatosis: conference statement—National Institutes of Health Consensus Development Conference.** *Arch Neurol* 1988;45: 575–78 Medline
4. Patel NB, Stacy GS. **Musculoskeletal manifestations of neurofibromatosis type 1.** *AJR Am J Roentgenol* 2012;199:W99–106 CrossRef Medline
5. Taleb FS, Guha A, Arnold PM, et al. **Surgical management of cervical spine manifestations of neurofibromatosis type 1: long-term clinical and radiological follow-up in 22 cases.** *J Neurosurg Spine* 2011; 14:356–66 CrossRef Medline
6. Goertz O, Langer S, Uthoff D, et al. **Diagnosis, treatment and survival of 65 patients with malignant peripheral nerve sheath tumors.** *Anticancer Res* 2014;34:777–83 Medline
7. Weiss B, Widemann BC, Wolters P, et al. **Sirolimus for progressive neurofibromatosis type 1-associated plexiform neurofibromas: a neurofibromatosis Clinical Trials Consortium phase II study.** *Neuro Oncol* 2015;17:596–603 CrossRef Medline
8. Jakacki RI, Dombi E, Steinberg SM, et al. **Phase II trial of pegylated interferon alfa-2b in young patients with neurofibromatosis type 1 and unresectable plexiform neurofibromas.** *Neuro Oncol* 2017;19: 289–97 CrossRef Medline
9. Ferguson MJ, Rhodes SD, Jiang L, et al. **Preclinical evidence for the use of sunitinib malate in the treatment of plexiform neurofibromas.** *Pediatr Blood Cancer* 2016;63:206–13 CrossRef Medline
10. Dombi E, Baldwin A, Marcus LJ, et al. **Activity of selumetinib in neurofibromatosis type 1–related plexiform neurofibromas.** *N Engl J Med* 2016;375:2550–60 CrossRef Medline
11. Ruggieri M, Polizzi A, Spalice A, et al. **The natural history of spinal neurofibromatosis: a critical review of clinical and genetic features.** *Clin Genet* 2015;87:401–10 CrossRef Medline
12. Jinnai T, Koyama T. **Clinical characteristics of spinal nerve sheath tumors: analysis of 149 cases.** *Neurosurgery* 2005;56:510–15; discussion 510–15 CrossRef Medline
13. Nguyen R, Dombi E, Akshintala S, et al. **Characterization of spinal findings in children and adults with neurofibromatosis type 1 enrolled in a natural history study using magnetic resonance imaging.** *J Neurooncol* 2015;121:209–15 CrossRef Medline
14. Patronas NJ, Courcoutsakis N, Bromley CM, et al. **Intramedullary and spinal canal tumors in patients with neurofibromatosis 2: MR imaging findings and correlation with genotype.** *Radiology* 2001; 218:434–42 CrossRef Medline

3D Pseudocontinuous Arterial Spin-Labeling MR Imaging in the Preoperative Evaluation of Gliomas

Q. Zeng, B. Jiang, F. Shi, C. Ling, F. Dong, and J. Zhang

ABSTRACT

BACKGROUND AND PURPOSE: Previous studies showed conflicting results concerning the value of CBF maps obtained from arterial spin-labeling MR imaging in grading gliomas. This study was performed to investigate the effectiveness of CBF maps derived from 3D pseudocontinuous arterial spin-labeling in preoperatively assessing the grade, cellular proliferation, and prognosis of gliomas.

MATERIALS AND METHODS: Fifty-eight patients with pathologically confirmed gliomas underwent preoperative 3D pseudocontinuous arterial spin-labeling. The receiver operating characteristic curves for parameters to distinguish high-grade gliomas from low-grade gliomas were generated. Pearson correlation analysis was used to assess the correlation among parameters. Survival analysis was conducted with Cox regression.

RESULTS: Both maximum CBF and maximum relative CBF were significantly higher in high-grade gliomas than in low-grade gliomas ($P <$ .001). The areas under the curve for maximum CBF and maximum relative CBF in distinguishing high-grade gliomas from low-grade gliomas were 0.828 and 0.863, respectively. Both maximum CBF and maximum relative CBF had no correlation with the Ki-67 index in all subjects and had a moderate negative correlation with the Ki-67 index in glioblastomas ($r = -0.475, -0.534$, respectively). After adjustment for age, a higher maximum CBF ($P = .008$) and higher maximum relative CBF ($P = .005$) were associated with worse progression-free survival in gliomas, while a higher maximum relative CBF ($P = .033$) was associated with better overall survival in glioblastomas.

CONCLUSIONS: 3D pseudocontinuous arterial spin-labeling–derived CBF maps are effective in preoperative evaluation of gliomas. Although gliomas with a higher blood flow are more malignant, glioblastomas with a lower blood flow are likely to be more aggressive.

ABBREVIATIONS: ASL = arterial spin-labeling; CASL = continuous ASL; GBM = glioblastoma; HGG = high-grade glioma; HR = hazard ratio; KPS = Karnofsky Performance Scale; LGG = low-grade glioma; max = maximum; OS = overall survival; pCASL = pseudocontinuous ASL; PFS = progression-free survival; ROC = receiver operating characteristic; WHO = World Health Organization

Glioma is the most common intracranial malignant tumor, accounting for almost 80% of primary malignant brain tumors.[1] Grading of gliomas is important for an optimal therapy plan and predicting outcome.[2,3] According to the World Health Organization (WHO) criteria, gliomas can be classified into 4 groups: grades I–IV. Grade I and grade II gliomas are considered low-grade gliomas (LGGs), while grade III and grade IV gliomas are regarded as high-grade gliomas (HGGs).

Advanced MR imaging techniques, such as MR perfusion, have been shown to be more effective than conventional MR imaging techniques in grading gliomas.[4,5] Dynamic susceptibility contrast perfusion imaging is the reference standard for evaluating tumor perfusion.[6,7] However, this technique relies on the intravenous application of a contrast medium, which is not suitable for patients who are allergic to this medium or who have renal failure.[8,9]

Arterial spin-labeling (ASL) is a noninvasive MR perfusion imaging technique for obtaining CBF maps. Some previous studies based on pulsed ASL and continuous ASL (CASL) have shown that the ASL-derived CBF maps have potential value in grading gliomas[8,10-15] and predicting their progression.[9,16,17] However, although pseudocontinuous ASL (pCASL) is considered an improved method over pulsed ASL and CASL,[18-20] a recent study reported that pCASL-derived CBF maps failed to accurately grade gliomas.[21]

Received February 8, 2017; accepted after revision May 22.

From the Departments of Neurosurgery (Q.Z., C.L., J.Z.), Radiology (B.J., F.D.), and Neurology (F.S.), Second Affiliated Hospital of Zhejiang University School of Medicine, Hangzhou, Zhejiang, China; and Brain Research Institute (J.Z.) and Collaborative Innovation Center for Brain Science (J.Z.), Zhejiang University, Hangzhou, Zhejiang, China.

This work was supported by the Natural Science Foundation of Zhejiang (grant No. LY13H180006) and the Medicine and Health Research Foundation of Hangzhou (grant No. 20140633B25).

Please address correspondence to Jianmin Zhang, MD, Department of Neurosurgery, Second Affiliated Hospital of Zhejiang University School of Medicine, 88 Jiefang Rd, Hangzhou, Zhejiang, China, 310009; e-mail: zjm135@vip.sina.com

Indicates open access to non-subscribers at www.ajnr.org

http://dx.doi.org/10.3174/ajnr.A5299

On the other hand, according to many previous studies, gliomas with higher tumor blood flow are commonly more malignant.[8-17] However, a recent study found a positive correlation between proliferation activity and levels of a hypoxia biomarker in glioblastoma (GBM),[22] suggesting that GBM with a lower blood flow might be more aggressive. Hence, the correlation between relative CBF and the grade of malignancy might be more complex in gliomas.

The purpose of this study was to examine the value of the CBF maps derived from 3D pCASL in preoperatively assessing the grade, cellular proliferation, and prognosis of gliomas. Additionally, we performed a subgroup analysis on patients with GBM.

MATERIALS AND METHODS

Patients

This was a retrospective study based on data collected from our prospective cohort of patients with gliomas who were hospitalized at the Department of Neurosurgery, Second Affiliated Hospital of Zhejiang University School of Medicine, between August 2013 and January 2015. This study was approved by the local ethics review board and was conducted in accordance with the ethical principles of the Declaration of Helsinki. Written informed consent was obtained from all participants. Fifty-eight patients with supratentorial cerebral gliomas, who underwent a preoperative MR imaging examination with a 3D pCASL sequence, were enrolled in this study. The preoperative Karnofsky Performance Scale (KPS) was administered in all patients when they were admitted to the hospital.

Imaging Data Acquisition

All subjects underwent MR imaging on a 3T system (Discovery MR750; GE Healthcare, Milwaukee, Wisconsin) with an 8-channel high-resolution receiver head coil. The CBF images were acquired with a 3D pCASL sequence with the following parameters: section thickness, 4 mm; number of sections, 36; FOV, 240 × 240 mm; matrix, 128 × 128; TR, 4632 ms; TE, 10.5 ms; flip angle, 111°; number of excitations, 3; labeling duration, 1450 ms; postlabeling duration, 1525 ms; and pixel bandwidth, 976.6 Hz/pixel. The scan time for this sequence was 4 minutes 29 seconds. In addition, a contrast-enhanced T2-FLAIR sequence was acquired after the injection of a gadolinium contrast agent.

Pathology

The median time interval between preoperative MR imaging and the operation was 4 days (range, 1–10 days). Three patients underwent only stereotactic biopsy, and the others underwent craniotomy. The histopathologic diagnosis was performed by pathologists on the basis of the WHO 2007 criteria.

The Ki-67 proliferating index was reported in 45 patients. In each case, areas with the highest number of positive-staining tumor nuclei were selected for calculating the Ki-67 index. According to previous literature,[23,24] patients with a Ki-67 index of ≥30% were assigned to the high Ki-67 index group and patients with a Ki-67 index of <30% were assigned to the low Ki-67 index group.

Follow-Up

Three patients who underwent stereotactic biopsy and 2 patients who died of operative complications were excluded in the postoperative follow-up. Among the other 53 patients, only 2 (3.9%) were lost to follow-up. Thus, 51 patients were included in the survival analysis. The median follow-up time was 30 months (range, 24–36 months). Overall survival (OS) was defined as the time from diagnosis until either death or the time the patient was last known to be alive (censused), and progression-free survival (PFS) was defined as the time from diagnosis until tumor progression, recurrence, or death or when the patient was last known to be alive (censused).[25]

Image Processing and Analysis

The CBF images were all coregistered to the contrast-enhanced T2-FLAIR images by using SPM12 (www.fil.ion.ucl.ac.uk/spm). The analysis of the images was performed with ImageJ, Version 1.49 (National Institutes of Health, Bethesda, Maryland). The ROIs were manually placed on the contrast-enhanced T2-FLAIR images by 1 expert neuroradiologist with 20 years' experience, who was blinded to the pathology of the tumors. Before ROIs were drawn, the image section that was speculated to contain the tumor area with the highest tumor blood flow was chosen by referring to the CBF maps. Areas with an abnormal signal in the enhanced T2-FLAIR images were all included. Another rectangular ROI was drawn to include contralateral gray matter areas. Then ROIs were copied to the corresponding CBF maps, as shown in Fig 1. The maximum CBF values (CBF_{max}) in ROIs were obtained. Then the relative CBF_{max} ($rCBF_{max}$) was calculated by dividing the CBF_{max} in the tumor ROI by the CBF_{max} in the contralateral ROI.

Interobserver Concordance

Another reader, a junior neurosurgeon who was blinded to the pathology, also delineated the ROIs of all tumors. The measurements from this reader were only used for the assessment of interobserver concordance. The $rCBF_{max}$ values measured by the 2 readers were compared by means of an intraclass correlation coefficient.

Statistical Analysis

All statistical analyses were performed with SPSS Statistics, Version 22 (IBM, Armonk, New York) and GraphPad Prism, Version 6.0 (GraphPad Software, San Diego, California). The significance level was set to $\alpha = .05$. $P < .05$ was statistically significant.

The normality assumption was tested with the Kolmogorov-Smirnov test. The data were expressed as mean ± SD. Interobserver reliability was with the intraclass correlation coefficient based on a 2-way random-effects model. The Pearson correlation analysis was used to assess the correlation among parameters.

The 1-way ANOVA followed by the Fisher least significant difference test was used to compare differences in parameters among multiple groups. The differences in parameters between the HGG and the LGG groups were compared using the independent samples *t* test. The receiver operating characteristic (ROC) curves for parameters in distinguishing HGG from LGG were generated. Optimal cutoff values were derived from ROC curves, and sensitivity, specificity, predictive values, and accuracy were calculated on the basis of these best cutoff values.

Survival analysis was conducted with the Cox regression for

both the univariate and multivariate analyses. Except for CBF parameters, 3 clinical features (age, sex, preoperative KPS) were also included in the survival analysis.

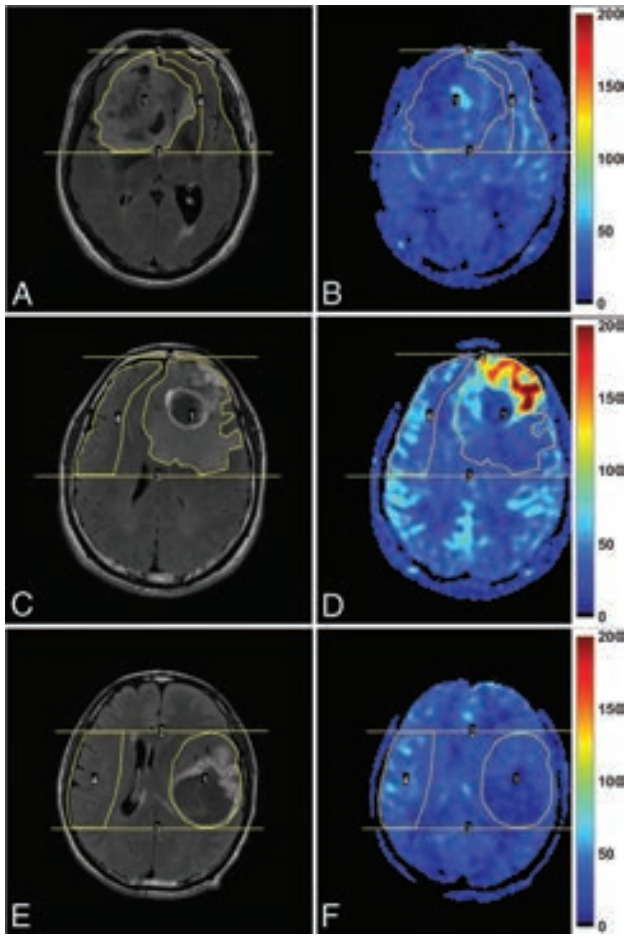

FIG 1. Enhanced T2-FLAIR images (*A*, *C*, and *E*) and CBF maps (*B*, *D*, and *F*) of a 69-year-old man with oligoastrocytoma (WHO grade II; Ki-67 index, 10%), a 42-year-old man with glioblastoma (WHO grade IV; Ki-67 index, 20%), and a 43-year-old man with glioblastoma (WHO grade IV; Ki-67 index, 60%), respectively. Note that blood flow is significantly elevated in the glioblastoma with a relatively low Ki-67 index, while it is not elevated in the glioblastoma with a very high Ki-67 index. The unit for CBF maps is milliliters/100 g/min.

Table 1: Measurements of absolute CBF_{max} and $rCBF_{max}$ in each type of pathologic tumor

Grade/Histology	No.	CBF_{max} (mL/100 g/min) Tumor	Contralateral	$rCBF_{max}$
Grade II ($n = 13$)				
Astrocytoma	5	75.4 ± 10.2[a,b]	83.2 ± 3.90	0.91 ± 0.18[c,d]
Oligoastrocytoma	4	74.8 ± 12.1[a,b]	93.2 ± 28.8	0.83 ± 0.16[c,d]
Oligodendroglioma	4	109.8 ± 47.8[e]	80.0 ± 9.6	1.38 ± 0.59[e,f]
Grade III ($n = 17$)				
Anaplastic astrocytoma	6	127.2 ± 84.8[e]	78.0 ± 23.6	1.51 ± 0.68[e,f]
Anaplastic oligoastrocytoma	7	125.1 ± 71.9[e]	82.4 ± 8.9	1.54 ± 0.88[e,f]
Anaplastic oligodendroglioma	4	212.5 ± 87.5	78.8 ± 16.6	2.75 ± 1.02
Grade IV ($n = 28$)				
Glioblastoma	28	171.5 ± 58.7	77.0 ± 10.9	2.25 ± 0.79

[a] $P < .01$, compared with glioblastoma.
[b] $P < .01$, compared with anaplastic oligoastrocytoma.
[c] $P < .001$, compared with glioblastoma.
[d] $P < .001$, compared with anaplastic oligoastrocytoma.
[e] $P < .05$, compared with anaplastic oligoastrocytoma.
[f] $P < .05$, compared with glioblastoma.

RESULTS

Patient Characteristics

Among these 58 patients with gliomas, there were 27 women and 32 men, with a mean age of 49.5 years (range, 26–76 years) and a mean KPS score of 82.9 (range, 30–100). According to the WHO 2007 criteria, there were 13 patients diagnosed with WHO grade II (astrocytomas, $n = 5$; oligoastrocytomas, $n = 4$; oligodendrogliomas, $n = 4$), 17 patients diagnosed with WHO grade III (anaplastic astrocytomas, $n = 6$; anaplastic oligoastrocytomas, $n = 7$; anaplastic oligodendrogliomas, $n = 4$), and 28 patients diagnosed with WHO grade IV (GBM, $n = 28$).

Interobserver Concordance

The manifestations of an LGG, a GBM with a low Ki-67 index, and a GBM with a high Ki-67 index in contrast-enhanced T2-FLAIR images and CBF maps are shown in Fig 1. Our evaluation of the interobserver concordance for parameters showed excellent agreement. The intraclass correlation coefficients for the measurement of tumor CBF_{max}, contralateral CBF_{max}, and $rCBF_{max}$ were as high as 0.995, 0.860, and 0.987, respectively. Furthermore, there was a very strong correlation between CBF_{max} and $rCBF_{max}$ ($r = 0.941$).

Parameters in Each Type of Pathologic Tumor

The measured parameters in each type of pathologic tumor are summarized in Table 1. The CBF_{max} of GBMs was only significantly higher than that of astrocytomas ($P = .002$) and oligoastrocytomas ($P = .005$), while the $rCBF_{max}$ of GBMs was significantly higher than that of astrocytomas ($P < .001$), oligoastrocytomas ($P < .001$), oligodendrogliomas ($P = .032$), anaplastic astrocytomas ($P = .03$), and anaplastic oligoastrocytomas ($P = .027$). Both the CBF_{max} and $rCBF_{max}$ of GBMs were lower than those of anaplastic oligodendrogliomas without statistical significance (both $P = .22$).

Both the CBF_{max} and $rCBF_{max}$ of anaplastic oligodendrogliomas were significantly higher than those of anaplastic astrocytomas ($P = .035$ and .013, respectively) and anaplastic oligoastrocytomas ($P = .027$ and .012, respectively), while those of oligodendrogliomas were higher than those of astrocytomas ($P = .4$ and .35, respectively) and oligoastrocytomas ($P = .42$ and .30, respectively) without statistical significances. Both the CBF_{max} and $rCBF_{max}$ of anaplastic oligodendrogliomas were significantly higher than those of oligodendrogliomas ($P = .021$ and .012, respectively).

The mean CBF_{max} and $rCBF_{max}$ were similar between astrocytomas and oligoastrocytomas, or between anaplastic astrocytomas and anaplastic oligoastrocytomas. No significant differences were detected among different pathologic types for contralateral CBF_{max} ($P = .50$).

Parameters in Each Tumor Grade

Both the absolute tumor CBF_{max} and $rCBF_{max}$ increased with an increase in grade of glioma, as shown in Table 2. In all gliomas, both the CBF_{max} and $rCBF_{max}$ of grade IV gliomas were significantly

higher than those of grade II gliomas ($P < .001$), and those of grade III gliomas were significantly higher than those of grade II gliomas ($P = .011$ and .009, respectively), while those of grade IV gliomas were higher than those of grade III gliomas without statistical significance ($P = .198$ and .070, respectively). After oligodendrogliomas and anaplastic oligodendrogliomas were excluded, significant differences between grade III gliomas and grade IV gliomas were detected for both CBF_{max} and $rCBF_{max}$ ($P = .025$ and .004, respectively).

Differentiation of LGG and HGG

There were significant differences between LGG and HGG for both CBF_{max} and $rCBF_{max}$ ($P < .001$), regardless of whether oligodendrogliomas and anaplastic oligodendrogliomas were excluded, as shown in Fig 2. The ROC curves for CBF_{max} and $rCBF_{max}$ in distinguishing HGG from LGG are shown in Fig 3, and the results of the ROC analysis are shown in Table 3. The area under curve, best cutoff value, sensitivity, and specificity for CBF_{max} were 0.828, 91 (mL/100 g/min), 84.4%, and 84.6%, respectively, in all gliomas and were 0.859, 91 (mL/100 g/min), 82.9%, and 100%, respectively, after oligodendrogliomas and anaplastic oligodendrogliomas were excluded. Those for $rCBF_{max}$ were 0.863, 1.19, 82.2%, and 84.6%, respectively, in all gliomas and were 0.916, 1.22, 80.5%, and 100%, respectively, after oligodendrogliomas and anaplastic oligodendrogliomas were excluded. Both CBF_{max} and $rCBF_{max}$ values allowed HGGs to be distinguished from LGGs, and the differential diagnosis was improved after oligodendrogliomas and anaplastic oligodendrogliomas were excluded.

Table 2: Measurements of absolute CBF_{max} and $rCBF_{max}$ in each WHO grade with or without the exclusion of oligodendrogliomas and anaplastic oligodendrogliomas

Patients/Grades	No.	CBF_{max} (mL/100 g/min) Tumor	CBF_{max} (mL/100 g/min) Contralateral	$rCBF_{max}$
All				
Grade II	13	85.8 ± 30.3	85.3 ± 16.4	1.03 ± 0.41
Grade III	17	146.4 ± 84.0[b]	80.0 ± 16.1	1.81 ± 0.96[c]
Grade IV	28	171.5 ± 58.7[d]	77.0 ± 10.9	2.25 ± 0.15[d]
Excluded[a]				
Grade II	9	75.1 ± 10.4	87.7 ± 18.6	0.88 ± 0.16
Grade III	13	126.1 ± 74.7[e]	80.4 ± 16.6	1.52 ± 0.77[b]
Grade IV	28	171.5 ± 58.7[d,f]	77.0 ± 10.9	2.25 ± 0.15[d,g]

[a] With oligodendrogliomas and anaplastic oligodendrogliomas excluded. Note the following *P* values in each patient group:
[b] $P < .05$, compared with grade II.
[c] $P < .01$, compared with grade II.
[d] $P < .001$, compared with grade II.
[e] $P = .05$, compared with grade II.
[f] $P < .05$, compared with grade III.
[g] $P < .01$, compared with grade III.

Correlation with the Ki-67 Index

In all patients, as shown in Fig 4, both CBF_{max} ($P = .565$) and $rCBF_{max}$ ($P = .652$) values were not correlated with the Ki-67 index. However, there was a moderate positive association between CBF_{max} and the Ki-67 index in the low Ki-67 index group ($P = .029$, $r = 0.399$), and a high inverse association between CBF_{max} and the Ki-67 index in the high Ki-67 index group ($P < .001$, $r = -0.775$). Similarly, $rCBF_{max}$ had a moderate positive correlation with the Ki-67 index in the lower Ki-67 index group ($P = .017$, $r = 0.432$) and a high inverse correlation with the Ki-67 index in the high Ki-67 index group ($P < .001$, $r = -0.784$). In addition, in GBM, both CBF_{max} ($P = .017$, $r = -0.475$) and rCBFmax ($P = .006$, $r = -0.534$) showed a moderate negative correlation with the Ki-67 index.

Survival Analysis

Fifty-one patients (13 grade II, 13 grade III, 25 grade IV) were included in the survival analysis. Table 4 shows the results obtained with the univariate Cox model for PFS and OS in both gliomas and GBMs. Sex had no association with PFS or OS in both gliomas and GBMs (all data, $P > .5$). In gliomas, higher CBF_{max}, higher $rCBF_{max}$, older age, and lower KPS were associated with worse PFS (hazard ratio [HR] = 1.005, 1.670, 1.036, 0.971, respectively; all data, $P < .05$), while CBF_{max} and $rCBF_{max}$ were not prognosis factors for OS ($P = .244$ and .232, respectively). In GBMs, lower CBF_{max}, lower $rCBF_{max}$, and older age tended to be associated with worse OS without statistical significances (HR = 0.993, 0.563, 1.030, respectively; $P = .070$, .065, and .103, respectively), while CBF_{max} and $rCBF_{max}$ were not associated with PFS ($P = .497$ and .644, respectively).

Either CBF_{max} or $rCBF_{max}$ were included in the multivariate Cox analysis for PFS in gliomas, together with age and KPS. Furthermore, CBF_{max} or $rCBF_{max}$ were also included in the multivariate Cox analysis for OS in GBM, together with age. The results showed that $rCBF_{max}$ was a significant independent prognostic factor for PFS in gliomas

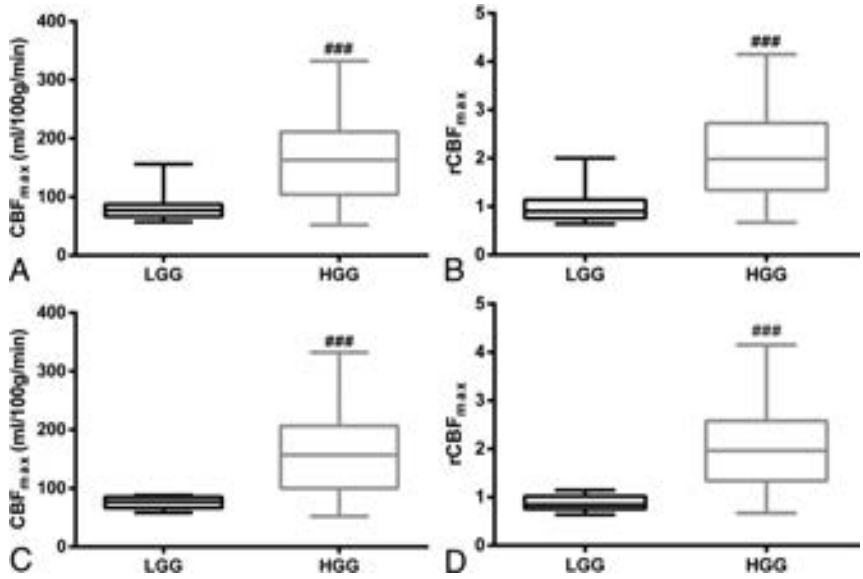

FIG 2. Boxplots of CBF_{max} (*A*) and $rCBF_{max}$ (*B*) in low-grade gliomas and high-grade gliomas for all subjects. The boxplots of CBF_{max} (*C*) and $rCBF_{max}$ (*D*) in LGGs and HGGs after the oligodendrogliomas and anaplastic oligodendrogliomas were excluded. ### indicates $P < .001$, compared with LGG.

($P = .005$) and OS in GBMs ($P = .033$), while CBF_{max} was only a significant independent prognosis factor for PFS in gliomas ($P = .008$), shown in Table 5. After adjustment for age, higher CBF_{max} (HR = 1.007) and higher $rCBF_{max}$ (HR = 1.707) were associated with worse PFS in gliomas, while higher $rCBF_{max}$ (HR = 0.490) was associated with better OS in GBM.

DISCUSSION

In this study, 3D pCASL-derived CBF maps were found to be effective in preoperatively assessing the grade and prognosis in gliomas. Another interesting finding was that CBF_{max} and $rCBF_{max}$ showed a dual relationship with the degree of malignancy in gliomas. In accordance with previous studies based on pulsed ASL and CASL,[8-17] both CBF_{max} and $rCBF_{max}$ obtained from pCASL increased with increasing grade of gliomas, and gliomas with higher CBF_{max} and $rCBF_{max}$ were associated with worse PFS. These findings suggest that gliomas with higher $rCBF_{max}$ are associated with a higher degree of malignancy. However, in GBMs, both CBF_{max} and $rCBF_{max}$ were found to have a significant negative correlation with the Ki-67 index. Also, GBMs with a lower $rCBF_{max}$ were associated with worse OS after adjustment for age. Thus, GBMs with lower blood flow seemed to be more aggressive.

Unlike quantification methods of DSC MR imaging, which require an accurate arterial input function, 1 advantage of the ASL sequence is that it can provide an absolute quantification of CBF.[9] In our study, a very strong correlation between CBF_{max} and $rCBF_{max}$ was reported. The results of $rCBF_{max}$ were similar to those of CBF_{max} in grading gliomas and evaluating the Ki-67 index, while $rCBF_{max}$ seemed to be more valuable in predicting the prognosis of gliomas and GBMs. These results suggest that ASL-derived absolute CBF is also useful in evaluating gliomas.

However, compared with the DSC perfusion MR imaging, one limitation of the application of ASL is the relatively low SNR.[15,20]

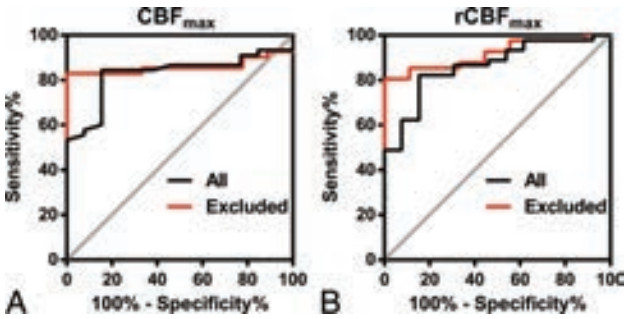

FIG 3. Receiver operating characteristic curves of CBF_{max} (*A*) and $rCBF_{max}$ (*B*) in distinguishing high- from low-grade gliomas, without (*black line*) or with (*red line*) oligodendrogliomas and anaplastic oligodendrogliomas excluded.

Table 3: ROC curve analyses of CBF_{max} and $rCBF_{max}$ in discriminating high- and low-grade gliomas

Parameters/Patients	AUC	Youden Index	Cutoff Value	Sensitivity (%)	Specificity (%)	PPV (%)	NPV (%)	Accuracy (%)
CBF_{max}								
All	0.828	0.690	91 mL/100 g/min	84.4	84.6	95.0	61.1	84.5
Excluded[a]	0.859	0.829	91 mL/100 g/min	82.9	100	100	56.3	86.0
$rCBF_{max}$								
All	0.863	0.668	1.19	82.2	84.6	94.9	57.9	82.8
Excluded[a]	0.916	0.805	1.22	80.5	100	100	52.9	84.0

Note:—AUC indicates area under the curve; PPV, positive predictive value; NPV, negative predictive value.
[a] With oligodendrogliomas and anaplastic oligodendrogliomas excluded.

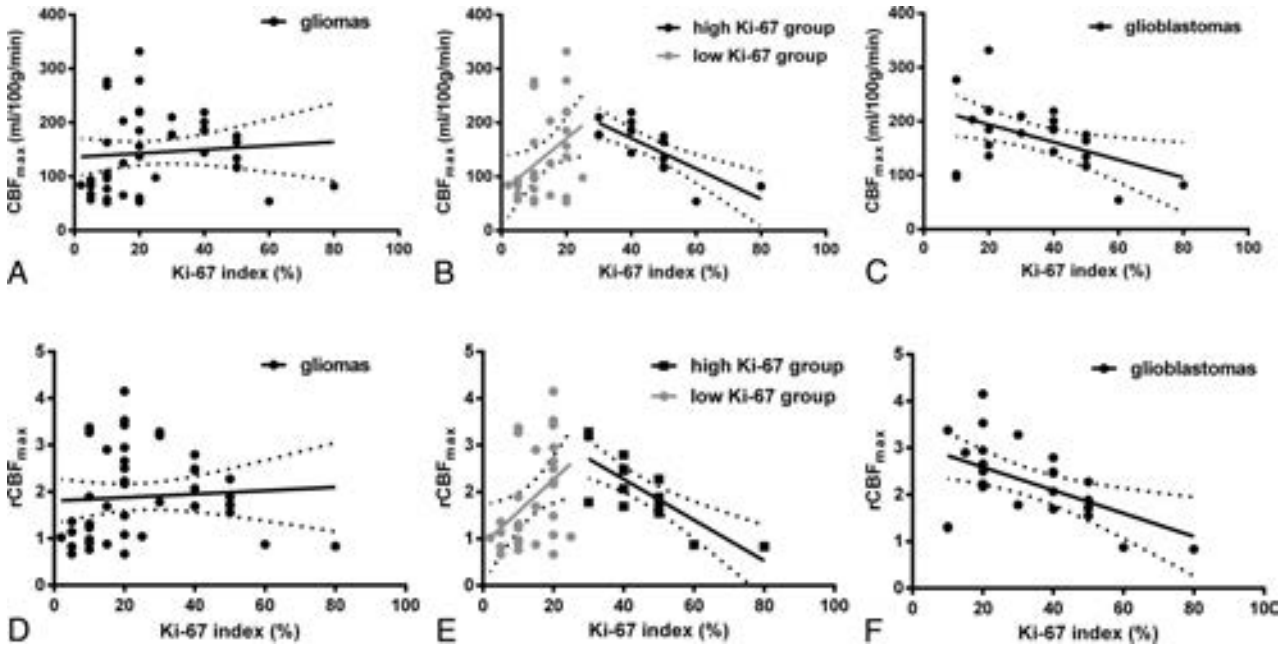

FIG 4. The linear regression of CBF_{max} (*A–C*) and $rCBF_{max}$ (*D–F*) with the Ki-67 index in all subjects (*A* and *D*), in the low and high Ki-67 groups (*B* and *E*), and in glioblastomas (*C* and *F*). The low Ki-67 group included patients with a Ki-67 index of <30%, and the high Ki-67 group included patients with a Ki-67 index of ≥30%.

CASL is an improved method, providing a higher tagging efficiency compared with pulsed ASL.[18] However, because of magnetization transfer effects, the magnetization in the target tissues will be reduced, which limits the application of this method.[18] In 2005, Garcia el al[19] proposed the pCASL method to overcome this disadvantage, and this method can improve not only the SNR but also the accuracy of CBF measurements.[18,20] Previous studies have shown that the pulsed ASL–derived and CASL-derived CBF maps have potential value in grading gliomas.[8,10-15] In the current study, pCASL-derived CBF maps were also found to be effective in grading gliomas. However, a previous study indicated that pCASL-derived CBF maps were unable to grade gliomas, in contradiction to our results.[21] In that study, compared with relative CBF derived from the dynamic contrast-enhanced MR imaging, the ASL-derived relative CBF was found to be relatively higher in LGGs but lower in HGGs. The potential explanation is not clear. More research may be required to evaluate the reliability of the CBF maps derived from pCASL.

Oligodendrogliomas and anaplastic oligodendrogliomas exhibit elevated relative CBV compared with astrocytic tumors of the same histologic grade.[26,27] Similarly, our study also found that both CBF_{max} and $rCBF_{max}$ were clearly elevated in oligodendrogliomas (not statistically significant) and anaplastic oligodendrogliomas (statistically significant) compared with other pathologic subtypes of the same histologic grade. In accordance with previous studies based on relative CBV,[26] ability of the CBF_{max} and $rCBF_{max}$ values in differentiating HGGs from LGGs improved after we excluded oligodendrogliomas and anaplastic oligodendrogliomas.

Furthermore, our results demonstrated a significantly higher CBF_{max} and $rCBF_{max}$ in anaplastic oligodendrogliomas than in oligodendrogliomas. These results conflicted with those of a previous study based on CASL-derived CBF_{max}.[12] However, a recent study by Fellah et al,[28] based on DSC-derived relative CBF, reported a result similar to that in our study. Several previous studies have also shown a significantly higher relative CBV in anaplastic oligodendrogliomas than in oligodendrogliomas,[28-31] while some other studies have reported a conflicting result.[32-34] The ability of perfusion parameters to distinguish oligodendrogliomas and anaplastic oligodendrogliomas needs to be evaluated further.

A previous study by Mayer et al[22] showed a positive correlation between proliferative activity and the level of a hypoxia biomarker in GBM. This molecular pathology finding is consistent with our finding that the Ki-67 index had a negative correlation with CBF_{max} and $rCBF_{max}$ in GBMs. However, the potential mechanism is not clear. Evans et al[35] found that higher grade gliomas were associated with more hypoxia. It is widely accepted that hypoxia will lead to the activation of the transcription of hypoxia-inducible factor-1 via stabilization of its α subunit.[36-38] One potential mechanism of this may result in lower tumor blood flow in GBMs, which causes severe hypoxia and, in turn, the activation of the transcription of hypoxia-inducible factor-1, leading to high proliferative activity through further downstream pathways. Another potential mechanism might be due to the inability of angiogenesis to keep up with tumor cell proliferation in certain GBMs that have a high proliferative activity. The explicit mechanism needs to be investigated further.

On the other hand, our study also found that GBMs with a lower $rCBF_{max}$ were associated with a worse OS but showed no association with PFS. This finding also suggests that a GBM with lower blood flow may cause severe hypoxia, causing it to become increasingly malignant. Some other studies have also found that hypoxia in GBM is related to a poor prognosis,[39] yet 2 previous studies based on ASL-derived CBF maps have reported a contradictory result.[16,17] However, 1 of those contradictory studies involved only 18 gliomas,[16] and another contradictory study had only performed qualitative analysis,[17] which reduced their reliability. It is well-known that the activity of hypoxia-inducible factor-1α–mediated pathways due to hypoxia will lead to migration and invasion of tumor cells.[40,41] In addi-

Table 4: Univariate Cox model for progression-free survival and overall survival in patients with gliomas and glioblastomas

	PFS			OS		
Variables	HR	95% CI	*P* Value	HR	95% CI	*P* Value
Gliomas ($n = 51$)						
Age	1.036	1.009–1.063	.008	1.043	1.014–1.073	.004
Sex[a]	0.957	0.670–1.368	.811	0.896	0.606–1.325	.582
KPS	0.971	0.953–0.989	.002	0.970	0.952–0.988	.002
CBF_{max}	1.005	1.001–1.010	.027	1.003	0.998–1.008	.244
$rCBF_{max}$	1.670	1.149–2.427	.007	1.246	0.869–1.785	.232
GBM ($n = 25$)						
Age	1.036	1.002–1.072	.039	1.030	0.994–1.067	.103
Sex[a]	0.851	0.547–1.323	.851	0.870	0.548–1.381	.555
KPS	0.986	0.963–1.008	.215	0.987	0.965–1.009	.242
CBF_{max}	0.997	0.989–1.005	.497	0.993	0.985–1.001	.070
$rCBF_{max}$	0.865	0.467–1.601	.644	0.563	0.306–1.035	.065

[a] Female versus male.

Table 5: Multivariate Cox model for progression-free survival in patients with gliomas and overall survival in patients with glioblastomas

		PFS in Gliomas			OS in GBM		
Parameters	Variables	HR	95% CI	*P* Value	HR	95% CI	*P* Value
Multivariate Cox model including CBF_{max}	CBF_{max}	1.007	1.002–1.012	.008	0.992	0.984–1.001	.066
	Age	1.043	1.015–1.071	.002	1.030	0.995–1.067	.097
	KPS[a]	–	–	.131[b]	–	–	–
Multivariate Cox model including $rCBF_{max}$	$rCBF_{max}$	1.707	1.174–2.483	.005	0.490	0.254–0.943	.033
	Age	1.038	1.011–1.065	.006	1.037	1.001–1.074	.045
	KPS[a]	–	–	.233[b]	–	–	–

[a] KPS was not included in the multivariate Cox analysis for OS in glioblastomas.
[b] Only the *P* value was presented for the variable, which was excluded from the Cox model with $P > .10$.

tion, hypoxia is known to induce resistance to radiation therapy and chemotherapy through several mechanisms.[42,43] This could explain why GBMs with a lower blood flow were more aggressive and were associated with a worse OS.

However, a previous study by Law et al[44] in 2008 found that GBMs with high relative CBV were significantly associated with a poor OS, while another study by Deike et al[45] in 2016 suggested that GBMs with a low blood supply may be associated with poor OS. The difference in results between these studies may be due to the different postoperative treatment strategies. Currently, concomitant radiochemotherapy has become the standard treatment for GBMs, and sometimes bevacizumab is also used to treat recurrent GBMs. Thus, resistance to radiation therapy and chemotherapy is now playing a more important role than before in the treatment of GBMs and will clearly influence the OS of patients with GBMs. A prospective study enrolling relatively large samples is needed to accurately evaluate the role of perfusion parameters in predicting the outcome of GBMs.

There were some limitations in our research. First, the sample size used for this study was not very large; therefore, some of the results may not be completely reliable, especially the results from the subgroup analysis. Further studies enrolling larger samples are needed to verify these results. Second, the postcontrast T2-FLAIR images were consulted when drawing the ROIs, so the ROI selection method presented in our study was not an accurate portrayal of a blind study. However, the resulting bias is hardly avoided, and it has also existed in many previous studies.[8-14] Compared with previous ROI selection methods, the method presented in our study is relatively objective, with an excellent intraclass correlation coefficient. Third, molecular pathology for gliomas, such as 1p19q deletion and *IDH1/2* mutations, was not routinely examined in our study. Further studies dividing gliomas or GBMs into subgroups by molecular pathology may provide further useful information.

CONCLUSIONS

3D pCASL-derived CBF maps are effective in preoperative evaluation of gliomas. Although gliomas with higher blood flow are associated with a higher degree of malignancy, GBMs with a lower blood flow are likely to be more aggressive.

ACKNOWLEDGMENTS

We thank Professor Yi Shen from the Department of Public Health, Zhejiang University School of Medicine, for his assistance in statistics, and Harry Lee from Zhejiang University for his assistance in editing the manuscript.

Disclosures: Qiang Zeng—*RELATED*: *Grant*: Hangzhou Municipal Health Bureau; *UNRELATED*: *Employment*: Second Affiliated Hospital of Zhejiang University College of Medicine. Biao Jiang—*RELATED*: *Grant*: Zhejiang Provincial Natural Science Foundation Committee; *UNRELATED*: *Employment*: Second Affiliated Hospital of Zhejiang University College of Medicine. Chenhan Ling—*RELATED*: *Grant*: Hangzhou Municipal Health Bureau; *UNRELATED*: *Employment*: Second Affiliated Hospital of Zhejiang University College of Medicine. Fei Dong—*UNRELATED*: *Employment*: Second Affiliated Hospital of Zhejiang University College of Medicine. Jianmin Zhang—*UNRELATED*: *Employment*: Second Affiliated Hospital of Zhejiang University College of Medicine; *Grants/Grants Pending*: The National Natural Science Foundation of China.

REFERENCES

1. Schwartzbaum JA, Fisher JL, Aldape KD, et al. **Epidemiology and molecular pathology of glioma.** *Nat Clin Pract Neurol* 2006;2:494–503 CrossRef Medline
2. Weller M, van den Bent M, Hopkins K, et al; European Association for Neuro-Oncology (EANO) Task Force on Malignant Glioma. **EANO guideline for the diagnosis and treatment of anaplastic gliomas and glioblastoma.** *Lancet Oncol* 2014;15:e395–e403 CrossRef Medline
3. Soffietti R, Baumert BG, Bello L, et al; European Federation of Neurological Societies. **Guidelines on the management of low-grade gliomas: report of an EFNS-EANO Task Force.** *Eur J Neurol* 2010;17:1124–33 CrossRef Medline
4. Roy B, Gupta RK, Maudsley AA, et al. **Utility of multiparametric 3-T MRI for glioma characterization.** *Neuroradiology* 2013;55:603–13 CrossRef Medline
5. Nguyen TB, Cron GO, Perdrizet K, et al. **Comparison of the diagnostic accuracy of DSC- and dynamic contrast-enhanced MRI in the preoperative grading of astrocytomas.** *AJNR Am J Neuroradiol* 2015;36:2017–22 CrossRef Medline
6. Knopp EA, Cha S, Johnson G, et al. **Glial neoplasms: dynamic contrast-enhanced T2*-weighted MR imaging.** *Radiology* 1999;211:791–98 CrossRef Medline
7. Law M, Yang S, Babb JS, et al. **Comparison of cerebral blood volume and vascular permeability from dynamic susceptibility contrast-enhanced perfusion MR imaging with glioma grade.** *AJNR Am J Neuroradiol* 2004;25:746–55 Medline
8. Furtner J, Schöpf V, Schewzow K, et al. **Arterial spin-labeling assessment of normalized vascular intratumoral signal intensity as a predictor of histologic grade of astrocytic neoplasms.** *AJNR Am J Neuroradiol* 2014;35:482–89 CrossRef Medline
9. Rau MK, Braun C, Skardelly M, et al. **Prognostic value of blood flow estimated by arterial spin labeling and dynamic susceptibility contrast-enhanced MR imaging in high-grade gliomas.** *J Neurooncol* 2014;120:557–66 CrossRef Medline
10. Fudaba H, Shimomura T, Abe T, et al. **Comparison of multiple parameters obtained on 3T pulsed arterial spin-labeling, diffusion tensor imaging, and MRS and the Ki-67 labeling index in evaluating glioma grading.** *AJNR Am J Neuroradiol* 2014;35:2091–98 CrossRef Medline
11. Kim HS, Kim SY. **A prospective study on the added value of pulsed arterial spin-labeling and apparent diffusion coefficients in the grading of gliomas.** *AJNR Am J Neuroradiol* 2007;28:1693–99 CrossRef Medline
12. Chawla S, Wang S, Wolf RL, et al. **Arterial spin-labeling and MR spectroscopy in the differentiation of gliomas.** *AJNR Am J Neuroradiol* 2007;28:1683–89 CrossRef Medline
13. Warmuth C, Gunther M, Zimmer C. **Quantification of blood flow in brain tumors: comparison of arterial spin labeling and dynamic susceptibility-weighted contrast-enhanced MR imaging.** *Radiology* 2003;228:523–32 CrossRef Medline
14. Kim MJ, Kim HS, Kim JH, et al. **Diagnostic accuracy and interobserver variability of pulsed arterial spin labeling for glioma grading.** *Acta Radiol* 2008;49:450–57 CrossRef Medline
15. Wolf RL, Wang J, Wang S, et al. **Grading of CNS neoplasms using continuous arterial spin labeled perfusion MR imaging at 3 Tesla.** *J Magn Reson Imaging* 2005;22:475–82 CrossRef Medline
16. Furtner J, Bender B, Braun C, et al. **Prognostic value of blood flow measurements using arterial spin labeling in gliomas.** *PLoS One* 2014;9:e99616 CrossRef Medline
17. Qiao XJ, Ellingson BM, Kim HJ, et al. **Arterial spin-labeling perfusion MRI stratifies progression-free survival and correlates with epidermal growth factor receptor status in glioblastoma.** *AJNR Am J Neuroradiol* 2015;36:672–77 CrossRef Medline
18. Wong EC. **New developments in arterial spin labeling pulse sequences.** *NMR Biomed* 2013;26:887–91 CrossRef Medline
19. Garcia DM, De Bazelaire C, Alsop D. **Pseudo-continuous flow driven adiabatic inversion for arterial spin labeling.** *Proc Int Soc Magn Reson Med* 2005;13:37

20. Fernández-Seara MA, Edlow BL, Hoang A, et al. **Minimizing acquisition time of arterial spin labeling at 3T.** *Magn Reson Med* 2008;59:1467–71 CrossRef Medline
21. Roy B, Awasthi R, Bindal A, et al. **Comparative evaluation of 3-dimensional pseudocontinuous arterial spin labeling with dynamic contrast-enhanced perfusion magnetic resonance imaging in grading of human glioma.** *J Comput Assist Tomogr* 2013;37:321–26 CrossRef Medline
22. Mayer A, Schneider F, Vaupel P, et al. **Differential expression of HIF-1 in glioblastoma multiforme and anaplastic astrocytoma.** *Int J Oncol* 2012;41:1260–70 CrossRef Medline
23. Schaffel R, Hedvat CV, Teruya-Feldstein J, et al. **Prognostic impact of proliferative index determined by quantitative image analysis and the International Prognostic Index in patients with mantle cell lymphoma.** *Ann Oncol* 2010;21:133–39 CrossRef Medline
24. Bottini A, Berruti A, Brizzi MP, et al. **Cytotoxic and antiproliferative activity of the single agent epirubicin versus epirubicin plus tamoxifen as primary chemotherapy in human breast cancer: a single-institution phase III trial.** *Endocr Relat Cancer* 2005;12:383–92 CrossRef Medline
25. Jain R, Poisson LM, Gutman D, et al. **Outcome prediction in patients with glioblastoma by using imaging, clinical, and genomic biomarkers: focus on the nonenhancing component of the tumor.** *Radiology* 2014;272:484–93 CrossRef Medline
26. Lev MH, Ozsunar Y, Henson JW, et al. **Glial tumor grading and outcome prediction using dynamic spin-echo MR susceptibility mapping compared with conventional contrast-enhanced MR: confounding effect of elevated rCBV of oligodendroglimoas [corrected].** *AJNR Am J Neuroradiol* 2004;25:214–21 Medline
27. Cha S, Tihan T, Crawford F, et al. **Differentiation of low-grade oligodendrogliomas from low-grade astrocytomas by using quantitative blood-volume measurements derived from dynamic susceptibility contrast-enhanced MR imaging.** *AJNR Am J Neuroradiol* 2005;26:266–73 Medline
28. Fellah S, Caudal D, De Paula AM, et al. **Multimodal MR imaging (diffusion, perfusion, and spectroscopy): is it possible to distinguish oligodendroglial tumor grade and 1p/19q codeletion in the pretherapeutic diagnosis?** *AJNR Am J Neuroradiol* 2013;34:1326–33 CrossRef Medline
29. Kapoor GS, Gocke TA, Chawla S, et al. **Magnetic resonance perfusion-weighted imaging defines angiogenic subtypes of oligodendroglioma according to 1p19q and EGFR status.** *J Neurooncol* 2009;92:373–86 CrossRef Medline
30. Whitmore RG, Krejza J, Kapoor GS, et al. **Prediction of oligodendroglial tumor subtype and grade using perfusion weighted magnetic resonance imaging.** *J Neurosurg* 2007;107:600–09 CrossRef Medline
31. Spampinato MV, Smith JK, Kwock L, et al. **Cerebral blood volume measurements and proton MR spectroscopy in grading of oligodendroglial tumors.** *AJR Am J Roentgenol* 2007;188:204–12 CrossRef Medline
32. Jenkinson MD, Smith TS, Joyce KA, et al. **Cerebral blood volume, genotype and chemosensitivity in oligodendroglial tumours.** *Neuroradiology* 2006;48:703–13 CrossRef Medline
33. Hilario A, Ramos A, Perez-Nuñez A, et al. **The added value of apparent diffusion coefficient to cerebral blood volume in the preoperative grading of diffuse gliomas.** *AJNR Am J Neuroradiol* 2012;33:701–07 CrossRef Medline
34. Xu M, See SJ, Ng WH, et al. **Comparison of magnetic resonance spectroscopy and perfusion-weighted imaging in presurgical grading of oligodendroglial tumors.** *Neurosurgery* 2005;56:919–26 CrossRef Medline
35. Evans SM, Judy KD, Dunphy I, et al. **Hypoxia is important in the biology and aggression of human glial brain tumors.** *Clin Cancer Res* 2004;10:8177–84 CrossRef Medline
36. Korkolopoulou P, Patsouris E, Konstantinidou AE, et al. **Hypoxia-inducible factor 1alpha/vascular endothelial growth factor axis in astrocytomas: associations with microvessel morphometry, proliferation and prognosis.** *Neuropathol Appl Neurobiol* 2004;30:267–78 CrossRef Medline
37. Mashiko R, Takano S, Ishikawa E, et al. **Hypoxia-inducible factor 1alpha expression is a prognostic biomarker in patients with astrocytic tumors associated with necrosis on MR image.** *J Neurooncol* 2011;102:43–50 CrossRef Medline
38. Birner P, Piribauer M, Fischer I, et al. **Vascular patterns in glioblastoma influence clinical outcome and associate with variable expression of angiogenic proteins: evidence for distinct angiogenic subtypes.** *Brain Pathol* 2003;13:133–43 Medline
39. Bekaert L, Valable S, Lechapt-Zalcman E, et al. **[18F]-FMISO PET study of hypoxia in gliomas before surgery: correlation with molecular markers of hypoxia and angiogenesis.** *Eur J Nucl Med Mol Imaging* 2017;44:1383–92 CrossRef Medline
40. Fujiwara S, Nakagawa K, Harada H, et al. **Silencing hypoxia-inducible factor-1alpha inhibits cell migration and invasion under hypoxic environment in malignant gliomas.** *Int J Oncol* 2007;30:793–802 Medline
41. Zagzag D, Lukyanov Y, Lan L, et al. **Hypoxia-inducible factor 1 and VEGF upregulate CXCR4 in glioblastoma: implications for angiogenesis and glioma cell invasion.** *Lab Invest* 2006;86:1221–32 CrossRef Medline
42. Toth RK, Warfel NA. **Strange bedfellows: nuclear factor, erythroid 2-like 2 (Nrf2) and hypoxia-inducible factor 1 (HIF-1) in tumor hypoxia.** *Antioxidants* 2017;6:27 CrossRef Medline
43. Liu H, Cai Y, Zhang Y, et al. **Development of a hypoxic radiosensitizer-prodrug liposome delivery DNA repair inhibitor Dbait combination with radiotherapy for glioma therapy.** *Adv Healthc Mater* 2017;6:1601377 CrossRef Medline
44. Law M, Young RJ, Babb JS, et al. **Gliomas: predicting time to progression or survival with cerebral blood volume measurements at dynamic susceptibility-weighted contrast-enhanced perfusion MR imaging.** *Radiology* 2008;247:490–98 CrossRef Medline
45. Deike K, Wiestler B, Graf M, et al. **Prognostic value of combined visualization of MR diffusion and perfusion maps in glioblastoma.** *J Neurooncol* 2016;126:463–72 CrossRef Medline

Diagnostic Accuracy of Neuroimaging to Delineate Diffuse Gliomas within the Brain: A Meta-Analysis

N. Verburg, F.W.A. Hoefnagels, F. Barkhof, R. Boellaard, S. Goldman, J. Guo, J.J. Heimans, O.S. Hoekstra, R. Jain, M. Kinoshita, P.J.W. Pouwels, S.J. Price, J.C. Reijneveld, A. Stadlbauer, W.P. Vandertop, P. Wesseling, A.H. Zwinderman, and P.C. De Witt Hamer

ABSTRACT

BACKGROUND: Brain imaging in diffuse glioma is used for diagnosis, treatment planning, and follow-up.

PURPOSE: In this meta-analysis, we address the diagnostic accuracy of imaging to delineate diffuse glioma.

DATA SOURCES: We systematically searched studies of adults with diffuse gliomas and correlation of imaging with histopathology.

STUDY SELECTION: Study inclusion was based on quality criteria. Individual patient data were used, if available.

DATA ANALYSIS: A hierarchic summary receiver operating characteristic method was applied. Low- and high-grade gliomas were analyzed in subgroups.

DATA SYNTHESIS: Sixty-one studies described 3532 samples in 1309 patients. The mean Standard for Reporting of Diagnostic Accuracy score (13/25) indicated suboptimal reporting quality. For diffuse gliomas as a whole, the diagnostic accuracy was best with T2-weighted imaging, measured as area under the curve, false-positive rate, true-positive rate, and diagnostic odds ratio of 95.6%, 3.3%, 82%, and 152. For low-grade gliomas, the diagnostic accuracy of T2-weighted imaging as a reference was 89.0%, 0.4%, 44.7%, and 205; and for high-grade gliomas, with T1-weighted gadolinium-enhanced MR imaging as a reference, it was 80.7%, 16.8%, 73.3%, and 14.8. In high-grade gliomas, MR spectroscopy (85.7%, 35.0%, 85.7%, and 12.4) and ^{11}C methionine–PET (85.1%, 38.7%, 93.7%, and 26.6) performed better than the reference imaging.

LIMITATIONS: True-negative samples were underrepresented in these data, so false-positive rates are probably less reliable than true-positive rates. Multimodality imaging data were unavailable.

CONCLUSIONS: The diagnostic accuracy of commonly used imaging is better for delineation of low-grade gliomas than high-grade gliomas on the basis of limited evidence. Improvement is indicated from advanced techniques, such as MR spectroscopy and PET.

ABBREVIATIONS: hsROC = hierarchic summary receiver operating characteristic; ROC = receiver operating characteristic; STARD = Standard for Reporting of Diagnostic Accuracy; CI = credibility interval; TP = true-positive; TN = true-negative; FP = false-positive; FN = false-negative

Diffuse gliomas are the most common primary brain tumors in adults, with an annual incidence of approximately 6 per 100,000. Despite advances in neurosurgery, radiation therapy, and chemotherapy, gliomas are fatal.[1] Brain imaging is indispensable for diagnosis, treatment planning, evaluation, and follow-up.

Received January 15, 2017; accepted after revision May 30.

From the Neurosurgical Center Amsterdam (N.V., F.W.A.H., W.P.V., P.C.D.W.H.), and Departments of Radiology and Nuclear Medicine (F.B., R.B., O.S.H.), Neurology (J.J.H., J.C.R.), Physics and Medical Technology (P.J.W.P.), and Pathology (P.W.), VU University Medical Center, Amsterdam, the Netherlands; Service of Nuclear Medicine and PET/Biomedical Cyclotron Unit (S.G.), l'université libre de Bruxelles–Hôpital Erasme, Brussels, Belgium; Shanghai Medical College (J.G.), Fudan University, Shanghai, China; Department of Radiology (R.J.), New York University School of Medicine, New York, New York; Department of Neurosurgery (M.K.), Osaka University Graduate School of Medicine, Osaka, Japan; Academic Neurosurgery Division (S.J.P.), Department of Clinical Neurosciences, Addenbrooke's Hospital, Cambridge, UK; Department of Neurosurgery (A.S.), University of Erlangen-Nuremberg, Erlangen, Germany; Department of Pathology (P.W.), Radboud University Medical Centre, Nijmegen, the Netherlands; Department of Clinical Epidemiology and Biostatistics (A.H.Z.), Academic Medical Center, University of Amsterdam, the Netherlands; and Institutes of Neurology and Healthcare Engineering (F.B.), University College London, London, UK.

This work was supported by a residency fellow grant from the Dutch Cancer Society (nr OAA/H1/VU 2015-7502 to N.V.) and an institutional grant from the Cancer Center Amsterdam (nr 2012-2-05 to P.C.D.W.H.).

Paper previously presented as a poster at: Annual Meeting of the Society for Neuro-Oncology, November 21–14, 2013; San Francisco, California; Annual Meeting of the European Association of Neurosurgical Societies, November 11–14, 2013; Tel Aviv, Israel.

Please address correspondence to Philip C. De Witt Hamer, MD, Neurosurgical Center Amsterdam, VU University Medical Center, 2F-010, De Boelelaan 1117, 1081 HV Amsterdam, the Netherlands; e-mail: p.dewitthamer@vumc.nl

Indicates article with supplemental on-line appendix.

Indicates article with supplemental on-line photos.

http://dx.doi.org/10.3174/ajnr.A5368

Although imaging standards to plan resection and radiation therapy vary between institutions and specialists, conventional imaging is in common use, typically consisting of T1-weighted MR imaging before and after gadolinium and T2/FLAIR-weighted imaging for gliomas. Of these conventional sequences, T2/FLAIR-weighted imaging is often considered as a reference for low-grade gliomas, and T1-weighted gadolinium-enhanced imaging, for high-grade gliomas in neurosurgical planning, combined with T2-weighted imaging in radiation therapy planning.[2,3]

Compared with other cancer types, accurate delineation of gliomas within the brain for treatment planning is particularly important due to the proximity of eloquent brain structures, which are vulnerable to surgery and radiation therapy.[4] Conversely, more extensive resections and boosted radiation therapy correlate with longer survival.[5-7] At the same time, clinical observations challenge the diagnostic accuracy of current imaging protocols: Gliomas recur even after a radiologically complete resection,[8,9] and glioma cells have been detected outside MR imaging abnormalities.[10,11] Brain imaging techniques, such as multivoxel spectroscopy and PET, were developed to improve tumor grading and delineation.[12,13]

Inherent in any regional treatment, such as surgery and radiation therapy, is the need to delineate a target volume, which mandates a dichotomous classification into tumor and normal tissue. Low- and high-grade gliomas have different treatment strategies and prognosis, while both are characterized by diffuse tumor infiltration. This supports our pooled analysis for diffuse glioma in addition to subgroup analysis by glioma grade. More accurate glioma delineation may improve the consistency between treatment results and survival. For instance, more accurate delineation may serve to identify patients eligible for more aggressive surgery than would have been considered on the basis of conventional imaging and may identify patients with glioma infiltration beyond meaningful surgical therapy so that useless and possibly harmful resections can be avoided.

The diagnostic accuracy of imaging techniques to delineate gliomas has not been systematically addressed, to our knowledge. In this meta-analysis, we estimate and compare the diagnostic accuracies of conventional imaging techniques and advanced MR imaging and PET to delineate newly diagnosed diffuse gliomas within brain tissue in adults.

MATERIALS AND METHODS

Search Strategy

We aimed to identify all publications reporting glioma imaging correlated with histopathology for the sampled locations. Our data sources were the National Library of Medicine (PubMed/MEDLINE, beginning in 1966) and the Excerpta Medica DataBASE (EMBASE, beginning in 1947), accessed on February 29, 2016, searching MeSH and Emtree subject headings (On-line Appendix: Methods 1). The publication language was restricted to Western languages; the publication date was restricted until January 1, 2016. References of identified studies were reviewed for further eligible publications in adherence with the Preferred Reporting Items for Systematic Reviews and Meta-Analyses (PRISMA) statement guidelines (http://prisma-statement.org/).

Study Selection Criteria

Studies were eligible for further analysis on the basis of 5 inclusion criteria: First, an adult population or subpopulation was required with patients at least 18 years of age. Second, only newly diagnosed diffuse gliomas of World Health Organization grades II–IV were included to avoid imaging artifacts from previous treatment. Third, brain imaging of any technique was allowed as a diagnostic test. Fourth, histopathology of tissue samples was required as a reference test. Fifth, histopathology of samples and imaging test measurements had to be directly correlated by surgical navigation with 3D coordinates. When duplicate reports on the same population were retrieved, only the report with the most complete data was used for analysis. Studies also including patients of pediatric age or pathology other than diffuse glioma were included if the population of interest could be extracted from the data. Postmortem studies were excluded to avoid bias from end-stage disease. For interobserver agreement on study inclusion, a κ statistic was used.[14]

Quality and Outcome Measures

Any study reporting glioma imaging correlated with histopathology was independently assessed in full text for quality criteria by 2 observers (N.V. and F.W.A.H, with 3 and 8 years of experience in clinical neurosurgery) using the Standard for Reporting of Diagnostic Accuracy (STARD) guidelines, a 25-item checklist to explore reporting quality.[15] Disagreements were resolved through adjudication by a third observer (P.C.D.W.H., with 15 years of experience in clinical neurosurgery). For interobserver agreement on quality assessment, the intraclass correlation coefficient was calculated. One observer extracted the study data (N.V.) on the imaging techniques, the histopathologic examination method, the colocalization method between imaging and histopathology, and the number of patients and samples categorized by glioma grades. The extracted data were verified by another observer (P.C.D.W.H.). Biopsy sample locations were categorized for each imaging technique as normal or abnormal signal according to the authors' test positivity criteria and as glioma or normal brain in correlated histopathologic examination according to the authors' definitions. We aimed to include individual sample data as much as possible, either by availability from the publication, by request for original data to corresponding authors (up to 3 times in case of nonresponse), or by estimation of data points from plots of image measurements versus tumor characteristics. If individual sample data were unavailable, we included the aggregated data as summaries of true-positive (TP), true-negative (TN), false-positive (FP), and false-negative (FN) samples. Accordingly, each imaging technique in every study provided at least 1 estimate of diagnostic accuracy.

Statistical Analysis

We used hierarchic summary receiver operating characteristic (hsROC) curve analysis with random effects for within-study and between-study variation to summarize estimates of the diagnostic accuracy for each imaging technique with >1 study available (On-line Appendix: Methods 2).[16] The available data allowed hierarchic analysis of samples within techniques. The estimates with 95% credibility intervals (CIs) consisted of the summary true-

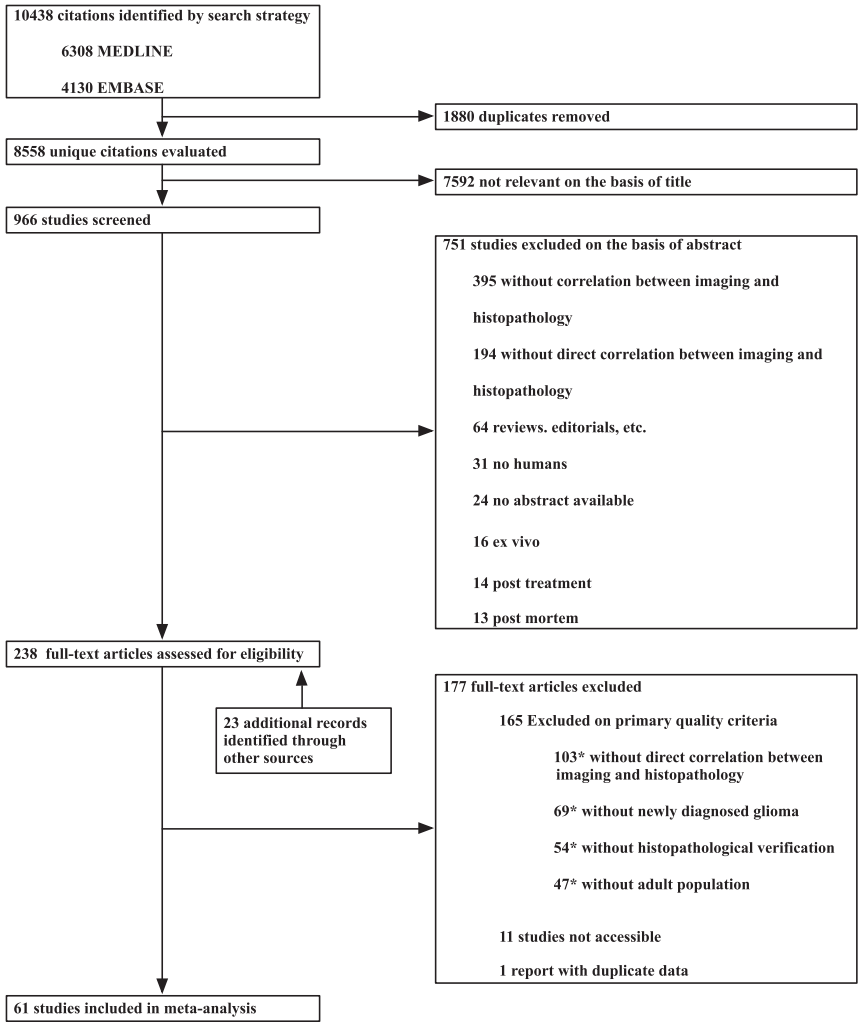

FIG 1. Flow chart of publication selection. The *asterisk* indicates that multiple exclusion criteria could apply to studies.

positive rate (sensitivity: TP / [TP + FN]), the summary false-positive rate (1-specificity: FP/ [FP + TN]), the diagnostic odds ratio ([TP/FN]/[FP/TN]),[17] and the summary area under the receiver operating characteristic (ROC) curve. Differences in estimates between imaging techniques in relation to reference imaging were also calculated and considered significant when the CI excluded zero. A Bayesian Markov chain Monte Carlo algorithm with 3 chains modeled the hsROC curve with the CI for each imaging technique on the basis of 5 parameters: the accuracy and its precision, the cut-point and its precision, and the scale parameter.[18] The accuracy and the cut-point were allowed to vary among studies; the scale was allowed to vary among imaging techniques. These parameters provide an hsROC curve with an operating point on the curve representing the summary true-positive and false-positive rates. A Bayesian hsROC analysis was used for the following reasons: First, this approach is considered the standard for meta-analysis of diagnostic accuracy, taking into account the correlation between the true-positive and false-positive rates.[18,19] Second, individual sample data and aggregated data, if individual data are unavailable, can be analyzed together per imaging technique to estimate its diagnostic accuracy.[20,21] Third, varying test positivity criteria for imaging in studies can be accommodated.[22] Fourth, partly missing data can be handled with this model. For the meta-analysis, vague priors were chosen for the prior distributions, so that the results primarily reflect inference from the presented data without prior knowledge. Normal distributions with mean of zero and variance of 10,000 represented the accuracy, cut-point and scale parameters, and inverse γ distributions, with a shape and rate of 0.01 representing the precisions. Uniform distributions were used as alternative vague priors. Summary estimates consisted of the median values with CIs of the posterior distributions. For the analysis, we used JAGS software, Version 4.0.1 (Jags Software; Newark, Delaware; http://mcmc-jags.sourceforge.net) from the rjags package (Version 4–3) for R statistical and computing software (http://www.r-project.org/). Sampling traces and distributions and Gelman-Rubin diagnostics were evaluated for evidence against convergence by using the coda package (Version 0.17.1; https://www.rdocumentation.org/packages/coda/versions/0.17-1).

Statistical tests for heterogeneity between studies are unavailable for diagnostic accuracy meta-analysis; therefore, heterogeneity was explored with subgroup analysis.[23] Sensitivity analysis included analysis of the following: 1) the subset of higher quality studies, considered those with a prospective design, including quantified sample data in at least 15 patients and qualifying for the methodologic description of both neuroimaging and histopathology[24]; 2) the subset of studies with individual patient data; and 3) alternative vague prior distributions. Subgroups of low-grade (World Health Organization grade II) and high-grade (World Health Organization grade III or IV) gliomas were reported separately. Publication bias was explored graphically.

RESULTS

The search strategy identified 8558 unique citations (Fig 1), of which 272 full-text publications were assessed for eligibility. Subsequently, 61 articles were included for meta-analysis on the basis of the 5 selection criteria. The interobserver agreement for inclusion was moderate ($\kappa = 0.47$; 95% CI, 0.37–0.57). A total of 3532 samples with correlated histopathologic examinations and imaging were included from 1309 patients with gliomas. For subgroup analysis by glioma grade, data could be extracted for 907 samples in 421 patients with low-grade gliomas and for 1380 samples in 814 patients with high-grade gliomas. Glioma subtypes, such as astrocytoma or oligodendroglioma, could not be analyzed in subgroups because data for these subgroups could usually not be

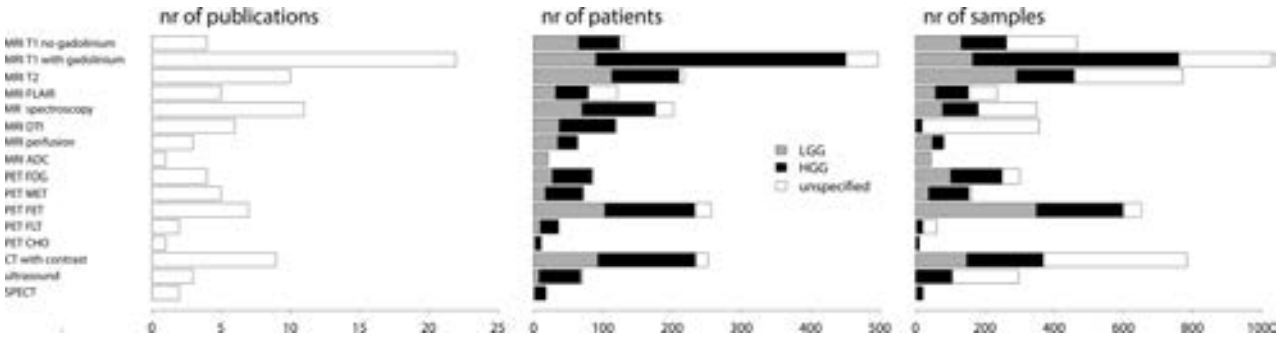

FIG 2. Number of publications, patients, and samples for imaging techniques categorized by glioma grades. LGG indicates low-grade glioma; HGG, high-grade glioma; FLT, ^{18}F fluorthymidine; nr, number.

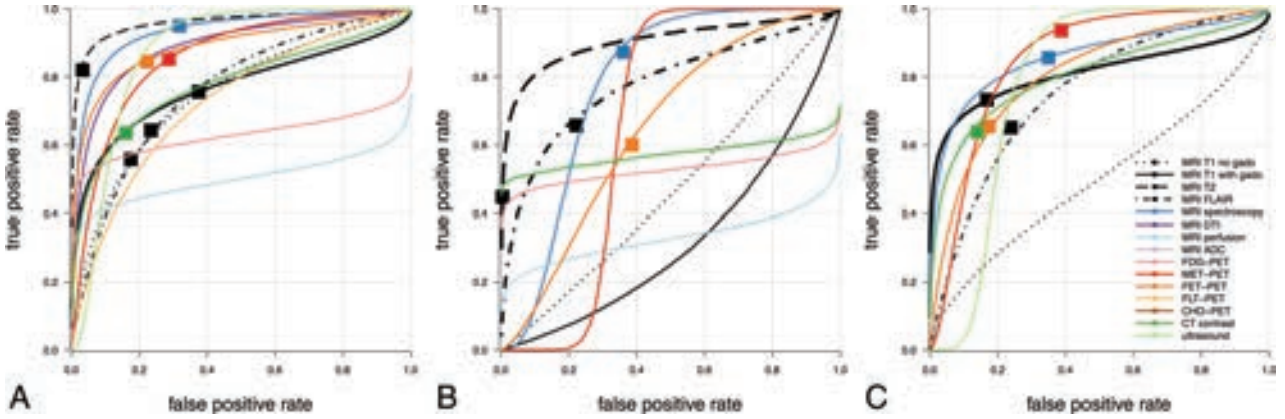

FIG 3. Summary hierarchic ROC curves of imaging techniques. Estimated summary ROC curves are plotted by imaging technique in ROC space for diffuse gliomas as a whole—that is, low- and high-grade gliomas combined (*A*), low-grade glioma (*B*), and high-grade glioma (*C*). The operating points of curves represent the estimated summary true-positive and false-positive rates as indicated by *solid squares*. *Solid squares* are missing when convergence is not reached. Color coding shows conventional MR imaging in black, advanced MR imaging in shades of blue, PET imaging in shades of red, and CT and sonography imaging in shades of green.

extracted. Individual sample data were available from 19 studies. The higher quality subset consisted of 29 studies.

The mean STARD score of the included studies was 13 ± 2.8. The interobserver agreement for STARD quality assessment was substantial (intraclass coefficient = 0.66; 95% CI, 0.49–0.78).

The included studies reported on 16 imaging techniques, including T1-weighted imaging before and after gadolinium, T2-, T2/FLAIR-, perfusion- and diffusion-weighted imaging (apparent diffusion coefficient), MR spectroscopy (choline to *N*-acetylaspartate ratio), diffusion tensor imaging (fractional anisotropy), and PET with these tracers: FDG, ^{11}C methionine (MET), ^{18}F fluoroethyltyrosine (FET), ^{18}F fluorthymidine, or ^{18}F or ^{11}C choline (Cho). Imaging protocols varied widely; for instance, 22 studies used 1.5T MR imaging field strength, 15 used 3T, 1 used 0.15T; and field strength was unspecified in 11 studies. The number of studies, patients, and samples for each imaging technique categorized by glioma grades is plotted in Fig 2.

The reference standard to distinguish tumor and normal brain in tissue samples for all studies was microscopic examination with hematoxylin-eosin staining and immunohistochemical analysis. Nine studies reported the reference standard as the labeling index of proliferating cells; 6 studies reported the reference standard as the tumor infiltration index; and 2 studies, as the cellularity index. We followed the authors' definition to differentiate normal brain and glioma.

The method to correlate the histopathology with imaging was frameless stereotactic needle biopsies in 27 studies, frame-based stereotactic needle biopsies in 14, neuronavigated resection biopsies in 12, and unspecified stereotactic needle biopsies in 8.

The hsROC curves of imaging techniques for diffuse glioma as a whole are plotted in Fig 3*A*, and for the subgroups of low- and high-grade gliomas, in Fig 3*B*, -*C*, respectively. The characteristics of these hsROC curves are listed in Fig 4.

The estimates of false-positive rates need to be interpreted with caution due to relative lack of data on true-negative samples. This "underrepresentation" of true-negatives and consequently bias in false-positive rates may be unbalanced across imaging techniques, creating additional biases when comparing the ROC curves.

In all gliomas considered, the area under the curve was highest for T2-weighted imaging (95.6%), followed by MR spectroscopy (93.3%). The false-positive rate was lowest in T2-weighted imaging (3.3%), followed by CT (16.0%); and the true-positive rate was highest for MR spectroscopy (95.0%), followed by sonography (93.3%). The diagnostic odds ratio was highest for T2-weighted imaging (152), followed by MR imaging spectroscopy (39.2).

For low-grade gliomas, the area under the curve was highest for T2-weighted imaging (89.0%), followed by MR spectroscopy (78.1%) and T2/FLAIR-weighted imaging (77.4%). The false-

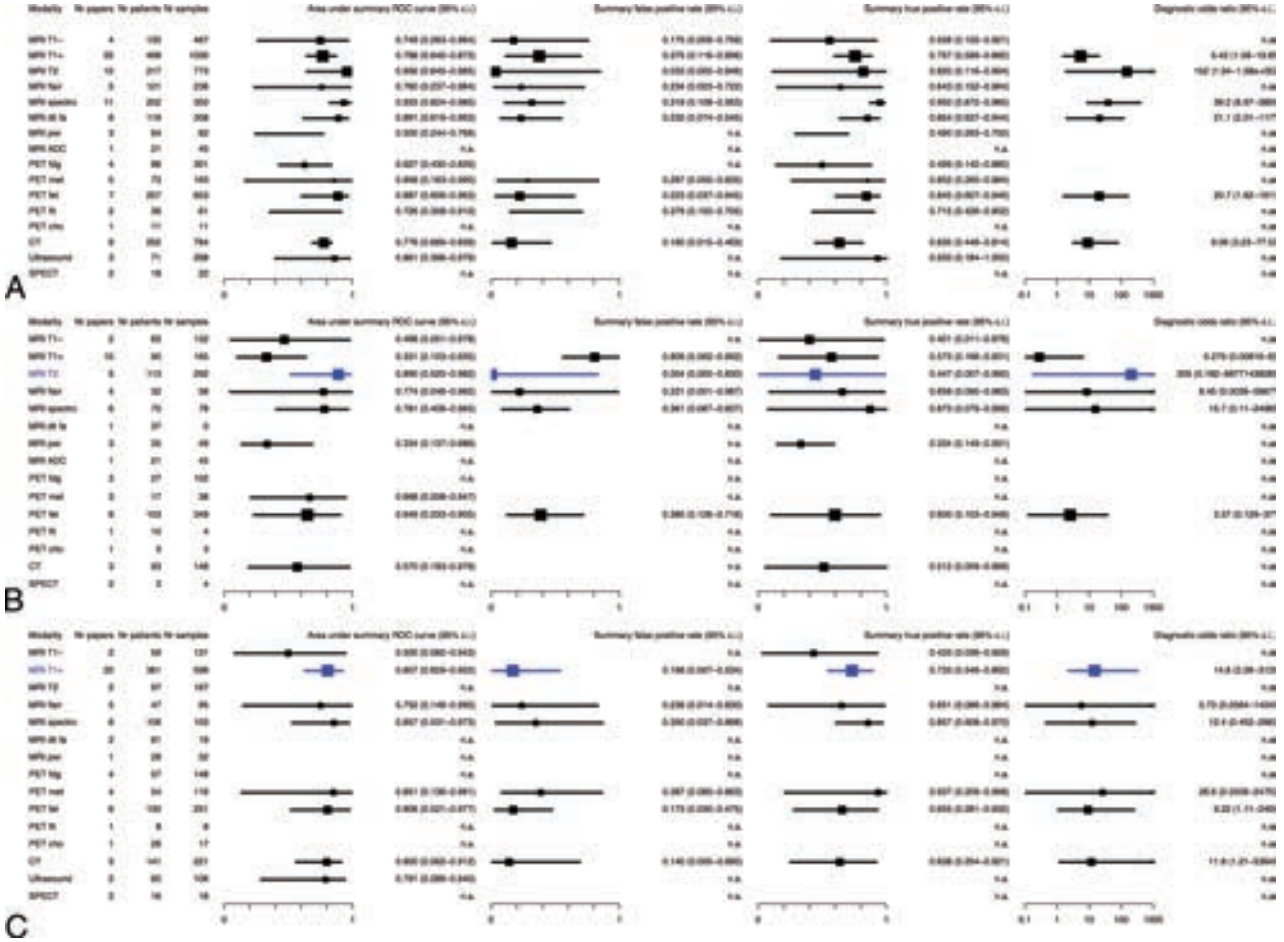

FIG 4. Diagnostic accuracy characteristics of imaging techniques. Diagnostic performance of imaging techniques expressed as area under the curve, summary false-positive rate, summary true-positive rate, and diagnostic odds ratio for diffuse gliomas as a whole—that is, low- and high-grade gliomas combined (*A*), low-grade glioma (*B*), and high-grade glioma (*C*). The medians of posterior distributions are plotted as *squares* proportional to the number of observations with 95% credibility intervals. The most common clinically used imaging technique is in blue as reference. n.a. indicates nonavailable data because either <3 studies were available or the posterior samples did not converge; fa, fractional anisotropy.

positive rate was lowest in T2-weighted imaging (0.4%), followed by T2/FLAIR-weighted imaging (22.1%); and the true-positive rate was highest for MR spectroscopy (87.3%), followed by T2/FLAIR-weighted imaging (65.8%). The diagnostic odds ratio was highest for T2-weighted imaging (205), followed by MR spectroscopy (15.7). Not surprising, the area under the curve was statistically significantly lower for T1-weighted gadolinium-enhanced imaging compared with T2-weighted imaging (difference of 54.4%; 95% CI, 8.4%–80.8%) and for perfusion-weighted imaging (difference of 54.1%; 95% CI, 7.8%–78.2%). Of note, T2-weighted imaging had a higher area under the curve, false-positive ratio, and diagnostic odds ratio in comparison with T2/FLAIR-weighted imaging, the other common clinically used MR imaging sequence.

For high-grade gliomas, the area under the curve was highest for MR spectroscopy (85.7%), followed by MET-PET (85.1%). The false-positive rate was lowest in CT (14.0%), followed by T1-weighted gadolinium-enhanced imaging (16.8%); and the true-positive rate was highest for MET-PET (93.7%), followed by MR spectroscopy (85.7%). The diagnostic odds ratio was highest for MET-PET (26.6), followed by T1-weighted gadolinium-enhanced imaging (14.8). MET-PET and MR spectroscopy had a higher area under the curve and true-positive rate in comparison with the common clinically used T1-weighted gadolinium-enhanced MR imaging (respectively, 80.7% and 73.3%). This came at the expense of higher false-positive rates for MET-PET and MR spectroscopy, respectively 38.7% and 35.0%. Most remarkable, CT with contrast had an area under the curve (80.0%) like that of T1-weighted gadolinium-enhanced MR imaging.

Sensitivity analysis demonstrated robustness against publication quality, individual sample data, and alternative vague priors (On-line Fig 1). Because statistical tests for heterogeneity were unavailable to take the association between sensitivity and specificity into account,[23] we inspected the plots of the study data and hsROC curve for each technique (On-line Fig 2), demonstrating considerable heterogeneity among studies, resulting in a relatively large CI. For many imaging techniques, the number of publications was too small to exclude publication bias (On-line Fig 3). Small studies with small areas under the curve or low false-positive rates may be missing for T1-weighted gadolinium-enhanced imaging and T2-weighted imaging.

DISCUSSION

The main findings of this meta-analysis for the diagnostic accuracy of neuroimaging to delineate diffuse gliomas are the following: 1) It is best with T2-weighted imaging, followed by MR spectroscopy. 2) It is better for low-grade gliomas with T2-weighted imaging than for high-grade gliomas with T1-weighted gadolinium-enhanced MR imaging; considering the area under the curve (89.0% versus 80.7%) and the diagnostic odds ratio (205 versus 14.8). 3) it may be improved in high-grade gliomas with MR spectroscopy or MET-PET. 4) It is not superior with T2/FLAIR-weighted imaging for low-grade gliomas. 5) It is not inferior with CT with contrast for high-grade gliomas. 6) It varies considerably between imaging techniques and shows heterogeneity between studies.

Thresholds for acceptable diagnostic accuracy of tumor imaging are undetermined. The accuracy of imaging for glioma delineation by MR imaging is, for instance, less than that for lesion detection in hepatocellular carcinoma by sonography, CT, or MR imaging.[25] It is comparable with detection of metastatic lymph nodes in non-small cell lung cancer by CT or MR imaging, but it is less than that of PET.[26,27] Moreover, it is less than that of the diagnosis of breast cancer by MR imaging.[28] These studies, however, address the radiologic diagnosis of cancer by imaging, not the delineation of infiltrative cancer within normal tissue. The identification of cancer cells within normal-appearing imaging regions seems to be specific for glioma.[10,29] We did not find meta-analyses of tumor delineation in other solid cancers.

The variation in diagnostic performance may be explained by the notoriously difficult diagnostic problem of delineating glioma cells, which gradually infiltrate brain tissue. Therefore, the concept of delineating a tumor by the presence or absence of cancer cells, on which ROC analysis is based, may oversimplify gradual glioma infiltration. Nevertheless, treatment target volumes are required for patient care.

Several factors may contribute to the observed variation in diagnostic performance. First, the scan protocols have not been standardized for any of these sequences. For the diagnostic standard of MR imaging, for instance, variation exists in scanner equipment, quality assessment and control, acquisition protocols, image processing, quantification, and interpretation by radiologists. Second, histopathologic examinations may vary due to incomplete sampling of heterogeneous tumors and interpretation differences among neuropathologists.[30-32] Third, the correlation between imaging measurements and histopathologic examination may be another source of variation. This colocalization depends on the precision of the navigated locations of tissue samples. Navigation precision has been found to be within several millimeters,[33,34] whereas tissue may be heterogeneous at smaller distances.[35]

Improvement of diagnostic accuracy to delineate gliomas for regional therapy requires an offset between increasing the true-positive rate and decreasing the false-positive rate. Increasing the true-positive rate may be preferable for tumor control, whereas decreasing the false-positive rate may be preferable for preservation of functional integrity. From the perspective of tumor control, the overestimation of diffuse glioma (ie, the inadvertent declaration of normal brain as diffuse glioma) would be more acceptable than underestimation. Nevertheless, this is only acceptable when at the same time, surgery aims to minimize neurologic deficits from removal of critical brain regions whether or not they are infiltrated by tumor. This is usually done by brain mapping of functions with the patient under local anesthesia to push the resection to the functional limits.[4] In other words, a more sensitive imaging delineation would be even more likely to require functional brain mapping as a safeguard against removal of critical brain regions potentially infiltrated by tumor. In this perspective, MR spectroscopy and PET might have the potential to increase the true-positive rate of glioma delineation for surgical strategies. However, a more sensitive tumor delineation should probably not prompt larger high-dose radiation fields because a similar safeguard against cognitive decline from radiation therapy is unavailable. Perhaps high-dose radiation therapy should rather focus on regions at high risk for tumor progression, whereas a lower dose could be acceptable in regions with a low risk for tumor progression.

Our observations may challenge current care standards. First, T2/FLAIR-weighted imaging has been proposed as the standard for radiologic response measurements in low-grade gliomas,[3] whereas our data indicate that T2-weighted imaging has better diagnostic performance before treatment than T2/FLAIR-weighted imaging. Second, MR imaging, including T1-weighted gadolinium-enhanced and T2-weighted imaging, is considered the standard for treatment planning and radiologic response measurements in high-grade gliomas,[2] whereas our data indicate that the diagnostic performance of CT with contrast to delineate high-grade gliomas before treatment is not necessarily inferior. Clearly, anatomy is better visualized with MR imaging than CT. Furthermore, subtle areas of disease progression that may be outside the main tumor mass are better identified on MR imaging than on CT.

Third, in particular for high-grade gliomas, there is room for improvement in tumor delineation. For instance, radiation oncology guidelines are heterogeneous regarding target delineation.[36-38] MR spectroscopy and PET hold promise as additives to the current standard, but availability and standardization are limitations to more widespread use. For a detailed discussion of these techniques, we suggest recent reviews.[39-43] Furthermore, T2-weighted imaging performed best for diffuse gliomas as a whole and for low-grade-gliomas but could not be estimated for high-grade gliomas in these data because quantitative information was only available from 2 studies. Nevertheless, T2-weighted imaging may contribute to better delineation of high-grade gliomas as well.

Strengths of this meta-analysis include a thorough search strategy, assessment of reporting quality by STARD criteria, and analysis using the hsROC method, whenever available, with individual sample data.

Our results should be interpreted within the limits of the quality of observational data that were retrieved with the limited number of patients and samples from publications with suboptimal reporting quality. Due to obvious reluctance to sample tissue outside imaging abnormalities, true-negative samples are underrepresented in these data; thus, estimates of false-positive rates are probably less reliable than those of true-positive rates. Further-

more, the available data only allowed indirect comparison of imaging techniques because only 2 studies were identified with quantitative head-to-head comparison of techniques.[44,45] Last, several potential biases in this meta-analysis should be considered.[46] Methodologic heterogeneity is likely to exist. Publication bias was suggested, though population bias is unlikely because all patients were required to have a glioma, control cases were excluded, and all samples from patients were examined with the same reference standard of histopathologic examination. Nevertheless, verification bias may be present because imaging characteristics have probably guided biopsy sampling strategies. The studies may be biased by patient selection, and we cannot exclude heterogeneity from subjective interpretation of image measurements. Furthermore, clinical heterogeneity is likely because in addition to unstandardized imaging and pathology protocols, positivity criteria of diagnostic and reference tests may have varied among studies.

The implication of our findings is that planning of surgery or radiation therapy for diffuse gliomas using current imaging protocols should be performed with caution because these have only moderate accuracy for glioma delineation based on limited evidence. The sensitivity of imaging to delineate all regions of existing tumor infiltration seems to be less than the specificity to rule out tumor from normal brain. The true-positive rate of conventional imaging for high-grade gliomas may be improved by MR spectroscopy and PET. Furthermore, future effort to quantify and improve this accuracy may aim at combinations of imaging and head-to-head comparison with molecular characterization as the criterion standard.

CONCLUSIONS

In this meta-analysis, the diagnostic accuracy of imaging for delineation of diffuse gliomas (low- and high-grade gliomas combined) is best with T2-weighted imaging, followed by MR spectroscopy. The diagnostic accuracy of the common clinically used imaging is better for low-grade gliomas with T2-weighted imaging than for high-grade gliomas with T1-weighted gadolinium-enhanced imaging. Improvement is indicated for high-grade gliomas using advanced imaging techniques, such as MR spectroscopy and PET. Current imaging protocols are based on limited evidence from heterogeneous studies, and future studies with head-to-head comparison and combinations of imaging techniques are required to improve glioma delineation.

Disclosures: Niels Verburg—*RELATED*: *Grant*: Dutch Cancer Society resident grant.

REFERENCES

1. Ricard D, Idbaih A, Ducray F, et al. **Primary brain tumours in adults.** *Lancet* 2012;379:1984–96 CrossRef Medline
2. Wen PY, Macdonald DR, Reardon DA, et al. **Updated response assessment criteria for high-grade gliomas: Response Assessment in Neuro-Oncology working group.** *J Clin Oncol* 2010;28:1963–72 CrossRef Medline
3. van den Bent MJ, Wefel JS, Schiff D, et al. **Response Assessment in Neuro-Oncology (a report of the RANO group): assessment of outcome in trials of diffuse low-grade gliomas.** *Lancet Oncol* 2011;12:583–93 CrossRef Medline
4. De Witt Hamer PC, Robles SG, Zwinderman AH, et al. **Impact of intraoperative stimulation brain mapping on glioma surgery outcome: a meta-analysis.** *J Clin Oncol* 2012;30:2559–65 CrossRef Medline
5. Sanai N, Polley MY, McDermott MW, et al. **An extent of resection threshold for newly diagnosed glioblastomas.** *J Neurosurg* 2011;115:3–8 CrossRef Medline
6. Capelle L, Fontaine D, Mandonnet E, et al; French Réseau d'Étude des Gliomes. **Spontaneous and therapeutic prognostic factors in adult hemispheric World Health Organization Grade II gliomas: a series of 1097 cases: clinical article.** *J Neurosurg* 2013;118:1157–68 CrossRef Medline
7. Einstein DB, Wessels B, Bangert B, et al. **Phase II trial of radiosurgery to magnetic resonance spectroscopy-defined high-risk tumor volumes in patients with glioblastoma multiforme.** *Int J Radiat Oncol Biol Phys* 2012;84:668–74 CrossRef Medline
8. Smith JS, Chang EF, Lamborn KR, et al. **Role of extent of resection in the long-term outcome of low-grade hemispheric gliomas.** *J Clin Oncol* 2008;26:1338–45 CrossRef Medline
9. Pichlmeier U, Bink A, Schackert G, et al; ALA Glioma Study Group. **Resection and survival in glioblastoma multiforme: an RTOG recursive partitioning analysis of ALA study patients.** *Neuro Oncol* 2008;10:1025–34 CrossRef Medline
10. Pallud J, Varlet P, Devaux B, et al. **Diffuse low-grade oligodendrogliomas extend beyond MRI-defined abnormalities.** *Neurology* 2010;74:1724–31 CrossRef Medline
11. Kelly PJ, Daumas-Duport C, Kispert DB, et al. **Imaging-based stereotaxic serial biopsies in untreated intracranial glial neoplasms.** *J Neurosurg* 1987;66:865–74 CrossRef Medline
12. la Fougère C, Suchorska B, Bartenstein P, et al. **Molecular imaging of gliomas with PET: opportunities and limitations.** *Neuro Oncol* 2011;13:806–19 CrossRef Medline
13. Waldman AD, Jackson A, Price SJ, et al; National Cancer Research Institute Brain Tumour Imaging Subgroup. **Quantitative imaging biomarkers in neuro-oncology.** *Nat Rev Clin Oncol* 2009;6:445–54 CrossRef Medline
14. Landis JR, Koch GG. **The measurement of observer agreement for categorical data.** *Biometrics* 1977;33:159–74 CrossRef Medline
15. Bossuyt PM, Reitsma JB, Bruns DE, et al; STARD Group. **STARD 2015: an updated list of essential items for reporting diagnostic accuracy studies.** *Radiology* 2015;277:826–32 CrossRef Medline
16. Rutter CM, Gatsonis CA. **A hierarchical regression approach to meta-analysis of diagnostic test accuracy evaluations.** *Stat Med* 2001;20:2865–84 CrossRef Medline
17. Glas AS, Lijmer JG, Prins MH, et al. **The diagnostic odds ratio: a single indicator of test performance.** *J Clin Epidemiol* 2003;56:1129–35 CrossRef Medline
18. Macaskill P. **Empirical Bayes estimates generated in a hierarchical summary ROC analysis agreed closely with those of a full Bayesian analysis.** *J Clin Epidemiol* 2004;57:925–32 CrossRef Medline
19. Harbord RM, Whiting P, Sterne JA, et al. **An empirical comparison of methods for meta-analysis of diagnostic accuracy showed hierarchical models are necessary.** *J Clin Epidemiol* 2008;61:1095–103 CrossRef Medline
20. Riley RD, Dodd SR, Craig JV, et al. **Meta-analysis of diagnostic test studies using individual patient data and aggregate data.** *Stat Med* 2008;27:6111–36 CrossRef Medline
21. Sutton AJ, Kendrick D, Coupland CA. **Meta-analysis of individual- and aggregate-level data.** *Stat Med* 2008;27:651–69 CrossRef Medline
22. Dukic V, Gatsonis C. **Meta-analysis of diagnostic test accuracy assessment studies with varying number of thresholds.** *Biometrics* 2003;59:936–46 CrossRef Medline
23. Leeflang MM, Deeks JJ, Gatsonis C, et al; Cochrane Diagnostic Test Accuracy Working Group. **Systematic reviews of diagnostic test accuracy.** *Ann Intern Med* 2008;149:889–97 CrossRef Medline
24. Rutjes AW, Reitsma JB, Di Nisio M, et al. **Evidence of bias and variation in diagnostic accuracy studies.** *CMAJ* 2006;174:469–76 CrossRef Medline
25. Chou R, Cuevas C, Fu R, et al. **Imaging techniques for the diagnosis**

of hepatocellular carcinoma: a systematic review and meta-analysis. *Ann Intern Med* 2015;162:697–711 CrossRef Medline
26. Silvestri GA, Gonzalez AV, Jantz MA, et al. **Methods for staging non-small cell lung cancer: diagnosis and management of lung cancer, 3rd ed—American College of Chest Physicians evidence-based clinical practice guidelines.** *Chest* 2013;143:e211S–50S CrossRef Medline
27. Zhang Y, Qin Q, Li B, et al. **Magnetic resonance imaging for N staging in non-small cell lung cancer: a systematic review and meta-analysis.** *Thorac Cancer* 2015;6:123–32 CrossRef Medline
28. Peters NH, Borel Rinkes IH, Zuithoff NP, et al. **Meta-analysis of MR imaging in the diagnosis of breast lesions.** *Radiology* 2008;246:116–24 CrossRef Medline
29. Lemée JM, Clavreul A, Aubry M, et al. **Characterizing the peritumoral brain zone in glioblastoma: a multidisciplinary analysis.** *J Neurooncol* 2015;122:53–61 CrossRef Medline
30. Kros JM, Gorlia T, Kouwenhoven MC, et al. **Panel review of anaplastic oligodendroglioma from European Organization For Research and Treatment of Cancer Trial 26951: assessment of consensus in diagnosis, influence of 1p/19q loss, and correlations with outcome.** *J Neuropathol Exp Neurol* 2007;66:545–51 CrossRef Medline
31. Scott CB, Nelson JS, Farnan NC, et al. **Central pathology review in clinical trials for patients with malignant glioma: a report of Radiation Therapy Oncology Group 83–02.** *Cancer* 1995;76:307–13 Medline
32. van den Bent MJ. **Interobserver variation of the histopathological diagnosis in clinical trials on glioma: a clinician's perspective.** *Acta Neuropathol* 2010;120:297–304 CrossRef Medline
33. Bjartmarz H, Rehncrona S. **Comparison of accuracy and precision between frame-based and frameless stereotactic navigation for deep brain stimulation electrode implantation.** *Stereotact Funct Neurosurg* 2007;85:235–42 CrossRef Medline
34. Zacest A, Berk C, Burchiel KJ. **Precision and accuracy of stereotactic targeting in patients undergoing repeat stereotactic surgery.** *Stereotact Funct Neurosurg* 2009;87:168–73 CrossRef Medline
35. Sottoriva A, Spiteri I, Piccirillo SG, et al. **Intratumor heterogeneity in human glioblastoma reflects cancer evolutionary dynamics.** *Proc Natl Acad Sci U S A* 2013;110:4009–14 CrossRef Medline
36. Zhao F, Li M, Kong L, et al. **Delineation of radiation therapy target volumes for patients with postoperative glioblastoma: a review.** *Onco Targets Ther* 2016;9:3197–204 CrossRefMedline
37. Niyazi M, Brada M, Chalmers AJ, et al. **ESTRO-ACROP guideline "target delineation of glioblastomas."** *Radiother Oncol* 2016;118:35–42 CrossRef Medline
38. Cabrera AR, Kirkpatrick JP, Fiveash JB, et al. **Radiation therapy for glioblastoma: executive summary of an American Society for Radiation Oncology Evidence-Based Clinical Practice Guideline.** *Pract Radiat Oncol* 2016;6:217–25 CrossRef Medline
39. Albert NL, Weller M, Suchorska B, et al. **Response Assessment in Neuro-Oncology working group and European Association for Neuro-Oncology recommendations for the clinical use of PET imaging in gliomas.** *Neuro Oncol* 2016;18:1199–208 CrossRef Medline
40. Fink JR, Muzi M, Peck M, et al. **Multimodality brain tumor imaging: MR imaging, PET, and PET/MR imaging.** *J Nucl Med* 2015;56:1554–61 CrossRef Medline
41. Langen KJ, Galldiks N, Hattingen E, et al. **Advances in neuro-oncology imaging.** *Nat Rev Neurol* 2017;13:279–89 CrossRef Medline
42. Brandão LA, Castillo M. **Adult brain tumors: clinical applications of magnetic resonance spectroscopy.** *Magn Reson Imaging Clin N Am* 2016;24:781–809 CrossRef Medline
43. Kalpathy-Cramer J, Gerstner ER, Emblem KE, et al. **Advanced magnetic resonance imaging of the physical processes in human glioblastoma.** *Cancer Res* 2014;74:4622–37 CrossRef Medline
44. Jain R, Gutierrez J, Narang J, et al. **In vivo correlation of tumor blood volume and permeability with histologic and molecular angiogenic markers in gliomas.** *AJNR Am J Neuroradiol* 2011;32:388–94 CrossRef Medline
45. Pauleit D, Floeth F, Hamacher K, et al. **O-(2-[18F]fluoroethyl)-L-tyrosine PET combined with MRI improves the diagnostic assessment of cerebral gliomas.** *Brain* 2005;128:678–87 CrossRef Medline
46. Lijmer JG, Bossuyt PMM, Heisterkamp SH. **Exploring sources of heterogeneity in systematic reviews of diagnostic tests.** *Stat Med* 2002;21:1525–37 CrossRef Medline

Imaging Biomarkers for Adult Medulloblastomas: Genetic Entities May Be Identified by Their MR Imaging Radiophenotype

V.C. Keil, M. Warmuth-Metz, C. Reh, S.J. Enkirch, C. Reinert, D. Beier, D.T.W. Jones, T. Pietsch, H.H. Schild, E. Hattingen, and P. Hau

ABSTRACT

BACKGROUND AND PURPOSE: The occurrence of medulloblastomas in adults is rare; nevertheless, these tumors can be subdivided into genetic and histologic entities each having distinct prognoses. This study aimed to identify MR imaging biomarkers to classify these entities and to uncover differences in MR imaging biomarkers identified in pediatric medulloblastomas.

MATERIALS AND METHODS: Eligible preoperative MRIs from 28 patients (11 women; 22–53 years of age) of the Multicenter Pilot-study for the Therapy of Medulloblastoma of Adults (NOA-7) cohort were assessed by 3 experienced neuroradiologists. Lesions and perifocal edema were volumetrized and multiparametrically evaluated for classic morphologic characteristics, location, hydrocephalus, and Chang criteria. To identify MR imaging biomarkers, we correlated genetic entities *sonic hedgehog* (*SHH*) *TP53* wild type, *wingless* (*WNT*), and non-*WNT*/non-*SHH* medulloblastomas (in adults, Group 4), and histologic entities were correlated with the imaging criteria. These MR imaging biomarkers were compared with corresponding data from a pediatric study.

RESULTS: There were 19 *SHH TP53* wild type (69%), 4 *WNT*-activated (14%), and 5 Group 4 (17%) medulloblastomas. Six potential MR imaging biomarkers were identified, 3 of which, hydrocephalus ($P = .03$), intraventricular macrometastases ($P = .02$), and hemorrhage ($P = .04$), when combined, could identify *WNT* medulloblastoma with 100% sensitivity and 88.3% specificity (95% CI, 39.8%–100.0% and 62.6%–95.3%). *WNT*-activated nuclear β-catenin accumulating medulloblastomas were smaller than the other entities (95% CI, 5.2–22.3 cm^3 versus 35.1–47.6 cm^3; $P = .03$). Hemorrhage was exclusively present in non-*WNT*/non-*SHH* medulloblastomas ($P = .04$; $n = 2/5$). MR imaging biomarkers were all discordant from those identified in the pediatric cohort. Desmoplastic/nodular medulloblastomas were more rarely in contact with the fourth ventricle (4/15 versus 7/13; $P = .04$).

CONCLUSIONS: MR imaging biomarkers can help distinguish histologic and genetic medulloblastoma entities in adults and appear to be different from those identified in children.

ABBREVIATIONS: AUC = area under the curve; CE = contrast-enhanced; CMB = classic medulloblastoma; DNMB = desmoplastic/nodular medulloblastoma; *SHH* = *sonic hedgehog*; WHO = World Health Organization; *WNT* = *wingless*

Medulloblastomas (World Health Organization [WHO] grade IV) rarely occur in adults. According to the United States registry analysis from the Surveillance, Epidemiology, and End-Results data base, incidence rates around 0.6 cases per million have been recorded, which is >50 times lower than the incidence of glioblastoma.[1-3] A higher age at diagnosis is a negative prognostic factor for survival, with a median overall survival currently between 7.7 and 9.7 years, provided patients receive the best medical care.[4] The 2016 revision of the WHO classification of CNS tumors introduced the concept of an integrative medulloblastoma diagnosis.[5] The diagnosis includes 4 histologically and 4 genetically defined entities known to have an influence on the

Received March 20, 2017; accepted after revision May 24.

From the Department of Radiology and Neuroradiology (V.C.K., C.R., S.J.E., H.H.S., E.H.), University Hospital Bonn, Bonn, Germany; Institute for Diagnostic and Interventional Neuroradiology (M.W.-M.), University Hospital Würzburg, Würzburg, Germany; Department of Neuropathology (T.P.), Brain Tumor Reference Center of the German Society for Neuropathology and Neuroanatomy, Bonn, Germany; Wilhelm Sander-Therapieeinheit NeuroOnkologie (C.R., P.H.) and Department of Neurology (C.R., P.H.), University Hospital Regensburg, Regensburg, Germany; Department of Neurology (D.B.), University Hospital Odense and Clinical Institute, University of Southern Denmark, Odense, Denmark; Department of Neurology (D.B.), University of Regensburg, Regensburg, Germany; and Deutsches Krebsforschungszentrum (D.T.W.J.), Division of Pediatric Neurooncology, Heidelberg, Germany.

Elke Hattingen and Peter Hau contributed equally to this work.

Prof. Hau received funding from Medac GmbH to conduct this study.

Paper previously presented at: Annual Meeting of the European Congress of Radiology, March 1–5, 2017 (SS711); Vienna, Austria.

Please address correspondence to Vera C. Keil, MD, Universitätsklinik Bonn, Radiologische Klinik, Sigmund-Freud-Str 25, D-53127 Bonn, Germany; e-mail: vera.keil@ukbonn.de

Indicates article with supplemental on-line photo.

http://dx.doi.org/10.3174/ajnr.A5313

course of the disease in both children and adults.[6-12] The genetic entities that are currently defined are *sonic hedgehog* (SHH)-activated (and exist with or without *TP53* mutation), *wingless* (WNT)-activated, and non-*SHH*/non-*WNT* (Groups 3 and 4) medulloblastomas. The defined histologic groups are classic (CMB), large cell anaplastic, desmoplastic/nodular (DNMB) medulloblastomas and medulloblastoma of extensive nodularity. The exact classification at the earliest possible time point is of great importance to evaluate prognosis and possible targeted therapies.

Radiogenomics is a dynamically evolving field in radiology based on standard diagnostic MR imaging. It seeks to identify so-called MR imaging biomarkers that may predict the genetic profile of a tumor, assuming that the genetic profile is reflected in a distinctive radiophenotype, and can also be of benefit when true genetic analysis is not available.[13] Only 1 study has been published in a predominantly pediatric cohort, which investigated a radiogenomic approach to differentiate genetically defined medulloblastoma entities.[14] The authors found that genetic entities were distinguishable by several MR imaging biomarkers such as tumor location or enhancement pattern. Different relative frequencies and varying prognostic influences of the genetic medulloblastoma entities between adult and pediatric cohorts suggest that MR imaging biomarkers identified in pediatric cohorts may be different from those in adult medulloblastoma.[8-10,12,15,16]

The Multicenter Pilot-study for the Therapy of Medulloblastoma of Adults (NOA-07) is the first prospective trial of an adult medulloblastoma cohort that systematically evaluated radiochemotherapy as the first-line treatment and included, among others, imaging biomarkers in its analysis. The study presented here is dedicated to identifying MR imaging biomarkers that will allow differentiation of medulloblastoma genetic entities based on the entirely adult NOA-07 cohort. Identification of such MR imaging biomarkers may facilitate presurgical tumor assessment and assist in the categorization of the differences between adult and pediatric MR imaging biomarkers.

MATERIALS AND METHODS

Patient and Imaging Data

This trial was registered at ClinicalTrials.gov (NCT01614132) and under the EudraCT number 2007-002560-10 (https://www.clinicaltrialsregister.eu/ctr-search/search?query=2007-002560-10) after approval by the ethics committee of the University of Regensburg, Regensburg, Germany (08-112-0058; substantial amendment of July 1, 2016) and of all participating sites. Between 2008 and 2014, 15 neuro-oncologic centers recruited 30 adult patients older than 21 years of age with suspected medulloblastomas. Medulloblastoma diagnosis was confirmed in all cases. Presurgical CT and MR imaging datasets were retrospectively analyzed involving multiparametric imaging criteria based on T1-weighted, T2-weighted, FLAIR, and contrast-enhanced T1-weighted sequences (available in $n = 28/30$) as well as apparent diffusion coefficient maps ($n = 23/30$, On-line Figure). In 2 of 30 cases, presurgical MR imaging data were not available.

Table 1: Adult and pediatric cohorts by histology and genetic status

	Adult (This Cohort, *n* = 28)	Pediatric (Perreault et al. 2014[14]) (*n* = 47)
Median age (range) (yr)	39.0 (33.4–41.3)	8.2 (0.9–33.9)
Male/female	1.5:1.0	2.4:1.0
Genetic entity (No.) (%)		
SHH	19 (67.9%)	13 (27.7%)
WNT	4 (14.2%)	4 (8.4%)
Group 4	5 (17.9%)	17 (36.2%)
Group 3	0 (0.0%)	13 (27.7%)
Histologic entity (No.) (%)		
Classic	13 (46.4%)	31 (66.0%)
Desmoplastic/nodular	15 (53.6%)	4 (8.5%)
Large cell anaplastic	0 (0.0%)	10 (21.3%)
Other subgroups	0 (0.0%)	2 (4.2%)

Note:—*SHH* indicates *sonic hedgehog*–activated medulloblastoma; *WNT*, *wingless*-activated medulloblastoma.

Data were compared with that in the cohort of Perreault et al,[14] in which 42 of 47 cases were pediatric (Table 1).

Imaging Criteria Definition and Analysis

Three neuroradiologists (E.H., M.W.-M., V.C.K., with 26, 28, and 6 years of experience, respectively) who were blinded to the histologic and genetic backgrounds of each patient, evaluated noncontrast-enhanced CT scans and MR imaging datasets (1.5T or 3T). Criteria were grouped as follows: 1) classic morphologic imaging characteristics applied to describe brain tumors, 2) Chang medulloblastoma staging criteria and tumor location,[17] 3) diagnostic criteria of hydrocephalus or brain stem compression, and 4) tumor and edema volumes and respective ratios.

Classic morphologic characteristics of brain tumors were defined as the following: enhancement pattern (strong, weak, nonenhancing), signal homogeneity (homogeneous, inhomogeneous), signal intensity (hypointense, isointense, hyperintense to gray matter) on nonenhanced T1-weighted and T2-weighted images, the sharpness of tumor margins, and the presence of cyst formation and hemorrhage. The presence of hemorrhage was diagnosed from either additional SWI or T2-weighted gradient-echo sequences or on presurgical CT.

Location criteria were the following: infiltration of the vermis, the hemispheres, or the brain stem/peduncular region, including contact with the lower rhombic lip, the eighth cranial nerve, the fourth ventricle, or the cerebellopontine angle. In addition, the presence of hydrocephalus, brain stem compression, midline shift, supratentorial growth, and multifocality was evaluated.

Medulloblastoma volumes were determined with commercially available software (tumor tracking tool, Intellispace Portal 5.0; Philips Healthcare, Best, the Netherlands) on automatically aligned contrast-enhanced T1WI (CET1WI) and T2-weighted images on the basis of manually defined signal-intensity thresholds. Perifocal edema was quantified on FLAIR datasets. Volume ratios were established as the following: 1) tumor volume ratio, which was defined as the volume fraction of the tumor part with exclusive T2 signal elevation and without the contrast-enhancing volume fraction (T2-weighted volume minus CET1WI volume divided by T2-weighted volume); and 2) edema-tumor ratio, which was defined as edema volume on FLAIR images divided by T2-weighted tumor volume.

Table 2: Comparative overview of MR imaging biomarkers for adult and pediatric cohorts regarding genetic entity discrimination

Adult Cohort Imaging Criteria (n = 28)	P Value	Correspondence	P Value	Pediatric Cohort Imaging Criteria (n = 47)[a]
Hemorrhage[b]	.04[b]	No[b]	NS	Blood products
Edema volume[b]	.02[b]	No[b]	NS	Edema present
Hydrocephalus[b]	.03[b]	NA	NA	NA
Chang M-stage ≥2[b] (Chang on CET1WI plus spinal tap)	.02[b]	NA	NA	NA
Contact with lower rhombic lip[b]	.03[b]	NA	NA	NA
Chang T-stage >T2 on T2WI[b]	.01[b]	NA	NA	NA
Contact with fourth ventricle[b]	.02[b]	Pseudocorrespondence	<.005[b]	Midline/fourth ventricle[b]
Infiltration of vermis	.80	No[b]		
Cysts	.82	Both NS	NS	Cyst
Contrast-enhancement homogeneity	.29	Both NS	NS	Enhancement pattern solid
Infiltration of cerebellar hemispheres	.08	No[b]	<.005[b]	Cerebellar hemisphere[b]
Contact with cerebellopontine angle	1.0	No[b]	<.005[b]	Contact with cerebellopontine angle[b]
Enhancement pattern	.81	No[b]	<.005[b]	Enhancement minimal to none[b]
Sharp margins	.63	No[b]	.03[b]	Ill-defined margins[b]
NA	NA	NA	NS	Enhancement pattern, other

Note:—NA indicates not available (parameter not analyzed); NS, criterion not significantly unbalancedly distributed, hence not identified a biomarker by Perreault et al.[14]
[a] Pediatric cohort: discovery cohort of Perreault el al.[14] No identical MR imaging biomarkers could be identified among imaging criteria of both cohorts.
[b] MR imaging biomarkers that were identified by significantly imbalanced distribution between genetic entities.

The criteria of Chang et al[17] were determined on the basis of tumor margins on both T2-weighted and CET1-weighted images. Macroscopically visible subependymal/ventricular metastases (Chang M-stage ≥2) were determined on CET1WI. Micrometastases (Chang M-stage 1) were previously investigated in the CSF at the time of diagnosis on the basis of the evaluation of 2 board-certified neuropathologists in all cases.[17]

Neuropathologic Evaluation

Medulloblastoma diagnoses had been confirmed at the German Brain Tumor Reference Center of the German Society for Neuropathology and Neuroanatomy by at least 2 board-certified neuropathologists. Classification was performed with histologic, immunohistochemical, and genetic analyses according to the revised WHO Classification of Tumors of the CNS 2016 as described in current Best Practice Guidelines.[18] Histologically and genetically defined medulloblastoma entities were available for all 28 patients. In addition, the whole genomic copy number and allelic distribution were analyzed by molecular inversion probe methodology without evidence of amplifications in *MYCC*, *MYCN*, or *GLI2* genes. One *SHH*-activated tumor was found to exhibit copy number losses of 9q and chromosome 14, typical for *SHH*-activated entities. A subgroup of samples was classified according their epigenetic subgroup by methylation arrays (450k array), which confirmed the genetically defined subgroups in all cases.[19,20] The complete analysis catalogue is listed in the On-line Figure.

Imaging criteria of the comparative pediatric cohort are listed in Table 2 extracted from the earlier publication.[14]

Statistics

Statistical analyses were designed by an independent biomathematician and performed with STATA 14.0 (StataCorp, College Station, Texas). Because no tentative assumptions regarding the relationship between imaging criteria and genetic or histologic status could be made, an exploratory statistical approach to identify possible MR imaging biomarkers involved testing imaging criteria against all other criteria with 2-sided Fisher exact or ANOVA testing (depending on whether categoric or continuous data were handled). Deliberately, no multiple testing correction approach was chosen to not overlook any possible significant associations.[21] Statistical significance was reached at $P < .05$.

Imaging criteria that were significantly associated with genetic criteria, according to the exploratory tests, were defined as potential imaging biomarkers. These were then assessed regarding their sensitivity and specificity in the differentiation of genetic entities. Evaluation involved both single and combined MR imaging biomarker applications and was based on an area under the curve (AUC) analysis.

To investigate potential differences between adult and pediatric biomarkers, we compared imaging biomarkers identified in the present study with those of a previous study involving a predominantly pediatric cohort.[14]

RESULTS

Patient Cohort

The cohort of adult patients with medulloblastoma in this NOA-07 substudy included 11 women and 17 men (detailed overview in Table 1). In this cohort, no *SHH*-activated *TP53*–mutated medulloblastomas were found, all were TP53 wild type. Histologically, no cases with large cell anaplastic histology or with extensive nodularity were present. All *WNT*-activated and non-*WNT*/non-*SHH* medulloblastomas were histologically CMB, while 4 of 15 *SHH*-activated medulloblastomas were DNMB ($P = .001$).

Imaging Biomarkers of Genetic Entities and Chromosomal Aberrations

Six categoric and continuous volumetric imaging criteria could be identified as MR imaging biomarkers to differentiate genetically defined entities of *SHH TP53* wild type, *WNT*-activated, and non-*SHH*/non-*WNT* Group 4 medulloblastomas in this cohort (Table 3). Notably, apart from hemorrhage, none of the classic MR imaging criteria used for tumor description, as defined in the "Materials and Methods" section, were identified as suitable MR imaging biomarkers.

The absence of the biomarker "hydrocephalus" was observed in 4 of 4 *WNT*-activated medulloblastomas. Hence, normally

Table 3: Imaging biomarkers for adult medulloblastoma genetic entity differentiation[a]

Imaging Biomarker	*P* Value	Genetic Entity		
		SHH (*n* = 19)	*WNT* (*n* = 4)	Group 4 (*n* = 5)
Hydrocephalus	.03[b]	12/19	0	4/5
Chang M-stage ≥2 (CET1WI)	.02[b]	10/19	0	1/5
Hemorrhage	.04[b]	0	0	2/5
Contact with fourth ventricle	.02[b]	3/19	3/4	3/5
Contact with lower rhombic lip	.03[b]	0	1/4	2/5
Chang T-stage >2 (T2WI)	.01[b]	17/19	1/4	4/5
Tumor volume on T2WI (median and 95% CI)	.06[c]	30.6 cm^3 (26.6–37.7 cm^3)	5.6 cm^3 (5.2–22.3 cm^3)	25.0 cm^3 (0.64–47.4 cm^3)

Note:—*SHH* indicates *sonic hedgehog*–activated medulloblastoma (only TP53 wild type in this cohort); *WNT*, *wingless*-activated medulloblastoma.

[a] Candidate imaging biomarkers for the differentiation of 3 different genetic medulloblastoma entities in this cohort (*SHH*, *WNT*, non-*SHH*/non-*WNT* Group 4) are listed on the left.

[b] Significant.

[c] Near significance when comparing all 3 groups.

sized ventricular spaces as a biomarker to differentiate *WNT*-activated lesions showed a high negative predictive value and a sensitivity of 100% (95% CI, 39.81%–100.0%; AUC, 0.83 [95% CI, 0.67–0.99]). However, the positive predictive value of having ruled out the other entities correctly was low (33.33%; 95% CI, 22.12%–46.8%), because 7 of 19 *SHH*-activated and 1 of 5 non-*SHH*/non-*WNT* medulloblastomas also showed no signs of hydrocephalus.

The absence of subependymal macrometastases (Chang M ≥2) identified *WNT*-activated lesions with 100% sensitivity (all *WNT* activated cases, Chang M <2; AUC, 0.73; 95% CI, 0.52–0.94). However, the positive predictive value was again low (21.0%; 95% CI, 16.42%–26.73%).

Hemorrhage was exclusively observed in non-*SHH*/non-*WNT* medulloblastomas ($n = 2/5$), resulting in a positive predictive value of 100% to identify this entity correctly; however, it had a low sensitivity (40.0%; 95% CI, 5.30%–85.34%; AUC, 0.70 [95% CI, 0.40–1.0]).

The combination of all 3 of the above-mentioned biomarkers to identify *WNT*-activated medulloblastomas increased the specificity to 88.30% (95% CI, 62.6%–95.32%) at a sensitivity of 100% (95% CI, 39.80%–100%) and a negative predictive value of 100%, because no *WNT*-activated lesions showed hemorrhage, hydrocephalus, or macrometastases (AUC, 0.92; 95% CI, 0.81–1.0). The positive predictive value was 50.0% (95% CI, 29.0%–71.0%) because 3 of 19 *SHH*-activated and 1 of 5 non-*SHH*/non-*WNT* lesions were also negative for all 3 criteria.

Differentiation of *WNT*-activated medulloblastomas from *SHH*-activated and non-*SHH*/non-*WNT* entities combined was also possible: *WNT*-activated nuclear β-catenin accumulating medulloblastomas were significantly smaller on T2-weighted images (median, 11.0 versus 37.7 cm^3; 95% CI, 5.2–22.3 versus 35.1–47.6 cm^3; $P = .03$). Tumor volume on T2-weighted images was at a 5% error limit not significantly different when comparing all 3 entities ($P = .06$, Table 3).

The differentiation of *SHH*-activated and non-*SHH*/non-*WNT* Group 4 lesions was possible on the basis of edema volumes (*SHH*-activated medulloblatoma: median edema, 5.1 cm^3; 95% CI, 3.3–8.0 cm^3; Group 4 median edema, 1.2 cm^3; 95% CI, 0.0–6.9 cm^3; AUC, 0.85 [95% CI, 0.63–1.0; $P = .02$]), while tumor at the fourth ventricle (*SHH*-activated medulloblastoma, 3 of 19 cases; Group 4, three of 5 cases; AUC, 7.21; 95% CI, 0.39–1.0), contact with the lower rhombic lip, and the presence of hemorrhage (both biomarkers: *SHH*-activated medulloblastoma in 0 of 19 cases; Group 4, two of 5 cases; AUC, 0.70; 95% CI, 0.39–1.0) were less reliable and not significant ($P = .14$, .18, and .18, respectively). A visualization of MR imaging biomarkers for all 3 genetically defined medulloblastoma entities is presented in Fig 1.

No significant association could be identified for any of the imaging criteria and the chromosomal status of the tumor.

Comparison with Previously Reported MR Imaging Biomarkers for Medulloblastoma Entities in Pediatric Patients

Relative frequencies of histologically and genetically defined medulloblastoma entities were different between both cohorts: None of the MR imaging biomarkers identified in the adult cohort corresponded to those identified in the comparative predominantly pediatric cohort (Table 2). "Midline/fourth ventricle contact" was a significant biomarker to identify non-*SHH*/non-*WNT* medulloblastomas in the pediatric cohort. Midline location of the lesion was not significant in our cohort (criterion "vermis"). Contact with the fourth ventricle was analyzed separately for the present adult cohort and was determined as a biomarker with excess representation in *WNT*-activated medulloblastomas (Table 3).

Imaging Characteristics of Histologically Defined Entities DNMB and CMB

Perifocal edema volume was significantly larger in DNMB ($n = 15$) than in CMB [$n = 13$; median, 8.74 cm^3 (95% CI, 5.71–11.73 cm^3) versus 2.31 cm^3 (95% CI, 1.12–5.74 cm^3); $P = .01$; AUC 0.83 (95% CI, 0.68–0.98)]. DNMBs were less frequently in contact with the fourth ventricle than CMBs [4 of 15 versus 7 of 13; $P = .04$; positive predictive value to identify CMB correctly, 63.6% (95% CI, 39.7%–82.3%); AUC, 0.7 (95% CI, 0.5–0.9)].

DISCUSSION

According to the recent revision of the WHO classification of brain tumors, the definition of genetic and histologic features of medulloblastoma is a prerequisite for a proper diagnosis of this tumor.[5] In both pediatric and adult patients, genetically and histologically defined entities were determined to be relevant for prognosis and patient outcome. Therefore, precise characterization of medulloblastomas can facilitate the design of personalized therapies.[14,15,20] Biomarkers based on standard MR imaging techniques have been successfully applied in the diagnosis of numerous brain lesions, including medulloblastomas.[13,22-27]

As part of the criteria of Chang et al,[17] MR imaging morphometric analyses are well-established for medulloblastomas and are relevant in the prognosis of both adult and pediatric cohorts.[28] However, entities of adult medulloblastomas seem to behave differently from the same entities in pediatric cohorts.[10,12,14] To our knowledge, this is the first study to date that analyzes MR imaging biomarkers for genetic entity discrimination of exclusively adult patients with medulloblastoma in comparison with a pediatric cohort. The imaging criteria used in this study differ slightly from those presented in the study of Perreault et al.[14] Because the present

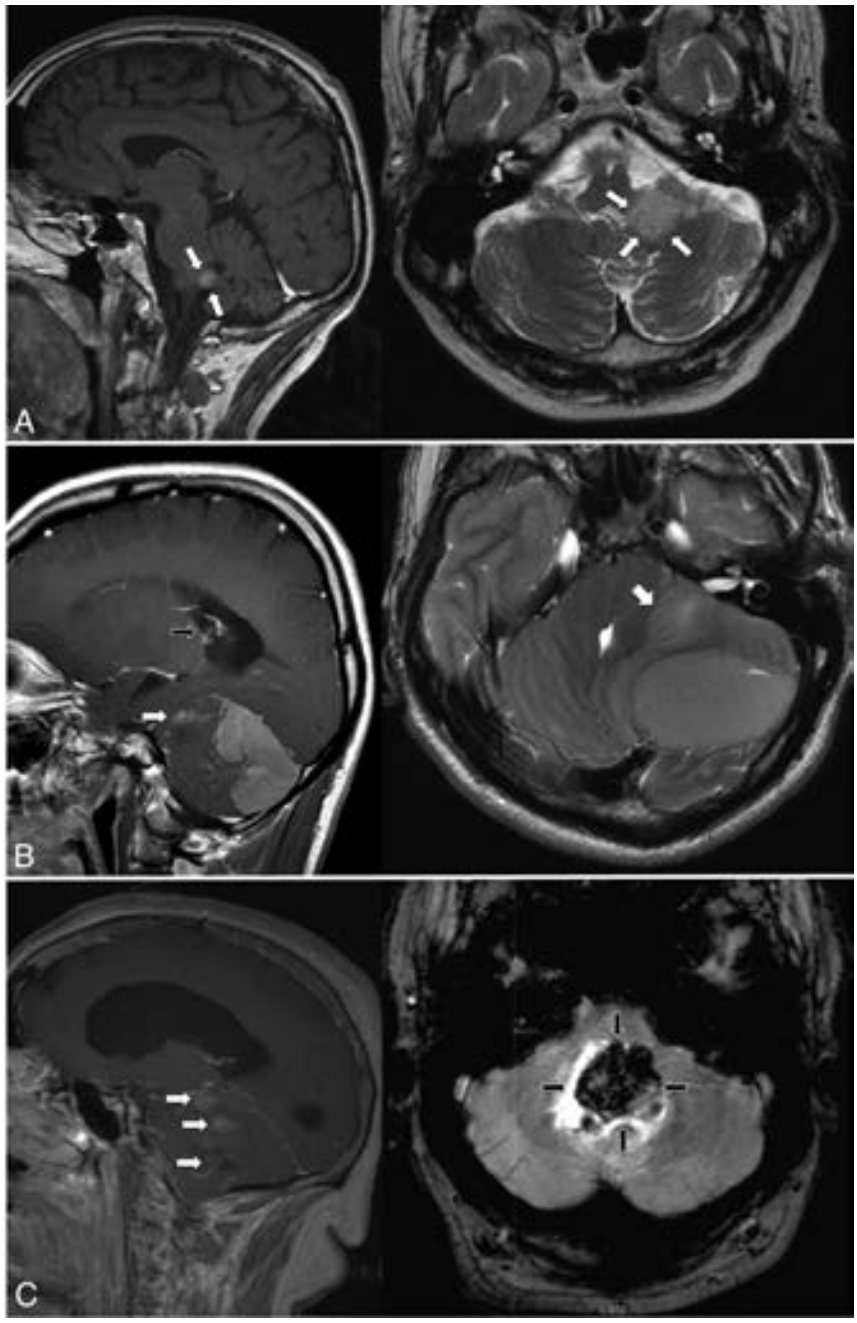

FIG 1. Characteristic imaging features of genetic medulloblastoma entities. Sagittal sections on the left; transverse sections on the right. *A*, Typical *WNT*-activated medulloblastoma, relatively small, in contact with the fourth ventricle (tumor margins marked with *white arrows*), no hydrocephalus. *B*, *SHH*-activated medulloblastoma with large tumor volume and macrometastases (sagittal image, *white arrow*) and large edema volume (transverse image, *white arrow*) and hydrocephalus (sagittal image, *black arrow*). *C*, Non-*SHH*/non-*WNT* Group 4 tumor showing macrometastases (sagittal image, *white arrows*), hydrocephalus, and hemorrhage (transverse image, *black arrows*) as distinguishing features.

study was a multicenter study, sequence parameters and image quality varied among the centers; these differences make the analysis more difficult.[14] In detail, the pediatric comparative cohort did not differentiate between 2 of the biomarkers in our cohort ("contact with the fourth ventricle" and "vermis/midline location") and did not include the Chang criteria or hydrocephalus. Remarkably, no coherent MR imaging biomarkers for the same genetic entities could be identified between adult and pediatric cohorts.

The cohort of adult medulloblastomas included in this study did not contain any *SHH*-activated *TP53* mutated cases or patients with large cell/anaplastic or extensively nodular histology, which are all common in pediatric cohorts.[4] Similarly, the relative frequencies of genetically defined medulloblastoma entities in this cohort differed from those in pediatric cohorts but were concordant with other adult cohorts.[9,12,14,16]

As a main result of our study, *WNT*-activated genetic entities of adult patients with medulloblastoma could be differentiated from *SHH*-activated *TP53* wild type and non-*SHH*/non-*WNT* Group 4 medulloblastomas by a combination of MR imaging biomarkers. Adult *WNT*-activated tumors were observed to be correlated to several imaging biomarkers, which might be described as their radiophenotype. At the time of tumor detection (and thus of neurologic symptoms), *WNT* tumors are in contact with the fourth ventricle, but without Chang M-stage ≥2 and are of small volume (lower Chang T-stages), in consequence without hydrocephalus. This finding might suggest that early midline location at the fourth ventricle induces neurologic symptoms, which allow diagnosis despite low tumor size. In contrast, most *SHH*-activated or non-*SHH*/non-*WNT* tumors were larger, multilocular, or focally metastatic and associated with hydrocephalus. Smaller, monofocal tumors can be more easily resected in total. This characteristic may also partially explain a frequently identified higher survival in these patients.[27] Most interesting, an association of *WNT*-activated medulloblastomas in the lower rhombic lip could only be confirmed for a minority of tumors in this trial, despite the embryologic association of *WNT*-activation within the lower rhombus.

The combination of 3 of 6 identified imaging biomarkers, hemorrhage, subependymal macrometastases, and hydrocephalus, allowed an optimal discrimination of *WNT*-activated medulloblastomas from the other 2 genetic entities in our cohort. All MR imaging biomarkers relevant for genetic entity discrimination in this cohort were, however, different from those identified for the comparative pediatric cohort. The pediatric cohort did not differentiate between 2 of the biomarkers in our cohort (contact with the fourth ventricle and vermis/midline location). Contact with the fourth ventricle is, therefore, a pseudo-

consistent biomarker between both cohorts because it was linked to the criterion midline location in the pediatric cohort, which was not identified as a biomarker in our study.

Commonly, medulloblastoma location is stratified into medial, cerebellopontine, and hemispheric lesions. However, attempts to use location criteria as biomarkers for differentiation of genetic medulloblastoma entities have yielded only inconsistent results.[14,29-31] Our cohort also exhibits this inconsistency, because no significant association between genetic entities and tumor location was observed. This may suggest that these location categories are not useful as biomarkers in adult medulloblastomas. A lack of association between cerebellar location and genetic entity is, to some extent, in conflict with findings that suggested that different medulloblastoma genetic entities had a spatially and cytologically distinct tumorigenesis.[7,29,32]

Classic morphologic tumor criteria such as signal homogeneity were not significantly associated with genetic entities in our study. This finding was strikingly different from the data of Perreault et al,[14] in which sharpness of tumor margins, enhancement pattern, and location categories were highly predictive of genetic entities (though tumor margins later proved not an adequate MR imaging biomarker when tested with the validation cohort of the pediatric study). Hemorrhage was the only classic morphologic tumor criterion in our cohort that exclusively occurred in Group 4 tumors. However, hemorrhage was also reported in *WNT*-activated medulloblastomas.[27,33] Therefore, this MR imaging biomarker should be re-evaluated in a larger independent cohort.

Considering the substantial amount of genetic and chromosomal factors investigated in this study, it remains surprising how many of these factors apparently do not result in a particular radiophenotype, especially when considering chromosomal aberrations. It can thus be postulated that the biologic impact of these factors cannot be quantified by standard MR imaging sequences. Quantitative MR imaging sequences and multifactorial computer-assisted image data analyses may, however, allow a better identification of biomarkers.[34]

As a limitation of our study, the comparative pediatric cohort comprised 4 adults (besides 43 children). However, the main limitation is the small size of our cohort. All findings regarding imaging biomarkers must, therefore, be taken as hypothesis-generating and should be tested for their validity in larger cohorts in the future. Different from our comparative pediatric cohort, in the discovery cohort of Perreault et al,[14] no validation cohort was available to test the identified MR imaging biomarkers for adult medulloblastoma genetic entity differentiation in a blinded setting. Further research is needed to determine why biomarkers for medulloblastoma entities in pediatric patients differed from adult biomarkers identified in this study and also why classic tumor imaging criteria were usually not relevant as MR imaging biomarkers in this study. Possible reasons can be statistical effects due to a small cohort size, different methods of image assessment, but also a true lack of influence of the genetic entity on medulloblastoma radiophenotype. An international prospective trial with larger patient numbers is planned and will be an opportunity to elaborate on these open questions.

CONCLUSIONS

Several MR imaging biomarkers could be identified in this cohort of adult patients with medulloblastoma and allowed successful presurgical discrimination of genetically as well as histologically defined medulloblastoma entities. MR imaging biomarkers used in differentiation of medulloblastomas in adults seem distinct from biomarkers in children. Both findings will need to undergo further validation by radiogenomic analyses of larger medulloblastoma cohorts.

Disclosures: Vera C. Keil—*UNRELATED*: *Payment for Lectures Including Service on Speakers Bureaus*: Philips Healthcare, *Comments*: 2015 invited talk in Switzerland, topic different from current study; *Travel/Accommodations/Meeting Expenses Unrelated to Activities Listed*: European Congress of Radiology, Vienna, *Comments*: oral presentation of study. Monika Warmuth-Metz—*UNRELATED*: *Board Membership*: Roche, *Comments*: adjudicator for the central review of imaging for the HERBY study (already closed); *Consultancy*: Italian Children's Hospital (Milano) and Russian Children's Cancer Hospital (Moscow), *Comments*: For the Milano hospital, I do the regular central evaluation for a diffuse intrinsic pontine glioma treatment study. For the Russian hospital, I do occasional evaluation of complicated cases of various brain tumors or brain lesions after treatment (eg, for leukemia); *Expert Testimony*: German Childhood Cancer Foundation (association of parents of affected children), *Comments*: funding for the central review of pediatric brain tumor imaging.* Torsten Pietsch—*UNRELATED*: *Consulting Fee or Honorarium*: Roche, Chugai Pharmaceutical Co, *Comments*: honoraria for talks; *Support for Travel to Meetings for the Study or Other Purposes*: Chugai Pharmaceutical Co, Affymetrix, *Comments*: travel support. Peter Hau—*RELATED*: *Grant*: Medac, *Comments*: educational grant for clinical trial, €5000 (US $5638.28)*; *UNRELATED*: *Consultancy*: Roche, Novocure, Eli Lilly and Company, Merck, *Comments*: consultant fees between €1000 (US $1141.65) and €2000 (US $2283.30); *Payment for Lectures Including Service on Speakers Bureaus*: Novocure, *Comments*: fees between €1000 (US $1141.65) and €2000 (US $2283.30); *Travel/Accommodations/Meeting Expenses Unrelated to Activities Listed*: Roche, Medac, *Comments*: Society for Neuro-Oncology meeting 2015 and 2017. *Money paid to the institution.

REFERENCES

1. Giordana MT, Schiffer P, Lanotte M, et al. **Epidemiology of adult medulloblastoma.** *Int J Cancer* 1999;80:689–92 Medline
2. Smoll NR. **Relative survival of childhood and adult medulloblastomas and primitive neuroectodermal tumors (PNETs).** *Cancer* 2012; 118:1313–22 CrossRef Medline
3. Thakkar JP, Dolecek TA, Horbinski C, et al. **Epidemiologic and molecular prognostic review of glioblastoma.** *Cancer Epidemiol Biomarkers Prev* 2014;23:1985–96 CrossRef Medline
4. Lai R. **Survival of patients with adult medulloblastoma: a population-based study.** *Cancer* 2008;112:1568–74 CrossRef Medline
5. Louis DN, Perry A, Reifenberger G, et al. **The 2016 World Health Organization Classification of Tumors of the Central Nervous System: a summary.** *Acta Neuropathol* 2016;131:803–20 CrossRef Medline
6. Padovani L, Sunyach MP, Perol D, et al. **Common strategy for adult and pediatric medulloblastoma: a multicenter series of 253 adults.** *Int J Radiat Oncol Biol Phys* 2007;68:433–40 CrossRef Medline
7. Gibson P, Tong Y, Robinson G, et al. **Subtypes of medulloblastoma have distinct developmental origins.** *Nature* 2010;468:1095–99 CrossRef Medline
8. Remke M, Hielscher T, Northcott PA, et al. **Adult medulloblastoma comprises three major molecular variants.** *J Clin Oncol* 2011;29: 2717–23 CrossRef Medline
9. Northcott PA, Hielscher T, Dubuc A, et al. **Pediatric and adult sonic hedgehog medulloblastomas are clinically and molecularly distinct.** *Acta Neuropathol* 2011;122:231–40 CrossRef Medline
10. Fellay CN, Frappaz D, Sunyach MP, et al. **Medulloblastomas in adults: prognostic factors and lessons from paediatrics.** *Curr Opin Neurol* 2011;24:626–32 CrossRef Medline
11. Taylor MD, Northcott PA, Korshunov A, et al. **Molecular subgroups of medulloblastoma: the current consensus.** *Acta Neuropathol* 2012; 123:465–72 CrossRef Medline

12. Zhao F, Ohgaki H, Xu L, et al. **Molecular subgroups of adult medulloblastoma: a long-term single-institution study.** *Neuro Oncol* 2016;18:982–90 CrossRef Medline
13. Colen RR, Hassan I, Elshafeey N, et al. **Shedding light on the 2016 World Health Organization Classification of Tumors of the Central Nervous System in the era of radiomics and radiogenomics.** *Magn Reson Imaging Clin N Am* 2016;24:741–49 CrossRef Medline
14. Perreault S, Ramaswamy V, Achrol AS, et al. **MRI surrogates for molecular subgroups of medulloblastoma.** *AJNR Am J Neuroradiol* 2014;35:1263–69 CrossRef Medline
15. Kool M, Korshunov A, Remke M, et al. **Molecular subgroups of medulloblastoma: an international meta-analysis of transcriptome, genetic aberrations, and clinical data of WNT, SHH, Group 3, and Group 4 medulloblastomas.** *Acta Neuropathol* 2012;123:473–84 CrossRef Medline
16. Lassaletta A, Ramaswamy V. **Medulloblastoma in adults: they're not just big kids.** *Neuro Oncol* 2016;18:895–97 CrossRef Medline
17. Chang CH, Housepian EM, Herbert C Jr. **An operative staging system and a megavoltage radiotherapeutic technic for cerebellar medulloblastomas.** *Radiology* 1969;93:1351–59 CrossRef Medline
18. Pietsch T, Haberler C. **Update on the integrated histopathological and genetic classification of medulloblastoma: a practical diagnostic guideline.** *Clin Neuropathol* 2016;35:344–52 CrossRef Medline
19. Hovestadt V, Jones DT, Picelli S, et al. **Decoding the regulatory landscape of medulloblastoma using DNA methylation sequencing.** *Nature* 2014;510:537–41 CrossRef Medline
20. Pietsch T, Schmidt R, Remke M, et al. **Prognostic significance of clinical, histopathological, and molecular characteristics of medulloblastomas in the prospective HIT2000 multicenter clinical trial cohort.** *Acta Neuropathol* 2014;128:137–49 CrossRef Medline
21. Rothman KJ. **No adjustments are needed for multiple comparisons.** *Epidemiology* 1990;1:43–46 CrossRef Medline
22. Yeom KW, Mobley BC, Lober RM, et al. **Distinctive MRI features of pediatric medulloblastoma subtypes.** *AJR Am J Roentgenol* 2013;200:895–903 CrossRef Medline
23. Bourgouin PM, Tampieri D, Grahovac SZ, et al. **CT and MR imaging findings in adults with cerebellar medulloblastoma: comparison with findings in children.** *AJR Am J Roentgenol* 1992;159:609–12 CrossRef Medline
24. Malheiros SM, Carrete H Jr, Stávale JN, et al. **MRI of medulloblastoma in adults.** *Neuroradiology* 2003;45:463–67 CrossRef Medline
25. Koeller KK, Rushing EJ. **From the archives of the AFIP: medulloblastoma: a comprehensive review with radiologic-pathologic correlation.** *Radiographics* 2003;23:1613–37 CrossRef Medline
26. Fruehwald-Pallamar J, Puchner SB, Rossi A, et al. **Magnetic resonance imaging spectrum of medulloblastoma.** *Neuroradiology* 2011;53:387–96 CrossRef Medline
27. Phoenix TN, Patmore DM, Boop S, et al. **Medulloblastoma genotype dictates blood brain barrier phenotype.** *Cancer Cell* 2016;29:508–22 CrossRef Medline
28. Kocakaya S, Beier CP, Beier D. **Chemotherapy increases long-term survival in patients with adult medulloblastoma: a literature-based meta-analysis.** *Neuro Oncol* 2016;18:408–16 CrossRef Medline
29. Grammel D, Warmuth-Metz M, von Bueren AO, et al. **Sonic hedgehog-associated medulloblastoma arising from the cochlear nuclei of the brainstem.** *Acta Neuropathol* 2012;123:601–14 CrossRef Medline
30. Teo WY, Shen J, Su JM, et al. **Implications of tumor location on subtypes of medulloblastoma.** *Pediatr Blood Cancer* 2013;60:1408–10 CrossRef Medline
31. Robinson GW. **Impact of tumor location on medulloblastoma subtyping and treatment.** *Pediatr Blood Cancer* 2013;60:1393–94 CrossRef Medline
32. Jaiswal AK, Mahapatra AK, Sharma MC. **Cerebellopointine angle medulloblastoma.** *J Clin Neurosci* 2004;11:42–45 CrossRef Medline
33. Shinojima N, Nakamura H, Tasaki M, et al. **A patient with medulloblastoma in its early developmental stage.** *J Neurosurg Pediatr* 2014;14:615–20 CrossRef Medline
34. Macyszyn L, Akbari H, Pisapia JM, et al. **Imaging patterns predict patient survival and molecular subtype in glioblastoma via machine learning techniques.** *Neuro Oncol* 2016;18:417–25 CrossRef Medline

Multinodular and Vacuolating Neuronal Tumor of the Cerebrum: A New "Leave Me Alone" Lesion with a Characteristic Imaging Pattern

R.H. Nunes, C.C. Hsu, A.J. da Rocha, L.L.F. do Amaral, L.F.S. Godoy, T.W. Watkins, V.H. Marussi, M. Warmuth-Metz, H.C. Alves, F.G. Goncalves, B.K. Kleinschmidt-DeMasters, and A.G. Osborn

ABSTRACT

SUMMARY: Multinodular and vacuolating neuronal tumor of the cerebrum is a recently reported benign, mixed glial neuronal lesion that is included in the 2016 updated World Health Organization classification of brain neoplasms as a unique cytoarchitectural pattern of gangliocytoma. We report 33 cases of presumed multinodular and vacuolating neuronal tumor of the cerebrum that exhibit a remarkably similar pattern of imaging findings consisting of a subcortical cluster of nodular lesions located on the inner surface of an otherwise normal-appearing cortex, principally within the deep cortical ribbon and superficial subcortical white matter, which is hyperintense on FLAIR. Only 4 of our cases are biopsy-proven because most were asymptomatic and incidentally discovered. The remaining were followed for a minimum of 24 months (mean, 3 years) without interval change. We demonstrate that these are benign, nonaggressive lesions that do not require biopsy in asymptomatic patients and behave more like a malformative process than a true neoplasm.

ABBREVIATIONS: DNET = dysembryoplastic neuroepithelial tumor; MVNT = multinodular and vacuolating neuronal tumor of the cerebrum

Multinodular and vacuolating neuronal tumor of the cerebrum (MVNT) was first described in 2013 as a benign seizure-associated lesion with a characteristic histopathologic appearance.[1]

The most recent (2016) *World Health Organization Classification of Tumors of the Central Nervous System*[2] includes MVNT as a unique cytoarchitectural pattern of gangliocytoma, though to date, it remains unclear whether MVNT is a true neoplastic process or a dysplastic hamartomatous/malformative lesion.[2,3]

Only a few cases of MVNT have been reported in the neuropathology literature.[1,3-6] We report 33 cases of presumed MVNT that exhibit a remarkably similar pattern of imaging findings that, in many of our cases, were followed for years without demonstrating interval change. Only 4 of our cases were biopsy-proven because most were asymptomatic and incidentally discovered.

In this article, we describe the nearly pathognomonic imaging appearance of MVNTs and suggest that these are nonaggressive "leave me alone" brain lesions, which do not require either biopsy or resection.

CASE SERIES

Case Selection

Fifty-three cases of presumed MVNTs were collected from the MR imaging archives of the multinational contributing authors. Imaging was performed between July 2006 and November 2016. All cases were characterized as a subcortical or juxtacortical lesion consisting of a small cluster of nodules (Fig 1). Patient records for each case were retrospectively reviewed, and demographic features, clinical symptoms prompting initial imaging, histopathology reports, and follow-up studies or subsequent development of neurologic symptoms were noted by each contributing author. Cases that did not have either biopsy proof or follow-up of at least 24 months were later excluded, resulting in 33 patients.

Imaging Analysis

All imaging studies were performed on either a 1.5T or a 3T scanner. In all studies, sequences performed included sagittal T1WI, axial FLAIR, and DWI. Depending on the scanner used, either a gradient-echo sequence or a susceptibility-weighted imaging sequence was performed. Thin-section steady-state sequences (FIESTA,

Received February 18, 2017; accepted after revision May 3.

From the Division of Neuroradiology (R.H.N., A.J.d.R., L.L.F.d.A., H.C.A.), Santa Casa de Sao Paulo School of Medical Sciences, Sao Paulo, Brazil; Division of Neuroradiology (R.H.N., A.J.d.R.), Diagnosticos da America SA, Sao Paulo, Brazil; Department of Medical Imaging (C.C.H., T.W.W.), Princess Alexandra Hospital, Brisbane, Queensland, Australia; Division of Neuroradiology (L.L.F.d.A., V.H.M.), Medimagem, Hospital da Beneficencia Portuguesa de Sao Paulo, Sao Paulo, Brazil; Department of Radiology (L.F.S.G.), Hospital Sirio Libanes, Sao Paulo, Brazil; Department of Radiology (L.F.S.G.), Medical School, Universidade de Sao Paulo, Sao Paulo, Brazil; Department of Neuroradiology (M.W.-M.), University Hospital Würzburg, Würzburg, Germany; Department of Radiology (F.G.G.), Children's Hospital of Brasilia, Brasilia, Brazil; Department of Pathology (B.K.K.-D.), University of Colorado, Aurora, Colorado; and Department of Radiology (A.G.O.), University of Utah, Salt Lake City, Utah.

Please address correspondence to Renato Hoffmann Nunes, MD, Santa Casa de Misericórdia de São Paulo, Serviço de Diagnóstico por Imagem, Rua Dr Cesário Motta Junior 112, Vila Buarque, São Paulo-SP/Brazil, 01221-020; e-mail: renatohn@hotmail.com; @renatohn

Indicates article with supplemental on-line table.

http://dx.doi.org/10.3174/ajnr.A5281

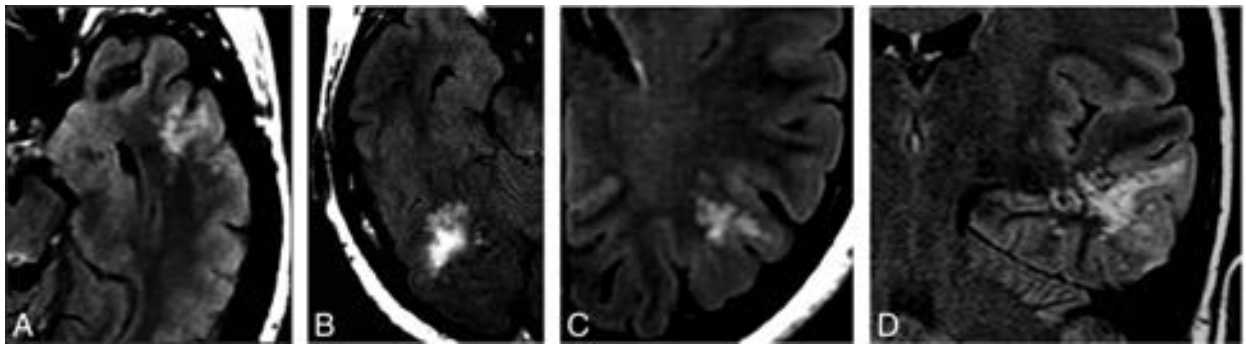

FIG 1. Typical imaging presentation on FLAIR. Selected axial (*A–C*) and coronal (*D*) FLAIR images of presumed MVNT demonstrate supratentorial hyperintense intra-axial lesions consisting of groups of multiple nodules, located on the subcortical ribbon and superficial subcortical white matter following the gyral contour. The images illustrate the variability in the size and location of the lesions and the degree of surrounding signal change (*A*, Case 21. *B*, Case 23. *C*, Case 7. *D*, Case 19).

Summary of findings of patients with presumed MVNT

Demographics	33 patients; mean age, 39 yr; female/male ratio (1.4:1)
Clinical data	Nonfocal headache (n = 16), possible seizure (n = 8), other reasons (n = 9)
	Follow-up scan 24–144 mo (mean, 36.8 mo)
Location	Parietal lobe (n = 9), frontal lobe (n = 8), temporal lobe (n = 6), occipital lobe (n = 2), >1 lobe (n = 8)
MRI findings (total)	
Hyperintense lesions on T2WI in comparison with the normal white matter	33 (100%)
Hyperintense lesions on FLAIR in comparison with the CSF	33 (100%)
Hypointense lesions on thin-section T2WI in comparison with the CSF	21 (100%)
Presence of abnormal white matter signal surrounding the bubble-like lesions	15 (45%)
Contrast enhancement	1 (3%)
Restricted diffusion or blooming on susceptibility-weighted imaging	0 (0%)

balanced FFE, CISS) were occasionally acquired. Gadolinium-enhanced T1WI was performed in all patients. Three neuroradiologists (R.H.N., A.J.d.R., and A.G.O., with 5, 22, and >35 years of experience, respectively) reviewed all individual cross-sectional images in a consensus analysis. Location, configuration, lesion size, and signal intensity on T1WI and T2WI, FLAIR, DWI, thin-section steady-state sequences, and postgadolinium T1WI were tabulated.

RESULTS

Demographic Data

Patient demographics, clinical presentation, and imaging findings in all 33 patients are summarized in the Table and detailed in the On-line Table. Patient ages ranged from 8 to 63 years, with a mean of 39 years (median, 41 years) at the time of initial diagnosis. There were 19 females and 14 males (female/male ratio, 1.4:1).

Imaging Findings

Size and Configuration. All lesions consisted of groupings of multiple (3 to >10) tiny discrete, sharply marginated, round or ovoid intra-axial nodules, ranging from 1 to 5 mm in diameter. They were all supratentorial and located on the inner surface of an otherwise normal-appearing cortex. The lesions often surrounded a sulcus, principally within the deep cortical ribbon and superficial subcortical white matter (Figs 1–3). Overall lesion size ranged from to 7 to 57 mm in maximum diameter, and mass effect was minimal or absent.

Location. Nine of 33 (27%) lesions were located in the parietal lobe, 8 (24%) were confined to the frontal lobe, and 6 (18%) were isolated to the temporal lobe. Only 2 lesions were located in the occipital lobe (4%). Eight (24%) affected more than 1 lobe.

Signal Intensity. Twenty-nine nodules (88%) were mildly hypo-/isointense relative to normal white matter, while the remainder were hypointense on T1-weighted spin-echo sequences. All nodules did not suppress on FLAIR (Figs 2–4) and were hyperintense on T2WI to normal white matter and hypointense in comparison with CSF. The differences in signal intensity on T2WI were better demonstrated on thin-section steady-state sequences (Fig 2), which were available for review in 21 patients (64%). The white matter surrounding or adjacent to the small nodules appeared normal in nearly half of patients (18/33). In 45%, confluent T2/FLAIR hyperintensity that spared the overlying cortex was present (Figs 1–3). No lesions exhibited restricted diffusion (Fig 3), and none showed blooming on susceptibility-weighted imaging.

Contrast Enhancement. Post-contrast enhancement was absent in all (Fig 3) except 1 lesion (97%). This lesion displayed a very subtle focus of enhancement along its medial margin.

Clinical Data

Presenting symptoms included nonfocal headache (n = 16) and suspected seizure (n = 8). Nine patients were scanned for other reasons, such as Bell's palsy, glioma, meningioma follow-up, neuroimaging surveillance of patients with known skin melanoma, and psychiatric evaluations.

Follow-up scans were available in all except 3 cases (all

of which were biopsy-proven), ranging from 24 to 144 months (mean, 36.8 months) following initial imaging. All (100%) were clinically indolent and unchanged in size or appearance.

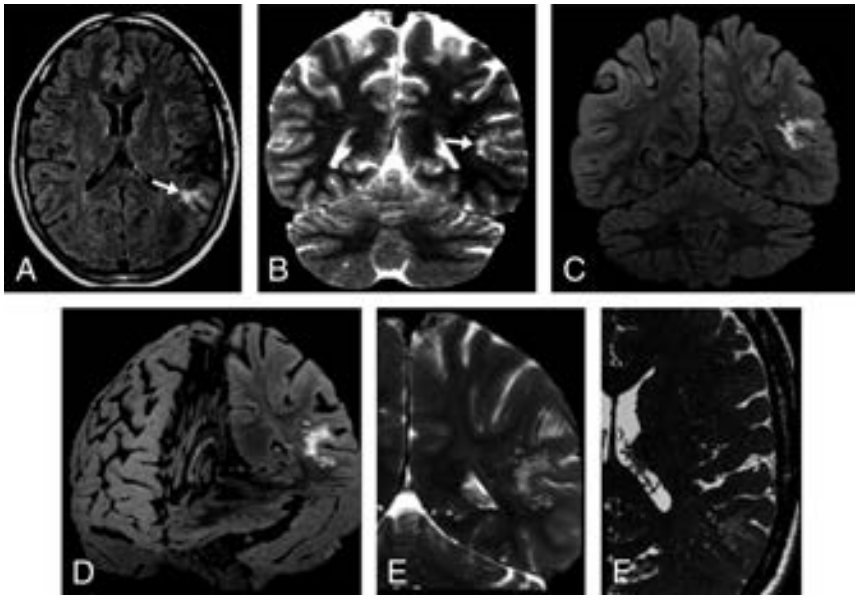

FIG 2. A 47-year-old woman who presented with nonfocal headache (case 1). Axial FLAIR (*A*) and coronal T2-weighted I (*B*) MR images demonstrate a left temporoparietal hyperintense subcortical lesion (*arrows*). The lesion had ill-defined borders, and the surrounding white matter appeared slightly hyperintense on T2/FLAIR. After 60 months of clinical stability, the study was performed on a 3T scanner. Coronal FLAIR (*C*), FLAIR 3D reconstruction (*D*), selected coronal T2WI (*E*), and selected axial thin-section T2WI (*F*) show the unchanged lesion located on the inner surface of otherwise normal-appearing left temporoparietal cortex surrounding a sulcus. The groups of multiple coalescent intralesional and perilesional nodules are better depicted. The images illustrate that the signal changes previously demonstrated in the surrounding white matter consist of innumerable very tiny nodules clustered together, sparing the overlying cortex.

Pathologic Findings

Because of their benign appearance and lack of relationship to specific clinical symptomatology, in most cases, the lesions were thought to be incidental. However, in 4 patients, the presenting clinical symptoms were potentially attributed to the identified lesion.

In 1 (case 10), even though the presenting symptoms (psychiatric) did not correlate with the lesion location, the neurosurgeons decided to resect the lesion to exclude a worrisome pathologic condition. Although initially the pathologic analysis was called "inconclusive," subsequent re-analysis of the slides showed multiple glioneuronal hamartomas fitting the histopathologic description of MVNT.

Another patient (case 26) presented with isolated seizure localized to the right temporal region, which correlated with the location of the subcortical lesion. The lesion was resected and the patient's symptoms resolved. Again, the initial pathologic analysis was called "inconclusive"; however, re-analysis of the histopathology showed 2 small areas of abnormal tissue consisting of glial and neuronal cells in a rarified background of focal microcyst formation, consistent with the histopathologic description of MVNT.

In another (case 31), the patient

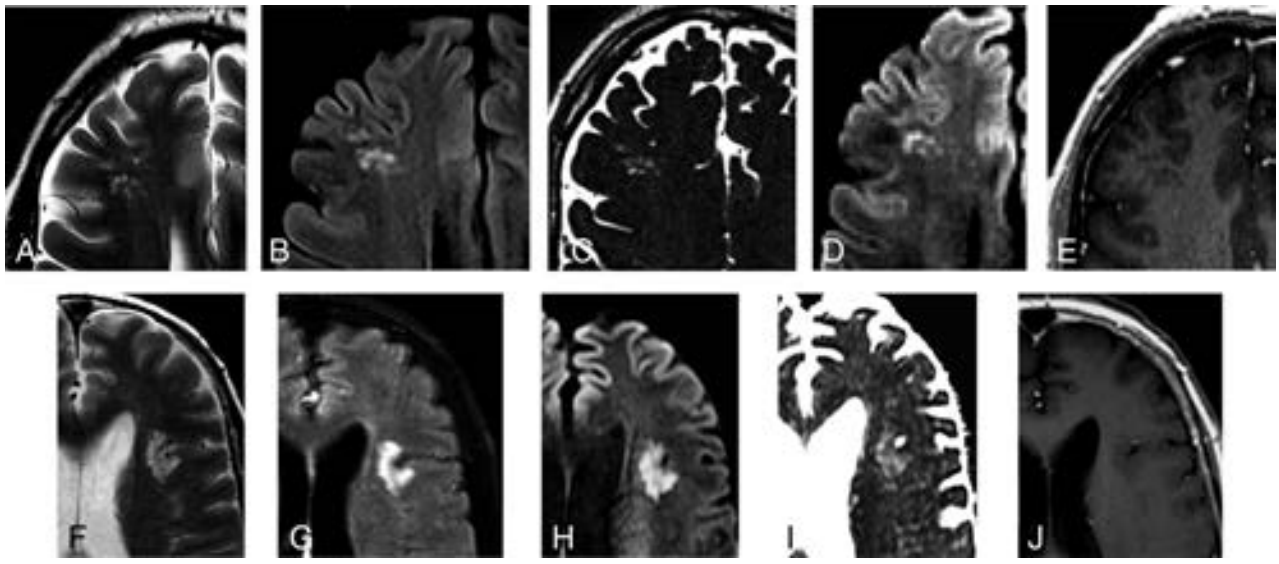

FIG 3. Most prevalent MR imaging presentations. A 50-year-old asymptomatic man with a history of skin melanoma (case 15). *A–E*, Selected axial MR images show a right frontal subcortical lesion consisting of groups of multiple nodules, hyperintense on FLAIR/T2WI (*A* and *B*). Selected axial thin-section T2WI (*C*) depicts mild hypointensity in comparison with the CSF. High signal is seen on an axial DWI (*D*) with high ADC values (not shown) due to the T2-shinethrough effect. No abnormal enhancement is depicted (*E*). No changes were detected on imaging follow-up after 25 months (not shown). A 41-year-old man who presented with nonfocal headache (case 8). *F–J*, Selected axial MR images reveal a left opercular subcortical lesion consisting of groups of multiple nodules, hyperintense on FLAIR/T2WI (*F* and *G*). High signal is seen on an axial DWI (*H*) with high ADC values (*I*) due to the T2-shinethrough effect. No abnormal enhancement is depicted (*J*). No changes were detected on imaging follow-up after 24 months (not shown).

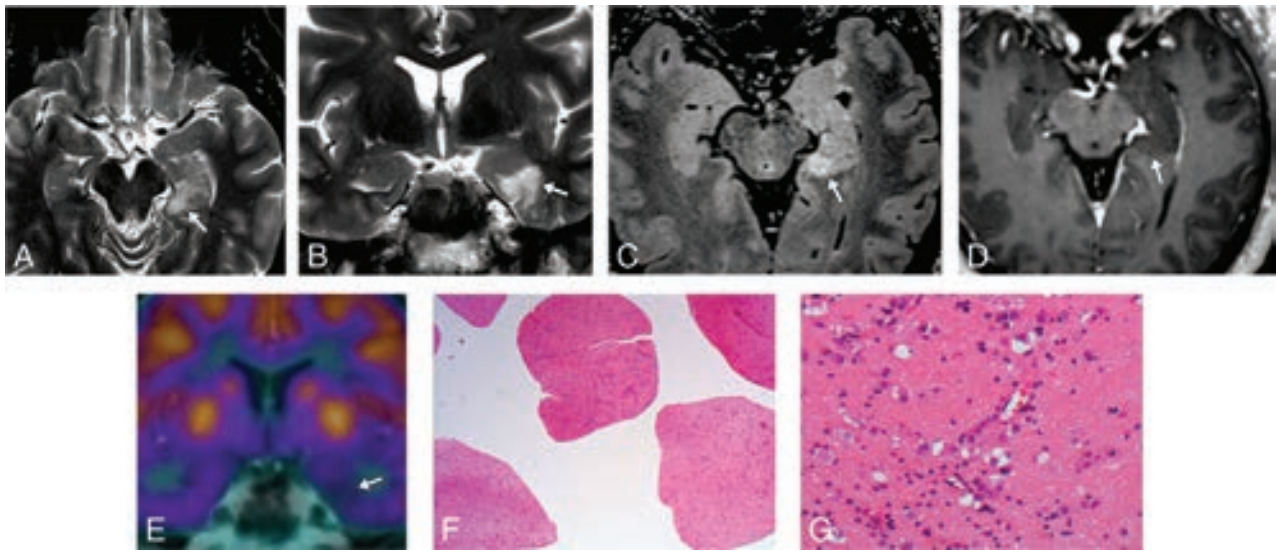

FIG 4. A 53-year-old male patient with temporal lobe epilepsy (case 31). *A–D*, MR imaging demonstrates a probable MVNT in the left parahippocampal gyrus (*arrows*). *E*, FDG-PET MR brain imaging shows focal hypometabolism in the left medial temporal lobe corresponding to the site of suspected lesion. *F* and *G*, Hematoxylin-eosin-stained histopathology slides demonstrate the abnormal clustering and vacuolation of the neuronal cells. Images were obtained with 20× magnification (*F*) and 200× magnification (*G*).

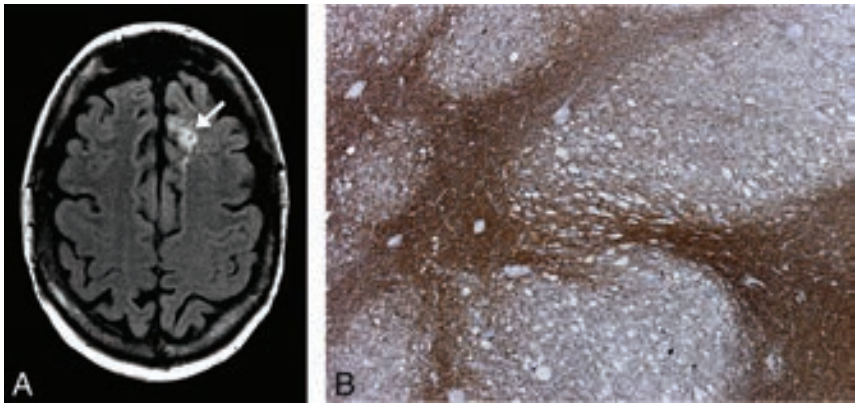

FIG 5. A 43-year-old male patient with headaches (case 33). *A*, Axial FLAIR image demonstrates a left frontal lobe lesion (*arrow*) consisting of multiple coalescent T2 and FLAIR hyperintense nodules located in the deep cortical ribbon and without mass effect. *B*, Low-power photomicrograph with immunohistochemistry staining for neurofibrillary protein shows positive staining between variably sized nonstaining vacuolating nodules.

presented with temporal lobe epilepsy. MRI evaluation showed a lesion in the left parahippocampal gyrus (Fig 4). Surgical resection of the lesion was performed and histopathology analysis revealed abnormal brain tissue in the left parahippocampal gyrus that included a population of cells showing neuronal features, many of which had vacuolation of a perikarya and a degree of clustering. Immunohistochemical stains confirmed a degree of nodularity and a weak immunoreactivity for synaptophysin on many neuronal cells, but most appeared negative for neuronal nuclear protein and neurofilament protein. There was variable background of positive dendritic staining for CD34. The lesion was also negative for *IDH1-R132H* mutation antibody, and staining was normal for *ATRX* and *p53*. The *Ki67* proliferation refraction was very low, and staining for *GFAP* showed varying background gliosis. Findings supported the diagnosis of MVNT.

In the other pathology-proven case (case 33), the patient presented with headaches (Fig 5). Brain MR imaging was performed and demonstrated a left frontal lobe lesion suggestive of MVNT. Histopathology and immunohistochemical stains confirmed the diagnosis.

DISCUSSION

MVNTs are distinctive neuronal lesions first described by Huse et al[1] in 2013 in a small case series of 10 patients. Since then, an additional 5 cases have been reported in the neuropathology literature.[3-6] Because so few reported cases were available, the new 2016 World Health Organization Classification of CNS neoplasms recognized MVNT as an entity but provisionally included it as a unique cytoarchitectural pattern of gangliocytoma, noting that it was unclear whether it is a truly neoplastic or dysplastic lesion.[2] This article examines the imaging and clinical spectrum of a large series of presumed MVNTs and delineates classic imaging findings of MVNT in an effort to prevent misdiagnosis and unnecessary biopsy.

Published cases[1,3-6] share similar histopathologic features, showing neuroepithelial cells with conspicuous stromal vacuolation arranged in nodules principally within the deep cortical ribbon and superficial subcortical white matter. These dysplastic cells typically orient perpendicular to the cortical surface, which correlates well with the radiologic appearance of clusters or a linear array of juxtacortical nodules. The constituent dysplastic cells exhibit immunopositivity for *HuC/HuD* and *Olig2*, associated with neurogenesis at an earlier stage of neuronal development. However, they show negativity or weak positivity for neuronal lineage markers that are present in mature neurons, therefore, revealing an early neuronal immunophenotype. To date, genetic

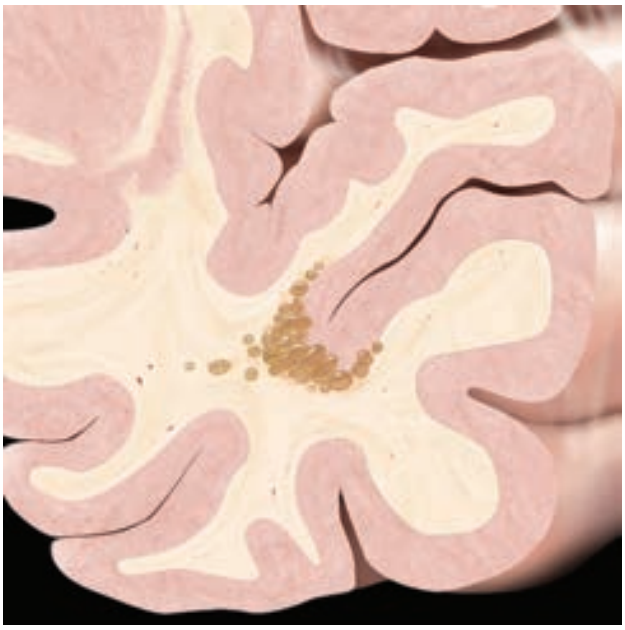

FIG 6. MVNT typical presentation graphic illustration. Schematic coronal view depicts a nodular "bubbly-appearing" lesion located on the inner surface of otherwise normal-appearing left temporal lobe cortex within the deep cortical ribbon and superficial subcortical white matter. Reprinted from *Osborn's Brain*[9] with permission from Elsevier.

analyses have failed to demonstrate characteristic molecular changes that specify a particular tumor subtype.[1,3-6] More recently, MVNTs have been shown to demonstrate overexpression of *α-internexin*, which is a major component of neurofilaments in interneurons and cerebellar granule cells. *INA* expression is seen in developing immature neurons. Again, these findings support the hypothesis that MVNT may represent a dysplastic early neuronal phenotype and may fall into a category between cortical malformation and harmatomatous lesions, which behave in a benign fashion.[3,6]

MVNTs exhibit a highly characteristic appearance on MR imaging. All lesions in our series consist of a cluster of variably sized nodular lesions located on the subcortical ribbon and superficial subcortical white matter following the gyral contour (Fig 6). They appear hyperintense on T2WI, do not suppress on FLAIR, and typically do not enhance or cause mass effect (Figs 2–4). Our findings are in accordance with those in the cases in the pathology literature.[1,3-6] The nonsuppression on FLAIR and the slightly hypointense signal compared with CSF on T2-weighted sequences observed in this series are possibly related to a high protein or solid component within the vacuolated areas. In almost half of our patients, the subcortical white matter adjacent to the small nodules are hyperintense on T2/FLAIR; this appearance is likely due to coalescence of many smaller clustered nodules and partial volume averaging (Fig 2), sometimes resembling a mass-like lesion as previously described.[3-6]

Most of our cases were imaged before the description of MVNT in the 2016 World Health Organization Classification and were initially diagnosed as enlarged perivascular spaces, focal cortical dysplasia, or dysembryoplastic neuroepithelial tumor (DNET). Although MVNT may have some overlapping imaging features with DNET and other cortically based tumors, the absence of cortical involvement and prominent mass effect and intra- or perilesional tumor nodules help to distinguish MVNTs.[3,6,7] Enlarged perivascular spaces may also have some similar imaging features; however, they typically exhibit CSF-like signal on all sequences, while MVNTs do not suppress on FLAIR. Prominent perivascular spaces that are below the resolution of 1.5 or 3T MR imaging may not suppress on FLAIR, but this pattern is usually described as an abnormal white matter signal surrounding other typical enlarged perivascular spaces, particularly in the anterior temporal region.[8]

While the most common clinical manifestation was an episode of seizure in the neuropathology literature,[1,3-6] in this series, possible seizure was only observed in a few patients (19%) and the remainder presented with nonspecific, nonfocal clinical manifestations. Most MVNTs are usually an incidental finding on imaging studies and may be more common than other neuronal and mixed glioneuronal tumors. The true prevalence of this lesion in asymptomatic individuals may have been underestimated in the neuropathology literature due to reporting bias because most are probably not resected.

It is still not clear whether multinodular and vacuolating neuronal tumor represents a neoplasm or malformation[2]; however, on the basis of our results, given the long stability of the imaging findings and clinical course, it is apparent that MVNT behaves in a benign, nonaggressive manner that is more like a hamartomatous lesion than a neoplasm. Imaging findings of MVNT are highly suggestive of the diagnosis. While a few MVNTs may be causative of seizure disorders and therefore require excision for clinical management, akin to DNET, most are asymptomatic lesions that are "leave me alone" entities. These lesions usually do not require biopsy, resection, or follow-up imaging unless and until it can be demonstrated that the visualized lesion is responsible for the symptoms.

Our retrospective study had clear limitations. Only half of our patients had adequate imaging follow-up to confirm stability with time. Another major limitation is that histopathology was only available for 4 cases. Nevertheless, the imaging findings of all presumed MVNTs were strikingly similar to the ones described in the neuropathology literature.

CONCLUSIONS

This large case series describes the typical MRI appearance of MVNT characterized by subcortical cluster of FLAIR hyperintense nodular lesions located on the inner surface of an otherwise normal-appearing cortex without enhancement or significant mass effect. Although the true nature of MVNT remains to be fully elucidated, the histopathology literature to-date favors a malformative lesion over a neoplasm. We emphasize that MVNT is a "leave me alone" brain lesion. When incidentally discovered, MVNT can be sufficiently managed on surveillance imaging to ensure stability and unnecessary surgery or biopsy should be avoided.

ACKNOWLEDGMENTS

We thank Thomas Robertson, BMedSc, MBBS(Hons), FRCPA, from the Department of Anatomical Pathology and Cytopathology, Royal Brisbane and Women's Hospital, Herston, Queens-

land, Australia, and Vaska Kasturi, FRCPA, from the Department of Pathology, Princess Alexandra Hospital, Australia, for their significant contribution in the pathology evaluation.

Disclosures: Ann G. Osborn—*UNRELATED*: *Consultancy*: Elsevier, *Comments*: led the Brain Team for neuroradiology content for books, STATdx, RADPrimer, 2014 to present; *Payment for Lectures Including Service on Speakers Bureaus*: Mallinckrodt, *Comments*: Neuroradiology from the Masters course, 2014–2015; *Royalties*: Elsevier, *Comments*: book royalties; *Stock/Stock Options*: Amirsys, *Comments*: exercised in June 2014 during acquisition of Amirsys from Elsevier.

REFERENCES

1. Huse JT, Edgar M, Halliday J, et al. **Multinodular and vacuolating neuronal tumors of the cerebrum: 10 cases of a distinctive seizure-associated lesion.** *Brain Pathol* 2013;23:515–24 CrossRef Medline
2. Louis DN, Perry A, Reifenberger G, et al. **The 2016 World Health Organization Classification of Tumors of the Central Nervous System: a summary.** *Acta Neuropathol* 2016;131:803–20 CrossRef Medline
3. Yamaguchi M, Komori T, Nakata Y, et al. **Multinodular and vacuolating neuronal tumor affecting amygdala and hippocampus: a quasi-tumor?** *Pathol Int* 2016;66:34–41 CrossRef Medline
4. Bodi I, Curran O, Selway R, et al. **Two cases of multinodular and vacuolating neuronal tumour.** *Acta Neuropathol Commun* 2014;2:7 CrossRef Medline
5. Fukushima S, Yoshida A, Narita Y, et al. **Multinodular and vacuolating neuronal tumor of the cerebrum.** *Brain Tumor Pathol* 2015;32:131–36 CrossRef Medline
6. Nagaishi M, Yokoo H, Nobusawa S, et al. **Localized overexpression of alpha-internexin within nodules in multinodular and vacuolating neuronal tumors.** *Neuropathology* 2015;35:561–68 CrossRef Medline
7. Shin JH, Lee HK, Khang SK, et al. **Neuronal tumors of the central nervous system: radiologic findings and pathologic correlation.** *Radiographics* 2002;22:1177–89 CrossRef Medline
8. Rawal S, Croul SE, Willinsky RA, et al. **Subcortical cystic lesions within the anterior superior temporal gyrus: a newly recognized characteristic location for dilated perivascular spaces.** *AJNR Am J Neuroradiol* 2014;35:317–22 CrossRef Medline
9. Osborn AG. *Osborn's Brain.* 2nd ed. Philadelphia: Elsevier; 2017:592

Age, Sex, and Racial Differences in Neuroimaging Use in Acute Stroke: A Population-Based Study

A. Vagal, P. Sanelli, H. Sucharew, K.A. Alwell, J.C. Khoury, P. Khatri, D. Woo, M. Flaherty, B.M. Kissela, O. Adeoye, S. Ferioli, F. De Los Rios La Rosa, S. Martini, J. Mackey, and D. Kleindorfer

ABSTRACT

BACKGROUND AND PURPOSE: Limited information is available regarding differences in neuroimaging use for acute stroke work-up. Our objective was to assess whether race, sex, or age differences exist in neuroimaging use and whether these differences depend on the care center type in a population-based study.

MATERIALS AND METHODS: Patients with stroke (ischemic and hemorrhagic) and transient ischemic attack were identified in a metropolitan, biracial population using the Greater Cincinnati/Northern Kentucky Stroke Study in 2005 and 2010. Multivariable regression was used to determine the odds of advanced imaging use (CT angiography/MR imaging/MR angiography) for race, sex, and age.

RESULTS: In 2005 and 2010, there were 3471 and 3431 stroke/TIA events, respectively. If one adjusted for covariates, the odds of advanced imaging were higher for younger (55 years or younger) compared with older patients, blacks compared with whites, and patients presenting to an academic center and those seen by a stroke team or neurologist. The observed association between race and advanced imaging depended on age; in the older age group, blacks had higher odds of advanced imaging compared with whites (odds ratio, 1.34; 95% CI, 1.12–1.61; $P < .01$), and in the younger group, the association between race and advanced imaging was not statistically significant. Age by race interaction persisted in the academic center subgroup ($P < .01$), but not in the nonacademic center subgroup ($P = .58$). No significant association was found between sex and advanced imaging.

CONCLUSIONS: Within a large, biracial stroke/TIA population, there is variation in the use of advanced neuroimaging by age and race, depending on the care center type.

ABBREVIATION: GCNKSS = Greater Cincinnati/Northern Kentucky Stroke Study

Stroke is the fifth leading cause of death and a leading cause of disability in the United States.[1] According to national mortality statistics from the Centers from Disease Control and Prevention, racial disparities in mortality were largest for stroke, among the leading causes of death.[2] The National Health and Nutrition Survey Epidemiologic Follow-Up Study[3] estimated that mortality due to cerebrovascular disease accounted for 28% of the difference in total mortality rates between blacks and whites. During 2010–2013, stroke mortality among those aged 45 and older varied by age and race. There was a markedly higher stroke death rate in non-Hispanic black individuals than in any of the other race-ethnicity groups, and a greater portion of their stroke deaths occurred at younger ages (45–64 years).[4] Studying trends in stroke incidence and case fatality is critical for the planning, implementation, and evaluation of the public health effort to decrease the burden of stroke in the United States.

Previous studies have shown compelling sex, racial, and socioeconomic disparities in the treatment and outcomes among patients with acute stroke.[5-7] Generally, racial minorities and women with acute stroke have lower quality hospital care,[5,8-13] including the use of imaging. These disparities can contribute to inequality in stroke outcomes and are a top research priority of

Received September 12, 2016; accepted after revision June 5, 2017.

From the Departments of Radiology (A.V.), Emergency Medicine (O.A.), and Neurology (K.A.A., P.K., D.W., M.F., B.M.K., S.F., F.D.L.R.L.R., S.M., D.K.), University of Cincinnati Medical Center, Cincinnati, Ohio; Department of Radiology (P.S.), Hofstra Northwell School of Medicine, Hempstead, New York; Department of Biostatistics and Epidemiology (H.S., J.C.K.), Cincinnati Children's Hospital Medical Center, Cincinnati, Ohio; Baptist Health Neuroscience Center (F.D.L.R.L.R.), Miami, Florida; University of New Mexico Health Sciences Center and Department of Neurology (F.D.L.R.L.R.), Albuquerque, New Mexico; and Department of Neurology (J.M.), Indiana University School of Medicine, Indianapolis, Indiana.

This work was supported by National Institute of Health grant R01NS30678.

Paper previously presented as oral presentation at: Annual Meeting of the American Society of Neuroradiology and the Foundation of the ASNR Symposium, May 21–26, 2016; Washington, DC.

Please address correspondence to Achala Vagal, MD, MS, Department of Radiology, University of Cincinnati Medical Center, 234 Goodman St, Cincinnati, OH 45267; e-mail: vagala@ucmail.uc.edu

Indicates open access to non-subscribers at www.ajnr.org

http://dx.doi.org/10.3174/ajnr.A5340

the National Institute of Neurologic Disorders and Stroke. The management of stroke begins with the appropriate diagnostic work-up. Imaging is an important component in both evaluation and decision-making in patients presenting with suspected acute stroke. In particular, early vascular imaging, such as CTA/MRA, is now critical for clinical decision-making in patients potentially eligible for endovascular therapy, and urgent brain MR imaging and vascular imaging are recommended in suspected transient ischemic attack.[14] Although numerous publications have highlighted the disparities in stroke care, very limited data describe demographic differences in neuroimaging use in a population. These observations motivated us to examine data from a large population-based cohort for evidence of systematically different imaging work-up in patients with stroke based on race, sex, or age. If the sources and causes of disparities in stroke care are recognized, these can then inform the setup of programs and initiatives to improve stroke care. This information will also be critical as we transition to value-based health care.

The Greater Cincinnati/Northern Kentucky Stroke Study (GCNKSS) is designed to investigate stroke incidence rates and case fatality in a biracial population (blacks and whites) of a 5-county region that includes the city of Cincinnati. Our objective was to assess whether race, sex, or age differences exist in neuroimaging use in routine acute stroke practice within this large, metropolitan, population-based cohort and whether these differences depend on care center type.

MATERIALS AND METHODS

Study Design/Study Population

This was a retrospective, population-based study of all adults (20 years of age and older) with acute stroke among residents of a 5-county region of Southwest Ohio and Northern Kentucky during 2005 and 2010. Patients with acute stroke (ischemic and hemorrhagic) and TIA were identified in a population of 1.3 million served by 15 different inpatient hospitals in the Greater Cincinnati/Northern Kentucky area. The GCNKSS involved ascertainment of all stroke events that occurred in the population in 2005 and 2010.

Methodology and Study Population of the GCNKSS

The detailed methodology of GCNKSS has been published before.[15] The study population is defined as all residents of the Greater Cincinnati/Northern Kentucky region, which includes 2 Southern Ohio counties and 3 contiguous Northern Kentucky counties that abut the Ohio River. The study population of the Greater Cincinnati/Northern Kentucky region consists of <3% Hispanic and other minorities; all self-identified black or white subjects were included in our analysis. There were 2 methods of screening: retrospective review of discharge diagnoses and prospective monitoring of emergency department visits and admission lists. To qualify as an incidence case, a person must have met the criteria for 1 of the 5 stroke/TIA subcategories, lived at a zip code within the 5-county region at the time of stroke onset, and had the onset of stroke in 2005 (between January 1, 2005, and December 31, 2005) or 2010 (between January 1, 2010, and December 31, 2010). Strokes were classified as first-ever or recurrent on the basis of evidence of prior clinical stroke in the medical record. The date and type of each prior stroke or TIA were recorded, and any neurologic deficit present before the current stroke or TIA was documented. We have current institutional review board approval at all the regional hospitals.

Clinical and Imaging Data Abstraction

Screening. Screening techniques were identical in both the 2005 and 2010 study periods. Study nurses prospectively screened the medical records of all inpatients with primary or secondary stroke–related *International Classification of Diseases, 9th Revision* discharge diagnoses from the 15 acute care hospitals in the study region. The *International Classification of Diseases, 9th Revision*-Clinical Modification codes (both primary and secondary discharge diagnoses) for retrieving medical records included 430–436. In addition, strokes not found by inpatient screening were ascertained by monitoring all stroke-related visits to hospital emergency departments (with the exception of the Cincinnati Children's Hospital Medical Center). Patient charts and imaging records abstracted by research nurses were reviewed by study physicians. Study physicians reviewed every abstract to verify whether a stroke or TIA had occurred and then assigned a stroke category and mechanism to each event on the basis of all available information, using definitions described previously.[16]

Stroke Case Adjudication. Study nurses and physicians were trained extensively before case review, and detailed instructions guided reviewers on screening, abstraction, and case review. Specifically, study physicians reviewed all data from each case, including clinical scenarios, presenting symptoms, and imaging (CT and/or MR imaging reports, and images if physician-requested). In addition, senior investigators reviewed a select sample of cases from all physician reviewers to ensure accuracy of case ascertainment, and any discrepancies or questionable cases were resolved by senior investigators.

We included all acute ischemic or hemorrhagic stroke or TIA cases ascertained in the hospital setting, including all emergency departments and inpatient services (direct admissions and in-hospital events). The cases included in this analysis were restricted to hospitalized patients because the collection of outpatient imaging performed in a nursing home or physician's office setting was not pursued in the study. Socioeconomic status was determined by the percentage below the poverty level within a respondent's US 2000 Census Tract of residence and dichotomized at high poverty ≥20%.[17]

Data Analysis

The proportion of noncontrast CT, CT angiograms, MR imaging, MR angiograms, and carotid sonograms within 2 days of stroke/TIA symptom onset was computed by sex, age (55 or younger or older than 55 years), and race (white or black) demographic groups. We specifically used the 2-day limit to capture all imaging performed for both acute stroke and TIA work-up. In our previous work,[18] we found a trend toward an increased incidence of ischemic stroke in the young (20–54 years of age) for both black and white patients. We used this same age limit (55 years) to dichotomize the current study group into young versus old.

We used multivariable logistic regression to determine the odds of advanced imaging use for the demographic variables of

interest (age, sex, and race), adjusting for additional covariates. We defined advanced imaging as additional CT or MR imaging, including CTA head and/or neck, MR imaging brain, and MRA head and/or neck. Covariates included NIHSS score; an indicator for high poverty (percentage below poverty level ≥20%); emergency department presentation; insurance; type of case (hemorrhagic, ischemic, or TIA); seen by the stroke team or neurologist; type of care center (academic or nonacademic); and study year (2005 or 2010). We defined "academic center" as one with a neurology residency program where neurology is the primary admitting service for patients with stroke. Interaction terms for study year by age, sex, and race and age by race, age by sex, and race by sex were evaluated in the model with a $P < .05$ considered statistically significant. Statistically significant interactions were described by stratification by the effect modifier. Last, we also stratified cases on the basis of type of care center to evaluate whether any observed associations were consistent across the type of care center, with further stratification by any significant effect modifiers.

RESULTS

In 2005, there were 3471 stroke/TIA events with imaging data available in 3226 patients; and in 2010, there were 3431 stroke/TIA events with imaging data available in 3213 patients. Because demographic differences in imaging use did not differ significantly between the calendar years 2005 and 2010, data for the 2 years were combined. The median age for the combined group was 72 years, 20% were black, 57% were women, and the median NIHSS score was 3 (Table 1). A higher proportion of men underwent MR imaging (55% versus 51%, $P < .01$) and MRA (36% versus 31%, $P < .01$) compared with women, with no sex differences in the use of NCCT, carotid sonography, or CTA. A higher proportion of blacks underwent NCCT (96% versus 92%), MR imaging (59% versus 51%), and MRA (41% versus 31%) compared with whites ($P < .01$), with no racial difference in CTA. Advanced imaging use (MR imaging, CTA, MRA) was higher in younger (55 years or younger) compared with older patients (older than 55 years) (68% versus 52%, $P < .01$), whereas older patients underwent a higher proportion of carotid sonography (43% versus 36%, $P < .01$) (Table 2).

Table 1: Demographics and clinical characteristics overall and by study year[a]

	All (*N* = 6902)	2005 (*n* = 3471)	2010 (*n* = 3431)
Age (median) (IQR)	72 (59–81)	72 (59–81)	71 (58–82)
Race			
Black	1355 (20%)	659 (19%)	696 (20%)
White	5505 (80%)	2791 (80%)	2714 (79%)
Other	42 (1%)	21 (1%)	21 (1%)
Sex, female	3906 (57%)	1968 (57%)	1938 (56%)
Percentage below poverty ≥20%	754 (11%)	399 (12%)	355 (10%)
Care center			
Academic	1026 (15%)	440 (13%)	586 (17%)
Nonacademic	5876 (85%)	3031 (87%)	2845 (83%)
ED presentation	6023 (87%)	2955 (85%)	3068 (89%)
Insurance			
Any	6319 (94%)	3159 (95%)	3160 (93%)
Self-pay	415 (6%)	172 (5%)	243 (7%)
NIHSS (median) (IQR)	3 (1–7)	3 (1–7)	2 (1–6)
Case type			
Hemorrhagic	821 (12%)	427 (12%)	394 (11%)
Ischemic	4412 (64%)	2147 (62%)	2265 (66%)
TIA	1669 (24%)	897 (26%)	772 (22%)
Seen by stroke team or neurologist	4287 (62%)	2006 (58%)	2281 (66%)

Note:—IQR indicates interquartile range; ED, emergency department.
[a] Data are No. (%) unless otherwise indicated.

Multivariable Analysis

After we adjusted for covariates, younger age (55 years or younger) was associated with higher odds of advanced imaging compared with older age (older than 55) (adjusted odds ratio, 1.90; 95% CI, 1.63–2.22; $P < .01$). Compared with white patients, black patients had significantly higher odds of additional advanced imaging (OR, 1.27; 95% CI, 1.08–1.49; $P < .01$). The odds of advanced imaging were also higher if patients presented to an academic center or were seen by a stroke team or neurologist. No statistically significant association was found between sex and advanced imaging (Table 3). A higher NIHSS score was associated with decreased advanced imaging (OR, 0.93; 95% CI, 0.92–0.94; $P < .01$).

We found a significant age-by-race interaction so that the association between race and advanced imaging was dependent on age. After we adjusted for covariates, in the older age group, black race was associated with higher odds of advanced imaging compared with white race (OR, 1.34; 95% CI, 1.12–1.61; $P < .01$). However, in the younger age group, the association between race and advanced imaging was not statistically significant (Table 3). No statistically significant interactions were found between study year and age, sex, and race, between age and sex, and between age and race.

In subgroup analyses by type of center, the age-by-race interaction persisted in the academic center subgroup ($P < .01$), but not in the nonacademic center subgroup ($P = .58$). In the academic center, in the older age group, black race was associated with higher odds of advanced imaging compared with white race

Table 2: Unadjusted neuroimaging use for stroke/TIA work-up by sex, age, and race for combined study periods of 2005 and 2010[a]

	Sex			Age (yr)			Race		
	Men (*n* = 2996)	Women (*n* = 3906)	*P* Value	55 or Younger (*n* = 1343)	Older Than 55 (*n* = 5559)	*P* Value	Black (*n* = 1355)	White (*n* = 5505)	*P* Value
NCCT	2778 (93%)	3649 (93%)	.26	1265 (94%)	5162 (93%)	.08	1296 (96%)	5091 (92%)	<.01
MRI	1633 (55%)	1983 (51%)	<.01	851 (63%)	2765 (50%)	<.01	801 (59%)	2788 (51%)	<.01
CTA	163 (5%)	184 (5%)	.17	130 (10%)	217 (4%)	<.01	81 (6%)	263 (5%)	.07
MRA	1075 (36%)	1206 (31%)	<.01	569 (42%)	1712 (31%)	<.01	561 (41%)	1703 (31%)	<.01
Any advanced imaging	1718 (57%)	2104 (54%)	<.01	916 (68%)	2906 (52%)	<.01	847 (63%)	2948 (54%)	<.01
Carotid sonography	1246 (42%)	1614 (41%)	.82	482 (36%)	2378 (43%)	<.01	417 (31%)	2425 (44%)	<.01

[a] Data are No. (%) unless otherwise indicated.

Table 3: Multivariable model for advanced imaging (CTA/MRI/MRA) for stroke/TIA work-up in the overall group stratified by age groups

	Overall		55 yr or Younger		Older Than 55 yr	
	OR (95% CI)	*P* Value	OR (95% CI)	*P* Value	OR (95% CI)	*P* Value
Age 55 yr or younger	1.90 (1.63–2.22)	<.01	–	–	–	–
Race, black (reference white)[a]	1.27 (1.08–1.49)	<.01	1.02 (0.73–1.41)	.92	1.34 (1.12–1.61)	<.01
Sex, male	1.06 (0.95–1.18)	.32	1.06 (0.81–1.39)	.69	1.06 (0.94–1.20)	.31
Academic	1.43 (1.20–1.71)	<.01	1.21 (0.85–1.72)	.29	1.51 (1.22–1.85)	<.01
High poverty	0.85 (0.69–1.03)	.10	0.71 (0.49–1.04)	.08	0.91 (0.73–1.15)	.44
ED presentation	1.95 (1.65–2.29)	<.01	2.74 (1.81–4.14)	.01	1.84 (1.54–2.19)	<.01
Insurance (any, reference self-pay)	0.91 (0.70–1.18)	.47	0.90 (0.63–1.28)	.56	0.94 (0.64–1.39)	.76
NIHSS score	0.93 (0.92–0.94)	<.01	0.93 (0.92–0.95)	<.01	0.93 (0.92–0.94)	<.01
Event type (reference TIA)						
ICH/SAH	1.22 (0.99–1.50)	.07	1.98 (1.26–3.12)	<.01	1.04 (0.82–1.33)	.72
Infarct	2.51 (2.19–2.88)	<.01	2.46 (1.78–3.41)	<.01	2.50 (2.16–2.91)	<.01
Seen by stroke team or neurologist	2.33 (2.07–2.63)	<.01	3.25 (2.38–4.43)	<.01	2.22 (1.95–2.53)	<.01
Study year 2010 (reference 2005)	1.66 (1.48–1.85)	<.01	1.77 (1.35–2.33)	<.01	1.64 (1.46–1.85)	<.01

Note:—ED indicates emergency department; ICH, intracranial hemorrhage.
[a] Race by age group interaction ($P = .04$).

Table 4: Multivariable model for advanced imaging (CTA/MRI/MRA) for stroke/TIA work-up stratified by care center type and age groups

	Academic Center (*n* = 1026)[a]				Nonacademic Centers (*n* = 5876)[b]			
	55 yr or Younger		Older Than 55 yr		55 yr or Younger		Older Than 55 yr	
	OR (95% CI)	*P* Value	OR (95% CI)	*P* Value	OR (95% CI)	*P* Value	OR (95% CI)	*P* Value
Race, black (reference white)	0.56 (0.30–1.04)	.07	1.80 (1.19–2.72)	<.01	1.25 (0.82–1.89)	.29	1.27 (1.04–1.55)	.02
Sex, male	1.00 (0.58–1.72)	.99	1.25 (0.88–1.78)	.22	1.12 (0.82–1.54)	.48	1.05 (0.92–1.20)	.46
High poverty	0.98 (0.51–1.85)	.94	0.74 (0.47–1.17)	.20	0.64 (0.40–1.03)	.07	0.98 (0.75–1.28)	.89
ED presentation	2.09 (0.89–4.91)	.09	1.79 (1.03–3.12)	.04	3.19 (1.94–5.24)	<.01	1.83 (1.52–2.20)	<.01
Insurance (any, reference self-pay)	0.77 (0.45–1.33)	.35	0.84 (0.45–1.56)	.58	0.92 (0.57–1.47)	.73	0.99 (0.61–1.60)	.95
NIHSS	0.94 (0.92–0.97)	<.01	0.94 (0.92–0.95)	<.01	0.91 (0.89–0.94)	<.01	0.93 (0.92–0.94)	<.01
Event type (reference TIA)								
ICH/SAH	0.99 (0.34–2.85)	.98	1.54 (0.80–2.96)	.20	2.46 (1.40–4.34)	<.01	0.87 (0.65–1.17)	.37
Infarct	2.12 (0.93–4.88)	.08	1.85 (1.10–3.11)	.02	2.44 (1.68–3.55)	<.01	2.58 (2.20–3.01)	<.01
Seen by stroke team or neurologist	2.39 (1.02–5.56)	.04	3.02 (1.75–5.20)	<.01	3.80 (2.68–5.38)	<.01	2.21 (1.93–2.53)	<.01
Study year 2010 (reference 2005)	3.84 (2.23–6.62)	<.01	1.88 (1.31–2.68)	<.01	1.38 (1.00–1.90)	.05	1.61 (1.42–1.83)	<.01

Note:—ED indicates emergency department; ICH, intracranial hemorrhage.
[a] In the academic care center subgroup: race by age group interaction ($P < .01$).
[b] In the nonacademic care center subgroup: race by age group interaction ($P = .58$).

(OR, 1.80; 1.12–1.61; $P < .01$). However, in the younger age group, the association between black race and advanced imaging was in the opposite direction and not statistically significant (Table 4). In the nonacademic center, black race was associated with higher odds of advanced imaging in both age groups (unstratified OR, 1.28; 95% CI, 1.07–1.53; $P < .01$).

DISCUSSION

The principal finding of our study is that younger patients (55 year or younger) and black patients were more likely to undergo advanced imaging for acute stroke/TIA work-up. Although men underwent a significantly higher proportion of MR imaging/MRA in unadjusted analyses, this association was not present after adjusting for covariates. Additionally, we did not find a significant difference in the use of advanced imaging by insurance or socioeconomic status.

Prior studies have shown demographic differences in the use of neuroimaging for acute stroke.[15,19] Large variation was reported among English public hospitals, where younger patients, men, and patients of higher socioeconomic status were more likely to undergo brain imaging (NCCT or MR imaging).[11] A study using the Canadian Stroke Registry found that very elderly patients were less likely to undergo carotid imaging compared with younger patients with acute ischemic stroke, though there was no association between age and the quality of stroke care.[17] In our analysis, a higher proportion of the older patients underwent carotid sonography rather than CTA or MRA, compared with younger patients. A possible explanation is that older patients are less suitable candidates for carotid endarterectomy or carotid artery stent placement due to other comorbidities, including dementia; therefore, advanced vascular imaging is less likely to be performed. Additionally, younger patients may have more stroke mimics, leading to increased advanced imaging.

The strength of our study is that it is the largest population-based dataset capturing detailed clinical information regarding stroke care in the United States, and it is one of the few studies with a substantial number of black patients. In addition, our dataset represents a large, metropolitan population representative of the United States population with respect to median age, median income, black race, female sex, and rate below the poverty level.[16,20]

There is a distinct advantage in using a population-based source of information regarding imaging use patterns. Popula-

tion-based epidemiologic studies of stroke fall into 2 broad classes: 1) surveillance studies, and 2) cohort studies; both are needed to fully understand stroke incidence and disparities. Just as cohort studies are critical to the understanding of the causes of stroke, surveillance studies are critical to determining the distribution of stroke; and both contribute to knowledge regarding important public health trends in stroke. Similarly, administrative data provide complementary data to population-based studies by providing access to large numbers of cases with lower costs. However, administrative data lack the ability to answer clinical questions, have incomplete ascertainment, and have limited access to special populations. Registries, such as Get With the Guidelines,[21] provide more clinical information than purely administrative data, though they are still limited compared with population-based studies. Providing data in these registries by hospitals demonstrates a willingness to participate in stroke quality-improvement projects, indicating a bias at the hospital level.

Most surprising, in contrast to concerns that blacks may receive less diagnostic work-up, we found that overall, blacks received more advanced imaging than whites. A possible explanation is that in our population, the only large, academic hospital in the region admits a greater proportion of black patients. Furthermore, the racial difference depended on age and type of care center, with potential differential access to stroke expertise. A retrospective analysis of US Department of Veterans Affairs Hospital systems also suggested sites of care as a factor for disparities by demonstrating that white patients at nonminority-serving hospitals had a significantly higher probability of undergoing carotid imaging than either black or white patients at minority-serving hospitals.[22] In addition, there may be clinical differences between strokes in blacks and whites in our study, including variations in vascular risk factors prompting advanced imaging work-up. We also found that the odds of advanced imaging were higher if patients were seen by a stroke team or neurologist, suggesting that physician factors can have a substantial effect on imaging use. This finding has also been demonstrated in a large retrospective cohort study examining factors affecting the use of outpatient imaging, where specialists ordered 43.6% compared with 27.5% ordered by primary care physicians.[23]

Disparity in health care is being increasingly recognized; hence, an overarching goal of the Healthy People 2020 initiative is "to achieve health equity, eliminate disparities, and improve the health of all groups" in the United States.[24] A recent study demonstrated a significant gap between metropolitan and nonmetropolitan area hospitals, especially with the rate of recombinant tissue plasminogen activator administration and provision of stroke education.[25] Even more alarming is that this rural-urban geographic disparity gap in rtPA use is increasing.[26] Several deficiencies contribute to the disparity in stroke care, including widespread geographic variation and access issues. Furthermore, the prehospital recognition of stroke is lower among minority patients compared with non-Hispanic whites and, similarly, lower for female compared with male patients,[27] highlighting the importance of identifying all links in the chain of stroke care. Lack of awareness, socioeconomic factors, cultural impediments, and potential existence of bias are additional barriers in the delivery of care.[5]

Change in the incidence and outcome of a disease and the reduction of clearly identified disparities in these rates and outcomes are the ultimate test of how well science has translated new discoveries into benefits for the population. Because stroke is the most frequent neurologic cause of death and a leading cause of major disability, it should be a primary focus for neurologic surveillance studies. Understanding use of standard of care (NCCT) versus advanced imaging (MR imaging/CTA/MRA) is important because additional diagnostic imaging, including vascular imaging, can help guide treatment decisions and elucidate etiology and recurrence risk in patients with stroke and TIA. The understanding of the differential use of imaging in various centers, different age groups, and the "at-risk" population is crucial to designing future interventions to reduce stroke risk and quantify the need for standardization of care.

There are a few important limitations to our study, including the retrospective nature. There is a potential for bias of incomplete case ascertainment, though our method of identification of hospitalized strokes is well-defined and remained consistent across the study periods. Despite the surveillance methods in place, it is possible that some cases of stroke and TIA were missed. Although imaging may have an effect on the detection and diagnosis of stroke, the case definition for stroke used in this analysis for both study periods was based strictly on clinical criteria, supported by imaging findings. Another limitation is that the neuroimaging use rates are from older 2005 and 2010 cohorts. We plan to study the imaging use in the 2015 GCNKSS cohort (data collection for the same is underway). Our study also does not have the ability to track how the use of imaging affected clinical decision-making and/or outcomes in the stroke population; however, this area is an important focus for future research.

CONCLUSIONS

Age- and race-related differences exist in the use of neuroimaging for patients with stroke/TIA, which depends on care center type. Clearly, much work is still needed to understand these disparities. Deconstructing the differences in utilization data must continue because this can provide an important basis for lines of inquiry into socioeconomic and access-to-stroke-care issues. These data are critical for focusing and monitoring the success of the public health effort in decreasing disability and mortality due to stroke.

Disclosures: Achala Vagal—*UNRELATED*: *Grant*: CTSA KL2 grant, TR001426-01*. Heidi Sucharew—*RELATED*: *Grant*: R01NS30678*; *UNRELATED*: *Employment*: Cincinnati Children's Hospital Medical Center*. Kathleen A. Alwell—*RELATED*: *Grant*: National Institutes of Health/National Institute of Neurological Disorders and Stroke, *Comments*: work on the National Institutes of Health grant NS30678*. Jane C. Khoury—*RELATED*: *Grant*: National Institutes of Health/National Institute of Neurological Disorders and Stroke. Pooja Khatri—*RELATED*: *Grant*: National Institutes of Health/National Institute of Neurological Disorders and Stroke*; *UNRELATED*: *Consultancy*: St. Jude's, Grand Rounds Experts, *Comments*: medicolegal consultations; *Royalties:* UpToDate; *Travel/Accommodations/Meeting Expenses Unrelated to Activities Listed*: Neuravi Clot Summit; *Other*: Genentech pays my department for my PRISMS Principal Investigator effort; Biogen pays me for Data and Safety Monitoring Board member effort*. Daniel Woo—*UNRELATED*: National Institute of Neurological Disorders and Stroke, *Comments*: NS036695, NS069763*. Matthew Flaherty—*RELATED*: *Grant*: National Institutes of Health; *Support for Travel to Meetings for the Study or Other Purposes*: National Institutes of Health. Brett M. Kissela—*UNRELATED*: *Grant*: National Institutes of Health, *Comments*: multiple grants, including the National Institutes of Health grant from which this work was produced, NS030678; others include NS041588 and RR026314*; *Support for Travel to Meetings for the Study or Other Purposes*: Janssen Pharmaceutica; *Comments*: I was paid to attend a meeting

for the end point adjudication committee (see next); *Fees for Participation in Review Activities such as Data Monitoring Boards, Statistical Analysis, Endpoint Committees, and the Like:* AbbVie and Janssen Pharmaceutica, *Comments*: end point adjudication committees for clinical trials sponsored by these 2 entities. Opeolu Adeoye—*RELATED*: *Grant*: National Institutes of Health/National Institute of Neurological Disorders and Stroke, *Comments*: research grant support; *Support for Travel to Meetings for the Study or Other Purposes*: National Institutes of Health/National Institute of Neurological Disorders and Stroke, *Comments*: research grant support; *UNRELATED*: *Grants/Grants Pending*: CereDx, *Comments*: research grant for stroke plasma biomarker diagnosis; *Patents (Planned, Pending or Issued)*: PCT/US2011/068095, *Comments*: patent for noninvasive neurologic monitoring device for intracranial hemorrhage; *Other*: Sense Diagnostics, *Comments*: cofounder of the company formed to develop the device referenced in the patent above. Simona Ferioli—*RELATED*: National Institutes of Health, *Comments*: GCNKSS*. Felipe De Los Rios La Rosa—*RELATED*: *Grant*: National Institutes of Health*. Jason Mackey—*RELATED*: *Grant*: National Institutes of Health/National Institute of Neurological Disorders and Stroke, R01 NS030678*; *UNRELATED*: *Grants/Grants Pending*: IUH-VFR-365, IUH/IUSM Strategic Research Initiative CTSI PDT, National Institutes of Health LRP recipient Indiana University CTSI KL2 award*. Dawn Kleindorfer—*RELATED*: *Grant*: National Institutes of Health, *Comments*: R01 grant*. *Money paid to the institution.

REFERENCES

1. Mozaffarian D, Benjamin EJ, Go AS, et al; Writing Group Members, American Heart Association Statistics Committee, Stroke Statistics Subcommittee. **Executive summary: Heart Disease and Stroke Statistics—2016 Update: a report from the American Heart Association.** *Circulation* 2016;133:447–54 CrossRef Medline
2. Centers for Disease Control and Prevention (CDC). **Disparities in deaths from stroke among persons aged <75 years: United States, 2002.** *MMWR Morb Mortal Wkly Rep* 2005;54:477–81 Medline
3. Cox CS, Mussolino ME, Rothwell ST, et al. **Plan and operation of the NHANES I Epidemiologic Followup Study, 1992.** *Vital Health Stat 1* 1997;1–231 Medline
4. Ingram DD, Montresor-Lopez JA. **Differences in stroke mortality among adults aged 45 and over: United States, 2010–2013.** *NCHS Data Brief* 2015:1–8 Medline
5. Cruz-Flores S, Rabinstein A, Biller J, et al American Heart Association Stroke Council, Council on Cardiovascular Nursing, Council on Epidemiology and Prevention, Council on Quality of Care and Outcomes Research. **Racial-ethnic disparities in stroke care: the American experience—a statement for healthcare professionals from the American Heart Association/American Stroke Association.** *Stroke* 2011;42:2091–116 CrossRef Medline
6. Boehme AK, Siegler JE, Mullen MT, et al. **Racial and gender differences in stroke severity, outcomes, and treatment in patients with acute ischemic stroke.** *J Stroke Cerebrovasc Dis* 2014;23:e255–61 CrossRef Medline
7. Nasr DM, Brinjikji W, Cloft HJ, et al. **Racial and ethnic disparities in the use of intravenous recombinant tissue plasminogen activator and outcomes for acute ischemic stroke.** *J Stroke Cerebrovasc Dis* 2013;22:154–60 CrossRef Medline
8. Mozaffarian D, Benjamin EJ, Go AS, et al; American Heart Association Statistics Committee and Stroke Statistics Subcommittee. **Heart disease and stroke statistics–2015 update: a report from the American Heart Association.** *Circulation* 2015;131:e29–322 CrossRef Medline
9. Di Carlo A, Lamassa M, Baldereschi M, et al; European BIOMED Study of Stroke Care Group. **Sex differences in the clinical presentation, resource use, and 3-month outcome of acute stroke in Europe: data from a multicenter multinational hospital-based registry.** *Stroke* 2003;34:1114–19 CrossRef Medline
10. Reeves MJ, Fonarow GC, Zhao X, et al; Get With The Guidelines-Stroke Steering Committee & Investigators. **Quality of care in women with ischemic stroke in the GWTG program.** *Stroke* 2009;40:1127–33 CrossRef Medline
11. Lazzarino AI, Palmer W, Bottle A, et al. **Inequalities in stroke patients' management in English public hospitals: a survey on 200,000 patients.** *PLoS One* 2011;6:e17219 CrossRef Medline
12. Rose KM, Rosamond WD, Huston SL, et al. **Predictors of time from hospital arrival to initial brain-imaging among suspected stroke patients: the North Carolina Collaborative Stroke Registry.** *Stroke* 2008;39:3262–67 CrossRef Medline
13. Jacobs BS, Birbeck G, Mullard AJ, et al. **Quality of hospital care in African American and white patients with ischemic stroke and TIA.** *Neurology* 2006;66:809–14 CrossRef Medline
14. Powers WJ, Derdeyn CP, Biller J, et al American Heart Association Stroke Council. **2015 American Heart Association/American Stroke Association Focused Update of the 2013 Guidelines for the Early Management of Patients with Acute Ischemic Stroke Regarding Endovascular Treatment: A Guideline for Healthcare Professionals from the American Heart Association/American Stroke Association.** *Stroke* 2015;46:3020–35 CrossRef Medline
15. Brinjikji W, El-Sayed AM, Rabinstein AA, et al. **Disparities in imaging utilization for acute ischemic stroke based on patient insurance status.** *AJR Am J Roentgenol* 2014;203:372–76 CrossRef Medline
16. Broderick J, Brott T, Kothari R, et al. **The Greater Cincinnati/Northern Kentucky Stroke Study: preliminary first-ever and total incidence rates of stroke among blacks.** *Stroke* 1998;29:415–21 CrossRef Medline
17. Saposnik G, Black SE, Hakim A, et al; Investigators of the Registry of the Canadian Stroke Network (RCSN), Stroke Outcomes Research Canada (SORCan) Working Group. **Age disparities in stroke quality of care and delivery of health services.** *Stroke* 2009;40:3328–35 CrossRef Medline
18. Kissela BM, Khoury JC, Alwell K, et al. **Age at stroke: temporal trends in stroke incidence in a large, biracial population.** *Neurology* 2012;79:1781–87 CrossRef Medline
19. Martin KD, Naert L, Goldstein LB, et al. **Comparing the use of diagnostic imaging and receipt of carotid endarterectomy in elderly black and white stroke patients.** *J Stroke Cerebrovasc Dis* 2012;21:600–06 CrossRef Medline
20. Kleindorfer DO, Lindsell C, Broderick J, et al. **Impact of socioeconomic status on stroke incidence: a population-based study.** *Ann Neurol* 2006;60:480–84 CrossRef Medline
21. Schwamm LH, Fonarow GC, Reeves MJ, et al. **Get With the Guidelines-Stroke is associated with sustained improvement in care for patients hospitalized with acute stroke or transient ischemic attack.** *Circulation* 2009;119:107–15 CrossRef Medline
22. Cheng EM, Keyhani S, Ofner S, et al. **Lower use of carotid artery imaging at minority-serving hospitals.** *Neurology* 2012;79:138–44 CrossRef Medline
23. Sistrom C, McKay NL, Weilburg JB, et al. **Determinants of diagnostic imaging use in primary care.** *Am J Manag Care* 2012;18:e135–44 Medline
24. *Healthy People 2020* [Internet]. Washington, DC: US Department of Health and Human Services, Office of Disease Prevention and Health Promotion. https://www.healthypeople.gov/2020/About-Healthy-People. Accessed June 2, 2017
25. Seabury S, Bognar K, Xu Y, et al. **Regional disparities in the quality of stroke care.** *Am J Emerg Med* 2017 Mar 19. [Epub ahead of print] CrossRef Medline
26. Gonzales S, Mullen MT, Skolarus L, et al. **Progressive rural-urban disparity in acute stroke care.** *Neurology* 2017;88:441–48 CrossRef Medline
27. Govindarajan P, Friedman BT, Delgadillo JQ, et al. **Race and sex disparities in prehospital recognition of acute stroke.** *Acad Emerg Med* 2015;22:264–72 CrossRef Medline

Improved Detection of Anterior Circulation Occlusions: The "Delayed Vessel Sign" on Multiphase CT Angiography

D. Byrne, G. Sugrue, E. Stanley, J.P. Walsh, S. Murphy, E.C. Kavanagh, and P.J. MacMahon

ABSTRACT

BACKGROUND AND PURPOSE: Multiphase CTA, a technique to dynamically assess the vasculature in acute ischemic stroke, was primarily developed to evaluate collateral filling. We have observed that it is also useful in identifying distal anterior circulation occlusions due to delayed anterior circulation opacification on multiphase CTA, an observation we term the "delayed vessel sign." We aimed to determine the usefulness of this sign by comparing multiphase CTA with single-phase CTA.

MATERIALS AND METHODS: All 23 distal anterior circulation occlusions during a 2-year period were included. Ten M1-segment occlusions and 10 cases without a vessel occlusion were also included. All patients had follow-up imaging confirming the diagnosis. Initially, the noncontrast CT and first phase of the multiphase CTA study for each patient were blindly evaluated (2 neuroradiologists, 2 radiology trainees) for an anterior circulation occlusion. Readers' confidence, speed, and sensitivity of detection were recorded. Readers were then educated on the "delayed vessel sign," and each multiphase CTA study was re-examined for a vessel occlusion after at least 14 days.

RESULTS: There was significant improvement in the sensitivity of detection of distal anterior circulation vessel occlusions ($P < .001$), overall confidence ($P < .001$), and time taken to interpret ($P < .001$) with multiphase CTA compared with single-phase CTA. Readers preferred MIP images compared with source images in >90% of cases.

CONCLUSIONS: The delayed vessel sign is a reliable indicator of anterior circulation vessel occlusion, particularly in cases involving distal branches. Assessment of the later phases of multiphase CTA for the delayed vessel sign leads to a significant improvement in the speed and confidence of interpretation, compared with single-phase CTA.

ABBREVIATIONS: MPCTA = multiphase CTA; SPCTA = single-phase CTA

The major recent development in acute stroke care, clot retrieval by thrombectomy, reduces disability and improves the quality of life in patients with proximal large-vessel occlusions.[1] Prompt brain imaging and precise localization of an intracranial vessel occlusion are important to aid in the selection of appropriate patients for treatment with intravenous thrombolysis and/or thrombectomy.[2-4]

CT angiography is performed immediately after noncontrast CT to assess vessel occlusion or stenoses and to evaluate the pial collateral status. Single-phase CTA (SPCTA, a single arterial phase study of the head and neck) is the most common CTA technique used to assess the intra- and extracranial vasculature.[5] Multiphase CTA (MPCTA) is a new supplementary technique, distinct from brain perfusion CT, that acquires intracranial images at 3 time points (phases) rather than just a single phase.[5] To date, MPCTA has been primarily used to obtain extra information on the extent of pial collateral filling.[2,6,7]

We have observed a simple imaging sign on MPCTA that assists in confirming the diagnosis of acute ischemic stroke. It appears especially useful when an occluded vessel is small (eg, M2 or M3 segments of the middle cerebral artery), a finding that may be easily overlooked with SPCTA alone. The "delayed vessel sign" refers to the presence of an artery distal to the point of occlusion/stenosis that is absent or poorly opacified on the initial angiographic phase but becomes more opacified on the delayed phases, appearing denser than the equivalent vessel on the opposite side (Figs 1 and 2). This sign can rapidly indicate the presence of an ipsilateral vessel occlusion.

The aim of our study was to determine whether educating

Received March 9, 2017; accepted after revision May 27.

From the Departments of Radiology (D.B., G.S., E.S., E.C.K., P.J.M.) and Stroke Medicine (S.M.), Mater Misericordiae University Hospital, Dublin, Ireland; Department of Radiology (J.P.W.), St. James's Hospital, Dublin, Ireland; School of Medicine (S.M., E.C.K., P.J.M.), University College Dublin, Dublin, Ireland; and Royal College of Surgeons in Ireland Medical School (S.M.), Dublin, Ireland.

Please address correspondence to D. Byrne, MD, Department of Radiology, Whitty Building, North Circular Rd, Mater Misericordiae University Hospital, Dublin 7, Ireland; e-mail: dbyrne.radiology@gmail.com

http://dx.doi.org/10.3174/ajnr.A5317

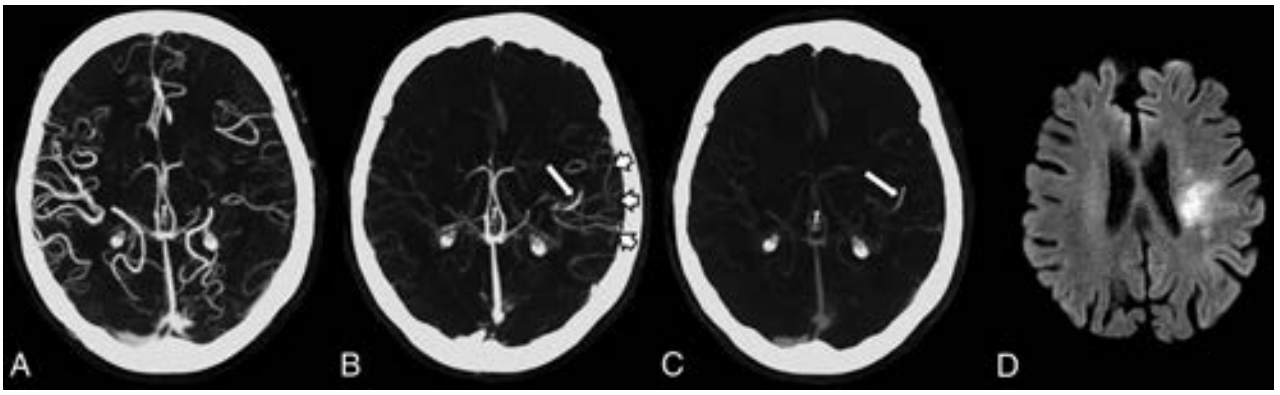

FIG 1. Multiphase CTA and follow-up MR imaging of an 83-year-old woman presenting with acute right upper limb weakness and dysphasia. *A*, Axial MIP of the first phase demonstrates subtle paucity of vessels in the distribution of the left MCA compared with the right side. *B*, Axial MIP of the second phase demonstrates the delayed vessel sign (*long arrow*). There is delayed enhancement of the distal left MCA via pial collateral vessels (*short arrows*). This vessel is not seen on the first phase due to the presence of an M2 vessel occlusion. *C*, Axial MIP of the third phase also demonstrates the "delayed" left MCA vessel (*long arrow*). *D*, DWI $b=1000$ image 2 weeks postpresentation demonstrates a recent infarct (*arrow*) in the same left MCA territory.

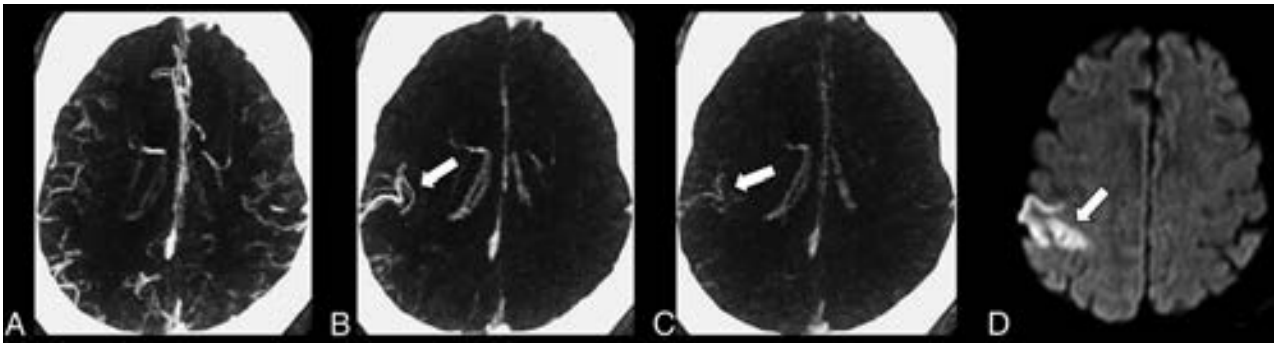

FIG 2. Multiphase CTA in a 65-year-old man with acute left-sided weakness. *A*, Axial MIP of the first phase without obvious asymmetry. *B* and *C*, Axial MIPs of the second and third phases demonstrate the delayed vessel sign (*arrow*) with opacification of a distal right MCA branch, which was not opacified on the first angiographic phase due to a proximal M2 vessel occlusion. *D*, DWI $b=1000$ image 24 hours postpresentation demonstrates an acute infarct (*arrow*) in the same right MCA territory.

radiologists of all levels of experience (resident to expert) on the delayed vessel sign would improve sensitivity, confidence, and speed in the detection of distal anterior circulation vessel occlusions compared with SPCTA alone.

MATERIALS AND METHODS

Patients and Distribution of Intracranial Vessel Occlusions

Approval for this study was obtained from the local ethics committee at Mater Misericordiae University Hospital. A senior radiology trainee (D.B.), not involved in the formal evaluation of the studies, selected all distal anterior (ie, M2/A2 segments or smaller) circulation occlusions in patients who presented to our institution after MPCTA became standard practice and who fulfilled the inclusion criteria (suspected acute ischemic stroke, having undergone NCCT and MPCTA, and follow-up cross-sectional imaging). This process identified 23 appropriate distal anterior circulation occlusions during the study period (January 2014 to September 2016). Ten consecutive M1 occlusions in the study period were also selected as a means of comparing the usefulness of the sign for the detection of larger vessel occlusions. In addition, the last 10 consecutive studies with normal findings with follow-up MR imaging available, obtained in the study period, were included to assess false-positives.

Of the 43 patients, 21 were women (mean age, 69 ± 16.5 years; range, 33–94 years). Before evaluation, vessel occlusions were deemed present or absent by a consensus of 2 neuroradiologists not involved in image evaluation who had access to follow-up imaging. The cases were randomly sorted to be evaluated by readers (neuroradiologists: P.J.M. with 10 years' experience and E.C.K. with 15 years' experience; radiology residents: G.S. with 2 years' experience, and E.S. with 3 years' experience).

Technical Parameters

Images were obtained with a 128-section multidetector CT scanner (Somatom Definition AS+; Siemens, Erlangen, Germany) at 120 kV, 90 mAs (effective) with a collimation of 128 × 0.6 mm. NCCT was performed from the skull base to the vertex. The first phase of the MPCTA was performed from the aortic arch to the skull vertex with the second and third phases performed from the skull base to the vertex. The first phase is timed to occur during the peak arterial phase with bolus monitoring of the descending thoracic aorta and is commenced after a 6-second delay. Eighty milliliters of intravenous contrast (iopamidol, Niopam; Bracco Imaging, Milan, Italy; 370 mg iodine per milliliter) is injected at a rate of 5 mL/s followed

Table 1: Results for radiology trainees[a]

	Distal Occlusions			Proximal M1 Occlusions			Normal Study Findings		
	SPCTA	MPCTA	*P* Value	SPCTA	MPCTA	*P* Value	SPCTA	MPCTA	*P* Value
Sensitivity (%)	71.7 (57.4–82.7)	100 (92.2–100)	<.001	100 (83.8–100)	100 (83.8–100)	NS	–	–	–
Confidence (1–5)	3.8 (3.6–4.0)	4.8 (4.6–4.9)	<.001	4.6 (4.3–4.8)	5.0	.08	3.6 (3.3–3.8)	5.0	<.001
Time (sec)	99 (90–107)	44 (40–49)	<.001	72 (65–79)	34 (30–37)	<.001	102 (93–112)	56 (51–61)	<.001

Note:—NS indicates not significant.
[a] Confidence intervals provided in parentheses.

Table 2: Results for neuroradiologists[a]

	Distal Occlusions			Proximal M1 Occlusions			Normal Study Findings		
	SPCTA	MPCTA	*P* Value	SPCTA	MPCTA	*P* Value	SPCTA	MPCTA	*P* Value
Sensitivity (%)	78.3 (64.4–87.7)	100 (92.2–100)	.004	100 (83.8–100)	100 (83.8–100)	NS	–	–	–
Confidence (1–5)	3.8 (3.7–4.0)	4.9 (4.8–5.0)	<.001	4.7 (4.5–4.9)	5.0	.08	3.7 (3.5–3.9)	4.9 (4.7–5.0)	<.001
Time (sec)	84 (78–90)	37 (34–41)	<.001	67 (60–74)	29 (26–32)	<.001	81 (78–85)	43 (39–47)	<.001

[a] Confidence intervals provided in parentheses.

by 40 mL of saline at a similar rate. The second and third phases are acquired after 11 and 22 seconds, respectively.

Thin sections (1 mm) are reconstructed for each phase, and maximum intensity projections with 5-mm section thickness are reconstructed at the scanner workstation in 3 planes (axial, sagittal, and coronal) for each phase.

Image Interpretation

Stage 1. The NCCT and SPCTA (ie, the first phase of an MPCTA study) were independently evaluated, and readers' confidence, speed, and sensitivity of detection were recorded. Readers were provided with a brief clinical history, NCCT, and source images of the SPCTA (ie, MIPs were initially not provided). On the NCCT, absence of hemorrhage, the presence or absence of a hyperdense vessel sign, and parenchymal infarction were recorded. Using SPCTA source images, readers were asked to record the presence and location of an intracranial vessel occlusion. A detailed analysis of all images generated was not expected. Intracranial vessel occlusions were classified as follows: right or left, anterior cerebral artery (A1, A2, or A3), and middle cerebral artery (M1, M2, M3). The time taken to complete the initial reading was recorded. Readers' degrees of confidence in their interpretation of each study were recorded with a 5-point Likert scale (1 = not at all confident, 2 = not very confident, 3 = neutral, 4 = confident, and 5 = very confident). Readers were then provided with the axial, coronal, and sagittal reconstructed MIP images and asked whether they preferred the source or reconstructed MIP images of the SPCTA.

Stage 2. After an interval of at least 2 weeks, all readers were educated on the delayed vessel. Readers were advised to immediately assess the second and third phases of the MPCTA rather than the first phase to aid in the detection of delayed enhancement. A positive delayed vessel sign is only present if a suspect vessel on the delayed phases is poorly opacified on the initial phase. If the delayed vessel sign was identified, the readers were advised to follow the vessel proximally and correlate with the linked initial angiographic phase to aid in the detection of the point of vessel occlusion.

Following this education, all readers re-evaluated the 43 cases but with access to the source images from the entire MPCTA study rather than just the initial phase. MIP reconstructions were initially withheld. Readers were asked to record the same findings as described in stage 1, but to also comment on the presence or absence of the delayed vessel sign and on which phase it was most pronounced. Readers were also asked to record the presence of concomitant pial vessel hyperenhancement (which refers to the presence of relatively asymmetric enhancing pial vessels on delayed phases of a MPCTA ipsilateral to an intracranial vessel occlusion) and to record on which of the 3 phases this was most obvious. Readers were then provided with reconstructed MIP images and asked whether they preferred the source or reconstructed MIP images of the MPCTA.

Statistical Analysis

The significance level was set at $P < .05$. The McNemar test was used to compare SPCTA with MPCTA results. To evaluate interrater agreement between readers, we used unweighted κ statistics and 95% confidence intervals. Agreement was quantified as fair ($\kappa = 0.21–0.40$), moderate ($\kappa = 0.41–0.60$), substantial ($\kappa = 0.61–0.80$), or almost perfect ($\kappa = 0.81–0.99$).

RESULTS

Distal Vessel Occlusions

There was a significant improvement in the sensitivity of the detection of distal (A2, A3, M2, M3) anterior circulation vessel occlusions on MPCTA compared with SPCTA ($P < .001$), from 75% to 100%. Among the 2 radiology trainees, 33 of 46 (total) distal occlusions were detected on SPCTA and all distal occlusions were detected with MPCTA. Among the 2 neuroradiologists, 36 of 46 (total) distal occlusions were detected on SPCTA and all distal occlusions were detected with MPCTA (Tables 1 and 2).

Among radiology trainees (Table 1), for distal anterior circulation occlusions, mean confidence improved from 3.8 for SPCTA to 4.8 for MPCTA ($P < .001$). The average time taken to interpret each case on SPCTA was 99 seconds and decreased to 44 seconds with MPCTA ($P < .001$). Among neuroradiologists (Table 2), for distal anterior circulation occlusions, the mean confidence was 3.8 for SPCTA, improving to 4.9 for MPCTA ($P < .001$). The average time taken to interpret each case on SPCTA was 84 seconds, decreasing to 37 seconds on MPCTA ($P < .001$).

M1 Occlusions

While all proximal (M1) occlusions were detected on both SPCTA and MPCTA by all readers, there was significant improvement in the speed of detection of M1 occlusions with MPCTA. There was also a trend toward improvement in the confidence of detection of M1 occlusions; however, this did not reach statistical significance ($P = .08$). Among radiology trainees, for proximal M1 occlusions, confidence improved from 4.6 with SPCTA to 5.0 with MPCTA ($P = .08$). The average time taken to interpret each case on SPCTA was 72 seconds, decreasing to 34 seconds on MPCTA ($P < .001$). Among neuroradiologists, for proximal M1 occlusions, the mean confidence was 4.7 for SPCTA, improving to 5.0 for MPCTA ($P = .08$). The average time taken to interpret each case on SPCTA was 67 seconds, decreasing to 29 seconds on MPCTA ($P < .001$).

Normal Study Findings

The average time taken to evaluate studies with normal findings without an intracranial vessel occlusion significantly decreased with MPCTA (49 seconds) compared with SPCTA (92 seconds) ($P < .001$), and readers' confidence significantly improved for studies with normal findings with MPCTA (4.9) compared with SPCTA (3.6) ($P < .001$).

General Findings

Both radiology trainees and neuroradiologists stated that in patients with an intracranial vessel occlusion, that they preferred and were more confident with their findings after MIP images were provided compared with source images (97.7% of MPCTA cases and 90.9% of SPCTA cases). Readers stated that they were more confident with MIP compared with source images in 100% of cases with normal findings without intracranial vessel occlusion.

Overall, the sensitivity of the delayed vessel sign for the presence of vessel occlusion was 96.2% (95% CI, 91.4%–98.3%) and specificity was 100% (95% CI, 91.2%–100%). Overall, the positive predictive value of the delayed vessel sign was 100% (95% CI, 97.1%–100%), and the negative predictive value was 88.9% (95% CI, 76.5%–95.1%).

With the Pearson correlation coefficient, there was a high correlation between the presence of the delayed vessel sign and pial vessel enhancement ($r = 0.6465$, $P < .001$).

Interrater agreement was almost perfect ($\kappa = 0.83$) between readers for distal anterior circulation intracranial occlusion detection with SPCTA and improved with MPCTA ($\kappa = 0.95$). Agreement was almost perfect for the presence of the delayed vessel sign in cases of distal anterior circulation intracranial vessel occlusion ($\kappa = 0.91$) and was substantial ($\kappa = 0.75$) for the presence of asymmetric pial vessel enhancement.

DISCUSSION

In our institution, MPCTA is the standard angiographic technique in the investigation of suspected acute ischemic stroke. Acute cerebral ischemia is a dynamic process requiring a dynamic diagnostic approach.[8] In this context, the evaluation of patients suspected of having acute ischemic stroke with single-phase CTA is inappropriate. While perfusion CT is an established stroke imaging technique (from which MPCTA-type images can also be generated),[9,10] it is not universally available at all times of day, especially in non-stroke centers. MPCTA is an alternative technique for achieving dynamic vascular imaging and may be more widely applicable. Additional software-based postprocessing is not required, and in our experience, accurate interpretation by the nonexpert (especially if comfortable with SPCTA) is readily possible after brief training.

MPCTA was primarily developed to improve the assessment of pial collaterals; however, we have found, consistent with other reports, that it also aids in the diagnosis of distal anterior circulation occlusions.[11,12] Our study provides an easily understood means by which MPCTA can improve the detection of more distal anterior circulation vessel occlusions. The previous studies,[11,12] also demonstrating the superiority of MPCTA over SPCTA, did not provide a clear mechanism by which this benefit is derived. We have found that the delayed vessel sign on CTA can be communicated and understood quickly and easily by all medical professionals involved in acute stroke care. We have shown that the education of radiologists of different levels of expertise (but particularly trainee radiologists) on the delayed vessel sign leads to an increase in the sensitivity and speed of detection of distal anterior circulation vessel occlusions. We have also found that confidence in interpretation increases significantly.

It is likely that the delayed vessel (most commonly the more distal branches of the MCA) enhances slowly due to retrograde opacification via pial collaterals. A process of retrograde opacification is supported by the strong correlation between the presence of the delayed vessel sign and pial enhancement, an association most evident on the same delayed phase (either second or third). Our sign is distinct from the "clot outline sign,"[13] which is seen on procedural arteriograms obtained before intra-arterial thrombolysis. This sign implies that the vessel in question is almost completely occluded and has minute blood flow past the clot (ie, antegrade flow). The delayed vessel sign, which we describe, is conceptually different because the vessel in question typically has total occlusion, which fills retrograde via collateral vessels. Unlike the clot outline sign, our study pertains to CTA, not procedural arteriography, and is used to assist in the diagnosis of distal anterior circulation occlusions rather than to predict treatment responders.

In this new era of endovascular treatment of proximal large-vessel occlusions, the detection and treatment of less severe stroke due to more distal vessel occlusion remain essential.[14] Recent data suggest that patients with proximal M2 occlusions may benefit from endovascular treatment; therefore, early accurate detection of these occlusions will likely become more important.[15,16] The role of intravenous thrombolysis with tenectaplase in mild stroke with distal vessel occlusion will be tested in the A Randomized Controlled Trial of TNK-tPA Versus Standard of Care for Minor Ischemic Stroke With Proved Occlusion trial (NCT02398656).

Patients are often initially triaged as having possible acute ischemic stroke by paramedics or other non-stroke specialists[17] and are referred for NCCT after early rapid clinical assessment.[17-20] The differential diagnosis of acute stroke from stroke mimics can be a challenge, especially in milder cases.[21] Many patients present to the hospital off-hours[22,23] when there may be less immediate

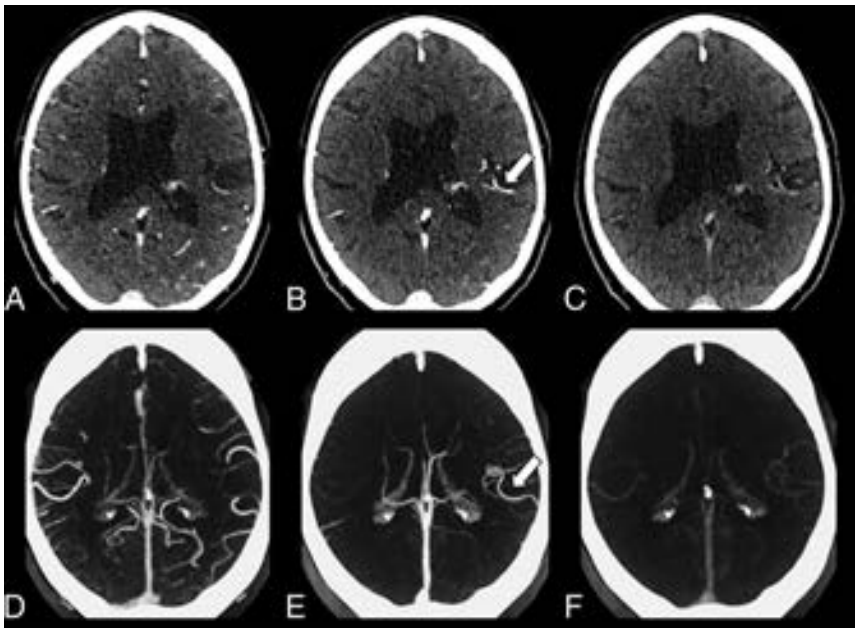

FIG 3. Multiphase CTA in a 78-year-old man with expressive dysphasia and right-sided weakness. *A*, Axial source image of the first phase of MPCTA without obvious asymmetry of the intracranial vasculature. *B*, The delayed vessel sign is identified on the second phase (*arrow*), indicative of a proximal occlusion. *C*, Axial source image of the third phase of the MPCTA. *D–F*, Axial MIPs of the first, second, and third phases of the same patient. The delayed vessel sign is more apparent on MIP image (*arrow*) of the second phase (*E*) compared with source images.

access to senior radiology personnel and hence greater reliance on trainee radiologists for the initial interpretation of imaging.[24,25] We think that this sign will aid in the rapid differentiation of stroke from stroke mimics.[20,26] MPCTA comprises a large number of images that can seem daunting to interpret, especially in the urgent clinical scenario of suspected ischemic stroke. The key to a quick, confident, and accurate MPCTA interpretation, especially in patients with an uncertain clinical diagnosis, is to immediately assess the later phases rather than the initial phase for the presence of the delayed vessel sign; this assessment can then accelerate the identification of a vessel occlusion.

The purpose of MIPs is to give an overview of the target vessel by generating a DSA-like image.[27] MIPs are known to increase the conspicuity of intracranial vessel occlusion and stenosis.[28] In 97.7% of MPCTA cases and in 90.9% of SPCTA cases in this study, both radiology trainees and neuroradiologists stated that they preferred and were more confident with their interpretation when MIP images were provided compared with source images alone. The delayed vessel sign was often more apparent on MIP compared with source images (Fig 3). Readers also reported that symmetric vessel enhancement in cases without an intracranial vessel occlusion was easier to appreciate on MIP compared with source images and reassured readers that no intracranial vessel occlusion was present.

This study was affected by several limitations. First, while all appropriate cases of distal anterior circulation occlusion were retrospectively selected, an element of bias in case selection cannot be excluded. For example, patients misdiagnosed as having a stroke mimic at presentation may not have received follow-up brain imaging and thus would not be included. Another limitation is that we did not use DSA as a criterion standard in the identification of an occlusion but rather used the consensus opinion of 2 neuroradiologists not involved in the study. Although the delayed vessel sign demonstrated a high negative predictive value in cases of distal occlusion, we hypothesize that the sign would be absent, or harder to appreciate, in patients with poor collateral supply in the ischemic territory. For example, in cases of basal ganglia and internal capsule infarction, territories supplied by lenticulostriate branches,[29] the delayed vessel sign will likely be absent because these vessels are perforator arteries and lack collateral blood supply.[30] In addition, the delayed vessel sign will be absent in cases of small cortical infarcts, which are often caused by occlusion of small pial vessels by microemboli.[31] The sign may falsely indicate an acute intracranial occlusion in several scenarios not encountered in this study population, for example in the setting of chronic intracranial occlusions/stenoses and acute or chronic extracranial occlusions. Readers were not timed on their interpretation of the entire angiographic dataset but only on the time to establish the presence or absence of a vessel occlusion. The times recorded in this study are not a true reflection of the interpretation time for the entire study. Our inclusion criteria limited the study to anterior circulation stroke because this is the most common type of intracranial vessel occlusion; however, the sign may also be applicable to the posterior circulation.

CONCLUSIONS

The delayed vessel sign is a reliable indicator of anterior circulation vessel occlusion and is particularly useful in cases involving distal branches that are not easily identified on a single-phase angiographic examination. Immediate assessment of the MIP reconstructions of the later phases of an MPCTA examination for the delayed vessel sign leads to a significant improvement in the speed and confidence of detecting vessel occlusions.

Disclosures: Sean Murphy—*UNRELATED*: *Travel/Accommodations/Meeting Expenses Unrelated to Activities Listed*: travel grants to attend the International Stroke Conference, Houston, Texas, February 2017; sponsorship to attend the European Stroke Conference, Prague, May 2017; sponsorship to attend the UK Stroke Forum, November 2016.

REFERENCES

1. Ganesalingam J, Pizzo E, Morris S, et al. **Cost-utility analysis of mechanical thrombectomy using stent retrievers in acute ischemic stroke.** *Stroke* 2015;46:2591–98 CrossRef Medline
2. Menon BK, Campbell BC, Levi C, et al. **Role of imaging in current acute ischemic stroke workflow for endovascular therapy.** *Stroke* 2015;46:1453–61 CrossRef Medline
3. Berkhemer OA, Fransen PS, Beumer D, et al. **A randomized trial of intraarterial treatment for acute ischemic stroke.** *N Engl J Med* 2015; 372:11–20 CrossRef Medline

4. Goyal M, Demchuk AM, Menon BK, et al; ESCAPE Trial Investigators. **Randomized assessment of rapid endovascular treatment of ischemic stroke.** *N Engl J Med* 2015;372:1019–30 CrossRef Medline
5. Menon BK, d'Esterre CD, Qazi EM, et al. **Multiphase CT angiography: a new tool for the imaging triage of patients with acute ischemic stroke.** *Radiology* 2015;275:510–20 CrossRef Medline
6. Kim EY, Shin DH, Noh Y, et al. **Comparison of imaging selection criteria for intra-arterial thrombectomy in acute ischemic stroke with advanced CT.** *Eur Radiol* 2016;26:2974–81 CrossRef Medline
7. Bang OY, Goyal M, Liebeskind DS. **Collateral circulation in ischemic stroke: assessment tools and therapeutic strategies.** *Stroke* 2015;46:3302–09 CrossRef Medline
8. Liebeskind DS, Alexandrov AV. **Advanced multimodal CT/MRI approaches to hyperacute stroke diagnosis, treatment, and monitoring.** *Ann N Y Acad Sci* 2012;1268:1–7 CrossRef Medline
9. Orrison WW Jr, Snyder KV, Hopkins LN, et al. **Whole-brain dynamic CT angiography and perfusion imaging.** *Clin Radiol* 2011;66:566–74 CrossRef Medline
10. Kortman HG, Smit EJ, Oei MT, et al. **4D-CTA in neurovascular disease: a review.** *AJNR Am J Neuroradiol* 2015;36:1026–33 CrossRef Medline
11. Volny O, Cimflova P, Kadlecova P, et al. **Single-phase versus multiphase CT angiography in middle cerebral artery clot detection: benefits for less experienced radiologists and neurologists.** *J Stroke Cerebrovasc Dis* 2017;26:19–24 CrossRef Medline
12. Yu AY, Zerna C, Assis Z, et al. **Multiphase CT angiography increases detection of anterior circulation intracranial occlusion.** *Neurology* 2016;87:609–16 CrossRef Medline
13. Christoforidis GA, Mohammad Y, Avutu B, et al. **Arteriographic demonstration of slow antegrade opacification distal to a cerebrovascular thromboembolic occlusion site as a favorable indicator for intra-arterial thrombolysis.** *AJNR Am J Neuroradiol* 2006;27:1528–31 Medline
14. Coutts SB, Modi J, Patel SK, et al. **What causes disability after transient ischemic attack and minor stroke? Results from the CT and MRI in the Triage of TIA and minor Cerebrovascular Events to Identify High Risk Patients (CATCH) Study.** *Stroke* 2012;43:3018–22 CrossRef Medline
15. Sheth SA, Yoo B, Saver JL, et al; UCLA Comprehensive Stroke Center. **M2 occlusions as targets for endovascular therapy: comprehensive analysis of diffusion/perfusion MRI, angiography, and clinical outcomes.** *J Neurointerv Surg* 2015;7:478–83 CrossRef Medline
16. Powers WJ, Derdeyn CP, Biller J, et al; American Heart Association Stroke Council. **2015 American Heart Association/American Stroke Association Focused Update of the 2013 Guidelines for the Early Management of Patients With Acute Ischemic Stroke Regarding Endovascular Treatment: A Guideline for Healthcare Professionals From the American Heart Association/American Stroke Association.** *Stroke* 2015;46:3020–35 CrossRef Medline
17. Harbison J, Massey A, Barnett L, et al. **Rapid ambulance protocol for acute stroke.** *Lancet* 1999;353:1935 CrossRef Medline
18. Audebert HJ, Saver JL, Starkman S, et al. **Prehospital stroke care: new prospects for treatment and clinical research.** *Neurology* 2013;81:501–08 CrossRef Medline
19. Goyal M, Menon BK, Hill MD, et al. **Consistently achieving computed tomography to endovascular recanalization <90 minutes: solutions and innovations.** *Stroke* 2014;45:e252–56 CrossRef Medline
20. Zerna C, Assis Z, d'Esterre CD, et al. **Imaging, intervention, and workflow in acute ischemic stroke: the Calgary approach.** *AJNR Am J Neuroradiol* 2016;37:978–84 CrossRef Medline
21. Kamal N, Hill MD, Blacquiere DP, et al. **Rapid assessment and treatment of transient ischemic attacks and minor stroke in Canadian emergency departments: time for a paradigm shift.** *Stroke* 2015;46:2987–90 CrossRef Medline
22. Yang CY, Chen YF, Lee CW, et al. **Multiphase CT angiography versus single-phase CT angiography: comparison of image quality and radiation dose.** *AJNR Am J Neuroradiol* 2008;29:1288–95 CrossRef Medline
23. Barber PA, Demchuk AM, Zhang J, et al. **Validity and reliability of a quantitative computed tomography score in predicting outcome of hyperacute stroke before thrombolytic therapy: ASPECTS Study Group—Alberta Stroke Programme Early CT Score.** *Lancet* 2000;355:1670–74 CrossRef Medline
24. Streifler JY, Benderly M, Molshatzki N, et al. **Off-hours admission for acute stroke is not associated with worse outcome–a nationwide Israeli stroke project.** *Eur J Neurol* 2012;19:643–47 CrossRef Medline
25. Sorita A, Ahmed A, Starr SR, et al. **Off-hour presentation and outcomes in patients with acute ischemic stroke: a systematic review and meta-analysis.** *Eur J Intern Med* 2014;25:394–400 CrossRef Medline
26. Coutts SB, Dubuc V, Mandzia J, et al; TEMPO-1 Investigators. **Tenecteplase-tissue-type plasminogen activator evaluation for minor ischemic stroke with proven occlusion.** *Stroke* 2015;46:769–74 CrossRef Medline
27. Ota H, Takase K, Rikimaru H, et al. **Quantitative vascular measurements in arterial occlusive disease.** *Radiographics* 2005;25:1141–58 CrossRef Medline
28. Lev MH, Farkas J, Rodriguez VR, et al. **CT angiography in the rapid triage of patients with hyperacute stroke to intraarterial thrombolysis: accuracy in the detection of large vessel thrombus.** *J Comput Assist Tomogr* 2001;25:520–28 CrossRef Medline
29. Djulejić V, Djulejić S, Georgievski B, et al. **Clinical significance of blood supply to the internal capsule and basal ganglia.** *J Clin Neurosci* 2016;25:19–26 CrossRef Medline
30. Kleine JF, Beller E, Zimmer C, et al. **Lenticulostriate infarctions after successful mechanical thrombectomy in middle cerebral artery occlusion.** *J Neurointerv Surg* 2017;9:234–39 CrossRef Medline
31. Touaoussa A, El Youssi H, El Hassani I, et al. **Disseminated intravascular coagulation: clinical and biological diagnosis** [in French]. *Ann Biol Clin (Paris)* 2015;73:657–63 CrossRef Medline

Concordance of Time-of-Flight MRA and Digital Subtraction Angiography in Adult Primary Central Nervous System Vasculitis

H. de Boysson, G. Boulouis, J.-J. Parienti, E. Touzé, M. Zuber, C. Arquizan, N. Dequatre, O. Detante, B. Bienvenu, A. Aouba, L. Guillevin, C. Pagnoux, and O. Naggara

ABSTRACT

BACKGROUND AND PURPOSE: 3D-TOF-MRA and DSA are 2 available tools to demonstrate neurovascular involvement in primary central nervous system vasculitis. We aimed to compare the diagnostic concordance of vessel imaging using 3D-TOF-MRA and DSA in patients with primary central nervous system vasculitis.

MATERIALS AND METHODS: We retrospectively identified all patients included in the French primary central nervous system vasculitis cohort of 85 patients who underwent, at baseline, both intracranial 3D-TOF-MRA and DSA in an interval of no more than 2 weeks and before treatment initiation. Two neuroradiologists independently reviewed all 3D-TOF-MRA and DSA imaging. Brain vasculature was divided into 25 arterial segments. Concordance between 3D-TOF-MRA and DSA for the identification of arterial stenosis was assessed by the Cohen κ Index.

RESULTS: Thirty-one patients met the inclusion criteria, including 20 imaged with a 1.5T MR unit and 11 with a 3T MR unit. Among the 25 patients (81%) with abnormal DSA findings, 24 demonstrated abnormal 3D-TOF-MRA findings, whereas all 6 remaining patients with normal DSA findings had normal 3D-TOF-MRA findings. In the per-segment analysis, concordance between 1.5T 3D-TOF-MRA and DSA was 0.82 (95% CI, 0.75–0.93), and between 3T 3D-TOF-MRA and DSA, it was 0.87 (95% CI, 0.78–0.91).

CONCLUSIONS: 3D-TOF-MRA shows a high concordance with DSA in diagnostic performance when analyzing brain vasculature in patients with primary central nervous system vasculitis. In patients with negative 3T 3D-TOF-MRA findings, the added diagnostic value of DSA is limited.

ABBREVIATIONS: COVAC = COhort of patients with primary VAsculitis of the Central nervous system; PCNSV = primary central nervous system vasculitis; RCVS = reversible cerebral vasoconstriction syndrome; SCA = superior cerebellar artery

The diagnosis of primary central nervous system vasculitis (PCNSV) relies on the evidence of isolated vascular involvement of CNS vessels in patients with persistent neurologic disorders. Complete work-up should exclude other conditions that may explain vascular changes, such as infection, malignancy, autoimmune disease, and other cerebral vasculopathies, especially reversible cerebral vasoconstriction syndrome (RCVS) or atherosclerosis.[1-4] Original diagnostic criteria from Calabrese and Mallek,[5] established in 1988, proposed that vascular involvement could be demonstrated with brain biopsy, which remains the criterion standard, or with DSA. DSA has a high sensitivity for the involvement of small vessels of up to 500 μm. However, it remains an invasive tool with the risk of rare complications.[6,7]

With the development and gradual improvement of MR imaging technologies, alternative options to image CNS vessels have become available and may be substitutes for DSA. MR imaging is now considered a requirement in all patients with a suspected

Received March 16, 2017; accepted after revision May 20.

From the Departments of Internal Medicine (H.d.B., B.B., A.A.) and Neurology (E.T.), Caen University Hospital, University of Caen-Normandie, Institut National de la Santé et de la Recherche Médicale Unite Mixte de Recherche 919, Caen, France; Department of Neuroradiology (G.B., O.N.), Centre Hospitalier Sainte-Anne, Université Paris-Descartes, Institut National de la Santé et de la Recherche Médicale Unite Mixte de Recherche 894, Paris, France; Biostatistics and Clinical Research Unit (J.-J.P.), Caen University Hospital, Caen, France; Department of Vascular Neurology (M.Z.), Centre Hospitalier Saint Joseph, Université Paris-Descartes, Institut National de la Santé et de la Recherche Médicale Unite Mixte de Recherche S 919, Paris, France; Department of Neurology (C.A.), Montpellier University Hospital, Institut National de la Santé et de la Recherche Médicale Unite Mixte de Recherche 894, Montpellier, France; Department of Neurology (N.D.), Lille University Hospital, Lille, France; Department of Neurology (O.D.), Grenoble Alpes University Hospital, Grenoble, France; Department of Internal Medicine (L.G.), Centre Hospitalier Cochin, Paris, France; and Vasculitis Clinic (C.P.), Division of Rheumatology, Mount Sinai Hospital, Toronto, Ontario, Canada.

This study was supported by an institutional grant from the French Ministry of Health (COVAC, 2009 PHRC 08017).

Please address correspondence to Hubert de Boysson, MD, MSc, Department of Internal Medicine, Caen University Hospital, University of Caen-Normandie, Ave de la Côte de Nacre, 14000 Caen, France; e-mail: deboysson-h@chu-caen.fr

Indicates open access to non-subscribers at www.ajnr.org

Indicates article with supplemental on-line table.

http://dx.doi.org/10.3174/ajnr.A5300

diagnosis of PCNSV. Noncontrast 3D-TOF-MRA sequences can demonstrate vascular changes, such as stenosis, occlusions, or fusiform dilation. However, in many patients, DSA is still performed, even if the brain 3D-TOF-MRA shows vascular abnormalities. Our aim was to compare the diagnostic concordance between noncontrast intracranial 3D-TOF-MRA and DSA in patients with PCNSV.

MATERIALS AND METHODS

This study was conducted in accordance with Good Clinical Practices and the Declaration of Helsinki. Inclusion in the cohort required patient informed consent, and the cohort was approved by the Paris-Cochin institutional review board (No. 12541).

The article was prepared in accordance with Strengthening the Reporting of Observational Studies in Epidemiology[8] and Standards for Reporting of Diagnostic Accuracy Studies (http://www.stard-statement.org/) guidelines.

Patients

We created a cohort of patients with definite diagnoses of PCNSV (COhort of patients with primary VAsculitis of the Central Nervous System [COVAC]) in 2010 in France using the well-established networks of the French Vasculitis Study Group, French NeuroVascular Society, and National Society of Internal Medicine. This cohort was supported by an institutional grant from the French Ministry of Health (COVAC, 2009 hospital project of clinical research [PHRC] 08017).

After the initial description of the first 52 enrolled patients,[9] the cohort increased to 85 patients at the time of the present study.

As previously mentioned, patients were older than 18 years of age at diagnosis and had evidence of cerebral vascular involvement on brain biopsy and/or CNS vessel imaging. They had all been followed up for at least 6 months after diagnosis (unless they died) and were thoroughly screened at the onset for any differential diagnosis. We excluded patients with other vasculopathies or conditions potentially associated with secondary CNS vasculitis (eg, systemic vasculitis, autoimmune disease, infection). RCVS was excluded for each patient on the basis of the following criteria: 1) clinical presentation (no severe or thunderclap headaches at presentation, unless a brain biopsy showed vasculitis), 2) persistence of some vascular lesions as defined on MRA performed >6 months after the initial diagnostic work-up, and 3) clinical follow-up.

For the present study, we retrospectively selected in the COVAC population patients who underwent baseline intracranial 3D-TOF-MRA and DSA before treatment initiation and within a 2-week interval. We did not include patients with both procedures having negative findings and negative or absent biopsy findings.

Study Variables and Definitions

For each patient, as previously described,[9] we collected standard demographic data, medical history, clinical symptoms at disease onset, laboratory test parameters, CSF results (considered abnormal when the leukocyte count was >5 cells/mL and/or the total protein level was >0.5 mg/mL), neuroimaging findings, and CNS histology, when available. Transmural inflammation of the vessel wall on a biopsy sample, with or without lymphocytic infiltrate, granuloma, and necrosis, defined biopsy-proved PCNSV.[10]

Neuroimaging Analysis

For each patient, all imaging examinations, including source images, were gathered in a digital anonymous format and forwarded for review by 2 neuroradiologists (with 14 [O.N.] and 6 [G.B.] years of experience in stroke imaging) who were blinded to clinical manifestations. Characteristics of each MR imaging unit were also collected. Proximal, second divisions, and subsequent branches of each cerebral artery and the vertebral artery, PICA, anterior inferior cerebellar artery, superior cerebellar artery (SCA), and basilar artery were analyzed with both procedures. For DSA and 3D-TOF-MRA analysis, in line with previous works, we differentiated large-, medium-, and small-sized vessels.[11,12] Intracranial internal carotid and proximal anterior (A1), middle (M1), and posterior (P1) cerebral arteries were considered large; second divisions (A2, M2, P2) and subsequent branches (>A2, >M2, >P2) were considered medium- and small-sized vessels, respectively. The vertebral and basilar arteries were considered large-sized vessels, whereas the PICA, anterior inferior cerebellar artery, and SCA were considered medium-sized vessels. We thus divided cerebral vasculature into 25 segments (left and right intracranial internal carotid arteries, A1, A2, >A2, M1, M2, >M2, P1, P2, >P2; vertebral artery; and PICA/anterior inferior cerebellar artery/SCA, and basilar artery). A vascular segment was considered involved in case of stenosis, fusiform dilation, or occlusion.

We thus analyzed concordance of 1.5T/3T 3D-TOF-MRA and DSA.

Statistical Analyses

Categoric variables are expressed as number (%), and quantitative variables, as median (range). Categoric variables were analyzed with the χ^2 test, and quantitative variables were analyzed with the Wilcoxon rank sum test.

The Cohen κ Concordance Index was used to analyze concordance between 3D-TOF-MRA and DSA in the global cerebral vasculature and in each vascular territory. Interrater agreement in identifying intracranial artery stenosis on DSA and 3D-TOF-MRA was studied with the Cohen κ Concordance Index. Any discordance between readers was adjudicated by consensus. The index values represent the following interpretations: poor ($\kappa <$ 0), slight (κ = 0–0.20), fair (κ = 0.21–0.40), moderate (κ = 0.41–0.60), substantial (κ = 0.61–0.80), and almost perfect (κ = 0.81–1).

Using DSA as a criterion standard, we calculated the sensitivity, specificity, accuracy, and positive and negative predictive values of MRA on per-patient and per-segment analyses. Statistical analyses were computed with JMP, Version 9.0.1, 2010 (SAS Institute, Cary, North Carolina), with $P < .05$ defining statistical significance.

RESULTS

Among the 85 patients included in COVAC, 31 (from 12 different centers) met the inclusion criteria and underwent both 3D-TOF-MRA and DSA at baseline. The demographic data, clinical manifestations, and main laboratory test results of the 31 enrolled patients are shown in Table 1. The other 54 patients were not included because they did not undergo both procedures before treatment (n = 21) or because of a lack of digitalized images to

Table 1: Characteristics at diagnosis of the 31 patients with primary central nervous system vasculitis[a]

Characteristics	Total (*n* = 31)	Unenrolled Patients (*n* = 54)	*P* Value
Demographic data			
Age (yr)	42 (24–65)	46 (18–79)	.73
Male/female	16:15	28:26	.98
Clinical manifestations			
Headaches	17 (55)	42 (78)	.03
Focal deficits	26 (84)	43 (80)	.63
Seizures	9 (29)	22 (41)	.28
Cognitive impairment	7 (23)	26 (48)	.02
Loss of consciousness	3 (10)	19 (35)	.01
Psychiatric disorders	6 (19)	13 (24)	.61
C-reactive protein, (mg/L)	3 (0–47)	5 (1–95)	.13
Abnormal CSF	18/29 (62)	35/53 (66)	.13
Leukocyte count (/mm^3)	6 (1–100)	8 (0–250)	.07
Protein concentration (mg/mL)	0.6 (0.2–4.1)	0.7 (0.1–2.8)	.19
Abnormal brain biopsy findings	8/16 (50)	18/26 (69)	.32
Abnormal DSA findings	25 (81)	26/41 (63)	.13
Abnormal MRA findings	24 (77)	25/44 (57)	.09

[a] Unless otherwise indicated, values are an absolute number (%) or median (range).

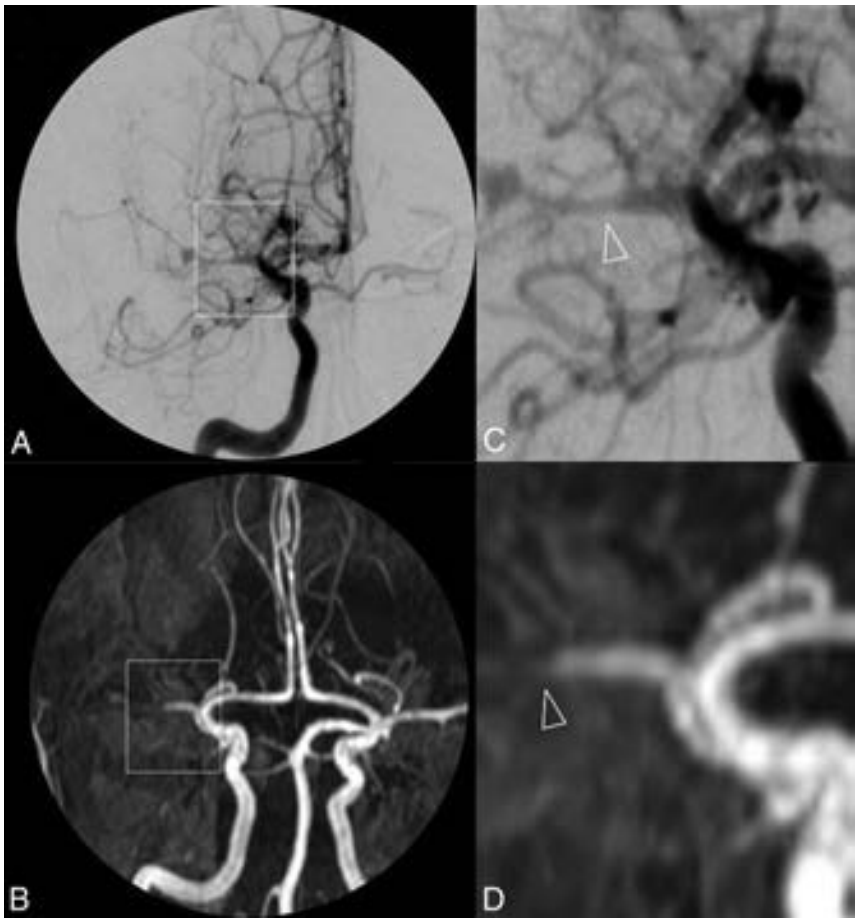

FIG 1. DSA (*A*) and 3D-TOF-MRA (*C*) with respective magnifications (*B* and *D*) of a patient with primary central nervous system vasculitis. A near-occlusive stenotic lesion of the proximal middle cerebral artery segment extending to both superficial branches with a pseudodilation of the bifurcation is shown. Arterial lumen irregularities are also observed in A2 segments of both anterior cerebral arteries.

review ($n = 33$). These excluded patients had more headaches, cognitive impairment, and loss of consciousness than those enrolled. They were more often in the biopsy-proved PCNSV group, and their DSA and 3D-TOF-MRA findings were often less positive compared with included patients, though the differences were not statistically significant. Excluded and enrolled patients did not differ in terms of other demographic data, laboratory tests, neuroimaging results, treatment, and outcome.

Sixteen (52%) of the 31 patients analyzed in this study had a brain biopsy that showed vasculitis features in 8 cases (50%). The 23 patients without histologic proof of vasculitis had DSA-diagnosed PCNSV and did not show any clinical or biologic signs compatible with another vessel-related disease, including RCVS, during a median follow-up of 43 months (range, 14–78 months).

Brain MRIs with T1-weighted, T2-weighted, fluid-attenuated inversion recovery, T1-weighted with gadolinium injection, gradient-echo T2*-weighted, and diffusion-weighted imaging with apparent diffusion coefficient mapping as well as 3D-TOF-MRA sequences were obtained on 1.5T and 3T MR imaging units in 20 and 11 patients, respectively. Characteristics of each MR imaging unit and sequence parameters are shown in the On-line Table. Interrater concordance in identifying intracranial artery lesions on DSA and 3D-TOF-MRA was excellent ($\kappa = 0.93$; 95% CI, 0.89–0.96; and $\kappa = 0.87$; 95% CI, 0.79–0.92, respectively).

Twenty-five (81%) patients had abnormal DSA findings, and 24 (77%) of them also had abnormal 3D-TOF-MRA findings (2 patients are presented in Figs 1 and 2). The patient with abnormal DSA findings but normal 3D-TOF-MRA findings had isolated small-vessel involvement, demonstrated by brain biopsy. The 6 patients with normal DSA findings (and normal 3D-TOF-MRA findings) had biopsy-proved PCNSV.

In a per-segment analysis, medians of 2 (range, 0–18) and 3 (range, 0–18) abnormal segments were observed on 3D-TOF-MRA and DSA ($P = .03$), respectively. 3D-TOF-MRA identified 116 of 141 (82.3%) abnormal segments as observed on DSA. The other 25 false-negative segments observed only on DSA but not on 3D-TOF-MRA were small-sized vessels in 16 cases, medium-sized vessels in 8 cases, and large-sized vessels in 1 case. Seven false-positive vascular segments were involved in MRA but not

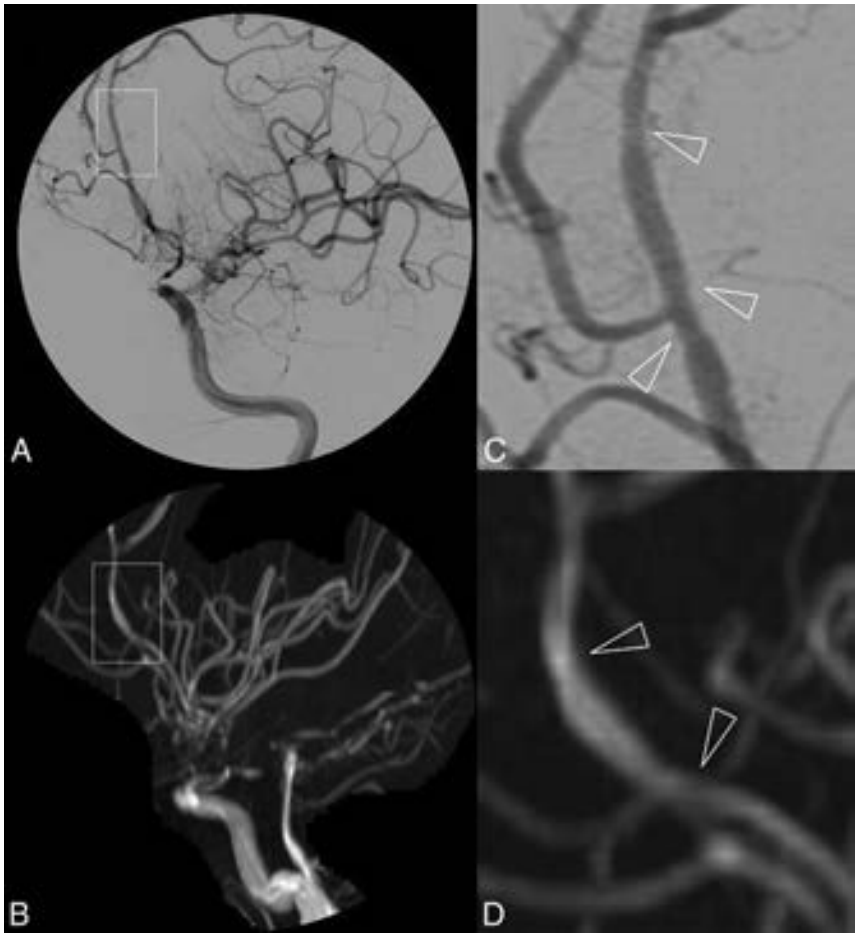

FIG 2. DSA (*A*) and 3D-TOF-MRA (*C*) with respective magnifications (*B* and *D*) of a patient with primary central nervous system vasculitis. Subtle irregularities of the arterial lumen of the A2–A3 segments of the left anterior cerebral artery are shown in a patient with otherwise near-occlusive stenoses of left intracranial internal carotid artery extending to the initial portion of the left MCA.

Table 2: Concordance between 1.5T/3T MRA and DSA on cerebral vascular segments in primary central nervous system vasculitis

	1.5T MR (κ; 95% CI)	3T MR (κ; 95% CI)
Intracranial internal carotid artery	1	1
A1	0.90 (0.73–1)	0.90 (0.75–1)
A2	0.83 (0.59–1)	0.83 (0.51–1)
>A2	0.57 (0.34–0.72)	0.86 (0.60–1)
M1	0.94 (0.81–1)	1
M2	0.90 (0.76–1)	0.91 (0.82–1)
>M2	0.69 (0.41–0.97)	0.74 (0.42–1)
P1	1	1
P2	0.60 (0.20–0.98)	1
>P2	0.64 (0.18–1)	1
V4	0.66 (0.38–1)	0.86 (0.62–1)
BA	0.83 (0.50–1)	1
PICA/AICA/SCA	0.88 (0.63–1)	1

Note:—BA indicates basilar artery.

on DSA: medium-sized vessels in 4 cases and small-sized vessels in 3.

There was a high degree of concordance between 3D-TOF-MRA and DSA (κ Index, 0.84; 95% CI, 0.79–0.89; $P < .0001$). Concordance between 1.5T 3D-TOF-MRA and DSA was 0.82 (95% CI, 0.75–0.93), and between 3T 3D-TOF-MRA and DSA, it was 0.87 (95% CI, 0.78–0.91). Detailed κ indices for each vascular segment according to the MR imaging unit are shown in Table 2.

All κ indices were >0.50, even for small-sized vessels. When we assessed small-vessel involvement, 3T 3D-TOF-MRA showed better results than 1.5T 3D-TOF-MRA.

The sensitivity, specificity, diagnostic accuracy, and positive and negative predictive values of all MRAs, 1.5T MRAs, and 3T MRAs, with DSA as the criterion standard, are shown in Table 3.

DISCUSSION

Our results indicate excellent concordance between noncontrast 3D-TOF-MRA and DSA in patients with PCNSV during the initial imaging work-up. For small-vessel involvement, 3T 3D-TOF-MRA detected more distal vascular involvement than 1.5T units.

In patients with suspected PCNSV, biopsy remains the best procedure to yield a diagnosis. In patients without or with negative biopsy findings, DSA is still considered the criterion standard for brain vessel imaging, but it is now performed less frequently than 3D-TOF-MRA in many centers because of its more invasive nature. Typical DSA findings of PCNSV include alternating areas of stenosis and dilation, referred to as beading, which can be smooth or irregular. These typically occur bilaterally but can also include single vessels. Although DSA lesion patterns (in PCNSV) have been described in detail,[6,7,13] no systematic comparison between 3D-TOF-MRA and DSA has been performed in PCNSV. In atherosclerosis or other vasculitis such as Takayasu arteritis, an excellent concordance was observed between MRA and DSA.[14-18] Herein, 3D-TOF-MRA was able to demonstrate vascular involvement in different vessels with an efficiency similar to that of DSA. However, DSA showed a larger FOV compared with MRA and remains a better tool to give a precise and exhaustive cartography of vascular lesions, especially in the most distal vascular segments. Moreover, flow saturation lowers the detection of distal stenoses in 3D-TOF-MRA and thus may also explain the better ability of DSA to assess distal vascular segments.[19]

As expected, compared with 1.5T units, 3T 3D-TOF MRA showed better sensitivity and concordance with DSA. In small-sized vessel involvement, a high degree of concordance was observed between 3D-TOF-MRA and DSA only for 3T units. However, isolated small-sized vessel PCNSV involves a subgroup of patients in whom DSA findings (and a fortiori 3D-TOF-MRA) are also mostly negative, and only biopsy can show vascular involvement in these patients.[9,20-22] In our first description of the French

Table 3: Diagnostic performance of 1.5T and 3T 3D-TOF-MRA in primary central nervous system vasculitis compared with DSA

	Sensitivity (%)	Specificity (%)	Accuracy (%)	PPV	NPV
Diagnosis per patient	96 (24/25)	100 (6/6)	96.77 (30/31)	100	85.7
Diagnosis per segment on all MR units ($n = 31$)	83.3 (116/141)	98.9 (627/634)	95.9 (743/775)	94.3	96.2
1.5 MR units ($n = 20$)	81.5 (75/92)	98.5 (402/408)	95.4 (477/500)	92.6	95.9
3T MR units ($n = 11$)	83.7 (41/49)	99.6 (225/226)	96.7 (266/275)	97.6	96.6

Note:—PPV indicates positive predictive value; NPV, negative predictive value.

cohort, as well as in another large study by Salvarani et al,[23] two-thirds of the patients with biopsy-proved PCNSV had negative DSA findings.[9] In the present study, 6 of our 7 patients with isolated small-sized vessel vasculitis demonstrated by biopsy had normal 3D-TOF-MRA and DSA findings. Hence, our results suggest that 3D-TOF-MRA could be performed as the first vascular imaging for patients with suspected PCNSV. When findings are negative, DSA could be the second imaging procedure, though our results showed that most patients would have negative DSA findings in this setting.

This study has limitations, including its retrospective design and relatively small sample size. Moreover, because this was a multicenter study, 3D-TOF-MRA was not performed with similar parameters in each center. The heterogeneity of MR imaging devices used at different sites and the use of 1.5T or 3T MR imaging are limitations because differences in acquisition parameters may influence both image quality and diagnosis. However, the demonstration of a good concordance between 1.5/3T 3D-TOF-MRA and DSA among manufacturers and MR imaging fields strengthens the conclusion that 3D-TOF-MRA can be used to demonstrate the involvement of multiple vessels in the working diagnosis of PCNSV. Regarding the visibility of distal branches on 3D-TOF-MRA, the use of a multislab technique may have led to misinterpretation and false-positives for distal stenoses. However, distal stenoses observed on 3D-TOF-MRA were also observed on DSA, reducing the probability of false-positivity.

The patients analyzed in this study may represent a subset of those with PCNSV (selection bias) because we observed some differences in excluded patients, limiting the generalizability of our results. However, more cases of small-sized-vessel PCNSV were apparent among excluded patients—that is, biopsy-proved PCNSV with normal neurovascular imaging findings. Neuroradiologists who performed the neuroimaging analyses were aware that all patients in the series had PCNSV, which might also have introduced a bias in their interpretation of the images. Interpretation of multiple vascular narrowings or stenosis, including differentiation between PCNSV and distal intracranial atherosclerosis or RCVS, remains challenging. To minimize a false-positive diagnosis of PCNSV, we definitely included patients in the French PCNSV register after at least 6 months of follow-up to analyze their clinical and radiologic evolutions under treatment. This inclusion criteria retrospectively strengthened the confidence in the diagnosis. Because RCVS is the main differential in diagnosis of PCNSV in the case of multifocal segmental stenosis of cerebral arteries, a significant limitation of this study is that no patients had initial high-resolution black-blood contrast-enhanced 3D-T1WI of the intracranial arterial wall. In addition, some studies have suggested that arterial wall imaging may enable differentiation between RCVS and PCNSV with specific imaging patterns.[24,25]

Although the present study suggests that demonstration of multifocal segmental stenosis of cerebral arteries on 3D-TOF-MRA may be sufficient to strengthen the diagnostic suspicion of PCNSV, DSA may also be necessary to add precise lesional mapping in the distal vasculature and rule out mimics. Finally, we performed per-patient and per-segment analyses. In the latter, we may have artificially increased the diagnostic performance of MRA because readers classified each segment as normal or pathologic, irrespective of the number of focal stenoses.

CONCLUSIONS

The present study adds new insights to the diagnostic approach for patients with suspected PCNSV. 3D-TOF-MRA showed excellent concordance with DSA in demonstrating multiple vascular lesions. Higher performance was observed in distal vascular analysis with 3T 3D-TOF-MRA than with 1.5T units. Additionally, in patients with negative 3D-TOF-MRA findings, particularly obtained on a 3T MR imaging unit, the DSA yield was low. Further studies are required to determine whether 3T 3D-TOF-MRA can replace DSA.

ACKNOWLEDGMENTS

The authors thank Dr Alison Johnson for proof-reading the manuscript.

Disclosures: Emmanuel Touzé—*UNRELATED*: *Board Membership*: Boehringer Ingelheim; *Payment for Lectures Including Service on Speakers Bureaus*: Boehringer Ingelheim, Bristol-Myers Squibb, Amgen, Pfizer, Bayer; *Travel/Accommodations/Meeting Expenses Unrelated to Activities Listed*: Teva Pharmaceutical Industries, Sanofi Genzyme. Mathieu Zuber—*UNRELATED*: *Board Membership*: Boehringer Ingelheim; *Consultancy*: Boehringer Ingelheim, Bayer; *Payment for Lectures Including Service on Speakers Bureaus*: Boehringer Ingelheim, Bayer, Sanofi. Christian Pagnoux—*UNRELATED*: *Board Membership*: Roche, Sanofi, ChemoCentryx, *Comments*: Less than €15,000 each during the past 5 years; *Consultancy*: Roche, Sanofi, ChemoCentryx, *Comments*: board and consultancy included, less than €15,000 each during the past 5 years; *Grants/Grants Pending*: Roche, *Comments*: educational in-aid grant <15,000 CAD in past 3 years; *Payment for Lectures Including Service on Speakers Bureaus*: Roche, *Comments*: Less than 5000 CAD during the past 3 years.

REFERENCES

1. Salvarani C, Brown RD Jr, Hunder GG. **Adult primary central nervous system vasculitis.** *Lancet* 2012;380:767–77 CrossRef Medline
2. Hajj-Ali RA, Calabrese LH. **Central nervous system vasculitis.** *Curr Opin Rheumatol* 2009;21:10–18 CrossRef Medline
3. Birnbaum J, Hellmann DB. **Primary angiitis of the central nervous system.** *Arch Neurol* 2009;66:704–09 Medline
4. Hajj-Ali RA, Singhal AB, Benseler S, et al. **Primary angiitis of the CNS.** *Lancet Neurol* 2011;10:561–72 CrossRef Medline
5. Calabrese LH, Mallek JA. **Primary angiitis of the central nervous system: report of 8 new cases, review of the literature, and proposal for diagnostic criteria.** *Medicine (Baltimore)* 1988;67:20–39 CrossRef Medline
6. Alhalabi M, Moore PM. **Serial angiography in isolated angiitis of the central nervous system.** *Neurology* 1994;44:1221–26 CrossRef Medline
7. Kadkhodayan Y, Alreshaid A, Moran CJ, et al. **Primary angiitis of the central nervous system at conventional angiography.** *Radiology* 2004;233:878–82 CrossRef Medline
8. von Elm E, Altman DG, Egger M, et al; STROBE Initiative. **The Strengthening the Reporting of Observational Studies in Epidemi-**

ology (STROBE) statement: guidelines for reporting observational studies. *PLoS Med* 2007;4:e296 CrossRef Medline
9. de Boysson H, Zuber M, Naggara O, et al; French Vasculitis Study Group and the French NeuroVascular Society. **Primary angiitis of the central nervous system: description of the first fifty-two adults enrolled in the French cohort of patients with primary vasculitis of the central nervous system.** *Arthritis Rheumatol* 2014;66:1315–26 CrossRef Medline
10. Miller DV, Salvarani C, Hunder GG, et al. **Biopsy findings in primary angiitis of the central nervous system.** *Am J Surg Pathol* 2009;33:35–43 CrossRef Medline
11. MacLaren K, Gillespie J, Shrestha S, et al. **Primary angiitis of the central nervous system: emerging variants.** *QJM* 2005;98:643–54 CrossRef Medline
12. Salvarani C, Brown RD Jr, Calamia KT, et al. **Primary central nervous system vasculitis: analysis of 101 patients.** *Ann Neurol* 2007;62:442–51 CrossRef Medline
13. Hellmann DB, Roubenoff R, Healy RA, et al. **Central nervous system angiography: safety and predictors of a positive result in 125 consecutive patients evaluated for possible vasculitis.** *J Rheumatol* 1992;19:568–72 Medline
14. Choi CG, Lee DH, Lee JH, et al. **Detection of intracranial atherosclerotic steno-occlusive disease with 3D time-of-flight magnetic resonance angiography with sensitivity encoding at 3T.** *AJNR Am J Neuroradiol* 2007;28:439–46 Medline
15. Demaerel P, De Ruyter N, Maes F, et al. **Magnetic resonance angiography in suspected cerebral vasculitis.** *Eur Radiol* 2004;14:1005–12 CrossRef Medline
16. Garg SK, Mohan S, Kumar S. **Diagnostic value of 3D contrast-enhanced magnetic resonance angiography in Takayasu's arteritis: a comparative study with digital subtraction angiography.** *Eur Radiol* 2011;21:1658–66 CrossRef Medline
17. Korogi Y, Takahashi M, Nakagawa T, et al. **Intracranial vascular stenosis and occlusion: MR angiographic findings.** *AJNR Am J Neuroradiol* 1997;18:135–43 Medline
18. Lee NJ, Chung MS, Jung SC, et al. **Comparison of high-resolution MR imaging and digital subtraction angiography for the characterization and diagnosis of intracranial artery disease.** *AJNR Am J Neuroradiol* 2016;37:2245–50 CrossRef Medline
19. Ozsarlak O, Van Goethem JW, Maes M, et al. **MR angiography of the intracranial vessels: technical aspects and clinical applications.** *Neuroradiology* 2004;46:955–72 CrossRef Medline
20. Benseler SM, deVeber G, Hawkins C, et al. **Angiography-negative primary central nervous system vasculitis in children: a newly recognized inflammatory central nervous system disease.** *Arthritis Rheum* 2005;52:2159–67 CrossRef Medline
21. Salvarani C, Brown RD Jr, Calamia KT, et al. **Primary central nervous system vasculitis with prominent leptomeningeal enhancement: a subset with a benign outcome.** *Arthritis Rheum* 2008;58:595–603 CrossRef Medline
22. de Boysson H, Boulouis G, Aouba A, et al. **Adult primary angiitis of the central nervous system: isolated small-vessel vasculitis represents distinct disease pattern.** *Rheumatology (Oxford)* 2017;56:439–44 CrossRef Medline
23. Salvarani C, Brown RD Jr, Christianson TJ, et al. **Adult primary central nervous system vasculitis treatment and course: analysis of one hundred sixty-three patients.** *Arthritis Rheumatol* 2015;67:1637–45 CrossRef Medline
24. Mandel DM, Matouk CC, Farb RI, et al. **Vessel wall MRI to differentiate between reversible cerebral vasoconstriction syndrome and central nervous system vasculitis: preliminary results.** *Stroke* 2012;43:860–62 CrossRef Medline
25. Obusez EC, Hui F, Hajj-Ali RA, et al. **High-resolution MRI wall imaging: spatial and temporal patterns of reversible cerebral vasoconstriction syndrome and central nervous system vasculitis.** *AJNR Am J Neuroradiol* 2014;35:1527–32 CrossRef Medline

In Vivo Imaging of Venous Side Cerebral Small-Vessel Disease in Older Adults: An MRI Method at 7T

C.E. Shaaban, H.J. Aizenstein, D.R. Jorgensen, R.L. MacCloud, N.A. Meckes, K.I. Erickson, N.W. Glynn, J. Mettenburg, J. Guralnik, A.B. Newman, T.S. Ibrahim, P.J. Laurienti, A.N. Vallejo, and C. Rosano, for the LIFE Study Group

ABSTRACT

BACKGROUND AND PURPOSE: Traditional neuroimaging markers of small-vessel disease focus on late-stage changes. We aimed to adapt a method of venular assessment at 7T for use in older adults. We hypothesized that poorer venular morphologic characteristics would be related to other small-vessel disease neuroimaging markers and a higher prevalence of small-vessel disease–Alzheimer disease risk factors.

MATERIALS AND METHODS: Venules were identified in periventricular ROIs on SWI and defined as tortuous or straight. The tortuosity ratio was defined as total tortuous venular length divided by total straight venular length. White matter hyperintensity burden (visually rated from 0 to 3) and the number of microbleeds (0, 1, >1) were determined. Differences in tortuous and straight venular lengths were evaluated. Relationships with demographic variables, allele producing the e4 type of *apolipoprotein E* (*APOE4*), growth factors, pulse pressure, physical activity, and Modified Mini-Mental State Examination were assessed via Spearman correlations.

RESULTS: Participants had 42% more tortuous venular tissue than straight (median, 1.42; 95% CI, 1.13–1.62). *APOE4* presence was associated with a greater tortuosity ratio ($\rho = 0.454$, $P = .001$), and these results were robust to adjustment for confounders and multiple comparisons. Associations of the tortuosity ratio with sex and vascular endothelial growth factor did not survive adjustment. Associations of the tortuosity ratio with other variables of interest were not significant.

CONCLUSIONS: Morphologic measures of venules at 7T could be useful biomarkers of the early stages of small-vessel disease and Alzheimer disease. Longitudinal studies should examine the impact of *apolipoprotein E* and vascular endothelial growth factor on the risk of venular damage.

ABBREVIATIONS: AD = Alzheimer disease; *APOE4* = allele producing the e4 type of *apolipoprotein E*; BDNF = brain-derived neurotrophic factor; IQR = interquartile range; LIFE MRI = Lifestyle Interventions and Independence for Elders Magnetic Resonance Imaging study; 3MS = Modified Mini-Mental State Examination; SVD = small-vessel disease; VEGF = vascular endothelial growth factor; WMH = white matter hyperintensities

Cerebral small-vessel disease (SVD) increases dementia risk[1] and vulnerability to Alzheimer disease (AD) neuropathology.[2] Neuroimaging methods investigating SVD have traditionally relied on WM hyperintensities (WMHs). However, WMH is a marker of late-stage SVD, reflecting advanced parenchymal damage, reduced CBF, and abnormalities of the small penetrating vessels.[3] Thus, there is a need for radiologic markers that capture the earlier stages of SVD relating directly to vessel health.

With aging and hypertension, arteries have a reduced ability to absorb flow pulsatility, thus transmitting highly pulsatile flow to the venules. Venular walls are well-equipped to handle low pulsatile and slow flow, but not highly pulsatile flow. Pulsatility-related damage can induce venular morphologic changes such as collagenosis, leading to loss of elasticity and lumen narrowing/occlusion, which, in turn, promote ischemia. Both collagenosis and

Received October 25, 2016; accepted after revision May 28, 2017.

From the Graduate School of Public Health, Department of Epidemiology (C.E.S., D.R.J., N.W.G., A.B.N., C.R.), Center for the Neural Basis of Cognition (C.E.S., H.J.A., D.R.J., K.I.E., C.R.), Departments of Psychiatry (H.J.A., R.L.M.), Biological Sciences (N.A.M.), Psychology (K.I.E.), Radiology (J.M., T.S.I.), Bioengineering (T.S.I.), and Immunology (A.N.V.). University of Pittsburgh, Pittsburgh, Pennsylvania; Department of Epidemiology and Public Health (J.G.), University of Maryland School of Medicine, Baltimore, Maryland; Laboratory for Complex Brain Networks (P.J.L.) and Department of Radiology (P.J.L.), Wake Forest University School of Medicine, Winston-Salem, North Carolina; and Department of Pediatrics (A.N.V.), Children's Hospital of Pittsburgh, Pittsburgh, Pennsylvania.

Research reported in this publication was supported by the National Institute on Aging under award Nos. U01 AG022376, F31 AG054084 (C.E.S.), R01 AG044474 (C.R.), and P30 AG024827. C.E.S. also received support from a training grant from the National Institute of General Medical Sciences under award No. T32 GM081760.

The content is solely the responsibility of the authors and does not necessarily represent the official views of the National Institutes of Health.

Please address correspondence to Caterina Rosano, MD, MPH, Department of Epidemiology, Graduate School of Public Health, University of Pittsburgh, 130 DeSoto St, 5139 Parran South, Pittsburgh, PA 15261; e-mail: rosanoc@edc.pitt.edu

Indicates open access to non-subscribers at www.ajnr.org

Indicates article with supplemental on-line appendix and table.

Indicates article with supplemental on-line photos.

http://dx.doi.org/10.3174/ajnr.A5327

tortuosity lead to reduced CBF and increased upstream resistance, exacerbating arterial pathology. Extravasation and inflammatory response, including focal perivascular parenchymal infiltration, can also occur, facilitated by the lack of tight junctions on the venous-side circulation.[4] Inflammatory cascades further damage the vasculature, reduce CBF, and compromise the BBB. These phenomena can become apparent as morphologic changes such as tortuosity, collagenosis, and thicker basal lamina. Such changes have been seen in vivo in AD[5] and in postmortem studies, and they appear more common with older age and in proximity to regions with WMHs.[6-8] Although the possibility has not been tested directly, venular morphologic alterations are considered to precede radiologically overt WMHs.

Ultra-high-field (7T) MR imaging has emerged as a noninvasive method to visualize venous microcirculation.[9,10] Specifically, SWI exploits the paramagnetic properties of deoxyhemoglobin to visualize venules without a contrast agent. Methods to quantify venules in multiple sclerosis,[11] sickle cell anemia,[12] CADASIL,[7,13] and, recently, AD[14] have been reported. However, venular characteristics in relation to cerebral SVD in aging are unknown.

Our primary aim was to demonstrate the feasibility of adapting published methods[11,12] to study venular characteristics in older adults. Our secondary aim was to evaluate the relationships of venular characteristics with neuroimaging markers of SVD—WMH and microbleeds—and variables relevant to SVD and AD. We hypothesized that poorer venular morphologic characteristics would be related to other SVD neuroimaging markers and a higher prevalence of SVD-AD risk factors.

MATERIALS AND METHODS

Participants

The Lifestyle Interventions and Independence for Elders Magnetic Resonance Imaging study (LIFE MRI) is a neuroimaging study within a randomized controlled trial, which demonstrated that physical activity prevents major mobility disability in at-risk community-dwelling older adults versus health education control (hazard ratio, 0.82, $P = .03$).[15] The study protocol was approved by the University of Pittsburgh institutional review board. All participants provided written informed consent. The present study ($n = 53$) used images from the baseline visit.

The LIFE study design has been previously reported.[16] The On-line Table shows inclusion/exclusion criteria. Participants were not screened for MR imaging on the basis of caffeine use due to minimal reported average caffeine-related signal change of veins in white matter ($-2 \pm 1.2\%$).[17] On-line Fig 1 shows participant flow.

Sample Characteristics

Age, race, and sex, self-reported by participants, were evaluated because of their association with SVD and AD.[18-22] *Apolipoprotein E* was genotyped by using TaqMan (TaqMan probe C__904973_10; Applied Biosystems, Life Technologies, Foster City, California) and pyrosequencing.[23] The allele producing the e4 type of *apolipoprotein E* (*APOE4*) is the strongest genetic risk factor for late-onset AD.[24] Pulse pressure (systolic blood pressure–diastolic blood pressure; average of 2-seated measurements) and physical activity were assessed because of their associations with AD[25,26] and SVD.[27,28] Physical activity was measured for 7 days by using hip-worn accelerometry (GT3X; Actigraph, Pensacola, Florida) as minutes per day of moderate physical activity. Finally, the Modified Mini-Mental State Examination (3MS)[29] was included as a measure of global cognition.

Growth Factors

The angiogenic factors vascular endothelial growth factor (VEGF)[30] and brain-derived neurotrophic factor (BDNF)[31] were measured via the Luminex system with kits (Human Cancer Panel and Neurodegenerative Disease Panel; EMD Millipore, Hercules, California). Fasting blood, collected by venipuncture, remained at room temperature for 30–60 minutes to clot and was then centrifuged at 1600 x g for 15 minutes at 4°C. Serum was aliquoted and immediately frozen at −70°C or lower and stored until analysis. Concentrations were determined with 2 sets of standard curves, with final values calculated according to standardized procedures we have validated.[32]

Potential Confounders

Self-reported antihypertensive medication use, which may affect pulse pressure, was recorded. Blood hemoglobin level was measured because it may affect venular conspicuity on SWI. We also recorded SWI voxel size, which varied among the participants.

Outcome Variables

Venular Characteristics. Axial susceptibility-weighted MRIs were obtained at the University of Pittsburgh MR Research Center by using a Rapid Biomedical (Rimpar, Germany) 8-channel head coil on a Siemens (Erlangen, Germany) 7T scanner (TR = 2000 ms, TE = 15 ms), acquired with $0.25 \times 0.25 \times 1.50$ mm ($n = 40$), $0.23 \times 0.23 \times 3.00$ mm voxels, interleave gap = 0.60 mm ($n = 12$), or with $0.50 \times 0.50 \times 1.00$ mm voxels ($n = 5$). When necessary, scans were resampled to 1.50-mm section thickness.

A 4×1 cm ROI was placed in each hemisphere, 1 section below the uppermost section on which ventricular CSF was visible. To maintain consistency, we placed the ROI on the basis of native-space landmarks, centered along the anteroposterior length of the ventricle, and on the lateral wall of the ventricle (On-line Fig 2). The ROI was chosen because it corresponds to regions known to be vulnerable to SVD,[5,13,14] is consistent with published methods,[11,12] and allows the greatest consistency in vessel orientation, with a clear course perpendicular to the length of the lateral ventricles. The minimum intensity projection was applied over 3 sections (4.5 mm) to improve visualization.[9]

Three raters (C.E.S., D.R.J., N.A.M.) were trained and overseen by a certified neuroradiologist (J.M.) and the study Principal Investigator (C.R.). First, published protocols were studied and discussed among the raters, neuroradiologist, Principal Investigator, and coinvestigators (H.J.A., R.L.M.). Next, the same 5 MRIs were rated by the raters, each blinded to the tracings of the other 2 raters. Last, each venular tracing was discussed among the raters and with the neuroradiologist and Principal Investigator regarding the presence/absence of the venule and straight/tortuous course. This discussion continued until the raters were proficient in tracing and the results of their consensus were consistent with the judgment of the neuroradiologist/Principal Investigator.

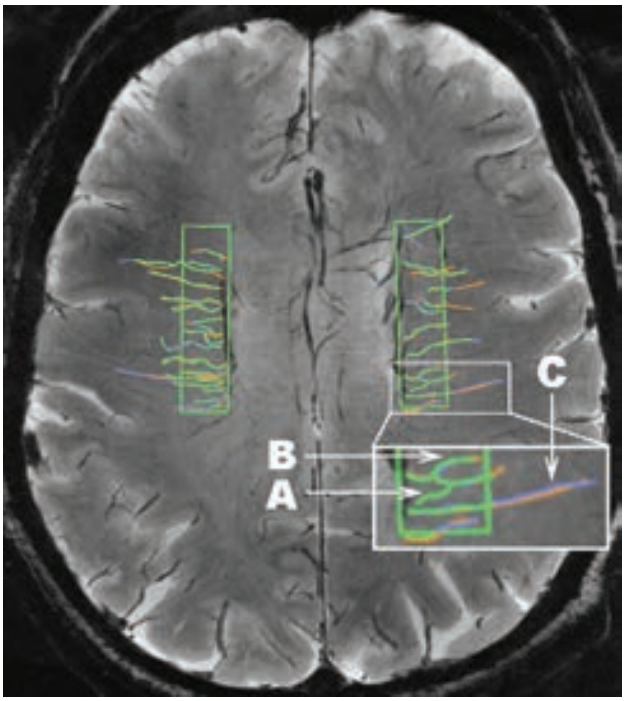

FIG 1. A sample consensus venular tracing on SWI at 7T across ROIs in both hemispheres in the LIFE MRI study. Each rater traces the venules. A different color (green, purple, orange) is assigned to each rater, and the 3 sets of tracings are then overlaid. Inset in white is shown at larger magnification at the bottom of the figure to illustrate: *A*, An example of a venule that would not be included in the dataset because it was traced by only 1 of the 3 raters (green). *B*, An example of a tortuous venule. *C*, An example of a straight venule.

Tracing was done with OsiriX Imaging Software (http://www.osirix-viewer.com).[33] Criteria to identify a venule were the following: a linear structure of intensity darker than the surrounding parenchyma; length, ≥3 mm; and coursing through the ROI for ≥3 mm (to reduce interrater variability of inclusion for vessels along the edge of the ROI). Most venules could be followed to obvious deep veins, and the dark appearance and orientation axial to the ventricles and deep within the white matter also helped to identify the origin of the vessels as venous. Venules were traced across their full length, even if they continued outside the ROI, to avoid artificial truncation. After all venules were traced, the presence/absence of a venule was adjudicated by consensus among raters. A venule was included only if ≥2 of the 3 raters had traced it (Fig 1). Next, the venular course (straight/tortuous) was rated during the consensus meeting. A vessel that ran free of inflection points ≥30° for most of its total length (>60%) was defined "straight"; otherwise the vessel was defined "tortuous." The length of each venule was computed as the median value of the lengths measured by the raters tracing that venule. The number and length of all consensus-traced venules were summed, and total and average lengths (total length/venule number) were obtained for each participant.

Tortuous venules are present in areas with WMHs[6]; thus, we evaluated tortuous and straight venules separately. The tortuosity ratio was calculated as the total tortuous length divided by the total straight length. Thus, a tortuosity ratio of >1 indicates greater tortuous venular length than straight length. Due to blood oxygen level–dependent–related signal blooming, measures of diameter may not have been accurate; thus, we did not quantify diameter.

White Matter Hyperintensities. WMH was imaged with T2WI (TR = 12,500 ms, TE = 55 ms, voxel size = 0.5 × 0.5 × 6.0 mm) and MPRAGE (TR = 3430 ms, TE = 3.54 ms, voxel size = 0.7 mm^3 isotropic) and was rated by a consensus of 2 raters (C.R., H.J.A.) with a 0–3 modified Fazekas rating scale.[34] Ratings consisted of the following: 0 = none: no punctate hyperintense areas or periventricular rims; 1 = mild: few punctate hyperintense areas and/or limited amount of hyperintense rims around the ventricular horns; 2 = moderate: multiple punctate hyperintense areas and/or larger rims around the ventricular horns; or 3 = severe: confluent subcortical hyperintense areas and/or rims all around the ventricles, including the horns and sides. Only 4/53 had no WMHs (WMH = 0), leaving 92% with at least mild WMHs; thus, we combined 0 and 1 to create a "none/mild" category. Because the distinction between periventricular and deep WMHs is not consistently meaningful, we did not differentiate them.[35]

Microbleeds. We classified cerebral microbleeds on the basis of Greenberg et al.[36] Two trained raters (N.A.M., E.L.T.) characterized microbleeds under the supervision of a neuroradiologist (J.M.). Microbleeds were defined as black or substantially hypointense on SWI, round or ovoid (confirmed on adjacent sections), and at least half surrounded by brain parenchyma. To take advantage of the ability of the 7T magnet to capture quite small microbleeds, we did not use a minimum size criterion. Final ratings were based on consensus, with disagreements mediated by the neuroradiologist. We counted the total number of microbleeds across all 64 sections of the axial SWI and categorized totals as 0, 1, or >1 microbleed.

Statistical Analysis

Descriptive statistics were calculated as counts and percentages, means and SDs, or medians and interquartile ranges (IQRs). Differences were tested with *t* tests, Wilcoxon rank sum tests, or χ^2 tests, $\alpha = .05$. We also determined the median tortuosity ratio and calculated the 95% CIs by using 10,000 bootstrapped samples.

We explored the relationships of the tortuosity ratio with other neuroimaging markers of SVD, including WMH and microbleeds; nonmodifiable factors, including demographic variables (age, race, and sex), and *APOE4*; potentially modifiable factors, including growth factors (VEGF and BDNF), pulse pressure (adjusted for antihypertensive medication use), and physical activity; 3MS; and hemoglobin, with Spearman correlations, $\alpha = .10$. Significant correlations with the tortuosity ratio were re-evaluated as partial correlations adjusted for hemoglobin and voxel size. A false discovery rate of 0.10 was used to correct for multiple comparisons.

Statistical analysis was performed in SAS, Version 9.4[37] and SPSS version 22.[38]

RESULTS

MR imaging study participants were younger and less likely to be non-Hispanic white than the non-MR imaging study participants (Table 1). Of MR imaging study participants, 15/47 with *APOE* data had at least 1 copy of the *APOE4* allele. Thus, representation

Table 1: Study sample characteristics in the LIFE study at the Pittsburgh site

	MRI Study (n = 53)	Non-MRI Study (n = 163)	P Value
Age (median) (IQR) (yr)	76.0 (5.8)	79.4 (9.0)	<.01[a]
Race, non-Hispanic white (No.) (%)	30 (56.6)	124 (76.1)	<.01[a]
Sex, female (No.) (%)	42 (79.2)	123 (75.5)	.57
APOE4 allele presence[b] (No.) (%)	15 (31.9)	27 (20.0)	.10
VEGF (median) (IQR) (pg/mL)	414.61 (370.17)	–	
BDNF (median) (IQR) (pg/mL)	19,780.30 (27,492.00)	–	
Pulse pressure (median) (IQR)	53 (13)	57 (18)	.06
Physical activity—daily moderate activity (median) (IQR) (min)	24.6 (31.6)	18.3 (22.7)	.05
3MS (median) (IQR)	93 (7)	92 (9)	.46
Severe WMH burden[c] (No.) (%)	11 (20.8)	–	
No microbleeds[d] (No.) (%)	21 (39.6)	–	
Confounders			
On antihypertensive medication (No.) (%)	39 (73.6)	119 (73.0)	.93
Hemoglobin level[e] (median) (IQR) (g/dL)	12.7 (1.2)	13.2 (2.0)	.22

[a] Significant.
[b] Available on $n = 47$ (MRI) and $n = 135$ (non-MRI).
[c] WMH: rated as 0 = none/mild, 1 = moderate, 2 = severe.
[d] Available on $n = 45$ due to scan quality or motion; the remaining 24 were split nearly evenly between 1 and >1.
[e] Available on $n = 47$ (MRI) and $n = 139$ (non-MRI).

Table 2: Venular length measures in LIFE MRI ($n = 53$) for tortuous and straight venules separately

	Tortuous	Straight	P Value[a]
Total length of venules (mean) (SD) (mm)[c]	156.87 (53.18)	111.41 (50.11)	<.001[b]
No. of venules (mean) (SD)	18.09 (5.87)	13.11 (5.34)	<.001[b]
Average length of venules (mean) (SD) (mm)	8.64 (0.87)	8.30 (1.42)	.07

[a] P values based on paired t tests comparing tortuous and straight venule characteristics.
[b] Significant.
[c] Venule lengths: for each participant, venules were traced in 4-cm^2 ROIs (1 in each hemisphere), their length was measured by 3 raters, and median length was computed for each vessel. Venules are characterized as straight or tortuous. The total straight and tortuous venular length in millimeters is calculated for each participant.

Table 3: Spearman correlations of tortuosity ratio with variables of interest to SVD and AD in LIFE MRI ($n = 53$)

	ρ	P Value
Age	−0.023	.87
Race	0.202	.15
Sex	−0.304	.03[a]
APOE4	0.454	.001[a]
Pulse pressure[b]	0.206	.14
VEGF	−0.236	.096[a]
BDNF	0.227	.11
Hemoglobin level	0.266	.07[a]
Physical activity—daily moderate activity (min)	−0.187	.20
3MS	0.199	.15

[a] Significant.
[b] Partial correlation of pulse pressure and tortuosity ratio adjusted for antihypertensive drug use.

of *APOE4* was higher than the 14% estimate among controls worldwide[39] but did not differ significantly from non-MR imaging participants. No or mild WMHs were seen in 58.5% of participants, while 20.8% each had moderate and severe WMHs. Regarding microbleeds, 39.6% of the sample had 0, 20.8% had 1, and 24.5% had >1.

The total length of tortuous vessels ranged from 26.25 to 246.36 mm, while the total straight length ranged from 16.72 to 217.65 mm. The overall length of tortuous venules was greater than that of straight venules (Table 2). Total tortuous length was 42% greater than total straight length (median tortuosity ratio, 1.4; 95% bootstrapped CI, 1.13–1.62) (On-line Fig 3). To examine whether this finding was due to number of venules or average length, we evaluated differences in those measures. The total number of tortuous venules ranged from 4 to 32, while total straight venules ranged from 2 to 24. There were more tortuous venules than straight ones. The range of average tortuous length was 6.56–10.93 mm, while the range of average straight length was 4.35–11.57 mm, and these average lengths were not significantly different. Thus, the difference in total tortuous and straight venular lengths was driven by a greater number of tortuous venules.

Correlations between neuroimaging markers of SVD and the tortuosity ratio were not significant. WMH correlated at $\rho = -0.125$, $P = .37$, and microbleeds correlated at $\rho = -0.059$, $P = .70$.

Among nonmodifiable variables associated with AD and SVD, sex was associated with the tortuosity ratio (Table 3). Males had a higher tortuosity ratio (median, 2.15; IQR, 0.98) than females (median, 1.31; IQR, 0.71). Those with at least 1 copy of the *APOE4* allele had a higher tortuosity ratio (median, 2.15; IQR, 1.78) than those without it (median, 1.21; IQR, 0.75). Associations with age and race were not significant ($P > .10$).

Among modifiable factors potentially influencing venular characteristics, a higher VEGF was associated with a lower tortuosity ratio. There were no significant associations with BDNF, pulse pressure (adjusted for antihypertensive use), physical activity, or 3MS score ($P > .10$). Results were similar when using a ratio of vessel counts instead of the ratio of total lengths.

The relationship of *APOE4* with venular tortuosity, but not the other findings, remained significant after false discovery rate correction of the P value ($P = .01$). Further adjustment for hemoglobin level and voxel size did not modify the association with *APOE4*.

DISCUSSION

We found that application of 7T SWI is feasible to image cerebral venular characteristics in vivo in older adults. This method is a novel way of visualizing an understudied component of the cerebral vasculature. Given associations of venular tortuosity with SVD[6] and AD[40,41] as well as increases in microvascular changes with age,[8] venular tortuosity may serve as a marker of declining cerebrovascular integrity. This method may afford earlier detection of SVD and has the advantage of characterizing venular morphology without contrast.

We also found that *APOE4* was associated with a higher tortuosity ratio, and this association was robust to adjustment for potential confounders and multiple comparisons. This result supports studies implicating *APOE4* in reduced vascular integrity.

The APOE4 protein can directly damage the vasculature.[42] *APOE* is associated with neuroimaging manifestations of SVD,[43,44] and there are indications that it is associated with microvascular changes. Mice expressing transgenic human *APOE4* have altered basement membrane protein expression.[45] In humans with AD, *APOE4* is associated with BBB disruption.[46] *APOE4* is associated with both increased deposition and reduced clearance of β amyloid.[42] Clearly, *APOE4* is central to the development of AD pathology, and our results suggest it could be implicated in venular damage. It is possible that β amyloid deposition induces venular damage. An AD mouse model showed that as β amyloid built up in the arterioles beginning at 5 months of age, venular mural cells were damaged by 7 months of age.[41] However, it is also possible that venular damage induces β amyloid deposition. In this same experimental model, further venular mural cell damage led to increased arteriolar β amyloid deposition and, most interesting, induction of venular tortuosity.[41] The temporality of venular damage and β amyloid deposition remains an open question. We were unable to collect amyloid imaging. Hence, future multimodal neuroimaging studies need to evaluate the timing and relationship of β amyloid burden and venular tortuosity.

Although our result is remarkably consistent with the proposed *APOE4*-mediated reduction of vascular integrity,[42] our study cannot clarify the underlying mechanisms. This limitation notwithstanding, *APOE4* being associated with venular tortuosity indicates the potential for risk stratification as an intervention strategy. Thus, other factors should be evaluated to offset *APOE4*-related risk.

We found a nonsignificant association of the tortuosity ratio with WMHs and microbleeds, which could be due to a lack of sensitivity in our visual ratings or the small sample size. Future larger studies should evaluate associations of the tortuosity ratio with WMH volume, a more sensitive measure compared with visual ratings. Alternatively, this lack of association may indicate that the tortuosity ratio is capturing novel, early information regarding vascular integrity. Future work should examine the relationships of the tortuosity ratio with other SVD neuroimaging markers and related cognitive and mobility impairment and clarify the temporal order of venular damage and other SVD neuroimaging manifestations. We predict that venular damage comes before traditional neuroimaging markers of SVD.

Our study has several limitations. The sample was not selected to have a particularly low or high SVD burden. Future studies should compare venular tortuosity ratios in those 2 groups. Larger samples will be needed to confirm associations with sex and VEGF. The venular measures are also 2D and, therefore, do not account for venules running out of the plane. However, this bias is nondifferential across our sample. Finally, MR imaging participants were younger and had a higher proportion of nonwhites, indicating that this sample may differ from that in the general community-dwelling older adult population.

Despite these limitations, our study has notable strengths. We applied ultra-high-field neuroimaging with a higher SNR than typically used to visualize novel venular characteristics. This allows smaller sample sizes at ultra-high-fields than would be required at lower field strengths. Because this neuroimaging study was also within a randomized controlled trial, these participants were extremely well-characterized, allowing us to control for potential confounding factors.

CONCLUSIONS

SWI at 7T offers a noninvasive method to image markers of cerebral venular integrity and fills an important gap in knowledge. Morphologic measures of venules at 7T could be useful biomarkers of the early stages of SVD and AD. Risk and protective factors, especially those that are modifiable, for these pathophysiologic changes should be evaluated. Future longitudinal multimodal studies characterizing venular integrity at 7T are warranted.

For the full LIFE study investigator listing, see the On-line Appendix.

ACKNOWLEDGMENTS

The authors thank Erica Lynn Tamburo for neuroimaging assistance and Joshua Michel for implementing standardized Luminex assays.

Disclosures: C.E. Shaaban—*RELATED*: *Grant*: National Institute on Aging, *Comments*: F31 AG054084,* Howard J. Aizenstein—*RELATED*: *Grant*: National Institutes of Health*; *UNRELATED*: *Grants/Grants Pending*: National Institutes of Health*; *Travel/Accommodations/Meeting Expenses Unrelated to Activities Listed*: National Institutes of Health. Dana R. Jorgensen—*UNRELATED*: *Grant*: National Heart, Lung, and Blood Institute, *Comments*: T32 HL083825. Rebecca L. MacCloud—*RELATED*: *Grant*: National Institutes of Health.* Nancy W. Glynn—*RELATED*: *Grant*: National Institutes of Health, *Comments*: I was funded by the parent National Institutes of Health grant that recruited the participants for this work.* Tamer S. Ibrahim—*UNRELATED*: *Grants/Grants Pending*: National Institutes of Health, *Comments*: R01 grants.* Paul J. Laurienti—*RELATED*: *Grant*: National Institutes of Health.* Abbe N. Vallejo—*RELATED*: *Grant*: National Institutes of Health, *Comments*: P30 AG024827.* Caterina Rosano—*RELATED*: *Grant*: R01AG044474*; *Support for Travel to Meetings for the Study or Other Purposes*: R01AG044474.* *Money paid to the institution.

REFERENCES

1. Prins ND, van Dijk EJ, den Heijer T, et al. **Cerebral white matter lesions and the risk of dementia.** *Arch Neurol* 2004;61:1531–34 CrossRef Medline
2. Rosano C, Aizenstein HJ, Wu M, et al. **Focal atrophy and cerebrovascular disease increase dementia risk among cognitively normal older adults.** *J Neuroimaging* 2007;17:148–55 CrossRef Medline
3. Wardlaw JM, Valdés Hernández MC, Muñoz-Maniega S. **What are white matter hyperintensities made of? Relevance to vascular cognitive impairment.** *J Am Heart Assoc* 2015;4:001140 CrossRef Medline
4. Bechmann I, Galea I, Perry VH. **What is the blood-brain barrier (not)?** *Trends Immunol* 2007;28:5–11 CrossRef Medline
5. Bouvy WH, Kuijf HJ, Zwanenburg JJ, et al; Utrecht Vascular Cognitive Impairment (VCI) Study group. **Abnormalities of cerebral deep medullary veins on 7 Tesla MRI in amnestic mild cognitive impairment and early Alzheimer's disease: a pilot study.** *J Alzheimers Dis* 2017;57:705–10 CrossRef Medline
6. Fazekas F, Kleinert R, Offenbacher H, et al. **Pathologic correlates of incidental MRI white matter signal hyperintensities.** *Neurology* 1993;43:1683–89 CrossRef Medline
7. Pettersen JA, Keith J, Gao F, et al. **CADASIL accelerated by acute hypotension: arterial and venous contribution to leukoaraiosis.** *Neurology* 2017;88:1077–80 CrossRef Medline
8. Moody DM, Brown WR, Challa VR, et al. **Periventricular venous collagenosis: association with leukoaraiosis.** *Radiology* 1995;194:469–76 CrossRef Medline
9. Haacke EM, Mittal S, Wu Z, et al. **Susceptibility-weighted imaging: technical aspects and clinical applications, Part 1.** *AJNR Am J Neuroradiol* 2009;30:19–30 Medline
10. Mittal S, Wu Z, Neelavalli J, et al. **Susceptibility-weighted imaging:**

technical aspects and clinical applications, Part 2. *AJNR Am J Neuroradiol* 2009;30:232–52 Medline
11. Sinnecker T, Bozin I, Dorr J, et al. **Periventricular venous density in multiple sclerosis is inversely associated with T2 lesion count: a 7 Tesla MRI study.** *Mult Scler* 2013;19:316–25 CrossRef Medline
12. Novelli EM, Elizabeth Sarles C, Jay Aizenstein H, et al. **Brain venular pattern by 7T MRI correlates with memory and haemoglobin in sickle cell anaemia.** *Psychiatry Res* 2015;233:18–22 CrossRef Medline
13. De Guio F, Vignaud A, Ropele S, et al. **Loss of venous integrity in cerebral small vessel disease: a 7-T MRI study in Cerebral Autosomal-Dominant Arteriopathy with Subcortical Infarcts and Leukoencephalopathy (CADASIL).** *Stroke* 2014;45:2124–26 CrossRef Medline
14. Kuijf HJ, Bouvy WH, Zwanenburg JJ, et al. **Quantification of deep medullary veins at 7 T brain MRI.** *Eur Radiol* 2016;26:3412–18 CrossRef Medline
15. Pahor M, Guralnik JM, Ambrosius WT, et al; LIFE study investigators. **Effect of structured physical activity on prevention of major mobility disability in older adults: the LIFE study randomized clinical trial.** *JAMA* 2014;311:2387–96 CrossRef Medline
16. Fielding RA, Rejeski WJ, Blair S, et al; LIFE Research Group. **The Lifestyle Interventions and Independence for Elders Study: design and methods.** *J Gerontol A Biol Sci Med Sci* 2011;66:1226–37 CrossRef Medline
17. Sedlacik J, Helm K, Rauscher A, et al. **Investigations on the effect of caffeine on cerebral venous vessel contrast by using susceptibility-weighted imaging (SWI) at 1.5, 3 and 7 T.** *Neuroimage* 2008;40:11–18 CrossRef Medline
18. de Leeuw FE, de Groot JC, Achten E, et al. **Prevalence of cerebral white matter lesions in elderly people: a population based magnetic resonance imaging study—the Rotterdam Scan Study.** *J Neurol Neurosurg Psychiatry* 2001;70:9–14 CrossRef Medline
19. Gao S, Hendrie HC, Hall KS, et al. **The relationships between age, sex, and the incidence of dementia and Alzheimer disease: a meta-analysis.** *Arch Gen Psychiatry* 1998;55:809–15 CrossRef Medline
20. Liao D, Cooper L, Cai J, et al. **The prevalence and severity of white matter lesions, their relationship with age, ethnicity, gender, and cardiovascular disease risk factors: the ARIC Study.** *Neuroepidemiology* 1997;16:149–62 Medline
21. Lindsay J, Laurin D, Verreault R, et al. **Risk factors for Alzheimer's disease: a prospective analysis from the Canadian Study of Health and Aging.** *Am J Epidemiol* 2002;156:445–53 CrossRef Medline
22. Steenland K, Goldstein FC, Levey A, et al. **A meta-analysis of Alzheimer's disease incidence and prevalence comparing African-Americans and Caucasians.** *J Alzheimers Dis* 2015;50:71–76 CrossRef Medline
23. Cavallari LH, Langaee TY, Momary KM, et al. **Genetic and clinical predictors of warfarin dose requirements in African Americans.** *Clin Pharmacol Ther* 2010;87:459–64 CrossRef Medline
24. Bertram L, McQueen MB, Mullin K, et al. **Systematic meta-analyses of Alzheimer disease genetic association studies: the AlzGene database.** *Nat Genet* 2007;39:17–23 CrossRef Medline
25. Beydoun MA, Beydoun HA, Gamaldo AA, et al. **Epidemiologic studies of modifiable factors associated with cognition and dementia: systematic review and meta-analysis.** *BMC Public Health* 2014;14:643 CrossRef Medline
26. Qiu C, Winblad B, Viitanen M, et al. **Pulse pressure and risk of Alzheimer disease in persons aged 75 years and older: a community-based, longitudinal study.** *Stroke* 2003;34:594–99 CrossRef Medline
27. Mitchell GF, van Buchem MA, Sigurdsson S, et al. **Arterial stiffness, pressure and flow pulsatility and brain structure and function: the Age, Gene/Environment Susceptibility–Reykjavik study.** *Brain* 2011;134(pt 11):3398–407 CrossRef Medline
28. Torres ER, Strack EF, Fernandez CE, et al. **Physical activity and white matter hyperintensities: a systematic review of quantitative studies.** *Prev Med Rep* 2015;2:319–25 CrossRef Medline
29. Teng EL, Chui HC. **The Modified Mini-Mental State (3MS) examination.** *J Clin Psychiatry* 1987;48:314–18 Medline
30. Gerhardt H. **VEGF and endothelial guidance in angiogenic sprouting.** *Organogenesis* 2008;4:241–46 CrossRef Medline
31. Alhusban A, Kozak A, Ergul A, et al. **AT1 receptor antagonism is proangiogenic in the brain: BDNF a novel mediator.** *J Pharmacol Exp Ther* 2013;344:348–59 CrossRef Medline
32. Dvergsten JA, Mueller RG, Griffin P, et al. **Premature cell senescence and T cell receptor-independent activation of CD8+ T cells in juvenile idiopathic arthritis.** *Arthritis Rheum* 2013;65:2201–10 CrossRef Medline
33. Rosset A, Spadola L, Ratib O. **OsiriX: an open-source software for navigating in multidimensional DICOM images.** *J Digit Imaging* 2004;17:205–16 CrossRef Medline
34. Fazekas F, Chawluk JB, Alavi A, et al. **MR signal abnormalities at 1.5 T in Alzheimer's dementia and normal aging.** *AJR Am J Roentgenol* 1987;149:351–56 CrossRef Medline
35. DeCarli C, Fletcher E, Ramey V, et al. **Anatomical mapping of white matter hyperintensities (WMH): exploring the relationships between periventricular WMH, deep WMH, and total WMH burden.** *Stroke* 2005;36:50–55 CrossRef Medline
36. Greenberg SM, Vernooij MW, Cordonnier C, et al; Microbleed Study Group. **Cerebral microbleeds: a guide to detection and interpretation.** *Lancet Neurol* 2009;8:165–74 CrossRef Medline
37. *The SAS System for Windows* [computer progam]. Cary: SAS Institute; 2013
38. *IBM SPSS Statistics for Windows* [computer progam]. Version 22.0. Armonk: IBM; 2013
39. ALZFORUM. AlzGene: Meta-Analysis of All Published AD Association Studies (Case-Control Only) APOE_e2/3/4 2010; http://www.alzgene.org/meta.asp?geneID=83. Accessed September 16, 2016
40. Cheung CY, Ong YT, Ikram MK, et al. **Microvascular network alterations in the retina of patients with Alzheimer's disease.** *Alzheimers Dement* 2014;10:135–42 CrossRef Medline
41. Lai AY, Dorr A, Thomason LA, et al. **Venular degeneration leads to vascular dysfunction in a transgenic model of Alzheimer's disease.** *Brain* 2015;138(pt 4):1046–58 CrossRef Medline
42. Zlokovic BV. **Cerebrovascular effects of apolipoprotein E: implications for Alzheimer disease.** *JAMA Neurol* 2013;70:440–44 CrossRef Medline
43. Brickman AM, Schupf N, Manly JJ, et al. **APOE ε4 and risk for Alzheimer's disease: do regionally distributed white matter hyperintensities play a role?** *Alzheimers Dement* 2014;10:619–29 CrossRef Medline
44. Yates PA, Villemagne VL, Ellis KA, et al. **Cerebral microbleeds: a review of clinical, genetic, and neuroimaging associations.** *Front Neurol* 2014;4:205 CrossRef Medline
45. Hawkes CA, Sullivan PM, Hands S, et al. **Disruption of arterial perivascular drainage of amyloid-beta from the brains of mice expressing the human APOE epsilon4 allele.** *PLoS One* 2012;7:e41636 CrossRef Medline
46. Zipser BD, Johanson CE, Gonzalez L, et al. **Microvascular injury and blood-brain barrier leakage in Alzheimer's disease.** *Neurobiol Aging.* 2007;28:977–86 CrossRef Medline

Basal Ganglia T1 Hyperintensity in Hereditary Hemorrhagic Telangiectasia

A. Parvinian, V.N. Iyer, B.S. Pannu, D.R. Apala, C.P. Wood, and W. Brinjikji

ABSTRACT

BACKGROUND AND PURPOSE: The implications of basal ganglia T1 hyperintensity remain unclear in patients with hereditary hemorrhagic telangiectasia. This study was performed to assess the prevalence of this imaging finding in a large cohort of patients with hereditary hemorrhagic telangiectasia and to identify any association between this phenomenon and other disease manifestations.

MATERIALS AND METHODS: In this retrospective study, we identified all patients at our institution diagnosed with definite hereditary hemorrhagic telangiectasia from 2001 to 2017. Patients who did not undergo brain MR imaging were excluded. Patient demographics, laboratory results, and hereditary hemorrhagic telangiectasia disease characteristics were noted. Basal ganglia hyperintensity was evaluated both qualitatively and quantitatively relative to the signal intensity in the ipsilateral thalami. Statistical analysis was performed with commercially available software.

RESULTS: A total of 312 patients (41% men, 59% women; mean age, 51 ± 18 years) with definite hereditary hemorrhagic telangiectasia were identified. Basal ganglia T1 hyperintensity was present in 23.4% of patients and demonstrated a statistically significant association with older age ($P < .001$), increased hepatic AVMs ($P < .001$), high cardiac output state ($P < .001$), hepatic failure ($P = .01$), elevated peak serum alkaline phosphatase level ($P = .03$), and increased total bilirubin count ($P = .03$). There was no significant association with sex, hereditary hemorrhagic telangiectasia genetic mutation status, parkinsonism, or serum transaminase levels.

CONCLUSIONS: Basal ganglia T1 hyperintensity occurs in >23% of patients with hereditary hemorrhagic telangiectasia and is associated with hepatic vascular malformations, hepatic dysfunction, and elevated cardiac output. The presence of this finding on screening MR imaging in patients with hereditary hemorrhagic telangiectasia should prompt further evaluation for visceral lesions causing arteriovenous shunting.

ABBREVIATIONS: ALT = alanine aminotransferase; *ALK1* = *activin receptor-like kinase 1*; AST = aspartate aminotransferase; *ENG* = *endoglin*; HHT = hereditary hemorrhagic telangiectasia

Hereditary hemorrhagic telangiectasia (HHT) is an autosomal dominant vascular disorder characterized by arteriovenous malformations in multiple visceral and mucocutaneous vascular beds. The Curaçao diagnostic criteria include the following: 1) the presence of spontaneous and recurrent epistaxis, 2) mucocutaneous telangiectasias, 3) visceral arteriovenous malformations, and 4) a first-degree relative diagnosed with HHT using the same criteria.[1] Patients who meet at least 3 criteria are given a definite diagnosis of HHT, while those meeting 2 criteria are diagnosed with possible or suspected HHT; patients meeting <2 criteria are considered unlikely to have HHT. Siblings and children of affected patients have a 50% risk of inheriting the disorder.[2]

The most common clinical presentation of HHT is epistaxis early in the second decade of life.[2] In hospitalized patients, epistaxis and gastrointestinal hemorrhage occur in approximately 16% and 11% of patients, respectively, while congestive heart failure occurs in nearly 20% of patients.[3] Visceral arteriovenous malformations predominantly involve the liver, lungs, and brain, and their prevalence is related to the specific underlying mutation.[4] Patients with mutations in the *endoglin* (*ENG*) gene (HHT-1) more often have cerebral and pulmonary AVMs, while patients with mutations in the *activin receptor-like kinase 1* (*ALK1*) gene (HHT-2) are more likely to have hepatic AVMs; the rare *SMAD family member 4* mutation is associated with juvenile colonic

Received March 26, 2017; accepted after revision May 28.

From the Departments of Radiology (A.P., B.S.P., D.R.A., C.P.W., W.B.) and Pulmonary and Critical Care Medicine (V.N.I.), Mayo Clinic, Rochester, Minnesota.

Please address correspondence to Ahmad Parvinian, MD, Mayo Clinic, 200 First St SW, Rochester, MN 55905; e-mail: Parvinian.Ahmad@mayo.edu

http://dx.doi.org/10.3174/ajnr.A5322

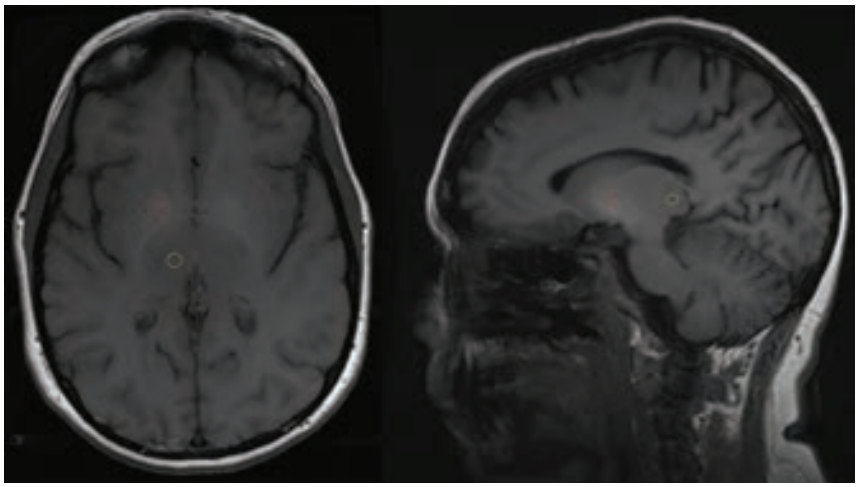

FIG 1. Axial and sagittal T1-weighted MR images of the brain demonstrating placement of ovoid ROIs on the basal ganglia (red) and ipsilateral thalamus (yellow).

polyposis.[5,6] The overall prevalence of cerebral AVMs is 10%, with a higher prevalence in HHT-1 versus HHT-2 (13.4% versus 2.4%).[7] Although clinically silent in nearly 45% of patients, AVMs may cause substantial morbidity, depending on their location, size, and the degree of arteriovenous shunting. Baseline brain MR imaging screening is recommended to minimize the risk of potentially fatal complications from cerebral AVMs.[8]

Some patients with HHT demonstrate abnormally increased basal ganglia signal intensity on T1-weighted MR images of the brain.[9-11] This finding has been attributed to intracranial deposition of paramagnetic manganese in hepatic arteriovenous shunting by hepatic AVMs.[11] However, the incidence and implications of this imaging finding remain unclear in the HHT population. Therefore, we conducted this study to assess the prevalence of basal ganglia T1 hyperintensity in a large cohort of patients with HHT and to identify any association between this phenomenon and other disease manifestations.

MATERIALS AND METHODS

Patient Population

This retrospective, single-institution study was approved by our institutional review board with a waiver of written informed consent and was performed in compliance with the Health Insurance Portability and Accountability Act. An initial patient list was generated by searching the institutional data base for all patients with HHT between January 2001 and January 2017. Inclusion criteria were the following: 1) patients with a definite diagnosis of HHT as defined by the Curaçao criteria, and 2) patients who underwent 1.5T or 3T MR imaging with at least 1 noncontrast T1-weighted scan. Patients without MR imaging of the brain were excluded from the study cohort.

Imaging Analysis

Basal ganglia hyperintensity was qualitatively determined relative to the signal intensity in the ipsilateral thalami. Quantitative measurements of signal intensity were obtained from 4- to 6-mm ovoid ROIs manually placed on the bilateral lentiform nuclei and thalami on axial or sagittal unenhanced T1-weighted images of the brain (Fig 1). In patients who underwent multiple MRIs, the earliest available scan was used to exclude gadolinium deposition as a cause for the increased T1 signal. The clinical record and relevant imaging were scrutinized to assess for potential confounders such as calcifications, toxins, hemorrhage, or ischemia.

Data Collection

The electronic medical record was reviewed to obtain patient demographics, laboratory values, and disease characteristics. Demographic information included age and sex. Laboratory studies disclosed the following values: total serum bilirubin, alkaline phosphatase, alanine aminotransferase, and aspartate aminotransferase, as well as cardiac output. HHT disease characteristics included the presence of mucocutaneous telangiectasias, epistaxis, family history, and genetic mutation status. Data regarding liver failure, dyskinesias, or clinical parkinsonism (tremor, bradykinesia, rigidity, and postural instability) were also collected. Relevant imaging was reviewed on the PACS to identify hepatic, pulmonary, and cerebral arteriovenous malformations (dysplastic vascular arterial and venous communication without an intervening capillary bed).

Patients were divided into 2 groups based on the presence or absence of basal ganglia hyperintensity, and the groups were compared with regard to the above-mentioned variables.

Statistical Analysis

Statistical analysis was performed with commercially available software (JMP 7; SAS Institute, Cary, North Carolina). Continuous variables were compared using the Student *t* test. The χ^2 test was used to compare categoric variables. P values $< .05$ were considered statistically significant.

RESULTS

Patient Population and Imaging Analysis

A total of 312 patients (41% men, 59% women; mean age, 51 ± 18 years) were included in the study cohort. A total of 73 patients had qualitatively bright basal ganglia on imaging analysis, and 239 patients had normal-appearing basal ganglia. The mean basal ganglia/thalamic ratio for the bright basal ganglia group versus the normal basal ganglia group was 1.27 ± 0.14 versus 1.07 ± 0.07 on the right side ($P < .001$) and 1.26 ± 0.13 versus 1.07 ± 0.07 on the left side ($P < .001$). Patient demographic and disease characteristics are summarized in Table 1. Representative cases are demonstrated in Figs 2 and 3.

Variables Associated with Basal Ganglia Hyperintensity

The presence of basal ganglia T1 hyperintensity demonstrated a statistically significant association with increased age (62 versus 48 years, $P < .001$), the presence of hepatic AVMs (49.3% versus 24.2%, $P < .001$), hepatic telangiectasias (23.3% versus 20.9%, $P < .001$), nasal telangiectasias (8.2% versus 2.1%, $P = .02$), increased peak cardiac output (7.9 versus 6.1 L/min, $P < .001$),

hepatic failure (5.4% versus 0.8%, $P = .01$), and elevated peak serum alkaline phosphatase levels (148 versus 108 U/L, $P = .03$) and elevated total bilirubin levels (0.88 versus 0.66, $P = .03$). There was no significant association with sex ($P = .62$), genetic mutation status ($P = .07$), parkinsonism (1.4% versus 1.3%, $P = .38$), or peak serum levels of alanine aminotransferase (ALT) (91 versus 53 U/L, $P = .35$) or aspartate aminotransferase (AST) (166 versus 51, $P = .28$). These findings are summarized in Table 2.

DISCUSSION

In this study, basal ganglia T1 hyperintensity was present in >23% of patients with definite HHT. There was a statistically significant association between this imaging finding and increased patient age, hepatic vascular malformations, hepatic dysfunction, and elevated cardiac output. There was no significant association with sex, genetic mutation status, cerebral AVMs, or gross neuropsychiatric derangement. These findings are in accordance with the prevailing hypothesis that intracranial deposition of paramagnetic manganese in the presence of hepatic AVMs is responsible for basal ganglia hyperintensity, a phenomenon that has been described in other disease processes in which hepatic metabolism of manganese is impaired or bypassed.[12] Moreover, these findings are important because they suggest that the degree of shunting required to produce basal ganglia hyperintensity appears to be associated with hepatic dysfunction and increased cardiac output, both of which may entail further metabolic derangements and a worse prognosis.

Table 1: Patient demographic and disease characteristics[a]

Demographics/Disease Characteristics	
Age (yr)	51 ± 18
Sex	
Male	129 (41%)
Female	183 (59%)
Mutation	
ENG	46 (14.7%)
ALK1	32 (10.3%)
AVM	
Cerebral	32 (10.3%)
Pulmonary	151 (48.4%)
Hepatic	94 (30.1%)
Telangiectasia	
Hepatic	67 (21.4%)
Nasal	11 (3.5%)
Liver failure	6 (1.9%)
Parkinsonism	4 (1.3%)
Serum laboratory values	
Total bilirubin (mg/dL)	0.71 ± 0.53
ALP (U/L)	118.4 ± 101
AST (U/L)	78.9 ± 456
ALT (U/L)	62.2 ± 202
Cardiac output (L/min)	6.6 ± 2.1

Note:—ALP indicates alkaline phosphatase; ALT, alanine aminotransferase.
[a] Data are means or No. (%).

The prevalence of basal ganglia hyperintensity in the present investigation was less than the rate described in a recent study of 139 patients (23% versus 38%); this prevalence may reflect the lower overall rate of hepatic AVMs in our cohort (30% versus 45%).[13] This could be due to a difference in the prevalence of *ENG* versus *ALK1* mutations in each study population, with hepatic AVMs and the high cardiac output state being much more common in those with the *ALK1* mutation. Older age, higher cardiac output, and increased prevalence of hepatic dysfunction in the bright basal ganglia group merit further discussion. Hepatic vascular involvement in HHT results in shunting involving portal vein to hepatic vein, hepatic artery to portal vein, or hepatic artery to hepatic vein. It is the hepatic artery–hepatic vein shunting that results in a high cardiac output state. A recent large nationwide study of patients with HHT in the United States found that most (~75%) patients with a high cardiac output state were older than 60 years of years of age.[3] Similarly, almost 60% of patients with cirrhosis were also older than 60 years of age in that study. Thus, the finding of high cardiac output and liver dysfunction among older patients in our study in the bright basal ganglia group is not a surprise.

Predicting liver disease in HHT is an important topic because substantial liver disease can often be present in otherwise asymptomatic patients. In a multivariate prediction model, Singh et al[14] reported that increasing age, female sex, higher alkaline phosphatase levels, and lower hemoglobin levels were all predictive of clinically significant liver disease among patients with HHT. Our study confirms these findings, with older age and higher alkaline phosphatase levels being more common in the bright basal ganglia group. Thus, it appears that bright basal ganglia occur more frequently in the same group of patients previously shown to have higher rates of clinically significant HHT-related liver disease. These congruent findings further validate our study hypothesis and results.

Manganese deposition has been associated with neurotoxicity in certain at-risk populations. In a recent study of workers with occupational exposure to manganese, Shin et al[15] found a dose-response relationship between T1 signal intensity and serum manganese levels and further described an inverse relationship between signal and neurobehavioral performance, positing that signal intensity may predict performance in workers exposed to the element. In the present study, increased basal ganglia signal intensity was not associated

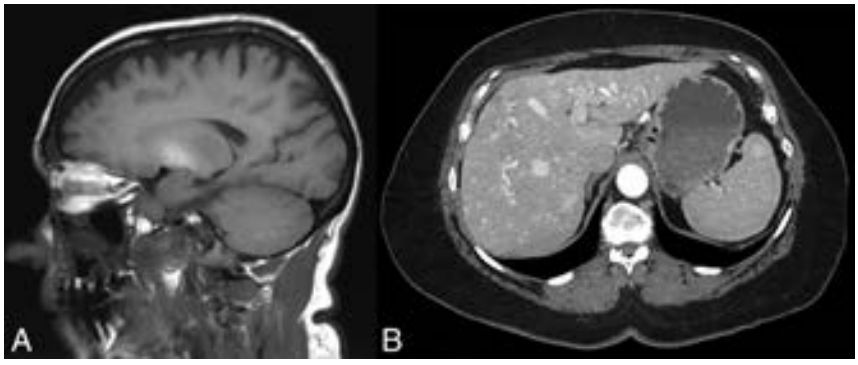

FIG 2. A representative patient with HHT and increased basal ganglia signal intensity on sagittal T1-weighted MR imaging (*A*) with a concurrent hyperenhancing hepatic AVM on arterial phase abdominal CT (*B*).

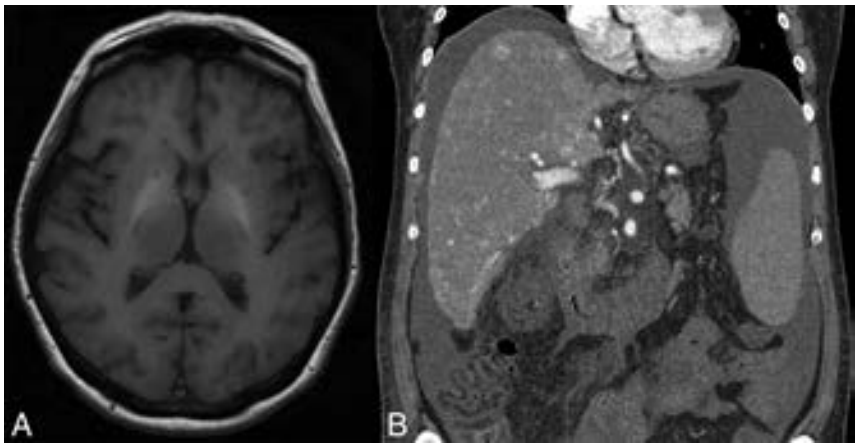

FIG 3. Another representative patient with HHT and increased basal ganglia signal intensity on axial T1-weighted MR imaging (*A*) with multiple hyperenhancing hepatic AVMs on coronal arterial phase abdominal CT (*B*).

Table 2: Variables associated with BG hyperintensity[a]

	BG Not Bright (*n* = 239, 76.6%)	BG Bright (*n* = 73, 23.4%)	*P* Value
Age (mean) (yr)	48 ± 17.9	62 ± 13.6	<.001
Sex			.62
Male	97 (40.6%)	32 (43.8%)	
Female	142 (59.4%)	41 (56.2%)	
Mean BG: thalamic intensity			
Right	1.07 ± 0.07	1.27 ± 0.14	<.001
Left	1.07 ± 0.07	1.26 ± 0.13	<.001
Mutation			.07
ENG	38 (15.9%)	8 (11.0%)	
ALK1	20 (8.4%)	12 (16.4%)	
AVM			
Cerebral	28 (11.7%)	4 (5.5%)	.12
Pulmonary	120 (50.2%)	31 (42.4%)	.03
Hepatic	58 (24.2%)	36 (49.3%)	<.001
Telangiectasia			
Hepatic	50 (20.9%)	17 (23.3%)	<.001
Nasal	5 (2.1%)	6 (8.2%)	.02
Liver failure	2 (0.8%)	4 (5.4%)	.01
Clinical parkinsonism	3 (1.3%)	1 (1.4%)	.38
Serum laboratory values (mean)			
Total bilirubin (mg/dL)	0.66 ± 0.40	0.88 ± 0.80	.03
ALP (U/L)	108 ± 80.2	148 ± 145	.03
AST (U/L)	51.2 ± 197	166 ± 862	.28
ALT (U/L)	52.7 ± 139	91.4 ± 327	.35
Cardiac output (L/min)	6.1 ± 1.8	7.9 ± 2.2	<.001

Note:—BG indicates basal ganglia; ALP, alkaline phosphatase; ALT, alanine aminotransferase.
[a] Data are No. (%) unless otherwise indicated.

with gross neurologic disturbances, though subclinical neurologic dysfunction may have existed at the time of imaging. Given the absence of overt neurologic manifestations, however, the association between basal ganglia T1 hyperintensity and liver dysfunction and elevated cardiac output highlights the importance of screening MR imaging.

Current guidelines recommend Doppler sonography or CT screening of adult patients with abnormal hepatic enzymes or clinical features suggestive of hepatic vascular malformations (ie, high output cardiac failure, liver failure, intestinal ischemia, or hepatic encephalopathy).[16] Our findings suggest that basal ganglia hyperintensity on screening brain MR imaging may be the only evidence of a subclinical hepatic AVM. In this setting, it may be appropriate to raise this possibility and recommend additional imaging and diagnostic studies to determine the presence of liver AVMs along with hepatic dysfunction and a high cardiac output state. Each of these entities worsens prognosis in patients with HHT and requires specific decisions with regard to follow-up and treatment options.[2] Most important, early detection of potentially consequential yet preclinical hepatic vascular malformations may facilitate timely intervention and ultimately lead to improved patient outcomes.

Limitations

Limitations of this study include its retrospective nature and the inherent weaknesses of nonprospective studies as well as the lack of formal neuropsychological assessment and lack of a corelation between basal ganglia deposits of manganese and serum manganese levels. Additionally, data were obtained during 2 decades from at least 15 different scanners and were therefore subject to variations in MR imaging technology and protocols and scan parameters; information pertaining to data obtained at 1.5T versus 3T was not available. The strengths of our study include the use of a well-characterized cohort of patients with HHT from a high-volume HHT center of excellence. In addition, each scan was carefully reviewed by a core group of experienced neuroradiologists with considerable experience in the field of HHT. Also, the availability of laboratory values and echocardiogram data from the electronic medical record allowed excellent statistical correlations to be made with increased basal ganglia T1 signal intensity.

CONCLUSIONS

Basal ganglia T1 hyperintensity due to manganese deposition occurs frequently in patients with HHT and was seen in >23% of this cohort. It was associated with older age and the presence of hepatic vascular malformations, hepatic dysfunction, and a high cardiac output state. The presence of this finding in patients with definite HHT should prompt a thorough evaluation for visceral AVMs and any associated systemic consequences.

Disclosures: Vivek Iyer—*UNRELATED*: *Consultancy*: Merck Pharmaceuticals, *Comments*: related to my work in chronic cough (site Principal Investigator for a phase 3 study); *Royalties*: *Mayo Clinic Internal Medicine Board Review* and *Mayo Clinic Interventional Cardiology Board Review*, *Comments*: I have authored a few chapters for these books and receive about US $100 a year in royalties.

REFERENCES

1. Shovlin CL, Guttmacher AE, Buscarini E, et al. **Diagnostic criteria for hereditary hemorrhagic telangiectasia (Rendu-Osler-Weber syndrome).** *Am J Med Genet* 2000;91:66–67 Medline
2. McDonald J, Pyeritz RE. **Hereditary hemorrhagic telangiectasia.** In: Pagon RA, Adam MP, Ardinger HH, et al, eds. *GeneReviews*. Seattle: University of Washington; 1993–2017. http://www.ncbi.nlm.nih.gov/books/NBK1351/. Accessed March 1, 2017 Medline
3. Brinjikji W, Wood CP, Lanzino G, et al. **High rates of bleeding complications among hospitalized patients with hereditary hemorrhagic telangiectasia in the United States.** *Ann Am Thorac Soc* 2016; 13:1505–11 CrossRef Medline
4. Shovlin CL. **Hereditary haemorrhagic telangiectasia: pathophysiology, diagnosis and treatment.** *Blood Rev* 2010;24:203–19 CrossRef Medline
5. Letteboer TG, Mager JJ, Snijder RJ, et al. **Genotype-phenotype relationship in hereditary haemorrhagic telangiectasia.** *J Med Genet* 2006;43:371–77 Medline
6. Sabbà C, Pasculli G, Lenato GM, et al. **Hereditary hemorrhagic telangiectasia: clinical features in ENG and ALK1 mutation carriers.** *J Thromb Haemost* 2007;5:1149–57 CrossRef Medline
7. Brinjikji W, Iyer VN, Wood CP, et al. **Prevalence and characteristics of brain arteriovenous malformations in hereditary hemorrhagic telangiectasia: a systematic review and meta-analysis.** *J Neurosurg* 2016 Oct 21. [Epub ahead of print] CrossRef Medline
8. Mandzia J, Henderson K, Faughnan M, et al. **Compelling reasons to screen brain in HHT.** *Stroke* 2001;32:2957–58 Medline
9. Kobayashi Z, Tani Y, Watabiki S, et al. **Brain MRI of hereditary hemorrhagic telangiectasia (HHT) with intrahepatic arteriovenous shunts.** *Intern Med* 2005;44:773–74 CrossRef Medline
10. Baba Y, Ohkubo K, Hamada K, et al. **Hyperintense basal ganglia lesions on T1-weighted images in hereditary hemorrhagic telangiectasia with hepatic involvement.** *J Comput Assist Tomogr* 1998;22: 976–79 CrossRef Medline
11. Oikonomou A, Chatzistefanou A, Zezos P, et al. **Basal ganglia hyperintensity on T1-weighted MRI in Rendu-Osler-Weber disease.** *J Magn Reson Imaging* 2012;35:426–30 CrossRef Medline
12. Maeda H, Sato M, Yoshikawa A, et al. **Brain MR imaging in patients with hepatic cirrhosis: relationship between high intensity signal in basal ganglia on T1-weighted images and elemental concentrations in brain.** *Neuroradiology* 1997;39:546–50 CrossRef Medline
13. Komiyama M, Terada A, Ishiguro T, et al. **Neuroradiological manifestations of hereditary hemorrhagic telangiectasia in 139 Japanese patients.** *Neurol Med Chir (Tokyo)* 2015;55:479–86 CrossRef Medline
14. Singh S, Swanson KL, Hathcock MA, et al. **Identifying the presence of clinically significant hepatic involvement in hereditary haemorrhagic telangiectasia using a simple clinical scoring index.** *J Hepatol* 2014;61:124–31 CrossRef Medline
15. Shin YC, Kim E, Cheong HK, et al. **High signal intensity on magnetic resonance imaging as a predictor of neurobehavioral performance of workers exposed to manganese.** *Neurotoxicology* 2007;28:257–62 CrossRef Medline
16. Faughnan ME, Palda VA, Garcia-Tsao G, et al; HHT Foundation International–Guidelines Working Group. **International guidelines for the diagnosis and management of hereditary haemorrhagic telangiectasia.** *J Med Genet* 2011;48:73–87 CrossRef Medline

Analysis of White Matter Damage in Patients with Multiple Sclerosis via a Novel In Vivo MR Method for Measuring Myelin, Axons, and G-Ratio

A. Hagiwara, M. Hori, K. Yokoyama, M. Nakazawa, R. Ueda, M. Horita, C. Andica, O. Abe, and S. Aoki

ABSTRACT

BACKGROUND AND PURPOSE: Myelin and axon volume fractions can now be estimated via MR imaging in vivo, as can the g-ratio, which equals the ratio of the inner to the outer diameter of a nerve fiber. The purpose of this study was to evaluate WM damage in patients with MS via this novel MR imaging technique.

MATERIALS AND METHODS: Twenty patients with relapsing-remitting MS with a combined total of 149 chronic plaques were analyzed. Myelin volume fraction was calculated based on simultaneous tissue relaxometry. Intracellular and CSF compartment volume fractions were quantified via neurite orientation dispersion and density imaging. Axon volume fraction and g-ratio were calculated by combining these measurements. Myelin and axon volume fractions and g-ratio were measured in plaques, periplaque WM, and normal-appearing WM.

RESULTS: All metrics differed significantly across the 3 groups ($P < .001$, except $P = .027$ for g-ratio between periplaque WM and normal-appearing WM). Those in plaques differed most from those in normal-appearing WM. The percentage changes in plaque and periplaque WM metrics relative to normal-appearing WM were significantly larger in absolute value for myelin volume fraction than for axon volume fraction and g-ratio ($P < .001$, except $P = .033$ in periplaque WM relative to normal-appearing WM for comparison between myelin and axon volume fraction).

CONCLUSIONS: In this in vivo MR imaging study, the myelin of WM was more damaged than axons in plaques and periplaque WM of patients with MS. Myelin and axon volume fractions and g-ratio may potentially be useful for evaluating WM damage in patients with MS.

ABBREVIATIONS: AVF = axon volume fraction; EDSS = Expanded Disability Status Scale; MVF = myelin volume fraction; NAWM = normal-appearing white matter; NODDI = neurite orientation dispersion and density imaging; PD = proton density; PWM = periplaque white matter; Vic = volume fraction of the intracellular compartment; Vec = volume fraction of the extracellular compartment; Viso = volume fraction of the CSF compartment

MR imaging, particularly T2-weighted imaging, is used for diagnosis and follow-up in patients with MS.[1] Advanced MR imaging modalities such as DTI, diffusional kurtosis imaging, *q*-space imaging, and MR spectroscopy have revealed abnormalities that were not apparent on conventional T2WI in the normal-appearing white matter (NAWM)[2,3] and periplaque white matter (PWM)[4,5] in the brains of patients with MS. A recently developed quantification pulse sequence called QRAPMASTER (an acronym derived from "quantification of relaxation times and proton density by multiecho acquisition of a saturation-recovery by using turbo spin-echo readout") has enabled the rapid simultaneous quantification of R1 and R2 relaxation rates and proton density (PD) in approximately 5 minutes, and thus enabled the use of these measurements in clinical practice.[6,7] Myelin volume fraction (MVF) can also be estimated based on R1, R2, and PD measurements.[8] The model hypothesizes 4 compartments in the brain: the myelin partial volume (or MVF), the cellular partial volume, the free water partial volume, and the excess parenchymal water partial volume. It assumes that the relaxation behavior of each compartment contributes to the effective relaxation behavior of an acquisition voxel as a whole. In this model, the magnetization exchange rates between tissue compartments are

Received March 15, 2017; accepted after revision May 24.

From the Departments of Radiology (A.H., M. Hori., M.N., R.U., M. Horita, C.A., S.A.) and Neurology (K.Y.), Juntendo University School of Medicine, Tokyo, Japan; Department of Radiology (A.H., O.A.), Graduate School of Medicine, University of Tokyo, Tokyo, Japan; and Department of Radiological Sciences (R.U.), Graduate School of Human Health Sciences, Tokyo Metropolitan University, Tokyo, Japan.

This work was supported by JSPS KAKENHI grant number 16K19852; grant number JP16H06280, Grant-in-Aid for Scientific Research on Innovative Areas - Resource and technical support platforms for promoting research "Advanced Bioimaging Support"; the Japan Radiological Society and Bayer Yakuhin (KJ-08); the Impulsing Paradigm Change through disruptive Technologies (ImPACT) Program of the Council for Science, Technology and Innovation (Cabinet Office, Government of Japan); and the program for Brain Mapping by Integrated Neurotechnologies for Disease Studies (Brain/MINDS) from the Japan Agency for Medical Research and Development, AMED.

Please address correspondence to Akifumi Hagiwara, MD, Department of Radiology, Juntendo University School of Medicine, 1-2-1, Hongo, Bunkyo-ku, Tokyo, Japan, 113-8421; e-mail: a-hagiwara@juntendo.ac.jp

Indicates open access to non-subscribers at www.ajnr.org

http://dx.doi.org/10.3174/ajnr.A5312

considered to be simulated by using Bloch estimation. MVF measured by this model has been validated by myelin staining of brain sections derived from cadavers.[9] We have previously reported that MVF, excess parenchymal water partial volume, R1, R2, and PD differed significantly across NAWM, PWM, and plaques.[10] In plaques, these parameters differed most from those in NAWM. The percentage differences in MVF and excess parenchymal water partial volume for plaques and PWM relative to NAWM differed significantly from those of R1, R2, and PD. It was concluded that MVF and excess parenchymal water partial volume are more sensitive to the MS disease process than R1, R2, and PD.

Neurite orientation dispersion and density imaging (NODDI) is one of the recently developed advanced diffusion metrics that assumes 3 compartments: a restricted intracellular compartment (Vic), a hindered extracellular compartment (Vec), and CSF with free diffusion (Viso).[11] Vic is attributed to the density of "neurites" (ie, axons and dendrites). As opposed to DTI, which is sensitive to the partial volume averaging of fiber orientations, NODDI incorporates the curving and fanning of fibers into the model and is considered to be more robust for estimating the volume of axons.[12] Even though it was not explicitly designed for handling the crossing of fibers, a preliminary study has also shown the robustness of the NODDI model for crossing fibers.[13]

The g-ratio, which is the ratio of the inner (axon only) to the outer diameter of a myelinated axon (axon plus myelin), is associated with speed of conduction.[14] Larger axons and thicker myelin sheaths give rise to faster conduction of electrochemical information, but there is a trade-off between these because of the limited space in the brain. G-ratio has a limited dynamic range in healthy WM[13] and depends on age[15-17] and region.[15,18] Stikov et al[12] developed a model that estimates "aggregate" g-ratio in a voxel via MR imaging. This model assumes that the g-ratios of all axons in a voxel are the same. Otherwise, the measured g-ratio would be the value if all of the myelin and axons were redistributed in a voxel such that all axons had the same g-ratio. Combining MVF, Viso, and Vic enables the calculation of axon volume fraction (AVF) and g-ratio. Notably, these measurements are specific to WM and not defined in GM.[13] These novel MR imaging methods in combination may differentiate between demyelination and axonal degeneration, whereas conventional T2WI or FLAIR images cannot. Remyelinated lesions are known to have thinner myelin sheaths and higher g-ratios than normal tissue.[19] G-ratio may also be useful for the evaluation of treatment effects in patients with MS.

The aim of the current study was to evaluate WM damage in patients with MS via novel MR imaging methods for quantifying MVF, AVF, and g-ratio.

MATERIALS AND METHODS

Study Participants

This prospective study recruited 24 patients with relapsing-remitting MS between April and July 2016. These patients were diagnosed according to standard criteria.[1,20,21] Of these patients, 1 did not have any plaques on brain MR imaging, the images of 1 were degraded by motion artifacts, and 2 had extensive WM abnormalities and it was difficult to evaluate focal plaques correctly. Therefore, these 4 patients were excluded, and 20 patients (5 men and 15 women; mean age, 46.7 years; age range, 31–67 years) were included in the analysis. The median Expanded Disability Status Scale (EDSS) score[22] at imaging was 1.3 (range, 0–7), and the mean disease duration was 11.5 ± 7.5 years. The institutional review board of Juntendo University Hospital approved this study, and written informed consent was obtained from all participants.

MR Imaging

All MR imaging was performed on a 3T system (Discovery MR750w; GE Healthcare, Milwaukee, Wisconsin) with a 24-channel head coil. All patients underwent MR relaxometry and diffusion-weighted, conventional T1-weighted, T2-weighted, and FLAIR imaging.

MR relaxometry was performed with a 2D axial pulse sequence. This is a multisection, multiecho, multisaturation delay saturation-recovery turbo spin-echo acquisition method in which images are collected with different combinations of TEs and saturation delay times.[6] In Juntendo University Hospital, combinations of 2 TEs and 4 delay times were used to generate a matrix of 8 complex images that were then used to quantify longitudinal R1 relaxation and transverse R2 relaxation rates and PD. The TEs used were 16.9 and 84.5 ms, and the delay times were 146, 546, 1879, and 3879 ms. The TR was 4.0 seconds. The other parameters used for MR relaxometry were as follows: FOV, 240 × 240 mm; matrix, 320 × 320; echo-train length, 10; bandwidth, 31.25 kHz; section thickness/gap, 4.0 mm/1.0 mm; sections, 30; and acquisition time, 7 minutes 12 seconds.

With the assumption that all the R1, R2, and PD values of myelin partial volume (or MVF), excess parenchymal water partial volume, cellular partial volume, and free water partial volume contribute to the effective R1, R2, and PD in each acquisition voxel, a model was produced to estimate partial volumes of these 4 compartments as described by Warntjes et al.[8] This was done by running Bloch equations and optimizing model parameters in a spatially normalized and averaged brain from a group of healthy controls. Using this model, MVF maps were created from R1, R2, and PD maps via SyMRI software (version 8.0; SyntheticMR, Linköping, Sweden). Although the more commonly used method (ie, quantitative magnetization transfer imaging) for estimating MVF to be used for calculating g-ratio requires a scaling factor to estimate MVF from measured macromolecular pool size based on proportionality,[12] we omitted this procedure because the method we used directly estimates the volume fraction of myelin in a voxel.[8] The R1, R2, and PD maps were also used to create synthetic T2WI with the following parameters: TR, 4500 ms; TE, 100 ms.

Conventional T1WI was obtained by using the following parameters: TR, 3294 ms; TE, 18 ms; TI, 908 ms; FOV, 240 × 216 mm; matrix, 352 × 256; echo-train length, 8; section thickness/gap, 4.0/1.0 mm; number of sections, 30. T2WI was obtained by using TR, 4500 ms; TE, 111 ms; FOV, 240 × 240 mm; matrix, 512 × 512; echo-train length, 24; bandwidth, 31.25 kHz; section thickness/gap, 4.0 mm/1.0 mm; and number of sections, 30. FLAIR images were obtained by using TR, 9000 ms; TE, 124 ms; TI, 2472 ms; FOV, 240 × 240 mm; matrix, 320 × 224; echo-train

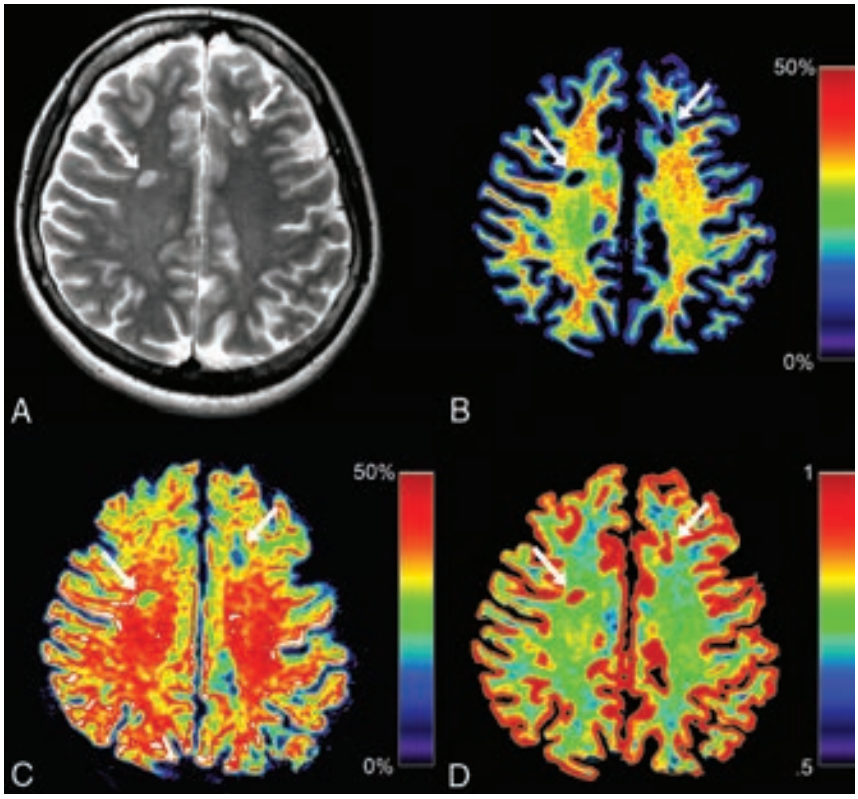

FIG 1. Representative images from a patient with MS. Synthetic T2WI (*A*) and maps of myelin volume fraction (*B*), axon volume fraction (*C*), and g-ratio (*D*) are shown. Two plaques are designated by arrows in these images. Even though myelin is severely damaged in these plaques (*B*, 5.53% and 7.23%), the degrees of axon damage are milder (*C*, 31.30% and 22.95%). Because myelin is severely damaged in these plaques, corresponding g-ratios are close to 1.00 (*D*, 0.94 and 0.91).

length, 16; section thickness/gap, 4.0/1.0 mm; and number of sections, 30.

Single-shot echo-planar imaging was performed for DWI by using 2 b-values (30 directions with $b = 1000$ seconds/mm^2 and 60 directions with $b = 2000$ seconds/mm^2). Non-DWI ($b = 0$ seconds/mm^2) was also acquired. An array spatial sensitivity encoding technique (ASSET) with an acceleration factor of 2 was used. Other parameters used for diffusion MR imaging were as follows: TR, 5000 ms; TE, 88.2 ms; diffusion gradient pulse duration, 41.184 ms; diffusion gradient separation, 29.596 ms; FOV, 256 × 256 mm; matrix, 256 × 256; echo-train length, 128; bandwidth, 1953.12 kHz; section thickness/gap, 4.0 mm/1.0 mm; sections, 30; and acquisition time, 7 minutes 40 seconds.

For DWI, distortions caused by eddy currents and motion effects were corrected by using affine whole-brain registration to $b = 0$ images with consideration of through-plane distortion in addition to in-plane distortion.[23] Images were then denoised by using multishell position-orientation adaptive smoothing based on the propagation-separation approach.[24,25] This algorithm does not assume a specific model and can be used for any diffusion model including NODDI. Instead of treating data from each shell separately, we treated the 2-shell diffusion data simultaneously for denoising to improve stability.[25]

We used the NODDI Matlab Toolbox5 (http://www.nitrc.org/projects/noddi_toolbox) to fit the NODDI model to the acquired and processed diffusion-weighted data to create maps of intracellular volume fraction (Vic), orientation dispersion index, and isotropic volume fraction (Viso). Extracting free diffusion compartment Viso, remaining Vic plus extracellular volume fraction Vec equals 1. The computational procedure for NODDI was accelerated by a convex optimization procedure that converts the nonlinear fitting into a linear one.[26]

Maps of AVF and g-ratio were obtained as described by Stikov et al.[12] Because transverse relaxation time T2 of myelin water is approximately 10 ms[27] and much shorter than the TE (88.2 ms in this study) for acquiring sufficient diffusion sensitization, the signal of myelin is negligible in the NODDI model, but the volume of myelin is not. In other words, the volume fractions estimated by NODDI correspond to nonmyelinated tissue. Therefore, AVF is given by the following equation:

$$AVF = (1 - MVF)(1 - Viso)Vic.$$

G-ratio is calculated by using fiber volume fraction (FVF) and AVF:

$$AVF/FVF = g^2.$$

MVF is:

$$MVF = FVF - AVF.$$

Thus, g-ratio is calculated as follows:

$$g = \sqrt{1/[1 + (MVF/AVF)]}.$$

These calculations were performed by using an in-house program developed with Matlab (MathWorks, Natick, Massachusetts). Linear transformation was performed to register the acquired images.

Image Analysis

Synthetic T2WI and maps of MVF, AVF, and g-ratio (Fig 1) were converted to DICOM files and analyzed by using OsiriX Imaging Software, Version 7.5 (http://www.osirix-viewer.com). An experienced neuroradiologist (A.H.) used conventional and synthetic MR images to confirm 150 plaques (defined as a WM area of more than 5 mm in diameter in the supratentorial area with abnormally high intensity on a T2WI). Of these, 1 plaque was new compared with the MR imaging performed 2 months earlier. None of the other lesions showed remarkable change compared with the MR imaging performed at least 1 year earlier. These 149 plaques were considered chronic and were used for ROI analysis. The mean number of plaques in the 20 patients was 7.45 ± 4.52. A.H. manually drew freehand ROIs on plaques, PWM, and NAWM on synthetic T2WI. An ROI was placed to encircle a plaque, and up to 4 ROIs, approximately half the size of the ROI of that plaque, were also placed on the PWM (defined as a normal-intensity WM area closest to and surrounding a plaque) (Fig 2).[4,5,10] The PWM ROIs were placed approximately 90° from the adjacent ROI to form a

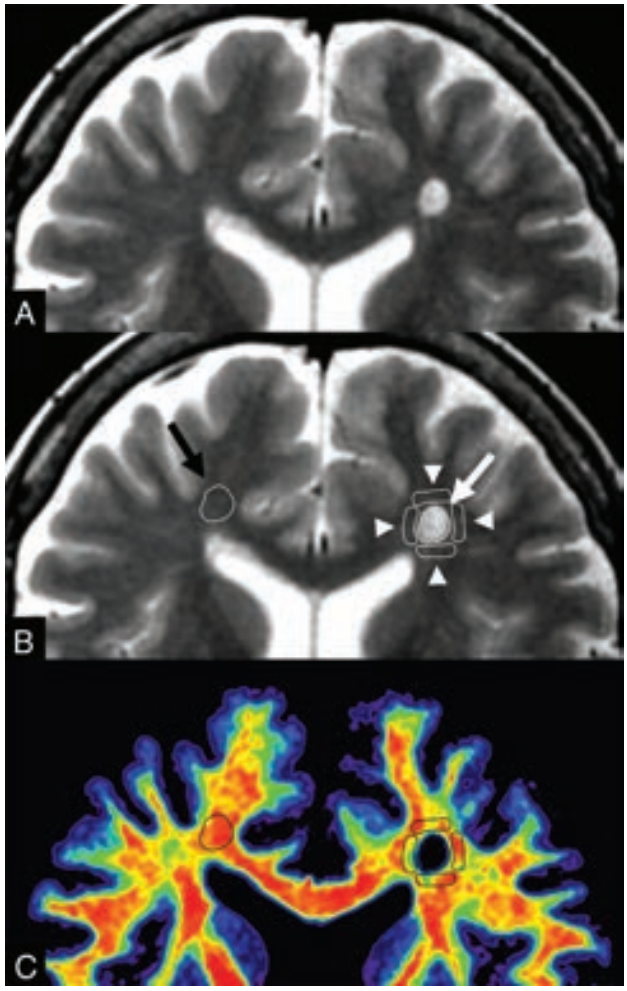

FIG 2. An example of ROI analysis in a patient with MS. The upper 2 images show the same synthetic T2WI without (*A*) and with (*B*) the placement of ROIs. A ROI (*white arrow*) was drawn on a plaque, and 4 ROIs (*arrowheads*) were placed on periplaque white matter to encircle the plaque. The ROI of the plaque was copied and pasted onto the contralateral normal-appearing white matter (*black arrow*). These ROIs were then copied and pasted onto maps of myelin volume fraction, axon volume fraction, and g-ratio. A map of the corresponding myelin volume fraction (*C*) is shown as an example.

box that surrounded the plaque. If a PWM ROI overlapped CSF, GM, or other plaques, it was discarded; 206 PWM ROIs were removed on this basis (ie, 390 PWM ROIs were used for analysis). The ROI of the plaque was copied and pasted on the contralateral NAWM. The mean ROI sizes were $45.17 \pm 30.19\ mm^2$ for plaques and $22.72 \pm 15.16\ mm^2$ for PWM. All the ROIs made on synthetic T2WI were copied and pasted onto the MVF, AVF, and g-ratio maps for the same patient, and the mean value of each ROI was recorded. To confirm the accuracy of ROI analyses, a second investigator (M. Horita) blinded to the patient information also independently conducted the same measurements.

Statistical Analysis

Because not all data were normally distributed, we used the Steel-Dwass test for multiple comparisons to compare MVF, AVF, and g-ratio values among plaques, PWM, and NAWM. The percentage changes of plaques or PWM relative to NAWM were also calculated and compared among different metrics (ie, MVF, AVF, and g-ratio). The signs of the percentage changes for MVF and AVF were inverted for statistical analysis because these values were higher overall in NAWM than in plaques and PWM. EDSS and disease duration were correlated with MVF, AVF, and g-ratio of NAWM averaged in each patient via the Spearman rank order correlation coefficient. A 2-sided P value $< .05$ was considered significant. All statistical analyses were performed with the software package R, version 3.2.1 (http://www.r-project.org/).

Table 1: Descriptive values of plaques, PWM, and NAWM

	MVF (%)[a]	AVF (%)[a]	G-Ratio (%)[a]
Plaques	5.97 ± 4.86	31.49 ± 10.39	0.93 ± 0.058
PWM	25.74 ± 4.42	39.08 ± 7.09	0.77 ± 0.049
NAWM	30.96 ± 3.74	44.10 ± 7.56	0.76 ± 0.051

[a] Values are mean ± SD. $P < .001$ for all metrics among each tissue type, except $P = .027$ for g-ratio between PWM and NAWM.

Table 2: Percentage changes of MVF, AVF, and g-ratio in plaques and PWM relative to NAWM

	MVF (%)[a]	AVF (%)[a]	G-Ratio (%)[a]
Plaques	80.78 ± 15.27	27.18 ± 25.27	23.81 ± 11.52
PWM	16.19 ± 14.82	9.31 ± 22.05	2.17 ± 8.24

[a] Values are mean ± SD. $P < .001$ for percentage changes of plaques and PWM relative to NAWM for comparisons among all metrics, except $P = .016$ for percentage change of plaques relative to NAWM when comparing between AVF and g-ratio, and $P = .033$ for percentage change of PWM relative to NAWM when comparing between MVF and AVF.

RESULTS

The results of ROI analysis and comparisons among plaques, PWM, and NAWM are shown in Table 1. MVF, AVF, and g-ratio all differed significantly among plaques, PWM, and NAWM. MVF and AVF were lower in plaques and PWM than in NAWM, with plaques showing the lowest value ($P < .001$), and g-ratio was higher in plaques and PWM than in NAWM, with plaques showing the highest value ($P < .001$, except $P = .027$ for g-ratio between PWM and NAWM).

The percentage changes of MVF, AVF, and g-ratio in plaques and PWM relative to NAWM are shown in Table 2. Those of MVF and AVF in plaques relative to NAWM differed significantly more from zero than that of g-ratio, with that of MVF differing the most from zero ($P < .001$, except $P = .016$ for comparison between those of AVF and g-ratio). Those of MVF and AVF in PWM relative to NAWM differed significantly more from zero than that of g-ratio, with that of MVF differing the most from zero ($P < .001$, except $P = .033$ for comparison between those of MVF and AVF).

The interobserver reproducibility between the 2 observers (A.H. and M. Horita) for the mean MVF values was measured. The interclass correlation coefficient for plaques was 0.84 (95% CI, 0.78–0.88), that for PWM was 0.94 (95% CI, 0.92–0.96), and that for NAWM was 0.89 (95% CI, 0.85–0.92).

Significant correlations with EDSS and disease duration were not found for MVF, AVF, and g-ratio of NAWM averaged in each patient (EDSS versus MVF, $P = .25$; EDSS versus AVF, $P = .87$; EDSS versus g-ratio, $P = .80$; disease duration versus MVF, $P = .25$; disease duration versus AVF, $P = .26$; disease duration versus g-ratio, $P = .22$).

DISCUSSION

The observation of lower MVF in plaques and PWM than in NAWM, with plaques showing the lowest value, is consistent with the results of our previous report.[10] In this study, AVF of PWM was also in between that of NAWM and plaques, with plaques showing the lowest value. However, the percentage changes of MVF for plaques and PWM relative to NAWM were higher than those of AVF. This implies that myelin was more damaged than axons in plaques and PWM. This corresponds to the results of previous histologic studies showing that demyelination is the primary event in patients with MS, and axons are relatively preserved in chronic plaques.[28] Even though Wallerian degeneration is known to cause axonal loss and contribute to secondary myelin degradation in PWM,[29,30] myelin loss may be the primary event in PWM as well as in plaques.[28] However, there is growing evidence that axonal damage is also a feature of MS that is associated with long-term disability and functional deficits.[31] For example, the average percentage change of AVF in plaques relative to NAWM in our study was 27.18%, lower than the value (68%) reported by Bjartmar et al[32] for histopathologic average axonal loss in MS lesions. However, their study involved the spinal cords of 5 paralyzed patients with MS with EDSS scores of ≥7.5, whereas the median EDSS score of the patients in our study was much lower (1.3), and the degrees of axonal damage in the patients in the 2 studies were presumably different. A greater number of patients would be required to stratify them according to EDSS to investigate patterns of myelin and axonal damage according to disease progression. In the current study, neither EDSS nor disease duration were significantly correlated with MVF, AVF, or g-ratio in NAWM. Correlations between clinical indicators and MVF, AVF, and g-ratio should also be re-evaluated in a larger study.

Our study is the first to report the g-ratio in the brains of a number of patients with MS. The average g-ratio of 0.76 in NAWM of patients with MS in this study is almost equal to the value of 0.75 in a patient with MS measured via MR imaging reported by Stikov et al.[12] In the current study, the average g-ratio of MS plaques was higher than that of NAWM (0.93 versus 0.76). This is consistent with a histologic study that showed myelin is thinner in plaques even after partial remyelination.[17] Although our result for the relationship of g-ratios between MS plaques and NAWM corresponds to the aforementioned report by Stikov et al,[12] the reported average g-ratio for plaques was 0.80 in that study, which is lower than that of the current study (0.93). This difference in g-ratios may be related to variations in the disease duration and differences in the methods used to measure g-ratio. In the current study, g-ratios in various regions were averaged, and the dependence of g-ratio on specific regions was not explored. Larger axons (eg, those in corticospinal tracts) are known to have greater g-ratios than smaller axons.[18,33]

There are various approaches for estimating MVF in the brain. Magnetization transfer imaging is one of these, and quantitative magnetization transfer imaging has shown a strong correlation with quantitative histology.[34] MR studies evaluating g-ratio have mostly been based on magnetization transfer imaging.[12,15,18] However, quantitative magnetization transfer imaging requires approximately 30 minutes for acquisition, and it is still unrealistic for routine use in a clinical setting. Quantitative magnetization transfer imaging first measures macromolecular pool size, and a coefficient for regressing it to MVF should be determined in each protocol.[12] The model based on tissue relaxometry used in the current study[8] directly estimates MVF in a voxel and can be used without determining a coefficient as is done by quantitative magnetization transfer imaging. Our report is the first to show g-ratios calculated with MVF measured via simultaneous tissue relaxometry. Although MVF calculated based on this tissue relaxometry has been validated in cadavers with no known brain diseases,[9] the methodology has not yet been histologically validated in brains with MS. In plaques, expected histology is heterogeneous, including myelin debris, poor remyelination, and remyelination with higher quality.[35] The extent to which MVF is affected by myelin debris may depend on the MR imaging technique used for estimation.[13]

The myelin model used in our study considers magnetization exchange rates between tissue compartments.[8] However, it does not explicitly incorporate a partial volume pool to account for magnetization transfer effects, which were shown to create an offset bias for steady-state approaches.[36] Magnetization transfer effects may result in small changes of our observed Carr-Purcell Meiboom-Gill multiecho signal amplitudes, which will propagate to the R2 estimations. In the model used in our study, however, myelin is estimated from combinations of the measured R1, R2, and PD values, and the effect of a potential offset in R2 is expected to be small. The inclusion of magnetization transfer effects and correction of a potential bias on our myelin water fraction measurements may be improvements in future works. Mossahebi et al[37] recently suggested a method to reduce the partial volume effect by CSF on the estimation of magnetization transfer. CSF partial volume is expected at the brain tissue interface with the surrounding CSF and is accounted for in the model used in our study by the incorporation of the free water partial volume compartment.

In addition to calculating MVF, measures of R1, R2, and PD acquired via simultaneous tissue relaxometry can also be used for synthesizing various contrast-weighted images, including T1-weighted, T2-weighted, FLAIR, double inversion recovery, or phase-sensitive inversion recovery images.[7,38-40] Thus, the need to obtain these images separately can be eliminated. The clinical usefulness of this specific tissue relaxometry with synthetic MR imaging has been shown in studies of patients with MS.[41,42]

The current study had some limitations. First, the sample size was small. Second, it did not include healthy controls. Third, only chronic plaques were investigated, and acute plaques may yield different results. Fourth, because the resolution of 2 techniques used for simultaneous tissue relaxometry and NODDI were not matched, there was a possibility of misregistration and partial volume effects.

CONCLUSIONS

This in vivo MR imaging study showed myelin to be more damaged than axons in plaques and PWM of patients with MS. The average g-ratio of NAWM was similar to a previously reported value[12] based on a single patient with MS, but that of plaques was higher than the value reported in that prior study, which was

measured by methods other than those used in the current study. MVF, AVF, and g-ratio have the potential to be useful for evaluating WM damage in patients with MS.

ACKNOWLEDGMENTS

We thank Araya Brain Imaging for technical support with data analysis. We are grateful to Dr. Marcel Warntjes and Dr. Nikola Stikov for providing us with the idea support and thoughtful comments on our manuscript.

Disclosures: Akifumi Hagiwara—*RELATED*: *Grants/Grants Pending*: JSPS KAKENHI, Advanced Bioimaging Support, Japan Radiological Society and Bayer Yakuhin, ImPACT Program, AMED, *Comments*: this work was supported by JSPS KAKENHI Grant Number 16K19852; grant number JP16H06280, Grant-in-Aid for Scientific Research on Innovative Areas - Resource and technical support platforms for promoting research "Advanced Bioimaging Support"; the Japan Radiological Society and Bayer Yakuhin (KJ-08); the Impulsing Paradigm Change through disruptive Technologies (ImPACT) Program of the Council for Science, Technology and Innovation (Cabinet Office, Government of Japan); and the program for Brain Mapping by Integrated Neurotechnologies for Disease Studies (Brain/MINDS) from the Japan Agency for Medical Research and development, AMED. Kazumasa Yokoyama—*UNRELATED*: *Other*: belonging to the department funded by Mitsubishi Tanabe Pharma, Hydrogen Health Medical Labo, ABIST, Melodian, Kenkoukazoku, Yamato, Biogen Idec Japan, Bayer, Nihon Pharmaceutical, Asahi Kasei Medical, Japan Blood Products Organization, MiZ, Ono Pharmaceutical.* Shigeki Aoki—*RELATED*: *Grant*: Brain/MINDS, ABiS*; *UNRELATED*: *Board Membership*: Bayer; *Consulting Fee or Honorarium*: SyMRI meeting chair; *Grants/Grants Pending*: Bayer, Daiichi-Sankyo, Eisai, Fuji-yakuhin, Fuji Film RI, Mediphysics, Toshiba, *Comments*: grant for diagnostic radiology*; *Payment for Lectures (including service on Speakers Bureaus)*: GE, Toshiba, Hitachi, Siemens, Bayer, Daiichisankyo, Eisai, Fuji-yakuhin, Fuji Film RI, Mediphysics, Novartis, Takeda, Biojen, *Comments*: honorarium for lectures/chair. *Money paid to the institution.

REFERENCES

1. Polman CH, Reingold SC, Banwell B, et al. **Diagnostic criteria for multiple sclerosis: 2010 revisions to the McDonald criteria.** *Ann Neurol* 2011;69:292–302 CrossRef Medline
2. Filippi M, Rocca MA, De Stefano N, et al. **Magnetic resonance techniques in multiple sclerosis: the present and the future.** *Arch Neurol* 2011;68:1514–20 CrossRef Medline
3. Yoshida M, Hori M, Yokoyama K, et al. **Diffusional kurtosis imaging of normal-appearing white matter in multiple sclerosis: preliminary clinical experience.** *Jpn J Radiol* 2013;31:50–55 CrossRef Medline
4. Guo AC, MacFall JR, Provenzale JM. **Multiple sclerosis: diffusion tensor MR imaging for evaluation of normal-appearing white matter.** *Radiology* 2002;222:729–36 CrossRef Medline
5. Hori M, Yoshida M, Yokoyama K, et al. **Multiple sclerosis: benefits of q-space imaging in evaluation of normal-appearing and periplaque white matter.** *Magn Reson Imaging* 2014;32:625–29 CrossRef Medline
6. Warntjes JB, Leinhard OD, West J, et al. **Rapid magnetic resonance quantification on the brain: optimization for clinical usage.** *Magn Reson Med* 2008;60:320–29 CrossRef Medline
7. Hagiwara A, Warntjes M, Hori M, et al. **SyMRI of the brain: rapid quantification of relaxation rates and proton density, with synthetic MRI, automatic brain segmentation, and myelin measurement.** *Invest Radiol* 2017 Mar 3. [Epub ahead of print] CrossRef Medline
8. Warntjes M, Engström M, Tisell A, et al. **Modeling the presence of myelin and edema in the brain based on multi-parametric quantitative MRI.** *Front Neurol* 2016;7:16 CrossRef Medline
9. Warntjes JBM, Persson A, Berge J, et al. **Myelin detection using rapid quantitative MR imaging correlated to macroscopically registered luxol fast blue–stained brain specimens.** *AJNR Am J Neuroradiol* 2017;38:1096–1102 CrossRef Medline
10. Hagiwara A, Hori M, Yokoyama K, et al. **Utility of a multiparametric quantitative MRI model that assesses myelin and edema for evaluating plaques, periplaque white matter, and normal-appearing white matter in patients with multiple sclerosis: a feasibility study.** *AJNR Am J Neuroradiol* 2017;38:237–42 CrossRef Medline
11. Zhang H, Schneider T, Wheeler-Kingshott CA, et al. **NODDI: practical in vivo neurite orientation dispersion and density imaging of the human brain.** *Neuroimage* 2012;61:1000–16 CrossRef Medline
12. Stikov N, Campbell JS, Stroh T, et al. **In vivo histology of the myelin g-ratio with magnetic resonance imaging.** *Neuroimage* 2015;118:397–405 CrossRef Medline
13. Campbell JS, Leppert IR, Narayanan S, et al. **Promise and pitfalls of g-ratio estimation with MRI.** arXiv:1701.02760v1 [physics.med-ph]. January 10, 2017. https://arxiv.org/abs/1701.02760v1. Accessed July 2, 2017
14. Rushton WA. **A theory of the effects of fibre size in medullated nerve.** *J Physiol* 1951;115:101–22 CrossRef Medline
15. Cercignani M, Giulietti G, Dowell NG, et al. **Characterizing axonal myelination within the healthy population: a tract-by-tract mapping of effects of age and gender on the fiber g-ratio.** *Neurobiol Aging* 2017;49:109–18 CrossRef Medline
16. Dean DC 3rd, O'Muircheartaigh J, Dirks H, et al. **Mapping an index of the myelin g-ratio in infants using magnetic resonance imaging.** *Neuroimage* 2016;132:225–37 CrossRef Medline
17. Melbourne A, Eaton-Rosen Z, Orasanu E, et al. **Longitudinal development in the preterm thalamus and posterior white matter: MRI correlations between diffusion weighted imaging and T2 relaxometry.** *Hum Brain Mapp* 2016;37:2479–92 CrossRef Medline
18. Mohammadi S, Carey D, Dick F, et al. **Whole-brain in-vivo measurements of the axonal g-ratio in a group of 37 healthy volunteers.** *Front Neurosci* 2015;9:441 Medline
19. Albert M, Antel J, Brück W, et al. **Extensive cortical remyelination in patients with chronic multiple sclerosis.** *Brain Pathol* 2007;17:129–38 CrossRef Medline
20. McDonald WI, Compston A, Edan G, et al. **Recommended diagnostic criteria for multiple sclerosis: guidelines from the International Panel on the diagnosis of multiple sclerosis.** *Ann Neurol* 2001;50:121–27 CrossRef Medline
21. Polman CH, Reingold SC, Edan G, et al. **Diagnostic criteria for multiple sclerosis: 2005 revisions to the "McDonald Criteria."** *Ann Neurol* 2005;58:840–46 CrossRef Medline
22. Kurtzke JF. **A new scale for evaluating disability in multiple sclerosis.** *Neurology* 1955;5:580–83 CrossRef Medline
23. Mohammadi S, Möller HE, Kugel H, et al. **Correcting eddy current and motion effects by affine whole-brain registrations: evaluation of three-dimensional distortions and comparison with slicewise correction.** *Magn Reson Med* 2010;64:1047–56 CrossRef Medline
24. Becker SM, Tabelow K, Voss HU, et al. **Position-orientation adaptive smoothing of diffusion weighted magnetic resonance data (POAS).** *Med Image Anal* 2012;16:1142–55 CrossRef Medline
25. Becker SM, Tabelow K, Mohammadi S, et al. **Adaptive smoothing of multi-shell diffusion weighted magnetic resonance data by msPOAS.** *Neuroimage* 2014;95:90–105 CrossRef Medline
26. Daducci A, Canales-Rodríguez EJ, Zhang H, et al. **Accelerated microstructure imaging via convex optimization (AMICO) from diffusion MRI data.** *Neuroimage* 2015;105:32–44 CrossRef Medline
27. Levesque IR, Pike GB. **Characterizing healthy and diseased white matter using quantitative magnetization transfer and multicomponent T(2) relaxometry: a unified view via a four-pool model.** *Magn Reson Med* 2009;62:1487–96 CrossRef Medline
28. Lucchinetti CF, Brück W, Rodriguez M, et al. **Distinct patterns of multiple sclerosis pathology indicates heterogeneity on pathogenesis.** *Brain Pathol* 1996;6:259–74 CrossRef Medline
29. Dziedzic T, Metz I, Dallenga T, et al. **Wallerian degeneration: a major component of early axonal pathology in multiple sclerosis.** *Brain Pathol* 2010;20:976–85 Medline
30. Simons M, Misgeld T, Kerschensteiner M. **A unified cell biological perspective on axon-myelin injury.** *J Cell Biol* 2014;206:335–45 CrossRef Medline
31. Haines JD, Inglese M, Casaccia P. **Axonal damage in multiple sclerosis.** *Mt Sinai J Med* 2011;78:231–43 CrossRef Medline
32. Bjartmar C, Kidd G, Mörk S, et al. **Neurological disability correlates**

with spinal cord axonal loss and reduced N-acetyl aspartate in chronic multiple sclerosis patients. *Ann Neurol* 2000;48:893–901 Medline
33. Graf von Keyserlingk D, Schramm U. **Diameter of axons and thickness of myelin sheaths of the pyramidal tract fibres in the adult human medullary pyramid.** *Anat Anz* 1984;157:97–111 Medline
34. West KL, Kelm ND, Carson RP, et al. **Myelin volume fraction imaging with MRI.** *Neuroimage* 2016 Dec 23. [Epub ahead of print] CrossRef Medline
35. Lampron A, Larochelle A, Laflamme N, et al. **Inefficient clearance of myelin debris by microglia impairs remyelinating processes.** *J Exp Med* 2015;212:481–95 CrossRef Medline
36. Liu F, Block WF, Kijowski R, et al. **Rapid multicomponent relaxometry in steady state with correction of magnetization transfer effects.** *Magn Reson Med* 2016;75:1423–33 CrossRef Medline
37. Mossahebi P, Alexander AL, Field AS, et al. **Removal of cerebrospinal fluid partial volume effects in quantitative magnetization transfer imaging using a three-pool model with nonexchanging water component.** *Magn Reson Med* 2015;74:1317–26 CrossRef Medline
38. Hagiwara A, Nakazawa M, Andica C, et al. **Dural enhancement in a patient with Sturge-Weber syndrome revealed by double inversion recovery contrast using synthetic MRI.** *Magn Reson Med Sci* 2016; 15:151–52 CrossRef Medline
39. Hagiwara A, Hori M, Suzuki M, et al. **Contrast-enhanced synthetic MRI for the detection of brain metastases.** *Acta Radiol Open* 2016;5: 2058460115626757 CrossRef Medline
40. Andica C, Hagiwara A, Nakazawa M, et al. **The advantage of synthetic MRI for the visualization of early white matter change in an infant with Sturge-Weber syndrome.** *Magn Reson Med Sci* 2016;15: 347–48 CrossRef Medline
41. Granberg T, Uppman M, Hashim F, et al. **Clinical feasibility of synthetic MRI in multiple sclerosis: a diagnostic and volumetric validation study.** *AJNR Am J Neuroradiol* 2016;37:1023–29 CrossRef Medline
42. Hagiwara A, Hori M, Yokoyama K, et al. **Synthetic MRI in the detection of multiple sclerosis plaques.** *AJNR Am J Neuroradiol* 2017;38: 257–63 CrossRef Medline

Pre- and Postcontrast 3D Double Inversion Recovery Sequence in Multiple Sclerosis: A Simple and Effective MR Imaging Protocol

P. Eichinger, J.S. Kirschke, M.-M. Hoshi, C. Zimmer, M. Mühlau, and I. Riederer

ABSTRACT

BACKGROUND AND PURPOSE: The double inversion recovery sequence is known to be very sensitive and specific for MS-related lesions. Our aim was to compare the sensitivity of pre- and postcontrast images of 3D double inversion recovery and conventional 3D T1-weighted images for the detection of contrast-enhancing MS-related lesions in the brain to analyze whether double inversion recovery could be as effective as T1WI.

MATERIALS AND METHODS: A postcontrast 3D double inversion recovery sequence was acquired in addition to the standard MR imaging protocol at 3T, including pre- and postcontrast 3D T1WI sequences as well as precontrast double inversion recovery of 45 consecutive patients with MS or clinically isolated syndrome between June and December 2013. Two neuroradiologists independently assessed precontrast, postcontrast, and subtraction images of double inversion recovery as well as T1WI to count the number of contrast-enhancing lesions. Afterward, a consensus reading was performed. Lin concordance was calculated between both radiologists, and differences in lesion detectability were assessed with the Student *t* test. Additionally, the contrast-to-noise ratio was calculated.

RESULTS: Significantly more contrast-enhancing lesions could be detected with double inversion recovery compared with T1WI (16%, 214 versus 185, $P = .007$). The concordance between both radiologists was almost perfect ($\rho_c = 0.94$ for T1WI and $\rho_c = 0.98$ for double inversion recovery, respectively). The contrast-to-noise ratio was significantly higher in double inversion recovery subtraction images compared with T1-weighted subtraction images (double inversion recovery, 14.3 ± 5.5; T1WI, 6.3 ± 7.1; $P < .001$).

CONCLUSIONS: Pre- and postcontrast double inversion recovery enables better detection of contrast-enhancing lesions in MS in the brain compared with T1WI and may be considered an alternative to the standard MR imaging protocol.

ABBREVIATIONS: DIR = double inversion recovery; GBCA = gadolinium-based contrast agent; CNR = contrast-to-noise ratio

Since the introduction of the double inversion recovery (DIR) sequence in 1994 by Redpath and Smith,[1,2] many studies have investigated the usefulness of DIR for the detection of inflammatory lesions in the brain in multiple sclerosis. In this sequence, the signals from both the CSF and normal white matter are suppressed simultaneously; thus, differentiation between gray matter and white matter is facilitated. Additionally, inflammatory lesions remain unsuppressed and appear hyperintense. The studies concluded that DIR is very sensitive and specific for MS lesions in the brain,[3-5] especially for intracortical lesions.[6-8] One group could also show that DIR provides the highest sensitivity in the detection of MS lesions in the infratentorial region compared with FLAIR and T2WI.[4] A similar benefit was found for an adapted DIR sequence in the spinal cord.[9] Due to the high sensitivity and specificity as well as the increasing availability of the DIR sequence, it is more often included in routine MR imaging protocols.

The standard MR imaging protocol for the examination of patients with MS commonly includes the intravenous administration of gadolinium-based contrast agents (GBCAs). The presence of contrast-enhancing lesions is important for the diagnosis and therapeutic strategies of MS and is listed in the revised McDonald criteria from 2010[10] and the magnetic resonance imaging in multiple sclerosis consensus guidelines[11] for the criteria of dissemination in time. Because the best sensitivity for enhancing lesions is achieved about 5–10 minutes after injection of a GBCA,[12] further sequences, usually T2WI, are performed for bridging the waiting time. However, these sequences should be carefully selected because the signal of contrast-enhancing lesions might be changed in modified T2WI sequences such as FLAIR[13,14] or DIR.[15,16]

Received March 26, 2017; accepted after revision June 2.

From the Department of Neuroradiology (P.E., J.S.K., C.Z., I.R.), Department of Neurology (M.-M.H., M.M.), Neuroimaging Center (M.M.), and Department of Radiology (I.R.), Klinikum rechts der Isar, Technische Universität München, Munich, Germany.

Please address correspondence to Isabelle Riederer, MD, Department of Neuroradiology, Klinikum rechts der Isar, Technische Universität München, Ismaninger Str 22, 81675 Munich, Germany; e-mail: isabelle.riederer@tum.de

http://dx.doi.org/10.3174/ajnr.A5329

One group found that contrast-enhancing parts of tumors appear hypointense in postcontrast DIR.[15] Furthermore, it has been shown recently that there is an altered signal intensity of active enhancing inflammatory MS lesions in postcontrast DIR of the brain.[16] This observation led to the recommendation to acquire DIR sequences before GBCA administration.

Here, we test the hypothesis that the signal loss on DIR images after GBCA administration can be used to detect active enhancing lesions. In particular, the aim was to compare the sensitivity of pre- and postcontrast images of 3D double inversion recovery and conventional 3D T1WI for the detection of contrast-enhancing MS-related lesions in the brain to analyze whether DIR could be as effective as T1WI.

MATERIALS AND METHODS

Patients

Patients were enrolled in a prospective study design, and data were analyzed retrospectively. In 45 consecutive patients between June and December 2013 (24 women, mean age, 38 ± 11 years; range, 19–62 years) with MS ($n = 38$; 37 relapsing-remitting, 1 secondary-progressive; median Expanded Disability Status Scale score, 1.7 ± 1.7, range, 0–6.5) or clinically isolated syndrome ($n = 7$), a DIR sequence was acquired after IV injection of a GBCA in addition to the standard in-house MR imaging protocol. The study was Health Insurance Portability and Accountability Act–compliant. The study protocol was approved by the local ethics committee, and written informed consent was obtained from all participants. All patients were examined due to a new clinical attack or for routine follow-up.

MR Imaging Acquisition

Scans were obtained on a 3T scanner (Achieva; Philips Healthcare, Best, the Netherlands) with a 16-channel array head coil. Our standard MR imaging protocol for patients with or suspicious for MS has a precontrast 3D DIR sequence and 3D T1WI sequences pre- and postcontrast (6 minutes after IV injection). For this study, an additional 3D DIR sequence was acquired following the postcontrast T1WI sequence, 12 minutes after GBCA injection. A GBCA (0.5 mmol/mL, gadoterate meglumine; Dotarem; Guerbet, Aulnay-sous-Bois, France) was injected intravenously at a concentration of 0.1 mmol/kg. MR imaging acquisition parameters of the 3D DIR sequence were as follows: acquired voxel size, 1.2 × 1.2 × 1.3 mm^3; acquisition matrix, 208 × 208; FOV, 250; TR, 5500 ms; TE, 328 ms; TI, 2550 ms; TSE factor, 173; number of sections, 300; acquisition time, 6 minutes; plane, sagittal. The parameters for the 3D T1WI sequence were the following: acquired voxel size, 1 × 1 × 1 mm^3; acquisition matrix, 240 × 240; FOV, 240 mm; TR, 9 ms; TE, 4 ms; number of sections, 170; acquisition time, 5 minutes and 55 seconds; plane, sagittal. Additionally, T2WI and FLAIR sequences were acquired routinely. The T2WI sequence had a spatial resolution of 1.0 × 1.0 × 1.5 mm^3, TR of 4000 ms, and a TE of 35 ms; the 3D FLAIR sequence had a spatial resolution of 1.0 × 1.0 × 1.5 mm^3, a TR of 10,000 ms, a TE of 140 ms, and a TI of 2750 ms.

MR Imaging Analysis

Data were analyzed retrospectively. DIR and T1WI scans were resliced and coregistered with SPM12 (http://www.fil.ion.ucl.ac.uk/spm/software/spm12) and subtracted by using a custom script written in Matlab (MathWorks, Natick, Massachusetts; R2015a, Version 8.5.0 197631). This script used the built-in registration in SPM and reslice-algorithms to perform a rigid body coregistration of the images with the precontrast image as the reference file and the postcontrast image as the source file. The coregistered images were subtracted ("precontrast-postcontrast" for DIR and "postcontrast-precontrast" for T1WI) and analyzed without further processing steps.

The sequences were reformatted with ITK-SNAP (www.itksnap.org)[17] in 1-mm axial sections. First, 2 neuroradiologists with 2 and 5 years' experience, respectively, assessed the images regarding the appearance of contrast-enhancing lesions. In a second step, both readers, blinded to diagnoses and clinical symptoms, independently assessed the images regarding the number of enhancing lesions by consulting precontrast, postcontrast, and subtraction images of DIR and T1WI in pseudorandom order by using ITK-SNAP. A contrast-enhancing lesion was defined as a 2-mm focal signal alteration in the brain tissue. A definite lesion count was derived from an additional consensus reading by both neuroradiologists by supplementary use of T2WI and FLAIR images. Additionally, lesions that were missed were classified with regard to localization (cortical/juxtacortical, periventricular, deep white matter, supra- or infratentorial).

Furthermore, the contrast-to-noise ratio (CNR) was calculated according to following formula:

$$CNR = (S_{lesion} - S_{nonaffected\ surrounding\ tissue})/SD_{nonaffected\ surrounding\ tissue},$$

where S_{lesion} and $S_{nonaffected\ surrounding\ tissue}$ represent the mean signal in an ROI in the lesion and normal-appearing surrounding brain tissue, respectively. $SD_{nonaffected\ surrounding\ tissue}$ is the SD of the normal-appearing surrounding brain tissue. Calculation and measurement of the mean values were performed with standard tools of ITK-SNAP.[17] The CNR was calculated in the largest lesion of each patient that was visible in all sequences.

Statistical Analysis

Differences in lesion number were calculated with the Wilcoxon signed rank test, and differences in the contrast-to-noise ratio were analyzed with a 2-sided Student *t* test for paired samples. The interobserver agreement was calculated with the Lin concordance (concordance correlation coefficient) by using the service of National Institute of Water and Atmospheric Research (http://services.niwa.co.nz/services/statistical/concordance). Significant differences were defined by $P < .05$ for the whole study.

RESULTS

In conformity with previous studies, active contrast-enhancing lesions appeared hypointense on postcontrast DIR,[15,16] and, consequently, hyperintense in subtraction images (precontrast minus postcontrast, Fig 1). Contrary to T1-weighted subtraction images, DIR subtraction images demonstrate only little or no contrast enhancement of blood vessels; thus, differentiation between a contrast-enhancing lesion and surrounding enhancing vessels is more difficult in T1WI, and lesion-to-background contrast appears higher in DIR subtraction images (Fig 2).

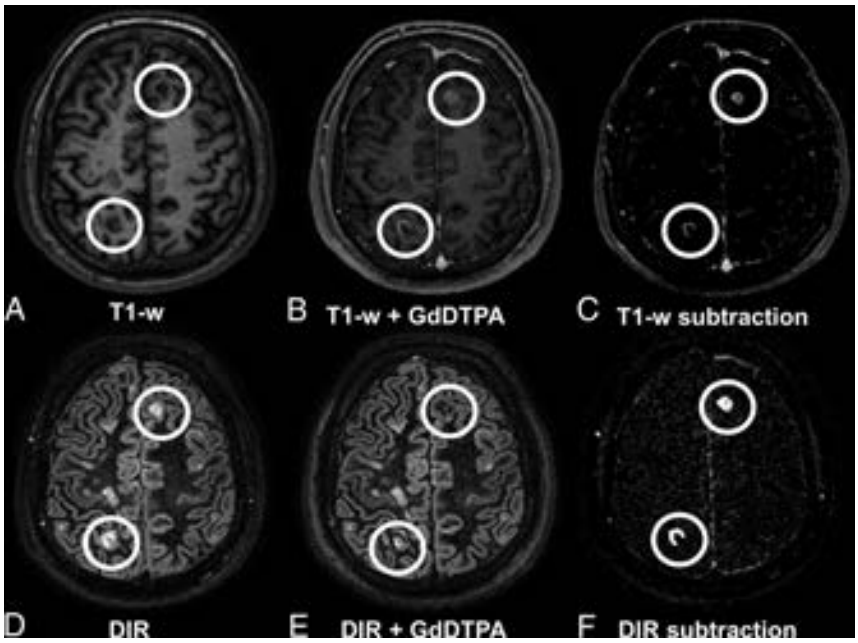

FIG 1. A 32-year-old male patient with relapsing-remitting MS with several lesions, including 2 contrast-enhancing juxta-/intracortical lesions in the left frontal and right parietal areas. Upper row (*A–C*): T1WI; lower row (*D–F*): DIR images with *A* and *D* being precontrast; *B* and *E*, postcontrast; and *C* and *F*, subtraction images. Enhancing lesions appear hypointense on postcontrast DIR and are visible in subtraction images. Note the high contrast of the lesions in the DIR subtraction image (*F*) compared with T1WI subtraction image (*C*).

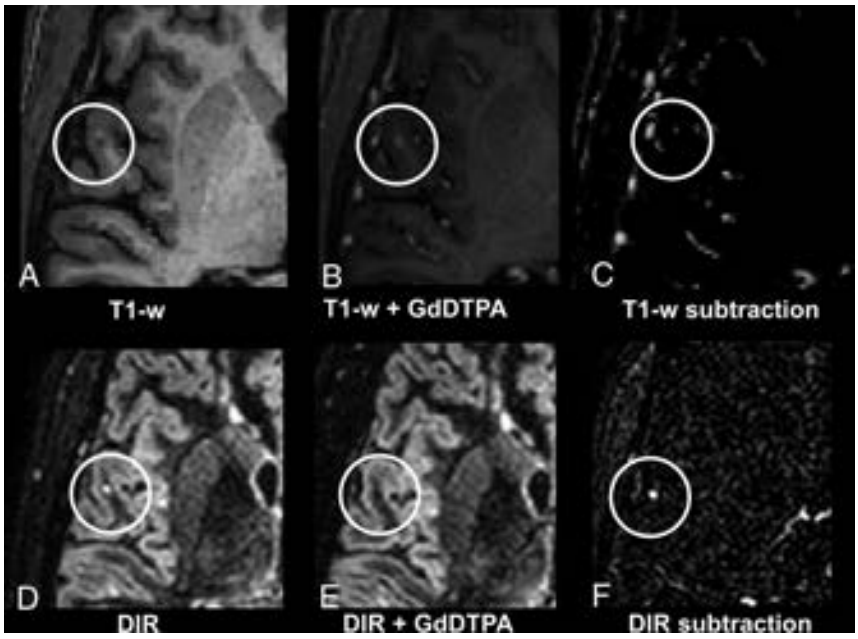

FIG 2. A 32-year-old male patient with relapsing-remitting MS. Upper row (*A–C*): T1WI; lower row (*D–F*): DIR images with *A* and *D* being precontrast; *B* and *E*, postcontrast; and *C* and *F*, subtraction images. Note the small juxtacortical lesion that is substantially more detectable in the DIR subtraction image (*F*) compared with the T1WI subtraction image (*C*). Contrary to DIR subtraction (*F*), in T1WI subtraction images (*C*), some contrast-enhancing vessels are visible near the lesion; thus, differentiation between an active contrast-enhancing lesion and surrounding enhancing vessels is difficult.

Lesion Count

Altogether, 16% more contrast-enhancing lesions could be detected in DIR images compared with T1WI (214 versus 185, $P = .007$). On average, 5 contrast-enhancing lesions per patient were detectable in DIR compared with 4 lesions per patient on conventional T1WI (range: 0–42 [DIR], 0–34 [T1WI]; mean: 4.8 ± 9.9 [DIR], 4.1 ± 8.9 [T1WI]). No lesion detected on T1WI was missed on DIR.

Of the 29 lesions missed on T1WI, 15 lesions were located juxtacortically; 5, periventricularly; 4, in the deep white matter supratentorially; and 5, infratentorially (2 cortically and 3 in the white matter). In Figs 2 and 3, examples of small juxtacortical lesions that can easily be missed in T1WI are shown.

In T1WI, 4 hyperintense signals in the brain tissue had been counted as lesions, though they had been classified as pulse artifacts after consulting the other available sequences in the context of the consensus reading (Fig 4). None of the hyperintense signal alterations in the DIR images were misdiagnosed.

The concordance between both radiologists was almost perfect, with slightly higher concordance for the DIR images (concordance correlation coefficient, $\rho_c = 0.94$ for T1WI and $\rho_c = 0.98$ for DIR).

Contrast-to-Noise Ratio

The contrast-to-noise ratio was significantly higher for DIR subtraction images (14.3 ± 5.5) compared with T1-weighted subtraction images (6.3 ± 7.1), postcontrast T1WI (1.7 ± 0.9), and postcontrast DIR (0.2 ± 0.5), respectively ($P < .001$).

DISCUSSION

In our study, we could show that pre- and postcontrast 3D DIR enables the detection of contrast-enhancing lesions in MS in the brain with higher sensitivity compared with pre- and postcontrast 3D T1WI. The total number of contrast-enhancing lesions found on DIR was significantly higher than those found on conventional T1WI, especially for small lesions in juxtacortical/intracortical localizations. Hence, our results suggest that DIR is not only superior to conventional T2-weighted sequences with regard to detection of cortical and WM lesions but may also constitute an alternative for T1-weighted contrast-enhanced sequences.

Several studies could show that the postcontrast fluid-attenuated inversion recovery sequence was useful for the detection of subtle enhancement due to blood-brain barrier dysfunc-

tion.[13,14,18] Because FLAIR and DIR differ only in an additional inversion recovery pulse in DIR—for the suppression of normal white matter—it is supposed that DIR is useful for the detection of contrast enhancement of MS lesions as well.

In fact, because it was discussed in a previous study that a single DIR sequence may be considered appropriate for MS monitoring,[19] the approach presented in this study could contribute to a minimally time-consuming MR imaging protocol, including the acquisition of postgadolinium images, with only DIR pre- and postcontrast (approximately a 12-minute protocol). On the other hand, such short protocols could have limited sensitivity for treatment-associated complications such as progressive multifocal leukoencephalopathy; therefore, further studies are necessary to analyze the sensitivity of DIR regarding opportunistic diseases. Furthermore, the T1WI sequence enables the quantification of brain atrophy that might occur in advanced stages of MS; however, this is actually not recommended in clinical routine because small changes might contribute to strong errors with a sensitivity of 67% and a specificity of 80%.[20] Still, because DIR sequences are more often included in routine MR imaging protocols for the assessment of MS, adding another DIR sequence after administration of a GBCA would be a notable time benefit if one decides to omit pre- and postcontrast T1WI.

We acknowledge limitations of our study. Most important, postcontrast DIR was always acquired after the acquisition of the T1WI sequence and thus delayed (6 minutes). It is well-known that the sensitivity of postcontrast images increases with the length of delay after administration of GBCAs.[12] Therefore, this increase might contribute to a bias toward a higher lesion count and contrast in DIR. However, the study of

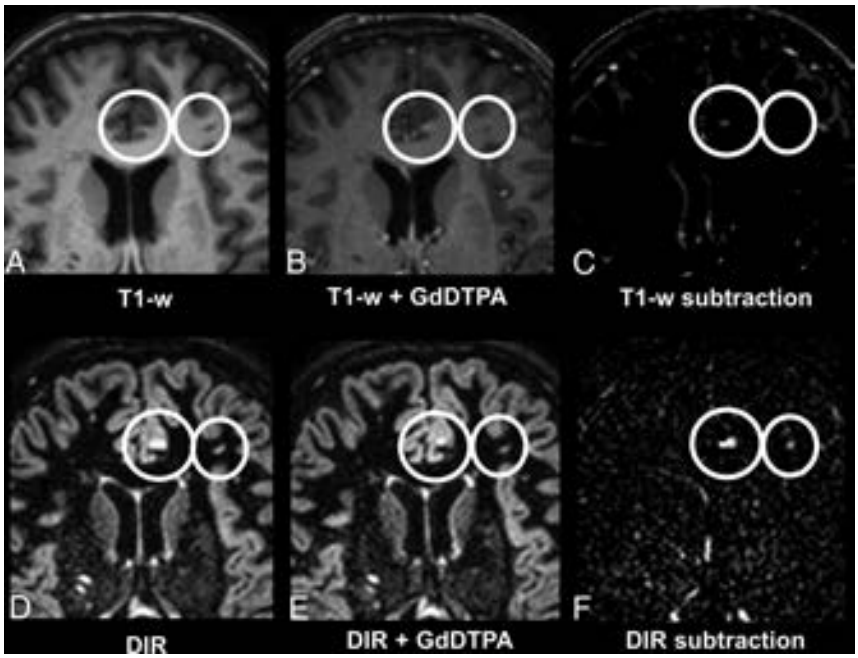

FIG 3. A 46-year-old female patient with relapsing-remitting MS. Upper row (*A–C*): T1WI; lower row (*D–F*): DIR images with *A* and *D* being precontrast; *B* and *E*, postcontrast; and *C* and *F*, subtraction images. Note that the small juxtacortical lesion is more detectable on the DIR subtraction image (*F*) compared with the T1-weighted subtraction image (*C*).

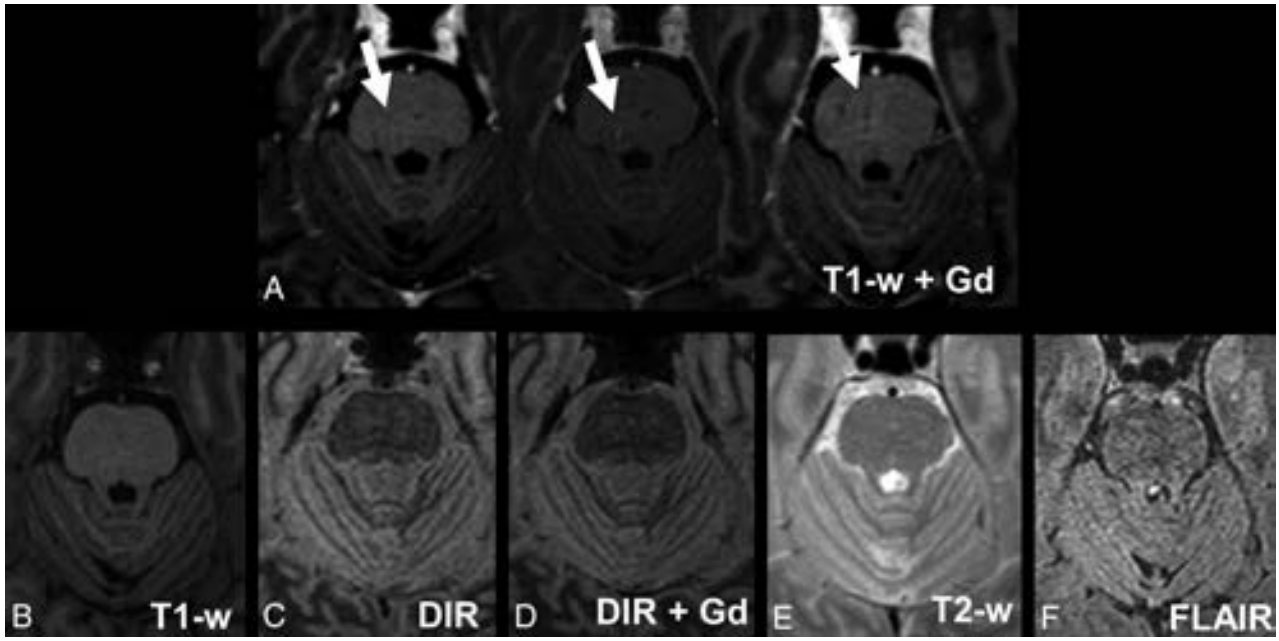

FIG 4. Pulsation artifacts detected in T1WI postcontrast. Images of a 52-year-old male patient with relapsing-remitting MS. Upper row: *A*, 3 consecutive postcontrast T1-weighted images; lower row: *B*, T1-weighted precontrast image. *C*, DIR precontrast image. *D*, DIR postcontrast image; *E*, T2WI; *F*, FLAIR. Note the small hyperintense signal alterations in the middle of the pons that are only visible on 3 consecutive T1-weighted postcontrast images and not on the other images.

Uysal et al[12] concluded that a delay of >5 minutes leads to only a minor additional benefit; they found no significant difference in lesion numbers with T1WI after 5 or 10 minutes, comparable with the timing of our study (6 and 12 minutes). A second limitation is that subtraction images have motion artifacts; thus, interpretation could be difficult if not impossible, in particular with the standard software of the main MR imaging vendors.

CONCLUSIONS

This study demonstrates that the DIR sequence, which has been shown to improve the visibility of MS-typical lesions in the brain compared with T2WI or FLAIR sequences, also enables detectability and visibility of MS-typical contrast-enhancing lesions in pre- and postcontrast DIR images at least equal to the detection with standard 3D T1WI in the brain. Further studies are necessary to evaluate whether subtraction DIR could be an alternative to T1WI or even reduce the protocol to only pre- and postcontrast DIR.

Disclosures: Jan S. Kirschke—*UNRELATED*: *Grants/Grants Pending*: European Research Council, Deutsche Forschungsgemeinschaft*; *Payment for Lectures Including Service on Speakers Bureaus*: Philips Healthcare. Muna-Miriam Hoshi—*UNRELATED*: *Travel/Accommodations/Meeting Expenses Unrelated to Activities Listed*: Bayer HealthCare, *Comments*: travel support for the annual meeting of the German Neurologic Society 2016. Claus Zimmer—*UNRELATED*: *Other*: C. Zimmer has served on scientific advisory boards for Philips Healthcare and Bayer Schering Pharma, serves as coeditor on the Advisory Board of Clinical Neuroradiology, has received speaker honoraria from Bayer Schering Pharma and Philips Healthcare, and has received research support and investigator fees for clinical studies from Biogen Idec, Quintiles, Merck Sharp & Dohme, Boehringer Ingelheim, Inventiv Health Clinical UK Ltd, Advance Corporation, BrainsGate, Pfizer, Bayer Schering Pharma, Novartis, Roche, Servier, Penumbra, WCT GmbH, Syngis, SSS International Clinical Research, PPD Germany GmbH, Worldwide Clinical Trials Ltd, phenox, Covidien, Actelion, Medivation, Medtronic, Harrison Clinical Research, Concentric, Penumbra, PHARMTRACE, Reverse Medical Corp, Premier Research Germany Ltd, Surpass Medical Ltd, and GlaxoSmithKline.* *Money paid to the institution.

REFERENCES

1. Redpath TW, Smith FW. **Imaging gray brain matter with a double-inversion pulse sequence to suppress CSF and white matter signals.** *MAGMA* 1994;2:451–55 CrossRef
2. Redpath TW, Smith FW. **Technical note: use of a double inversion recovery pulse sequence to image selectively grey or white brain matter.** *Br J Radiol* 1994;67:1258–63 CrossRef Medline
3. Vural G, Keklikoğlu HD, Temel Ş, et al. **Comparison of double inversion recovery and conventional magnetic resonance brain imaging in patients with multiple sclerosis and relations with disease disability.** *Neuroradiol J* 2013;26:133–42 CrossRef Medline
4. Wattjes MP, Lutterbey GG, Gieseke J, et al. **Double inversion recovery brain imaging at 3T: diagnostic value in the detection of multiple sclerosis lesions.** *AJNR Am J Neuroradiol* 2007;28:54–59 Medline
5. Seewann A, Kooi EJ, Roosendaal SD, et al. **Postmortem verification of MS cortical lesion detection with 3D DIR.** *Neurology* 2012;78:302–08 CrossRef Medline
6. Geurts JJ, Pouwels PJ, Uitdehaag BM, et al. **Intracortical lesions in multiple sclerosis: improved detection with 3D double inversion-recovery MR imaging.** *Radiology* 2005;236:254–60 CrossRef Medline
7. Calabrese M, De Stefano N, Atzori M, et al. **Detection of cortical inflammatory lesions by double inversion recovery magnetic resonance imaging in patients with multiple sclerosis.** *Arch Neurol* 2007;64:1416–22 CrossRef Medline
8. Simon B, Schmidt S, Lukas C, et al. **Improved in vivo detection of cortical lesions in multiple sclerosis using double inversion recovery MR imaging at 3 Tesla.** *Eur Radiol* 2010;20:1675–83 CrossRef Medline
9. Riederer I, Karampinos DC, Settles M, et al. **Double inversion recovery sequence of the cervical spinal cord in multiple sclerosis and related inflammatory diseases.** *AJNR Am J Neuroradiol* 2015;36:219–25 CrossRef Medline
10. Polman CH, Reingold SC, Banwell B, et al. **Diagnostic criteria for multiple sclerosis: 2010 revisions to the McDonald criteria.** *Ann Neurol* 2011;69:292–302 CrossRef Medline
11. Filippi M, Rocca MA, Ciccarelli O, et al; MAGNIMS Study Group. **MRI criteria for the diagnosis of multiple sclerosis: MAGNIMS consensus guidelines.** *Lancet Neurol* 2016;15:292–303 CrossRef Medline
12. Uysal E, Erturk SM, Yildirim H, et al. **Sensitivity of immediate and delayed gadolinium-enhanced MRI after injection of 0.5 M and 1.0 M gadolinium chelates for detecting multiple sclerosis lesions.** *AJR Am J Roentgenol* 2007;188:697–702 CrossRef Medline
13. Bonzano L, Roccatagliata L, Levrero F, et al. **In vitro investigation of poor cerebrospinal fluid suppression on fluid-attenuated inversion recovery images in the presence of a gadolinium-based contrast agent.** *Magn Reson Med* 2008;60:220–23 CrossRef Medline
14. Mathews VP, Caldemeyer KS, Lowe MJ, et al. **Brain: gadolinium-enhanced fast fluid-attenuated inversion-recovery MR imaging.** *Radiology* 1999;211:257–63 CrossRef Medline
15. Harris RJ, Cloughesy TF, Pope WB, et al. **Pre- and post-contrast three-dimensional double inversion-recovery MRI in human glioblastoma.** *J Neurooncol* 2013;112:257–66 CrossRef Medline
16. Hodel J, Badr S, Outteryck O, et al. **Altered signal intensity of active enhancing inflammatory lesions using post-contrast double inversion recovery MR sequence.** *Eur Radiol* 2017;27:637–41 CrossRef Medline
17. Yushkevich PA, Piven J, Hazlett HC, et al. **User-guided 3D active contour segmentation of anatomical structures: significantly improved efficiency and reliability.** *Neuroimage* 2006;31:1116–28 CrossRef Medline
18. Eisele P, Griebe M, Szabo K, et al. **Investigation of leptomeningeal enhancement in MS: a postcontrast FLAIR MRI study.** *Neurology* 2015;84:770–75 CrossRef Medline
19. Khangure SR, Khangure MS. **MR imaging in multiple sclerosis: the accuracy of 3D double inversion recovery at 3 Tesla and the potential for single sequence imaging.** *Neuroradiol J* 2011;24:92–99 CrossRef Medline
20. De Stefano N, Stromillo ML, Giorgio A, et al. **Establishing pathological cut-offs of brain atrophy rates in multiple sclerosis.** *J Neurol Neurosurg Psychiatry* 2016;87:93–99 CrossRef Medline

Dual-Energy CT in Enhancing Subdural Effusions that Masquerade as Subdural Hematomas: Diagnosis with Virtual High-Monochromatic (190-keV) Images

U.K. Bodanapally, D. Dreizin, G. Issa, K.L. Archer-Arroyo, K. Sudini, and T.R. Fleiter

ABSTRACT

BACKGROUND AND PURPOSE: Extravasation of iodinated contrast into subdural space following contrast-enhanced radiographic studies results in hyperdense subdural effusions, which can be mistaken as acute subdural hematomas on follow-up noncontrast head CTs. Our aim was to identify the factors associated with contrast-enhancing subdural effusion, characterize diffusion and washout kinetics of iodine in enhancing subdural effusion, and assess the utility of dual-energy CT in differentiating enhancing subdural effusion from subdural hematoma.

MATERIALS AND METHODS: We retrospectively analyzed follow-up head dual-energy CT studies in 423 patients with polytrauma who had undergone contrast-enhanced whole-body CT. Twenty-four patients with enhancing subdural effusion composed the study group, and 24 randomly selected patients with subdural hematoma were enrolled in the comparison group. Postprocessing with syngo.via was performed to determine the diffusion and washout kinetics of iodine. The sensitivity and specificity of dual-energy CT for the diagnosis of enhancing subdural effusion were determined with 120-kV, virtual monochromatic energy (190-keV) and virtual noncontrast images.

RESULTS: Patients with enhancing subdural effusion were significantly older (mean, 69 years; 95% CI, 60–78 years; $P < .001$) and had a higher incidence of intracranial hemorrhage ($P = .001$). Peak iodine concentration in enhancing subdural effusions was reached within the first 8 hours of contrast administration with a mean of 0.98 mg/mL (95% CI, 0.81–1.13 mg/mL), and complete washout was achieved at 38 hours. For the presence of a hyperdense subdural collection on 120-kV images with a loss of hyperattenuation on 190-keV and virtual noncontrast images, when considered as a true-positive for enhancing subdural effusion, the sensitivity was 100% (95% CI, 85.75%–100%) and the specificity was 91.67% (95% CI, 73%–99%).

CONCLUSIONS: Dual-energy CT has a high sensitivity and specificity in differentiating enhancing subdural effusion from subdural hematoma. Hence, dual-energy CT has a potential to obviate follow-up studies.

ABBREVIATIONS: DECT = dual-energy CT; ESDE = enhancing subdural effusion; HU = Hounsfield unit; SDH = subdural hematoma; SECT = single-energy CT; VNC = virtual noncontrast

Diffusion of contrast material into the subdural space following intravascular contrast administration can result in hyperdense enhancing subdural effusions (ESDEs) on follow-up noncontrast head CTs.[1,2] These effusions can be mistaken for subdural hematomas (SDHs).[1,2] Three case reports have previously described ESDEs, all following intra-arterial contrast administration during conventional angiography with resolution documented on short-term follow-up CT examinations.[1,2]

We have frequently observed ESDEs in our busy level 1 trauma center, where patients usually undergo admission contrast-enhanced whole-body CT followed by serial noncontrast head CTs for documented or suspected traumatic brain injury. Because ESDEs can be mistaken for SDHs, lack of awareness of this entity can potentially result in needless delays in instituting thromboprophylaxis and trigger unnecessary follow-up CT studies. Patients with polytrauma usually require thromboprophylaxis to prevent deep vein thrombosis. A number of authors have posited a mandatory 24- to 72-hour period of documented stability of intracranial bleeds before beginning thromboprophylaxis.[3-6] Hence, early discrimination of SDHs from ESDEs has important clinical implications.

Received March 12, 2017; accepted after revision May 25.

From the Department of Diagnostic Radiology and Nuclear Medicine (U.K.B., D.D., G.I., K.L.A.-A., T.R.F.), R Adams Cowley Shock Trauma Center, University of Maryland Medical Center, Baltimore, Maryland; and Department of Environmental Health Sciences (K.S.), Bloomberg School of Public Health, Johns Hopkins University, Baltimore, Maryland.

Please address correspondence to Thorsten R. Fleiter, MD, 22 S. Greene St, Department of Radiology, University of Maryland Medical Center, Baltimore, MD 21201; e-mail: tfleiter@gmail.com

Indicates article with supplemental on-line photos.

http://dx.doi.org/10.3174/ajnr.A5318

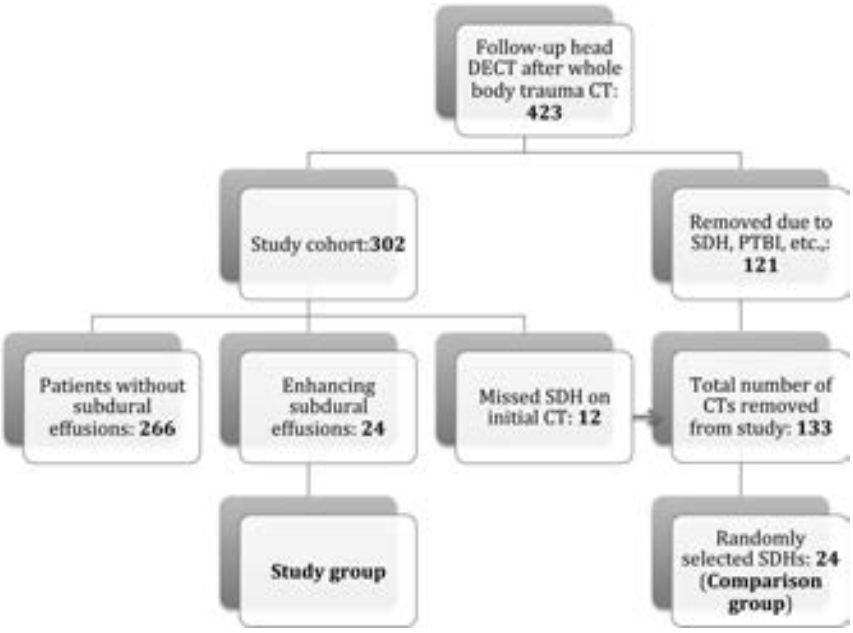

FIG 1. Flowchart shows the patient-selection process. PTBI indicates penetrating traumatic brain injury.

On single-energy CT (SECT), the hyperattenuation caused by hemorrhage and contrast medium is difficult to distinguish due to overlapping Hounsfield units (HU).[1,2,7,8] Present recommendations for differentiating SDH from ESDE involve serial follow-up imaging.[1,2] ESDEs shows rapid washout of contrast, hence decreasing hyperattenuation, while SDH retains hyperattenuation from blood for 2–3 weeks.[1,2,9] Dual-energy CT (DECT) can potentially obviate follow-up scans by differentiating iodine from hemorrhage.[7,10,11] Iodine overlay maps and virtual noncontrast (VNC) images can discriminate contrast and hemorrhage with a high degree of accuracy.[11] If VNC images can be used to reliably identify hematoma, even in the presence of iodine, differentiation between ESDEs and SDHs can be a simple and straightforward task. The utility of DECT in diagnosing ESDE was recently demonstrated in a case in which a subdural hyperdense collection that developed after endovascular treatment of an intracranial aneurysm was hyperdense on iodine-overlay images and hypodense on VNC images.[12] This evidence suggests that DECT may play a vital role in providing an early definitive diagnosis without the need for follow-up CT studies to document resolution of ESDEs.

The purpose of this study was to identify the factors associated with ESDE, characterize the diffusion and washout kinetics of iodine in ESDE, and assess the utility of DECT in differentiating ESDE from SDH.

MATERIALS AND METHODS

This retrospective study was Health Insurance Portability and Accountability Act–compliant, and permission was obtained from our institutional review board. Informed consent was waived. The study was conducted at a high-volume level 1 trauma center. The inclusion criteria were the following: 1) a history of blunt trauma with acquisition of contrast-enhanced whole-body CT at the time of admission between May 15, 2016, and November 10, 2016; 2) acquisition of follow-up noncontrast DECT of the head within 72 hours of the admission CT; 3) a radiology report describing a new SDH or hyperdense subdural collection on follow-up head CT; and 4) patients 18 years of age or older. Patients were excluded for the following reasons: 1) There was an SDH on the admission CT; 2) the mechanism of injury was penetrating rather than blunt trauma; and 3) craniectomy, craniotomy, ventricular drain, or pressure-monitoring-device placement was performed, violating the integrity of the meninges.

Subjects

A search of our Radiology Information System data base from the designated time period yielded 423 patients with at least 1 follow-up head CT performed with DECT within 72 hours of the initial study. At our institution, patients with intracranial injuries, persistent altered mental status, and on anticoagulation without intracranial injuries tend to be evaluated by follow-up head CT, at the discretion of the neurosurgery team. A radiology resident reviewed the head CT reports from this patient cohort for specific data, which included type of intracranial bleed, age, sex, mechanism of injury, and list of interventional procedures. There were 121 patients with SDHs on the initial study or meningeal disruption caused by either penetrating head injuries or interventional procedures performed before a follow-up head DECT was obtained. These patients were excluded from the cohort. The mean age of the final cohort consisting of 302 patients was 47 years (95% CI, 45–50 years), with 211 men and 91 women. The reports identified 36 patients with new SDHs or hyperdense subdural collections on the first follow-up study. All head CT studies of these 36 patients were further reviewed by a radiologist (reviewer R1) with 8 years of experience to exclude patients with missed SDHs on initial CT as well as hyperdense subdural collections that failed to completely washout on subsequent studies.

Hyperdense subdural collections that failed to show complete washout of contrast were considered enhancing SDHs. Enhancing SDHs show partial washout with clearance of the density contributed by iodine and retain the density from blood on follow-up studies. Twelve such patients with SDHs were excluded from the study group. The remaining 24 patients who had ESDEs on follow-up with subsequent washout of contrast constituted the study group. A 75-year-old woman with posttraumatic SAH developed ESDE after infusion of 250 mL of contrast media (iohexol, Omnipaque 240 and Omnipaque 300; GE Healthcare, Piscataway, New Jersey) for cerebral angiography, but not after whole-body CT with 100 mL of Omnipaque 300, and was therefore excluded from the study. Figure 1 shows the patient-selection flowchart. An equal number of patients with SDH on

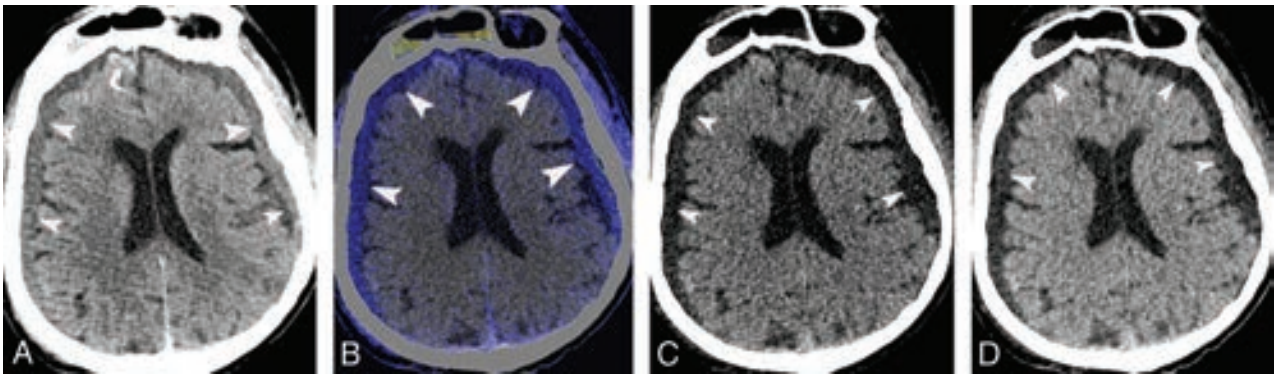

FIG 2. A 75-year-old woman who developed bilateral enhancing subdural effusion on a follow-up study obtained 11 hours after contrast infusion. Axial 120-kV image shows hyperdense subdural effusions (*arrowheads*, *A*) and right frontal subarachnoid hemorrhage (*curved arrow*, *B*). Iodine-overlay image shows contrast-stained subdural effusions (*arrowheads*). Virtual high-monochromatic (190-keV) (*C*) and virtual noncontrast (*D*) images show hypoattenuation (*arrowheads*) in the fluid.

follow-up DECT were randomly selected from our data base as a comparison group to measure the sensitivity and specificity of DECT in diagnosing ESDE.

Reference Standard

The presence of ESDE was determined with initial and follow-up images. Absence of SDH on the initial study, evolution of new hyperdense subdural collection on first follow-up CT (Fig 2*A* and On-line Fig 1*A*), and subsequent washout of hyperattenuation in follow-up studies were used as evidence for ESDE.[1,2,12]

Imaging Technique and Contrast Medium Injection

Admission whole-body CT examinations were performed on a DECT (Somatom Force; Siemens) or 64-channel SECT scanner (Brilliance; Philips Healthcare, Best, the Netherlands). Whole-body CT involves a noncontrast head CT followed by contrast-enhanced CT of the neck, chest, abdomen, and pelvis. The studies were performed after injection of 100 mL of iodinated contrast media (Omnipaque 350) with a split bolus, with 60 mL injected at 5 mL/s and 40 mL injected at 4 mL/s. The contrast injection was followed by a 50-mL saline injection at 4 mL/s.

Follow-up head CT studies were performed with a DECT or SECT scanner, depending on scanner availability. DECT images were obtained with the x-ray tubes at 80 kV and Sn150 kV. "Sn" denotes the use of additional tin filter that increases the mean photon energy of the respective spectrum. Scan parameters were as follows: rotation time, 0.5 seconds; pitch, 0.55. The reference milliampere-second was 273 mAs for the Sn150-kV and 410 mAs for the 80-kV tube. Original dual-energy datasets were reconstructed with an increment of 1 mm and section thicknesses of 1- and 5-mm for the 120-kV-equivalent mixed DECT images with an adaptive iterative reconstruction algorithm (ADMIRE, Siemens) with strength levels of 2 and 5, respectively. Automatic tube current modulation (CARE Dose4D; Siemens) was used in all patients. The mean CT dose index volume and dose-length product were 31.45 ± 2.95 mGy and 609.62 ± 76.79 mGy × cm, respectively.

Image Analysis of DECT

For measuring the diffusion and washout kinetics of iodine into the subdural effusions, all of the follow-up dual-energy datasets for head CTs from each patient, performed within 72 hours of the admission scan, were transferred to a postprocessing workstation (syngo.via, version VB10B; Siemens) to quantify iodine in the subdural space. If we included the first follow-up DECT data from the 24 patients, there were 47 follow-up DECT datasets, which were analyzed for evaluating iodine diffusion and washout kinetics. The maximum number of DECT studies from each patient evaluated was 3. Many of the patients had a combination of DECT and SECT follow-up studies. In such patients, DECT datasets were used for evaluating iodine diffusion and washout kinetics, while all the follow-up studies (both DECT and SECT) were used to evaluate subsequent washout of hyperattenuation to confirm the diagnosis of ESDE. A modified brain hemorrhage application was used, with the bone beam-hardening box checked and changes to the standard parameters in the syngo.via dual-energy configuration of gray-scale (window level = 31; width = 54) and dual-energy (window level = 28; width = 66), was made for the color look-up table. Similarly, the material decomposition algorithm was modified into hemorrhage, 80/75 HU (80 kV/Sn150 kV); CSF, 16/5 HU (80 kV/Sn150 kV); and iodine, with the relative contrast medium adjusted to a value of 3.46.

Reviewer R1 performed postprocessing of the data. From the original low- and high-kilovolt datasets, a VNC series and functional and quantitative iodine series were derived. In the functional images, the presence of iodine was indicated by blue in a special color-coded look-up table, with intensity corresponding to the relative concentration of iodine (Fig 2*B*). The software allows quantitative analysis of ROIs. After selection on the iodine image, the software calculated the concentration of iodine in milligrams/milliliter and the ROI size in square millimeters.

This algorithm also calculates the attenuation (HU) values from VNC and virtual 120-kV images and iodine-related attenuation. On each side of the cerebral convexities, 3 different ROIs of 0.2 cm^2 were used at different image sections. To promote uniformity in the measurements, we used approximately the same anatomic locations for the ROIs on sequential follow-up CT studies. The reviewer was blinded to the color-overlay images to prevent ROI placement over the maximum concentration of contrast medium for measuring the respective values. From the different

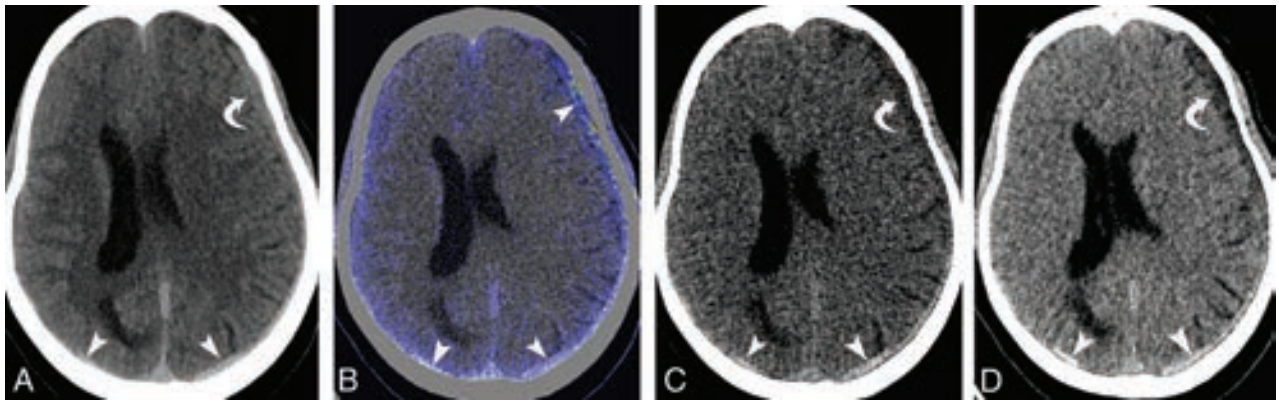

FIG 3. A 55-year-old man with left cerebral convexity and right occipital acute subdural hematomas with enhancement of a left subdural hematoma on a follow-up study obtained 6 hours after contrast infusion. Follow-up axial 120-kV (*A*) and iodine-overlay (*B*) images show hyperdense and contrast-stained subdural hematomas, respectively (*arrowheads*). Virtual high-monochromatic (190-keV) (*C*) and virtual noncontrast (*D*) images show hyperattenuation corresponding to the hematoma over the occipital lobes and left temporal lobe (*arrowheads*) and hypoattenuation corresponding to the enhancing component of hematoma over the left frontal lobe (*curved arrow*).

Table 1: Comparison of DECT findings differentiating ESDE from SDH

Diagnosis	Traditional Mixed (120-kV) Images	High-Monochromatic (190-keV) Images	VNC Images	Iodine-Overlay Images
ESDE	Hyperdense	Hypodense	Hypodense	Positive
SDH	Hyperdense	Hyperdense	Hyperdense	Positive/negative

ROIs, the mean iodine concentration and VNC-, mixed 120-kV-, and iodine-related attenuation were calculated. At the same time, the maximum thickness of the effusion was measured.

Two experienced radiologists performed DECT image analysis, reviewer R2 with 8 years and reviewer R3 with 5 years of experience. For each of the first follow-up studies performed on the DECT, axial 120-kV (standard gray-scale), 190-keV (virtual monochromatic energy), and VNC images created on a workstation were loaded onto a dedicated work list. Apart from the VNC images, we used 190-keV images due to the theoretic ability to achieve iodine removal because the energy used is far away from the *k*-edge of iodine, thus greatly decreasing the iodine attenuation to negligible values. Blinded to the initial and follow-up head CT findings, each radiologist reviewed the images, interpreting the 120-kV and 190-keV images separately. The studies were assessed for the presence or absence of hyperdense (relative to CSF) subdural collections on each set of images and were scored as nominal variables. In the final step, the VNC images were given as the third set, and reviewers were asked to score the density of subdural collections in a similar fashion. The presence of a hyperdense subdural collection on 120-kV images with loss of hyperattenuation on 190-keV and VNC images is considered a true-positive for ESDE (Fig 2 and On-line Fig 1), while hyperattenuation on all the 3 sets is considered SDH (Fig 3 and On-line Fig 2). Discrepancies between the assessments of the 2 reviewers were resolved by adjudication by another reviewer (R4 with 10 years of experience). Criteria used to differentiate ESDE from SDH are given in Table 1.

Statistical Analysis

Statistical analysis was performed by K.S., with statistical software (JMP 12; SAS Institute, Cary, North Carolina). Differences between the ESDE group and those without were determined with odds ratios and χ^2 and Wilcoxon tests. The strongest independent associations were determined by regression analysis. One-way analysis was used to determine the iodine concentrations, and contingency tables were used to determine sensitivity and specificity. κ statistics were used to test interobserver reliability in assessing CT variables by the radiologists and to test the agreement between nominal scores that were derived from the density of subdural collections on 190-keV and VNC images.

RESULTS

Among the 24 patients with ESDE, there were 18 men and 6 women. The incidence of ESDE in patients with trauma with follow-up head CT was 8.2%. The mean age of the patients with ESDE was 69 years (95% CI, 60–78 years). Patients with ESDE were significantly older than those without ($P < .001$), with an incidence of 13% in patients older than 50 years of age. There were 12 patients with bilateral and 12 with unilateral ESDEs, with a mean thickness of 4.2 mm (95% CI, 3.7–4.8 mm). The ESDEs mainly involved the frontal, parietal, and temporal lobes. None of the patients had mass effect or midline shift.

Table 2 shows the differences in the CT findings between patients with ESDE and those without. There was a higher association of ESDE with intracranial hemorrhage ($P = .001$), specifically with subarachnoid hemorrhage ($P = .002$). There was no association with cerebral contusions ($P = 0.97$) or CT evidence of diffuse axonal injury ($P = 0.33$). None of the patients with ESDE had epidural hematoma. According to stepwise logistic regression analysis, age was the most reliable predictor of ESDE ($P < .001$), followed by the presence of intracranial hemorrhage ($P = .002$).

Diffusion and Washout Kinetics of Iodine

All 24 patients had their first DECT follow-up from 4 to 24 hours after whole-body CT (median, 7 hours; interquartile range, 4). The peak concentration of iodine in ESDEs was reached in the scans obtained within the first 8 hours of contrast administration, with a mean of 0.98 mg/mL (95% CI, 0.81–1.13 mg/mL). The mean value of iodine concentration was 0.71 (95% CI, 0.48–0.94 mg/mL) in the scans obtained between 8 and 16 hours, and 0.41 (95% CI, 0.16–0.67), between 16 and 38 hours, reflecting gradual

Table 2: CT findings in ESDE and the control groups

Finding	ESDE Group (No.) (*n* = 24)	Non-ESDE Group (No.) (*n* = 266)	Odds Ratio (95% CI)	*P* Value
SAH	16	94	3.7 (1.52–8.97)	.002
Contusions	7	79	0.98 (0.39–2.46)	.97
Diffuse axonal injury	2	11	2.12 (0.44–10.2)	.33
Normal CT findings	4	136	5.15 (1.7–15.5)	.001

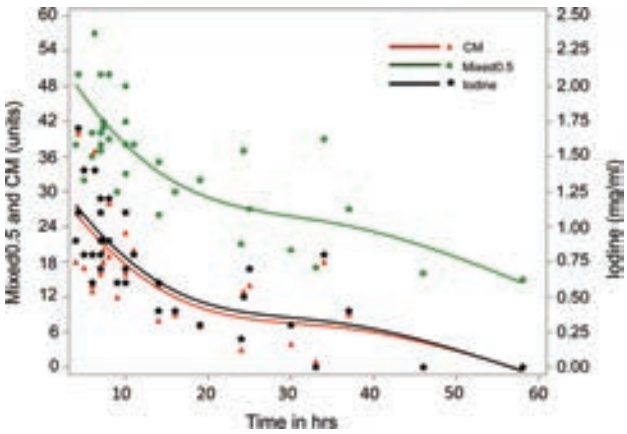

FIG 4. Time-concentration curve. Spline graph using penalized B-spline shows iodine (milligrams/milliliter), attenuation (HU) related to contrast media (CM), and mixed 120-kV (Mixed 0.5) images versus hours (hrs) after contrast administration.

washout. Complete washout was observed after 38 hours (Fig 4). The maximum concentration of iodine found in our group was 1.7 mg/mL on a study performed after 4.5 hours of contrast administration. None of the studies retained contrast beyond 38 hours. Iodine concentration and iodine-related attenuation had a correlation coefficient of 0.99 (95% CI, 0.98–0.99). The regression coefficient indicated that for every additional 0.1 mg/mL of iodine, the iodine-related attenuation increased by an average of 2.4 HU. The maximum attenuation reached in the subdural effusions was 67 HU (median, 35 HU; interquartile range, 16 HU) on mixed 120-kV images. The mean density of the subdural effusions as related to VNC images was found to be 19.98 HU (95% CI, 18.98–20.98 HU), corresponding to baseline attenuation of subdural effusion. Figure 4 shows the time-concentration curves of iodine with inclusion of attenuation related to contrast media and overall attenuation on mixed 120-kV images.

Specificity of Virtual High-Monochromatic Energy (190-keV) and VNC Images

All ESDEs were correctly interpreted as hyperdense subdural fluid on mixed 120-kV images and hypodense fluid on 190-keV and VNC images, because 190-keV and VNC images remove iodine. Twenty-two of the 24 SDHs were correctly interpreted as hyperattenuated subdural collections on 120-kV, 190-keV, and VNC images, and the remaining 2 studies were falsely interpreted as ESDE. Both of these were enhancing SDHs. The presence of a subdural collection on 120-kV images with loss of hyperattenuation on 190-keV images, when considered as true-positive for ESDE, had a sensitivity of 100% (95% CI, 85.75%–100%) and specificity of 91.67% (95% CI, 73%–99%). There was a perfect agreement ($\kappa = 1$) between 190-keV and VNC images with regard to the nominal scores that were derived to define the density of the subdural collection. There was almost perfect interobserver agreement between the 2 radiologists ($\kappa = 0.88$; 95% CI, 0.72–1).

DISCUSSION

We analyzed the factors associated with ESDE and the ability of DECT to discriminate ESDE from SDH in patients with trauma after whole-body CT. According to our results, patients with ESDE were significantly older ($P < .001$) and tended to have intracranial hemorrhage ($P = .001$). The results demonstrate that DECT can differentiate ESDE from SDH with high sensitivity and specificity.

Hyperattenuation caused by hemorrhage and contrast medium is difficult to discriminate on SECT because effusions can demonstrate varying densities.[1,2,7,8] Some patients with ESDE have very high densities (range, 97–200 HU) as opposed to blood (range, 28–82 HU; mean, 54 HU), and some have lower densities (35 HU), depending on the degree of iodine dilution in the effusion.[1,2,8] If the attenuation exceeds the value expected for blood, it can be assumed to have an iodine component, but this does not exclude an underlying SDH because contrast is known to diffuse into SDH (Fig 3 and On-line Fig 2).[7,13] Similarly, iodine overlay maps help in identifying contrast in subdural collections but do not differentiate ESDEs from enhancing SDHs (Fig 3*B*).[7,10] Hence, one has to rely on 190-keV or VNC images to identify a hematoma even when mixed with iodine (Fig 3*C*, -*D* and On-line Fig 2*C*, -*D*), to consistently differentiate enhancing SDH from ESDE.

Virtual high-monochromatic (190-keV) and VNC image reconstruction relies on the same measurement of attenuation differences in an ROI using 2 different effective x-ray spectra of a dual-energy scanner. The difference is that the percentage of the attenuation contributed by iodine in each voxel is subtracted or replaced in the VNC images but not in the virtual monochromatic images. Instead the attenuation contribution of the detected material is projected for a given kiloelectron volt in monochromatic images. However, the attenuation contribution of iodine is negligible at 190-keV and therefore should be comparable with the VNC approach of iodine subtraction or virtual replacement. (Fig 2*C*, -*D* and On-line Fig 1*C*, -*D*).[14,15] We have demonstrated that high-monochromatic images can be used in place of VNC images to identify ESDE after excluding iodine from the images. However, there were 2 SDHs that were falsely interpreted as ESDEs. Both of these were enhancing SDHs with a large enhancing component and a smaller SDH component (Fig 3*C*, -*D*). The reviewers overlooked the hematoma component on both 190-keV and VNC images and misinterpreted them. Hence, we recommend radiologists considering an enhancing SDH before diagnosing ESDE and carefully reviewing the 190-keV and VNC images for possible underlying small SDHs.

The reported cases by Zamora and Lin[1] and Rennert and Hamer[2] followed intra-arterial administration of contrast during angiography with use of 260 mL of Imeron 300 (iopamidol; Bracco, Milan, Italy) in 1 patient.[1,2] Our patients differ from those in these previous reports because the contrast was administered intravenously at moderate doses (100 mL). Zamora and Lin did

not mention the amount of contrast administered in their 2 patients during cerebral angiography; however, we presume that the contrast used was significantly higher than that of our patients. The reports had 2 patients with a high attenuation of 97 and 200 HU in the effusion and 1 patient with an attenuation of 35 HU, respectively. However, none of our effusions reached the high attenuation previously reported. The maximum attenuation reached in our subjects was 67 HU (median, 35 HU; Q_3–Q_1, 16 HU). The differences may be due to the lower dose of contrast used in our patients and also the intravenous route of administration.

Rennert and Hamer[2] proposed that the intra-arterial route of administration was a predisposing factor contributing to ESDEs. We believe that the route of contrast administration likely plays a role along with the amount of contrast used because 1 of our patients developed ESDE after intra-arterial administration of a large dose of contrast (250 mL) during cerebral angiography, but not after intravenous administration of a moderate contrast dose (100 mL) during whole-body CT. Zamora and Lin[1] proposed that the presence of SAH increases dural endothelial permeability with extravasation of contrast material by triggering a neuroinflammatory response, while Rennert and Hamer ascribed the increase in permeability to osmotic disruption caused by hyperosmolar contrast media. Our results suggest that diffusion of contrast into the subdural space is unlikely to be solely related to the inflammatory theory because this phenomenon is also seen in patients without SAH and in patients without any demonstrable intracranial abnormalities. Furthermore, osmotic disruption may not be an essential element of ESDE development because the capillaries of the dura are naturally fenestrated and allow free passage of contrast media into the dural extracellular space, depending on the hydrostatic pressure, producing enhancement.[16]

On the basis of the results of our study, with age being the strongest predictor, we propose an alternate theory: We postulate that the pathophysiology of ESDE follows that of patients with intracranial hypotension. According to the Monroe-Kellie rule, intracranial volume is constant and is represented by the sum volume of brain substance, CSF, and blood.[17,18] Therefore, with cerebral volume loss associated with advanced age, there will be a compensatory increase in CSF and intracranial blood volume. The increase in intracranial blood volume manifests in the form of dural vasodilation, greater concentration of contrast in dural vasculature, and subdural effusions.[17-21] Dural venous engorgement causes leakage of intravascular, nonhemorrhagic fluid across a hydrostatic pressure gradient into the subdural space, carrying contrast with it because the dural vasculature lacks tight junctions, thus not contributing to the blood-brain barrier.[17] Similar to effusions in intracranial hypotension, enhancing effusions involve frontoparietal areas and are thin (4.2 mm; 95% CI, 3.7–4.8 mm) without mass effect on the brain.[20,22] The intrinsic high density of this effusion (mean, 19.98 HU; 95% CI, 18.98–20.98 HU) on VNC images may be related to the concentration of protein in the fluid, as is seen in subdural fluid in patients with intracranial hypotension.[20]

Finally, we believe that these ESDEs do not represent traumatic subdural hygromas because hygromas tend to develop between 1 and 2 weeks after head injury rather than within the first few days.[13,23] Moreover, studies have demonstrated that contrast does not influx into subdural hygromas.[13]

Limitations

Quantification of iodine in the subdural space is limited by noise (eg, scatter). Increasing the radiation dose from our parameters achieved by setting off CARE Dose would have been optimum, but it would have resulted in more radiation. The use of the modified brain hemorrhage protocol in syngo.via in our image analysis might have minimized the errors caused by beam-hardening, the wrong kernel, or any other wrong scan parameters.

CONCLUSIONS

DECT has high sensitivity and specificity in differentiating ESDE from SDH with a potential to obviate follow-up studies.

REFERENCES

1. Zamora CA, Lin DD. **Enhancing subdural effusions mimicking acute subdural hematomas following angiography and endovascular procedures: report of 2 cases.** *J Neurosurg* 2015;123:1184–87 CrossRef Medline
2. Rennert J, Hamer OW. **Large subdural effusions after angiography mimicking acute subdural hematoma.** *J Comput Assist Tomogr* 2010; 34:249–50 CrossRef Medline
3. Farooqui A, Hiser B, Barnes SL, et al. **Safety and efficacy of early thromoboembolism chemoprophylaxis after intracranial hemorrhage from traumatic brain injury.** *J Neurosurg* 2013;119:1576–82 CrossRef Medline
4. Phelan HA, Wolf SE, Norwood SH, et al. **A randomized double-blinded, placebo-controlled pilot trial of anticoagulation in low-risk traumatic brain injury: the Delayed Versus Early Enoxaparin Prophylaxis I (DEEP I) study.** *J Trauma* 2012;73:1434–41 CrossRef Medline
5. Norwood SH, Berne JD, Rowe SA, et al. **Early venous thromboembolism prophylaxis with enoxaparin in patients with blunt traumatic brain injury.** *J Trauma* 2008;65:1021–26; discussion 1026–27 Medline
6. Koehler DM, Shipman J, Davidson MA, et al. **Is early venous thromboembolism prophylaxis safe in trauma patients with intracranial hemorrhage.** *J Trauma* 2011;70:324–29 CrossRef Medline
7. Gupta R, Phan CM, Leidecker C, et al. **Evaluation of dual-energy CT for differentiating intracerebral hemorrhage from iodinated contrast material staining.** *Radiology* 2010;257:205–11 CrossRef Medline
8. Willmann JK, Roos JE, Platz A, et al. **Multidetector CT: detection of active hemorrhage in patients with blunt abdominal trauma.** *AJR Am J Roentgenol* 2002;179:437–44 CrossRef Medline
9. Bodanapally UK, Sours C, Zhuo J, et al. **Imaging of traumatic brain injury.** *Radiol Clin North Am* 2015;53:695–715, vii CrossRef Medline
10. Phan CM, Yoo AJ, Hirsch JA, et al. **Differentiation of hemorrhage from iodinated contrast in different intracranial compartments using dual-energy head CT.** *AJNR Am J Neuroradiol* 2012;33:1088–94 CrossRef Medline
11. Postma AA, Das M, Stadler AA, et al. **Dual-energy CT: what the neuroradiologist should know.** *Curr Radiol Rep* 2015;3:16 CrossRef Medline
12. Tan LA, Chen M, Muñoz LF. **Letter to the editor: utility of dual-energy CT in differentiating contrast extravasation from intracranial hematoma.** *J Neurosurg* 2016;124:279–80 CrossRef Medline
13. Mori K, Maeda M. **Delayed magnetic resonance imaging with GdD-DTPA differentiates subdural hygroma and subdural effusion.** *Surg Neurol* 2000;53: 303–10; discussion 310–11 CrossRef Medline
14. Shinohara Y, Sakamoto M, Iwata N, et al. **Usefulness of monochromatic imaging with metal artifact reduction software for computed**

tomography angiography after intracranial aneurysm coil embolization. *Acta Radiol* 2014;55:1015–23 CrossRef Medline
15. Potter CA, Sodickson AD. **Dual-energy CT in emergency neuroimaging: added value and novel applications.** *Radiographics* 2016;36:2186–98 CrossRef Medline
16. Sage MR. **Kinetics of water-soluble contrast media in the central nervous system.** *AJNR Am J Neuroradiol* 1983;4:897–906 CrossRef Medline
17. Fishman RA, Dillon WP. **Dural enhancement and cerebral displacement secondary to intracranial hypotension.** *Neurology* 1993;43:609–11 CrossRef Medline
18. Paldino M, Mogilner AY, Tenner MS. **Intracranial hypotension syndrome: a comprehensive review.** *Neurosurg Focus* 2003;15:ECP2 Medline
19. Brightbill TC, Goodwin RS, Ford RG. **Magnetic resonance imaging of intracranial hypotension syndrome with pathophysiological correlation.** *Headache* 2000;40:292–99 CrossRef Medline
20. Mokri B, Parisi JE, Scheithauer BW, et al. **Meningeal biopsy in intracranial hypotension: meningeal enhancement on MRI.** *Neurology* 1995;45:1801–07 CrossRef Medline
21. Koss SA, Ulmer JL, Hacein-Bey L. **Angiographic features of spontaneous intracranial hypotension.** *AJNR Am J Neuroradiol* 2003;24:704–06 Medline
22. Pannullo SC, Reich JB, Krol G, et al. **MRI changes in intracranial hypotension.** *Neurology* 1993;43:919–26 CrossRef Medline
23. Yamada H, Watanabe T, Murata S, et al. **Developmental process of chronic subdural collections of fluid based on CT scan findings.** *Surg Neurol* 1980;13:441–48 Medline

Assessment of Iron Deposition in the Brain in Frontotemporal Dementia and Its Correlation with Behavioral Traits

R. Sheelakumari, C. Kesavadas, T. Varghese, R.M. Sreedharan, B. Thomas, J. Verghese, and P.S. Mathuranath

ABSTRACT

BACKGROUND AND PURPOSE: Brain iron deposition has been implicated as a major culprit in the pathophysiology of neurodegeneration. However, the quantitative assessment of iron in behavioral variant frontotemporal dementia and primary progressive aphasia brains has not been performed, to our knowledge. The aim of our study was to investigate the characteristic iron levels in the frontotemporal dementia subtypes using susceptibility-weighted imaging and report its association with behavioral profiles.

MATERIALS AND METHODS: This prospective study included 46 patients with frontotemporal dementia (34 with behavioral variant frontotemporal dementia and 12 with primary progressive aphasia) and 34 age-matched healthy controls. We performed behavioral and neuropsychological assessment in all the subjects. The quantitative iron load was determined on SWI in the superior frontal gyrus and temporal pole, precentral gyrus, basal ganglia, anterior cingulate, frontal white matter, head and body of the hippocampus, red nucleus, substantia nigra, insula, and dentate nucleus. A linear regression analysis was performed to correlate iron content and behavioral scores in patients.

RESULTS: The iron content of the bilateral superior frontal and temporal gyri, anterior cingulate, putamen, right hemispheric precentral gyrus, insula, hippocampus, and red nucleus was higher in patients with behavioral variant frontotemporal dementia than in controls. Patients with primary progressive aphasia had increased iron levels in the left superior temporal gyrus. In addition, right superior frontal gyrus iron deposition discriminated behavioral variant frontotemporal dementia from primary progressive aphasia. A strong positive association was found between apathy and iron content in the superior frontal gyrus and disinhibition and iron content in the putamen.

CONCLUSIONS: Quantitative assessment of iron deposition with SWI may serve as a new biomarker in the diagnostic work-up of frontotemporal dementia and help distinguish frontotemporal dementia subtypes.

ABBREVIATIONS: ACE = Addenbrooke's Cognitive Examination; AD = Alzheimer disease; ALS = amyotrophic lateral sclerosis; bvFTD = behavioral variant frontotemporal dementia; FrSBe = Frontal System Behavioral Scale; FTD = frontotemporal dementia; PPA = primary progressive aphasia

Frontotemporal dementia (FTD) is an early-onset dementia characterized by changes in behavior, personality, and language abilities. The major clinical presentations are frontal or behavioral variant FTD (bvFTD) with personality and behavioral changes, and the language variant known as primary progressive aphasia (PPA), with either prominent isolated expressive language deficits, progressive nonfluent aphasia, or prominent language comprehension and semantic deficits, semantic dementia.[1] Because standard neuropsychological testing often fails to detect the disease in its early stages and the behavioral changes predate neuropsychological deficits,[2] a major clinical challenge is to develop a biomarker for the early and accurate diagnosis of FTD.

Several neurodegenerative disorders such as Alzheimer disease (AD),[3] Parkinson disease,[4] multiple sclerosis,[5] amyotrophic lateral sclerosis (ALS),[6,7] neuroferrinopathy, panthothenate-kinase-2–associated neurodegeneration, and aceruloplasminemia[8] have been found to be associated with excessive iron accumulation. Also, our previous study in ALS demonstrated abnormal brain

Received January 27, 2017; accepted after revision June 5.

From the Cognition and Behavioural Neurology Section, Department of Neurology (R.S., T.V., P.S.M.) and Department of Imaging Sciences and Interventional Radiology (C.K., B.T.), Sree Chitra Tirunal Institute for Medical Sciences and Technology, Trivandrum, Kerala, India; Department of Radiodiagnostics (R.M.S.), Medical College, Trivandrum, Kerala, India; Integrated Divisions of Cognitive and Motor Aging (Neurology) and Geriatrics (Medicine) (J.V.), Albert Einstein College of Medicine, Bronx, New York; and Department of Neurology (P.S.M.), National Institute of Mental Health and Neurosciences, Banglore, Karnataka, India.

This study was supported by grants from National Institute on Aging (grant No. R21AG029799 and R01AG039330-01) to P.S.M.

Please address correspondence to P.S. Mathuranath, MD, National Institute of Mental Health and Neurosciences, Hosur Rd, Banglore, Karnataka, India 560029; e-mail: psmathu@yahoo.com

Indicates open access to non-subscribers at www.ajnr.org
Indicates article with supplemental on-line photo.
http://dx.doi.org/10.3174/ajnr.A5339

iron deposition in the posterior bank of the motor cortex, and this could be a potential biomarker for ALS.[9] Recently, there has been an increasing interest concerning in vivo quantitative estimation of nonheme iron in the pathophysiology of AD.[10,11] Postmortem studies have indicated neurodegeneration with brain iron deposition in FTD-ALS[12] and Pick disease.[13] A recent study in postmortem brains suggested that iron-impaired homeostasis possibly plays a crucial role in the pathogenesis of frontotemporal lobar degeneration.[14]

The neuropathologic basis of neurodegeneration in frontotemporal lobar degeneration is highly linked to different proteinopathies such as TAR DNA-binding protein 43 and fused in sarcoma proteins,[25,26] which have been found to be responsible for the focal atrophy in frontotemporal and subcortical areas.[17] De Reuck et al[14] found a significantly higher iron load in fused in sarcoma and TAR DNA–binding protein subgroups than in those with τ-frontotemporal lobar degeneration. Although it is widely accepted that the excessive iron accumulation contributes to neurodegeneration, it is not yet clear whether this is a primary or secondary event of the disease process. Iron is an important element for normal brain function due to its critical role in oxidative metabolism, DNA synthesis, and other enzymatic cellular processes. The metabolism of iron depends on the human hemochromatosis protein located on the cell membrane, which regulates uptake of iron by modulating the binding affinity of the transferrin receptor for iron-loaded transferrin.[18] Also the line of evidence indicates that the genetic variant of human hemochromatosis protein, namely H63D polymorphism in frontotemporal lobar degeneration, can foster the increased iron deposition in the basal ganglia regions.[19] In light of these new findings, the search for a biomarker capable of detecting cell death in anatomically specific patterns could be useful, similar to FDG-PET imaging in dementia, but at a lower cost and without any ionizing radiation exposure.

In recent years, susceptibility-weighted imaging has been confirmed as a tool to quantify iron deposition in the brain, which exploits magnetic susceptibility differences among tissues.[20,21] SWI is a 3D gradient technique that uses both magnitude and phase data, separately and together, to enhance the susceptibility differences among tissues. SWI has been shown to be more sensitive to nonheme iron (ferritin) than other conventional techniques.[22] The present study was conducted to unravel the regional changes in the iron concentration in the brains of patients with FTD. This in vivo measurement could potentially offer a good diagnostic tool for identifying the disease and studying the underlying pathophysiologic mechanisms. The goal of the present study was to quantify iron deposition in bvFTD and PPA in comparison with age-matched controls using SWI and to correlate these findings with behavioral test measures.

MATERIALS AND METHODS

Subjects

A total of 46 patients with FTD (34 with bvFTD, 12 with PPA [7 with semantic dementia and 5 with progressive nonfluent aphasia]) and 34 controls were included in the study after we obtained signed informed consent from the participants and their caregivers. The study had approval from the institutional ethics committee. The patients were recruited from the Memory and Neurobehavioral Clinic at Sree Chitra Tirunal Institute for Medical Sciences and Technology, a tertiary referral center in Trivandrum City, Kerala, India. The initial clinical diagnosis of FTD was established by an experienced cognitive neurologist (P.S.M.) as per the published FTD consensus criteria[1] and was subsequently confirmed by neuropsychological and neuroimaging examinations. All the patients with bvFTD met the recently published criteria by Rascovsky et al,[23] and those with PPA met Mesulam criteria.[24] Further, the PPA variants were identified based on the guidelines of an international group of PPA investigators.[25] We excluded patients with a history of cerebral ischemic infarction or hemorrhage, head trauma, alcohol abuse, cardiovascular and major psychiatric diseases, or a history of depressive illness and epilepsy or other neurologic disorders. The age-matched controls with no history of major neurologic or psychiatric illnesses and no contraindications for MR imaging were recruited from the local community and subjected to the same assessment as for FTD.

The cognitive assessment was performed with a neuropsychological battery that was validated for the local elderly population as described previously.[26] The test battery included the brief cognitive test of the Mini-Mental State Examination and the detailed global cognitive test of the Addenbrooke's Cognitive Examination (ACE). Furthermore, patients underwent a behavioral assessment test with the Frontal System Behavioral Scale (FrSBe), which investigates behaviors associated with frontal system damage such as apathy, disinhibition, and executive dysfunction.

Image Acquisition

All images were acquired on a 1.5T whole-body scanner (Avanto; Siemens, Erlangen, Germany) equipped with an 8-channel phased array head coil. In all subjects, sagittal T1-weighted images were acquired to locate the prescribed positions of the anterior/posterior commissures. Conventional T1-weighted and T2-weighted images were acquired with MR imaging sections aligned parallel to the anterior/posterior commissure line to screen the subjects for other cerebral anatomic abnormalities such as traumatic brain injury, old hemorrhagic infarcts, and so forth. SWI imaging was performed with a 3D spoiled gradient recalled-echo sequence with the following parameters: TR/TE, 49/40 ms; flip angle, 20°; section thickness, 2.1 mm; number of sections, 56; FOV, 250 × 203 mm; matrix size, 260 × 320. For the analysis, the images were high-pass-filtered with a low spatial frequency kernel and a central matrix size of 64 × 64. The resulting image is the SWI filtered phase image. The filtered phase image served as an indicator of phase variations and hence the concentration of iron. The details of the measurement of iron in the order of micrograms of iron/gram of tissue are described elsewhere.[9,20,21] The 3D FLASH volumetric scans were also acquired for the anatomic localization based on surface landmarks.

Image Analysis

All the susceptibility-weighted images were examined by 2 certified and experienced neuroradiologists (C.K.) and (B.T.). The high-pass-filtered images were analyzed with signal processing in nuclear MR software (SPIN; MR Imaging Institute for Biomedical Research, Detroit, Michigan). Both the SWI and phase images

Table 1: Demographic, clinical, and behavioral data comparison[a]

	Controls	bvFTD	PPA	*P* Value (Group Effect)
Age (yr)[b]	61.07 ± 6.15	61.18 ± 11.96	64.64 ± 3.98	.55
Sex[c]	18/16	23/11	8/4	.33
FrSBe				
Apathy	19.36 ± 10.55	30.26 ± 11.72	27.58 ± 13.16	.003
Disinhibition	15.86 ± 2.12	33.74 ± 9.27	24 ± 8.07	<.001
Executive dysfunction	20.41 ± 5.68	56.65 ± 16.93	34 ± 9.73	<.001
Neuropsychological test scores				
MMSE	28.66 ± 1.11	18.9 ± 7.71	22.82 ± 5.51	<.001
ACE	92.45 ± 7.03	53.29 ± 24.9	55.9 ± 20.59	<.001

[a] Bonferroni post hoc tests compare differences between groups; both MMSE and ACE scores were absent in 8 patients with bvFTD and 2 with PPA.
[b] Student *t* test
[c] χ^2 test.

Table 2: Iron content (micrograms of iron/gram of tissue) of each region in bvFTD, PPA, and the control group

				Bonferroni-Corrected *P* Value[a]		
Region	Controls	bvFTD	PPA	bvFTD vs Controls	PPA vs Controls	bvFTD vs PPA
LSFG	13.17 ± 5.78	24.35 ± 10.02	18.61 ± 4.23	<.001[b]	.123	.09
RSFG	12.55 ± 5.51	25.36 ± 9.82	18.45 ± 5.11	<.001[b]	.75	.03[b]
LPCG	35.16 ± 10.03	40.17 ± 7.39	37.14 ± 8.28	.064	1.00	.914
RPCG	33.46 ± 14.29	41.74 ± 7.1	39.2 ± 12.11	.012[b]	.416	1.00
LAC	17.21 ± 7.71	21.31 ± 5.72	18.57 ± 4.21	.034[b]	1.00	.634
RAC	16.72 ± 5.7	22.15 ± 6.1	17.97 ± 3.79	.001[b]	1.00	.092
LIN	12.44 ± 5.4	15.91 ± 7.09	15.33 ± 5.33	.074	.512	1.00
RIN	11.86 ± 5.59	16.55 ± 7.83	14.14 ± 2.78	.01[b]	.883	.793
LCAU	25.76 ± 12.05	29.00 ± 12.46	27.19 ± 4.88	.756	1.00	1.00
RCAU	24.96 ± 13.46	31.43 ± 13.79	25.87 ± 7.32	.13	1.00	.609
LPUT	20.96 ± 11.23	26.98 ± 8.95	21.18 ± 5.33	.037[b]	1.00	.227
RPUT	20.61 ± 9.5	27.84 ± 8.12	21.13 ± 6.49	.003[b]	.06	.066
LGP	27.58 ± 10.25	30.66 ± 9.08	28.39 ± 7.58	.55	1.00	1.00
RGP	26.65 ± 7.27	32.3 ± 11.51	28.11 ± 8.68	.053	1.00	.585
LFWM	13.96 ± 6.61	14.67 ± 5.91	15.21 ± 3.17	1.00	1.00	1.00
RFWM	13.65 ± 5.98	17.08 ± 6.77	13.30 ± 4.64	.078	1.00	.217
LHP	12.28 ± 7.60	15.64 ± 7.07	15.58 ± 4.09	.156	.493	1.000
RHP	11.95 ± 6.6	17.01 ± 8.82	14.89 ± 4.21	.024[b]	.671	1.00
LTP	13.72 ± 5.44	21.90 ± 8.69	19.67 ± 5.16	<.001[b]	.041[b]	1.00
RTP	13.25 ± 5.9	23.41 ± 8.71	18.77 ± 4.35	<.001[b]	.07	.166
LRN	27.29 ± 11.07	30.39 ± 10.99	27.90 ± 7.99	.709	1.00	1.00
RRN	24.21 ± 9.13	31.58 ± 12.66	24.69 ± 9.05	.02[b]	1.00	.177
LSN	26.78 ± 11.63	30.90 ± 9.90	28.05 ± 10.64	.365	1.00	1.00
RSN	26.64 ± 12.49	31.0 ± 11.25	27.85 ± 11.09	.403	1.00	1.00
LDN	20.71 ± 8.84	23.26 ± 7.86	21.41 ± 7.47	.633	1.00	1.00
RDN	19.93 ± 6.5	24.03 ± 8.41	20.47 ± 3.96	.064	1.00	.424

Note:—RTP indicates right temporal pole; LTP, left temporal pole; LIN, left insula; RIN, right insula; LCAU, left caudate; RCAU, right caudate; RPUT, right putamen; LPUT, left putamen; LGP, left globus pallidus; RGP, right globus pallidus; LFWM, left frontal white matter; RFWM, right frontal white matter; LHP, left head and body of the hippocampus; RHP, right head and body of the hippocampus; LRN, left red nucleus; RRN, right red nucleus; RSN, right substantia nigra; LSN, left substantia nigra; RSFG, right superior frontal gyrus; LSFG, left superior frontal gyrus; LDN, left dentate nucleus; RDN, right dentate nucleus; RPCG, right precentral gyrus just anterior to central sulcus; LPCG, left precentral gyrus just anterior to central sulcus; LAC, left gray matter abutting and posterior to the cingulate sulcus along with adjacent medial frontal lobe; RAC, right gray matter abutting and posterior to the cingulate sulcus along with adjacent medial frontal lobe.
[a] Bonferroni post hoc tests compare differences among groups.
[b] Significant.

were used for the analysis. Initially, the brightness and contrast of the images were adjusted and magnified 2 times to obtain the anatomic landmark of each structure. Second, ROIs were determined and drawn manually on respective SWI sections with extreme care to minimize partial volume effects. The regions were selected on the basis of known functions of different parts of the brain and the published structural MR imaging studies that had objectives comparable with those in our study. Many of these studies have described significant GM volume loss in the frontal, insular, anterior cingulate, caudate, putaminal, thalamic, and temporal polar regions in bvFTD[27-29] and predominant temporal (temporal pole, anterior hippocampus) and extratemporal (ventromedial prefrontal cortex, insula, anterior cingulate, caudate) regions in PPA.[28,30,31] Hence, the ROIs were drawn on both hemispheres with the help of e-anatomy of IMAIOS (https://www.imaios.com/en/e-Anatomy/Head-and-Neck/Brain-MRI-3D) and included the following: the GM at the precentral gyrus just anterior to central sulcus, adjacent subcortical WM and CSF in the central sulcus, the superior frontal gyrus medial to superior frontal sulcus, temporal pole, insula, basal ganglia regions (caudate), putamen, globus pallidus, substantia nigra, red nucleus, frontal WM, anterior cingulate defined by the gray matter abutting and posterior to the cingulate sulcus along with adjacent medial frontal lobe, hippocampus including its head and body, and, finally, the dentate nucleus (On-line Figure). Inferior and middle frontotemporal regions were avoided in the analysis specifically to reduce the contribution of susceptibility artifacts of the skull base. Finally, each ROI was copied to phase images for measuring the mean phase values. To ensure the consistency in measurement, phase values were measured independently by 2 observers (R.S. and R.M.S.).

To compare data across patients, we assumed that the CSF in each patient contained zero iron.[32] Hence, the iron content in an ROI was directly proportional to the shift in phase between the CSF and the particular ROI.

Statistical Analysis

Statistical analysis was performed with the Statistical Package for the Social Sciences 20.0 (IBM, Armonk, New York). The age and sex distribution among subjects was compared with the Student *t* test and χ^2 test, respectively. The interrater agreement between the 2 observers on iron measurement was calculated with κ statistics. The comparison among the mean values of neuropsychological scores, behavioral scores, and iron in each ROI between groups was performed by 1-way ANOVA analysis with a post hoc Bonferroni procedure.

All statistical tests were set at a significance of $P < .05$. Finally, a linear regression analysis was performed to assess the correlation between iron content and behavioral scores.

RESULTS

Subject Characteristics

The demographic, neuropsychological, and behavioral data are summarized in Table 1. The patients and controls were comparable on age ($P = .5$), and sex ($P = .33$). The patients with bvFTD were significantly worse than those with PPA on FrSBe scores of apathy, disinhibition, and executive dysfunction. Furthermore, those with bvFTD and PPA demonstrated pathologic scores on the ACE and MMSE compared with controls. The direct comparison between patient groups revealed significantly greater behavioral scores of disinhibition and executive dysfunction in bvFTD compared with PPA.

Quantitative Measurement of Brain Iron Content in a Patient with FTD

We observed a very good interrater agreement ($\kappa = 0.88$) between the 2 raters in the quantitative measurement of iron values.

The quantitative assessment of brain iron deposition (micrograms of iron/gram of tissue) in the various regions in patients with FTD demonstrated significantly increased iron levels in bilateral superior frontal gyrus ($P < .001$), bilateral temporal pole ($P < .001$), bilateral anterior cingulate ($P = .001$ for the right and $P = .034$ for the left), bilateral putamen ($P = .003$ for the right and $P = .037$ for the left), right precentral gyrus just anterior to central sulcus ($P = .012$), right insula ($P = .01$), right hippocampus ($P = .024$), and right red nucleus ($P = .02$) in patients with bvFTD compared with controls (Table 2).

In patients with PPA, a significant iron level was noted in the left temporal pole ($P = .041$) and a trend toward significance in the right temporal pole ($P = .073$). A direct comparison between those with bvFTD and PPA showed an increased iron deposition in the right superior frontal gyrus ($P = .03$) in those with bvFTD (Fig 1).

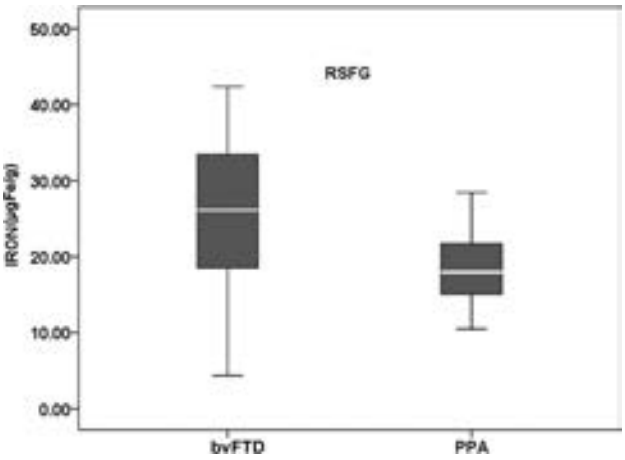

FIG 1. Boxplot showing iron content in the superior frontal gyrus in the direct comparison among patient groups. RSFG indicates right superior frontal gyrus.

Relationship between Cortical Brain Iron Deposition and Behavioral Scores

Linear regression analysis examining the relationship between cortical iron deposition and FrSBe subscores found a significant positive association between the iron content in the right superior frontal gyrus and apathy scores ($r^2 = 0.36$, $P < .001$) and the right putamen and disinhibition scores ($r^2 = 0.25$, $P = .003$) (Fig 2). No association was found between the iron content of any of the examined regions and executive dysfunction scores. The patients with PPA did not show any correlation with iron content and any of the behavioral scores.

DISCUSSION

In this study, we quantified the extent of brain iron deposition in the cortical and subcortical regions of patients with FTD in comparison with controls and correlated this with behavioral measures. To our knowledge, no other previous studies have performed a quantitative in vivo assessment of brain iron deposition in patients with FTD.

Pathologic accumulation of brain iron is shown in various neurodegenerative diseases including AD.[33] A previous postmortem study with 7T MR imaging on the detection of microbleeds in FTD demonstrated an iron overload in the basal ganglia.[34] The investigators also found a large number of microbleeds in the frontal cerebral cortex with gradient-echo T2*-weighted MR imaging sections. Also, a recent postmortem study confirmed the presence of iron in the deep gray nuclei in FTD brains.[14] Activated microglial cells and iron are known to accumulate at the neuro-

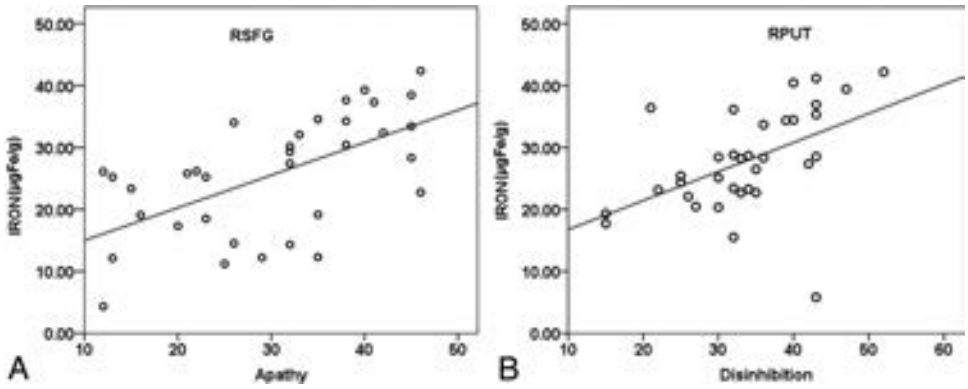

FIG 2. Correlation between iron concentration (micrograms of iron/gram of tissue) in the right superior frontal gyrus (RSFG) (*A*) and apathy, and the right putamen (RPUT) (*B*) and disinhibition scores in patients with bvFTD.

degenerative sites in AD and Parkinson disease.[35] These microglial cells have been implicated in maintaining the iron homeostasis in the brain by scavenging excess iron.[36] It has been reported that chronic microglial activation in FTD can cause the expression of progranulin and the production of proinflammatory mediators by phosphor-τ–positive neurons, which may contribute to neuronal death and disease progression.[37]

Prior studies have proved the efficacy of SWI in the quantitative assessment of cerebral iron content in subjects with dementia.[3,4,10] Wang et al[10] identified increased iron content in the hippocampus, head of the caudate, lenticular nucleus, and thalamus in those with amnestic mild cognitive impairment and AD compared with controls. Further, Zhou et al[3] demonstrated that SWI phase values of the bilateral hippocampus, globus pallidus, caudate, substantia nigra, and putamen were significantly different between those with AD and controls, which had a higher correlation coefficient with MMSE scores. Recently, Wu et al[4] suggested that a quantitative assessment of iron in the substantia nigra and globus pallidus with SWI may be useful for the early diagnosis and evaluation of the degree of disease in Parkinson disease.

The strength of the present study is the quantitative assessment of brain iron deposition in the frontal, temporal, and basal ganglia regions in FTD subtypes in comparison with controls without dementia using SWI. We found significantly increased levels of iron in the bilateral superior frontal gyrus, temporal pole, anterior cingulate, and putamen along with the right hemispheric insula, precentral gyrus, hippocampus, and red nucleus in patients with bvFTD compared with controls. The patients with PPA only showed significant iron levels in the left temporal pole in comparison with controls. A direct comparison revealed significant iron deposition in the right superior frontal gyrus in patients with bvFTD.

Earlier studies proved significant GM and WM degeneration in the frontoinsular-striatial-temporal regions in bvFTD[27,38,39] and more severe temporal atrophy in PPA.[39,40] Recently, De Reuck et al[14] analyzed the postmortem brains of patients with neurodegenerative and cerebrovascular disease and observed the most significant iron deposition in the claustrum, caudate, and putamen and comparatively lesser significant deposition in the globus pallidus, thalamus, and subthalamic nucleus in those with FTD compared with controls. These findings support our observation of increased iron deposition in the basal ganglia regions. Moreover, our volumetric results in the same patient group showed characteristic atrophy patterns in the basal ganglia (R.S. et al, unpublished data, 2016), which corroborate previous findings.[41] Notably, a prior tractography analysis in the human brain demonstrated well-established connections within the frontostriatal networks.[42] The significant iron deposition in the red nucleus of those with bvFTD may be due to its strong functional coherence with prefrontal, insular, temporal, parietal, thalamic, and hypothalamic regions.[43] In fact, the amount of iron deposition in the superior frontal gyrus and putamen correlated with the behavioral manifestations, as measured by the FrSBe, which has been implicated in the behavioral studies in FTD.[44,45] The role of the putamen in disinhibition may be due to its afferent connections to the medial, orbital, and dorsolateral prefrontal regions as well as its link with the prefrontal and motor circuits.[46] Therefore the regional iron deposition, as measured by SWI, may be used as a novel biomarker in the diagnosis of FTD subtypes.

This study has some limitations. Our sample size in PPA was relatively small. Also, some of the subjects were unable to complete the neuropsychological tests due to a more advanced stage of the disease. Although our patient group had characteristic symptomatology and conformed to the diagnostic criteria, pathologic confirmation of FTD has not been established for all subjects. Hence, future longitudinal studies on larger samples with neuropathologic data and higher resolution scanners (3T or 7T) could help verify and consolidate our conclusions. Nevertheless, this study provides insight into an angle for pursuing the search for biomarkers in FTD.

CONCLUSIONS

The results of the study showed that SWI could be a potential biomarker for measuring iron deposition in the FTD brain and iron increases in the frontal and temporal regions of patients. The study also demonstrated a significant correlation between regional iron content and behavioral profiles.

Disclosures: R. Sheelakumari—*RELATED*: *Grant*: National Institute on Aging*. Tinu Varghese—*RELATED*: *Grant*: National Institute on Aging.* Bejoy Thomas—*UNRELATED*: *Grants/Grants Pending*: GE Healthcare, *Comments*: Coinvestigator in an unrelated project*; *Patents (Planned, Pending or Issued)*: Indian patent application filed.* Joe Verghese—*RELATED*: *Grant*: National Institutes of Health, *Comments*: Kerala-Einstein Study: Healthy Lifestyle, Vascular Disease, and Cognitive Decline; type, R01 AG039330-01; role, Principal Investigator; agency, National Institute on Aging, Fogarty Institute*. Pavagadha Mathuranath—*RELATED*: *Grant*: National Institute on Aging, *Comments*: grant Nos. R21AG029799 and R01AG039330-01 to P.S.M.* *Money paid to the institution.

REFERENCES

1. Neary D, Snowden JS, Gustafson L, et al. **Frontotemporal lobar degeneration: a consensus on clinical diagnostic criteria.** *Neurology* 1998;51:1546–54 CrossRef Medline
2. Perry RJ, Graham A, Williams G, et al. **Patterns of frontal lobe atrophy in frontotemporal dementia: a volumetric MRI study.** *Dement Geriatr Cogn Disord* 2006;22:278–87 CrossRef Medline
3. Zhou B, Li S, Huijin H, et al. **The evaluation of iron content in Alzheimer's disease by magnetic resonance imaging: phase and R2* methods.** *Adv Alzheimer Dis* 2013;2:51–59 CrossRef
4. Wu SF, Zhu ZF, Kong Y, et al. **Assessment of cerebral iron content in patients with Parkinson's disease by the susceptibility-weighted MRI.** *Eur Rev Med Pharmacol Sci* 2014;18:2605–08 Medline
5. Ropele S, de Graaf W, Khalil M, et al. **MRI assessment of iron deposition in multiple sclerosis.** *J Magn Reson Imaging* 2011;34:13–21 CrossRef Medline
6. Adachi Y, Sato N, Saito Y, et al. **Usefulness of SWI for the detection of iron in the motor cortex in amyotrophic lateral sclerosis.** *J Neuroimaging* 2015;25:443–51 CrossRef Medline
7. Kwan JY, Jeong SY, Van Gelderen P, et al. **Iron accumulation in deep cortical layers accounts for MRI signal abnormalities in ALS: correlating 7 Tesla MRI and pathology.** *PLoS One* 2012;7:e35241 CrossRef Medline
8. Batista-Nascimento L, Pimentel C, Menezes RA, et al. **Iron and neurodegeneration: from cellular homeostasis to disease.** *Oxid Med Cell Longev* 2012;2012:128647 CrossRef Medline
9. Sheelakumari R, Madhusoodanan M, Radhakrishnan A, et al. **A potential biomarker in amyotrophic lateral sclerosis: can assessment of brain iron deposition with SWI and corticospinal tract degeneration with DTI help?** *AJNR Am J Neuroradiol* 2016;37:252–58 CrossRef Medline
10. Wang D, Zhu D, Wei XE, et al. **Using susceptibility-weighted images to quantify iron deposition differences in amnestic mild cognitive**

impairment and Alzheimer's disease. *Neurol India* 2013;61:26–34 CrossRef Medline
11. Raven EP, Lu PH, Tishler TA, et al. **Increased iron levels and decreased tissue integrity in hippocampus of Alzheimer's disease detected in vivo with magnetic resonance imaging.** *J Alzheimers Dis* 2013;37:127–36 CrossRef Medline
12. Santillo AF, Skoglund L, Lindau M, et al. **Frontotemporal dementia-amyotrophic lateral sclerosis complex is simulated by neurodegeneration with brain iron accumulation.** *Alzheimer Dis Assoc Disord* 2009;23:298–300 CrossRef Medline
13. Ehmann WD, Alauddin M, Hossain TI, et al. **Brain trace elements in Pick's disease.** *Ann Neurol* 1984;15:102–04 CrossRef Medline
14. De Reuck JL, Deramecourt V, Auger F, et al. **Iron deposits in postmortem brains of patients with neurodegenerative and cerebrovascular diseases: a semi-quantitative 7.0 T magnetic resonance imaging study.** *Eur J Neurol* 2014;21:1026–31 CrossRef Medline
15. Mackenzie IA, Neumann M, Bigio EH, et al. **Nomenclature and nosology for neuropathologic subtypes of frontotemporal lobar degeneration: an update.** *Acta Neuropathol* (*Berl*) 2010;119:1–4 CrossRef Medline
16. Neumann M, Rademakers R, Roeber S, et al. **A new subtype of frontotemporal lobar degeneration with FUS pathology.** *Brain J Neurol* 2009;132(pt 11):2922–31 CrossRef Medline
17. Garibotto V, Borroni B, Agosti C, et al. **Subcortical and deep cortical atrophy in frontotemporal lobar degeneration.** *Neurobiol Aging* 2011;32:875–84 CrossRef Medline
18. Feder JN, Penny DM, Irrinki A, et al. **The hemochromatosis gene product complexes with the transferrin receptor and lowers its affinity for ligand binding.** *Proc Natl Acad Sci U S A* 1998;95:1472–7 CrossRef Medline
19. Gazzina S, Premi E, Zanella I, et al. **Iron in frontotemporal lobar degeneration: a new subcortical pathological pathway?** *Neurodegener Dis* 2016;16:172–78 CrossRef Medline
20. Haacke EM, Ayaz M, Khan A, et al. **Establishing a baseline phase behavior in magnetic resonance imaging to determine normal vs. abnormal iron content in the brain.** *J Magn Reson Imaging* 2007;26:256–64 CrossRef Medline
21. Haacke EM, Makki M, Ge Y, et al. **Characterizing iron deposition in multiple sclerosis lesions using susceptibility weighted imaging.** *J Magn Reson Imaging* 2009;29:537–44 CrossRef Medline
22. Thomas B, Somasundaram S, Thamburaj K, et al. **Clinical applications of susceptibility weighted MR imaging of the brain: a pictorial review.** *Neuroradiology* 2008;50:105–16 Medline
23. Rascovsky K, Hodges JR, Knopman D, et al. **Sensitivity of revised diagnostic criteria for the behavioural variant of frontotemporal dementia.** *Brain* 2011;134:2456–77 CrossRef Medline
24. Mesulam MM. **Primary progressive aphasia.** *Ann Neurol* 2001;49:425–32 Medline
25. Gorno-Tempini ML, Hillis AE, Weintraub S, et al. **Classification of primary progressive aphasia and its variants.** *Neurology* 2011;76:1006–14 CrossRef Medline
26. Mathuranath PS, Cherian JP, Mathew R, et al. **Mini mental state examination and the Addenbrooke's cognitive examination: effect of education and norms for a multicultural population.** *Neurol India* 2007;55:106–10 CrossRef Medline
27. Bertoux M, O'Callaghan C, Flanagan E, et al. **Fronto-striatal atrophy in behavioral variant frontotemporal dementia and Alzheimer's disease.** *Front Neurol* 2015;6:147 CrossRef Medline
28. Nguyen T, Bertoux M, O'Callaghan C, et al. **Grey and white matter brain network changes in frontotemporal dementia subtypes.** *Transl Neurosci* 2013;4:410–18
29. Whitwell JL, Przybelski SA, Weigand SD, et al. **Distinct anatomical subtypes of the behavioural variant of frontotemporal dementia: a cluster analysis study.** *Brain* 2009;132(pt 11):2932–46 CrossRef Medline
30. Seelaar H, Rohrer JD, Pijnenburg YAL, et al. **Clinical, genetic and pathological heterogeneity of frontotemporal dementia: a review.** *J Neurol Neurosurg Psychiatry* 2011;82:476–86 CrossRef Medline
31. Duval C, Bejanin A, Piolino P, et al. **Theory of mind impairments in patients with semantic dementia.** *Brain* 2012;135(pt 1):228–41 CrossRef Medline
32. Haacke EM, Cheng NY, House MJ, et al. **Imaging iron stores in the brain using magnetic resonance imaging.** *Magn Reson Imaging* 2005;23:1–25 CrossRef Medline
33. Rouault TA, Cooperman S. **Brain iron metabolism.** *Semin Pediatr Neurol* 2006;13:142–48 CrossRef Medline
34. De Reuck J, Deramecourt V, Cordonnier C, et al. **Detection of microbleeds in post-mortem brains of patients with frontotemporal lobar degeneration: a 7.0-Tesla magnetic resonance imaging study with neuropathological correlates.** *Eur J Neurol* 2012;19:1355–60 CrossRef Medline
35. Ward RJ, Crichton RR, Taylor DL, et al. **Iron and the immune system.** *J Neural Transm (Vienna)* 2011;118:315–28 CrossRef Medline
36. Connor JR, Boeshore KL, Benkovic SA, et al. **Isoforms of ferritin have a specific cellular distribution in the brain.** *J Neurosci Res* 1994;37:461–65 CrossRef Medline
37. Ridolfi E, Barone C, Scarpini E, et al. **The role of the innate immune system in Alzheimer's disease and frontotemporal lobar degeneration: an eye on microglia.** *Clin Dev Immunol* 2013;2013:939786 CrossRef Medline
38. Boccardi M, Sabattoli F, Laakso MP, et al. **Frontotemporal dementia as a neural system disease.** *Neurobiol Aging* 2005;26:37–44 CrossRef Medline
39. Borroni B, Brambati SM, Agosti C, et al. **Evidence of white matter changes on diffusion tensor imaging in frontotemporal dementia.** *Arch Neurol* 2007;64:246–51 CrossRef Medline
40. Agosta F, Scola E, Canu E, et al. **White matter damage in frontotemporal lobar degeneration spectrum.** *Cereb Cortex* 2012;22:2705–14 CrossRef Medline
41. Josephs KA. **Frontotemporal dementia and related disorders: deciphering the enigma.** *Ann Neurol* 2008;64:4–14 CrossRef Medline
42. Leh SE, Ptito A, Chakravarty MM, et al. **Fronto-striatal connections in the human brain: a probabilistic diffusion tractography study.** *Neurosci Lett* 2007;419:113–18 CrossRef Medline
43. Nioche C, Cabanis EA, Habas C. **Functional connectivity of the human red nucleus in the brain resting state at 3T.** *AJNR Am J Neuroradiol* 2009;30:396–403 Medline
44. Eslinger PJ, Moore P, Antani S, et al. **Apathy in frontotemporal dementia: behavioral and neuroimaging correlates.** *Behav Neurol* 2012;25:127–36 CrossRef Medline
45. Halabi C, Halabi A, Dean DL, et al. **Patterns of striatal degeneration in frontotemporal dementia.** *Alzheimer Dis Assoc Disord* 2013;27:74–83 CrossRef Medline
46. Macfarlane MD, Jakabek D, Walterfang M, et al. **Striatal atrophy in the behavioural variant of frontotemporal dementia: correlation with diagnosis, negative symptoms and disease severity.** *PLoS One* 2015;10:e0129692 CrossRef Medline

Multicenter Experience with FRED Jr Flow Re-Direction Endoluminal Device for Intracranial Aneurysms in Small Arteries

M.A. Möhlenbruch, O. Kizilkilic, M. Killer-Oberpfalzer, F. Baltacioglu, C. Islak, M. Bendszus, S. Cekirge, I. Saatci, and N. Kocer

ABSTRACT

BACKGROUND AND PURPOSE: Flow diverters are emerging as an endovascular treatment alternative for proximally located intracranial aneurysms. However, treatment of aneurysms at and beyond the circle of Willis is not well-established. We assessed the clinical safety and efficacy of the Flow Re-Direction Endoluminal Device Jr (FRED Jr) dedicated to small-vessel diameters between 2.0 and 3.0 mm.

MATERIALS AND METHODS: This was a multicenter observational clinical study of 42 patients with 47 aneurysms treated by a flow-direction technique with the FRED Jr. The primary end point for clinical safety was the absence of death, major or minor stroke, and TIA. The primary end point for treatment efficacy was complete and near-complete occlusion according to the O'Kelly-Marotta grading scale at follow-up after 1, 6, and 12 months.

RESULTS: The FRED Jr deployment was technically successful in all cases. In 39/42 (93%) patients, the primary safety end point was reached; in the 3 remaining patients, 1 disabling ischemic stroke, 1 minor stroke with complete recovery at discharge, and 1 TIA were observed. Two asymptomatic, completely reversible side-branch occlusions occurred. Angiographic (DSA or flat panel CT) and clinical follow-up were available after 1 month in 41/47 (87%), 6 months in 27/47 (57%), and 12 months in 11/47 (23%) aneurysms. The primary efficacy end point was reached at 1 month in 27/41 (66%), at 6 months in 21/27 (78%), and at 12 months in 11/11 (100%) aneurysms.

CONCLUSIONS: Deployment of the FRED Jr is safe and effective in the treatment of intracranial aneurysms located in small vessels.

ABBREVIATIONS: ACA = anterior cerebral artery; AcomA = anterior communicating artery; FPCT = flat panel CT; FRED Jr = Flow Re-Direction Endoluminal Device Jr; OKM = O'Kelly-Marotta grading scale

The application of flow diversion with different flow-diverter stents for the treatment of intracranial aneurysms has gained increasing acceptance during the past several years.[1] A braided nitinol mesh with 30%–40% metal-covered surface area is the mainstay of the stent design. Expansion of the flow diverter at the aneurysm base notably decreases flow and subsequently induces thrombosis. The blood, diverted from the aneurysm sac, continues to flow through the porous mesh of the flow diverter following the pressure difference from the parent vessel to smaller branches.[2,3] Due to its singular design, a metal-covered inner stent layer with low permeability and an outer, more porous and stable stent scaffold, the Flow Re-Direction Endoluminal Device (FRED; MicroVention, Tustin, California) may be superior to other flow diverters, providing safer delivery and more effective occlusion of the aneurysm.[4-9] The FRED Jr (MicroVention) has a similar dual-layer design and is the first flow diverter dedicated to small vessels (ie, ≤3 mm). In the past, the flow diverter was not widely used in the treatment of distal circulation aneurysms due to their relatively superficial anatomy and good accessibility for microsurgical clipping. Furthermore, the delivery of the device into the relatively small-caliber vessels of the distal circulation was considered technically difficult.[10] However, clinical experience with such potential complications has rarely been reported.[11-16] Here, we report on our multicenter experience of the FRED Jr

Received February 24, 2017; accepted after revision May 24.

From the Department of Neuroradiology (M.A.M., M.B.), Heidelberg University Hospital, Heidelberg, Germany; Department of Neuroradiology (O.K., C.I., N.K.), Cerrahpasa Medical Faculty, Istanbul University, Istanbul, Turkey; Department of Neurology/Research Institute of Neurointervention (M.K.-O.), Paracelsus Medical University, Salzburg, Austria; Department of Radiology (F.B.), Marmara University School of Medicine, Istanbul, Turkey; Department of Radiology (S.C.), Koru and Bayindir Hospital, Ankara, Turkey; and Department of Radiology (S.C., I.S.), Yüksek Ihtisas University, Koru Hospital, Ankara, Turkey.

Paper previously presented, in part, at: Seminar of the Anatomy Biology Clinical Correlations - Working group in Interventional Neuroradiology, January 15–20, 2017; Val d'Isère, France.

Please address correspondence to Markus A. Möhlenbruch, MD, Department of Neuroradiology, Heidelberg University Hospital, Im Neuenheimer Feld 400, 69120 Heidelberg, Germany; e-mail: markus.moehlenbruch@med.uni-heidelberg.de

Indicates article with supplemental on-line appendix and tables.

http://dx.doi.org/10.3174/ajnr.A5332

flow diverter endovascular treatment of aneurysms in small cerebral vessels and present the feasibility, safety, and effectiveness of this treatment.

MATERIALS AND METHODS

Patient Selection

Local ethics committees approved this observational study, and informed consent was obtained from all subjects before treatment and chart review. The clinical and radiologic records of all consecutive subjects enrolled in a prospective registry of subjects treated with the FRED Jr at 6 centers (On-line Appendix) between October 2015 and December 2016 were reviewed retrospectively. Two operators (M.A.M. and N.K.) gathered and analyzed the data independently. Data collection included demographics; aneurysm features, including type, size, and location; vessel diameter and angulation; details of the endovascular treatment; clinical presentation; follow-up imaging; and clinical outcome. A multidisciplinary team (vascular neurosurgeons, interventional neuroradiologists) made treatment decisions on a case-by-case basis. The only inclusion criterion for treatment with the FRED Jr was an intracranial aneurysm located on a parent vessel with a 3-mm diameter.

Antiplatelet Therapy

In 4 centers (Cerrahpasa Medical Faculty, Heidelberg University Hospital, Marmara University School of Medicine, Paracelsus Medical University), the standard antiplatelet therapy included daily dual antiplatelet medication with 100–300 mg of aspirin and 75 mg of clopidogrel (loading dose, 300 mg), starting no less than 5 days before the procedure and maintaining the therapy for a minimum of 3–6 months after the procedure. After 3–6 months, the patients were switched to aspirin only for a minimum of 6 months or for life. In 2 centers (Yüksek Ihtisas University, Koru and Bayindir Hospital), a daily mono-antiplatelet medication was initiated with prasugrel, 10 mg (loading dose 40 mg), for 6 months and continued with aspirin thereafter. This regimen was also used in the first 4 centers in case of clopidogrel nonresponse. Platelet inhibition was tested with different methods, such as VerifyNow (Accumetrics, San Diego, California) or light transmission aggregometry either 1 day or immediately before endovascular treatment. Concurrent with the procedure, a bolus of standard heparin (70–100 IU/kg) initiated anticoagulation, which was maintained through intravenous administration to sustain an activated clotting time of 250–300 seconds or 2–2.5 times that of baseline.

FRED Jr

The FRED Jr flow diverter was designed to treat aneurysms located in small intracranial vessels. This stent comprises 2 integrated nitinol braided inner and outer layers. The inner layer is of lower porosity, braided in a 36-wire format; and the outer stent layer is of higher porosity, braided in a 16-wire format. This dual-layer design encompasses approximately 90% of its total length, with single-layer flares (part of the outer layer) at each end. These flares, 4 at each end of the stent, are assembled with platinum markers for radiopacity. Two interwoven tantalum wires integrate both layers and provide radiopaque visibility along the dual-layer length of the stent. The FRED Jr is currently recommended for vessel diameters from 2.0 to 3.0 mm. Available FRED Jr sizes are 2.5- and 3.0-mm diameters with working lengths (dual-layer coverage) between 8 and 37 mm. The stainless steel delivery microwire has a radiopaque tip and is shortened to reside only within the proximal portion of the FRED Jr device during deployment. As long as the flared ends and a minimal portion of the proximal working length remain within the 0.021-inch delivery microcatheter (Headway 21, MicroVention), the Fred Jr pusher allows resheathing and the device can be repositioned to optimize the position across the aneurysm neck. As soon as the total length of the stent is released from the microcatheter, it fully expands to its final deployed position.

Description of Technique

All patients were treated under general anesthesia via a transfemoral approach. Through a femoral sheath, a 6F–8F guiding catheter was advanced into the carotid or vertebral artery. Next, the target vessel was analyzed via biplane angiography and 3D rotational angiography. On the basis of the observed length of the aneurysm neck, a flow diverter was chosen with the aim of ensuring arterial wall coverage and an overlap of the inner mesh of at least 2 mm beyond the proximal and distal margins of the aneurysm neck. With a standard microguidewire, a Headway 21 microcatheter was maneuvered beyond the aneurysm neck. Then the flow diverter was unsheathed under roadmap guidance. This was achieved through slow withdrawal of the delivery microcatheter while, at the same time, holding or gently pushing the delivery wire to achieve complete expansion and wall apposition of the flow diverter for 2–3 minutes. In cases of incomplete opening, seen on 2D or 3D angiography, an in-stent percutaneous transluminal angioplasty with a balloon microcatheter was implemented. If additional aneurysm coiling was required to achieve aneurysm occlusion, the initially used microcatheter was jailed between the parent vessel wall and the flow diverter at its deployment.

Evaluation of End Points

Safety. Clinical evaluation was performed by a board-certified neuroradiologist, neurosurgeon, or neurologist immediately postprocedure, at 2 hours after the procedure, on the following day, and at discharge. Patient outcomes were assessed with the modified Rankin Scale. The primary end point for clinical safety was the absence of mortality, stroke (major or minor), and TIA. Technical safety was assessed by the attending neurointerventionalist on conventional DSA and, in some cases, additionally with 3D-DSA and/or flat panel CT (FPCT). Technical safety features of the flow diverter included navigation, radiopacity, deployment, expansion, and vessel wall apposition.

Efficacy. Treatment results were graded according to the O'Kelly-Marotta (OKM) grading scale for assessment of cerebral aneurysms treated by flow diversion.[17] The initial occlusion grade was composed of the initial degree of filling (A = total, B = subtotal, C = entry remnant, D = no filling) and the degree of stasis (prolongation of stasis into 1 = arterial, 2 = capillary, 3 = venous phase). On follow-up examinations, only the degree of filling was rated with digital subtraction angiography or FPCT according to

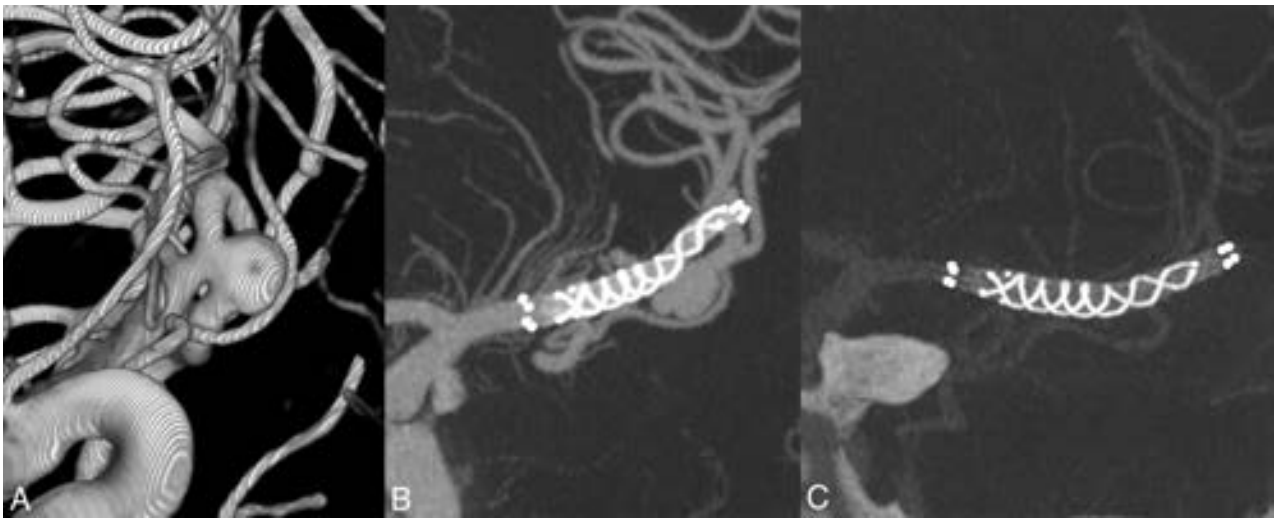

FIG 1. Patient 6 with a bifurcation aneurysm of the middle cerebral artery (3D-DSA, *A*) and after implantation of a FRED Jr in the M1 and superior MCA trunk (arterial FPCT, *B*). At 3-month follow-up, complete occlusion was observed (venous FPCT, *C*).

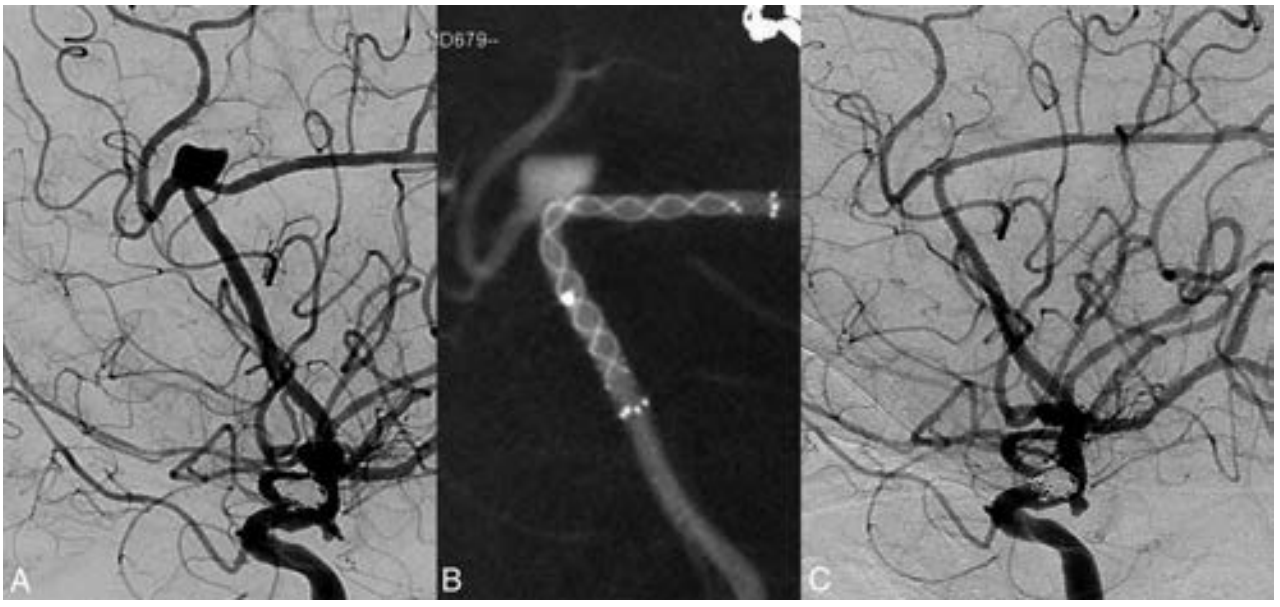

FIG 2. Patient 23 with an A2/A3 aneurysm of the anterior cerebral artery (*A*), and after deployment of a FRED Jr (*B*). At 6-month follow-up, complete occlusion was observed (*C*).

the OKM scale for comparison with the immediate results. The primary end point for treatment efficacy was complete and near-complete occlusion (ie, OKM C and D) at follow-up after 1, 6, and 12 months.

Statistics

Differences in variable distribution between groups were compared using Kruskal-Wallis tests for continuous variables and χ^2 tests for categoric variables. Significant results on univariate analysis were included in an ordered categoric regression model to measure their combined effect. All statistical analysis was undertaken with SPSS, Version 22.0 (IBM, Armonk, New York).

RESULTS

Baseline Patient and Aneurysm Characteristics

Forty-two patients (26 female; median age, 53 years; age range, 15–80 years) with 47 aneurysms were included. Demographics of all enrolled patients and features of the treated aneurysms are shown in the On-line Table 1. On-line Table 2 lists clinical details and angiographic imaging features. Representative cases are presented in Figs 1–3.

Eighteen aneurysms originated from the middle cerebral artery; 13, from the anterior cerebral artery (ACA) distal to anterior communicating artery (AcomA); 11, from the AcomA or A1/A2 junction of the ACA; 2, from the posterior cerebral artery; 1, from the superior cerebellar artery; and 1, from the vertebral artery at the V4 level. One was located at the tip of the terminal segment of the ICA. We included 35 saccular aneurysms, 9 fusiform/dissecting aneurysms, and 2 giant aneurysms (including 1 partially thrombosed aneurysm) and 1 blisterlike aneurysm. One aneurysm was symptomatic with a neurologic deficit, and 1 aneurysm was in the subacute stage after SAH.

The target lesion had been previously treated in 11 patients:

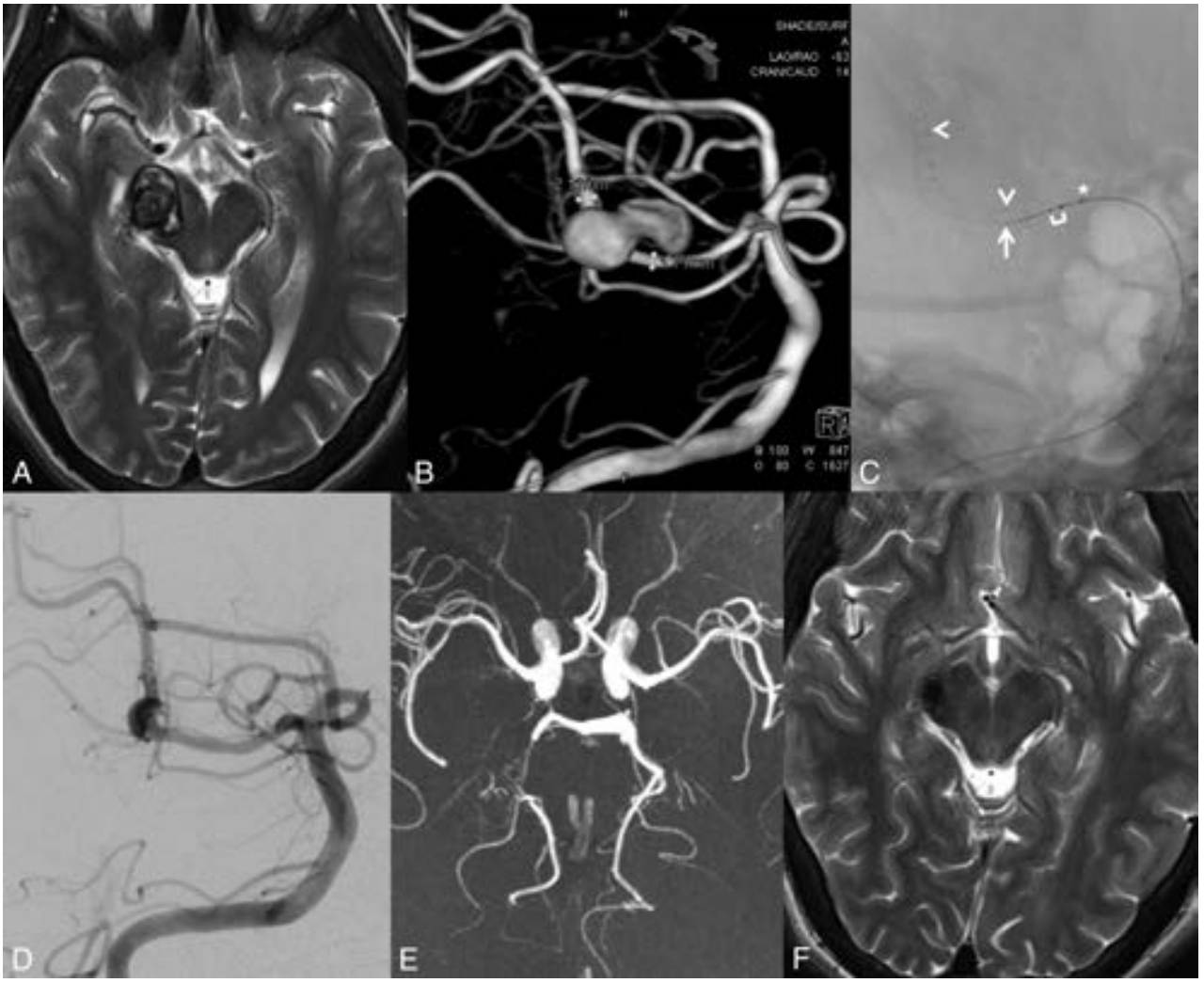

FIG 3. Patient 35 with a partially thrombosed giant aneurysm originating from the posterior cerebellar artery (T2, *A*; 3D-DSA, *B*). After deployment of a FRED Jr (*arrowheads* indicating the flow-diverting working zone, *arrow* pointing to the tip of the delivery wire, *bracket* showing the delivery wire markers where normally the proximal stent markers are compressed within the microcatheter, *asterisk* indicating the tip of the microcatheter; *C*), the aneurysm filling is reduced (*D*). At 12-month follow-up, the aneurysm is almost completely shrunken (TOF *E*; T2, *F*).

Five aneurysms had been coiled previously and developed a reperfusion. Two aneurysms were treated with flow diverters (the superior cerebellar artery with the Pipeline Embolization Device, Covidien, Irvine, California; and A2 with the Silk flow diverter, Balt Extrusion, Montmorency, France), but the aneurysms did not occlude during follow-up. Additionally, 4 aneurysms had regrowth after initial clipping.

Technical Results

The FRED Jr could always (all patients, all aneurysms) be successfully maneuvered to the target area and deployed across the aneurysm base to achieve complete coverage. However, in 2 cases (AcomA and A1/A2 junction), a longer version of the FRED Jr than initially chosen was implanted to ensure complete neck coverage. A single flow diverter was sufficient to treat the aneurysm in all cases.

The median aneurysm diameter was 6 mm (range, 1.3–25.2 mm) with a median neck size of 4 mm (range, 1.3–14.5 mm). The stented parent vessels had a median diameter of 2.4 mm (range, 1.4–3.6 mm) proximally and 2.1 mm (range, 1.5–3.4 mm) distally. The median degree of angulation of the parent artery was 95° (range, 10°–170°). In 1 case, concomitant coils were used to pack the aneurysm because of its multilobulated morphology. In-stent angioplasty after flow-diverter deployment was performed in 1 patient with a dissecting MCA aneurysm and distal stenosis of the parent artery. In 2 cases, a mild (<50%) stenosis of the FRED Jr after deployment was detected without the need for in-stent angioplasty. In 22/47 (47%) aneurysms, an immediate impact on the degree of stasis (OKM grading scale) could be observed on angiography at the end of the endovascular procedure, and the angiographic degree of filling (OKM grading scale) was changed immediately in 11/47 cases (23%).

Clinical Outcome and Procedure-Related Complications

The primary safety end point could be observed in 39/42 (93%) treated patients. One major stroke occurred in a patient with an atherosclerotic fusiform M1 aneurysm. After extubation, the patient had a hemiparesis. Immediate DSA control showed

the stent in place with perfusion of all MCA branches. The MR imaging control showed watershed infarctions. The patient was discharged with an mRS 3 and recovered to mRS 2 at 3 months after treatment.

A minor stroke developed in a patient with an A1/A2 aneurysm. This patient woke up with a transient hemiparesis. Immediate MR imaging control showed an embolic shower in the ACA territory. The patient was discharged with an mRS 1 and recovered to mRS 0 at 3 months after treatment. Another patient with an MCA bifurcation aneurysm experienced transient ischemic symptoms (slight hemiparesis) 2 hours after FRED Jr placement, induced by an occlusion of the inferior MCA trunk on DSA. Complete resolution of symptoms was observed within 1 hour after intravenous tirofiban injection, with complete reopening of the trunk on control DSA.

Diminished flow in the adjacent vessels was detected within 30 minutes after deployment in a patient with a pericallosal aneurysm. After intravenous tirofiban injection, the flow changed to normal within 10 minutes and the patient did not show any neurologic deficit after extubation. The same patient presented, after normal findings on 3-month follow-up MR imaging, with multiple enhancing brain lesions at 6-month follow-up MR imaging. The patient was never symptomatic, and after 1 month of steroids, the enhancing lesions had disappeared completely. Another patient with a giant MCA aneurysm experienced an upper trunk MCA occlusion immediately after deployment. After intravenous tirofiban, the upper trunk reopened, and the patient was asymptomatic after extubation.

There was no statistically significant association between any pretreatment patient or aneurysm characteristic and the occurrence of these procedure-related complications.

Follow-Up

Complete angiographic (DSA or FPCT) and clinical follow-up was performed after a median of 1 month in 41/47 (87%) aneurysms, after a median of 6 months in 27/47 (57%) aneurysms, and after a median of 12 months in 11/47 (23%) aneurysms. Seventy-one percent of patients (30/42) had at least 1 DSA examination at follow-up. At 1-month follow-up, 6/41 (15%) aneurysms showed complete occlusion (OKM D), and 21/41 (51%) aneurysms, a near-complete occlusion (OKM C). At 6-month follow-up, in 19/27 (70%) aneurysms, complete occlusion was observed (OKM D) and near-complete aneurysm occlusion was seen in 2/27 (7%). A complete filling was not detected in any of the followed aneurysms at 6 months. At 12-month follow-up, 8/11 (73%) aneurysms were still completely occluded (OKM D), while 3/11 (27%) aneurysms remained at near-complete occlusion (OKM C). Regardless of the follow-up timing, the primary end point for efficacy was reached in 32/41 (78%) aneurysms with any follow-up.

No cases of in-stent stenosis, in-stent thrombosis, or migration of the FRED Jr implant were observed on follow-up DSA or FPCT. So far, no retreatment has been performed.

The performed χ^2 and Kruskal-Wallis H tests showed no statistically significant differences among the different occlusion grades at 1, 6, or 12 months for any pretreatment patient or aneurysm characteristics.

DISCUSSION

In this clinical multicenter observational study, the FRED Jr device was assessed for the treatment of intracranial aneurysms in small arteries. While conventional microsurgical clipping or coiling with possible ballooning or stent placement remains the treatment of choice, few studies in the past have investigated the use of flow diverters in small vessels.[11-16] This new generation of intracranial flow diverters dedicated to vessels of ≤3 mm may provide a promising alternative for the safe and effective treatment of these challenging aneurysms. In this series, all treated aneurysms were completely covered by the flow diverter at postprocedural follow-up. The primary end point for clinical safety (ie, absence of mortality and stroke [major or minor] or transient ischemic attack) was achieved in 39/42 (93%) patients treated with the FRED Jr device. These findings are comparable with those in previous studies that focused on distal-circulation aneurysms treated with various intracranial flow diverters (in most cases the Pipeline Embolization Device), with up to 17.6% transient neurologic deficits, up to 10.7% permanent neurologic deficits, and no mortality.[11-16]

Procedural Success

In the present study, successful deployment of the FRED Jr device could be achieved in all cases. In 2 cases, a longer version of the FRED Jr was implanted because foreshortening of the initial FRED Jr was too pronounced, especially at the base of the aneurysm. Insufficient opening (>50%) of the FRED Jr, which has been reported for other available flow diverters in up to 10% of cases, did not occur with the FRED Jr.[18,19] Unsheathing and release of the FRED Jr was performed slowly for several minutes in a controlled fashion by retracting the delivery microcatheter only, to facilitate correct expansion and complete deployment of the FRED Jr. The so-called push/pull technique was usually not required. Should incomplete opening occur, despite these precautions, a complete retrieval of the FRED Jr device should be performed by simply resheathing it into the delivery microcatheter. In previous case series, delayed retraction of the flow diverter occurred, but this was not found in our series.[11,19] Furthermore, on follow-up, no in-stent stenosis or changes in stent morphology such as "fish mouth" (ie, inward crimping of 1 or both ends of flow diverter) or "foreshortening" phenomena, which were described in a series by Kocer et al[4] with the first version of FRED, were observed.

Angiographic Outcome

Occlusion results for the FRED Jr during early follow-up were promising. Immediately after FRED Jr deployment, a change in the degree of contrast stasis inside the aneurysm was noted in >47% of cases, similar to results of the "regular" FRED.[5] After 6 months, complete aneurysm occlusion, defined as an OKM grade of D, could be observed in 19/27 (70%) cases, which, on the Raymond and Roy scale, would correspond to grade I.[20]

Our efficacy rate was in line with the complete occlusion rate at 6–12 months of 33%–79% seen in previous studies, which had focused on distal circulation aneurysms with various intracranial flow diverters (in most cases the Pipeline Embolization Device was used).[11-14,16]

Potential Advantages

Advantages of the recently introduced FRED Jr may include the following: 1) enhanced outward stability of the stent toward the wall of the parent vessel due to the design (dual-layer) of the FRED Jr device and long sizes (available up to 41 mm), which provide a scaffolding effect. Most important, a single device can be used to achieve aneurysm occlusion in a single treatment session, while previously, the treatment of fusiform or giant aneurysms may have required telescoping implantation of >1 flow diverter or 2 sequential procedures (scaffolding stent followed by flow-diverter implantation). 2) The lower number of wires (16 wires in the outer stent compared with 48 wires in the Silk or Pipeline device, for example) may result in lower friction within the delivery microcatheter, allowing a smoother deployment of longer stents. 3) Stent opening will be more reliable because radial force vectors of the inner and outer stent will add up. This feature is especially critical when deployment includes vessels with >90° angulation. 4) Laminar blood flow might be improved by the dual-layer design and higher pore attenuation. Compared with the 48 wires of the Pipeline and Silk, the FRED Jr device consists of 16 outer nitinol wires and 36 inner nitinol wires with 2 tantalum integration wires. 5) The short inner stent will result in lower vessel wall coverage in the longitudinal direction (shortest, 8 mm, available on the market). The inner stent is designed to limit the working layer to the neck of the aneurysm and to spare adjacent branches, while maintaining the patency of these vessels. 6) The delivery microcatheter, Headway 21, is the smallest available delivery system on the market, with an outer distal diameter of 2F compared with Vaso 21 (Balt Extrusion) (outer distal diameter, 2.4F) for Silk, and Marksman (outer distal diameter, 2.8F) for Pipeline. 7) The delivery wire always stays inside the flow diverter. Therefore, the risk of vessel perforation, especially in small vessels, might be lower.

The main differences of the FRED Jr compared with the FRED are the following: 1) the dual-layer design of FRED Jr consisting of 16 + 36 wires instead of 16 + 48 wires for the FRED. This resulted in a lower metal coverage of the vessel wall with the FRED Jr (approximately 30% versus approximately 35%–40% with FRED). 2) The delivery wire system of the FRED Jr has no distal tip. 3) For FRED Jr delivery, a 0.021-inch microcatheter is adequate, whereas the FRED requires a 0.027-inch microcatheter.

Clinical Outcome and Complications

Overall, the primary safety end point could not be achieved in 3 patients (7%). However, only 1 patient had resulting permanent neurologic deficits (major stroke, 2%). The selected FRED Jr, in this case with an atherosclerotic fusiform M1 aneurysm, seemed too long and compromised the perfusion in 1 M2 branch. MR imaging control showed watershed infarctions. The patient was discharged with a hemiparesis and recovered to mRS 2 at 3 months after treatment. The minor stroke occurred in a patient with an A1/A2 aneurysm. The immediate MR imaging control showed an embolic shower in the ACA territory, which was probably because several attempts were needed to deploy the FRED Jr in a satisfactory position. The remaining symptomatic patient with a TIA had an occlusion of the lower MCA trunk, which is probably related to the Coandă effect (see below). Asymptomatic thrombosis of covered side branches was detected within 30 minutes after deployment in a patient with a pericallosal aneurysm and in another patient with a giant MCA bifurcation aneurysm. After intravenous tirofiban injection, the thrombosis resolved completely within 20 minutes. These 2 side-branch occlusions are likely device-related, such as incomplete wall apposition with emerging thrombus formation. However, the possibility of insufficient opening of the FRED Jr was ruled out by FPCT, and both patients had a good response to antiplatelet therapy in prior tests.

Immediate thrombosis of a covered side branch can be explained by the Coandă effect, a phenomenon in which a jet flow attaches itself to a nearby surface and remains attached even when the surface curves away from the initial jet direction.[21] The patient with the pericallosal aneurysm presented at follow-up with multiple enhancing brain lesions, similar to those described by Cruz et al,[22] suggesting a foreign body reaction, potentially caused by shedding of the hydrophilic coating. The patient never developed any symptoms, and after 1 month of steroids, the enhancing lesions had disappeared.

Three of 5 complications occurred in patients with MCA aneurysms, which are known to pose a higher risk of thromboembolic complications.[16,18]

Limitations

We conducted a multicenter, retrospective, observational study; therefore, there was inherent selection bias associated with it. The overall number of patients was small, and no statistical significance was discovered in univariate or multivariate analyses, likely owing to the lack of power. Moreover, the relatively recent adoption of FRED Jr in clinical use and the short follow-up period in our study imply that the durability of the treatment and long-term consequences with FRED Jr remain to be determined. To the best of our knowledge, however, this is the largest study of aneurysms located on small vessels treated with flow diverters, and our data demonstrate that the FRED Jr is a safe and effective form of treatment for aneurysms located on small arteries that are challenging for both conventional microsurgical and endovascular techniques.

CONCLUSIONS

In this first observational study of the FRED Jr for the treatment of distally located intracranial aneurysms, a high degree of safety and a high rate of complete aneurysm occlusion were observed. Long-term durability and safety should be proved by larger series. Our results support the notion that the use of intracranial micro-flow diverters, such as reported herein, may increase the armamentarium of procedural techniques for the neurointerventionalist, especially for targeting distally located aneurysms in which parent vessel diameters are ≤3 mm.

ACKNOWLEDGMENTS

The authors wish to thank Susanne Bonekamp and Sedat Giray Kandemirli for assistance with manuscript preparation.

Disclosures: Markus A. Möhlenbruch—*UNRELATED*: *Payment for Lectures Including Service on Speakers Bureaus*: Codman, Medtronic, MicroVention, phenox, Stryker. Monika Killer-Oberpfalzer—*UNRELATED*: *Board Membership*: research grant, MicroVention/Terumo.* Civan Islak—*UNRELATED*: *Consultancy*: Covidien; *Patents*

(Planned, Pending or Issued): 4D detachable embolic coil (US Pub No: US0327868A1); *Stock/Stock Options*: NDI Inc, *Comments*: 10%. Martin Bendszus—*UNRELATED*: *Board Membership*: DSMB for Vascular Dynamics; *Consultancy*: Codman, Roche, Guerbet, Boehringer Ingelheim; *Grants/Grants Pending*: Deutsche Forschungsgemeinschaft, Dietmar Hopp Foundation, Novartis, Siemens, Guerbet, Stryker, Covidien*; *Payment for Lectures Including Service on Speakers Bureaus*: Novartis, Roche, Guerbet, Teva, Bayer HealthCare Pharmaceuticals, Codman. Saruhan Cekirge—*UNRELATED*: *Consultancy:* Medtronic; *Consulting Fee or Honorarium*: MicroVention. Isil Saatci—*UNRELATED*: *Consultancy*: Medtronic. Naci Kocer—*UNRELATED*: *Consultancy*: MicroVention*; *Payment for Lectures Including Service on Speakers Bureaus*: MicroVention, *Comments*: I also have a proctoring agreement with MicroVention.* *Money paid to the institution.

REFERENCES

1. Brinjikji W, Murad MH, Lanzino G, et al. **Endovascular treatment of intracranial aneurysms with flow diverters: a meta-analysis.** *Stroke* 2013;44:442–47 CrossRef Medline
2. Cebral JR, Mut F, Raschi M, et al. **Analysis of hemodynamics and aneurysm occlusion after flow-diverting treatment in rabbit models.** *AJNR Am J Neuroradiol* 2014;35:1567–73 CrossRef Medline
3. Kallmes DF, Ding YH, Dai D, et al. **A second-generation, endoluminal, flow-disrupting device for treatment of saccular aneurysms.** *AJNR Am J Neuroradiol* 2009;30:1153–58 CrossRef Medline
4. Kocer N, Islak C, Kizilkilic O, et al. **Flow Re-direction Endoluminal Device in treatment of cerebral aneurysms: initial experience with short-term follow-up results.** *J Neurosurg* 2014;120:1158–71 CrossRef Medline
5. Möhlenbruch MA, Herweh C, Jestaedt L, et al. **The FRED flow-diverter stent for intracranial aneurysms: clinical study to assess safety and efficacy.** *AJNR Am J Neuroradiol* 2015;36:1155–61 CrossRef Medline
6. Alherz AI, Tanweer O, Flamini V. **A numerical framework for the mechanical analysis of dual-layer stents in intracranial aneurysm treatment.** *J Biomech* 2016;49:2420–27 CrossRef Medline
7. Briganti F, Leone G, Ugga L, et al. **Safety and efficacy of flow redirection endoluminal device (FRED) in the treatment of cerebral aneurysms: a single center experience.** *Acta Neurochir (Wien)* 2016;158:1745–55 CrossRef Medline
8. Drescher F, Weber W, Berlis A, et al. **Treatment of intra- and extracranial aneurysms using the Flow-Redirection Endoluminal Device: multicenter experience and follow-up results.** *AJNR Am J Neuroradiol* 2017;38:105–12 CrossRef Medline
9. Luecking H, Engelhorn T, Lang S, et al. **FRED flow diverter: a study on safety and efficacy in a consecutive group of 50 patients.** *AJNR Am J Neuroradiol* 2017;38:596–602 CrossRef Medline
10. Brouillard AM, Sun X, Siddiqui AH, et al. **The use of flow diversion for the treatment of intracranial aneurysms: expansion of indications.** *Cureus* 2016;8:e472 CrossRef Medline
11. Pistocchi S, Blanc R, Bartolini B, et al. **Flow diverters at and beyond the level of the circle of Willis for the treatment of intracranial aneurysms.** *Stroke* 2012;43:1032–38 CrossRef Medline
12. Martin AR, Cruz JP, O'Kelly C, et al. **Small pipes: preliminary experience with 3-mm or smaller Pipeline flow-diverting stents for aneurysm repair prior to regulatory approval.** *AJNR Am J Neuroradiol* 2015;36:557–61 CrossRef Medline
13. Lin N, Lanzino G, Lopes DK, et al. **Treatment of distal anterior circulation aneurysms with the Pipeline Embolization Device: a US multicenter experience.** *Neurosurgery* 2016;79:14–22 CrossRef Medline
14. Martínez-Galdámez M, Romance A, Vega P, et al. **Pipeline endovascular device for the treatment of intracranial aneurysms at the level of the circle of Willis and beyond: multicenter experience.** *J Neurointerv Surg* 2015;7:816–23 CrossRef Medline
15. Puri AS, Massari F, Asai T, et al. **Safety, efficacy, and short-term follow-up of the use of Pipeline Embolization Device in small (<2.5 mm) cerebral vessels for aneurysm treatment: single institution experience.** *Neuroradiology* 2016;58:267–75 CrossRef Medline
16. Gawlitza M, Januel AC, Tall P, et al. **Flow diversion treatment of complex bifurcation aneurysms beyond the circle of Willis: a single-center series with special emphasis on covered cortical branches and perforating arteries.** *J Neurointerv Surg* 2016;8:481–87 CrossRef Medline
17. O'Kelly CJ, Krings T, Fiorella D, et al. **A novel grading scale for the angiographic assessment of intracranial aneurysms treated using flow diverting stents.** *Interv Neuroradiol* 2010;16:133–37 CrossRef Medline
18. Brinjikji W, Lanzino G, Cloft HJ, et al. **Risk factors for ischemic complications following Pipeline Embolization Device treatment of intracranial aneurysms: results from the IntrePED Study.** *AJNR Am J Neuroradiol* 2016;37:1673–78 CrossRef Medline
19. Lubicz B, Collignon L, Raphaeli G, et al. **Flow-diverter stent for the endovascular treatment of intracranial aneurysms: a prospective study in 29 patients with 34 aneurysms.** *Stroke* 2010;41:2247–53 CrossRef Medline
20. Raymond J, Guilbert F, Weill A, et al. **Long-term angiographic recurrences after selective endovascular treatment of aneurysms with detachable coils.** *Stroke* 2003;34:1398–403 CrossRef Medline
21. Kocer N. *Giant Intracranial Aneurysms: A Case-Based Atlas of Imaging and Treatment.* New York: Springer; 2016:68–70
22. Cruz JP, Marotta T, O'Kelly C, et al. **Enhancing brain lesions after endovascular treatment of aneurysms.** *AJNR Am J Neuroradiol* 2014;35:1954–58 CrossRef Medline

Clinical Impact of Flat Panel Volume CT Angiography in Evaluating the Accurate Intraoperative Deployment of Flow-Diverter Stents

F. Clarençon, F. Di Maria, J. Gabrieli, E. Shotar, V. Degos, A. Nouet, A. Biondi, and N.-A. Sourour

ABSTRACT

BACKGROUND AND PURPOSE: The deployment of flow-diverter stents may be difficult to analyse on regular DSA. The purpose of our study was to investigate the clinical impact of stent-dedicated flat panel volume CT angiography to evaluate intraoperatively the satisfactory deployment of flow-diverter stents.

MATERIALS AND METHODS: From January 2009 to April 2015, 83 consecutive patients (mean age, 51 years; 62 women) were treated in our institution with flow-diverter stents. Eighty-seven aneurysms (82 unruptured, 5 ruptured; 77 anterior, 10 posterior circulation) were treated in these 83 patients (4 patients had 2 aneurysms, both treated by means of flow-diverter stents). One patient was treated for a traumatic carotid cavernous fistula. In 80% of the cases (68/85) a flat panel volume CT angiography was performed in the angiographic suite just after the flow-diverter stent deployment. Stent visualization was assessed by 2 independent reviewers. The clinical impact of stent malapposition was evaluated.

RESULTS: Flow-diverter stent visualization was satisfactory in 73.5% of the cases. In 2 cases (2.9%) the flat panel volume CT angiography prompted the operator to perform an additional intrastent angioplasty for a condition that was previously underestimated. Four patients (4.7%) experienced acute thromboembolic complications; 3 others had delayed thromboembolic complications. Only 1 of these patients had thromboembolic complications (acute or delayed) related to stent misdeployment, which was easily managed intraoperatively with no clinical consequence.

CONCLUSIONS: Flat panel volume CT angiography is an interesting tool to depict flow-diverter stent misdeployment and may encourage the operator to perform intrastent angioplasty (2.9% of the cases in our experience) to reduce the risks of thromboembolic complications.

ABBREVIATIONS: FDS = flow-diverter stent; FPV-CTA = flat panel volume CT angiography

Flow-diverter stents (FDSs) have gained acceptance in recent years for the treatment of intracranial aneurysms, especially giant and large ones.[1,2] This new-generation stent shifted the paradigm of treatment for intracranial aneurysms and now helps in treating intracranial aneurysms that were previously considered as challenging or even impossible to treat by endovascular means.[3] However, one of the drawbacks for their use is their poor radiopacity.[4] Indeed, despite the addition of radiopaque strands in the design of these stents, their visibility remains poor, hampering the visualization of their accurate deployment by the operator during the procedure. Flat panel volume CT angiography (FPV-CTA) is now increasingly used to evaluate the deployment of regular intracranial stents in cases of stent-assisted coiling,[5-7] and has shown its effectiveness to depict kinking/misdeployment. However, the potential of this technique has been poorly reported for FDSs.

The purpose of our study was to evaluate the potential of the FPV-CTA to display the accurate deployment of FDSs and to evaluate the clinical impact of FDS misdeployment depicted by this technique.

MATERIALS AND METHODS

Patient Demographics/Aneurysm Characteristics

All patient demographics and aneurysm characteristics are summarized in Table 1. From January 2009 to April 2015, 87 intracranial aneurysms (82 unruptured, 5 acutely ruptured; 77 anterior, 10 posterior circulation) were treated in 83 consecutive patients (mean age, 51 ± 12.1 years; age range, 20–77 years; 62 women, 21 men), during 85 embolization procedures (4 patients had 2 aneu-

Received March 18, 2017; accepted after revision June 9.

From the Departments of Interventional Neuroradiology (F.C., J.G., E.S., N.-A.S.), Anesthesiology (V.D.), and Neurosurgery (A.N.), Pitié-Salpêtrière Hospital. Paris France; Paris VI University (F.C., J.G., E.S., V.D.), Pierre et Marie Curie, Paris. France; Department of Interventional Neuroradiology (F.D.M.), Foch Hospital, Suresnes, France; and Department of Neuroradiology and Endovascular Therapy (A.B.), Besançon University Hospital, Besançon, France.

Please address correspondence to Frédéric Clarençon, MD, PhD, Department of Neuroradiology, Pitié-Salpêtrière Hospital, 47 Bd de l'Hôpital, 75013 Paris, France; e-mail: fredclare5@msn.com

http://dx.doi.org/10.3174/ajnr.A5343

Table 1: Patient demographics and aneurysm characteristics

Demographics/Characteristics	Overall Population	Patients Who Underwent FPV-CTA
No. of patients	83	68
Age (mean ± SD)	51 ± 12	51 ± 12
Female (no., %)	62 (75)	51 (75)
No. of aneurysms	87	70
Direct CC fistula (no.)	1	1
No. of procedures	84	70
Aneurysm locations		
Anterior circulation (no., %)	76 (87.4)	63 (90)
Paraclinoid ICA (no., %)	36 (41.4)	28 (40)
Cavernous ICA (no., %)	20 (23)	17 (24)
ACA/AComA (no., %)	7 (8)	6 (8.6)
ICA terminus (no., %)	4 (4.6)	4 (5.7)
AChoA/PComA (no., %)	4 (4.6)	4 (5.7)
MCA (no., %)	4 (4.6)	3 (4.3)
Petrous ICA (no., %)	1 (1.1)	1 (1.4)
Posterior circulation	11 (12.6)	7 (10)
Vertebral artery (no., %)	5 (5.7)	3 (4.3)
BA (no., %)	3 (3.4)	1 (1.4)
PCA (no., %)	2 (2.3)	2 (2.9)
SCA (no., %)	1 (1.1)	1 (1.45)
Aneurysm maximum diameter (mean ± SD)	9.2 ± 6.5	9.8 ± 6.5
Aneurysm neck (mean ± SD)	5.4 ± 3	5.4 ± 3
Acutely ruptured aneurysms (no., %)	5 (5.7)	3 (4.3)
Recanalized aneurysms (no., %)	16 (18.4)	13 (18.6)
Previously clipped (no., %)	2 (2.3)	2 (2.9)
Previously coiled (no., %)	14 (16.1)	11 (15.7)

Note:—ACA indicates anterior cerebral artery; AChoA, anterior choroidal artery; AComA, anterior communicating artery; BA, basilar artery; CC, carotid cavernous; PCA, posterior cerebral artery; PComA, posterior communicating artery; SCA, superior cerebellar artery.

rysms, both treated by means of FDS; in 2 cases, 2 aneurysms were treated with the same FDS). The mean maximum diameter of the aneurysms was 9.2 ± 6.5 mm; the mean neck size was 5.4 ± 3 mm. In 16 cases (18%), FDS was used for the treatment of a recurrence in an aneurysm previously treated by coiling (n = 13; 14.9%), by FDS (n = 1; 1.1%), or clipping (n = 2; 2.3%). In addition, 1 patient (Patient #43) was treated for a traumatic carotid cavernous fistula.

Endovascular Treatment

All procedures were performed under general anesthesia. In all except 1 case of blood-blister aneurysm, patients received dual antiplatelet therapy (clopidogrel and aspirin) before the treatment, which was pursued for 3–6 months after the procedure. Aspirin was then pursued for a total of 1 year. In all except 1 case (blood-blister aneurysm treated in emergency), the sensitivity to clopidogrel as well as to aspirin was evaluated by using the Multiplate aggregation test (Roche, Basel, Switzerland). In most cases, full anticoagulation was performed during the treatment, with an activated clotting time target between 2- to 3-fold the baseline. For the patient treated in emergency for the blood-blister aneurysm, the antithrombotic protocol was as follows: oral clopidogrel, 300 mg, 4 hours before the endovascular treatment, then continuous IV heparin (activated clotting time, 2- to 3-fold the baseline), and finally an IV bolus of aspirin (250 mg) during the procedure. Then the dual antiplatelet therapy (clopidogrel, 75 mg and aspirin, 250 mg) was pursued for 6 months and aspirin alone for an 6 additional months.

For patients who were resistant to clopidogrel, clopidogrel was replaced by ticagrelor (90 mg, twice a day) for 6 months.

The patients were all treated with a FDS (Pipeline Embolization Device [Covidien, Irvine, California] in 58 cases [67%], Silk [Balt Extrusion, Montmorency, France] in 14 cases [16%], NeuroEndoGraft [Stryker Neurovascular, Kalamazoo, Michigan] in 10 cases [11.5%], and FRED [MicroVention, Tustin, California] in 5 cases [5.7%]). In 12/85 cases (14%), 2 FDSs or more were used for the treatment of the same aneurysm. On average, 1.15 ± 0.4 FDSs were used per patient (range, 1–3).

In 80% of the cases (68/85), an FPV-CTA was performed in the angiographic suite just after the stent(s) deployment. The remaining 20% of cases corresponded to the cases treated in our early experience for which no FPV-CTA was performed or to cases for which raw data were not available on the PACS. In 37% of the cases (21/68), coils were already present in the aneurysm sac (either in case of recanalized coiled aneurysm or when the aneurysm was coiled before the FPV-CTA). In 15/68 cases (22%), the delivery microcatheter was kept in place (ie, within the lumen of the FDS) during the FPV-CTA acquisition (Fig 1). In one case, an FPV-CTA was performed with a jailed microcatheter inside the aneurysm sac (Fig 2).

All the patients explored by means of FPV-CTA had the same imaging protocol detailed below.

Acquisition Protocol

All FPV-CTAs were performed by using the same protocol. Via the guiding catheter used for the stent deployment, we proceeded to an intra-arterial injection in the parent vessel of iohexol, 300 mg I/mL, diluted at 20% with saline. All the FPV-CTAs were performed in the same biplane angiographic suite (Axiom Artis dBC [Siemens, Erlangen, Germany]); C-arm FPV-CTA characteristics were as follow: 200° of rotation (from 100° left oblique projection to 100° right oblique projection); 1 image/0.4° (20s-1KDR protocol). Twenty mm^3 of the 20% diluted contrast media were injected at 1 mL/s at the beginning of the CT-rotational acquisition. Secondary reconstructions were performed on a dedicated workstation (Artis Workplace; Siemens). For these reconstructions, a 512 × 512 matrix was used with a volume of view as small as possible, adapted to the length of the FDS. The voxel size was 0.14 mm. A batch of about 500 images was obtained from this reconstruction, with 5-mm thick sections and no intersection gap.

Evaluation Criteria

All FPV-CTA acquisitions were independently reviewed by 2 observers (F.C. and F.D.M.) with 5 and 6 years, experience, respec-

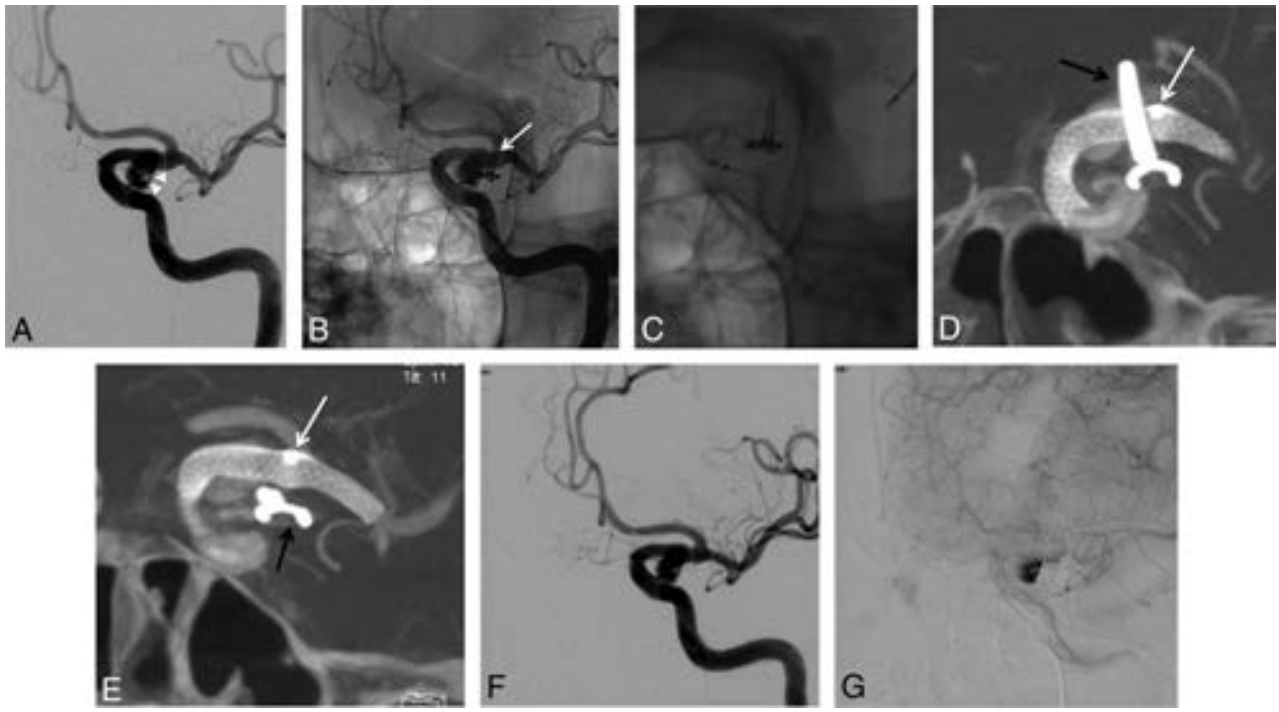

FIG 1. A 51-year-old woman presenting a recurrence of a left unruptured PComA aneurysm previously clipped. *A*, DSA in working projection showing the 5.2 × 5.0 mm recurrence with a 4.7 mm neck (*arrowheads*). *B*, Unsubtracted snapshot of the DSA in working projection displaying the clip (*white arrow*). *C*, Unsubtracted snapshot during the deployment of the FDS (Pipeline Embolization Device) from the left M1 segment to the carotid siphon. *D* and *E*, Snapshots from the FPV-CTA acquisition performed with 20% contrast media intra-arterial injection through the guiding catheter; MIP reconstruction. Satisfactory deployment of the stent is seen. Note the presence of the clip from the previous treatment (*black arrows*) and the microcatheter's tip, left in the FDS lumen during the acquisition (*white arrows*). Note that neither the clip nor the microcatheter's tip hamper the FDS visualization. *F* and *G*, Final DSA in working projection after FDS deployment (*F*, early phase; *G*, late phase). Stagnation of the contrast media within the aneurysm sac is seen at late phase (*G*). PComA indicates posterior communicating artery.

tively, in interventional neuroradiology. The FPV-CTA volumes were analyzed on a dedicated workstation (Leonardo workstation) with the aid of thin section multiplanar reconstructions (mainly in a plane perpendicular to the great axis of the parent artery) and MIP (thickness, 5 mm) reconstructions. The following criteria were independently evaluated by both observers: quality of the FDS visualization (poor/fair/good); the rate of the FDS visualized (not visualized/partial visualization/complete visualization); and the presence of misdeployment (kinking/misopening/twisted stent). In cases of stent misdeployment, the location of the misdeployment was graded as follows: proximal, central, or distal. Discrepancies between the 2 observers were settled in consensus. Finally, the presence of contrast media stagnation in the aneurysm sac was evaluated in consensus.

Statistical Analysis

Interrater agreement was performed by means of a weighted κ test.

κ index $\leq$0.40 was considered as poor agreement; between 0.41–0.60 as moderate agreement; between 0.61–0.80 as good agreement; and from 0.81–1 as excellent agreement.[8]

Influence of the following factors on FDS visualization was evaluated: age, sex, aneurysm location (ie, anterior/posterior circulation), aneurysm maximum diameter, aneurysm neck, presence of coils/clips, microcatheter in place within the FDS lumen, and presence of contrast media stagnation in the aneurysm sac. All statistical tests were performed by means of the STATA software (Version 11; StataCorp, College Station, Texas). A P value $<$.05 was considered as statistically significant.

Ethical Statement

Neither approval of the institutional review board nor patient informed consent are required by the ethics committee of our institution (Pitié-Salpêtrière Hospital) for retrospective analyses of patient records and imaging data.

RESULTS

FDS Visualization

Data regarding FDS evaluation are summarized in Table 2.

Interrater agreement was fair (k = 0.38) for the stent visualization quality (poor/fair/good) on FPV-CTA, moderate (k = 0.49) for the proportion of the stent visualized (partial/complete), and moderate (k = 0.57) for the analysis of the deployment quality (satisfactory/misopening). The analysis in consensus showed a satisfactory visualization of the FDS in 83.8% of the cases, a complete visualization of the FDS in 73.5% of the cases, and a misopening of the FDS in 11.8% of the cases (Figs 3 and 4). Univariate analysis showed that only the aneurysm's maximum diameter had an influence on stent visualization ($P < .001$). On the contrary, age, sex, aneurysm location (ie, anterior/posterior circulation), presence of coils/clipping, stent type, and number of stents had no influence on the visualization quality of the FDS (Table 3). In addition, the presence of the microcatheter inside the FDS during the acquisition (observed in 15/68 cases [22%]), the

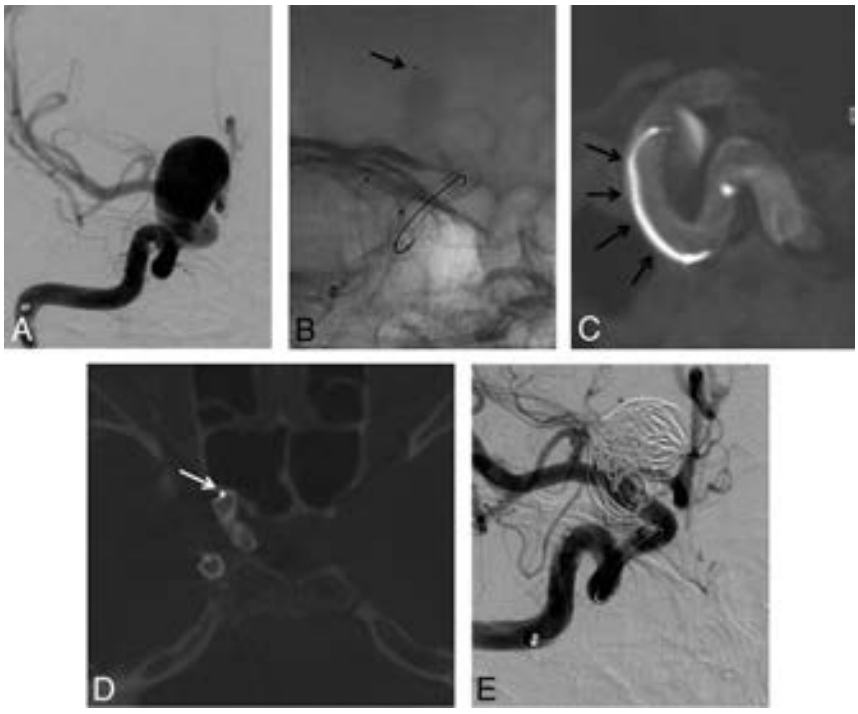

FIG 2. A 40-year-old woman treated for an incidental large right carotid ophthalmic aneurysm. *A*, Right ICA DSA in working projection showing the large paraclinoid aneurysm. *B*, Plain x-ray snapshot in working projection after the deployment of the FDS (Pipeline Embolization Device) in the parent artery, with a microcatheter jailed in the aneurysm sac (*arrow*). *C*, FPV-CTA acquisition, MIP reconstruction in sagittal view showing the satisfactory deployment of the FDS with the microcatheter jailed between the FDS and the wall of the parent artery (*arrows*). *D*, FPV-CTA, axial view. The jailed microcatheter is seen between the FDS and the wall of the parent artery (*arrow*). *E*, Final control DSA in working projection after loose coiling of the sac. Satisfactory exclusion of the sac is seen.

Table 2: Interrater agreements and analysis in consensus for the evaluation of FPV-CTAs

Interrater agreements	
Stent visualization quality	$\kappa = 0.38$
Stent rate visualized	$\kappa = 0.49$
Misdeployment	$\kappa = 0.57$
Analysis in consensus	
Good visualization	83.8%
Fair/poor visualization	16.2%
Complete visualization	73.5%
Partial visualization	27%
Satisfactory opening	88.2%
Misdeployment	11.8%

presence of a jailed microcatheter (observed in 1/68 cases [1.5%]), or the presence of contrast media stagnation (observed in 4/68 cases [6%]) had no influence on visualization quality of the FDS (Table 3). Multivariate analysis showed that both the presence of coils inside the aneurysm sac and an intrasaccular contrast media stagnation during the FPV-CTA decreased the visualization quality of the FDS ($P = .015$ and .02, respectively).

FDS Misopening/Additional Angioplasty

Misopening was depicted on FPV-CTA in 11.8% (8/68) of the cases. In 2.9% (2/68) of the cases, the misopening was visible only on the FPV-CTA. On the contrary, no case of malapposition was seen only on plain x-ray and missed by the FPV-CTA. No malapposition was seen in the case with a jailed microcatheter. In 2/8 cases (25%), the misopening was located at the distal aspect of the FDS; in 3/8 cases (37.5%), it was located at the proximal aspect. In the remaining 3 cases (37.5%) the misopening was observed in the central aspect of the FDS.

Clinical Consequences of Misdeployment Depicted

Seven (10.3%) intrastent angioplasties were performed after FDS deployment. In 5 cases (7.4%), the angioplasty was performed because major misopening was depicted on DSA before the FPV-CTA was performed. In the remaining 2 cases (2.9%), the misopening that led the operator to perform angioplasty was only seen on FPV-CTA (Figs 3 and 4). Interestingly, in both cases, the FDS were NeuroEndoGrafts.

Complications

Overall thromboembolic complication rate was 9.4% (8/85); the symptomatic thromboembolic complication rate was 7% (6/85). Thromboembolic complications leading to neurologic sequelae were recorded in 4.7% (4/85) of the cases. Acute thromboembolic complications (ie, intraoperative or in the immediate postoperative period) occurred in 4.7% of the cases (4/85); among them, only 2 (2.3%) were responsible for neurologic sequelae. Only 1 (1.2%) thromboembolic complication related to misopening or kinking of the FDS was recorded. In this case, a clot formed inside the FDS, which was misopened in its central aspect. This incomplete opening was obvious on DSA, and the clot resolved after intrastent angioplasty and IV injection of a bolus of abciximab. No clinical consequence was recorded in the latter patient. Three delayed (≥ 4 months) ischemic complications were recorded. These 3 cases have been previously reported.[9] None of these delayed ischemic complications were related to FDS misopening or kinking. Interestingly, in 1 case, a delayed stenosis located at the distal aspect of the FDS was depicted after a thromboembolic event occurred, whereas no misopening was seen on the FPV-CTA performed intraoperatively.[9]

DISCUSSION

FDSs are a new tool in the armamentarium of the interventional neuroradiologist that may help in treating intracranial aneurysms previously considered as uncoilable or very challenging to treat with regular techniques.[10]

Despite their potential for the treatment of difficult aneurysms, one of the major limitations for their use is their poor radiopacity. Indeed, to increase their pushability and conformability, the use of radiopaque components in the design of the FDS is limited because they dramatically increase their stiffness.[11]

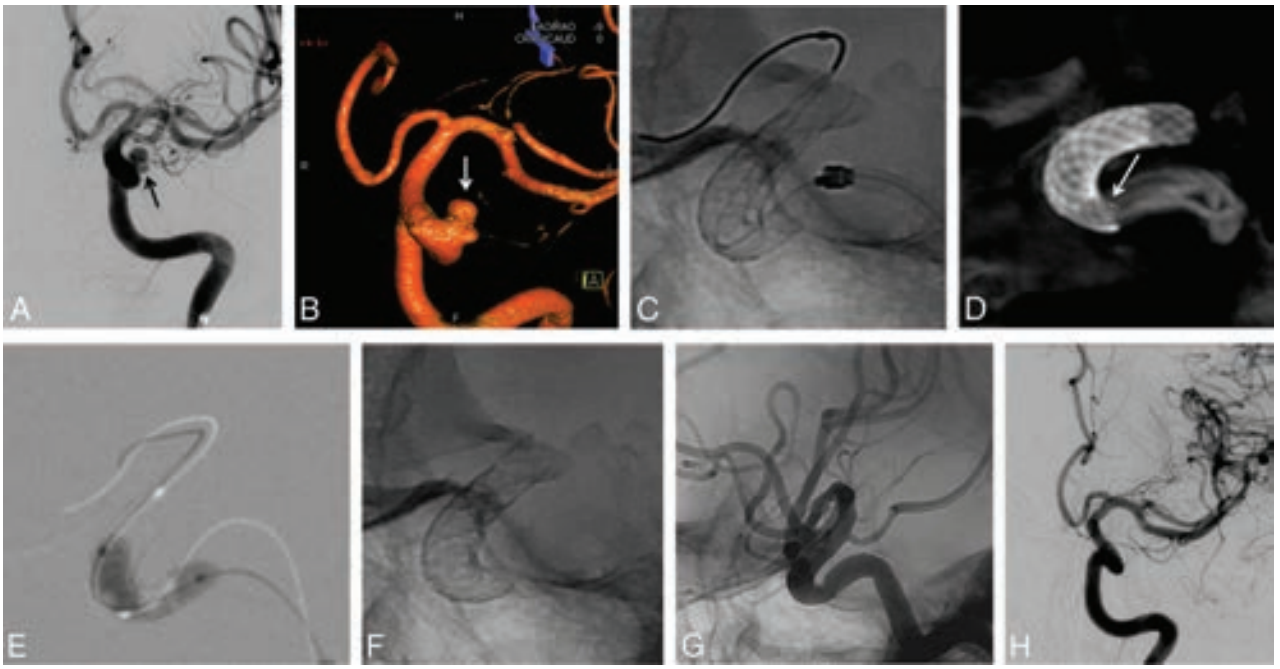

FIG 3. A 52-year-old woman treated for an unruptured left carotid ophthalmic large-neck aneurysm. *A*, Left ICA DSA in working projection (*A*) and 3D rotational angiography (*B*) showing the bi-lobed paraclinoid aneurysm with a large neck. Two overlapped FDSs (NeuroEndoGraft) were deployed in the carotid siphon to cover the aneurysm neck. *C*, Unsubtracted plain x-ray in lateral projection; the satisfactory opening of the distal FDS is demonstrated, but the proximal aspect of the proximal FDS is not clearly seen. *D*, FPV-CTA (sagittal view MIP reconstruction clearly separates the 2 FDSs and confirms an incomplete opening of the proximal aspect of the proximal FDS (*arrow*), which was subsequently treated by intrastent balloon angioplasty (*E*). *F* and *G*, Plain x-ray snapshots (*F*, without and *G*, with contrast media injection) in lateral projection showing a satisfactory opening of the FDS. *H*, One-year follow-up DSA in working projection showing the complete occlusion of the aneurysm.

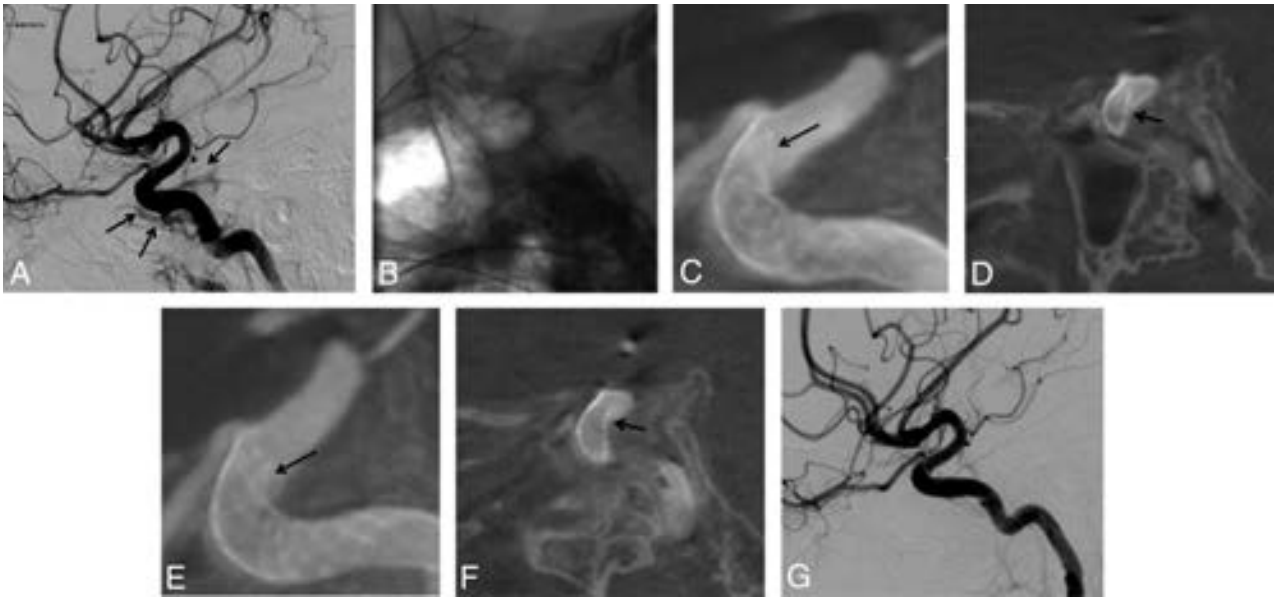

FIG 4. A 30-year-old man treated for a traumatic left carotid cavernous fistula, 1 month after a severe traumatic brain injury. *A*, Left ICA DSA in lateral projection before stent placement. Note the filling of the ipsilateral cavernous sinus (*arrows*). Treatment with an FDS covering the ICA's arterial tear was chosen. One FDS (NeuroEndoGraft) was deployed in the carotid siphon to cover the arterial tear. *B*, Unsubtracted snapshot after the stent deployment. No obvious malapposition of the stent is seen. *C* and *D*, FPV-CTA after the stent deployment in sagittal MIP reconstruction (*C*) and thin section sagittal oblique reconstruction (*D*). This acquisition clearly shows a narrowing of the distal aspect of the FDS (*arrow*) that prompted the operator to perform an intrastent balloon angioplasty. *E* and *F*, Postangioplasty FPV-CTA (*E*, sagittal view, MIP reconstruction; *F*, thin-section sagittal oblique reconstruction) shows incomplete but satisfactory opening of the distal aspect of the FDS (*arrow*). *G*, One-year follow-up DSA showing the complete cure of the traumatic fistula.

FPV-CTA is a CT-like acquisition performed via a rotation of the C-arm–mounted flat panel around the patient's head that can be easily performed in the angiographic suite. Since its early development, it has shown its potential to depict intraprocedural bleeding[12] and also to provide accurate imaging of endovascular implants.[13,14] The potential of FPV-CTA has been shown for the

Table 3: Univariate and multivariate analyses

Variables	Poor/Fair FDS Visualization	Good FDS Visualization	Univariate Analysis (*P* Value)	Multivariate Analysis (*P* Value)
Age, yr (mean ± SD)	51.5 ± 12.7	51.5 ± 12.3	.12	.7
Female (no., %)	7 (64)	44 (77)	.45	.61
Anterior location (no., %)	10 (90)	51 (89)	1	.94
Acute rupture (no., %)	0 (0)	3 (5)	1	.64
Recanalization/recurrence	4 (36)	7 (12)	.73	.34
Aneurysm max. diameter, mm (mean ± SD)	15.5 ± 8.2	8.7 ± 5.2	<.001[a]	.06
Aneurysm neck, mm (mean ± SD)	6.35 ± 3.65	5.1 ± 2.2	.13	.795
Stent type (PED; no., %)	36 (63)	8 (73)	.73	.96
No. of stents (mean ± SD)	1.2 ± 0.5	1.1 ± 0.3	.25	.92
Additional coils (no., %)	8 (73)	14 (25)	.004[a]	.015[a]
Microcatheter in place (no., %)	2 (18)	11 (19)	1	.28
Contrast media stagnation (no., %)	2 (18)	2 (3.5)	.12	.02[a]

Note:—max indicates maximum; PED, Pipeline Embolization Device.
[a] Statistically significant difference.

accurate visualization of intracranial stents (laser-cut[5,15,16] as well as braided stents[7]). It helps to see precisely the struts of the stent and may allow the depiction of a kinking, twisting, or stent misopening. FPV-CTA protocols have been developed either without injection[5] or with diluted contrast material injection.[17,18] The major advantage of protocols with contrast material injection (IV or intra-arterial) is that they may help to depict intrastent thrombus or endoleak (ie, contrast media filing between the FDS and the inner wall of the parent artery) caused by incorrect apposition of the stent.

Only scant data are available in the literature on the potential of FPV-CTA by intra-arterial[4,7] or IV[17] injection for the visualization of FDSs and its clinical impact. Such protocols have been used to evaluate the accuracy of the FDS deployment intraoperatively[4] and for follow-up imaging.[4,17] The potential of the visualization of the accurate deployment of FDS appears of tremendous importance owing to the fact that most intraoperative, postprocedure, or delayed complications, like thromboembolic events or even stent occlusion, seem to be related to FDS kinking or misdeployment.[19] In our series, we did not record any symptomatic ischemic complication caused by kinking or misdeployment of the FDS. The absence of such complications in our series may be explained by the fact that we widely used FPV-CTA (80% of the cases) to evaluate the FDS deployment and performed intrastent angioplasty in case of inaccurate wall apposition of the FDS. In addition, some cases of delayed aneurysm rupture have been linked to endoleak caused by incomplete deployment of the FDS. These endoleaks may lead to filling of the aneurysm with no exit for the blood trapped in the aneurysm sac.[20] No such complication occurred in our series. Consequently, we think that FPV-CTA should be systematically performed after FDS deployment because it may reduce the complication rate observed with these devices, one of the main drawbacks for their use.

To the best of our knowledge, we present the largest series of patients treated by FDS who underwent intraoperative FPV-CTA, and the only one for which an interrater agreement was evaluated and for which risk factors for poor/fair FDS visualization were assessed. This protocol provides, in a single acquisition, information on stent deployment, intrastent thrombosis, or stenosis and helps to see precisely which side arteries are covered by the FDS. We chose intra-arterial rather than an IV contrast media injection for the FPV-CTA acquisition to reduce the risk of poor opacification of the parent artery because of nonproper acquisition time. In addition, a 20% contrast material dilution (20% contrast media/80% saline) was chosen to avoid bright opacification of the parent vessel that would have hampered the visualization of the FDS.

In our series, satisfactory visualization of the FDS was reached in 83.8% of the cases; complete FDS visualization was observed in 73.5% of the cases. Interrater agreement was poor for stent visualization quality ($k = 0.38$) and moderate for the rate of FDS visualization ($k = 0.49$). However, the depiction of misopening was more reproducible ($k = 0.57$). Malapposition of the FDS was observed in 11.8% of the cases, which prompted the operator to perform an intrastent angioplasty in 7.4% of the cases (2.9% on the basis of FPV-CTA alone). In the series by Kizilkilic et al,[4] FPV-CTA results led to additional maneuvers (intrastent angioplasty or telescopic stent deployment) in 13% of the cases.

The only factors that were found by the multivariate analysis to be reducing the FDS visualization were the presence of coils and the presence of contrast media stagnation ($P = .015$ and .02, respectively). Consequently, we recommend performing the FPV-CTA acquisition before additional coiling when coils are needed (especially for large and giant aneurysms). To avoid contrast media stagnation in the aneurysm sac (frequently seen in giant and large aneurysms) that may hamper the FDS visualization, we recommend rinsing the parent artery with saline through the guiding catheter before performing the FPV-CTA. However, this rinsing may sometimes be insufficient when major intrasaccular stagnation is obtained after the FDS deployment. Interestingly, FPV-CTA acquisitions with the microcatheter inside the FDS lumen did not reduce the visualization quality. In addition, in the only case in which a jailed microcatheter was present in our series, no malapposition was observed. However, the presence of a jailed microcatheter may hamper the FDS deployment, especially in cases of the parent artery presenting huge curves.

Limitations of the Study

Our study presents some limitations. First, this is a monocenter retrospective study. Second, the population involved was a middle-sized one ($n = 83$). However, the relatively low volume of the population involved could be explained by the fact that the indi-

cations for FDS treatment are still nowadays limited because of a significant increased complication risk compared with regular endovascular techniques.[21] Second, no metallic artifact reduction algorithm was used in our series. These algorithms may be very useful when coils or clipping are already present before the stent deployment (recanalized aneurysms).[6,14,22] However, our results reflect the regular clinical practice because these algorithms are only available in few centers with angiographic suites optimized to clinical research. Finally, the proportion of FDS brands used for the treatment of the patients was not evenly distributed. Indeed, in most cases, a Pipeline Embolization Device was used (58/85; 68%). This heterogeneity made the comparison between the different FDSs for the quality of the deployment impossible.

CONCLUSIONS

FPV-CTA is a useful tool to depict FDS misdeployment/misopening, which may be not visible on plain x-ray. In 2.9% of the cases, the results of the FPV-CTA prompted investigators to perform intrastent angioplasty to avoid acute or delayed thromboembolic complication. We thus recommend performing FPV-CTA systematically after stent deployment in patients treated with FDS.

Disclosures: Frédéric Clarençon—*UNRELATED*: *Payment for Lectures including Service on Speakers Bureaus*: Medtronic, Guerbet, Balt Extrusion; *Other*: Codman Neurovascular, *Comments*: Study Core Lab. Alessandra Biondi—*RELATED: Consulting Fee or Honorarium*: Medtronic, Stryker Neurovasular, *Comments*: consultant and proctor; *UNRELATED*: *Consultancy*: Phenox. Nader-Antoine Sourour—*RELATED*: *Consulting Fee or Honorarium*: Medtronic, Balt Extrusion, Microvention; *UNRELATED*: *Stock/Stock Options:* Medina.

REFERENCES

1. Briganti F, Napoli M, Tortora F, et al. **Italian multicenter experience with flow-diverter devices for intracranial unruptured aneurysm treatment with periprocedural complications–a retrospective data analysis.** *Neuroradiology* 2012;54:1145–52 CrossRef Medline
2. Brinjikji W, Murad MH, Lanzino G, et al. **Endovascular treatment of intracranial aneurysms with flow diverters: a meta-analysis.** *Stroke* 2013;44:442–47 CrossRef Medline
3. Brinjikji W, Cloft HJ, Fiorella D, et al. **Estimating the proportion of intracranial aneurysms likely to be amenable to treatment with the Pipeline embolization device.** *J Neurointerv Surg* 2013;5:45–48 CrossRef Medline
4. Kizilkilic O, Kocer N, Metaxas GE, et al. **Utility of VasoCT in the treatment of intracranial aneurysm with flow-diverter stents.** *J Neurosurg* 2012;117:45–49 CrossRef Medline
5. Clarençon F, Piotin M, Pistocchi S, et al. **Evaluation of stent visibility by flat panel detector CT in patients treated for intracranial aneurysms.** *Neuroradiology* 2012;54:1121–25 CrossRef Medline
6. van der Bom IM, Hou SY, Puri AS, et al. **Reduction of coil mass artifacts in high-resolution flat detector conebeam CT of cerebral stent-assisted coiling.** *AJNR Am J Neuroradiol* 2013;34:2163–70 CrossRef Medline
7. Poncyljusz W, Zwarzany Ł, Safranow K. **Visualization of novel microstents in patients with unruptured intracranial aneurysms with contrast-enhanced flat panel detector CT.** *Eur J Radiol* 2015;84:1313–17 CrossRef Medline
8. Landis JR, Koch GG. **The measurement of observer agreement for categorical data.** *Biometrics* 1977;33:159–74 CrossRef Medline
9. Guédon A, Clarençon F, Di Maria F, et al. **Very late ischemic complications in flow-diverter stents: a retrospective analysis of a single-center series.** *J Neurosurg* 2016;125:929–35 CrossRef Medline
10. Wakhloo AK, Gounis MJ. **Revolution in aneurysm treatment: flow diversion to cure aneurysms: a paradigm shift.** *Neurosurgery* 2014;61 Suppl 1:111–20 CrossRef Medline
11. Hoffmann T, Gugel S, Beuing O, et al. **Radiopacity assessment of neurovascular implants.** *Current Directions in Biomedical Engineering* 2016;2:533–36 CrossRef
12. Struffert T, Richter G, Engelhorn T, et al. **Visualisation of intracerebral haemorrhage with flat-detector CT compared to multislice CT: results in 44 cases.** *Eur Radiol* 2009;19:619–25 CrossRef Medline
13. Psychogios MN, Scholz B, Rohkohl C, et al. **Impact of a new metal artefact reduction algorithm in the noninvasive follow-up of intracranial clips, coils, and stents with flat-panel angiographic CTA: initial results.** *Neuroradiology* 2013;55:813–18 CrossRef Medline
14. Stidd DA, Theessen H, Deng Y, et al. **Evaluation of a metal artifacts reduction algorithm applied to postinterventional flat panel detector CT imaging.** *AJNR Am J Neuroradiol* 2014;35:2164–69 CrossRef Medline
15. Levitt MR, Cooke DL, Ghodke BV, et al. **"Stent view" flat-detector CT and stent-assisted treatment strategies for complex intracranial aneurysms.** *World Neurosurg* 2011;75:275–78 CrossRef Medline
16. Richter G, Engelhorn T, Struffert T, et al. **Flat panel detector angiographic CT for stent-assisted coil embolization of broad-based cerebral aneurysms.** *AJNR Am J Neuroradiol* 2007;28:1902–08 CrossRef Medline
17. Yu SC, Lee KT, Lau TW, et al. **Intravenous C-arm conebeam CT angiography following long-term flow-diverter implantation: technologic evaluation and preliminary results.** *AJNR Am J Neuroradiol* 2016;37:481–86 CrossRef Medline
18. Ebrahimi N, Claus B, Lee CY, et al. **Stent conformity in curved vascular models with simulated aneurysm necks using flat-panel CT: an in vitro study.** *AJNR Am J Neuroradiol* 2007;28:823–29 Medline
19. Benndorf G, Strother CM, Claus B, et al. **Angiographic CT in cerebrovascular stenting.** *AJNR Am J Neuroradiol* 2005;26:1813–18 Medline
20. Darsaut TE, Rayner-Hartley E, Makoyeva A, et al. **Aneurysm rupture after endovascular flow diversion: the possible role of persistent flows through the transition zone associated with device deformation.** *Interv Neuroradiol* 2013;19:180–85 CrossRef Medline
21. Naggara ON, Lecler A, Oppenheim C, et al. **Endovascular treatment of intracranial unruptured aneurysms: a systematic review of the literature on safety with emphasis on subgroup analyses.** *Radiology* 2012;263:828–35 CrossRef Medline
22. Chintalapani G, Chinnadurai P, Srinivasan V, et al. **Evaluation of C-arm CT metal artifact reduction algorithm during intra-aneurysmal coil embolization: assessment of brain parenchyma, stents and flow-diverters.** *Eur J Radiol* 2016;85:1312–21 CrossRef Medline

Packing Density Necessary to Reach a High Complete Occlusion Rate in Circumferential Unruptured Intracranial Aneurysms Treated with Stent-Assisted Coil Embolization

R.T. Tosello, U.C. Batista, B.J.A. Pereira, and R.L. Piske

ABSTRACT

BACKGROUND AND PURPOSE: This study is a homogeneous series of circumferential unruptured intracranial aneurysms with large necks treated with stent-assisted coil embolization. Our purpose was to demonstrate which value of packing density is required to produce a durable occlusion.

MATERIALS AND METHODS: We retrospectively evaluated all patients with unruptured intracranial aneurysms who were treated with stent-assisted coil embolization having late angiographic control between 2004 and 2014, in a single large cerebrovascular referral center. To calculate the packing density, aneurysm volume, and coil volume, we used an on-line system.

RESULTS: In 49 circumferential unruptured intracranial aneurysms treated with stent-assisted coil embolization, 38.7% ($n = 19$) had complete occlusion in the immediate control. Of those with incomplete occlusion, 80% ($n = 24$) progressed to complete occlusion in the late angiographic follow-up. At late angiographic control, 87.7% ($n = 43$) of aneurysms were completely occluded. All aneurysms with a packing density of ≥19% were completely occluded. Packing density was the only statistically significant predictor of complete occlusion. None of the aneurysms with complete occlusion at immediate control or at late angiographic control had recurrence.

CONCLUSIONS: In circumferential aneurysms treated with stent-assisted coil embolization, packing density is the main predictor of complete occlusion. In this type of aneurysm, a packing density of ≥19% was enough to reach complete occlusion; knowing this is important to avoid higher packing densities that have more risk.

ABBREVIATIONS: PD = packing density; SACE = stent-assisted coil embolization; UIA = unruptured intracranial aneurysm

Unruptured intracranial aneurysms (UIAs) are present in 3% of the adult population and are increasingly detected due to more frequent use of noninvasive angiographic diagnostic imaging.[1-3]

Endovascular coiling for the treatment of intracranial aneurysms was first introduced into clinical use in 1990, and since then, the greatest concern has been the high recanalization rate, recently estimated to be approximately 20%.[4,5] This occurs more often in large-neck aneurysms,[6] which are currently treated with stent-assisted coil embolization (SACE).

In unassisted coil embolization, higher packing density (PD) rates are correlated with lower recanalization rates.[7-10] It is likely that in SACE treatment, the packing density necessary to reach a stable complete occlusion is lower, but there is no homogeneous study to confirm that possibility, to our knowledge.

The purpose of this study was to demonstrate which value of PD is likely to produce durable occlusion in a homogeneous series of circumferential, large-neck UIAs treated with SACE in a single cerebrovascular referral center.

MATERIALS AND METHODS

The study protocol was approved by a local institutional review board. This is a single-center retrospective review of our data bank from February 2004 to June 2014. Clinical and image records were independently reviewed by a member of the research team who did not participate in the treatment of any of the included patients. The patient demographics, treatment details and effects, results of follow-up, and complications were recorded.

All patients were treated under general anesthesia, and stent-assisted coiling was performed on a biplane Integris Allura FD20/30 angiographic system (Philips Healthcare, Best, the Netherlands). Regular techniques were used, including prior use of dual antiplatelet therapy.

Received March 6, 2017; accepted after revision May 18.

From the Centro de Neuro-Angiografia, Hospital Beneficência Portuguesa de São Paulo-SP, Paulo-SP, Brazil.

Please address correspondence to Renato Tavares Tosello, MD, Rua Joao Moura, 975 Apt 131, Edifício Eliana; e-mail: retosello@hotmail.com

http://dx.doi.org/10.3174/ajnr.A5303

Table 1: Relationship between the location and number of the aneurysms

Location	No.	%
Middle cerebral artery	11	22.4%
Anterior communicating artery	9	18.4%
Basilar artery	5	10.2%
Posterior communicating artery	5	10.2%
Bifurcation of the internal carotid artery	5	10.2%
Internal carotid artery	3	6.1%
Pericallosal artery	2	4.1%
Others	9	18.4%
Total	49	100%

From the 310 aneurysms in 271 patients treated with SACE, we selected 49 unruptured circumferential wide-neck aneurysms, not previously treated in 47 patients, with 3D reconstruction angiography before treatment and at least 1 late angiographic control. The mean time from the operation until the first follow-up was 7.0 months. Wide-neck aneurysms were defined as having at least 1 of the following criteria: neck size $\geq$ 4 mm, dome-to-neck ratio $<$ 1.5, or a cylindric neck.

To calculate the packing density, volume of aneurysms, and volume of coils, we used an on-line system available at www.angiocalc.com. This calculation was based on the shape and size of the aneurysm and on the type and size of the coils. All aneurysms treated with coils that did not have calculations based on this site were excluded.

Of the 47 patients, 15 were men, and 32, women. The mean age was 56.7 years. Of the 49 aneurysms, 32 had wide necks ($>$4 mm), 42 had unfavorable dome-to-neck ratios ($<$1.5 mm), 26 had wide necks and unfavorable dome-to-neck ratios, and 2 had cylindric necks.

The relationship between the location and number of aneurysms is shown in Table 1.

Aneurysm obliteration rates on the immediate control and first follow-up angiograms were classified as complete (100%); any opacity in the neck or sac of the aneurysm was considered incomplete obliteration.

In the late angiographic control, we evaluated the rate of progression from incomplete to complete occlusion and whether there was recurrence of an aneurysm with initial complete occlusion. We compared these data with the location of the aneurysm, the volume of the aneurysm and coils, the PD, and the type of stent used.

We used 4 types of stents: the Neuroform stent (Stryker Neurovascular, Kalamazoo, Michigan) in 35 procedures, the LEO stent (Balt Extrusion, Montmorency, France) in 16 procedures, the Enterprise stent (Codman & Shurtleff, Raynham, Massachusetts) in 2 procedures, and the Solitaire stent (Solitaire AB neurovascular remodeling device; Covidien, Irvine, California) in 1 procedure.

Statistical Analysis

Statistical analysis was performed by using R statistical and computing software, Version 3.2.2 (http://www.r-project.org/). For the relationships between volume and packing and volume and incomplete occlusion, the Pearson correlation coefficient was calculated. To obtain the relationship among age, sex, aneurysm volume, packing density, and volume of coils and complete occlusion at 6-month follow-up, we used logistic regression. We also calculated the corresponding 95% confidence interval to verify the existence of the relationship. The relationships between a high percentage of PD and complete occlusion and between large aneurysms and incomplete occlusion were assessed with logistic regression analysis. P values $<$ .05 indicated a significant difference.

RESULTS

In the immediate control, complete occlusion occurred in 38.7% of aneurysms (n = 19), and incomplete occlusion, in 61.2% aneurysms (n = 30). However, of those who had incomplete occlusion, 80% (n = 24) progressed to complete occlusion and the remaining 20% (n = 6) had incomplete occlusion (Fig 1). At the late angiographic control, 43 aneurysms (87.7%) had complete occlusion. There was no aneurysm recurrence in the first follow-up for those aneurysms that were completely occluded in the immediate control.

The mean volume of the 49 aneurysms was 175.2 mm^3 (median, 329.7 mm^3; range, 4.2–4849.9 mm^3). The mean coil volume was 38.5 mm^3 (median, 54.7 mm^3; range, 1.5–396.3 mm^3), and the average PD was 37.9% (median, 28.6%; range, 2.8%–54.9%).

Above 19% of PD, all aneurysms were completely occluded, independent of their volume (Fig 2).

According to Fig 2, the aneurysms were subdivided into 2 groups on the basis of volume: A, $<$179.6 mm^3 (n = 37); B, $>$179.6 mm^3. In group A, all aneurysms except 1 had complete occlusion, independent of their PD. The only aneurysm incompletely occluded in this group was one in which we could not deploy a necessary second coil due to the impossibility of recatheterizing the aneurysm sac after the first coil. In group B, complete occlusion was reached for all aneurysms with a PD of $>$19%. Aneurysms of $>$179.59 mm^3 had a larger diameter, between 7.0 and 7.8 mm.

The statistically significant correlation coefficient ($P < .05$) between aneurysm volume and PD was -0.42 (95% CI, -0.62 to -0.15; $P = .003$), and the correlation between aneurysm volume and incomplete aneurysm occlusion was -0.44 (95% CI, 0.18–0.64; $P = .002$). The correlation coefficient between coil volume and PD was 0.26 (95% CI, -0.50 to 0.02; $P = .071$), which is not statistically significant. Large volumes of coils are used in large aneurysms, which tend to have lower PD.

A multivariate analysis with predictive factors of complete aneurysm obliteration, including age, aneurysm volume, PD, and volume of coils, showed that the only statistically significant predictive factor was PD (Table 2).

Procedure-related complications occurred in 3 patients (6.4%, 3/47). In 2 patients (4.1%, 2/49), there was thrombosis of the stent after its release; one was treated with an intravenous infusion of a loading dose of abciximab (ReoPro), and the other, with an intra-arterial injection of tirofiban (Aggrastat) and mechanical thrombolysis, with full opening of the parent vessel. Both had a transient deficit and full recovery in 3 and 4 days, respectively. One patient (2.1%, 1/47) had an asymptomatic vertebral artery dissection, and a stent was placed at the site of dissection. There was no neurologic deficit in any of the 3 patients at discharge.

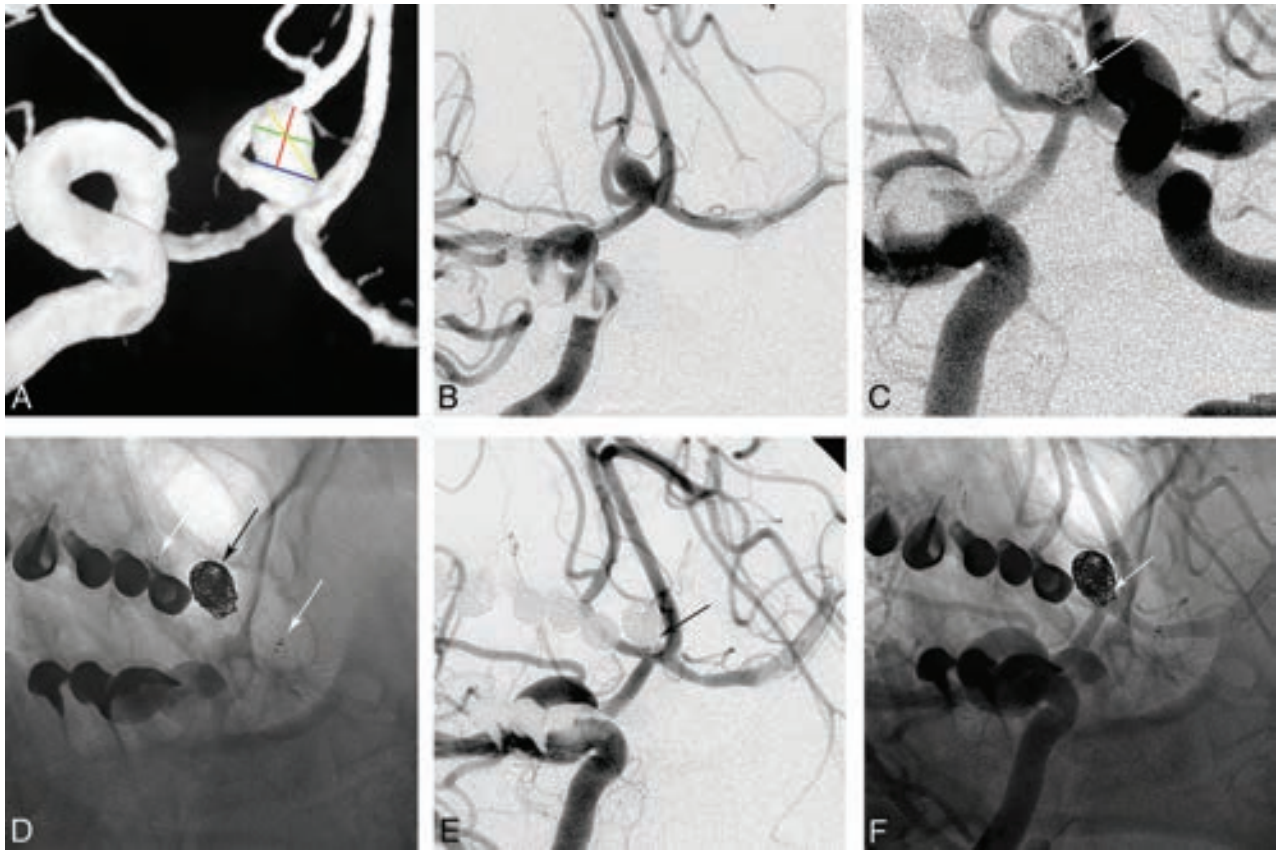

FIG 1. A 62-year-old man presenting with a small, incidental aneurysm of the anterior communicating artery. A 3D rotational angiogram (*A*) was obtained before the embolization. Measurements were made of the neck (*blue line*), diameter parallel to the neck (*green line*), height (*red line*), and largest diameter (*yellow line*). Projection work after a right internal carotid contrast injection (*B*) shows the relation of the anterior communicating artery aneurysm to the anterior cerebral arteries. Final control after simultaneous contrast injections in the internal carotid artery. *C* and *D*, Residual neck flow (*white arrow*) after stent-assisted coil embolization (stent, *white arrows*; coils, *black arrow*). Six-month angiographic controls (*E* and *F*) show the evolution to complete occlusion (*black* and *white arrows*).

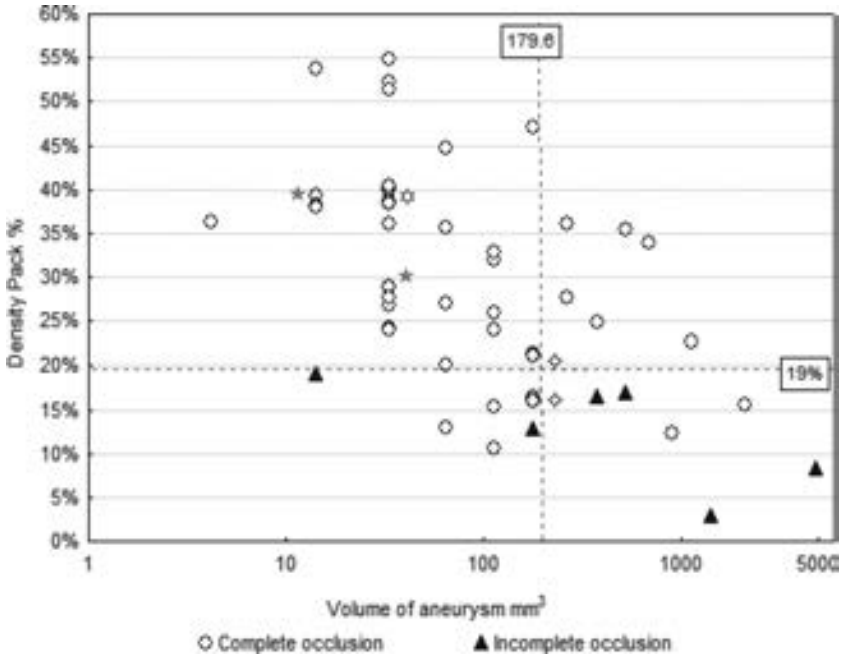

FIG 2. Results of the Pearson test, demonstrating that above 19% packing density, all aneurysms had complete occlusion. Regarding the volume, aneurysms above 179.6 mm^3 had a higher rate of incomplete occlusion when the packing density was below 19%. If >1 aneurysm is overlapping, note the following symbols: ✧, 2 aneurysms, ★, 3 aneurysms, ✡, 4 aneurysms.

DISCUSSION

Stent-assisted coil treatment for large-neck aneurysms has shown a higher rate of evolution to complete occlusion in the follow-up and a lower rate of late aneurysm recanalization compared with nonstented aneurysms.[6,8,11-14] The mechanisms involved are hemodynamic modification of the inflow angle to the sac, the presence of more metal on the neck, and the scaffold provided by the stent and coils favoring better endothelialization.[6,15-17] It is thought that the main predictor of immediate and late complete occlusion and the absence of aneurysm recurrence is the PD.[8,11,12,18-22]

However, we supposed that to achieve a higher PD, it is necessary to place several coils inside the aneurysm, increasing the treatment time, the risk of thromboembolic and hemorrhagic complications, and the cost of the procedure.

Gallas et al[23] found that 26% of aneurysms had an incomplete occlusion among 1036 aneurysms treated with coils.

Table 2: Multivariate analysis of predictive factors for complete occlusion

	Relative Risk	95% CI	*P* Value
Sex	0.933	0.254–6.045	.929
Age	0.746	0.089–2.345	.684
Volume of the aneurysm	1.001	1.000–1.002	.079
Packing density[a]	0.876	0.657–0.955	.012
Volume of the coils	1.005	0.998–1.011	.123

[a] Significance level is .05.

Raymond and Roy[7] reported that incomplete occlusion in the immediate control of aneurysms treated with coils is a risk factor for aneurysm recanalization. Piotin et al[11] reported that aneurysms treated with SACE had lower recanalization rates than nonstented aneurysms. Lawson et al[22] identified PD as a predictor of complete occlusion in aneurysms treated with SACE.

Chalouhi et al[8,13] found an adequate PD of 12%–22% for complete occlusion of aneurysms in angiographic follow-up tests in 290 aneurysms treated with SACE, but the aneurysm recurrence rate was not reported.

Unlike others, our study considered only circumferential saccular UIAs, homogenizing the group to find the PD required for a high complete aneurysm occlusion rate, with low rates of recurrence and complications during the procedure.

Our study presented a rate of 38.7% ($n = 19$) with complete occlusion and 61.2% ($n = 30$) with incomplete occlusion in the immediate control. Of those in the latter group, 80% ($n = 24$) progressed to complete occlusion in the late angiographic follow-up.

PD is the main predictor of complete occlusion and aneurysm recurrence. Our study found all aneurysms with PD ≥19% with initial incomplete occlusion evolved to complete occlusion in the late angiographic follow-ups, with a statistically significant relationship between the variable PD and the first follow-up, in agreement with the study of Chalouhi et al.[8] Aneurysms with low PD (<19%) tended to not evolve to complete occlusion. None of the aneurysms that were completely occluded had recurrence, emphasizing the relevance of the flow-remodeling theory in the use of stents.[6,15-17]

However, aneurysms with smaller (<100 mm^3) and moderate (100–1150.3 mm^3) volumes had high rates of complete occlusion (96% and 85%, respectively), compared with aneurysms with greater volume (>1150.3 mm^3), demonstrating that smaller aneurysm volume can reach a better PD value with higher complete occlusion rates than those of large aneurysms, as described in the literature.[5,6,9,11,12,18,24] There was no statistically significant relation between the volume and packing density of an aneurysm: The *P* value was .079 (statistical significance, $P < .05$), probably due to the low number of aneurysms.

Sluzewski et al[9] reported that all aneurysms with packing densities of >24% and a volume of <600 mm^3, treated with coil embolization, had complete occlusion. We found that all aneurysms with packing densities of ≥19% independent of their volume had complete occlusion. This finding shows that stents help neck endothelization, requiring fewer coils to reach complete occlusion.[17]

No patient with complete occlusion in our study needed retreatment, and our complication rate was 6%. All patients were discharged without neurologic deficits and none died.

A limitation of our study is its retrospective, no randomization design in a single center with a small sample due to the inclusion of only circumferential UIAs. Another limitation is the use of a variety of regular stents and coils.

Today with the advancement of technology, new stents with lower porosity or double layers (eg, LVIS Blue, Lvis, Lvis Jr; MicroVention, Tustin, California) may produce different results, needing specific studies.

CONCLUSIONS

This study shows that the SACE technique has high rates of evolution from incomplete-to-complete occlusion of aneurysms, without recurrence. The PD is the main predictor for complete aneurysm occlusion. All aneurysms with PD of ≥19% achieved complete occlusion. For small aneurysms, the rate of complete occlusion was higher than in large aneurysms because it is difficult to achieve an optimal packing density in large aneurysms. The PD needed to occlude large-neck aneurysms treated with stents is lower than in those without stents.

REFERENCES

1. Wiebers DO, Whisnant JP, Huston J 3rd, et al; International Study of Unruptured Intracranial Aneurysms Investigators. **Unruptured intracranial aneurysms: natural history, clinical outcome, and risks of surgical and endovascular treatment.** *Lancet* 2003;362:103–10 CrossRef Medline
2. Etminan N, Brown RD Jr, Beseoglu K, et al. **The unruptured intracranial aneurysm treatment score: a multidisciplinary consensus.** *Neurology* 2015;85:881–89 CrossRef Medline
3. Seibert B, Tummala RP, Chow R, et al. **Intracranial aneurysms: review of current treatment options and outcomes.** *Front Neurol* 2011; 2:45 CrossRef Medline
4. Molyneux AJ, Kerr RS, Birks J, et al; ISAT Collaborators. **Risk of recurrent subarachnoid haemorrhage, death, or dependence and standardised mortality ratios after clipping or coiling of an intracranial aneurysm in the International Subarachnoid Aneurysm Trial (ISAT): long-term follow-up.** *Lancet Neurol* 2009;8:427–33 CrossRef Medline
5. Mascitelli JR, Oermann EK, De Leacy RA, et al. **Predictors of treatment failure following coil embolization of intracranial aneurysms.** *J Clin Neurosci* 2015;22:1275–81 CrossRef Medline
6. Colby GP, Paul AR, Radvany MG, et al. **A single center comparison of coiling versus stent assisted coiling in 90 consecutive paraophthalmic region aneurysms.** *J Neurointerv Surg* 2012;4: 116–20 CrossRef Medline
7. Raymond J, Roy D. **Safety and efficacy of endovascular treatment of acutely ruptured aneurysms.** *Neurosurgery* 1997;41:1235–45; discussion 1245–46 CrossRef Medline
8. Chalouhi N, Dumont AS, Hasan D, et al. **Is packing density important in stent-assisted coiling?** *Neurosurgery* 2012;71:381–86; discussion 386–87 CrossRef Medline
9. Sluzewski M, van Rooij WJ, Slob MJ, et al. **Relation between aneurysm volume, packing, and compaction in 145 cerebral aneurysms treated with coils.** *Radiology* 2004;231:653–58 CrossRef Medline
10. Chueh JY, Vedantham S, Wakhloo AK, et al. **Aneurysm permeability following coil embolization: packing density and coil distribution.** *J Neurointerv Surg* 2015;7:676–81 CrossRef Medline
11. Piotin M, Blanc R, Spelle L, et al. **Stent-assisted coiling of intracranial aneurysms: clinical and angiographic results in 216 consecutive aneurysms.** *Stroke* 2010;41:110–15 CrossRef Medline
12. Chalouhi N, Jabbour P, Singhal S, et al. **Stent-assisted coiling of intracranial aneurysms: predictors of complications, recanalization, and outcome in 508 cases.** *Stroke* 2013;44:1348–53 CrossRef Medline
13. Chalouhi N, Starke RM, Koltz MT, et al. **Stent-assisted coiling**

versus balloon remodeling of wide-neck aneurysms: comparison of angiographic outcomes. *AJNR Am J Neuroradiol* 2013;34:1987–92 CrossRef Medline

14. Hong Y, Wang YJ, Deng Z, et al. **Stent-assisted coiling versus coiling in treatment of intracranial aneurysm: a systematic review and meta-analysis.** *PLoS One* 2014;9:e82311 CrossRef Medline
15. Tanemura H, Ishida F, Miura Y, et al. **Changes in hemodynamics after placing intracranial stents.** *Neurol Med Chir (Tokyo)* 2013;53:171–78 CrossRef Medline
16. Tateshima S, Tanishita K, Hakata Y, et al. **Alteration of intraaneurysmal hemodynamics by placement of a self-expandable stent: laboratory investigation.** *J Neurosurg* 2009;111:22–27 CrossRef Medline
17. Lopes D, Sani S. **Histological postmortem study of an internal carotid artery aneurysm treated with the Neuroform stent.** *Neurosurgery* 2005;56:E416; discussion E CrossRef Medline
18. Geyik S, Yavuz K, Yurttutan N, et al. **Stent-assisted coiling in endovascular treatment of 500 consecutive cerebral aneurysms with long-term follow-up.** *AJNR Am J Neuroradiol* 2013;34:2157–62 CrossRef Medline
19. Sadato A, Adachi K, Hayakawa M, et al. **Effects of anatomic characteristics of aneurysms on packing density in endovascular coil embolization: analysis of a single center's experience.** *Neurosurg Rev* 2016;39:109–14; discussion 114 CrossRef Medline
20. Ozretić D, Radoš M, Pavliša G, et al. **Long-term angiographic outcome of stent-assisted coiling compared to non-assisted coiling of intracranial saccular aneurysms.** *Croat Med J* 2015;56:24–31 CrossRef Medline
21. Bouillot P, Brina O, Ouared R, et al. **Particle imaging velocimetry evaluation of intracranial stents in sidewall aneurysm: hemodynamic transition related to the stent design.** *PLoS One* 2014;9:e113762 CrossRef Medline
22. Lawson MF, Newman WC, Chi YY, et al. **Stent-associated flow remodeling causes further occlusion of incompletely coiled aneurysms.** *Neurosurgery* 2011;69:598–603; discussion 603–04 CrossRef Medline
23. Gallas S, Januel AC, Pasco A, et al. **Long-term follow-up of 1036 cerebral aneurysms treated by bare coils: a multicentric cohort treated between 1998 and 2003.** *AJNR Am J Neuroradiol* 2009;30:1986–92 CrossRef Medline
24. Yang H, Sun Y, Jiang Y, et al. **Comparison of stent-assisted coiling vs coiling alone in 563 intracranial aneurysms: safety and efficacy at a high-volume.** *Neurosurgery* 2015;77:241–47; discussion 247 CrossRef Medline

The Use and Utility of Aspiration Thrombectomy in Acute Ischemic Stroke: A Systematic Review and Meta-Analysis

D. Wei, J.R. Mascitelli, D.A. Nistal, C.P. Kellner, J.T. Fifi, J.D. Mocco, and R.A. De Leacy

ABSTRACT

BACKGROUND: Thrombectomy trials are often specifically interpreted as evidence for the effectiveness of stent retrievers. The effectiveness of other thrombectomy techniques such as aspiration thrombectomy should be validated through further investigation and review.

PURPOSE: To evaluate published treatment times and clinical outcomes in patients treated with aspiration thrombectomy or ADAPT (A Direct Aspiration, First Pass Technique) for acute ischemic stroke.

DATA SOURCES: A systematic literature review was performed following Preferred Reporting Items for Systematic Reviews and Meta-Analyses (PRISMA) guidelines. MEDLINE, Scopus, and the Cochrane trial register were searched on November 8, 2016.

STUDY SELECTION: Twenty studies ($n = 1523$ patients) were included in this review and meta-analysis. One of these studies was prospective, and the rest were retrospective.

DATA ANALYSIS: Meta-analysis was performed by using a random effects model. Data and publication bias were visualized with forest plots and funnel plots.

DATA SYNTHESIS: Five studies investigated aspiration thrombectomy only, and 16 studies investigated ADAPT. Of the 16 studies on ADAPT, the rate of successful recanalization (TICI 2b/3) was 89.3% (95% CI, 85.4%–92.3%). The proportion of patients with good clinical outcome (90-day mRS $\leq$2) was 52.7% (95% CI, 48.0%–57.4%).

LIMITATIONS: Studies on ADAPT were retrospective, and there was heterogeneity between studies for successful recanalization ($P < .001$) and good clinical outcome ($P < .001$). There was evidence of publication bias for recanalization rates ($P = .01$), but not for clinical outcomes ($P = .42$).

CONCLUSIONS: ADAPT and aspiration thrombectomy are effective approaches to thrombectomy, with high recanalization rates and excellent clinical outcomes reported in the literature. Aspiration thrombectomy is a promising neurointervention, but large prospective randomized studies are needed to validate its utility.

ABBREVIATION: ADAPT = A Direct Aspiration, First Pass Technique

Endovascular therapy has recently been shown to be an effective intervention and is now the standard of care for acute ischemic stroke.[1-5] Broadly, there are 2 categories of techniques in endovascular treatment for stroke: 1) stent-based thrombectomy using retrievable stents with or without aspiration catheter and 2) aspiration thrombectomy using aspiration catheter alone. A Direct Aspiration, First Pass Technique (ADAPT) describes using aspiration thrombectomy as the first-line treatment with the possibility of adjuvant treatment if recanalization is not initially achieved. ADAPT is a commonly used thrombectomy technique among neurointerventionalists, but its effectiveness relative to stent-based thrombectomy has not been established.

Five randomized controlled clinical trials in 2015 (MR CLEAN, ESCAPE, REVASCAT, SWIFT PRIME, and EXTEND IA) demonstrated that thrombectomy is superior to intravenous alteplase for stroke caused by large vessel occlusions.[1-5]

Received March 7, 2017; accepted after revision May 24.

From the Departments of Neurosurgery (D.W., J.R.M., D.A.N., C.P.K., J.T.F., J.D.M., R.A.D.L.), Neurology (J.T.F.), and Radiology (R.A.D.L.), Mount Sinai Health System, New York, New York.

Please address correspondence to Reade A. De Leacy, MD, Department of Neurosurgery, Mount Sinai Health System, 1450 Madison Ave, Klingenstein Clinical Center, 1-North, New York, NY 10029; e-mail: reade.deleacy@mountsinai.org; @rdeleacymd

Indicates article with supplemental on-line tables.

Indicates article with supplemental on-line photos.

http://dx.doi.org/10.3174/ajnr.A5309

Thrombectomy was specifically limited to stent retrievers in some protocols and was the first-line treatment for most patients in these trials. These trials are often specifically interpreted as evidence for the effectiveness of stent retrievers. The effectiveness of other thrombectomy techniques such as aspiration thrombectomy should be validated through further investigation and review.

In this systematic review, we evaluated the effectiveness of aspiration alone and ADAPT and reviewed their advantages and disadvantages relative to stent-based thrombectomy. We also compared treatment times and clinical outcomes for patients treated with aspiration thrombectomy alone and patients who required further treatment with stent retriever.

METHODS

Literature Search and Study Categorization

This review was conducted in accordance with PRISMA (Preferred Reporting Items for Systematic Reviews and Meta-Analyses) guidelines.[6] A systematic review was performed on November 8, 2016 by using MEDLINE, Scopus, and the Cochrane trial register data bases. The search term was "(aspiration OR suction) AND stroke AND (thrombectomy OR endovascular OR neurointervention)." Duplicates were removed from records identified in the data base search. Articles were then screened based on title and abstract. The remaining papers underwent full-text review. Inclusion criteria were 1) the study must contain at least 20 patients treated with ADAPT or aspiration thrombectomy for acute ischemic stroke; 2) the study must include either a measure of treatment time or a measure of clinical outcome for patients treated with aspiration thrombectomy; and 3) the study must be written in English.

Aspiration thrombectomy and ADAPT are inconsistently defined in the literature. Terminology for aspiration thrombectomy includes thromboaspiration; forced arterial suction thrombectomy, or FAST; modified Penumbra System (Penumbra, Alameda, California); manual aspiration thrombectomy, or MAT; and ADAPT.[7-10] Manual aspiration thrombectomy has variably been used to refer to stent-based thrombectomy under aspiration and to aspiration thrombectomy itself.[9] ADAPT has a similar semantic fluidity, with some studies by using ADAPT and aspiration thrombectomy interchangeably. ADAPT has also been called sequential endovascular thrombectomy approach, or SETA; switching strategy for mechanical thrombectomy; and first-line aspiration.[11]

In this review, we define ADAPT as using aspiration thrombectomy on the first pass with the option of subsequent adjuvant treatment if recanalization is not achieved.[12] We chose to define ADAPT in this way because allowing neurointerventionalists to switch to other thrombectomy methods after initial attempts at aspiration thrombectomy is a more clinically pragmatic approach.[11] Furthermore, the ADAPT acronym explicitly specifies direct aspiration as a first pass and does not limit subsequent passes to aspiration.[12]

In contrast to "ADAPT" studies, we define "asp only" studies as ones that limit neurointervention to aspiration thrombectomy regardless of the initial ability to achieve recanalization. We make a distinction between "ADAPT-asp only" patients who received only aspiration under the ADAPT paradigm and "asp only" patients who were restricted to aspiration thrombectomy by treatment protocol. Patients treated with only aspiration under the ADAPT paradigm often achieved recanalization during initial passes with aspiration thrombectomy and did not require subsequent passes with stent retrievers. In contrast, "ADAPT-asp + adjuvant" patients often were not able to achieve recanalization with initial attempts at aspiration thrombectomy, and "asp only" patients continued with aspiration thrombectomy despite unsuccessful initial passes with aspiration thrombectomy. Patients who received only aspiration under the ADAPT paradigm might therefore represent less complicated cases, and we categorized them separately from patients restricted to an aspiration-only protocol.

Data Extraction

Demographic information, baseline characteristics, treatment, and clinical outcomes were extracted from studies that met the inclusion criteria. Demographic information included number of patients, age, and sex. Baseline characteristics include NIHSS at hospital admission and location of the occlusion. Treatment includes devices used, the proportion of patients who received IV-tPA before thrombectomy, onset-to-puncture times, puncture-to-recanalization times, proportion of patients treated with aspiration thrombectomy alone, and proportion of patients treated with stent retriever after attempt with aspiration thrombectomy (ADAPT). Clinical outcomes include TICI 2b/3 recanalization rate, rate of symptomatic intracerebral hemorrhage, rate of embolic occlusion in new territories, 90-day mRS, and 90-day mortality.

Statistical Analysis

Recanalization rates and clinical outcomes were assessed by meta-analysis. Cochran Q test and I^2 test were used to detect heterogeneity. Significant heterogeneity was defined as either a Cochran Q greater than the χ^2 critical value at 10% level of significance or an I^2 value greater than 50%. A random effects model was used for meta-analysis. All statistical analyses were performed by using the R language for statistical programming (http://www.r-project.org/).

RESULTS

Study Selection

The data base search yielded 708 studies from MEDLINE (270), Scopus (402), and Cochrane (36). Study selection is summarized in the flow diagram (Fig 1). Among these studies, the THRACE trial and the THERAPY trial were randomized controlled clinical trials with at least 20 patients treated with aspiration thrombectomy.[13,14] The THRACE trial compared thrombectomy after intravenous alteplase with intravenous alteplase alone. Of 141 patients treated with thrombectomy, 23 (16%) were patients treated with aspiration.[14] Outcome data specific to these 23 patients was not available, and this study was not included in this review. The THERAPY trial investigated whether aspiration thrombectomy after intravenous alteplase is superior to intravenous alteplase alone. The trial was terminated because of the loss of equipoise from the publication of MR CLEAN and the establishment of endovascular

therapy with intravenous alteplase as the standard of care.[13] The results of the trial are therefore underpowered, but are included in this meta-analysis. Ultimately, 20 studies comprising 1523 patients were selected for review (Table 1, On-line Tables 1 and 2).[7-13,15-27] Nineteen of these studies were retrospective, and 1 was prospective. Treatment times and clinical outcomes are summarized in Table 1.

Of the 20 studies included in this review, 5 followed an aspiration-only approach to treatment and 16 used an ADAPT paradigm. One study included both an aspiration-only group and an ADAPT group.[11] Four of the ADAPT studies included descriptive statistics for the subgroup of patients who were only treated with aspiration and the subgroup of patients with subsequent passes of adjuvant treatment after initial passes with aspiration thrombectomy (On-line Tables 3 and 4).[18,21,23,26]

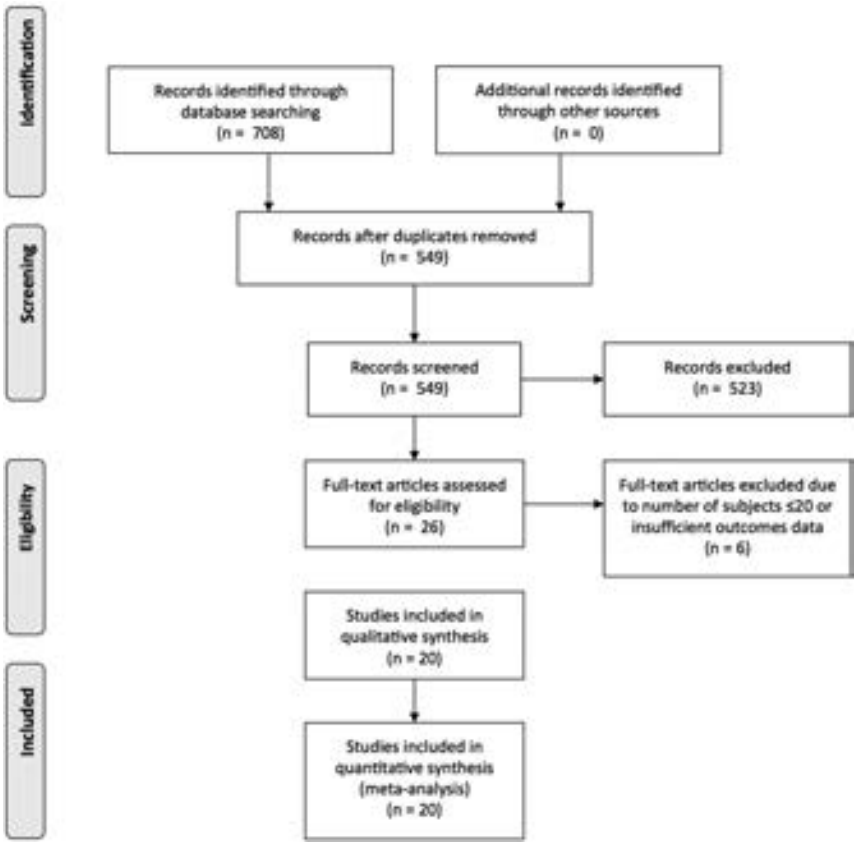

FIG 1. PRISMA flow diagram on study inclusion.

ADAPT Meta-Analysis and Study Heterogeneity

A meta-analysis of 16 ADAPT studies was performed for rates of successful recanalization (TICI 2b/3) and good clinical outcome (90-day mRS ≤2). The TICI 2b/3 recanalization rate was 89.3% (95% CI, 85.4%–92.3%) (Fig 2). Among patients treated with ADAPT, 52.7% (95% CI, 48.0%–57.4%) had a good clinical outcome (Fig 3). Cochran Q test and I^2 test suggest significant heterogeneity between studies for successful recanalization ($Q = 54.5$; $df = 15$; $I^2 = 72.5\%$; $P < .001$) and good clinical outcome ($Q = 27.8$; $df = 12$; $I^2 = 56.8\%$; $P < .001$). Tests for funnel plot asymmetry found evidence of publication bias for recanalization rates ($P = .01$), but not for clinical outcomes ($P = .42$) (On-line Figs 1 and 2).

Table 1: Treatment times and clinical outcomes by study

Study	Treatment	No. of Patients	OTP (min)	PTR (min)	Final TICI 2b/3 (%)	90-Day mRS ≤2 (%)	90-Day Mortality (%)	Asp Only (%)	Asp + Adjuvant (%)
Mocco et al,[13] 2016	Asp only	50	227	NA	70 (30/43)	38	12	NA	NA
Park et al,[10] 2016	Asp only	32	234	33	84	78	3	NA	NA
Eom et al,[7] 2014	Asp only	32	281	76	88	NA	25	NA	NA
Hwang et al,[8] 2013	Asp only	20	276	63	65	45	0	NA	NA
Kang et al,[11] 2013 (period 1)	Asp only	61	292	60	74	49	NA	NA	NA
Delgado Almandoz et al,[15] 2016	ADAPT	45	224	50	89	56	18	NA	NA
Hungerford et al,[16] 2016	ADAPT	154	454	40	95	53	10	81	19
Kabbasch et al,[18] 2016	ADAPT	30	189	26	90	43	20	70	30
Kim et al,[20] 2016	ADAPT	25	236	53	72	84	0	81	19
Kowoll et al,[21] 2016	ADAPT	54	179	41	93	NA	NA	56	44
Lapergue et al,[22] 2016	ADAPT	124	247	45	82	53	23	55	45
Mascitelli et al,[27] 2016	ADAPT	76	295	NA	92	NA	NA	58	42
Romano et al,[23] 2016	ADAPT	152	227	58	76	51	8	63	29
Vargas et al,[26] 2016	ADAPT	191	468	37	94	54	15	76	23
Jankowitz et al,[17] 2015	ADAPT	112	267	70	86	46	31	59	41
Kim et al,[9] 2015	ADAPT	70	238	34	91	60	3	91	9
Turk et al,[24] 2014a	ADAPT	98	507	37	95	39	19	78	22
Turk et al,[25] 2014b	ADAPT	64	NA	NA	95	47	NA	NA	NA
Turk et al,[12] 2014c	ADAPT	37	342	28	97	NA	NA	76	24
Kang et al,[11] 2013 (period 2)	ADAPT	74	233	68	85	68	NA	NA	NA
Kang et al,[19] 2011	ADAPT	22	318	40	82	46	14	82	18

Note:—Asp indicates aspiration; NA, not available; OTP, onset-to-puncture; PTR, puncture-to-recanalization.

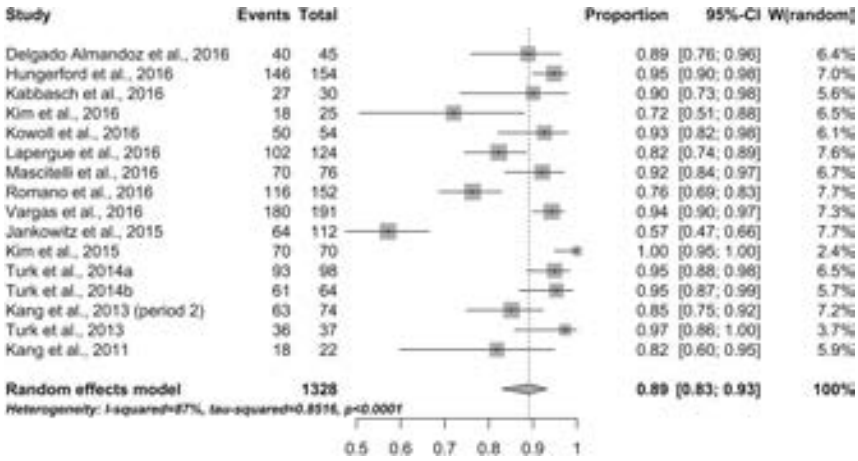

FIG 2. Forest plot of TICI 2b/3 recanalization rates by study.

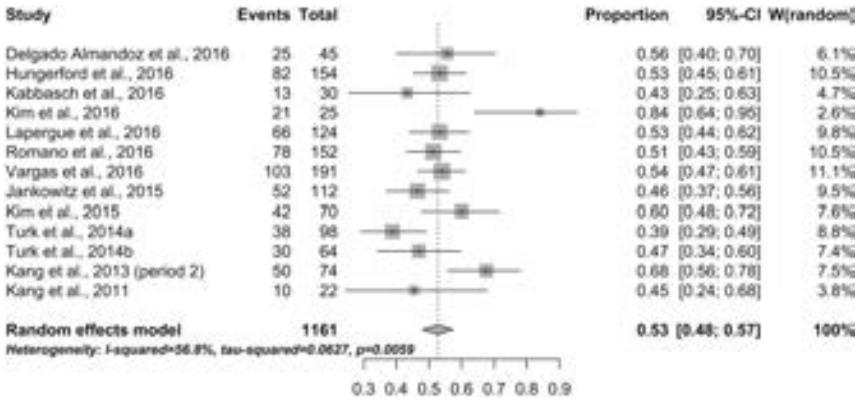

FIG 3. Forest plot of good outcomes (90-day mRS ≤90) by study.

DISCUSSION

Endovascular treatment of acute ischemic stroke with large vessel occlusion more than doubles the odds of a good clinical outcome compared with medical treatment alone and is now considered the standard of care.[28] Aspiration thrombectomy is a form of endovascular treatment that may have advantages over stent retrievers with respect to puncture-to-recanalization times, recanalization rates, cost-effectiveness, and clinical outcomes.[15,18,29] In this literature review, we categorized studies involving treatment with aspiration thrombectomy into 3 categories: 1) patients treated under an aspiration-only paradigm, 2) patients treated under ADAPT who only received aspiration thrombectomy, and 3) patients treated under ADAPT.

Aspiration Thrombectomy

Comparatively few studies assess aspiration thrombectomy without adjuvant therapy, and 5 studies were included in this review. The THERAPY trial was a randomized controlled clinical trial comparing aspiration thrombectomy after intravenous alteplase to medical treatment with alteplase alone. Aspiration thrombectomy with the Penumbra System was the procedure specified in the study protocol; however, 13% of patients were nonetheless treated with a stent retriever. A Penumbra 3D separator was also used in 25% of patients. Although the trial was underpowered because of early termination from loss of equipoise, trends were seen in superior clinical outcomes for aspiration thrombectomy. Ninety-day mortality was 12% for aspiration thrombectomy and 23.9% for medical treatment ($P = .18$). In the per-protocol population, good clinical outcome as measured by ordinal mRS had a 2.2 odds ratio ($P = .05$) in favor of aspiration thrombectomy.[13] An earlier retrospective study by Eom et al[7] similarly found aspiration thrombectomy superior to intra-arterial fibrinolysis. Aspiration thrombectomy had faster procedure times as well as higher rates of recanalization and good clinical outcomes in this study on basilar artery occlusions.

In another retrospective study, Hwang et al[8] found that aspiration thrombectomy for distal internal carotid occlusion strokes had superior recanalization rates and clinical outcomes compared with mechanical clot disruption. Patients treated with aspiration thrombectomy had a TICI 2b/3 recanalization rate of 64.7% (11/17) compared with 16.7% (1/6) for mechanical clot disruption ($P = .04$). Aspiration thrombectomy was also more likely to lead to good clinical outcome, with 45% (9/20) of patients having a 90-day mRS ≤2 compared with 16% (3/19) for mechanical clot disruption ($P = .05$). Park et al[10] evaluated the effectiveness of aspiration thrombectomy for more distally located large vessel occlusions. Aspiration thrombectomy successfully recanalized 84% (27/32) of patients with M2 occlusions, resulting in a good clinical outcome (90-day mRS ≤2) for 78% (25/32) of patients.

Kang et al[11] compared the aspiration-only paradigm with the ADAPT paradigm in a period-to-period analysis. There was a trend toward superior TICI 2b/3 recanalization rates for ADAPT over aspiration-only ($P = .10$), which became significant for difficult cases requiring at least 3 passes ($P = .03$). Overall, the aspiration-only paradigm may have superior clinical outcomes compared with intravenous medical management, intra-arterial fibrinolysis, and mechanical clot disruption. Aspiration only, however, may be inferior to the ADAPT paradigm.[8,11,13]

ADAPT–Aspiration Only

Among the 16 studies included in this review that used ADAPT, 4 provided descriptive statistics for the subgroup that received only aspiration thrombectomy. Patients who received only aspiration under the ADAPT paradigm had shorter puncture-to-recanalization times than patients who were also treated with stent retriever or other adjuvant therapies.[18,21,23,26] This is expected because ADAPT calls for aspiration as a first attempt, so patients successfully treated with aspiration would have fewer passes and shorter treatment times than patients who had subsequent passes. The potential advantages of ADAPT may be especially realized in pa-

tients who are recanalized early through aspiration thrombectomy. In patients treated under ADAPT, 56%–91% were treated by aspiration alone.[9,21]

ADAPT

Comparisons of puncture-to-recanalization times, recanalization rates, and clinical outcomes between ADAPT and stent-based thrombectomy have been inconclusive and have had conflicting results.[15,20,22,29] Kim et al[20] found that ADAPT has longer puncture-to-recanalization times than stent-based thrombectomy for M2 occlusions. Turk et al[29] reported the opposite and found faster treatment times for ADAPT, whereas Lapergue et al[22] did not report a significant difference in treatment times despite patients treated under ADAPT having more passes overall. Both Turk et al[29] and Lapergue et al[22] reported higher recanalization rates for ADAPT; however, this did not translate to a significant difference in 90-day clinical outcome. In contrast, Delgado Almandoz et al[15] reported no difference in treatment times despite more passes and no difference in recanalization, but found an advantage for ADAPT in clinical outcomes.

A meta-analysis of 16 studies was performed to assess rates of recanalization and good clinical outcome for ADAPT. The TICI 2b/3 recanalization rate was 89.3% (95% CI, 85.4%–92.3%) and the rate of 90-day mRS ≤2 was 52.7% (95% CI, 48.0%–57.4%). Goyal et al[28] conducted a patient-level meta-analysis of MR CLEAN, ESCAPE, REVASCAT, SWIFT PRIME, and EXTEND IA. These 5 randomized clinical trials used predominantly stent-based thrombectomy for first-line neurointervention and had an overall recanalization rate of 70.5% (402/570) and good clinical outcome rate of 46.0% (291/633) (On-line Table 5). Although recanalization and good clinical outcome rates were lower for the stent retriever meta-analysis than the lower bound of the 95% CI for this ADAPT meta-analysis, different inclusion criteria between studies and significant heterogeneity in the ADAPT meta-analysis limit interpretation of the relative utility of these thrombectomy techniques.

ADAPT has furthermore been reported to result in fewer complications with intracerebral hemorrhage, fewer cases of subarachnoid hemorrhage, and shorter length-of-stay in an intensive care unit.[15,29] These advantages have not been consistently found to be significant in the literature, and there does not appear to be a consensus on whether ADAPT offers any clinical advantages to stent-based thrombectomy with respect to complications.[22,29] Unlike stent-based thrombectomy, however, patients with subcortical infarctions treated with ADAPT do not demonstrate an increase in hemorrhage, which may be because of aspiration thrombectomy having less of a shearing effect on vascular endothelium.[16] Aspiration thrombectomy may therefore have a role in expanding inclusion criteria for endovascular stroke treatment.

Factors Affecting Success of Aspiration Thrombectomy

Choice of aspiration catheter may affect success with aspiration thrombectomy. As new aspiration catheters are introduced and neurointerventionalists become more experienced, success rates with aspiration thrombectomy are expected to improve.[29] It is worth noting that treatment with aspiration alone does not necessarily translate to use of a single device. Jankowitz et al[17] reported that a single aspiration catheter was able to achieve recanalization in 41% of patients, and an additional catheter was necessary in 18% of patients. Nonetheless, aspiration thrombectomy is more cost-effective and requires fewer resources than stent-based thrombectomy.[29]

The techniques used in aspiration thrombectomy and characteristics of large vessel occlusion may factor into relative success with aspiration thrombectomy and stent-based thrombectomy. Aspiration thrombectomy is particularly challenging with tortuosity, and a stent retriever may be the preferred method of treatment when the occlusion is located immediately distal to a severe acute angulation.[20] Young age of the patient, however, has been found to be associated with successful revascularization when using aspiration thrombectomy.[27] In Mascitelli et al,[27] average age of the patient in cases with successful aspiration thrombectomy was 66.5 years, and average age of the patient in cases of aspiration failure was 74.1 years ($P = .03$).

Clot composition may influence the ease of thrombectomy, and it is possible certain types of clots are more amenable to different treatment modalities. Kang et al[11] found that the ADAPT paradigm of switching to a stent retriever after initial failure with aspiration thrombectomy led to greater rates of recanalization than continued attempts with aspiration thrombectomy. Conversely, Kim et al[30] used aspiration thrombectomy to successfully revascularize 83.3% of patients who were recalcitrant to initial passes with a stent retriever. Aspiration thrombectomy and stent-based thrombectomy may have unique roles in acute stroke neurointervention, and future studies may identify factors that predict favorable response to each endovascular treatment.

Limitations and Future Directions

Limitations of this study include heterogeneity in the studies that met inclusion criteria for meta-analyses as well as evidence of publication bias for recanalization rate. Furthermore, most of the studies included in this review used ADAPT as the treatment protocol. There is a paucity of literature directly comparing aspiration thrombectomy with stent-based thrombectomy. Nearly all studies, including all studies assessing ADAPT, were retrospective. The COMPASS trial and ASTER trial are 2 randomized controlled trials designed to assess the potential noninferiority of ADAPT compared with stent-based thrombectomy. One of these trials (ASTER) has finished recruitment and the other (COMPASS) is ongoing. The results from these trials will hopefully address a gap in the literature on the effectiveness of the ADAPT approach.

CONCLUSIONS

This systematic review confirms that ADAPT and aspiration thrombectomy are effective approaches to thrombectomy for acute ischemic stroke. Meta-analysis found ADAPT is associated with 89.3% of patients achieving TICI 2b/3 recanalization and 52.7% having a 90-day mRS ≤2. A limitation of this review is that there are few studies investigating aspiration thrombectomy without adjuvant therapy, and only retrospective studies of ADAPT were available for meta-analysis. Furthermore, the ADAPT meta-analyses have significant heterogeneity with evidence of publication bias in recanalization rates, which may limit interpretation of

these results. Prospective studies are necessary to directly assess the utility of aspiration thrombectomy and ADAPT.

Disclosures: Johanna Fifi—*UNRELATED*: *Consultancy*: Penumbra, MicroVention; *Grants/Grants Pending*: Stryker; *Payment for Lectures (including service on Speakers Bureaus)*: Penumbra. J,D. Mocco—*UNRELATED*: *Consultancy*: Rebound Medical, Endostream, Synchron, Cerebrotech, TSP, Pulsar; *Grants/Grants Pending*: Stryker Neurovascular, Penumbra, Medtronic, Microvention*; *Stock/Stock Options*: Blockade Medical, TSP, Cerebrotech; *Other*: Apama, The Stroke Project, Endostream, Synchron, Cerebrotech, NeurVana, NeuroTechnology Investors, *Comments*: investor/ownership. Reade De Leacy—*UNRELATED*: *Consultancy*: Medical Metrics, Dfine, *Comments*: spine interventional company. *Money paid to the institution.

REFERENCES

1. Berkhemer OA, Fransen PS, Beumer D, et al. **A randomized trial of intraarterial treatment for acute ischemic stroke.** *N Engl J Med* 2015; 372:11–20 CrossRef Medline
2. Campbell BC, Mitchell PJ, Kleinig TJ, et al. **Endovascular therapy for ischemic stroke with perfusion-imaging selection.** *N Engl J Med* 2015;372:1009–18 CrossRef Medline
3. Goyal M, Demchuk AM, Menon BK, et al. **Randomized assessment of rapid endovascular treatment of ischemic stroke.** *N Engl J Med* 2015;372:1019–30 CrossRef Medline
4. Jovin TG, Chamorro A, Cobo E, et al. **Thrombectomy within 8 hours after symptom onset in ischemic stroke.** *N Engl J Med* 2015;372: 2296–306 CrossRef Medline
5. Saver JL, Goyal M, Bonafe A, et al. **Stent-retriever thrombectomy after intravenous t-PA vs. t-PA alone in stroke.** *N Engl J Med* 2015; 372:2285–95 CrossRef Medline
6. Moher D, Liberati A, Tetzlaff J, et al. **Preferred reporting items for systematic reviews and meta-analyses: the PRISMA statement.** *J Clin Epidemiol* 2009;62:1006–12 CrossRef Medline
7. Eom YI, Hwang YH, Hong JM, et al. **Forced arterial suction thrombectomy with the Penumbra reperfusion catheter in acute basilar artery occlusion: a retrospective comparison study in 2 Korean university hospitals.** *AJNR Am J Neuroradiol* 2014;35:2354–59 CrossRef Medline
8. Hwang YH, Kang DH, Kim YW, et al. **Outcome of forced-suction thrombectomy in acute intracranial internal carotid occlusion.** *J Neurointerv Surg* 2013;5 suppl 1:i81–84 CrossRef Medline
9. Kim YS, Kwak HS, Chung GH, et al. **Manual aspiration thrombectomy using the Penumbra catheter in patients with acute M1 occlusion: a single-center study.** *Interv Neuroradiol* 2015;21:694–99 CrossRef Medline
10. Park JS, Kwak HS. **Manual aspiration thrombectomy using Penumbra catheter in patients with acute M2 occlusion: a single-center analysis.** *J Korean Neurosurg Soc* 2016;59:352–56 CrossRef Medline
11. Kang DH, Kim YW, Hwang YH, et al. **Switching strategy for mechanical thrombectomy of acute large vessel occlusion in the anterior circulation.** *Stroke* 2013;44:3577–79 CrossRef Medline
12. Turk AS, Spiotta A, Frei D, et al. **Initial clinical experience with the ADAPT technique: a direct aspiration first pass technique for stroke thrombectomy.** *J Neurointerv Surg* 2014;6:231–37 CrossRef Medline
13. Mocco J, Zaidat OO, von Kummer R, et al. **Aspiration thrombectomy after intravenous alteplase versus intravenous alteplase alone.** *Stroke* 2016;47:2331–38 CrossRef Medline
14. Bracard S, Ducrocq X, Mas JL, et al. **Mechanical thrombectomy after intravenous alteplase versus alteplase alone after stroke (THRACE): a randomised controlled trial.** *Lancet Neurol* 2016; 15:1138–47 CrossRef Medline
15. Delgado Almandoz JE, Kayan Y, Young ML, et al. **Comparison of clinical outcomes in patients with acute ischemic strokes treated with mechanical thrombectomy using either Solumbra or ADAPT techniques.** *J Neurointerv Surg* 2016;8:1123–28 CrossRef Medline
16. Hungerford JP, Hyer M, Turk AS, et al. **Impact of ASPECT scores and infarct distribution on outcomes among patients undergoing thrombectomy for acute ischemic stroke with the ADAPT technique.** *J Neurointerv Surg* 2016 Aug 22. [Epub ahead of print] CrossRef Medline
17. Jankowitz B, Grandhi R, Horev A, et al. **Primary manual aspiration thrombectomy (MAT) for acute ischemic stroke: safety, feasibility and outcomes in 112 consecutive patients.** *J Neurointerv Surg* 2015; 7:27–31 CrossRef Medline
18. Kabbasch C, Möhlenbruch M, Stampfl S, et al. **First-line lesional aspiration in acute stroke thrombectomy using a novel intermediate catheter: initial experiences with the SOFIA.** *Interv Neuroradiol* 2016;22:333–39 CrossRef Medline
19. Kang DH, Hwang YH, Kim YS, et al. **Direct thrombus retrieval using the reperfusion catheter of the Penumbra system: forced-suction thrombectomy in acute ischemic stroke.** *AJNR Am J Neuroradiol* 2011;32:283–87 CrossRef Medline
20. Kim YW, Son S, Kang DH, et al. **Endovascular thrombectomy for M2 occlusions: comparison between forced arterial suction thrombectomy and stent retriever thrombectomy.** *J Neurointerv Surg* 2017;9:626–30 CrossRef Medline
21. Kowoll A, Weber A, Mpotsaris A, et al. **Direct aspiration first pass technique for the treatment of acute ischemic stroke: initial experience at a European stroke center.** *J Neurointerv Surg* 2016;8:230–34 CrossRef Medline
22. Lapergue B, Blanc R, Guedin P, et al. **A direct aspiration, first pass technique (ADAPT) versus stent retrievers for acute stroke therapy: an observational comparative study.** *AJNR Am J Neuroradiol* 2016; 37:1860–65 CrossRef Medline
23. Romano DG, Cioni S, Vinci SL, et al. **Thromboaspiration technique as first approach for endovascular treatment of acute ischemic stroke: initial experience at nine Italian stroke centers.** *J Neurointerv Surg* 2017;9:6–10 CrossRef Medline
24. Turk AS, Frei D, Fiorella D, et al. **ADAPT FAST study: a direct aspiration first pass technique for acute stroke thrombectomy.** *J Neurointerv Surg* 2014;6:260–64 CrossRef Medline
25. Turk AS, Turner R, Spiotta A, et al. **Comparison of endovascular treatment approaches for acute ischemic stroke: cost effectiveness, technical success, and clinical outcomes.** *J Neurointerv Surg* 2015;7: 666–70 CrossRef Medline
26. Vargas J, Spiotta A, Fargen K, et al. **Long term experience using the ADAPT technique for the treatment of acute ischemic stroke.** *J Neurointerv Surg* 2017;9:437–41 CrossRef Medline
27. Mascitelli JR, Kellner CP, Oravec CS, et al. **Factors associated with successful revascularization using the aspiration component of ADAPT in the treatment of acute ischemic stroke.** *J Neurointerv Surg* 2017;9:636–40 CrossRef Medline
28. Goyal M, Menon BK, van Zwam WH, et al. **Endovascular thrombectomy after large-vessel ischaemic stroke: a meta-analysis of individual patient data from five randomised trials.** *Lancet* 2016;387: 1723–31 CrossRef Medline
29. Turk AS 3rd, Campbell JM, Spiotta A, et al. **An investigation of the cost and benefit of mechanical thrombectomy for endovascular treatment of acute ischemic stroke.** *J Neurointerv Surg* 2014;6:77–80 CrossRef Medline
30. Kim SK, Yoon W, Moon SM, et al. **Outcomes of manual aspiration thrombectomy for acute ischemic stroke refractory to stent-based thrombectomy.** *J Neurointerv Surg* 2015;7:473–77 CrossRef Medline

Endovascular Treatment of Dural Arteriovenous Fistulas of the Transverse and Sigmoid Sinuses Using Transarterial Balloon-Assisted Embolization Combined with Transvenous Balloon Protection of the Venous Sinus

E. Piechowiak, F. Zibold, T. Dobrocky, P.J. Mosimann, D. Bervini, A. Raabe, J. Gralla, and P. Mordasini

ABSTRACT

BACKGROUND AND PURPOSE: Combined transarterial balloon-assisted endovascular embolization with double-lumen balloon microcatheters and concomitant transvenous balloon protection was described as a promising treatment technique for dural arteriovenous fistulae of the transverse and sigmoid sinus. The purpose of this study was to evaluate the technical efficacy and safety of this combined treatment technique.

MATERIALS AND METHODS: Nine consecutive patients presenting with dural arteriovenous fistulas of the transverse and sigmoid sinuses underwent combined transarterial and transvenous balloon-assisted endovascular embolization. Prospectively collected data were reviewed to assess the technical success rate, complication rate, and clinical outcome.

RESULTS: Six patients presented with clinically symptomatic Borden type I, and 3 patients, with Borden type II dural arteriovenous fistulas of the transverse and sigmoid sinuses (3 men, 6 women; mean age, 50.4 years). Transarterial embolization was performed with a double-lumen balloon with Onyx and concomitant transvenous sinus protection with a dedicated venous remodeling balloon. Complete angiographic occlusion at the latest follow-up (mean, 4.8 months) was achieved in 6 patients, and near-complete occlusion, in 2 patients. Clinical cure or remission of symptoms was obtained in 6 and 2 patients, respectively. One patient with a residual fistula underwent further treatment in which the dural arteriovenous fistula was cured by sinus occlusion. Complete occlusion of the dural arteriovenous fistula was visible on the follow-up angiography after final treatment in 8 patients. One patient refused follow-up angiography but was free of symptoms. There were no immediate or delayed postinterventional complications.

CONCLUSIONS: Transarterial balloon-assisted embolization of dural arteriovenous fistulas of the transverse and sigmoid sinuses with combined transvenous balloon protection is safe and offers a high rate of complete dural arteriovenous fistula occlusion and remission of clinical symptoms.

ABBREVIATION: dAVF = dural arteriovenous fistula

During the past few decades, endovascular embolization has become the first-line treatment for a wide range of dural arteriovenous fistulas (dAVFs). Several transarterial and transvenous endovascular approaches have been advocated. Preliminary studies on the use of double-lumen balloon microcatheters for transarterial embolization of dAVFs with Onyx (Covidien, Irvine, California) have shown encouraging results. These studies have reported high occlusion rates, reduction of reflux into the feeding artery, a reduced quantity of injected Onyx and peri-interventional time, and low complication rates.[1-9] In addition, transvenous balloon-assisted sinus protection during transarterial embolization has been reported to be another useful adjunct to the endovascular treatment of dAVFs.[10-12] Transvenous balloon protection of the recipient sinus has mainly been associated with a reduction in inadvertent occlusion of the lumen of a functioning sinus, preservation of venous patency, facilitation of occlusion of abnormal arteriovenous connections within the sinus wall and separate venous channels, and increased penetration of embolic material by retrograde reflux into other dural feeders of the fistula network. Techniques aiming to preserve the underlying sinus may have lower complication rates than sinus-occluding

Received March 13, 2017; accepted after revision June 1.

From the University Institute of Diagnostic and Interventional Neuroradiology (E.P., F.Z., T.D., J.G., P.M., P.J.M.) and Department of Neurosurgery (D.B., A.R.), Inselspital, University of Bern, Bern, Switzerland.

Jan Gralla and Pasquale Mordasini contributed equally to the study.

Please address correspondence to Pasquale Mordasini, MD, MSc, University Institute of Diagnostic and Interventional Neuroradiology, University of Bern, Inselspital, Freiburgstr 10, 3010 Bern, Switzerland; e-mail: pasquale.mordasini@insel.ch

Indicates open access to non-subscribers at www.ajnr.org

Indicates article with supplemental on-line table.

http://dx.doi.org/10.3174/ajnr.A5333

embolization techniques, in which the recipient venous sinus has to be sacrificed.[13] Therefore, transarterial balloon-assisted embolization with a concomitant transvenous balloon protection technique theoretically has the advantages of both techniques combined; this combination leads to increased occlusion and reduced complication rates.

The purpose of this study was to report the angiographic and clinical outcomes of patients with dAVFs of the transverse and sigmoid sinuses treated with a combined approach of transarterial balloon-assisted endovascular embolization and double-lumen balloon microcatheters with concomitant transvenous balloon protection.

MATERIALS AND METHODS

Between August 2015 and September 2016, nine consecutive patients presented at our institution with symptomatic dAVFs of the transverse and sigmoid sinuses and were treated by combined transarterial and transvenous balloon-assisted endovascular embolization. Clinical and angiographic data were collected in a clinical data base and retrospectively analyzed.

Clinical data, including age, sex, clinical presentation, and clinical follow-up, were recorded. Angiographic data, including location and type of fistula (according to the Borden and Cognard classifications); feeding arteries; the angiographic outcome immediately after the treatment and during the follow-up angiography (at 3–6 months); and treatment-related data on arterial access, embolic agent, and technical and other related complications, were collected. Clinical deterioration, stroke, intracranial hemorrhage, and cranial nerve palsy were considered treatment-related complications. A technical complication was defined as any technical problem with the material used or any medical problem occurring during the intervention, including vessel perforation, inadvertent embolization of nontarget vessels, and failure to complete the treatment.

In patients who had Borden type I dAVFs, endovascular treatment was offered after reaching interdisciplinary consensus if intolerable clinical symptoms were present and if patients were actively asking for treatment.

Angiographic and Clinical Analysis

The imaging material was analyzed in detail by 2 experienced neuroradiologists (E.P. and P.M., with 8 and 12 years of experience, respectively), one of whom had no involvement in the treatment. Angiographic outcome was descriptively defined as complete occlusion if no residual fistula was visible; as near-complete occlusion with minimal residual fistula, if there was a 90%–99% occlusion rate; and as residual fistula, if an occlusion rate of <90% was achieved. To determine the clinical course, we asked patients before and immediately after the treatment, as well as during the follow-up examination (3–6 months), about the subjective improvement or deterioration of their symptoms, especially the intensity of the tinnitus. The outcome was categorized as better, equal to, and worse than before treatment. Clinical cure was defined as complete absence of previous symptoms.

Endovascular Technique

All endovascular interventions were performed by the same trained neuroradiologists (P.M., J.G.) with the patient under general anesthesia using a biplane neuroangiography suite (Artis zee; Siemens, Erlangen, Germany). After puncture of the left femoral vein and right femoral artery, an 8F guiding catheter was placed in the internal jugular vein and the external carotid artery on the side of the fistula (Guider Softip; Boston Scientific, Fremont, California). Transarterial navigation into the most promising arterial feeder was performed with a double-lumen dimethyl-sulfoxide–resistant balloon microcatheter (4 × 10 mm, Scepter C; MicroVention, Tustin, California) over a 0.014-inch microwire (SilverSpeed-14; Covidien). A distal position at the site of the fistula or close to the fistula could be achieved in all cases. Nimodipine (2 mg) was added to the continuous flushing line (1000 mL of saline) to facilitate distal navigation and to avoid or minimize mechanically induced vasospasm. Subsequently, via the transvenous route, a dedicated compliant dimethyl-sulfoxide–resistant venous remodeling balloon (8 × 80 mm, Copernic RC; Balt Extrusion, Montmorency, France) was navigated into the affected sinus covering the site of the fistula. After carefully inflating the transarterial double-lumen balloon, we performed microcatheter embolization with Onyx-18 and/or Onyx-20 under the roadmap technique (Fig 1). Simultaneously, the venous balloon was repeatedly temporarily inflated during transarterial Onyx injection for a maximum of 2–5 minutes. Inflation pressure was manually adapted to prevent Onyx migration into the main sinus lumen and to simultaneously achieve better penetration into the fistulous connections within and around the sinus wall (Fig 1).

After termination of the liquid embolic injection, the transarterial and transvenous balloons were deflated and retrieved without any complications. A 4-vessel diagnostic angiography was performed at the end of every procedure to check for complete occlusion or residual fistula (Figs 2 and 3). Technical and procedural details are summarized in the On-line Table.

RESULTS

Six patients presented with clinically symptomatic Borden type I; and 3, patients with Borden type II dAVFs of the transverse and sigmoid sinuses (3 cases of Cognard type I; 3 cases of Cognard type IIa; 1 case of Cognard type IIb; 2 cases of Cognard type IIa + b).[14,15] Of these 9 patients, 3 were men and 6 were women. The mean age was 50.4 years (range, 24–66 years). Clinical symptoms at presentation were intolerable tinnitus in all 9 patients and additional headache in 3 patients. No patient had experienced dAVF-related hemorrhage. One patient (No. 7) presented with persistent intolerable tinnitus after 3 previous unsuccessful attempts at transarterial embolization, with residual fistula, while the other 8 patients presented with a newly diagnosed dAVF. Patient clinical characteristics are summarized in the On-line Table.

Overall, complete angiographic occlusion was achieved in 6 patients, and near-complete angiographic occlusion with minimal residual fistula, in 2 of the 9 patients after 1 embolization (88.9%), leading to clinical cure or remission of symptoms. In Borden type I fistulas with residual shunt, no transformation to a higher grade was noted postintervention, and all Borden type II fistulas with residual shunts were downgraded to Borden type I fistulas. Of the 6 patients with near-complete occlusion and minimal residual fistulas immediately after treatment, 5 patients showed complete clinical cure during follow-up of whom 4 pa-

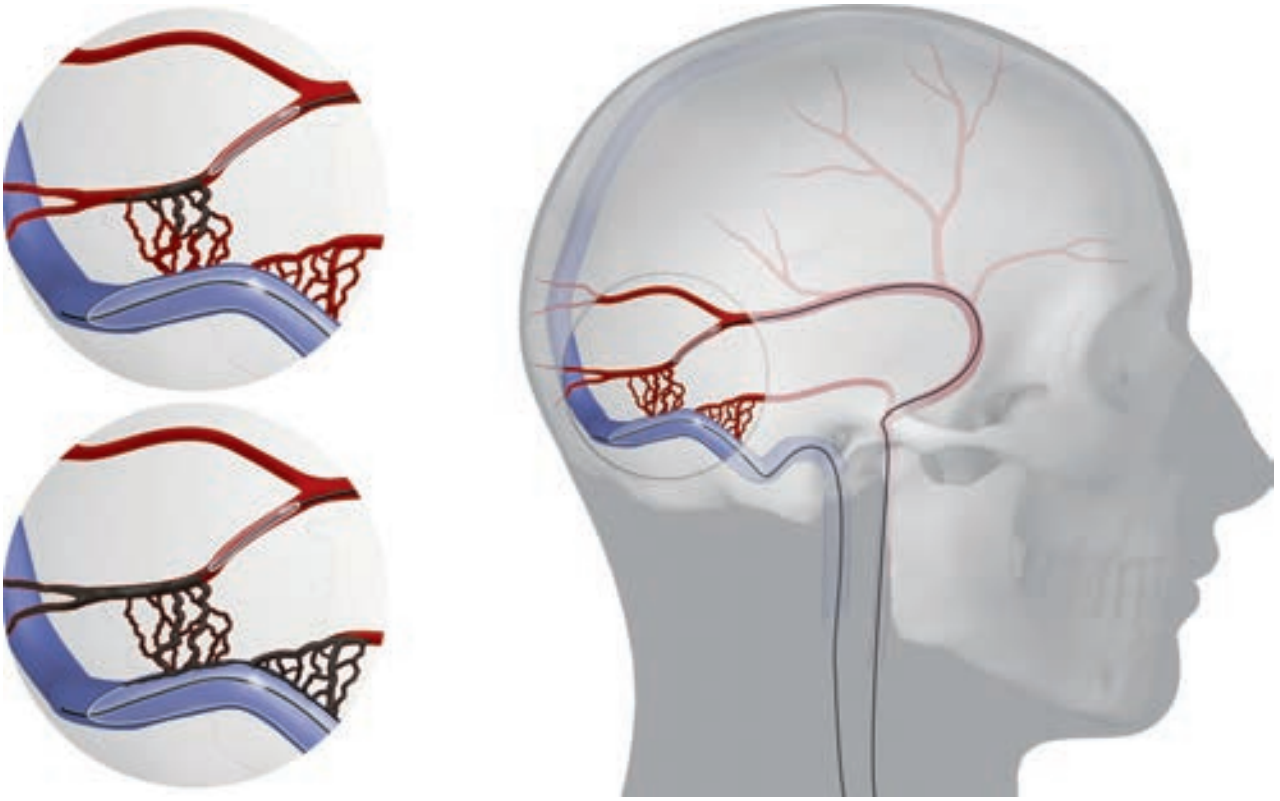

FIG 1. Demonstration of the technique combining transarterial balloon-assisted embolization and transvenous balloon protection in the endovascular treatment of dAVFs of the transverse and sigmoid sinuses. Onyx injection during inflation of the balloons with Onyx penetration throughout the feeding arteries and total occlusion of the fistula.

tients showed a proven spontaneous complete occlusion of the fistula during follow-up imaging (1 patient with a residual fistula and residual tinnitus had a second treatment session, and the fistula was cured by sinus occlusion; 1 patient refused to undergo any follow-up imaging due to clinical cure). Eight patients underwent a single endovascular treatment session. Routine clinical or angiographic follow-up or both were performed after 2–6 months, and records were available for 8 of the 9 patients (mean follow-up, 4.8 months). Two patients refused to undergo the 6-month follow-up angiography due to clinical cure. There were no immediate or delayed permanent postinterventional complications.

Transarterial navigation of the balloon microcatheter to the target position in a main feeder close to the fistula point where Onyx injection was intended to start was possible in all 9 patients; this target was the middle meningeal artery. Embolization was performed from a single arterial feeder, and it was possible to place the venous remodeling balloon within the affected sinus segment in all patients. There were no technical difficulties or complications associated with balloon placement, inflation, deflation, or retrieval.

In 1 patient (No. 6) diagnosed with a Borden type II fistula, embolic material migrated into the proximal vein of Labbé despite venous balloon protection, most likely through a parallel dural channel not protected by the balloon. Consequently, the intervention was stopped prematurely to prevent further propagation of embolic material. No impairment of patency of the vein of Labbé was noted, and it was still contributing to the drainage of brain parenchyma. The patient had an uneventful clinical course, with no improvement of his initial intolerable tinnitus. Follow-up angiography demonstrated the residual Borden type I dAVF at the level of the distal sigmoid sinus. Progressive occlusion of the transverse and proximal sigmoid sinuses at the level of the previously embolized portion of the dAVF and at the level of the jugular bulb was noted. Because the distal sigmoid sinus was exclusively draining the fistula without any contribution of the cerebral veins, the residual dAVF was treated secondarily by transvenous sinus occlusion with coils and Onyx. Complete occlusion of the dAVF and complete remission of the tinnitus were achieved. Therefore, after the final treatment, all patients were free of symptoms, and 8 of 9 had an angiographic occlusion of the dAVF (1 patient with a minimal residual fistula refused to undergo any follow-up imaging).

DISCUSSION

In our small series of patients with dAVFs, we achieved complete occlusion or reduction of flow to a minimal residual fistula in 88.9% of the cases after 1 embolization attempt, with complete improvement of the initial symptoms during follow-up. One patient with a residual fistula was treated again, which led to occlusion of the parent sinus followed by clinical cure. There were no immediate or delayed permanent postinterventional complications.

During the past few decades, endovascular embolization with liquid embolic material, particles, or coils has become the first-line treatment for a wide range of dAVFs. Several transarterial and transvenous endovascular approaches have been advocated. Recent technical improvements include the introduction of dimeth-

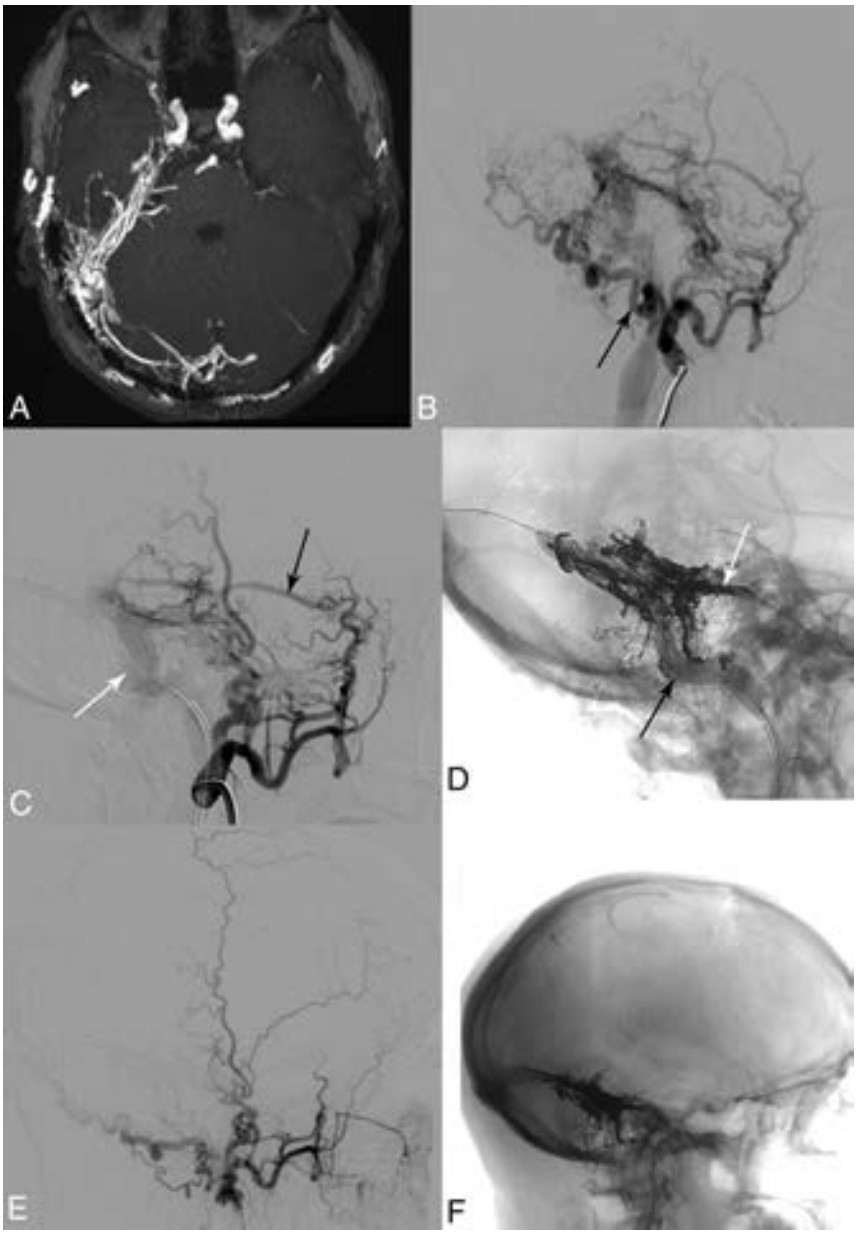

FIG 2. A 51-year-old man (patient 7) after 3 unsuccessful endovascular treatment attempts 10 years ago showing a progressive Borden I fistula on the right. *A*, Time-of-flight angiography. *B*, Right external carotid artery angiogram shows feeding arteries from the middle meningeal artery, occipital artery (*black arrow*), meningohypophyseal trunk (not visible), posterior auricular artery, artery of the falx cerebelli (not visible), subarcuate artery, and vertebral artery (not visible). *C*, Right external carotid artery angiogram after positioning of the venous balloon in the right transverse and sigmoid sinuses (8 × 80 mm, Copernic RC; *white arrow*). Middle meningeal artery (*black arrow*). *D*, Fluoroscopic image depicting the inflated venous balloon (*black arrow*), the arterial double-lumen balloon microcatheter in the middle meningeal artery, partially hidden behind Onyx (4 × 10 mm, Scepter C; *white arrow*), and the cast of Onyx-18. *E*, Right external carotid artery angiogram after embolization of the fistula with complete occlusion. *F*, Fluoroscopic image shows Onyx-18 distribution after complete occlusion of the dural fistula.

yl-sulfoxide–compatible double-lumen balloon microcatheters for transarterial embolization and dedicated especially designed venous balloons for transvenous sinus protection. Combining the advantages of transarterial balloon-assisted embolization with transvenous balloon protection seems to be a promising treatment strategy. Formerly, use of the technique had only been reported in small case series as part of different endovascular treatment approaches for dAVFs.[2,8,13]

The introduction of dimethyl-sulfoxide–compatible double-lumen balloon microcatheters for transarterial embolization of dAVFs with Onyx has shown encouraging results in preliminary studies, with high occlusion and low complication rates.[1-9,16] In the largest study available, Kim et al[5] compared the results of transarterial Onyx embolization for dAVFs using a double-lumen balloon with those obtained by using a nonballoon microcatheter. The use of a double-lumen balloon microcatheter led to an increased immediate complete occlusion rate, decreased procedure time, decreased Onyx injection time, and a decrease in the number of feeders requiring embolization compared with the group treated with a nonballoon microcatheter. The main advantages of double-lumen balloon-assisted embolization are immediate control of the antegrade flow of the embolic material without the need for proximal plug formation, more effective distal penetration into the fistula and possibly into the distal portion of other arterial feeders, and the prevention of reflux into adjacent arteries.[5] The larger profile and greater stiffness of the balloon microcatheter compared with dedicated low-profile embolization microcatheters mean that a satisfactory distal injection position may not be reachable due to small vessel caliber or tortuosity.[3] In our series, delivery of the balloon microcatheter was possible through the middle meningeal artery in all cases; this artery usually has a rather straight course, facilitating microcatheterization. The potential risk of vessel rupture as a result of overinflation of the balloon[2] can be avoided by carefully inflating the balloon under fluoroscopic control.

Transvenous balloon protection during transarterial embolization was first proposed by Shi et al[8] with a small compliant balloon originally designed for aneurysm remodeling. The introduction of a large dedicated dimethyl-sulfoxide–resistant single-lumen compliant balloon catheter for transvenous sinus occlusion (8 × 80 mm, Copernic RC) has facilitated this adjunctive technique and paved the way for its wider use. The advantages of transvenous balloon protection during simultaneous transarterial embolization include the prevention of inadvertent occlusion of the lumen of a functioning sinus required for cerebral venous drainage and propagation of embolic material into adjacent cortical or deep cerebral veins. Ertl et al[13] recently

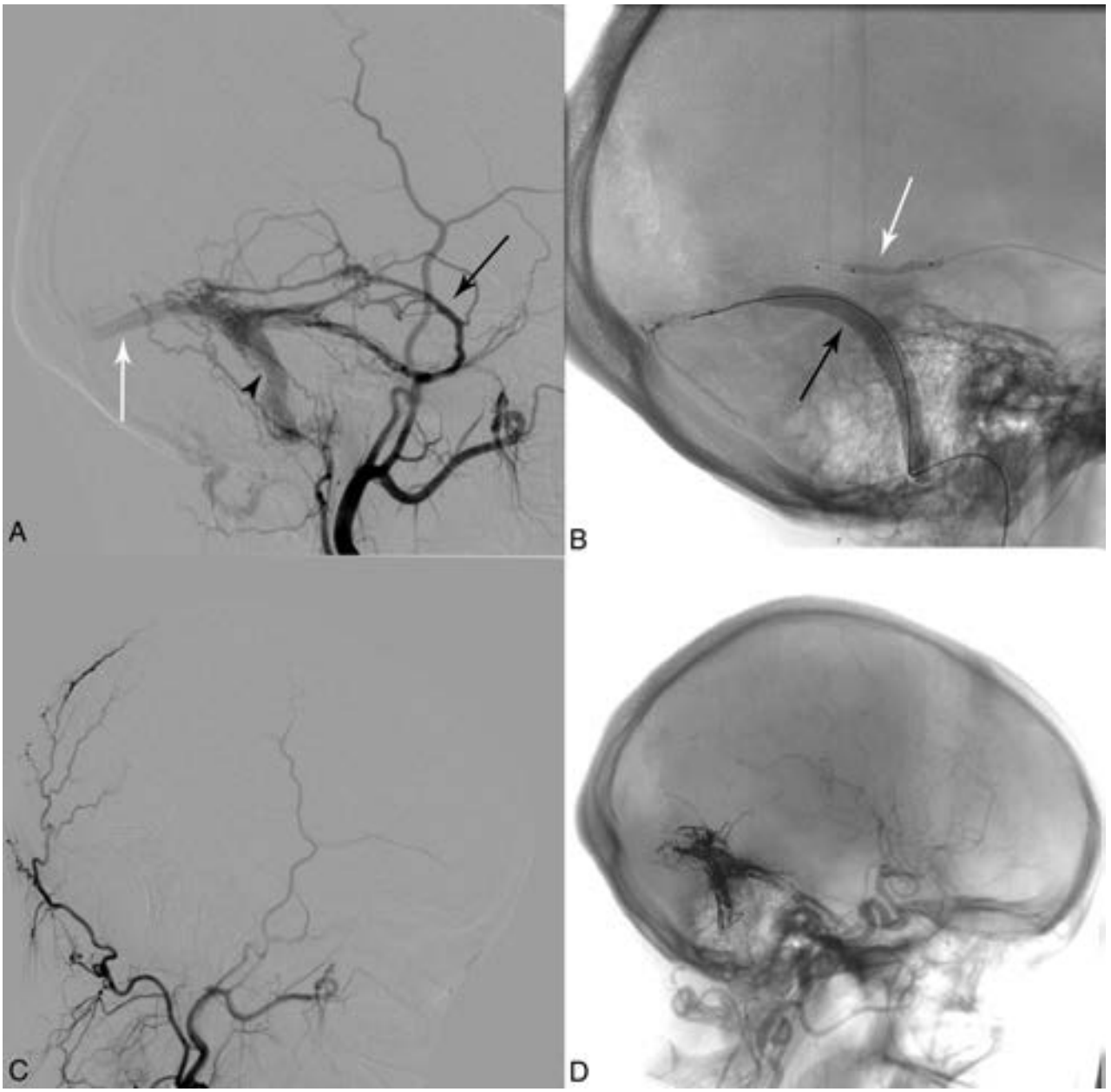

FIG 3. A 24-year-old woman (patient 1) with a Borden II fistula on the left. *A*, Baseline left external carotid artery angiogram with feeding arteries from the middle meningeal artery (*black arrow*), occipital artery, and meningohypophyseal trunk (not visible). Transverse sinus (*white arrow*); sigmoid sinus (*black arrowhead*). *B*, Fluoroscopic image showing an inflated venous balloon (8 × 80 mm Copernic RC; *black arrow*) and arterial double-lumen balloon catheter in the middle meningeal artery (4 × 10 mm, Scepter C; *white arrow*). *C*, Left external carotid artery angiogram (2-month follow-up) after embolization of the fistula showing complete occlusion. *D*, Fluoroscopic image depicting Onyx-18 distribution after complete occlusion of the dural fistula.

conducted a retrospective comparison of sinus-preserving and sinus-occluding endovascular treatment techniques for low- and intermediate-grade dAVFs involving the transverse and sigmoid sinuses (Cognard type I–IIb). A higher rate of permanent fistula occlusion was achievable with sinus-occluding techniques than with the sinus-preserving technique (93% versus 71%), but this came at the cost of a higher complication rate (33% versus 0%). These results are in accordance with our findings using a combined transarterial and transvenous approach for sinus-preserving dAVF embolization, showing no permanent complications and a high rate of remission of clinical symptoms with a single treatment session. Two-thirds of our patient population presented with a low-grade dAVF with a known benign natural history and thus relative and no vital treatment indication, despite the disturbing tinnitus. Every treatment attempt should aim for the lowest risk of complications and the most favorable benefit-risk ratio.

Despite a small residual shunt in 5 patients, after the embolization session, all patients experienced remission of clinical symptoms with spontaneous complete occlusion in 4 patients during follow-up and subsequently complete clinical cure (1 patient refused the follow-up angiography due to clinical cure). Furthermore, transvenous balloon placement in the sinus was helpful to understand the vascular anatomy of the fistula network and its

venous drainage during embolization. Parallel venous channels as recipients for the arterial shunt into the transverse/sigmoid sinus and multiple arteriovenous connections within the dural wall and not the sinus itself can be observed.[17-19] These venous recipient structures may be obscured and not distinctly identified during angiography and transarterial embolization. The use of transvenous balloon protection with inflation of the balloon within the main sinus lumen, covering the entire length of the diseased sinus, facilitates the identification and occlusion of these abnormal arteriovenous connections within the sinus wall and separates venous channels by enabling increased penetration of embolic material by retrograde reflux into other dural feeders of the fistula network. At the same time, the technique allows sinus patency control and provides continuous injection of liquid embolic material, minimizing the risk of leakage into the sinus.[8,10-12]

Although no permanent clinical complications occurred in our series, inadvertent propagation of Onyx into the proximal vein of Labbé was noted despite balloon inflation inside the main sinus lumen in 1 patient (No. 6), most probably the result of retrograde leakage of liquid embolic material along a parallel channel. This finding emphasizes the necessity of monitoring and adjusting balloon pressure appropriately and carefully observing the Onyx penetration along the dural sinus. An inflation time of 2–5 minutes has been used with temporary deflation of the balloon during cessation of Onyx injection to avoid venous infarction due to prolonged transvenous balloon occlusion, especially in the dominant sinus or in those cases involving normal cortical veins.[11]

The limitations of our study include its retrospective nature, the small sample size, and, for some patients, the short follow-up period. However, the results were obtained in consecutive patients with a defined pathology who were treated with a standardized endovascular approach.

CONCLUSIONS

In our small series of patients with dAVFs of the transverse and sigmoid sinuses, we found no relevant adverse events and a high cure rate with a technique combining transarterial balloon-assisted embolization and transvenous balloon protection. Long-term follow-up and larger patient series are necessary to further assess its efficacy and durability.

Disclosures: Jan Gralla—*UNRELATED*: *Consultancy*: Medtronic and Penumbra, *Comments*: Global Principal Investigator of STAR and SWIFT-DIRECT (Medtronic), Clinical Events Committee member of the ProMISe Study (Penumbra)*; *Grants/Grants Pending*: Swiss National Foundation, *Comments*: research grant for MRI in stroke*. *Money paid to the institution.

REFERENCES

1. Andreou A, Ioannidis I, Nasis N. **Transarterial balloon-assisted glue embolization of high-flow arteriovenous fistulas.** *Neuroradiology* 2008;50:267–72 CrossRef Medline
2. Chiu AH, Aw G, Wenderoth JD. **Double-lumen arterial balloon catheter technique for Onyx embolization of dural arteriovenous fistulas: initial experience.** *J Neurointer Surg* 2014;6:400–03 CrossRef Medline
3. Dabus G, Linfante I, Martinez-Galdámez M. **Endovascular treatment of dural arteriovenous fistulas using dual lumen balloon microcatheter: technical aspects and results.** *Clin Neurol Neurosurg* 2014;117:22–27 CrossRef Medline
4. Huo X, Li Y, Jiang C, et al. **Balloon-assisted endovascular treatment of intracranial dural arteriovenous fistulas.** *Turk Neurosurg* 2014; 24:658–63 CrossRef Medline
5. Kim JW, Kim BM, Park KY, et al. **Onyx embolization for isolated type dural arteriovenous fistula using a dual-lumen balloon catheter.** *Neurosurgery* 2016;78:627–36 CrossRef Medline
6. Kim ST, Jeong HW, Seo J. **Onyx embolization of dural arteriovenous fistula, using Scepter C balloon catheter: a case report.** *Neurointervention* 2013;8:110–14 CrossRef Medline
7. Paramasivam S, Niimi Y, Fifi J, et al. **Onyx embolization using dual-lumen balloon catheter: initial experience and technical note.** *J Neuroradiol* 2013;40:294–302 CrossRef Medline
8. Shi ZS, Loh Y, Duckwiler GR, et al. **Balloon-assisted transarterial embolization of intracranial dural arteriovenous fistulas.** *J Neurosurg* 2009;110:921–28 CrossRef Medline
9. Spiotta AM, Miranpuri AS, Vargas J, et al. **Balloon augmented Onyx embolization utilizing a dual lumen balloon catheter: utility in the treatment of a variety of head and neck lesions.** *J Neurointerv Surg* 2014;6:547–55 CrossRef Medline
10. Choi BJ, Lee TH, Kim CW, et al. **Reconstructive treatment using a stent graft for a dural arteriovenous fistula of the transverse sinus in the case of hypoplasia of the contralateral venous sinuses: technical case report.** *Neurosurgery* 2009;65:E994–96; discussion E996 CrossRef Medline
11. Jittapiromsak P, Ikka L, Benachour N, et al. **Transvenous balloon-assisted transarterial Onyx embolization of transverse-sigmoid dural arteriovenous malformation.** *Neuroradiology* 2013;55:345–50 CrossRef Medline
12. Zhang Y, Li Q, Huang QH. **Embolization of a superior sagittal sinus dural arteriovenous fistula under intrasinus balloon protection: a case report.** *Interv Neuroradiol* 2015;21:94–100 CrossRef Medline
13. Ertl L, Brückmann H, Kunz M, et al. **Endovascular therapy of low- and intermediate-grade intracranial lateral dural arteriovenous fistulas: a detailed analysis of primary success rates, complication rates, and long-term follow-up of different technical approaches.** *J Neurosurg* 2017;126:360–67 CrossRef Medline
14. Borden JA, Wu JK, Shucart WA. **A proposed classification for spinal and cranial dural arteriovenous fistulous malformations and implications for treatment.** *J Neurosurg* 1995;82:166–79 CrossRef Medline
15. Cognard C, Gobin YP, Pierot L, et al. **Cerebral dural arteriovenous fistulas: clinical and angiographic correlation with a revised classification of venous drainage.** *Radiology* 1995;194:671–80 CrossRef Medline
16. Jagadeesan BD, Grigoryan M, Hassan AE, et al. **Endovascular balloon-assisted embolization of intracranial and cervical arteriovenous malformations using dual lumen co-axial balloon microcatheters and Onyx: initial experience.** *Neurosurgery* 2013 Feb 25. [Epub ahead of print] CrossRef Medline
17. Caragine LP, Halbach VV, Dowd CF, et al. **Parallel venous channel as the recipient pouch in transverse/sigmoid sinus dural fistulae.** *Neurosurgery* 2003;53:1261–66; discussion 1266–67 CrossRef Medline
18. Hamada Y, Goto K, Inoue T, et al. **Histopathological aspects of dural arteriovenous fistulas in the transverse-sigmoid sinus region in nine patients.** *Neurosurgery* 1997;40:452–56; discussion 456–58 Medline
19. Nishijima M, Takaku A, Endo S, et al. **Etiological evaluation of dural arteriovenous malformations of the lateral and sigmoid sinuses based on histopathological examinations.** *J Neurosurg* 1992;76: 600–06 CrossRef Medline

Anatomic Location of Tumor Predicts the Accuracy of Motor Function Localization in Diffuse Lower-Grade Gliomas Involving the Hand Knob Area

S. Fang, J. Liang, T. Qian, Y. Wang, X. Liu, X. Fan, S. Li, Y. Wang, and T. Jiang

ABSTRACT

BACKGROUND AND PURPOSE: The accuracy of preoperative blood oxygen level–dependent fMRI remains controversial. This study assessed the association between the anatomic location of a tumor and the accuracy of fMRI-based motor function mapping in diffuse lower-grade gliomas.

MATERIALS AND METHODS: Thirty-five patients with lower-grade gliomas involving motor areas underwent preoperative blood oxygen level–dependent fMRI scans with grasping tasks and received intraoperative direct cortical stimulation. Patients were classified into an overlapping group and a nonoverlapping group, depending on the extent to which blood oxygen level–dependent fMRI and direct cortical stimulation results concurred. Tumor location was quantitatively measured, including the shortest distance from the tumor to the hand knob and the deviation distance of the midpoint of the hand knob in the lesion hemisphere relative to the midline compared with the normal contralateral hemisphere.

RESULTS: A 4-mm shortest distance from the tumor to the hand knob value was identified as optimal for differentiating the overlapping and nonoverlapping group with the receiver operating characteristic curve (sensitivity, 84.6%; specificity, 77.8%). The shortest distances from the tumor to the hand knob of ≤4 mm were associated with inaccurate fMRI-based localizations of the hand motor cortex. The shortest distances from the tumor to the hand knob were larger ($P = .002$), and the deviation distances for the midpoint of the hand knob in the lesion hemisphere were smaller ($P = .003$) in the overlapping group than in the nonoverlapping group.

CONCLUSIONS: This study suggests that the shortest distance from the tumor to the hand knob and the deviation distance for the midpoint of the hand knob on the lesion hemisphere are predictive of the accuracy of blood oxygen level–dependent fMRI results. Smaller shortest distances from the tumor to the hand knob and larger deviation distances for the midpoint of hand knob on the lesion hemisphere are associated with less accuracy of motor cortex localization with blood oxygen level–dependent fMRI. Preoperative fMRI data for surgical planning should be used cautiously when the shortest distance from the tumor to the hand knob is ≤4 mm, especially for lower-grade gliomas anterior to the central sulcus.

ABBREVIATIONS: BOLD = blood oxygen level–dependent; DCS = direct cortical stimulation; DD = deviation distance for the midpoint of the hand knob on the lesion hemisphere; D-min = the shortest distance from the tumor to the hand knob

The sensorimotor area is divided by a central sulcus. Because the anterior structure is responsible for motor function, brain tumors in this area cause transient motor function deficits and even permanent paralysis.[1] It is crucial to identify the motor cortex accurately, especially areas relevant to hand movement. Previous studies have investigated various ways of localizing the motor cortex. The hypothesis that the hand knob (hand

Received March 13, 2017; accepted after revision June 4.

From the Department of Neurosurgery (S.F., Y.W., T.J.), Beijing Tiantan Hospital, Capital Medical University, Beijing, China; Beijing Neurosurgical Institute (S.F., J.L., Y.W., X.L., X.F., Y.W., T.J.), Capital Medical University, Beijing, China; MR Collaborations NE Asia (T.Q.), Siemens Healthcare, Beijing, China; Functional Neuroradiology Center (S.L.), Beijing Neurosurgical Institute, Beijing, China; and Beijing Institute for Brain Disorders Brain Tumor Center (T.J.), Beijing, China.

S. Fang, J. Liang, and T. Qian contributed equally to this article.

This study was supported by funds from the National High Technology Research and Development Program of China (863 program) (2015AA020504), the National Basic Research Program of China (No. 2015CB755500), and the National Natural Science Foundation of China (No. 81601452).

Please address correspondence to Tao Jiang, MD, PhD, Beijing Neurosurgical Institute, Capital Medical University, 6, Tiantanxili, Beijing, 100050, China; e-mail: taojiang1964@163.com; Yinyan Wang, MD, Department of Neurosurgery, Beijing Tiantan Hospital, Capital Medical University, 6, Tiantanxili, Beijing, 100050, China; e-mail: tiantanyinyan@126.com

Indicates open access to non-subscribers at www.ajnr.org

Indicates article with supplemental on-line appendix.

Indicates article with supplemental on-line photos.

http://dx.doi.org/10.3174/ajnr.A5342

motor cortex), whose shape resembles the Greek letter Ω the in axial plane, represents the hand motor cortex is well-recognized.[2] However, due to morphologic deviations, tumor infiltration, and edema, hand knobs cannot be localized through typical structural landmarks.[3-5] Hence, a novel method is needed to localize the motor cortex to achieve higher accuracy and reliability.

Blood oxygen level–dependent (BOLD) fMRI is a reliable preoperative method for mapping functional regions of the brain that allows assessment of the function of cortical and subcortical regions.[6] BOLD fMRI helps neurosurgeons determine surgical strategy before an operation.[7,8] Recently, fMRI was applied to help guide intraoperative direct cortical stimulation (DCS), the criterion standard for mapping the functional cortex.[9,10] Motor cortical mapping was considered more accurate compared with language mapping via BOLD fMRI.[11-15] However, inaccurate localizations may sometimes misguide the process of motor functional preservation.[11,16,17] In individual cases, BOLD fMRI identified the motor cortex on the posterior central gyrus[18] or failed to localize the motor cortex.[19] Here, we investigated the factors that affect the accuracy of motor area localization with BOLD fMRI.

Previous studies have suggested that inaccurate BOLD fMRI results are associated with certain tumor locations, neurovascular uncoupling, and functional reorganization.[3,20-23] That tumor locations affect BOLD fMRI signals has been verified.[21,24] Unfortunately, how tumor locations impact BOLD fMRI accuracy has not been quantified, to our knowledge. Tumors localized posterior to the central sulcus may not invade the precentral gyrus because of the barrier formed by the central sulcus and the ascending branch of the cingulate sulcus.[25] It is unclear whether tumor location (anterior or posterior to the central sulcus) influences the accuracy of BOLD fMRI mapping.

This study investigated the association of tumor locations with the accuracy of BOLD fMRI–based localization using quantitatively assessed radiographic characteristics. Two parameters were assessed, namely the shortest distance from tumor to the hand knob (D-min) and the deviation distance for the midpoint of the hand knob on the lesion hemisphere (DD). We hypothesized the following: 1) Smaller D-min and larger DD would be associated with relatively poor BOLD fMRI accuracy, and 2) tumors anterior to the hand knob would notably decrease BOLD fMRI accuracy.

MATERIALS AND METHODS

Patients

Thirty-five patients with lower-grade gliomas whose tumor involved motor areas were enrolled in this retrospective study. All patients underwent preoperative fMRI evaluations and awake craniotomy with intraoperative brain mapping between January 2014 and February 2016 at the Glioma Therapy Center at Beijing Tiantan Hospital. The criteria for inclusion were the following: 1) age older than 18 years, 2) no history of surgical treatment or radiation therapy, 3) no preoperative paralysis, 4) no contraindications to MR imaging, 5) distance from the tumor to the hand knob area of <20 mm, and 6) pathologically confirmed diffuse lower-grade gliomas. Subjects were subdivided into group A (the glioma was located anterior to the central sulcus) or group P (the glioma was located posterior to the central sulcus). We recruited 16 healthy subjects as the control group. This study was approved by the ethics committee of the Beijing Tiantan Hospital. Informed consent was obtained from all participants included in this study.

Anatomic Images: fMRI

MR imaging was performed with a Magnetom Prisma 3T scanner (Siemens, Erlangen, Germany). Anatomic images of each lesion were collected with T1 magnetization prepared rapid acquisition of gradient echo (TR, 2300 ms; TE, 2.3 ms; flip angle, 8°; FOV, 240×240 mm^2; voxel size, $1.0 \times 1.0 \times 1.0$ mm^3; sections, 192; section thickness, 1 mm) and T2-weighted imaging (TR, 5000 ms; TE, 105 ms; flip angle, 150°; FOV, 240×240 mm^2; voxel size, $0.5 \times 0.5 \times 3$ mm^3; sections, 33; section thickness, 3 mm).

Each subject received training for grasping before BOLD fMRI scans within 3 days of the scan. During the fMRI scan, subjects performed a motor task 4 times (twice with the ipsilateral hand and twice with the contralateral hand). The subjects grasped their hands at 1 Hz for 30 seconds, then rested for 30 seconds, and repeated this sequence 3 times during each scan. Before each scan, the magnetic field required 8 seconds to stabilize (On-line Fig 1). The subject relaxed for 20 seconds before each scan. The echo-planar imaging sequence collected the fMRI data (TR, 2000 ms; TE, 30 ms; flip angle, 90°; FOV, 240×240 mm^2; voxel size, $3.0 \times 3.0 \times 3.0$ mm^3; sections, 30; section thickness, 3 mm).

DCS during Awake Craniotomy

Within 3 days after BOLD fMRI scans, all patients underwent awake craniotomy and intraoperative brain mapping with DCS to identify the hand motor cortex by one of the authors, who has considerable experience in awake craniotomy. The procedure was similar to that in previously published reports.[16,26] We used an Ojemann Cortical Stimulator (Integra Life, Plainsboro, New Jersey) to stimulate the cortical and subcortical structures 3 times (intensity, 2–6 mA; frequency, 60 Hz; square wave and duration, 1 ms). We recorded unconscious hand movements during stimulation as positive controls. If at least 2 of the 3 stimulations induced hand movement, we labeled that position as a positive hand motor area, which should be protected during tumor removal. Each positive site was recorded by intraoperative photographs. Patients were anesthetized again after brain mapping and tumor resection. During DCS, no seizures occurred.

BOLD fMRI Data Processing

All BOLD fMRI data were processed with SPM8 software (http://www.fil.ion.ucl.ac.uk/spm/). The processing sequence was as follows: 1) realignment, 2) section timing, 3) smoothing, and 4) coregistering individual T1 images. In the smoothing step, a Gaussian kernel was used with a full width at the half maximum of 6 mm. The BOLD data were analyzed with a general linear model (family-wise error, $P < .05$). Up to 300 voxels were selected from the BOLD fMRI results to represent the hand motor area.

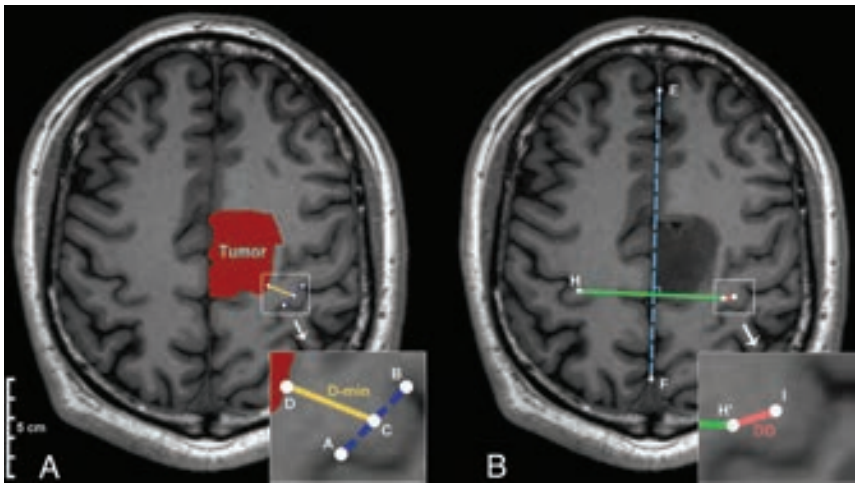

FIG 1. The mathematic model used to quantify the anatomic characteristics (the original magnification of the smaller pictures was ×200%). *A*, Representation of the calculation of D-min. Points A and B represent the ends of the hand knob. Point C represents the midpoint of the hand knob on the lesion hemisphere. Point D is a point on the tumor boundary that is closest to the Point C. D-min is shown as the *gold line*. *B*, The WAN model was used to calculate the DD. The *dotted blue line* indicates the midline of the brain. Points H and I are the midpoints of the hand knobs on the healthy and lesion hemispheres, respectively. Point H′ is the point that mirrors H on the basis of the midline of the brain (*dotted blue line).* The *pink line* represents the DD.

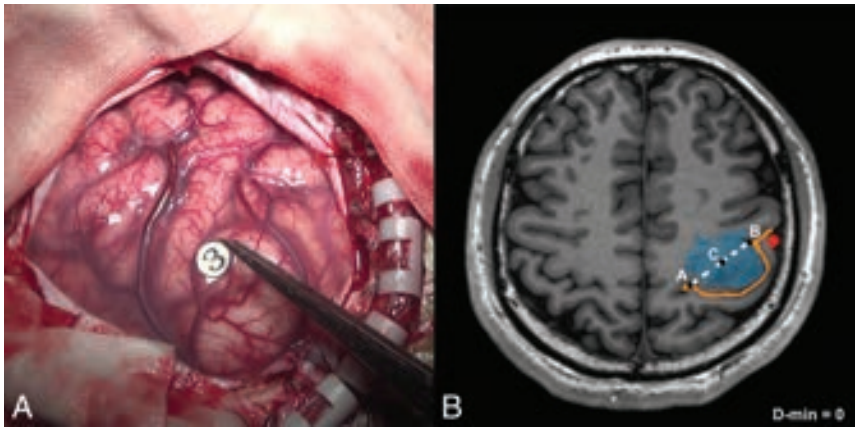

FIG 2. Example of the DCS-positive site and D-min (patient No. 9). *A*, The hand motor area is identified by intraoperative brain mapping. The marker 3 represents thumb buckling when stimulated in this region. *B*, Points A and B represent the ends of the hand knob. The midpoint of the hand knob (point C) in the lesion hemisphere is shown (midpoint of line AB). In this case, the shortest distance from the tumor to the hand knob is zero. The blue region is the tumor, the orange line is the central sulcus (with the Ω sign), and the red region is blood oxygen level—dependent functional MR imaging results.

Anatomic Structure Data Analysis

Two parameters were established for this study. The first, D-min, represented the shortest distance from the tumor to the midpoint between both ends of the hand knob. The other, DD, represented the distance deviation between the hand knob midpoint in the lesion hemisphere and the equivalent hand knob midpoint in the healthy, contralateral hemisphere.

MRIcron (http://www.mccauslandcenter.sc.edu/mricro/mricron) was used to define the reference plane. In the axial plane, the reference plane was defined as the point where both sides of the hand knob were completely visible. Both D-min and DD were calculated at the reference plane.

D-min (Fig 1*A*), the midpoint of the hand knob (point C) in the lesioned hemisphere, was calculated on the basis of both of the hand knob end point coordinates (ie, points A and B). Subsequently, the point nearest on the tumor boundary (point D) to the midpoint of the hand knob (point C) was identified. Finally, D-min was calculated according to the coordinates of points C and D (calculative details are in the On-line Appendix, Part 1).

A mathematic model called WAN was generated to calculate the DD (Fig 1*B*). In the model, the coordinates of the midpoint in the healthy hemisphere (point H) and the midpoint in the lesioned hemisphere (point I) were calculated on the basis of both of their hand knob end point coordinates. The midline (blue dotted line) was calculated on the basis of points E and F, which were located on either side of the falx cerebri intersection. In addition, the midpoint (point H′) that mirrored point H was calculated on the basis of the line EF. Finally, the DD was calculated according to the coordinates of point H′ and point I (calculative details are in the On-line Appendix, Part 2).

DCS Results and Overlap Index Calculation

To characterize the region of positive stimulation by DCS, a global region of 5-mm diameter was defined on the basis of each positive site. This region was manually drawn by 2 neuroradiologists independently according to intraoperative photographs (Fig 2*A*). If their selections varied from each other by >5%, another neuroradiologist with 20 years of experience made the final decision regarding the region location.

The number of overlapping voxels between BOLD fMRI results and DCS regions was calculated via Matlab 2014a (MathWorks, Natick, Massachusetts). The overlap index was calculated via the formula (in this study, the total voxels of BOLD = 300):

$$\text{Overlap Index} = \frac{\text{Number of Overlapping Voxels}}{\text{Total Voxels of BOLD}} \times 100\%.$$

The nonoverlap phenomenon was defined as the overlap index equal to zero (Fig 3). In contrast, the overlap phenomenon was defined as the overlap index greater than zero (Fig 4).

Statistical Analysis

A χ^2 test was performed for the distribution of several attributes (including sex, age, lesion hemisphere, World Health Organiza-

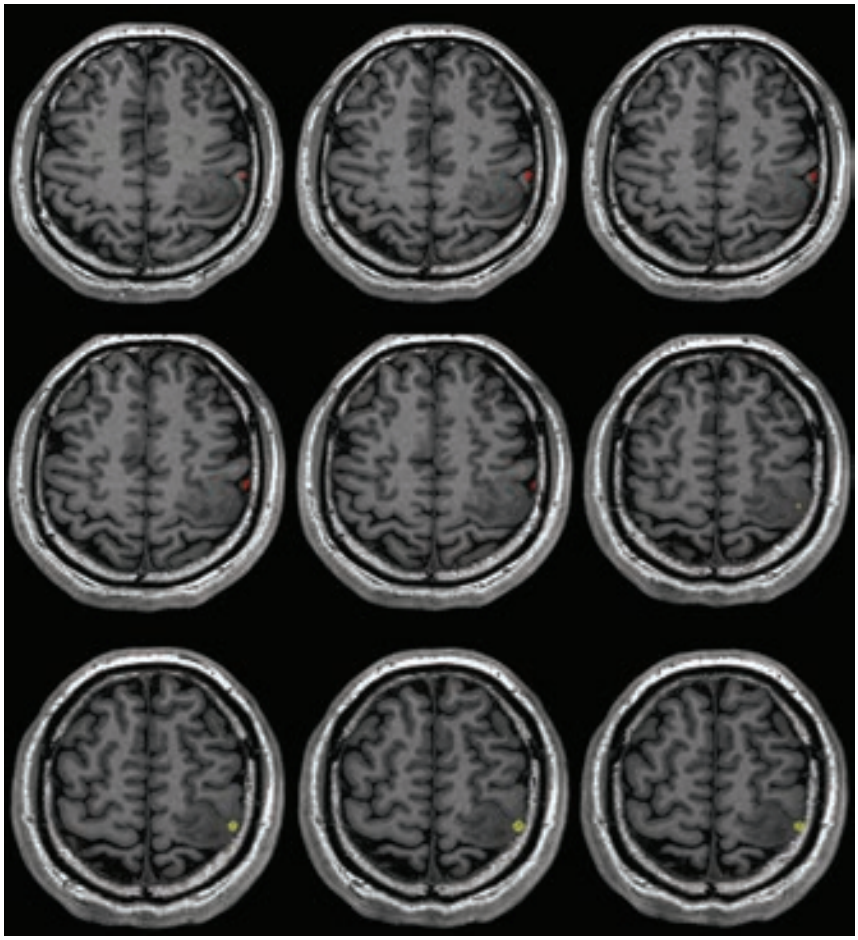

FIG 3. An example of the nonoverlapping phenomenon (patient No. 9). There was no region overlapping between the BOLD fMRI and DCS results. The red region is the BOLD fMRI results. The yellow region is the DCS results.

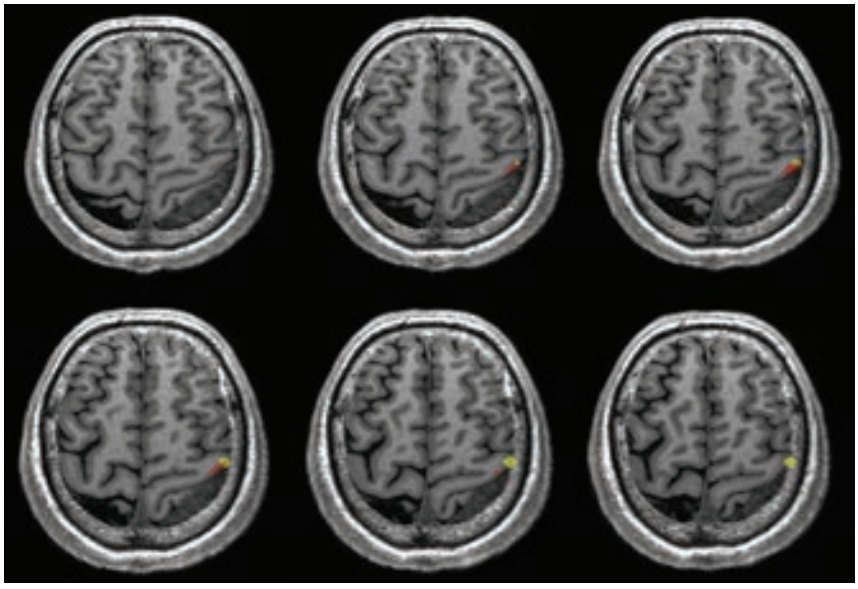

FIG 4. An example of the overlapping phenomenon (patient No. 16). There were some overlapping regions between the BOLD fMRI and DCS results. The red region is the BOLD fMRI results. The yellow region is the DCS results.

tion grade, and preoperative epilepsy history). A Student *t* test was used to analyze the differences in D-min and DD between the 2 patient groups. All results are presented as mean ± SD. The receiver operating characteristic curve was generated with GraphPad Prism 6.0c software (GraphPad Software, San Diego, California). The level of significance was .05 (2-tailed) for each statistical test.

RESULTS

Patients

Thirty-five patients met our inclusion criteria (Table 1). Eighteen of them were older than 40 years of age. All were right-handed. Fourteen patients (40%) had a preoperative seizure history. Twenty-six (74.3%) had grade II gliomas, and the others had grade III gliomas. There were no statistical differences in general characteristics with respect to overlapping or nonoverlapping phenomena.

In terms of anatomic characteristics (Table 2), 20 gliomas were anterior to the hand knob and 15 gliomas were posterior to it (Fig 5). The mean tumor volume was 50.76 ± 25.12 mm^3, the mean D-min was 7.50 ± 5.28 mm, and the mean DD was 9.38 ± 1.36 mm.

There were 16 subjects (1 women, 15 men) in the control group. Their mean age was 25.6 ± 1.0 years, and only 2 patients were right-handed.

Association between D-min and Motor Area Localization

The mean D-min for the nonoverlapping group was smaller than that for the overlapping group (3.02 ± 0.88 mm versus 9.07 ± 1.01 mm, respectively; $P = .002$, *t* test; Fig 6*A*). The receiver operating characteristic curve analysis indicated that 4 mm was the optimal cutoff value (84.6% sensitivity; 77.8% specificity; area under the curve, 0.844) to predict nonoverlapping phenomena (Fig 6*B*).

Overlap Index between BOLD fMRI and DCS Results

In group A, a significant difference in the overlap index was identified between the D-min ≤4-mm group and the D-min >4-mm group (17.2% ± 7.5% versus 59.1% ± 10.5%, respectively; $P = .005$, On-line Fig 2*B*). Con-

versely, no difference was found between the D-min ≤4-mm group and the D-min >4-mm group in group P (33.5% ± 22.5% versus 56.6% ± 9.4%, respectively; $P = .275$, On-line Fig 2*C*).

Table 1: General characteristics for the patient group

Characteristics	Value (%)	*P* Value
Sex		.19
Male	26 (74.3)	
Female	9 (25.7)	
Age		.71
40 years or older	18 (51.4)	
Younger than 40 years	17 (48.6)	
Handedness		–
Left	0 (0)	
Right	35 (100)	
Lesion hemisphere		.43
Left	21 (60)	
Right	14 (40)	
Preoperative seizure history		.71
Seizure	14 (40)	
No seizure	21 (60)	
WHO pathologic grade		.39
II	26 (74.3)	
III	9 (25.7)	
Overlapping results		–
Overlapping	26 (74.3)	
Nonoverlapping	9 (25.7)	
Intraoperative seizure		–
Yes	0 (0)	
No	35 (100)	

Note:—WHO indicates World Health Organization.

Table 2: Anatomic characteristics of the patient group

Characteristics	Value
Tumor volume (mean) (mm^3)	50.76 ± 25.12
D-min (mean) (mm)	7.50 ± 5.28
DD (mean) (mm)	9.38 ± 1.36
Tumor location	
Anterior to hand knob (group A) (No.)	20 (57.1%)
Posterior to hand knob (group P) (No.)	15 (42.9%)

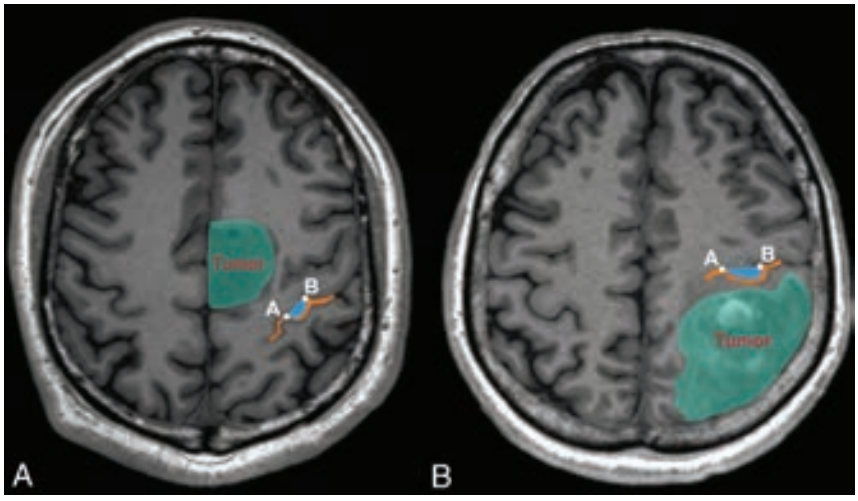

FIG 5. An example of tumor and hand knob locations. *A*, The tumor was anterior to the hand knob. *B*, The tumor was posterior to the hand knob. The *orange line* is the central sulcus, and the *blue region* is the hand knob. Points A and B represent both ends of the hand knob.

Hand Knob Deviation and Nonoverlapping Phenomena

In the WAN model, we evaluated the symmetry of the bilateral hand knob in patient and control groups by measuring the DD. The DD of the patient group was significantly larger than that of the control group (9.38 ± 1.36 mm versus 4.16 ± 0.74 mm; $P = .015$, *t* test; On-line Fig 3).

The DD for the patient group was larger in the nonoverlapping group than in the overlapping group (17.59 ± 4.00 mm versus 7.06 ± 0.71 mm, respectively; $P = .003$, *t* test; On-line Fig 4*A*). In group A, a statistical difference in DD was found between the overlapping group and the nonoverlapping group (nonoverlapping group, 20.88 ± 5.45 mm; overlapping group, 6.30 ± 0.90 mm; $P = .001$, *t* test; On-line Fig 4*B*), whereas no significant difference existed in group P (overlapping group, 7.95 ± 1.12 mm; nonoverlapping group, 10.99 ± 3.21 mm, respectively; $P = .280$, *t* test; On-line Fig 4).

DISCUSSION

Identifying the hand motor cortex accurately is crucial when planning surgery for gliomas involving the functional motor cortex. At present, BOLD fMRI is the prevalent noninvasive preoperative method used to localize the motor cortex. However, the accuracy of BOLD fMRI remains contested. Previous studies have concluded that unreliable BOLD fMRI results are associated with neurovascular uncoupling, particular tumor locations, tumor grades, cooperation of patients, task selection, and functional reorganization.[9,27-30] Although the BOLD fMRI signals are affected by tumor locations,[21,24] the impact of tumor location on BOLD fMRI accuracy has not been quantified. Thus, in our study, we investigated how tumor location affected BOLD fMRI accuracy via some locational characteristics such as D-min and DD.

On the basis of the regression model, the calculated voxel values were positively related to the degree of activation. A previous study[31] considered the top 2% of the highly activated voxels as the functional area. Similarly, we allowed a maximum of 300 voxels from the BOLD fMRI results, to exclude a large number of irrelevant voxels.

BOLD fMRI takes advantage of variations in blood hemoglobin levels to identify the relevant functional cortex.[32] The mechanism relies on neurovascular coupling. When neurons are activated, the oxygen-hemoglobin level increases rapidly and remains high until activation ceases in relevant areas. Coincidentally, the oxygen-hemoglobin exhibits a type of diamagnetism that acts as an endogenous contrast medium, thus revealing relevant activated areas.[33]

Due to limitations of BOLD fMRI,[34] false-negative results may appear in the presence of neurovascular uncoupling. Thus, the actual functional area may not be displayed completely, and the BOLD fMRI results may be unreliable.[28,35,36] Alterations in hemodynamics and the microenvironment are the primary reasons.[21,33,37] First, gliomas impair cerebral vascular reactions and reduce CBV

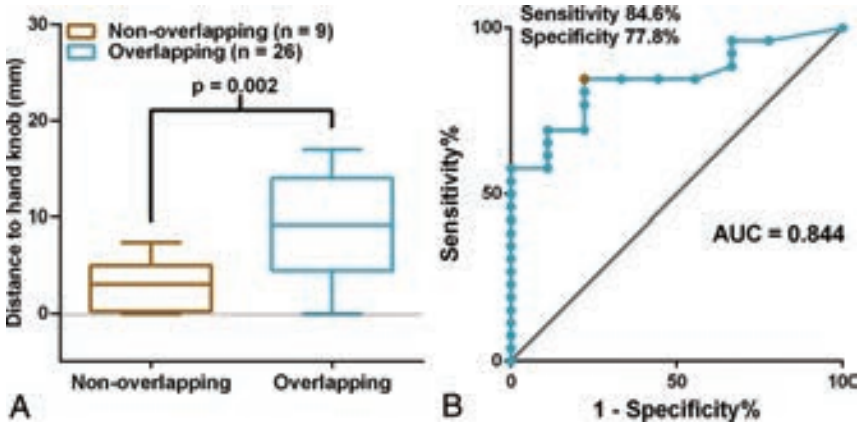

FIG 6. The relationship between D-min and the nonoverlapping phenomena of BOLD fMRI and a comparison with DCS results. *A*, The boxplot shows that D-min is significantly different between the overlapping and nonoverlapping groups (*t* test). The *middle line* in each box is the mean value; the horizontal boundaries of the boxes are the first and third quartiles. The *topmost line* is the maximum value, and the *bottommost line* is the minimum value. *B*, Receiver operating characteristic curves are used to assess whether the BOLD fMRI and DCS results overlap. The results for sensitivity are plotted against 1-specificity to compare BOLD fMRI versus DCS. The gray line is the reference line. The *red point* represents the optimal point for which the best cutoff value was 4 mm, with a sensitivity of 84.6% and a specificity of 77.8%. AUC indicates area under the curve.

and CBF.[21,34] This process raises the level of deoxygenated hemoglobin that is paramagnetic and reduces BOLD signals.[22] Second, gliomas change the microenvironment of surrounding tissues.[33,38] Abnormal astrocyte proliferation decreases potassium reabsorption, which reduces the oxygen supply and elevates deoxygenated hemoglobin levels.[39] Previous studies illustrated that gliomas induce neurovascular uncoupling.[35,36] Furthermore, the higher-grade gliomas are associated with a greater probability of neurovascular uncoupling.[15,17,21,22] Our results demonstrated that if D-min were ≤4 mm, nonoverlapping phenomena occurred more frequently than when D-min was >4 mm. We speculate that this outcome is due to neurovascular uncoupling. A previous study verified that gliomas caused a decline in BOLD fMRI activation by neurovascular uncoupling when the glioma was near the primary motor cortex.[40] Our results were consistent with this theory to some extent. However, another study suggested that the distance between the tumor and primary motor cortex was no more likely than tumor type in influencing BOLD fMRI activation.[41] This finding may be because all patients in that study had glioblastomas rather than lower-grade gliomas. On the basis of previous studies,[15,17,21,22] we believe that the degree of neurovascular uncoupling in our patients was not greater than that in patients with glioblastomas. Hence, we believe that D-min significantly affects BOLD fMRI accuracy in lower-grade gliomas.

Distortion and movement of hand knobs may decrease the accuracy of BOLD fMRI results. Hand knobs will be moved and become distorted when gliomas grow and invade surrounding structures.[3-5] By comparing DD, we found that hand knobs moved more obviously in the patient group than in the control group. Hand knob distortion decreased the number of true-positive voxels in relevant regions. However, the number of positive voxels stimulated by DCS was unchanged.[26] Hence, the overlap indexes decreased. This result could explain the significant difference in overlap between the group with a D-min of <4 mm and the group with a D-min of >4 mm. This finding may also explain the larger DD in the nonoverlapping group than in the overlapping group. Hence, we believe that distortion and movement of hand knobs may decrease the accuracy of BOLD fMRI results.

We found that the accuracy of BOLD fMRI results was associated with glioma location. The structure of the primary motor cortex is unique. The cingulate sulcus and the central sulcus constitute an obstruction that divides the precentral and posterior central gyri completely.[25] A prior study showed that the pre- and postcentral sulci were only linked by the paracentral lobule, which was responsible for foot movement.[42] Because of its special structure, it is easier for gliomas to invade the precentral gyrus from anterior areas. In contrast, it is difficult for gliomas that grow on the posterior central gyrus to invade the precentral gyrus directly. Hence, we hypothesized that gliomas that grow anterior to the central sulcus compared with those growing posterior to it would influence the BOLD fMRI accuracy more. To test our theory, we divided patients into group A or P. We found significant differences in both D-min and DD in group A, but not in group P. This finding corresponded with our hypothesis. Thus, we concluded that anterior gliomas influenced the BOLD fMRI accuracy more obviously than posterior gliomas. The limited number of samples in our study made it difficult to verify this finding. In the future, we will recruit more patients to verify our hypothesis.

Besides neurovascular uncoupling and tumor locations, there are other factors that may cause the inaccuracy of BOLD fMRI mapping, including task selection, the cooperation of patients, and cognitive status.[12,33] Grasping is one of the traditional tasks used to identify the motor cortex and has been used in many previous studies.[16,43,44] Poor cooperation and impaired cognitive status of the patient could reduce the quality of BOLD fMRI.[33,45] To reduce the above influences, we enrolled patients without preoperative paralysis, and each patient was trained to achieve good performance in hand grasping before the BOLD fMRI scans.

CONCLUSIONS

This study suggests that D-min and DD are predictive of the accuracy of BOLD fMRI results. A smaller D-min and larger DD are associated with less accuracy of motor area localization with BOLD fMRI. One should be cautious in the use of preoperative fMRI data for surgical planning when D-min is smaller than 4 mm, especially for a lower-grade glioma located anterior to the central sulcus.

ACKNOWLEDGMENTS

We thank Stefan Huwer from Siemens for support with image collection.

Disclosures: Tianyi Qian—*UNRELATED*: *Employment*: Siemens.

REFERENCES

1. Chang EF, Clark A, Smith JS, et al. **Functional mapping-guided resection of low-grade gliomas in eloquent areas of the brain: improvement of long-term survival—clinical article.** *J Neurosurg* 2011;114:566–73 CrossRef Medline
2. Yousry TA, Schmid UD, Alkadhi H, et al. **Localization of the motor hand area to a knob on the precentral gyrus: a new landmark.** *Brain* 1997;120(pt 1):141–57 CrossRef Medline
3. Hou BL, Bhatia S, Carpenter JS. **Quantitative comparisons on hand motor functional areas determined by resting state and task BOLD fMRI and anatomical MRI for pre-surgical planning of patients with brain tumors.** *Neuroimage Clin* 2016;11:378–87 CrossRef Medline
4. Pujol J, Deus J, Acebes JJ, et al. **Identification of the sensorimotor cortex with functional MRI: frequency and actual contribution in a neurosurgical context.** *J Neuroimaging* 2008;18:28–33 CrossRef Medline
5. Gabriel M, Brennan NP, Peck KK, et al. **Blood oxygen level dependent functional magnetic resonance imaging for presurgical planning.** *Neuroimaging Clin N Am* 2014;24:557–71 CrossRef Medline
6. Majos A, Tybor K, Stefańczyk L, et al. **Cortical mapping by functional magnetic resonance imaging in patients with brain tumors.** *Eur Radiol* 2005;15:1148–58 CrossRef Medline
7. Talacchi A, Turazzi S, Locatelli F, et al. **Surgical treatment of high-grade gliomas in motor areas: the impact of different supportive technologies—a 171-patient series.** *J Neurooncol* 2010;100:417–26 CrossRef Medline
8. Spena G, D'Agata F, Panciani PP, et al. **Supratentorial gliomas in eloquent areas: which parameters can predict functional outcome and extent of resection?** *PLoS One* 2013;8:e80916 CrossRef Medline
9. Pirotte B, Voordecker P, Neugroschl C, et al. **Combination of functional magnetic resonance imaging-guided neuronavigation and intraoperative cortical brain mapping improves targeting of motor cortex stimulation in neuropathic pain.** *Neurosurgery* 2008;62:941–56 Medline
10. De Witt Hamer PC, Robles SG, Zwinderman AH, et al. **Impact of intraoperative stimulation brain mapping on glioma surgery outcome: a meta-analysis.** *J Clin Oncol* 2012;30:2559–65 CrossRef Medline
11. Bartos R, Jech R, Vymazal J, et al. **Validity of primary motor area localization with fMRI versus electric cortical stimulation: a comparative study.** *Acta Neurochir (Wien)* 2009;151:1071–80 CrossRef Medline
12. Trinh VT, Fahim DK, Maldaun MV, et al. **Impact of preoperative functional magnetic resonance imaging during awake craniotomy procedures for intraoperative guidance and complication avoidance.** *Stereotact Funct Neurosurg* 2014;92:315–22 CrossRef Medline
13. Ille S, Sollmann N, Hauck T, et al. **Impairment of preoperative language mapping by lesion location: a functional magnetic resonance imaging, navigated transcranial magnetic stimulation, and direct cortical stimulation study.** *J Neurosurg* 2015;123:314–24 CrossRef Medline
14. Ille S, Sollmann N, Hauck T, et al. **Combined noninvasive language mapping by navigated transcranial magnetic stimulation and functional MRI and its comparison with direct cortical stimulation.** *J Neurosurg* 2015;123:212–25 CrossRef Medline
15. Holodny AI, Schulder M, Liu WC, et al. **The effect of brain tumors on BOLD functional MR imaging activation in the adjacent motor cortex: implications for image-guided neurosurgery.** *AJNR Am J Neuroradiol* 2000;21:1415–22 Medline
16. Lehéricy S, Duffau H, Cornu P, et al. **Correspondence between functional magnetic resonance imaging somatotopy and individual brain anatomy of the central region: comparison with intraoperative stimulation in patients with brain tumors.** *J Neurosurg* 2000;92:589–98 CrossRef Medline
17. Holodny AI, Schulder M, Liu WC, et al. **Decreased BOLD functional MR activation of the motor and sensory cortices adjacent to a glioblastoma multiforme: implications for image-guided neurosurgery.** *AJNR Am J Neuroradiol* 1999;20:609–12 Medline
18. Due-Tonnessen P, Rasmussen I, Berntsen EM, et al. **Identifying the central sulcus in patients with intra-axial lesions: a multicenter study comparing conventional presurgical MRI to topographical analysis and BOLD-fMRI.** *J Comput Assist Tomogr* 2014;38:1–8 CrossRef Medline
19. Zhang D, Fox MD, Leuthardt EC, et al. **Preoperative sensorimotor mapping in brain tumor patients using spontaneous fluctuations in neuronal activity imaged with functional magnetic resonance imaging: initial experience.** *Neurosurgery* 2009;65:226–36 Medline
20. Vassal M, Charroud C, Deverdun J, et al. **Recovery of functional connectivity of the sensorimotor network after surgery for diffuse low-grade gliomas involving the supplementary motor area.** *J Neurosurg* 2017;126:1181–90 CrossRef Medline
21. Hou BL, Bradbury M, Peck KK, et al. **Effect of brain tumor neovasculature defined by rCBV on BOLD fMRI activation volume in the primary motor cortex.** *Neuroimage* 2006;32:489–97 CrossRef Medline
22. Fujiwara N, Sakatani K, Katayama Y, et al. **Evoked-cerebral blood oxygenation changes in false-negative activations in BOLD contrast functional MRI of patients with brain tumors.** *Neuroimage* 2004;21:1464–71 CrossRef Medline
23. Agarwal S, Sair HI, Yahyavi-Firouz-Abadi N, et al. **Neurovascular uncoupling in resting state fMRI demonstrated in patients with primary brain gliomas.** *J Magn Reson Imaging* 2016;43:620–26 CrossRef Medline
24. Wang L, Chen D, Olson J, et al. **Re-examine tumor-induced alterations in hemodynamic responses of BOLD fMRI: implications in presurgical brain mapping.** *Acta Radiol* 2012;53:802–11 CrossRef Medline
25. Shah KB, Hayman LA, Chavali LS, et al. **Glial tumors in Brodmann area 6: spread pattern and relationships to motor areas.** *Radiographics* 2015;35:793–803 CrossRef Medline
26. Duffau H, Capelle L, Denvil D, et al. **Usefulness of intraoperative electrical subcortical mapping during surgery for low-grade gliomas located within eloquent brain regions: functional results in a consecutive series of 103 patients.** *J Neurosurg* 2003;98:764–78 CrossRef Medline
27. Picht T, Wachter D, Mularski S, et al. **Functional magnetic resonance imaging and cortical mapping in motor cortex tumor surgery: complementary methods.** *Zentralbl Neurochir* 2008;69:1–6 CrossRef Medline
28. Majos A, Bryszewski B, Kośla KN, et al. **Process of the functional reorganization of the cortical centers for movement in GBM patients: fMRI study.** *Clin Neuroradiol* 2017;27:71–79 CrossRef Medline
29. Ulmer JL, Hacein-Bey L, Mathews VP, et al. **Lesion-induced pseudodominance at functional magnetic resonance imaging: implications for preoperative assessments.** *Neurosurgery* 2004;55:569–79; discussion 580–81 CrossRef Medline
30. Xie J, Chen XZ, Jiang T, et al. **Preoperative blood oxygen level-dependent functional magnetic resonance imaging in patients with gliomas involving the motor cortical areas.** *Chin Med J (Engl)* 2008;121:631–35 Medline
31. Qiu TM, Yan CG, Tang WJ, et al. **Localizing hand motor area using resting-state fMRI: validated with direct cortical stimulation.** *Acta Neurochir (Wien)* 2014;156:2295–302 CrossRef Medline
32. Ogawa S, Lee TM, Kay AR, et al. **Brain magnetic resonance imaging with contrast dependent on blood oxygenation.** *Proc Natl Acad Sci U S A* 1990;87:9868–72 CrossRef Medline
33. D'Esposito M, Deouell LY, Gazzaley A. **Alterations in the BOLD fMRI signal with ageing and disease: a challenge for neuroimaging.** *Nat Rev Neurosci* 2003;4:863–72 CrossRef Medline
34. Ulmer JL, Krouwer HG, Mueller WM, et al. **Pseudo-reorganization of language cortical function at fMR imaging: a consequence of tumor-induced neurovascular uncoupling.** *AJNR Am J Neuroradiol* 2003;24:213–17 Medline
35. Zacà D, Jovicich J, Nadar SR, et al. **Cerebrovascular reactivity mapping in patients with low grade gliomas undergoing presurgical sensorimotor mapping with BOLD fMRI.** *J Magn Reson Imaging* 2014;40:383–90 CrossRef Medline

36. Chen CM, Hou BL, Holodny AI. **Effect of age and tumor grade on BOLD functional MR imaging in preoperative assessment of patients with glioma.** *Radiology* 2008;248:971–78 CrossRef Medline
37. Sakatani K, Murata Y, Fujiwara N, et al. **Comparison of blood-oxygen-level-dependent functional magnetic resonance imaging and near-infrared spectroscopy recording during functional brain activation in patients with stroke and brain tumors.** *J Biomed Opt* 2007; 12:062110 CrossRef Medline
38. Schwarzbauer C, Heinke W. **Investigating the dependence of BOLD contrast on oxidative metabolism.** *Magn Reson Med* 1999;41:537–43 Medline
39. Paulson OB, Newman EA. **Does the release of potassium from astrocyte endfeet regulate cerebral blood flow?** *Science* 1987;237:896–98 CrossRef Medline
40. Liu WC, Feldman SC, Schulder M, et al. **The effect of tumour type and distance on activation in the motor cortex.** *Neuroradiology* 2005; 47:813–19 CrossRef Medline
41. Fraga de Abreu VH, Peck KK, Petrovich-Brennan NM, et al. **Brain tumors: the influence of tumor type and routine MR imaging characteristics at BOLD functional MR imaging in the primary motor gyrus.** *Radiology* 2016;28:876–83 CrossRef Medline
42. Wang Y, Hao Y, Zhou J, et al. **Direct current stimulation over the human sensorimotor cortex modulates the brain's hemodynamic response to tactile stimulation.** *Eur J Neurosci* 2015;42:1933–40 CrossRef Medline
43. Krings T, Reinges MH, Erberich S, et al. **Functional MRI for presurgical planning: problems, artefacts, and solution strategies.** *J Neurol Neurosurg Psychiatry* 2001;70:749–60 CrossRef Medline
44. Möller M, Freund M, Greiner C, et al. **Real time fMRI: a tool for the routine presurgical localisation of the motor cortex.** *Eur Radiol* 2005;15:292–95 CrossRef Medline
45. Pujol J, Conesa G, Deus J, et al. **Clinical application of functional magnetic resonance imaging in presurgical identification of the central sulcus.** *J Neurosurg* 1998;88:863–69 CrossRef Medline

Flat Panel Angiography in the Cross-Sectional Imaging of the Temporal Bone: Assessment of Image Quality and Radiation Dose Compared with a 64-Section Multisection CT Scanner

G. Conte, E. Scola, S. Calloni, R. Brambilla, M. Campoleoni, L. Lombardi, F. Di Berardino, D. Zanetti, L.M. Gaini, F. Triulzi, and C. Sina

ABSTRACT

BACKGROUND AND PURPOSE: Cross-sectional imaging of the temporal bone is challenging because of the complexity and small dimensions of the anatomic structures. We evaluated the role of flat panel angiography in the cross-sectional imaging of the temporal bone by comparing its image quality and radiation dose with a 64-section multisection CT scanner.

MATERIALS AND METHODS: We retrospectively collected 29 multisection CT and 29 flat panel angiography images of normal whole-head temporal bones. Image quality was assessed by 2 neuroradiologists, who rated the visualization of 30 anatomic structures with a 3-point ordinal scale. The radiation dose was assessed with an anthropomorphic phantom.

RESULTS: Flat panel angiography showed better image quality than multisection CT in depicting the anterior and posterior crura of the stapes, the footplate of the stapes, the stapedius muscle, and the anterior ligament of the malleus ($P < .05$). In contrast, multisection CT showed better image quality than flat panel angiography in assessing the tympanic membrane, the bone marrow of the malleus and incus, the tendon of the tensor tympani, the interscalar septum, and the modiolus of the cochlea ($P < .05$). Flat panel angiography had a significantly higher overall image quality rating than multisection CT ($P = .035$). A reduction of the effective dose of approximately 40% was demonstrated for flat panel angiography compared with multisection CT.

CONCLUSIONS: Flat panel angiography shows strengths and weaknesses compared with multisection CT. It is more susceptible to artifacts, but due to the higher spatial resolution, it shows equal or higher image quality in assessing some bony structures of diagnostic interest. The lower radiation dose is an additional advantage of flat panel angiography.

ABBREVIATIONS: FPA = flat panel angiography; FPCT = flat panel CT; H_T = equivalent dose; MSCT = multisection CT; TLD = thermoluminescent dosimeter

Cross-sectional imaging of the temporal bone is challenging because of the complexity and small dimensions of the anatomic structures. Multisection CT (MSCT) represents the technique of choice for the study of the temporal bones. It is noninvasive and provides a high spatial resolution (~0.4 mm in-plane and ~0.5 mm in section thickness) that allows radiologists to visualize most of the anatomic structures and detect pathologic changes.[1] On occasion, however, more invasive examinations, such as an exploratory operation, may be required to achieve a diagnosis or to clarify the pathologic processes depicted by MSCT.[2]

Flat panel CT (FPCT) has recently provided an alternative method with ultra-high isotropic spatial resolution (~150 × 150 × 150 μm^3).[3,4] Some studies have investigated the image quality of FPCT in the delineation of postmortem normal temporal bone anatomy: FPCT showed higher image quality compared with MSCT when isolated temporal specimens were scanned but showed similar image quality in cadaveric whole-head specimens.[1,2,3,5] The diagnostic value of FPCT has been reported to be high in the assessment of conductive hearing loss.[6]

All these studies have been using prototype scanners or dedicated scanners to perform FPCT of the temporal bone. Radiologic assessment of the fine bony structures of the ear can also be performed with angiographic systems equipped with flat panel detectors, but the use of this technique is still uncommon. Recently, flat

Received January 17, 2017; accepted after revision May 22.

From the Postgraduation School of Radiodiagnostics (G.C., S.C.) and Department of Pathophysiology and Transplantation (F.T.), Università degli Studi di Milano, Milan, Italy; Neuroradiology Unit (E.S., L.L., F.T., C.S.) and Health Physics Unit (R.B., M.C.), Fondazione Istituto Di Ricovero e Cura a Carattere Scientifico Ca'Granda Ospedale Maggiore Policlinico, Milan, Italy; and Audiology Unit (F.D.B., D.Z.) and Otolaryngology Unit (L.M.G.), Department of Clinical Sciences and Community Health, Fondazione Istituto Di Ricovero e Cura a Carattere Scientifico Ca'Granda Ospedale Maggiore Policlinico, Università degli Studi di Milano, Milan, Italy.

Please address correspondence to Giorgio Conte, MD, Postgraduation School in Radiodiagnostics, Università degli Studi di Milano, Via Festa del Perdono 7, 20122 Milan, Italy; e-mail: giorgioconte.unimed@gmail.com

Indicates article with supplemental on-line tables.

Indicates article with supplemental on-line photos.

http://dx.doi.org/10.3174/ajnr.A5302

panel angiography (FPA) was used in the cross-sectional imaging assessment of cochlear implants and metallic prostheses after middle ear reconstructive surgery because it is less susceptible to metallic artifacts.[7-9] However, the image quality of FPA of the normal temporal bone has not yet been investigated in patients during clinical practice, and radiation exposure has not been assessed so far, to our knowledge. It was our expectation that FPA could provide better image quality at lower radiation exposure compared with MSCT.

The purpose of our study was to test the value of FPA in the cross-sectional imaging of the temporal bone in a cohort of patients during clinical practice by comparing its image quality and radiation dose with those in 64-section MSCT.

MATERIALS AND METHODS

Patients

The use of FPA in our department began in January 2015 for the postoperative assessment of patients with cochlear implants,[7] after its radiation exposure was tested on a phantom. Thereafter, the use of FPA was extended to other clinical indications on the basis of its proved image quality. FPA and MSCT were randomly performed. FPA was always preferred to MSCT because of the results of the phantom dose experiments (see the "Radiation Dose Assessment" paragraph in the "Results" section) but was performed whenever the unit was available, the latter being largely dedicated to endovascular procedures. Otherwise MSCT was performed.

For this study, from January 2015, we collected 29 consecutive MSCT scans and 29 consecutive FPA scans of normal temporal bones, obtained in our department. Temporal bones were defined as normal according to the following criteria: 1) no pathologic findings on MSCT or FPA, and 2) no history of otologic disorders on the imaged side as evidenced by the patient's medical record. Each examination was performed to investigate or rule out suspected abnormalities in the contralateral temporal bone, including cholesteatoma, otosclerosis, middle and inner ear congenital malformations, and complications of otitis.

This retrospective study received review board approval; patient informed consent was waived.

MSCT and FPA Protocols

MSCT examinations were performed with a 64-section CT scanner (Optima CT660; GE Healthcare, Milwaukee, Wisconsin). The MSCT scan included both temporal bones, with the following scan parameters: current, 200 mA; voltage, 120 kV; pitch, 0.531:1; rotation time, 1 second; section collimation, 0.625 mm; FOV, 22 cm^2; matrix, 512 × 512; scan length, 105 mm. The scan time was 5.63 seconds. The CT dose index volume was 62.1 mGy, and the dose-length was 652 mGy × cm. The images were reconstructed from the raw data with a 512 × 512 matrix and a 10-cm FOV, leading to a 0.195 × 0.195 mm pixel size in the plane of acquisition. A bone sharpening filter (Bone Plus; GE Healthcare) was used.

FPA was performed with an angiographic system (Allura Xper FD20; Philips Healthcare, Best, the Netherlands), including a digital flat panel detector, 30 × 40 cm with a source-to-image-receptor distance of 120 cm. The FPA scan included both temporal bones of the patient's head, with the following scan parameters: current, 260 mA; voltage, 80 kV; FOV, 20 × 15 cm^2; voxel size, 0.14 × 0.14 × 0.14 mm^3; scan height, 150 mm. By rotating 240° (from 60° to 300°) passing through the posterior part of the head and avoiding the anterior part, the pivoting C-arm of the angiography unit acquires a volume dataset of up to 622 projections, with a scan time of 25 seconds. The dose-area product was 10,650 mGy × cm^2, and the air kerma was 121 mGy. Each temporal bone was reprocessed separately into a small FOV. Postprocessing of this volume dataset was performed with reconstruction software (Allura 3D-RA 6.3.0/XperCt 3.1.0; Philips Healthcare), offering all the possibilities of standard 3D-postprocessing such as multiplanar reformations, curved reformations, volume-rendering technique, shaded surface display technique, and MIP. Depending on the number of additional procedures running, the average reconstruction time was approximately 10 minutes.

Assessment of Image Quality

Two neuroradiologists with >3 years of experience in otoradiology independently evaluated each examination separately on a PACS viewer. The readers were permitted to scroll through the image sections, change the CT window level and width, perform MPR and MIP of the volume data, and zoom in and out in any order.

First, the radiologists defined each scan as adequate or inadequate according to the presence of artifacts, including head movements. Thirty anatomic structures were identified, listed in Online Table 1. For each of the structures, the investigators rated the quality of visualization with an ordinal scale as follows: Zero indicated that the anatomic structure could not be identified; 1, the anatomic structure could be identified but was not well-delineated from the surrounding structures; and 2, the anatomic structure could be identified and was well-delineated from the surrounding structures. For each examination, the summed score represented the overall image quality, ranging from 0 to 60 points (maximum, 2 points × 30 structures). The 2 readers' average scores (continuous variables) were used to compare differences between MSCT and FPA.

Furthermore, each reader placed a circular ROI (approximately 50 mm^2) in the inner portion of the external acoustic canal, avoiding surrounding bony structures and the tympanic membrane. The signal was defined as the mean CT attenuation value within the ROI, and the noise, as the SD of the CT attenuation values within the ROI. The signal-to-noise ratio was calculated. The 2 readers' average signal, noise, and SNR were used to compare MSCT and FPA.

Nominal variables were represented as relative percentages, and continuous variables were represented as the mean ± SD. A χ^2 test for nominal data and a Mann-Whitney test for continuous data were used to compare MSCT and FPA. The Kolmogorov-Smirnov test was used to test the normality of the continuous variables, and an unpaired Student *t* test or Mann-Whitney test was used to compare the 2 groups, as appropriate. The Spearman rank correlation coefficient was used to assess the degree of correlation between SNR and the summed score for each group. To analyze the interobserver agreement, we dichotomized into 2

groups ("visualized" = 1; and "not visualized" = 0). The observers' sensitivity in detecting each anatomic structure was calculated, and interobserver agreement was expressed as a percentage of agreement. The κ statistic, which estimates the proportion of interobserver agreement above that expected by chance, was computed for each anatomic structure. Differences were considered statistically significant with $P < .05$. The statistical analysis was performed with SPSS 20 statistical software (IBM, Armonk, New York).

Radiation Dose Assessment

We used an anthropomorphic Rando Alderson phantom (Rando Alderson Research Laboratories, Long Island, City, New York) for radiation dose assessment. The phantom represented an average male and was composed of a human skeleton embedded in tissue-equivalent material. A thermoluminescent dosimeter (TLD) (GR-200 Thermoluminescent Detector; 360RAD, Beijing, China) consisting of LiF, Mg, Cu, and P materials (https://www.thermofisher.com/order/catalog/product/SCP18815) with an intrinsic dose detector limit of approximately 1 microsievert (μSv) was used. The TLDs were inserted into the Rando phantom at sites corresponding to organs or tissues (listed in On-line Table 2) of interest in the head and neck region.[10] In addition, we placed TLDs outside on the phantom orbits to estimate the dose on the eye lenses. Four TLDs were placed at each site to obtain the average, the SD, and the variation coefficient. For each technique (MSCT and FPA), 3 scans were obtained to provide a more reliable measure of radiation in the dosimeters, minimizing the changes related to the phantom positioning.

Estimation percentages of irradiated tissue were retrieved from the literature and used to calculate the equivalent dose (H_T) to a tissue or organ in μSv.[10,11] Effective dose (E), expressed in μSv, was calculated with the following equation: $E = \Sigma wT \times H_T$, where E is the product of the tissue-weighting factor (wT), which represents the relative contribution of that organ or tissue to the overall risk, and the H_T. The whole body was found by the summation of the weighted equivalent doses to all tissues or organs exposed. The International Commission on Radiologic Protection 103/2007 tissue-weighting factors were used to calculate E.[12]

RESULTS

Image Quality Assessment

All 29 MSCT and FPA scans were considered adequate by both readers. In particular, no FPA scan showed excessive head movement, necessitating the repetition of the examination. The MSCT and FPA groups did not differ in age (49.0 ± 6.9 versus 46.8 ± 12.5 years; $P = .466$), sex (female/male: 19:10 versus 18:11; $P = .785$), or side (right/left: 16:13 versus 15:14; $P = .792$). MSCT had higher signal (938.4 ± 21.0 versus 767.0 ± 86.8; $P < .001$), lower noise (61.5 ± 14.4 versus 236.2 ± 44.0; $P < .001$), and higher SNR (16.39 ± 3.8 versus 3.5 ± 1.1; $P < .001$) compared with FPA.

MSCT showed better image quality than FPA in assessing the tympanic membrane, bone marrow of the malleus and incus, tendon of tensor tympani, interscalar septum and modiolus of the cochlea (all statistics, $P < .05$; On-line Table 1 and On-line Fig 1). FPA showed better image quality than MSCT in assessing the anterior and posterior crura of the stapes (On-line Fig 2), footplate of the stapes (On-line Fig 2), incudostapedial joint (On-line Fig 3), and stapedius muscle and anterior ligament of the malleus (all statistics, $P < .05$; On-line Table 1). No significant difference in terms of image quality was found between MSCT and FPA in the assessment of the remaining anatomic structures (On-line Table 1). FPA had a significantly higher overall image quality (summed score) than MSCT ($P = .035$; On-line Table 1). Data on the observer sensitivity and interobserver agreement are summarized in On-line Table 3. The summed score of FPA correlated with the SNR ($R = 0.44$, $P = .02$), while no correlation was found between the summed scores of MSCT and SNR ($R = 0.21$, $P = .26$).

Table 1: Equivalent doses (H_T) for each organ of interest

Sites	FPA	MSCT
Bone marrow	2.4	3.24
Esophagus	0.15	0.37
Thyroid	1.48	3.74
Skin	0.33	2.09
Bone surface	6.05	6.89
Salivary glands	32.44	57.26
Brain	21.33	32.71
Lymphatic nodes	0.69	1.15
Muscle	0.69	1.15
Extrathoracic region	12.93	26.6
Oral mucosa	15.71	25.21
Pituitary	24.31	45.84
Eyes	5.09	51.15
Eye lens	1.77	45.9

Table 2: Tissue-weighting factors and effective doses of FPA and MSCT for each organ

Sites	Tissue-Weighting Factors (ICRP 103 Version)	FPA	MSCT
Bone marrow	0.12	0.29	0.39
Esophagus	0.04	0.01	0.01
Thyroid	0.04	0.06	0.15
Skin	0.01	0.00	0.02
Bone surface	0.01	0.06	0.07
Salivary glands	0.01	0.32	0.57
Brain	0.01	0.21	0.33
Lymphatic nodes			
Muscle	0.12	0.28	0.5
Extrathoracic region			
Oral mucosa	Mean dose on remainder organs[a]		
Effective dose (mSv)		1.23	2.04

Note:—ICRP indicates International Commission on Radiological Protection.
[a] Remainder organs are: adrenals, extrathoracic region, gall bladder, heart, kidneys, lymphatic nodes, muscle, oral mucosa, pancreas, prostate or uterus/cervix, small intestine, spleen, thymus. For remainder organs a tissue-weighting factor of 0.05 is assigned according to the IRCP 103 version. The effective dose for the extrathoracic region and the oral mucosa, respectively, corresponds to the mean dose on remainder organs.

Radiation Dose Assessment

Doses of the TLD sites are reported in On-line Table 2 and represented in On-line Fig 4; equivalent doses and effective doses for each organ are reported in Tables 1 and 2, respectively.

DISCUSSION

Image Quality Assessment

Our study demonstrates that FPA provides higher image quality in the cross-sectional imaging of the temporal bone compared with a 64-section MSCT scanner. To the best of our knowledge,

no previous studies have assessed the image quality of FPA in delineating normal temporal bone anatomy.

The image quality of FPCT prototypes or dedicated FPCT scanners has already been assessed in isolated temporal bone specimens, resulting in better image quality compared with MSCT.[1,3,13] However, these results are not clinically useful because FPCT prototypes are not available for clinical use in humans; the use of dedicated FPCT scanners in isolated temporal bone specimens does not represent the real clinical setting. Whole-head specimens absorb more low-energy photons, and radiation penetration is lower because the mass between the radiation source and the detector is greater.

A previous study showed that a dedicated FPCT scanner did not provide improvement in image quality in scanning whole-head temporal bone specimens compared with MSCT.[1] Our results are partially in agreement with these results. Although the overall image quality of FPA was better than MSCT, FPA improved the visualization of some structures (ie, stapes, stapedius muscle, anterior malleus ligament, chorda tympani), but it showed a limited value in the visualization of other structures (ie, modiolus, the interscalar septum of the cochlea, the tympanic membrane, bone marrow of the malleus and incus). Some technical aspects are pertinent to understanding these heterogeneous results.

The high isotropic spatial resolution of FPA ($0.14 \times 0.14 \times 0.14$ mm) provided more detailed cross-sectional images and allowed us to obtain multiplanar reformations with the same spatial resolution as in the original plane. In contrast, MSCT had a lower spatial resolution (0.64-mm thickness and 0.2×0.2 mm in-plane resolution), and the anisotropic voxel shape led to a loss of detail in the MPR images. The higher spatial resolution of FPA was particularly useful for the depiction of small bone structures such as the stapes and its components but was less useful for the visualization of larger bone structures, such as the malleus and incus, which were well-visualized by MSCT.

FPA had different technical disadvantages compared with MSCT, including a longer acquisition time, more susceptibility to artifacts, and lower contrast resolution and SNR. The longer acquisition time of FPA (25 versus 5.6 seconds) can render the scanning more susceptible to motion artifacts. Beam-hardening and scattering artifacts were evident in FPA, creating bright streaks in the image. Beam-hardening occurs in high-attenuation tissue, such as the temporal bone, where low-energy photons are more easily absorbed and high-energy photons pass through.[14] Thus, beam transmission does not follow the simple exponential decay seen with a monochromatic x-ray. FPA cannot use the same algorithms that MSCT adopts to correct for beam-hardening because they require that the complete object (ie, the temporal bone) fit into the FOV; FPA uses a small FOV (20×25 cm) and does not completely compute the temporal bone.[15]

Scattering artifacts are due to the deviation of some photons when they pass through the whole-head tissues. The diverted photons impact the wrong detector (ie, not the detector parallel to the x-ray source), and tissue density information is distorted.[1] In FPA, unlike MSCT, scatter intensities may severely impair image quality because the entire volume, as opposed to a few planes in MSCT, contributes to the scattered radiation.[4] Beam-hardening and scattering artifacts explain why FPA visualized small bone structures surrounded by soft-tissue (ie, the modiolus and interscalar septum of the cochlea) or small soft-tissue structures surrounded by bony structures (ie, bone marrow of the malleus and incus) less optimally than MSCT. In addition, scattering artifacts were responsible for the low contrast resolution of FPA, which did not attain improved depiction of small soft-tissue structures immersed in air space (ie, suspensory ligaments, tendons of the tensor tympani and tympanic membrane) compared with MSCT, as one could expect. The high susceptibility to artifacts explains the higher image noise and the lower signal and SNR measured in the FPA images. We demonstrated that when artifacts decreased and SNR increased, the overall image quality of FPA improved.

Considering our results, it is important to define when the use of FPA is preferable to MSCT for the cross-sectional imaging of the temporal bone. FPA is recommended only in patients with high compliance to avoid head motion artifacts due to the longer acquisition time. We always preferred FPA in the assessment of the middle and inner ear because it shows equal or better image quality than MSCT in depicting almost all bony structures of diagnostic interest. Although FPA could fail in the assessment of the modiolus and the interscalar septum because of motion, beam-hardening, and scattering artifacts, we also recommend FPA for the assessment of suspected cochlear malformations in pediatric patients. In fact, beam-hardening and scattering artifacts are usually less evident in pediatric patients due to their smaller head volume. In uncooperative pediatric patients, we perform FPA with the patient under sedation in the same session with the MR imaging study, if planned, to avoid 2 separate sedations. Otherwise MSCT with low-dose protocol is preferred. FPA is highly recommended in the assessment of cochlear implants and metallic prostheses after middle ear reconstructive surgery, as previously reported in the literature.[7-9] Regarding the cross-sectional imaging of the outer ear, we use FPA for the assessment of the bony external auditory canal, as in cases of suspected external auditory canal atresia or osteoma, which may be associated with middle ear malformations. In contrast, we do not use FPA for the assessment of pathologies that can involve the soft tissues of the periauricular region, such as malignant otitis externa because of the low contrast resolution of FPA.

Radiation Dose Assessment

According to our results, the lower radiation dose is the main advantage of FPA in the assessment of the temporal bone. Compared with MSCT, FPA showed a reduction of the effective dose of up to 40% (1.23 versus 2.04 mSv). We observed that the equivalent dose of FPA decreased approximately 76% for the lenses of the eye and 40% for the thyroid, which are the most radiosensitive tissues in the head and neck region.

To the best of our knowledge, no previous studies have compared radiation doses between FPCT or FPA and MSCT in the assessment of the temporal bone. In the literature, similar data were only reported for FPCT in the assessment of the maxillofacial region, reflecting the widespread use of FPCT in dental radiology.[10,16-19] In previous studies considering radiation exposure of FPCT and MSCT in the assessment of the temporal bone, the dose

was provided by the manufacturers[2] or recorded from the scanner console.[13]

The lower equivalent dose of FPA is due to 3 main reasons: The first is related to the scan parameters because the dose change is approximately proportional to the square of the tube voltage (kilovolt) and proportional to the current (milliampere).[20] Thus, the lower tube voltage of FPA determines a reduction of the dose though its current is higher. Second, FPA has a smaller FOV than MSCT, allowing a further reduction in exposure as well as scanning of the whole mastoid area together with the middle and inner ears, which may be essential for some diagnoses.[13] Third, the semicircular trajectory of our x-ray source, posterior to the head, explains the conspicuous reduction in radiation dose to the lenses of the eyes and the thyroid. Regions situated in the primary beam of the x-ray source receive a higher dose than regions far from the source.

Some limitations of our study must be acknowledged. We did not perform a within-subject analysis, with each patient undergoing both examinations, for ethical reasons; however, this limitation was overcome by enrolling a large number of subjects. We do not know whether our results will be completely reproducible with other angiography systems because of the different technology and reconstruction algorithms provided by various manufacturers. Our image quality assessment was focused on the delineation of the normal ear anatomy, so we do not know if the described improvements of FPA can improve the diagnosis of pathologic processes. Finally, we did not compare the FPA system and FPCT scanner, so we do not know if the latter remains the first choice for the temporal bone assessment.

CONCLUSIONS

FPA can be adopted for the cross-sectional imaging of the temporal bone, showing strengths and weaknesses compared with MSCT. FPA can fail in depicting structures, as discussed in this article, because of motion, beam-hardening, and scattering artifacts that impair the contrast resolution. However, due to its higher spatial resolution, FPA showed equal or higher image quality than MSCT in assessing bony structures of considerable diagnostic interest for radiologists. The lower radiation dose is an additional advantage of FPA, showing a reduction of the effective dose of up to 40% compared with MSCT.

REFERENCES

1. Fatterpekar GM, Doshi AH, Dugar M, et al. **Role of 3D CT in the evaluation of the temporal bone.** *Radiographics* 2006;26(suppl 1): S117–32 CrossRef Medline
2. Majdani O, Thews K, Bartling S, et al. **Temporal bone imaging: comparison of flat panel volume CT and multisection CT.** *AJNR Am J Neuroradiol* 2009;30:1419–24 CrossRef Medline
3. Gupta R, Bartling SH, Basu SK, et al. **Experimental flat-panel high-spatial-resolution volume CT of the temporal bone.** *AJNR Am J Neuroradiol* 2004;25:1417–24 Medline
4. Gupta R, Cheung AC, Bartling SH, et al. **Flat-panel volume CT: fundamental principles, technology, and applications.** *Radiographics* 2008;28:2009–22 CrossRef Medline
5. Dalchow CA, Weber Al, Yanagihara N, et al. **Digital volume tomography: radiologic examinations of the temporal bone.** *AJR Am J Roentgenol* 2006;186:416–23 CrossRef Medline
6. Dalchow CV, Weber AL, Bien S, et al. **Value of digital volume tomography in patients with conductive hearing loss.** *Eur Arch Otorhinolaryngol* 2006;263:93–99 CrossRef Medline
7. Pearl MS, Roy A, Limb CJ. **High-resolution secondary reconstructions with the use of flat panel CT in the clinical assessment of patients with cochlear implants.** *AJNR Am J Neuroradiol* 2014;35: 1202–08 CrossRef Medline
8. Zaoui K, Kromeier J, Neudert M, et al. **Flat panel CT following stapes prosthesis insertion: an experimental and clinical study.** *Eur Radiol* 2012;22:837–44 CrossRef Medline
9. Zaoui K, Kromeier J, Neudert M, et al. **Clinical investigation of flat panel CT following middle ear reconstruction: a study of 107 patients.** *Eur Radiol* 2014;24:587–94 CrossRef Medline
10. Ludlow JB, Ivanovic M. **Comparative dosimetry of dental CBCT devices and 64-slice CT for oral and maxillofacial radiology.** *Oral Surg Oral Med Oral Pathol Oral Radiol Endod* 2008;106:106–14 CrossRef Medline
11. Kim DS, Rashsuren O, Kim EK. **Conversion coefficients for the estimation of effective dose in cone-beam CT.** *Imaging Sci Dent* 2014; 44:21–29 CrossRef Medline
12. **The 2007 Recommendations of the International Commission on Radiological Protection: ICRP Publication 103.** *Ann ICRP* 2007;37: 1–332 CrossRef Medline
13. Peltonen LI, Aarnisalo AA, Kortesniemi MK, et al. **Limited cone-beam computed tomography imaging of the middle ear: a comparison with multislice helical computed tomography.** *Acta Radiol* 2007;48:207–12 CrossRef Medline
14. Brooks RA, Di Chiro G. **Beam hardening in x-ray reconstructive tomography.** *Phys Med Biol* 1976;21:390–98 CrossRef Medline
15. Schlicht FA, Kunze H. **Beam hardening correction for flat-panel computed tomography devices.** In: *Proceedings of the International Meeting on Fully-Dimensional Image Reconstruction in Radiology and Nuclear Medicine,* Newport, Rhode Island. June 1–4, 2015
16. Cohen M, Kemper J, Mobes O, et al. **Radiation dose in dental radiology.** *Eur Rad* 2002;12:634–37 CrossRef Medline
17. Li G. **Patient radiation dose and protection from cone-beam computed tomography.** *Imaging Sci Dent* 2013;43:63–69 CrossRef Medline
18. Loubele M, Bogaerts R, Van Dijck E, et al. **Comparison between effective radiation dose of CBCT and MSCT scanners for dentomaxillofacial applications.** *Eur J Radiol* 2009;71:461–68 CrossRef Medline
19. Veldhoen S, Schollchen M, Hanken H, et al. **Performance of cone-beam computed tomography and multidetector computed tomography in diagnostic imaging of the midface: a comparative study on phantom and cadaver scans.** *Eur Rad* 2017;27:790–800 CrossRef Medline
20. Kaira MK, Maher MM, Toth TL, et al. **Strategies for CT radiation dose optimization.** *Radiology* 2004;230:619–28 CrossRef Medline

Measurement for Detection of Incomplete Partition Type II Anomalies on MR Imaging

K.L. Reinshagen, H.D. Curtin, A.M. Quesnel, and A.F. Juliano

ABSTRACT

BACKGROUND AND PURPOSE: Incomplete partition type II of the cochlea, commonly coexisting with an enlarged vestibular aqueduct, can be a challenging diagnosis on MR imaging due to the presence of a dysplastic spiral lamina–basilar membrane neural complex, which can resemble the normal interscalar septum. The purpose of this study was to determine a reproducible, quantitative cochlear measurement to assess incomplete partition type II anomalies in patients with enlarged vestibular aqueducts using normal-hearing ears as a control population.

MATERIALS AND METHODS: Retrospective analysis of 27 patients with enlarged vestibular aqueducts (54 ears) and 28 patients (33 ears) with normal audiographic findings who underwent MR imaging was performed. Using reformatted images from a cisternographic 3D MR imaging produced in a plane parallel to the lateral semicircular canal, we measured the distance (distance X) between the osseous spiral lamina-basilar membrane complex of the upper basal turn and the first linear signal void anterior to the basilar membrane.

RESULTS: The means of distance X in patients with normal hearing and prospectively diagnosed incomplete partition type II were, respectively, 0.93 ± 0.075 mm (range, 0.8–1.1 mm) and 1.55 ± 0.25 mm (range, 1–2.1 mm; $P < .001$). Using 3 SDs above the mean of patients with normal hearing (1.2 mm) as a cutoff for normal, we diagnosed 21/27 patients as having abnormal cochleas; 4/21 were diagnosed retrospectively. This finding indicated that almost 20% of patients were underdiagnosed. Interobserver agreement with 1.2 mm as a cutoff between normal and abnormal produced a κ score of 0.715 (good).

CONCLUSIONS: Incomplete partition type II anomalies on MR imaging can be subtle. A reproducible distance X of ≥1.2 mm is considered abnormal and may help to prospectively diagnose incomplete partition type II anomalies.

ABBREVIATIONS: DRIVE = driven equilibrium; EVA = enlarged vestibular aqueduct; IP-II = incomplete partition type II

Incomplete partition type II (IP-II, scala communis) is one of many congenital malformations associated with sensorineural hearing loss. IP-II has been characterized as a cochlea with a normal proximal basilar turn and a deficient interscalar septum between the upper turns.[1,2] In combination with an enlarged vestibular aqueduct (EVA), this anomaly was first described by Carlo Mondini[3] and is frequently referred to as the "Mondini" deformity. Correlation among CT, MR imaging, and histopathology in this entity has indicated that a band of low signal on MR imaging extending from the lateral modiolus to the lateral wall of the cochlea (closest to the middle ear) near the upper middle turn corresponds to a band of tissue representing the dysplastic osseous spiral lamina–basilar membrane neural complex. This dysplastic structure contains neurosensory elements, including the dendritic processes of the spiral ganglion neurons and a dysplastic organ of Corti on top of the basilar membrane of the middle turn.[4] The dysplastic osseous spiral lamina–basilar membrane neural complex has an MR imaging appearance that can mimic that of the interscalar septum. Thus, the IP-II anomaly may be under-recognized on MR imaging.

The presence of an EVA can sometimes herald an underlying IP-II anomaly. Radiologically, IP-II is most often diagnosed in conjunction with EVA, possibly because of limitations in the radiologic diagnosis of IP-II based on current methods and because the EVA draws the radiologist's attention to a subtle cochlear anomaly. In a recent study using high-resolution CT and 1.5T MR imaging, 92% (54/59) of ears were found to have IP-II with an EVA and 8% (5/59) of ears had an isolated IP-II anomaly.[5] In contrast, on histologic examination of human temporal bone specimens, 91% (20/22) of ears with IP-II were found to have no associated EVA, suggesting that isolated IP-II cochlear anomalies may be radiologically underdiagnosed.[6]

Received January 31, 2017; accepted after revision June 1.

From the Departments of Radiology (K.L.R., H.D.C., A.F.J.) and Otolaryngology (A.M.Q.), Massachusetts Eye and Ear, Harvard Medical School, Boston, Massachusetts.

Please address correspondence to Katherine L. Reinshagen, MD, Department of Radiology, Massachusetts Eye and Ear, 243 Charles St, Boston, MA 02114; e-mail: katherine_reinshagen@meei.harvard.edu

http://dx.doi.org/10.3174/ajnr.A5335

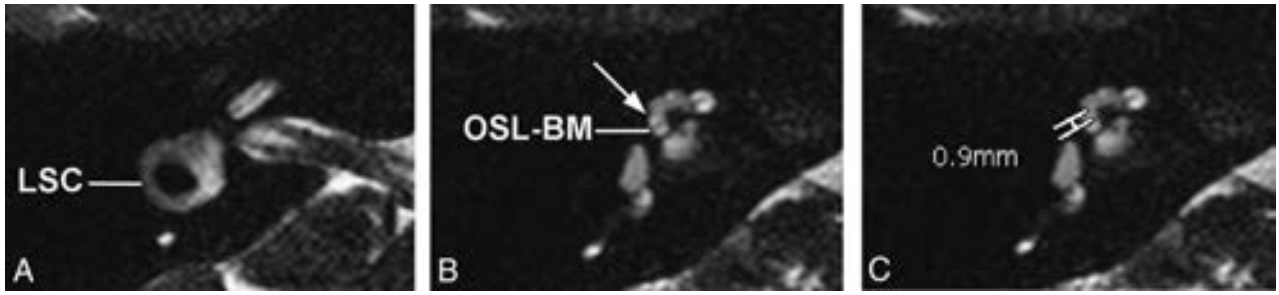

FIG 1. Axial 3D cisternographic (DRIVE) fast-recovery TSE MR imaging of the right temporal bone in a patient with normal hearing. *A*, Reformatted images parallel to the lateral semicircular canal (LSC) are created. Once created, the lateral semicircular canal is seen in its entirety on a single reformatted image. *B*, The osseous spiral lamina–basilar membrane complex of the upper basal turn (OSL-BM) and the first T2-hypointense linear band (*arrow*), in this case representing the interscalar septum, are demonstrated. *C*, A caliper is then placed to measure the distance between the OSL-BM and the linear band (distance X).

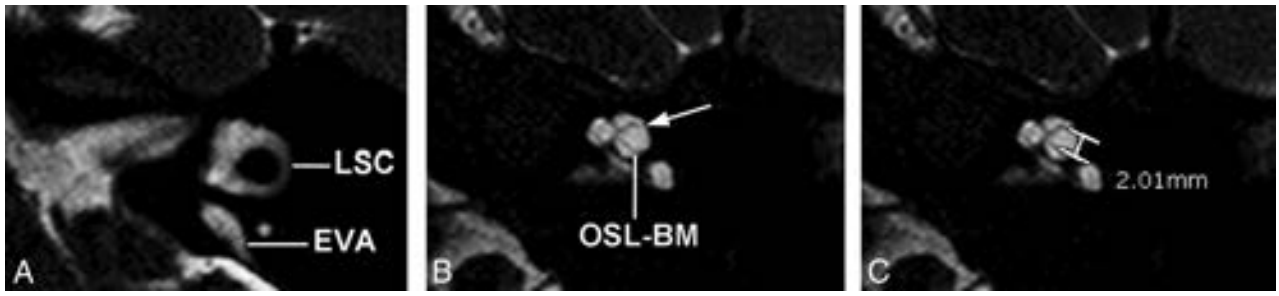

FIG 2. Axial 3D cisternographic (DRIVE) fast-recovery TSE MR image of the right temporal bone in a patient with a prospectively diagnosed IP-II anomaly. *A*, Reformatted images parallel to the lateral semicircular canal (LSC) are created. Once created, the lateral semicircular canal is seen in its entirety on a single reformatted image. Note the enlarged vestibular aqueduct. *B*, The osseous spiral lamina–basilar membrane complex of the upper basal turn (OSL-BM) and the first T2-hypointense linear band (*arrow*), in this case representing a band of dysplastic osseous spiral lamina–basilar membrane neural complex, are demonstrated. *C*, A caliper is then placed to measure the distance between the OSL-BM and the linear band (distance X).

Because the morphologic diagnosis of IP-II can be challenging on MR imaging, our study aimed to determine a quantitative, reproducible measurement technique on MR imaging that would aid in the diagnosis of IP-II. A secondary aim of the study was to determine the prevalence of prospectively underdiagnosed cases of IP-II in patients with enlarged vestibular aqueducts. We hypothesized that because of the partial absence of the interscalar septum in IP-II, the measured distance X would be larger in IP-II than in normal-hearing ears and, when used retrospectively, would help identify missed cases of IP-II.

MATERIALS AND METHODS

Following institutional review board approval, we conducted a retrospective analysis of high-resolution 1.5 and 3T MR imaging temporal bone studies performed between 2005 and 2015 at the Massachusetts Eye and Ear. Patients who underwent a high-resolution 3D heavily T2-weighted cisternographic sequence (axial T2 3D driven equilibrium [DRIVE], Philips Healthcare, Best, the Netherlands; axial CISS, Siemens, Erlangen, Germany) and had a radiologic diagnosis of an enlarged vestibular aqueduct were selected. A separate, consecutively chosen, control group with normal audiographic findings, discussed in the following paragraph, was included in the study. The imaging acquisition parameters for the 3T T2-DRIVE were set as follows: TR, 1700 ms; TE, 190 ms; NEX, 3; spacing, 0.5 mm; matrix, 412 × 337; scan time, 4 minutes 37 seconds. The imaging acquisition parameters for the CISS sequence were set as follows: TR, 12.25 ms; TE, 5.90 ms; NEX, 1; matrix, 230 × 1024. An 8-channel head coil was used. Patients younger than 5 years were sedated by the anesthesia team.

Twenty-seven patients with enlarged vestibular aqueducts who underwent MR imaging were found in the PACS. Twenty-six of the 27 patients underwent MR imaging for assessment of sensorineural hearing loss. One patient did not have a history of sensorineural hearing loss or an audiogram in the electronic medical record but, rather, was being imaged to assess a possible temporal bone lesion. Thirty-three ears in 28 additional consecutive patients referred by otologists and having undergone MR imaging for unilateral hearing loss, vertigo, or dizziness were used as a healthy control dataset. The asymptomatic, contralateral normal ear in these patients with unilateral hearing loss was used. The healthy control set of patients had audiograms that confirmed normal hearing in the ears used in the dataset.

Reformatted images of the cochlea were created with the MPR tool at the radiologist's viewer (SYNAPSE 3D; Fujifilm Medical Systems, Tokyo, Japan) in a plane parallel to the lateral semicircular canal, a reproducible landmark (Figs 1*A* and 2*A*). This plane is perpendicular to the distal limb of the first and second turns of the cochlea. Two observers (K.L.R. and A.F.J.) independently measured the perpendicular distance from the osseous spiral lamina–basilar membrane complex in the upper basal turn (closest to the middle ear) to the point at which the first linear signal void distal (anterior) to the osseous spiral lamina–basilar membrane complex contacts the lateral cochlear wall on magnified images.

For the purpose of this study, this is referred to as distance X. In healthy patients, the distal signal void is the interscalar septum; in patients with abnormal findings, it is presumed to be the dysplastic osseous spiral lamina–basilar membrane neural complex. Examples of these measurements are provided (Figs 1*B*, -*C*, and 2*B*, -*C*). When available, CT images in a reformatted plane parallel to the lateral semicircular canal were reviewed in the setting of discordant findings.

Statistical analysis was performed with GraphPad Prism software (GraphPad Software, San Diego, California). *P* values were calculated with an unpaired *t* test to compare the mean and SDs between patients with prospectively diagnosed cochlear anomalies and normal-hearing ears. The κ interobserver score was calculated on the basis of the observed agreements regarding whether a cochlea was abnormal or normal.

RESULTS

The 33 normal-hearing ears in 28 patients were studied (mean age, 16.7 years; range, 6 months to 32 years; Table). Patients with normal hearing had distance X measurements ranging from 0.8 to 1.1 mm and a mean distance X measurement of 0.93 ± 0.075 mm. With these patients as a normal reference, a cutoff of 1.2 mm was used to define the lower limit of abnormal because this was >3 SDs (greater than the 99.7th percentile) above the mean of healthy patients.

The 27 patients with enlarged vestibular aqueducts had a mean age of 24.9 years (range, 5 months to 65 years; Table). Prospectively, 17 of the 27 patients (63%) were diagnosed with EVA and IP-II anomalies. These patients were diagnosed prospectively on the basis of the classic imaging qualitative morphologic abnormalities seen in IP-II primarily on CT, but also applied to MR imaging, including the presence of a flattened interscalar ridge (anchor point) between the upper basal and upper middle turns and the cystlike undersegmented appearance of the cochlea.[1,6] The mean distance X measurement when there was a cochlear abnormality identified prospectively was 1.55 ± 0.25 mm (range, 1–2.1 mm). One patient who was thought to have a bilateral IP-II anomaly prospectively had a distance X measurement of <1.2 mm in 1 ear, which was included in this cohort. The mean distance X measurement among these patients with cochlear malformations was statistically different from that of patients with normal hearing, $P < .001$. Figure 3 demonstrates the mean distance X measurements, along with the range of values within 2 SDs above and below the mean, in patients with prospectively diagnosed IP-II anomalies and those with normal-hearing ears.

Ten of the 27 patients with enlarged vestibular aqueducts were not prospectively diagnosed with IP-II anomalies; however, 4 of these 10 had abnormal distance X measurements of ≥1.2 mm. Therefore, 4/21 (19%) patients found to have abnormal cochleas were identified retrospectively. Three of these 4 patients also underwent CT. In 1 patient, expected flattening of the interscalar ridge (anchor point) between the upper basal and upper middle turns was not seen; however, the modiolus of the abnormal cochlea appeared deficient. The other 2 patients had subtle findings of flattening of the interscalar ridge (anchor point), a deficient modiolus, and absence of the lateral interscalar septum. Figure 4*A* demonstrates the typical CT findings of IP-II from 1 of the 3 patients who subsequently underwent CT. The corresponding MR imaging demonstrates subtle morphologic features and has a widened distance X (Fig 4*B*).

Interobserver agreement to determine abnormal and normal cochleas based on the 1.2-mm cutoff was good with a calculated κ score of 0.715.

Patient demographics

	Normal-Hearing Ears	Patients with EVA
Total No. of patients	28 (33 ears studied)	27 (54 ears studied)
Mean patient age (yr)	16.7	24.9
SD of patient age (yr)	11.0	21.5
P value	.08	

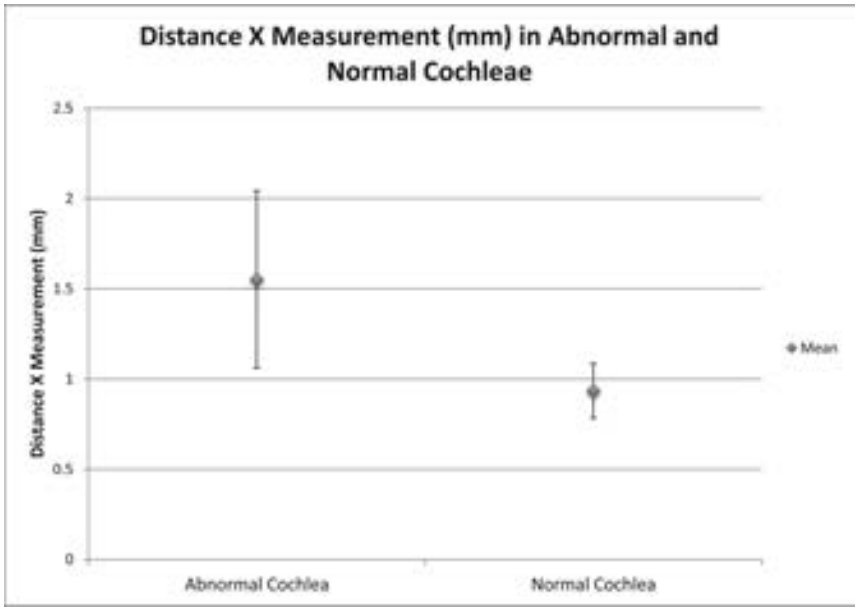

FIG 3. Graph demonstrating the mean distance X measurements ± 2 SDs in patients with prospectively diagnosed IP-II anomalies and individuals with normal hearing.

DISCUSSION

In patients with a congenital cause of sensorineural hearing loss, an IP-II anomaly of the cochlea is one of the most frequently detected imaging findings. Qualitative appearances of the cochlea on CT have been described in IP-II, including a consistent loss of the interscalar septum and flattening of the interscalar ridge (anchor point) between the upper basal and upper middle turns of the cochlea.[6] This flattened interscalar ridge may be less apparent on MR imaging because assessment of the bony contour is less optimal. Because more pediatric patients are now undergoing MR imaging for assessment of sensorineural hearing loss, scrutiny of the internal segmentation of the cochlea is important to avoid missing a diagnosis of IP-II.

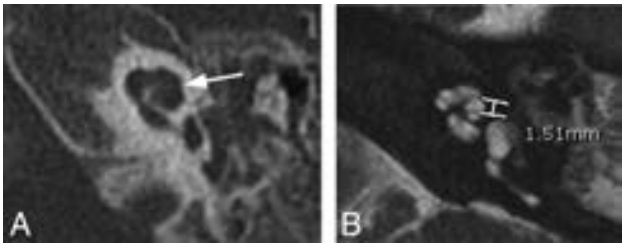

FIG 4. Axial CT and MR images of 1 of the 4 patients who was found, in retrospect, to have abnormal distance X measurements on MR imaging. *A*, On CT, the typical findings of IP-II including flattening of the interscalar ridge (anchor point) between the upper basal and upper middle turns (*arrow*) are demonstrated and confirm the presence of an IP-II anomaly. *B*, Corresponding MR image, on which distance X is found to be greater than 1.2 mm.

The heavily T2-weighted cisternographic sequence is routinely used in temporal bone imaging and can be performed across MR imaging vendor platforms at both 1.5- and 3T field strengths. On a heavily T2-weighted cisternographic sequence, the basilar membrane of the distal first turn of the cochlea is visible as a hypointense line extending from the modiolus to the lateral wall of the cochlea. Just distal (anterior) to this line, the interscalar septum is normally visible. In IP-II, this segment of the interscalar septum is absent. However, in IP-II, there is a thin T2-hypointense band extending from the lateral modiolus to the lateral wall of the cochlea in the same approximate location, having an appearance similar to that of a slightly malpositioned interscalar septum. On histology, this band corresponds to the dysplastic osseous spiral lamina–basilar membrane neural complex of the second turn and contains neurosensory elements, including a dysplastic organ of Corti on top of a dysplastic basilar membrane.[4] We hypothesized that a quantitative measurement between the basilar membrane of the upper basal turn of the cochlea and the first T2-hypointense band (distance X) on MR imaging would help differentiate a normal cochlea with an interscalar septum from the IP-II anomaly with the dysplastic osseous spiral lamina–basilar membrane neural complex.

To create a reproducible standardized measurement technique, we identified a plane parallel to the lateral semicircular canal and used axial reconstructions along this plane for measurements. This plane is perpendicular to the distal limb of the first and second turns of the cochlea and can be readily produced at the viewer side with integrated multiplanar reformat tools within most PACS. Distance X measurements in patients with normal hearing had a narrow range from 0.8 to 1.1 mm between the basilar membrane of the upper basal turn and the first low T2 signal band. In the healthy patient, this band represents the anterolateral interscalar septum. The mean distance X measurement was 0.94 ± 0.075 mm. Of note, none of the patients with normal hearing had a distance X measurement exceeding 1.1 mm. Despite the large range in patient age of the normal-hearing ears, the distance X measurement stayed within a relatively small size range, consistent with the development of the cochlea being complete in the embryologic stage.[7] Distance X measurements in individuals with normal hearing were statistically different from those in patients believed to have IP-II anomalies based on morphologic, qualitative assessment (mean, 1.55 ± 0.25 mm). Prospectively, 1 patient who was thought to have only an EVA on MR imaging and a suspected bilateral IP-II anomaly prospectively using CT morphology had a distance X measurement of <1.2 mm by both observers (1 and 1.1 mm) in 1 ear. This was considered to be a false-negative, suggesting that measurement criteria should be applied as an adjunct to morphologic criteria. We believe that this false-negative was due to motion degradation on the scan, affecting image quality.

We believed those patients with distance X measurements above 1.2 mm, 3 SDs above the mean, or a measurement greater than the 99.7th percentile to have abnormal cochleas. This method was shown to have good interobserver reliability. With a normal upper limit of 1.2 mm, 78% (21/27) of patients with enlarged vestibular aqueducts had a coexistent cochlear anomaly. This finding was similar to that in other reported studies that have shown EVAs in the presence of cochlear anomalies as high as 76%.[8] Our study confirms that the EVA has a high association with additional cochlear anomalies.

Retrospective analysis demonstrated that some patients with enlarged vestibular aqueducts might be underdiagnosed with regard to a coexistent cochlear anomaly. Almost one-fifth (4/21) of the patients with EVAs and abnormal cochleas by measurement were found retrospectively. We attribute the presence of a neural band in the lateral cochlea extending to the upper middle turn as a potential reason for the underdiagnosis because the dysplastic osseous spiral lamina–basilar membrane neural complex may be mistaken for a slightly malpositioned or even normally located interscalar septum, thus making this diagnosis more challenging.

Limitations

The major limitation of this study is that only patients with enlarged vestibular aqueducts were assessed. While EVA is commonly associated with cochleovestibular anomalies, cochleovestibular anomalies can also be isolated findings, and these were not assessed. Because a secondary aim of this study was to find underdiagnosed cochlear anomalies, searching our data base for cochlear anomalies alone would be insufficient. Because coexistent cochlear anomalies have been reported in as many as 76% of EVA anomalies,[8] we decided to focus our attention on this subgroup of patients with hearing loss.

Another limitation of this study is the relatively small sample size. The number of patients with enlarged vestibular aqueducts on MR imaging was relatively rare in our study population. Most of our cases of EVA had been discovered on CT with no further MR imaging performed. Further studies with larger sample sizes may be helpful to confirm our findings.

Theoretically, severe endolymphatic hydrops can displace the osseous spiral lamina–basilar membrane complex toward the scala tympani. However, this phenomenon has only been recognized in the apical turn in severe cases of endolymphatic hydrops in human temporal bone specimens and has not been described in the basal turn.[9]

CONCLUSIONS

The IP-II anomaly is a subtle MR imaging finding. In IP-II, a band of tissue, which histologically represents a combination of dysplastic neural tissue, basilar membrane, and the osseous spiral

lamina, can have an appearance similar to that of an interscalar septum on heavily T2-weighted cisternographic sequences. With a standardized plane parallel to the lateral semicircular canal, a measurement from the basilar membrane of the upper basal turn of the cochlea (closest to the middle ear) to the first T2-hypointense band (distance X) of >1.2 mm should be considered abnormal. Knowledge of the presence of the dysplastic osseous spiral membrane–basilar membrane neural complex and use of a quantitative measurement may help to prospectively reduce missed cochlear anomalies, particularly with an enlarged vestibular aqueduct.

Disclosures: Hugh D. Curtin—*UNRELATED*: *Royalties*: Elsevier, *Comments*: royalties for textbook.

REFERENCES

1. Sennaroglu L, Saatci I. **A new classification for cochleovestibular malformations.** *Laryngoscope* 2002;112:2230–41 CrossRef Medline
2. Sennaroglu L, Saatci I. **Unpartitioned versus incompletely partitioned cochleae: radiologic differentiation.** *Otol Neurotol* 2004;25:520–29; discussion 529 Medline
3. Mondini C. **Minor works of Carlo Mondini: the anatomical section of a boy born deaf.** *Am J Otol* 1997;18:288–93 CrossRef Medline
4. Leung KJ, Quesnel AM, Juliano AF, et al. **Correlation of CT, MR, and histopathology in incomplete partition-II cochlear anomaly.** *Otol Neurotol* 2016;37:434–37 CrossRef Medline
5. Kontorinis G, Goetz F, Giourgas A, et al. **Radiological diagnosis of incomplete partition type I versus type II: significance for cochlear implantation.** *Eur Radiol* 2012;22:525–32 CrossRef Medline
6. Makary C, Shin J, Caruso P, et al. **A histological study of scala communis with radiological implications.** *Audiol Neurootol* 2010;15:383–93 CrossRef Medline
7. Bast T, Anson B. *The Temporal Bone and the Ear*. Springfield: Charles C Thomas; 1949
8. Davidson HC, Harnsberger HR, Lemmerling MM, et al. **MR evaluation of vestibulocochlear anomalies associated with large endolymphatic duct and sac.** *AJNR Am J Neuroradiol* 1999;20:1435–41 Medline
9. Nadol J. **Disorders of unknown or multiple causes.** In: Merchant S, Nadol J, Schuknecht; HF, eds. *Schuknecht's Pathology of the Ear.* 3rd ed. Shelton, Conneticut: People's Medical Publishing House; 2010:571–627

Localizing the L5 Vertebra Using Nerve Morphology on MRI: An Accurate and Reliable Technique

M.E. Peckham, T.A. Hutchins, S.E. Stilwill, M.K. Mills, B.J. Morrissey, E.A.R. Joiner, R.K. Sanders, G.J. Stoddard, and L.M. Shah

ABSTRACT

BACKGROUND AND PURPOSE: Multiple methods have been used to determine the lumbar vertebral level on MR imaging, particularly when full spine imaging is unavailable. Because postmortem studies show 95% accuracy of numbering the lumbar vertebral bodies by counting the lumbar nerve roots, attention to lumbar nerve morphology on axial MR imaging can provide numbering clues. We sought to determine whether the L5 vertebra could be accurately localized by using nerve morphology on MR imaging.

MATERIALS AND METHODS: One hundred eight cases with full spine MR imaging were numbered from the C2 vertebral body to the sacrum with note of thoracolumbar and lumbosacral transitional states. The origin level of the L5 nerve and iliolumbar ligament were documented in all cases. The reference standard of numbering by full spine imaging was compared with the nerve morphology numbering method. Five blinded raters evaluated all lumbar MRIs with nerve morphology technique twice. Prevalence and bias-adjusted κ were used to measure interrater and intrarater reliability.

RESULTS: The L5 nerve arose from the 24th presacral vertebra (L5) in 106/108 cases. The percentage of perfect agreement with the reference standard was 98.1% (95% CI, 93.5%–99.8%), which was preserved in transitional and numeric variation states. The iliolumbar ligament localization method showed 83.3% (95% CI, 74.9%–89.8%) perfect agreement with the reference standard. Inter- and intrarater reliability when using the nerve morphology method was strong.

CONCLUSIONS: The exiting L5 nerve can allow accurate localization of the corresponding vertebrae, which is essential for preprocedure planning in cases where full spine imaging is not available. This neuroanatomic method displays higher agreement with the reference standard compared with previously described methods, with strong inter- and intrarater reliability.

ABBREVIATIONS: LSTV = lumbosacral transitional vertebrae; PABAK = prevalence-adjusted bias-adjusted κ; PSV = presacral vertebrae; VNV = vertebral numeric variation

Accurate and reliable spine numbering is important for the diagnosis of pathology and preprocedure planning. This can be challenging in patients with vertebral numeric variation (VNV) or lumbosacral transitional vertebrae (LSTV), particularly when full spine imaging is unavailable. VNV refers to the variation of the total number of presacral vertebrae (PSV). Approximately 89% of the population have 24 PSV (5 lumbar-type vertebrae), 8% have 25 PSV (6 lumbar-type vertebrae), and 3% have 23 PSV (4 lumbar-type vertebrae).[1] LSTV are congenital spinal anomalies in which an elongated transverse process of the last lumbar vertebra fuses with the "first" sacral segment to varying degrees.[2] The morphologic variation of LSTV can range from partial/complete L5 sacralization to partial/complete S1 lumbarization.[3,4] The prevalence of LSTV in the population varies throughout the literature because of differences in definition and diagnostic modalities.[1,4-6] LSTV can also vary with sex, with lumbarization of S1 seen more commonly in women and sacralization found to be more common in men.[3] A person can have VNV without LSTV, or conversely, one can have LSTV without VNV.[1] Approximately 5% of subjects have been found to have both.[1]

Multiple anatomic landmarks have been used to determine the lumbar vertebral level in cases without full spine imaging. A leading method of localizing the iliolumbar ligament, most frequently arising from L5, has been found less accurate in the setting of

Received March 10, 2017; accepted after revision May 23.

From the Neuroradiology Division (M.E.P., T.A.H., G.J.S., L.M.S.) and Musculoskeletal Division (S.E.S., M.K.M., R.K.S.), Departments of Radiology and Imaging Sciences (B.J.M., E.A.R.J.), University of Utah Health Sciences Center, Salt Lake City, Utah.

Paper previously presented at the American Society of Spine Radiology Annual Symposium, February 23–26, 2017; San Diego, California. (Awarded 1st place in the Mentor Award category.)

Please address correspondence to Miriam E. Peckham, MD, Neuroradiology Division, Departments of Radiology and Imaging Sciences, University of Utah Health Sciences Center, 30 North, 1900 East, #1A071, Salt Lake City, UT 84132; e-mail: Miriam.Peckham@hsc.utah.edu; @Miriam_Peckham

http://dx.doi.org/10.3174/ajnr.A5311

LSTV and VNV.[7-11] Other landmarks, including the level of the conus, right renal artery, superior mesenteric artery, aortic bifurcation, and iliac crest height, are also less accurate.[9,12-14] Choosing the appropriate level for surgical or interventional procedures is essential and relies on accurately and reliably numbering the spine in patients with "normal" anatomy as well as those with variant or transitional anatomy.[4,15] This is especially important in patients with LSTV and/or VNV undergoing surgical planning, as up to 32% of neurosurgeons have reported an event of wrong-level spinal surgery occurring at least once in their careers.[16] LSTV can also create challenges for approach in interventional pain procedures and can increase the risk of iatrogenic vascular injury.[17]

Multiple imaging modalities have been used to evaluate LSTV and VNV, with MR imaging found to be most reliable.[18] Anteroposterior radiographs have demonstrated high intermodality agreement with MR imaging.[19] Studies show that one can accurately number the vertebrae by counting down from C2 to the sacrum on sagittal MR imaging by using a cross-referencing tool.[1,8,19,20] Although most counting methods have focused on the ossified structures, 1 postmortem study numbered the vertebrae by dorsal spinal nerve morphology and found up to 95% probability that the lower spinal nerves correspond to their respective spinal segment.[21] We hypothesized that nerve morphology on lumbar spine MR imaging would aid in L5 vertebra localization, particularly when full spine imaging was not available. We aimed 1) to determine whether MR imaging morphologic features of the lumbar nerves could be used to distinguish the lower lumbar levels and 2) to apply these characteristics in localizing the L5 vertebra.

MATERIALS AND METHODS

This retrospective study, performed over 7 months, was approved by the institutional review board and investigators were compliant with the Health Insurance Portability and Accountability Act.

Patients

We searched our picture archiving and communication system for patients aged 18 years and older who had MR imaging of the full spine and radiographic imaging (CT or radiographs) of the thoracolumbar and lumbosacral junctions within the last 4 years (2013–2016). Patients without these studies were excluded. Patients with congenital vertebral segmentation anomalies were also excluded because of the possibility of associated nerve anomalies. The indications for most of these studies were back pain and metastatic disease, and patients were included if the osseous structures and nerves could be delineated.

Vertebral Body Count

Two investigators, a neuroradiology faculty member (L.M.S.) with more than 10 years' experience in spine imaging and a neuroradiology fellow (M.E.P.), reviewed each case and documented the total number of presacral vertebrae by counting down from C2 to the sacrum on MR imaging. Radiographic images of the thoracic and lumbar spine were reviewed to document rib count as well as evaluate transitional anatomy at the thoracolumbar and lumbosacral junctions. O'Driscoll staging[22] and the Castellvi method[23] were used to classify the lumbosacral anatomy. The level of the iliolumbar ligament and L5 nerve were also documented in all cases.

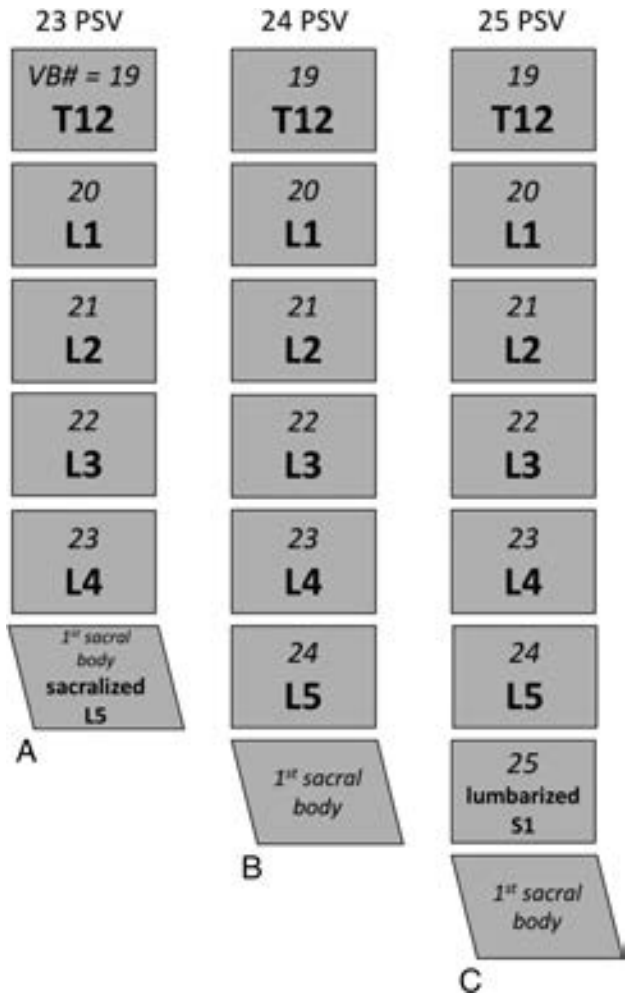

FIG 1. Graphic demonstrating our method for vertebral body numbering. When counting down from C2, patients with only 4 lumbar-type vertebral bodies (sacralized L5) have 23 PSV (*A*), patients with 5 lumbar-type vertebral bodies have 24 PSV (*B*), and patients with 6 lumbar-type vertebral bodies (lumbarized S1) have 25 PSV (*C*).

Vertebral numbering was performed as follows: the first 7 vertebrae were considered cervical, and the next 12 vertebrae were considered to be thoracic even in cases with an anomalous number of ribs.[1] In the cases with 13 rib-bearing vertebrae, we considered it "lumbar thoracization" with L1 having supranumery ribs. After T12, the vertebrae were counted as lumbar-type, extending to the level of the lumbosacral junction. Based on morphology and laterality per the Castellvi classification,[23] if the lower lumbar transverse processes had either unilateral or bilateral nonfused articulations with the sacrum (partial L5 sacralization), they were classified as either Castellvi 1 or 2. If the transverse processes were either unilaterally or bilaterally fused to the sacrum (complete L5 sacralization), the LSTV were classified as either Castellvi 3 or 4. The total number of PSV was the sum of cervical, thoracic, and lumbar segments. The 24th vertebra was considered L5 in all cases, even in those with VNV or LSTV (Fig 1). In LSTV cases, a patient with partial L5 sacralization (unilateral or bilateral assimilation joints without osseous fusion) was considered to have 24

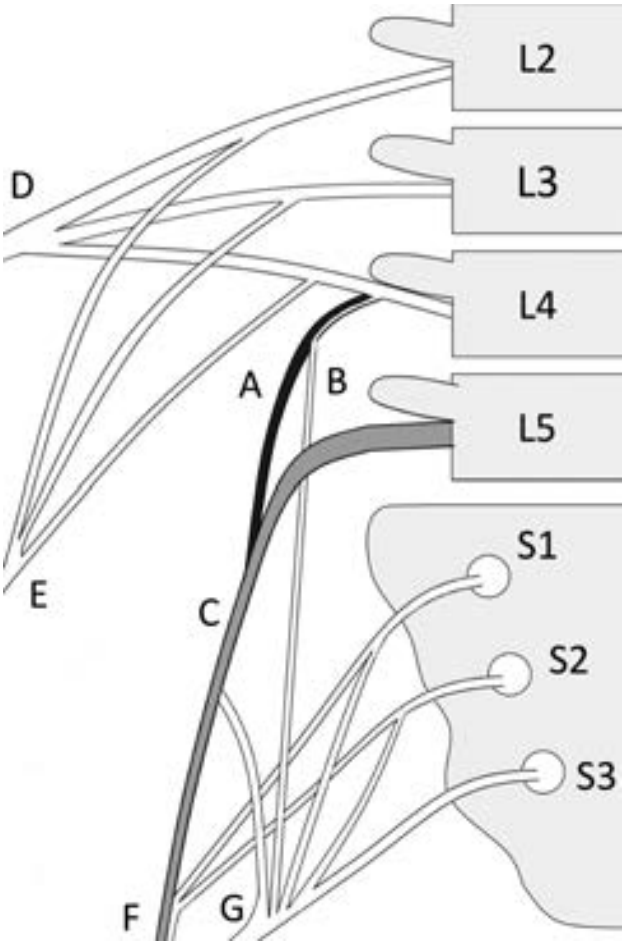

FIG 2. Schematic demonstrating the divisions of the lumbosacral plexus. The L4 nerve divides soon after exiting the neural foramen into peroneal (black) (A) and tibial (B) components, with the peroneal component joining the lateral fibers of L5 (gray) (C). The L4 nerve also contributes to both the femoral (D) and obturator (E) nerves. L5 is the only lumbar nerve that does not have a proximal division. Branches of L4–S2 make up the common peroneal nerve (F), and branches of L4–S3 make up the tibial nerve (G), which together comprise components of the sciatic nerve (not illustrated). The MRI morphology of the L4 peroneal component and L5 nerve are of special importance for localization; thus, they are shaded in this figure.

PSV, whereas a patient with complete L5 sacralization (unilateral or bilateral assimilation joints with osseous fusion) was considered to have 23 PSV. By the same Castellvi classification method, in those patients with lumbarization of S1, the patient was considered to have 24 PSV when S1 was partially lumbarized and 25 PSV if S1 was completely lumbarized.[1,23]

L5 Nerve Localization

The L5 nerve was identified by using 3 anatomic characteristics. First, L5 is typically the only lumbar nerve that does not split proximally and was identified on MR imaging by its nonsplitting course (Fig 2). Second, the insertion of the L4 peroneal branch along the lateral aspect of the L5 nerve, commonly seen at the level of the sacrum in patients with normal anatomy, was a helpful characteristic (Fig 3). Finally, the caliber of nerves along the sacrum aided in localization; specifically, the nonsplitting L5 nerve was approximately twice the caliber of the L4 peroneal branch at the level of the sacrum. This sign was particularly helpful in thinner patients, in whom the psoas muscle obscured the exiting L4 nerve (Fig 4).

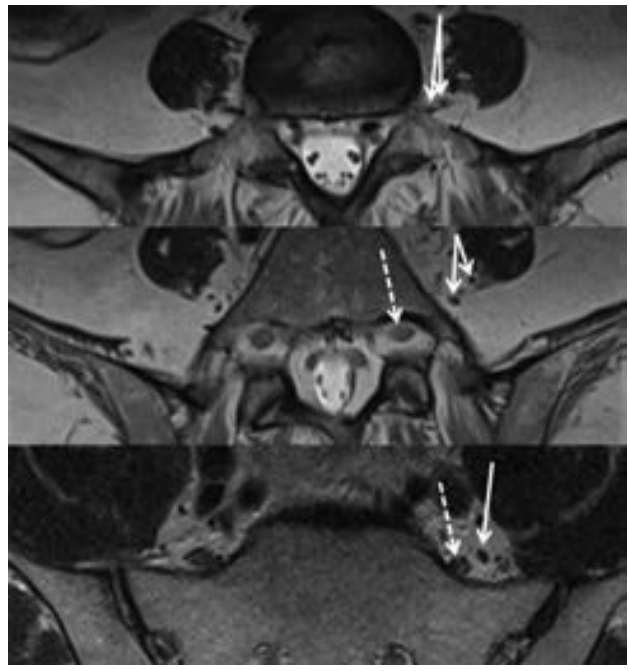

FIG 3. Consecutive cranial to caudal axial T2-weighted MR images demonstrate L4 and L5 nerve root anatomy. The L4 nerve root splits proximally into tibial and peroneal branches (*solid arrows*). The peroneal branch extends caudally and joins with the L5 nerve root (*dashed arrow*) along its anterolateral aspect at the level of the lateral sacrum.

Interrater and Intrarater Reliability

Five blinded raters of various stages of training, including 2 residents (2nd year and 4th year), 1 junior faculty member (1 year postfellowship), and 2 senior faculty members (5 and 7 years postfellowship) from both neuroradiology and musculoskeletal radiology subspecialties reviewed all 108 MR imaging lumbar spines in random order on 2 occasions, separated by 2 months. Before reviewing the cases, the raters were given a brief tutorial on lumbosacral plexus anatomy, MR imaging nerve appearance, and the method of nerve morphology numbering. Each rater was asked to localize the L5 nerve on lumbar spine MR imaging and determine normal (5 lumbar-type vertebral bodies) or LSTV anatomy (ie, lumbarized S1 or sacralized L5) by using the nerve morphology method and lumbosacral osseous anatomy. No other imaging was provided. Those results were compared with the reference standard as determined by full spine MR imaging.

Statistical Analyses

Patient sample size was determined by the rate of variant anatomy in the population with more than 100 patients chosen to achieve a 95% CI. Descriptive statistics were calculated for PSV. To verify the reliability of the nerve morphology method for denoting L5, we determined at which spinal level the L5 nerve exited and expressed this as a percentage agreement with the reference standard labeling. Although the κ coefficient is more widely familiar, it has an anomaly when data are clumped into 1 cell of the cross-tabulation table between raters. Therefore, the more relevant and ap-

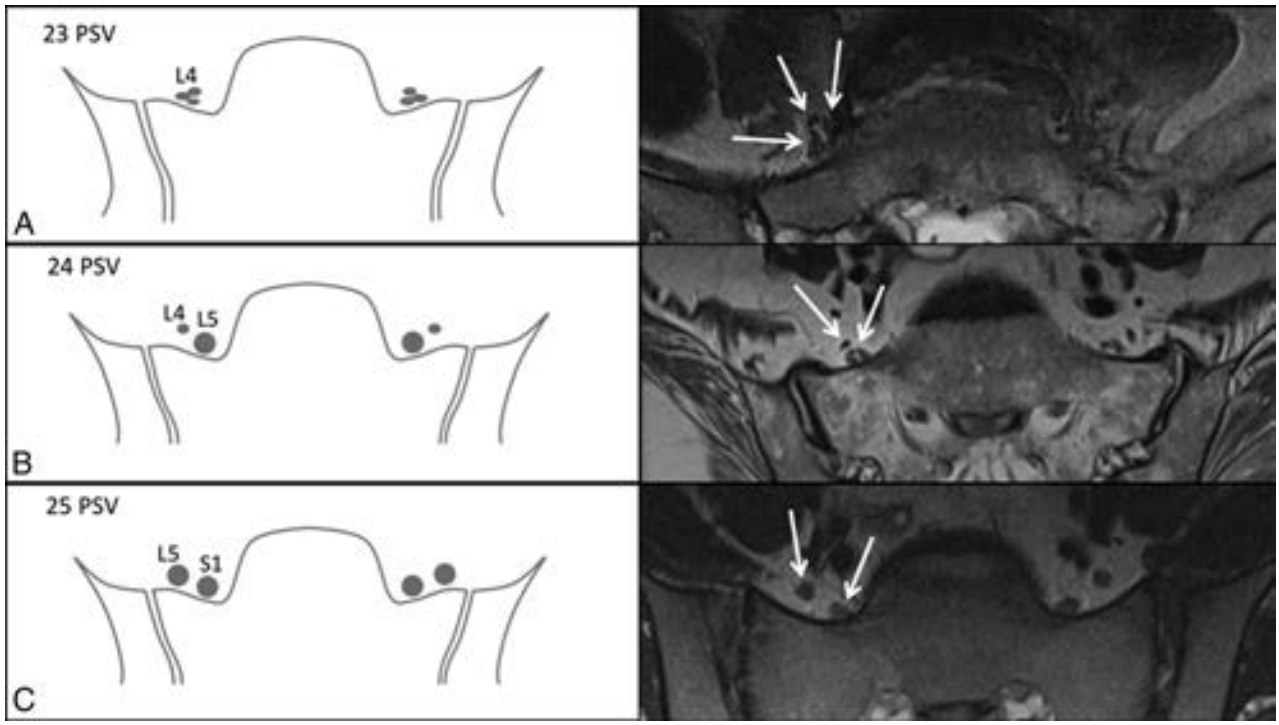

FIG 4. Axial T2-weighted MR images at the level of the sacrum with corresponding graphics demonstrating how the caliber of the nerve roots along the sacrum can be used to identify the number of lumbar vertebral segments. In patients with 4 lumbar segments, the L4 nerve root is seen splitting over the lateral sacrum (*A*, *arrows*). In patients with 5 lumbar segments, the peroneal branch of L4 joins the L5 nerve root, which is twice the caliber of L4 (*B*, *arrows*). In patients with more than 5 lumbar segments, 2 nerves of similar caliber will be seen along the lateral sacral wing, representing L5 laterally and S1 medially (*C*, *arrows*).

propriate prevalence-adjusted bias-adjusted κ, or PABAK, was used to measure interrater and intrarater reliability, which gives the true proportion of agreement beyond chance agreement regardless of unbalanced data patterns.[24] Although a formula for computing the PABAK interreliability for more than 2 raters simultaneously is not available, using the mean PABAK and range of confidence limits provides a reasonable approximation of the interrater reliability of the 5 raters simultaneously. Statistical analyses were performed by using commercial statistical analysis software (STATA Statistical Software: Release 14; StataCorp, College Station, Texas).

RESULTS

One hundred eight patients were randomly selected from this data base inquiry (60 females). The combined subject group ranged in age from 18–90 years (mean, 51.9 years ± 16.9). The female patients ranged in age from 18–90 (mean, 50.1 years), and the male patients ranged in age from 29–87 (mean, 54.1 years).

Vertebral Body Count

Sixteen of 108 patients had VNV (14.8%), 7 of whom had 23 PSV (6.5%) and 9 of whom had 25 PSV (8.3%). Ninety-two patients had 24 PSV (86%). Thirty of 108 patients had LSTV (29.7%) with 24 of these patients having Castellvi type 1 or 2 and 6 having Castellvi type 3a or 3b. None of the patients had Castellvi type 4. Nine of 16 patients with VNV also had LSTV.

Twelve patients had hypoplastic ribs at T12, 8 of whom also had LSTV. In addition, 6 patients had 13 rib-bearing vertebral bodies, and none of these patients had LSTV. One patient had only 11 rib-bearing thoracic vertebrae and 6 non–rib-bearing bodies (total of 24 PSV) with partial sacralization of L5. One patient had bilateral cervical ribs at C7.

L5 Nerve Localization

The L5 nerve was identified in all patients and arose from the 24th PSV (L5) in 106/108 cases. The percentage of perfect agreement with the reference standard was 98.1% (95% CI, 93.5%–99.8%). This agreement was preserved in cases with LSTV and VNV. In the 2 cases that were incongruous with the reference standard, the L5 nerve arose from a lumbarized S1 vertebra, and in both of these cases, there was variant thoracolumbar anatomy with supranumery ribs at L1. The percentage of perfect agreement with the reference standard when using the iliolumbar ligament localization method was 83.3% (95% CI, 74.9%–89.8%), accurately identifying the level L5 in 90/108 cases. In the cases of nonagreement, either the iliolumbar ligament did not arise from the 24th PSV, arose from 2 different levels, accessory ligaments were present, or the ligaments were difficult to identify.

Interrater and Intrarater Reliability

Computing PABAK for all possible pairs of comparisons of interrater reliability yielded a range of 0.83–0.96. The average PABAK was excellent at 0.89 (Table 1). The interrater reliability between each rater, and the reference standard are reported in Table 2. The intrarater reliability comparing a rater's scores on 2 separate occasions is reported in Table 3.

Table 1: PABAK interrater reliability coefficients between each pair of raters with 95% CI[a]

Rater	2	3	4	5
1	0.91 (0.83–0.99)	0.96 (0.91–1.0)	0.91 (0.83–0.99)	0.89 (0.80–0.98)
2		0.94 (0.88–1.0)	0.85 (0.75–0.95)	0.83 (0.73–0.94)
3			0.91 (0.83–0.99)	0.85 (0.75–0.95)
4				0.83 (0.73–0.94)

[a] Interrater reliabilities between each pair of raters ranged from 0.83–0.96. The average coefficient was 0.89. The smallest 95% CI lower limit was 0.73, and the largest upper limit was 1.0. Although a formula for computing the PABAK interreliability for more than 2 raters simultaneously is not available, using this mean and range of confidence limits provides a reasonable approximation of the interrater reliability of the 5 raters simultaneously (PABAK, 0.89; 95% CI, 0.73–1.0).

Table 2: Interrater reliability between each rater and the reference standard

Rater	PABAK Coefficient (95% CI)
1	0.91 (0.83–0.99)
2	0.81 (0.70–0.92)
3	0.87 (0.78–0.96)
4	0.85 (0.75–0.95)
5	0.94 (0.88–1.0)

Table 3: Intrarater reliability comparing each rater's scoring on 2 separate occasions

Rater	PABAK Coefficient (95% CI)
1	0.92 (0.85–0.99)
2	0.85 (0.75–0.95)
3	0.91 (0.83–0.99)
4	0.89 (0.80–0.98)
5	0.78 (0.65–0.89)

DISCUSSION

Developing an accurate and reliable method for numbering the lumbar vertebrae when complete spine imaging is not available has been difficult, especially in patients with LSTV and VNV. We found that the neuroanatomic MR imaging features of the exiting L5 nerve can allow accurate localization of the L5 vertebra.

Embryologically, the neural structures arise from the ectoderm, whereas the osseous scaffold arises from the mesoderm. The notochord is central to the development of the spine, acting as a frame for organization of the mesodermal cells from which eventually arises the vertebral column. Signal from the notochord and neural tube during the sixth week leads to chondrification and ultimately ossification.[25,26] The cervical spinal segments demonstrate morphologic stability with a fixed number of 7 vertebrae, whereas the thoracic and lumbar segments can vary.[27-29] An association of transitional thoracolumbar junction anatomy with concomitant LSTV has been noted.[7] Although the osseous structures show variation in up to 16% of the population, the neural structures have been shown to have less variability.[1,6,21,25,26]

The L5 nerve can be localized on MR imaging by using the morphologic features of the lumbosacral plexus. First, L5 is typically the only lumbar nerve without proximal branching. The L1–L4 nerves all split proximally just after exiting the neural foramen. The "normal" L4 nerve contributes to the femoral and obturator nerves. A posterior fascicle of L4 joins the lateral surface of L5 proximally, eventually making up the lateral/peroneal part of the sciatic nerve. This L4 contribution to the peroneal component of the sciatic nerve is small (Fig 2). Along with L4, the L5–S2 nerves contribute to the common peroneal and tibial components of the sciatic nerve. One can follow the first "nonsplitting" nerve to determine the level of the L5 vertebral body. For example, if the first nonsplitting nerve is tracked back to the first sacral body, it supports the patient only having 4 lumbar-type vertebrae with sacralization of L5 (23 PSV) (Fig 1*A*). If the first nonsplitting nerve is tracked back to a vertebral body 2 levels above the first sacral body, it supports the patient having more than 5 lumbar-type vertebrae (lumbarization of S1, 25 PSV) (Fig 1*C*). Second, the L4 peroneal branch inserts along the lateral aspect of the L5 nerve, commonly at the level of the sacrum in patients with nonvariant anatomy. Third, the caliber of nerves along the sacrum can aid with localization; that is, the nonsplitting L5 nerve is approximately twice the size of the L4 peroneal branch at the level of the sacrum. Differences in nerve caliber along the sacrum can be useful for localization in patients with a paucity of abdominal fat where the psoas muscle obscures L4 and when there are confounding adjacent small vascular structures. In patients with 23 PSV, the larger caliber L5 nerve arises from the first sacralized foramen, and the L4 nerve divides along the lateral sacrum (Fig 4*A*). In patients with 24 PSV, both the peroneal branch of L4 and the L5 nerve are present along the lateral sacrum, with L5 approximately twice the caliber of the L4 peroneal branch (Fig 4*B*). In patients with 25 PSV, the nerves coursing along the sacrum will be of similar caliber as they represent the L5 and S1 nerve roots (Fig 4*C*). Given that the nerves can vary in size such that L5 may not be equal in size to S1 in all cases but slightly smaller, caliber should not be used in isolation of the other morphologic characteristics.

Assessment of nerve morphology can be challenging in patients with severe neural foraminal narrowing and facet disease, which obscure evaluation of the proximal nerves, and when there is pathology deforming the nerve (eg, peripheral nerve sheath tumors or chronic inflammatory demyelinating polyneuropathy). Patients with congenital vertebral segmentation anomalies (eg, hemivertebrae) also present a numbering challenge because there may be concomitant variant lumbosacral plexus anatomy (ie, duplicated nerves). An additional potential pitfall includes when the patient's L4 peroneal branch is borderline in caliber, not distinctly <50% the size of L5 along the lateral sacrum. In these cases, one should follow the nerves proximally to determine whether 1 of the nerves divides; otherwise, additional studies (eg, CT chest and abdomen) may be helpful for vertebral body counting. This nerve morphology method works best with sequential axial images so that the nerves can be tracked to the exiting neural foramen. Different types of conjoined nerve roots may pose another numbering challenge, albeit less common.[30] As is advocated by most radiologists, the imaging report should state how the vertebral bodies were numbered and if there is transitional or variant anatomy to avoid confusion for the referring clinician.

The 2 cases where the nerve morphology method was discordant with the reference standard demonstrated nerves with L5 morphology arising from a lumbarized S1 in patients with 25 PSV. The L5 nerves split proximally, which made them more consistent with L4 morphology. In both cases, there was "lumbar thoracization" with 13 rib-bearing vertebrae without LSTV. Although the 4 other patients with 13 rib-bearing vertebrae followed the expected nerve morphology, we highlight the importance of being aware of altered lumbosacral nerve distribution in the set-

ting of transitional thoracolumbar anatomy. We posit that in patients with transitional thoracolumbar anatomy and 25 PSV, the L5 nerve assumes "the role of the L4 nerve," providing the peroneal component of the forming sciatic nerve trunk, whereas the sciatic nerve trunk is made up predominantly by the S1 nerve root.[31]

Alternatively, there may be "thoracic lumbarization" in which there are 11 rib-bearing vertebral bodies and 6 non–rib-bearing bodies. In this situation, the L4 nerve may contribute the peroneal component, and the L5 nerve may contribute the tibial component to the forming sciatic nerve at 1 spinal level higher than in normal anatomy. This may not be revealing in the nerve morphology, as in our 1 patient with 11 rib-bearing vertebrae and 6 non–rib-bearing vertebrae (total of 24 PSV). A low number of the population have thoracolumbar transitional anatomy, reflecting why this nerve morphology technique works the majority of the time (95% by postmortem studies). Although using nerve morphology is not a perfect technique, it does enable lumbar spine numbering to be rapidly deduced on MR imaging and quickly provides clues for when further evaluation with vertebral counting is warranted.

The nerve method is based on the morphologic characteristics of the exiting spinal nerves; however, some studies suggest that there are some variations in the "physiologic" nerve. Intraoperative electrophysiologic monitoring of evoked electromyography in patients with 24 PSV compared with 25 PSV showed that the "L6" nerve was equivalent to the S1 nerve root not only morphologically, but also physiologically as it innervated the biceps femoris.[32] Seyfert[33] used the cremasteric reflex in 50 male patients and correlated it to spine imaging. He found that the lumbosacral dermatome lies more ventrally in patients with a cranial displacement of the thoracolumbar or lumbosacral vertebral transition, which may reflect the variant plexus position. Kim et al[34] performed selective nerve root blocks by using electrical stimulation in patients having transitional vertebrae with lumbosacral radiculopathy. They found that the distribution of motor and sensory symptoms caused by the lumbarized S1 (L6) nerve root stimulation was similar to that of the S1 nerve root stimulation in the normal configuration, whereas the distribution of motor and sensory symptoms caused by the sacralized L4 nerve root stimulation was similar to that of L5 nerve root stimulation in the normal configuration.

The high interrater reliability and overall strong intrarater reliability of this method shows that it can be realistically implemented across subspecialties and is reproducible in the hands of users. Familiarity of the lumbosacral plexus anatomy is easily attained by the practicing radiologist and facilitates application of this neuroanatomic method of spine numbering. There is variability in how practitioners number the spine, without taking into account LSTV and VNV. We believe this nerve method will provide consistency in reporting between readers. Using nerve morphology can also aid in anatomic localization for symptoms that follow specific nerve distributions. This can be useful both in diagnostic studies and interventional spine procedures and is especially helpful in patients with variant anatomy. Localizing the L5 nerve is the key for preprocedural planning and typically only the osseous structures are used as preprocedural/procedural assessment modalities (eg, radiographs and fluoroscopy). Identifying the L5 nerve and determining the corresponding vertebral level will allow appropriate localization during procedures.

CONCLUSIONS

The level of the exiting L5 nerve can allow accurate localization of the corresponding vertebrae, particularly when full spine imaging is not available. This neuroanatomic method displays higher agreement with the reference standard compared with previously described methods. The strong inter- and intrarater reliability illustrates that this method can provide consistency in reporting between readers and is essential for accuracy in preprocedure planning.

REFERENCES

1. Paik NC, Lim CS, Jang HS. **Numeric and morphological verification of lumbosacral segments in 8280 consecutive patients.** *Spine* 2013; 38:E573–78 CrossRef Medline
2. Hughes RJ, Saifuddin A. **Imaging of lumbosacral transitional vertebrae.** *Clin Radiol* 2004;59:984–91 CrossRef Medline
3. Mahato NK. **Relationship of sacral articular surfaces and gender with occurrence of lumbosacral transitional vertebrae.** *Spine J* 2011; 11:961–65 CrossRef Medline
4. Konin GP, Walz DM. **Lumbosacral transitional vertebrae: classification, imaging findings, and clinical relevance.** *AJNR Am J Neuroradiol* 2010;31:1778–86 CrossRef Medline
5. Apazidis A, Ricart PA, Diefenbach CM, et al. **The prevalence of transitional vertebrae in the lumbar spine.** *Spine J* 2011;11:858–62 CrossRef Medline
6. Tang M, Yang XF, Yang SW, et al. **Lumbosacral transitional vertebra in a population-based study of 5860 individuals: prevalence and relationship to low back pain.** *Eur J Radiol* 2014;83:1679–82 CrossRef Medline
7. Carrino JA, Campbell PD Jr, Lin DC, et al. **Effect of spinal segment variants on numbering vertebral levels at lumbar MR imaging.** *Radiology* 2011;259:196–202 CrossRef Medline
8. Bressler EL. **Numbering of lumbosacral transitional vertebrae on MRI**. *AJR Am J Roentgenol* 2007;188:W210; author reply W211 CrossRef Medline
9. Tureli D, Ekinci G, Baltacioglu F. **Is any landmark reliable in vertebral enumeration? A study of 3.0-Tesla lumbar MRI comparing skeletal, neural, and vascular markers.** *Clin Imaging* 2014;38:792–96 CrossRef Medline
10. Farshad-Amacker NA, Lurie B, Herzog RJ, et al. **Is the iliolumbar ligament a reliable identifier of the L5 vertebra in lumbosacral transitional anomalies?** *Eur Radiol* 2014;24:2623–30 CrossRef Medline
11. Hughes RJ, Saifuddin A. **Numbering of lumbosacral transitional vertebrae on MRI: role of the iliolumbar ligaments.** *AJR Am J Roentgenol* 2006;187:W59–65 CrossRef Medline
12. Farshad-Amacker NA, Aichmair A, Herzog RJ, et al. **Merits of different anatomical landmarks for correct numbering of the lumbar vertebrae in lumbosacral transitional anomalies.** *Eur Spine J* 2015; 24:600–08 CrossRef Medline
13. Tokgoz N, Ucar M, Erdogan AB, et al. **Are spinal or paraspinal anatomic markers helpful for vertebral numbering and diagnosing lumbosacral transitional vertebrae?** *Korean J Radiol* 2014;15: 258–66 CrossRef Medline
14. Lee CH, Seo BK, Choi YC, et al. **Using MRI to evaluate anatomic significance of aortic bifurcation, right renal artery, and conus medullaris when locating lumbar vertebral segments.** *AJR Am J Roentgenol* 2004;182:1295–300 CrossRef Medline
15. Crawford CH 3rd, Glassman SD, Gum JL, et al. **Conflicting calculations of pelvic incidence and pelvic tilt secondary to transitional lumbosacral anatomy (lumbarization of S-1): case report.** *J Neurosurg Spine* 2017;26:45–49 CrossRef Medline

16. Jhawar BS, Mitsis D, Duggal N. **Wrong-sided and wrong-level neurosurgery: a national survey.** *J Neurosurg Spine* 2007;7:467–72 CrossRef Medline
17. Josiah DT, Boo S, Tarabishy A, et al. **Anatomical differences in patients with lumbosacral transitional vertebrae and implications for minimally invasive spine surgery.** *J Neurosurg Spine* 2017;26:137–43 CrossRef Medline
18. Farshad-Amacker NA, Lurie B, Herzog RJ, et al. **Interreader and intermodality reliability of standard anteroposterior radiograph and magnetic resonance imaging in detection and classification of lumbosacral transitional vertebra.** *Spine J* 2014;14:1470–75 CrossRef Medline
19. Paik NC, Lim CS, Jang HS. **Numbering of vertebrae on MRI using a PACS cross-referencing tool.** *Acta Radiol* 2012;53:785–89 CrossRef Medline
20. Shabshin N, Schweitzer ME, Carrino JA. **Anatomical landmarks and skin markers are not reliable for accurate labeling of thoracic vertebrae on MRI.** *Acta Radiol* 2010;51:1038–42 CrossRef Medline
21. Prat D, Gagnard G, Cousineau J. **Numbering of the dorsal spinal nerve roots in man from the 12th thoracic nerve to the coccygeal nerve** [Article in French]. *Bull Assoc Anat (Nancy)* 1983;67:331–36 Medline
22. O'Driscoll CM, Irwin A, Saifuddin A. **Variations in morphology of the lumbosacral junction on sagittal MRI: correlation with plain radiography.** *Skeletal Radiol* 1996;25:225–30 CrossRef Medline
23. Castellvi AE, Goldstein LA, Chan DP. **Lumbosacral transitional vertebrae and their relationship with lumbar extradural defects.** *Spine (Phila Pa 1976)* 1984;9:493–95 CrossRef
24. Byrt T, Bishop J, Carlin JB. **Bias, prevalence and kappa.** *J Clin Epidemiol* 1993;46:423–29 CrossRef Medline
25. Scaal M. **Early development of the vertebral column.** *Semin Cell Dev Biol* 2016;49:83–91 CrossRef Medline
26. Thawait GK, Chhabra A, Carrino JA. **Spine segmentation and enumeration and normal variants.** *Radiol Clin North Am* 2012;50:587–98 CrossRef Medline
27. Galis F. **Why do almost all mammals have seven cervical vertebrae? Developmental constraints, Hox genes, and cancer.** *J Exp Zool* 1999;285:19–26 CrossRef Medline
28. Narita Y, Kuratani S. **Evolution of the vertebral formulae in mammals: a perspective on developmental constraints.** *J Exp Zool B Mol Dev Evol* 2005;304:91–106 CrossRef Medline
29. Wigh RE. **Classification of the human vertebral column: phylogenetic departures and junctional anomalies.** *Med Radiogr Photogr* 1980;56:2–11 Medline
30. Postacchini F, Urso S, Ferro L. **Lumbosacral nerve-root anomalies.** *J Bone Joint Surg Am* 1982;64:721–29 CrossRef Medline
31. Chang HS, Nakagawa H. **Altered function of lumbar nerve roots in patients with transitional lumbosacral vertebrae.** *Spine (Phila Pa 1976)* 2004;29:1632–35; discussion 1635 CrossRef Medline
32. Hinterdorfer P, Parsaei B, Stieglbauer K, et al. **Segmental innervation in lumbosacral transitional vertebrae (LSTV): a comparative clinical and intraoperative EMG study.** *J Neurol Neurosurg Psychiatry* 2010;81:734–41 CrossRef Medline
33. Seyfert S. **Dermatome variations in patients with transitional vertebrae.** *J Neurol Neurosurg Psychiatry* 1997;63:801–03 CrossRef
34. Kim YH, Lee PB, Lee CJ, et al. **Dermatome variation of lumbosacral nerve roots in patients with transitional lumbosacral vertebrae**. *Anesth Analg* 2008;106:1279–83 CrossRef Medline

Test-Retest and Interreader Reproducibility of Semiautomated Atlas-Based Analysis of Diffusion Tensor Imaging Data in Acute Cervical Spine Trauma in Adult Patients

D.J. Peterson, A.M. Rutman, D.S. Hippe, J.G. Jarvik, F.H. Chokshi, M.R. Reyes, C.H. Bombardier, and M. Mossa-Basha

ABSTRACT

BACKGROUND AND PURPOSE: DTI is a tool for microstructural spinal cord injury evaluation. This study evaluated the reproducibility of a semiautomated segmentation algorithm of spinal cord DTI.

MATERIALS AND METHODS: Forty-two consecutive patients undergoing acute trauma cervical spine MR imaging underwent 2 axial DTI scans in addition to their clinical scan. The datasets were put through a semiautomated probabilistic segmentation algorithm that selected white matter, gray matter, and 24 individual white matter tracts. Regional and white matter tract volume, fractional anisotropy, and mean diffusivity values were calculated. Two readers performed the nonautomated steps to evaluate interreader reproducibility. The coefficient of variation and intraclass correlation coefficient were used to assess test-retest and interreader reproducibility.

RESULTS: Of 42 patients, 30 had useable data. Test-retest reproducibility of fractional anisotropy was high for white matter as a whole (coefficient of variation, 3.8%; intraclass correlation coefficient, 0.93). Test-retest coefficient-of-variation ranged from 8.0%–18.2% and intraclass correlation coefficients from 0.47–0.80 across individual white matter tracts. Mean diffusivity metrics also had high test-retest reproducibility (white matter: coefficient-of-variation, 5.6%; intraclass correlation coefficient, 0.86) with coefficients of variation from 11.6%–18.3% and intraclass correlation coefficients from 0.57–0.74 across individual tracts, with better agreement for larger tracts. The coefficients of variation of fractional anisotropy and mean diffusivity both had significant negative relationships with white matter volume (26%–27% decrease for each doubling of white matter volume, $P < .01$).

CONCLUSIONS: DTI spinal cord segmentation is reproducible in the setting of acute spine trauma, specifically for larger white matter tracts and total white or gray matter.

ABBREVIATIONS: CV = coefficient of variation; ICC = intraclass correlation coefficient; FA = fractional anisotropy; MD = mean diffusivity

DTI is a technique that provides microstructural evaluation not afforded by conventional MR imaging techniques.[1] In various disease states, DTI has been extensively investigated in brain applications and can detect abnormalities in otherwise normal-appearing brain regions[2,3] and is able to predict outcomes.[4] Early DTI use shows promise in detecting spinal cord abnormalities associated with spinal cord injury,[5,6] demyelinating diseases,[7] spondylotic myelopathy,[8] HIV myelopathy,[9] and various inflammatory and vascular myelopathies.[10] In acute spinal cord trauma, DTI has shown value in assessing microstructural injury, differentiating between hemorrhagic and nonhemorrhagic contusions, and strong correlation with clinical injury scores.[5]

Similar to brain DTI, tract-based white matter analysis of the spinal cord may offer additional insight into white matter characteristics in both healthy and diseased states.[11-13] Current methods of evaluating spine DTI data, however, are either purely qualitative assessments or labor-intensive hand-drawn ROIs that may be prone to reader-related variability/imprecision and poor reproducibility. In brain DTI, completely automated methods are available to reliably parcel the brain,[14] with application to clinical care.[15] Recently, a set of tools has been released as part of the

Received April 15, 2017; accepted after revision June 5.

From the Departments of Radiology (D.J.P., A.M.R., D.S.H., J.G.J., M.M.-B.) and Rehabilitation Medicine (M.R.R., C.H.B.), University of Washington, Seattle, Washington; and Department of Radiology (F.H.C.), Emory University, Atlanta, Georgia.

This work was supported by the Association of University Radiologists GE Radiology Research Academic Fellowship (AUR GERRAF) and the Administration for Community Living, National Institute on Disability Independent Living and Rehabilitation Research grant 90SI5006.

Paper previously presented at: American Society of Spine Radiology Annual Symposium, February 23–26, 2017; San Diego, California and the American Society of Neuroradiology Annual Meeting, April 22–27, 2017; Long Beach, California.

Please address correspondence to Mahmud Mossa-Basha, MD, Department of Radiology, University of Washington, 1959 NE Pacific St, Box 357115, Seattle, WA 98195; e-mail: mmossab@uw.edu; @mossabas

Indicates open access to non-subscribers at www.ajnr.org
Indicates article with supplemental on-line tables.
Indicates article with supplemental on-line photos.
http://dx.doi.org/10.3174/ajnr.A5334

"Spinal Cord Toolbox" that can allow for spinal cord registration, segmentation, and parcellation.[16] The Spinal Cord Toolbox (https://www.nitrc.org/projects/sct/) has been applied to flaccid myelitis on T2-weighted imaging,[17] functional imaging of the spine,[18] and T2*, DTI, and inhomogeneous magnetization transfer sequences in healthy patients at a range of ages.[19] To date, evaluation of the reproducibility of spinal cord segmentation and analysis algorithms such as the Spinal Cord Toolbox when using DTI sequences has been lacking. In addition, the reproducibility of DTI in the setting of acute spinal cord trauma has yet to be evaluated. Determination of these characteristics is particularly important in the setting of trauma evaluation, where the presence of factors such as pain or cognitive dysfunction from associated injuries, medication effect, susceptibility artifact from metallic fusion hardware, or the presence of external lines may impact image acquisition and interpretation.

In this study, we evaluated the test-retest reproducibility of a semiautomated atlas-based technique for extracting tract-specific and level-specific diffusion metrics in patients with acute cervical spine trauma. Furthermore, we also assessed the influence of reader-induced variability on the parcellation process.

MATERIALS AND METHODS

Subjects

After institutional review board approval (Harborview Medical Center), 42 consecutive patients presenting with acute cervical spinal trauma were prospectively recruited through an institutional review board–approved waiver of consent and scanned by using an imaging protocol that included 2 separate axial DTI acquisitions. Inclusion criteria were: 1) clinical concern for cervical spinal cord injury, 2) undergoing MR imaging of the cervical spine within 72 hours of initial injury, and 3) adult patient ≥18 years of age. The exclusion criteria were: 1) spine surgery or hardware for treatment of spinal injury within the scanning field, 2) pregnancy, and 3) known spinal cord disease or previous injury that would affect DTI metrics.

MR Imaging Acquisition

MR imaging scanning was performed on a 3T Trio scanner (Siemens, Erlangen, Germany). The scanning protocol included 2D sagittal T1 FLAIR, T2, STIR, axial T2, and 2-axial DTI acquisitions. For the current study, axial DTI and sagittal STIR sequences were used in processing and analysis, and thus, the parameters are listed. Axial DTI sequences are single-shot echo-planar acquisitions with reduced field of view in the anteroposterior dimension and 10 directions of diffusion, which were acquired during the same scan session with the following parameters: TR, 2600 ms; TE, 90 ms; 0.85 × 0.85 mm in-plane resolution; 200 mm × 100 mm field of view; section thickness, 5 mm; 0 intersection gap; 6 averages; bandwidth, 1766 Hz/pixel; and generalized autocalibrating partially parallel acquisition, 2. For each acquisition, images were acquired with spherically distributed b-vectors at a b-value of 750 seconds/mm^2, along with 6 interspersed minimally weighted B0 volumes. A total of 22–28 sections were acquired for the DTI scan with 11–14 cm of coverage in the foot-to-head direction depending on needed coverage, with a scan time of 3 minutes 30 seconds to 4 minutes 28 seconds. The advanced shim mode and dynamic field correction options were activated to reduce B0 and eddy current distortions, respectively. Axial DTI extended from the foramen magnum to the C7–T1 vertebral body level in the craniocaudal direction. The sagittal STIR sequence had the following parameters: TR, 3700 ms; TE, 47 ms; field of view, 220 × 220 mm; TI, 230 ms; section thickness, 3 mm; in-plane resolution, 1 × 0.7 mm; parallel imaging acceleration, 2; 2 averages; and bandwidth, 252 Hz/pixel. The axial DTI scans were performed at the beginning and end of the MR imaging scan. Before performance of the final DTI scan, the scanner table was removed from the MR imaging scanner, with removal of the detachable coils, and the patient was repositioned in craniocaudal and right-to-left directions. The coils were subsequently placed again and the table reintroduced into the scanner. Localizers were repeated and the DTI scan field of view was repositioned for the second scan. Patients were not removed from the scanner table or room because of concern for patient safety relating to injuries that would limit patient mobility and function and could potentially result in additional patient discomfort and/or injury. In this setting, we felt that patient repositioning and relocalization would be sufficient for reproducibility assessment.

Analysis Pipeline

An image analysis pipeline was constructed, which takes an axial DTI dataset and a sagittal STIR image as input and gives vertebral level-specific DTI metrics in total gray matter and white matter, regional white matter (dorsal, lateral, and ventral), and within 30 labeled white matter tracts (see On-line Tables 1–3 for individual white matter tracts analyzed). The core of the parcellation procedure is a coordinate transformation that maps the subject-space spinal image onto a labeled template. This transformation is the concatenation of a section-wise spine-straightening transformation, then an affine transformation, and then a final nonlinear warp. This warp is a symmetric normalization transformation[20] as implemented in Advanced Normalization Tools (http://stnava.github.io/ANTs/)[21] by using mutual information as the cost function. The template used is the MNI-poly-AMU template with labeled probabilistic ROIs. This template was created by labeling, co-registering and averaging high-quality T2 images from 16 healthy patients. A complete description of the template is available in Fonov et al[22] and in the Spinal Cord Toolbox on-line documentation (https://sourceforge.net/p/spinalcordtoolbox/wiki/MNI-Poly-AMU/).

The full parcellation pipeline includes the following steps (summarized in Fig 1), with command-line utilities in single quotes: 1) Diffusion datasets were corrected for motion and eddy current–induced distortions by using 'sct_dmri_moco'. 2) The tensor was calculated by using FSL's 'dtifit' (http://fsl.fmrib.ox.ac.uk/fsl/fsl-4.1.9/fdt/fdt_dtifit.html) by using weighted least squares fitting. 3) A spinal cord–stripping routine ('sct_propseg') was then run separately on both the STIR image and the mean DWI. This routine models the spinal cord surface as a tubular mesh, which is deformed until it matches the edges of the spinal cord. 4) At this point, manual intervention is required to identify the vertebral levels, which is done on the STIR image by placing single-point 3D ROIs, performed by a reader blinded to clinical information and other imaging findings. 5) After step 3 is finished, the vertebral levels are mapped onto the diffusion images by crossmodal registration of the STIR to the mean DWI by using

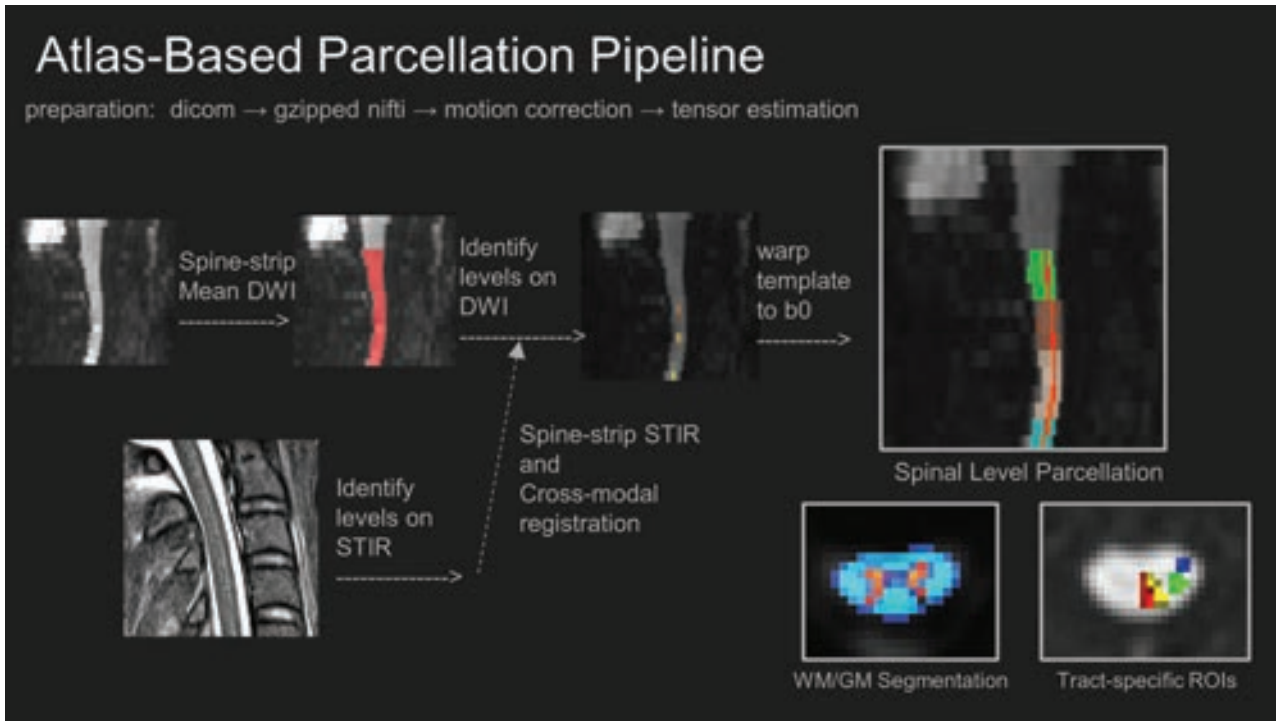

FIG 1. Atlas-based parcellation pipeline of DTI of the cervical spinal cord.

'sct_register_multimodal'. After determining the STIR-to-mean DWI transformation, the same transformation was applied to the 3 manually defined point ROIs, yielding mean DWI with labeled vertebral levels. 6) The MNI-poly-AMU spinal cord atlas[22] was then registered to the diffusion dataset with 'sct_warp_template'. This utility finds the subject-to-template composite transformation described above, then applies the reverse transformation to the template, thereby mapping the atlas ROIs into individual subject space. Registration and white matter–gray matter segmentation at the level of spinal cord injury is shown in On-line Fig 1. 7) Spine and tract-level fractional anisotropy (FA) and mean diffusivity (MD) values were obtained with 'sct_extract_metrics' by using the default maximum-likelihood method, which is a Bayesian parameter estimation method that has been shown to yield more accurate values than a simple weighted average.[23] Further documentation on these utilities and a description of their default parameters is available on the Spinal Cord Toolbox Web site (https://sourceforge.net/p/spinalcordtoolbox/wiki/tools/). The processing pipeline was coded by using makefiles and run through 'make,' following the approach described by Askren et al.[24] The pipeline was run on a Debian 7 workstation, with FSL version 2.0.9 (http://www.fmrib.ox.ac.uk/fsl), and Spinal Cord Toolbox version 2.2.

To evaluate the influence of manual intervention, a second reader, a neuroradiologist with 6 years' experience interpreting spine MR imaging, independently repeated step 4 (the only step requiring manual intervention) while also blinded to clinical information and other imaging findings.

In 8 cases, the fully automated spinal cord–stripping routine failed to produce a satisfactory mask because of poor initial estimates of the center of the spinal cord. In these cases, 3 single-point ROIs were placed within the spinal cord to seed the propagating segmentation.

Statistical Analysis

Pairs of measurements from each reader or each acquisition were compared to assess test-retest and interreader reproducibility of region volume, FA, and MD. Reproducibility was assessed visually by using Bland-Altman plots. Test-retest and interreader reproducibility were also summarized by using the within-paired standard deviation, the coefficient of variation (CV) (calculated as [100% × the within-paired standard deviation]/mean) and the intraclass correlation coefficient (ICC). Qualitative interpretation of ICC values are as follows: 0–.20 = poor; 0.21–0.40 = fair; 0.41–0.60 = moderate; 0.61–0.80 = good; and 0.81–1 = excellent.[8] For test-retest reproducibility, these metrics were calculated separately for each reader, and then the metrics from the readers were averaged. Similarly, for interreader reproducibility, these metrics were calculated separately for each acquisition, and then the metrics from the acquisitions were averaged. Standard errors of these metrics were calculated by using the nonparametric bootstrap, where patients were resampled to account for dependence between vertebral levels of the same patient.[25] These standard errors were multiplied by 2 to represent the approximate 95% CI and presented as metric (2× standard error) to show the precision of the metric estimates. A generalized estimating equations log-linear model was used to estimate the linear trend between CV and white matter volume. All statistical calculations were conducted with the statistical computing language R (version 3.1.1; http://www.r-project.org/). Throughout, 2-sided t tests were used, with statistical significance defined as $P < .05$.

RESULTS

Patient Data

Of the 42 patients recruited, 12 had insufficient image quality because of motion ($n = 9$), susceptibility from metal artifact ($n = 2$),

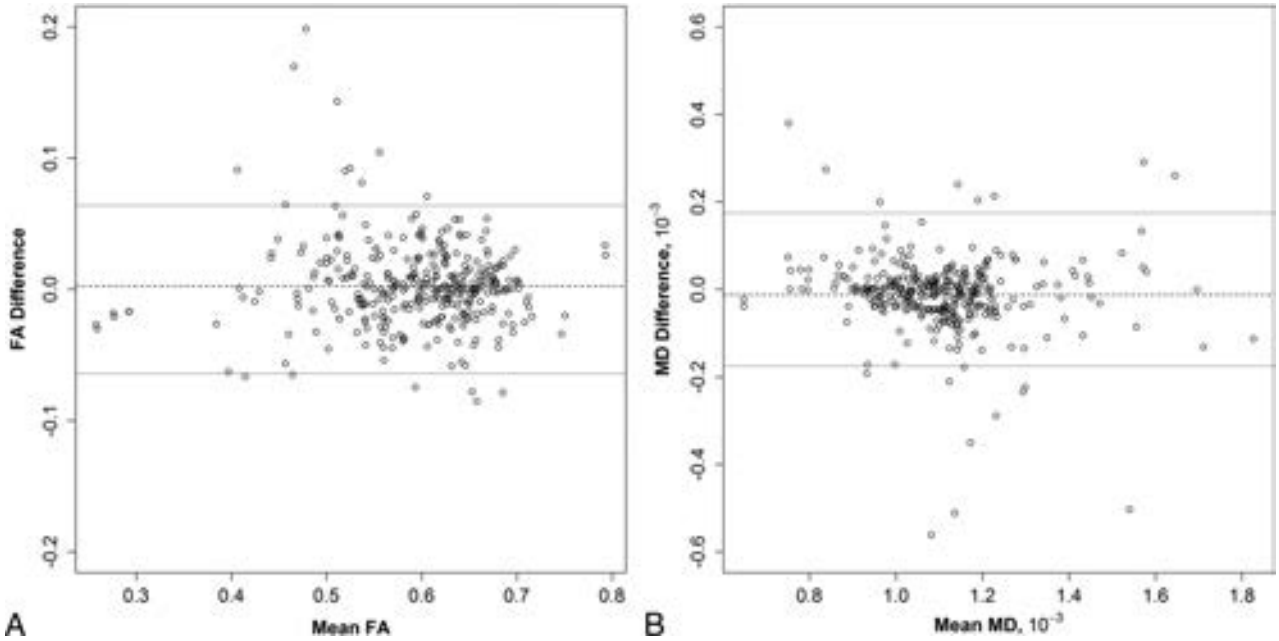

FIG 2. *A*, Bland-Altman plots of scan and re-test measurements of FA. The *dashed line* indicates the mean difference between measurements, and the *dotted lines* indicate the limits of agreement. Each reader's measurements are shown separately. *B*, Bland-Altman plots of scan and re-test measurements of MD. The *dashed line* indicates the mean difference between measurements, and the *dotted lines* indicate the limits of agreement. Each reader's measurements are shown separately.

or coverage ($n = 1$) and were excluded. Among the 30 remaining patients, 9 (30%) were woman, with ages ranging from 18–91 years (median, 41 years). At the time of imaging, 6 patients had an acute spinal cord contusion, 1 had moderate degenerative stenosis, and the remaining patients had no evidence of spinal cord injury or appreciable abnormality on conventional MR imaging or diffusion trace maps. Both readers could extract DTI metrics from 174 cervical levels (mean, 5.8 ± 1.1 per subject) from both scans.

These 174 levels were segmented into up to 30 white matter tracts. However, the left and right lateral reticulospinal, medial reticulospinal, and medial longitudinal fasciculus tracts could not be segmented on >95% of levels because of small size relative to the imaging resolution and were excluded, leaving 24 of 30 tracts available for analysis (On-line Fig 2). Among the 24 remaining tracts, the following tracts could not be segmented on some levels (reported by number not segmentable on the left/right sides out of 174 total levels): fasciculus cuneatus (1/0), fasciculus gracilis (1/0), rubrospinal (3/1), spino-olivary (0/1), tectospinal (33/35), lateral vestibulospinal (64/69), ventrolateral reticulospinal (67/72), ventral corticospinal (74/73), and ventral reticulospinal (85/88) tracts. After excluding these tract levels, of the original 4176 potential tract segments (174 × 24), there were 3509 total white matter tract segments per level available for analysis.

Test-Retest Reproducibility

White matter volume and the volume of individual white matter tracts had test-retest CVs of 7.7% and 13.2%, respectively (On-line Table 1). The volume of the ventral reticulospinal tract had the highest CV of 36.9%, but this was also the smallest tract assessed (mean volume, 5 ± 3 mm^3).

The test-retest reproducibility of FA metrics was high for the white matter as a whole (CV, 3.8%; ICC, 0.93) and, to a lesser extent, among all individual white matter tracts as a group (CV, 10.8%; ICC, 0.81) (On-line Table 2, Fig 2*A*). Across the individual white matter tracts, the test-retest CV ranged from 8.0% (fasciculus cuneatus) to 18.2% (ventral reticulospinal tract), and the test-retest ICC ranged from 0.47 (ventral reticulospinal tract) to 0.80 (lateral corticospinal tract). As noted, the ventral reticulospinal tract was the smallest tract on average, and in general, reproducibility improved with increasing white matter volume of the analyzed tract (Fig 3). The test-retest CV of FA decreased by 26.6% (95% CI, 22.6%–30.3%; $P = .008$) for each doubling of white matter volume.

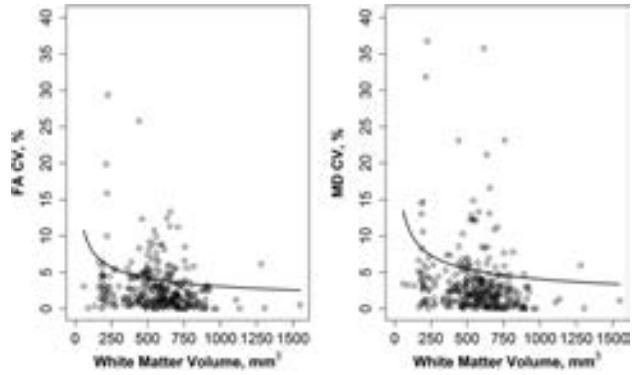

FIG 3. CV of FA (*left panel*) and MD (*right panel*), calculated per test-retest pair, versus the white matter volume. The generalized estimating equations–based estimate of mean CV is shown by the *bold curve*. CV increased with decreasing white matter tract volume for both FA ($P = .008$) and MD ($P < .001$).

Similarly, the test-retest reproducibility of MD metrics was high for the white matter as a whole (CV, 5.6%; ICC, 0.86) and for the individual white matter tracts (CV, 14.5%; ICC, 0.75) (On-line Table 3, Fig 2*B*), though the CV estimates ($P < .001$ and $P = .035$) and ICC estimates ($P < .001$ and $P < .001$) of MD over the

white matter and individual tracts were statistically significantly lower than those for FA. For each tract, the test-retest CV ranged from 11.6% (fasciculus cuneatus) to 18.3% (ventral reticulospinal tract), and the test-retest ICC ranged from 0.57 (ventral reticulospinal tract) to 0.74 (spino-olivary tract). As with FA, the MD of the ventral reticulospinal tract had the lowest reproducibility among the tracts assessed, likely because of its small size. Similar to FA, the test-retest CV of MD decreased by 25.5% (95% CI, 23.9%–27.1%; $P < .001$) for each doubling of white matter volume (Fig 3).

Interreader Reproducibility

Interreader reproducibility of FA metrics was generally numerically higher than the corresponding test-retest reproducibility estimates (On-line Table 2), with the interreader CV <10% and ICC >0.80 for all individual tracts except the ventral reticulospinal tract (CV, 13.0%; ICC, 0.73) and ventral corticospinal tract (CV, 11.2%; ICC, 0.76). Interreader reproducibility of MD metrics was also numerically higher than the corresponding test-retest reproducibility estimates (On-line Table 3), though the interreader reproducibility of MD of the whole white matter and individual tracts as a group were statistically significantly lower than those for FA ($P < .01$ for all comparisons). The interreader CV and ICC of MD were <15% and >0.70, respectively, for all individual white matter tracts except for the rubrospinal tract (CV, 16.9%; ICC, 0.65).

DISCUSSION

We report the first study to evaluate the test-retest and interreader reproducibility of semiautomated atlas-based segmentation of DTI of the cervical spinal cord in patients with acute trauma. Atlas-based parcellation of spinal cord DTI data shows good to excellent test-retest reproducibility for volume of gray matter, white matter (total), and individual tracts. Test-retest reproducibility for FA and MD for individual white matter tracts ranged from moderate to good, whereas the test-retest reproducibility was good to excellent for total white matter, gray matter, and white matter regions (ventral, lateral, and dorsal white matter stations). Cervical spinal cord tract-specific diffusion metrics are especially reproducible within the larger, major white matter tracts, with a lower degree of reproducibility in smaller white matter tracts. This is likely a product of in-plane image resolution, and with higher resolution acquisitions, DTI metrics of smaller white matter tracts of interest would likely be more reproducible and analyzable. Estimates of test-retest variability can be used for sample size planning in future longitudinal studies that use spinal cord DTI to measure outcomes. The manual step of identifying the vertebral levels and repeated cord segmentation introduces only limited variability in the extracted metrics of moderately sized and larger parcels, as shown by overall good to excellent interreader agreement.

A few prior studies have investigated the reproducibility of DTI of the spinal cord mainly by using manual ROI evaluation. In an analysis of 40 healthy control patients, Brander et al[26] used whole cord and right, left, and posterior manual ROIs as well as tractography-based analysis for quantitative DTI metric assessments. There was excellent and good intrareader and good interreader agreement for whole cord FA and ADC values, respectively, when using ICC. There was excellent intrareader agreement for tractography-based analysis for all metrics. In 10 pediatric patients with chronic spinal cord injury, Mulcahey et al[6] assessed the scan-rescan reproducibility of DTI metrics in pediatric patients with chronic spinal cord injury by using whole cord manual ROIs drawn at each level of the cervical spinal cord. The ICC ranged from 0.50–0.89 for FA depending on the cervical spinal cord level, MD ranged from 0.80–0.95, axial diffusivity ranged from 0.82–0.94, and radial diffusivity ranged from 0.82–0.94. Smith et al[27] evaluated the scan-rescan and interreader reproducibility of DTI in 9 health volunteers, with manual ROIs placed over the right and left side of the spinal cord and over the dorsal columns. There was no significant difference between readers or between scans for each ROI placement. The normalized Bland-Altman difference for interreader assessment was 1.89%–2.06% and for test-retest evaluation was 2.38–4.54%. These studies showed interreader, intrareader, and scan-rescan reproducibility of spinal cord DTI by using manual ROI assessment in healthy volunteers and patients with chronic spinal cord injury, similar to our results that show reproducibility of DTI metrics by using semiautomated segmentation in the setting of acute trauma.

Our study is the first to evaluate spine DTI reproducibility in patients with acute cervical spine trauma in a clinical setting. This study indicates that the use of spine DTI in clinical patients with acute cervical spine trauma is feasible and reproducible. Although only 30 of 42 DTI cases had 2 sets of useable DTI data, 4 of the 9 cases discarded because of motion artifact degrading 1 of the DTI acquisitions had a useable first DTI scan. Thus, in clinical use for spinal cord assessment, 34 of 42 cases (80%) would have been adequate. The spine DTI reproducibility studies cited above relied on manual ROIs that are more labor intensive and cumbersome and do not provide tract-specific information compared with atlas-based segmentation evaluation algorithms. Frequently, the ROIs used were whole cord, which provides limited data on disease impact on white matter specifically, especially considering the variations in DTI metrics between white and gray matter as well as the potential microstructural differences in disease influence between these tissues. Cheran et al[5] previously established the value of DTI of the spine in acute trauma by using whole cord ROIs (gray and white matter included), with correlation of DTI values to clinical scores. The current study uses a segmentation algorithm that provides tract-specific metrics that can confer increased specificity with respect to clinical injury scores compared with whole-cord ROIs.

Establishing the reproducibility of DTI of the spine in a clinical environment has the potential to further its use in disease states in which it has shown promise. DTI can detect spinal cord abnormalities in multiple sclerosis,[7] neuromyelitis optica,[10] HIV myelopathy,[9] and spondylotic myelopathy[8] when conventional MR imaging appears normal and could potentially better guide treatment. In addition, DTI provides quantitative microstructural data that may show improved association with clinical presentation compared with conventional imaging, and its inclusion may be able to better predict outcomes.[28]

This investigation has some limitations. First, 12 of 42 patients had to be excluded for unusable image sets. Imaging patients with acute spine trauma is challenging because motion artifact can be significant, and complete compliance cannot be guaranteed. Ex-

tended scan sessions can introduce significant discomfort, and repeating motion-corrupted scans was not feasible. Furthermore, having 1 corrupted run (out of 2) was enough to disqualify a patient from this analysis. A second limitation is that patients were not removed from the table or room between DTI scans. To attenuate this limitation, patients had the coils removed and were repositioned on the table and relocalized, with subsequent repositioning of the axial DTI field of view. Considering significant patient injuries and limited patient mobility and function, we felt this was an adequate step for reproducibility while keeping subject safety in mind. The DTI sequences were not cardiac-gated for control of spinal cord motion because of the time cost and lack of clinical feasibility in this population; cardiac gating could double scan time in some cases in a population that often requires immediate medical care and is motion-prone.

CONCLUSIONS

This work is an initial step toward using automated parcellation of spinal cord DTI in acute traumatic cervical spinal cord injury. The established test-retest and interreader reproducibility of these measures may inform the development of future studies focused on DTI as an imaging biomarker in diagnostic and therapeutic interventions in this patient population.

Disclosures: Daniel Hippe—*RELATED*: *Grant*: Association of University Radiologists and GE Healthcare, *Comments*: AUR GE Radiology Research Academic Fellowship (GERRAF) Award; *UNRELATED*: *Grants/Grants Pending*: GE Healthcare, Philips Healthcare, Toshiba America Medical Systems, *Comments*: statistical work on other projects. Jeffrey Jarvik—*UNRELATED*: *Consultancy*: HealthHelp, UpToDate, *Comments*: radiology benefits management company and on-line evidence-based publication; *OTHER RELATIONSHIPS*: AUR GERRAF Board of Review, Radiological Society of North America Clinical Trials Workshop Faculty. Falgun Chokshi—*RELATED*: *Grants/Grants Pending*: AUR GERRAF, *Comments*: career development grant cosponsored by the AUR and GE, Inc. All funds are paid to Emory School of Medicine. I do not get any direct funds from GE or AUR*. Maria Reyes—*UNRELATED*: *Grants/Grants Pending*: Craig H. Neilsen Foundation, *Comments*: grant to our department supporting academic time related to an educational program for spinal cord injury, unrelated to the manuscript topic*. Charles Bombardier—*RELATED*: *Grants/Grants Pending*: National Institute on Disability, Independent Living and Rehabilitation Research*. Mahmud Mossa-Basha—*RELATED*: *Grants/Grants Pending*: AUR GERRAF grant*. *Money paid to the institution.

REFERENCES

1. Basser PJ, Pierpaoli C. **Microstructural and physiological features of tissues elucidated by quantitative-diffusion-tensor MRI.** *J Magn Reson B* 1996;111:209–19 CrossRef Medline
2. Brandstack N, Kurki T, Tenovuo O. **Quantitative diffusion-tensor tractography of long association tracts in patients with traumatic brain injury without associated findings at routine MR imaging.** *Radiology* 2013;267:231–39 CrossRef Medline
3. Gratsias G, Kapsalaki E, Kogia S, et al. **A quantitative evaluation of damage in normal appearing white matter in patients with multiple sclerosis using diffusion tensor MR imaging at 3 T.** *Acta Neurol Belg* 2015;115:111–16 CrossRef Medline
4. Yuh EL, Cooper SR, Mukherjee P, et al. **Diffusion tensor imaging for outcome prediction in mild traumatic brain injury: a TRACK-TBI study.** *J Neurotrauma* 2014;31:1457–77 CrossRef Medline
5. Cheran S, Shanmuganathan K, Zhuo J, et al. **Correlation of MR diffusion tensor imaging parameters with ASIA motor scores in hemorrhagic and nonhemorrhagic acute spinal cord injury.** *J Neurotrauma* 2011;28:1881–92 CrossRef Medline
6. Mulcahey MJ, Samdani A, Gaughan J, et al. **Diffusion tensor imaging in pediatric spinal cord injury: preliminary examination of reliability and clinical correlation.** *Spine* 2012;37:E797–803 CrossRef Medline
7. Naismith RT, Xu J, Klawiter EC, et al. **Spinal cord tract diffusion tensor imaging reveals disability substrate in demyelinating disease.** *Neurology* 2013;80:2201–09 CrossRef Medline
8. Curvo-Semedo L, Lambregts DM, Maas M, et al. **Rectal cancer: assessment of complete response to preoperative combined radiation therapy with chemotherapy–conventional MR volumetry versus diffusion-weighted MR imaging.** *Radiology* 2011;260:734–43 CrossRef Medline
9. Mueller-Mang C, Law M, Mang T, et al. **Diffusion tensor MR imaging (DTI) metrics in the cervical spinal cord in asymptomatic HIV-positive patients.** *Neuroradiology* 2011;53:585–92 CrossRef Medline
10. Rivero RL, Oliveira EM, Bichuetti DB, et al. **Diffusion tensor imaging of the cervical spinal cord of patients with neuromyelitis optica.** *Magn Reson Imaging* 2014;32:457–63 CrossRef Medline
11. O'Donnell LJ, Westin CF, Golby AJ. **Tract-based morphometry for white matter group analysis.** *NeuroImage* 2009;45:832–44 CrossRef Medline
12. Reich DS, Smith SA, Jones CK, et al. **Quantitative characterization of the corticospinal tract at 3T.** *AJNR Am J Neuroradiol* 2006;27:2168–78 Medline
13. Yushkevich PA, Zhang H, Simon TJ, et al. **Structure-specific statistical mapping of white matter tracts.** *Neuroimage* 2008;41:448–61 CrossRef Medline
14. Fischl B. **FreeSurfer.** *Neuromage* 2012;62:774–81 CrossRef Medline
15. Brewer JB. **Fully-automated volumetric MRI with normative ranges: translation to clinical practice.** *Behav Neurol* 2009;21:21–28 CrossRef Medline
16. De Leener B, Lévy S, Dupont SM, et al. **SCT: Spinal Cord Toolbox, an open-source software for processing spinal cord MRI data.** *Neuroimage* 2017;145:24–43 CrossRef Medline
17. McCoy DB, Talbott JF, Wilson M, et al. **MRI atlas-based measurement of spinal cord injury predicts outcome in acute flaccid myelitis.** *AJNR Am J Neuroradiol* 2017;38:410–17 CrossRef Medline
18. Eippert F, Kong Y, Winkler AM, et al. **Investigating resting-state functional connectivity in the cervical spinal cord at 3T.** *Neuroimage* 2017;147:589–601 CrossRef Medline
19. Taso M, Girard OM, Duhamel G, et al. **Tract-specific and age-related variations of the spinal cord microstructure: a multi-parametric MRI study using diffusion tensor imaging (DTI) and inhomogeneous magnetization transfer (ihMT).** *NMR Biomed* 2016;29:817–32 CrossRef Medline
20. Tustison NJ, Avants BB. **Explicit B-spline regularization in diffeomorphic image registration.** *Front Neuroinform* 2013;7:39 CrossRef Medline
21. Avants BB, Tustison NJ, Stauffer M, et al. **The Insight ToolKit image registration framework.** *Front Neuroinform* 2014;8:44 CrossRef Medline
22. Fonov VS, Le Troter A, Taso M, et al. **Framework for integrated MRI average of the spinal cord white and gray matter: the MNI-Poly-AMU template**. *Neuroimage* 2014;102 Pt 2:817–27 CrossRef Medline
23. Lévy S, Benhamou M, Naaman C, et al. **White matter atlas of the human spinal cord with estimation of partial volume effect.** *Neuroimage* 2015;119:262–71 CrossRef Medline
24. Askren MK, McAllister-Day TK, Koh N, et al. **Using make for reproducible and parallel neuroimaging workflow and quality-assurance.** *Front Neuroinform* 2016;10:2 CrossRef Medline
25. Davison AC, Hinkley DV. *Bootstrap Methods and Their Application.* Cambridge: Cambridge University Press; 1997
26. Brander A, Koskinen E, Luoto TM, et al. **Diffusion tensor imaging of the cervical spinal cord in healthy adult population: normative values and measurement reproducibility at 3T MRI.** *Acta Radiol* 2014;55:478–85 CrossRef Medline
27. Smith SA, Jones CK, Gifford A, et al. **Reproducibility of tract-specific magnetization transfer and diffusion tensor imaging in the cervical spinal cord at 3 Tesla.** *NMR Biomed* 2010;23:207–17 CrossRef Medline
28. Agosta F, Absinta M, Sormani MP, et al. **In vivo assessment of cervical cord damage in MS patients: a longitudinal diffusion tensor MRI study.** *Brain* 2007;130:2211–19 CrossRef Medline

Yield of Image-Guided Needle Biopsy for Infectious Discitis: A Systematic Review and Meta-Analysis

A.L. McNamara, E.C. Dickerson, D.M. Gomez-Hassan, S.K. Cinti, and A. Srinivasan

ABSTRACT

BACKGROUND: Image-guided biopsy is routinely conducted in patients with suspected discitis, though the sensitivity reported in the literature ranges widely.

PURPOSE: We applied a systematic review and meta-analysis to estimate the yield of image-guided biopsy for infectious discitis.

DATA SOURCES: We performed a literature search of 4 data bases: PubMed, Cochrane CENTRAL Register of Controlled Trials, Embase.com, and Scopus from data base inception to March 2016.

STUDY SELECTION: A screen of 1814 articles identified 88 potentially relevant articles. Data were extracted for 33 articles, which were eligible if they were peer-reviewed publications of patients with clinical suspicion of discitis who underwent image-guided biopsy.

DATA ANALYSIS: Patients with positive cultures out of total image-guided biopsy procedures were pooled to estimate yield with 95% confidence intervals. Hypothesis testing was performed with an inverse variance method after logit transformation.

DATA SYNTHESIS: Image-guided biopsy has a yield of approximately 48% (793/1763), which is significantly lower than the open surgical biopsy yield of 76% (152/201; $P < .01$). Biopsy in patients with prior antibiotic exposure had a yield of 32% (106/346), which was not significantly different from the yield of 43% (336/813; $P = .08$) in patients without prior antibiotic exposure.

LIMITATIONS: The conclusions of this meta-analysis are primarily limited by the heterogeneity of the included studies.

CONCLUSIONS: Image-guided biopsy has a moderate yield for the diagnosis of infectious discitis, which is significantly lower than the yield of open surgical biopsy. This yield is not significantly affected by prior antibiotic use.

Discitis (also referred to as vertebral osteomyelitis, spondylitis, or spondylodiscitis) is an infectious process of the disc space and/or associated vertebral body. The reported incidence ranges between 4–24 per million per year[1] and has been increasing over recent years because of intravenous drug use, immunocompromised hosts, and the increasing use of spinal instrumentation and surgery.[2] The infection can be classified as granulomatous (tuberculosis and other mycobacterial pathogens) or pyogenic[1]; the most common pyogenic infectious agent is *Staphylococcus aureus*.[3]

Clinical presentation of discitis involves the insidious onset of constant back pain with neurologic deficits in one-third of cases.[2] Diagnosis is often delayed because of the nonspecific symptoms and results in prolonged morbidity and poorer clinical outcomes including prolonged neurologic deficits.[2] Treatment generally consists of antibiotics for 6–8 weeks, with surgical debridement necessary in cases of compression of neurologic structures or failure of antibiotic therapy.[4]

The diagnosis of discitis can be made based on a combination of clinical signs, laboratory tests, and imaging. Clinical signs include elevated white blood cell count, persistent low back pain, and laboratory tests including elevated C-reactive protein and erythrocyte sedimentation rate as well as positive blood cultures.[1,2] The clinical standard imaging technique is contrast-enhanced MR imaging, particularly early in the disease process.[1,2,5] MR imaging has a high sensitivity (96%) and specificity (92%) for discitis.[6] Typical MR imaging findings include an increase in fluid

Received March 31, 2017; accepted after revision June 7.

From the University of Michigan Health System (A.L.M., D.M.G.-H., S.K.C., A.S.), Ann Arbor, Michigan; and University of California, San Francisco (E.C.D.), San Francisco, California.

Abstract previously presented at: Radiological Society of North America Scientific Assembly and Annual Meeting, November 27 to December 2, 2016; Chicago, Ilinois.

Please address correspondence to Alyssa McNamara, MD, 1500 E Medical Center Dr, Ann Arbor, MI 48109; e-mail: alyssamcn@gmail.com

Indicates article with supplemental on-line photos.

http://dx.doi.org/10.3174/ajnr.A5337

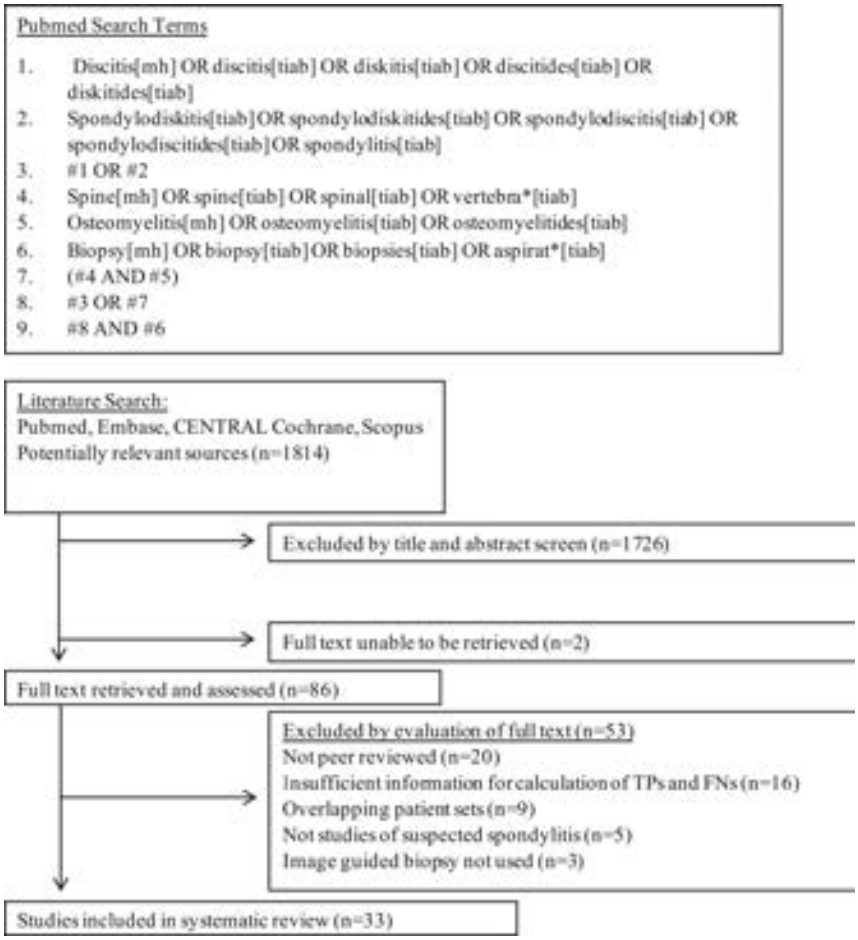

FIG 1. PubMed search structure and search flow diagram. Mh indicates Medical Subject Heading; tiab, Title and Abstract; TP, true-positive; FN, false-negative.

signal on T2-weighted sequences and postcontrast enhancement of the disc, vertebral bodies, or the surrounding soft tissues.[7]

When clinical findings are suggestive of discitis, but blood cultures are negative, microbiologic confirmation through direct biopsy is a frequently used subsequent diagnostic strategy.[3] Microbiologic diagnosis allows for confirmation of the diagnosis of infectious discitis as well as identification of the microorganism to tailor antibiotic therapy. The reported sensitivity of biopsy has ranged widely within the literature between 31% and 91%.[8-9] Lower sensitivity has been associated with antibiotic use and percutaneous rather than surgical biopsy.[10-14] Current Infectious Diseases Society of America guidelines recommend percutaneous biopsy in cases of suspected discitis without positive blood cultures and treating empirically in cases of positive blood cultures.[3] In cases of negative percutaneous biopsy, Infectious Diseases Society of America guidelines recommend repeating the image-guided biopsy or proceeding to surgical biopsy to improve sensitivity.[3]

Given the broad range of reported sensitivity in the literature, the current study aimed to evaluate the literature with regard to the yield of image-guided biopsy in suspected cases of discitis. We performed a systematic review of image-guided biopsy in suspected cases of discitis. We identified 1 other systematic review and meta-analysis on this topic, performed by Pupaibool et al,[15] which found the sensitivity of CT-guided biopsy to be 52.2%, though this meta-analysis did not consider cases of discitis with prior surgical intervention (a common and clinically important indication for image-guided biopsy), did not assess many subgroups, and evaluated only 358 abstracts as opposed to the 1814 abstracts we identified as potentially relevant. In our study, the studies were compared in a meta-analysis of sensitivity, as well as the following subgroup analyses: open surgical versus image-guided biopsy, prior antibiotic exposure, type of image guidance, biopsy technique, pathogen detected, and pathogen detection technique (polymerase chain reaction versus culture).

MATERIALS AND METHODS

Protocol and Registration

A review protocol was designed according to PRISMA guidelines and registered with the PROSPERO register (ID CRD42016039121).

Eligibility Criteria

Eligible studies were peer-reviewed journal articles containing empiric data on the yield of image-guided biopsy in discitis. The inclusion criteria were as follows: a) peer-reviewed journal publication on human patients; b) patients were clinically suspected of having infectious discitis before biopsy; c) biopsy samples were obtained via CT- or fluoroscopic-guided procedure; and d) reported data necessary to extract true-positive and false-negative biopsy culture results.

Search

An experienced reference librarian assisted with designing the search strategy. The search strategy was designed with synonyms identified through index searching with MeSH. The following electronic data bases were searched: PubMed, Cochrane CENTRAL Register of Controlled Trials, Embase.com, and Scopus. The search was open to articles from data base inception to March 3, 2016 and was not restricted to the English language. An example of the search structure used in PubMed is illustrated in Fig 1.

Study Selection

The title/abstract screening was completed independently by 2 reviewers with DistillerSR (Evidence Partners, Cambridge, United Kingdom). Disagreements were resolved by consensus discussion between the 2 reviewers. Non-English literature was translated with Google Translate (Google, Mountain View, California). The full-text articles of relevant references were acquired and independently reviewed for inclusion. Disagreements were resolved by consensus discussion by the 2 reviewers.

Study characteristics

Author	Year	Reference Standard[a]	Image Guidance	Biopsy Type	Pathogens	Prior Antibiotics	TP	FN	FP	TN	Total Patients
Spira et al[21]	2016	MRI	CT	Core	Mixed	NR	10	24			34
Agarwal et al[5]	2016	Mixed	Mixed	Core	Mixed	Mixed	30	94			124
Brinjikji et al[22]	2015	MRI	Mixed	NR	Mixed	Mixed	38	39			77
Kim et al[23]	2015	NR	NR	NR	Pyogenic	None	38	52			90
Chang et al[18]	2015	Histopathology	CT	Core	Mixed	Mixed	29	26	4	29	88
Garg et al[24]	2014	Mixed	CT	Core	Mixed	Mixed	16	68			84
Choi et al[19]	2014	MRI	Mixed	NR	Mixed	Mixed	12	32	1		45
Tachibana et al[25]	2014	NR	NR	NR	Pyogenic	NR	11	17			28
Gras et al[26]	2014	MRI	CT	NR	Pyogenic	None	7	6			13
Aagaard et al[27]	2013	Mixed	NR	NR	Pyogenic	NR	59	77			136
Kim et al[28]	2013	Mixed	Fluoroscopy	Core	Mixed	None	51	83			134
Gasbarrini et al[29]	2012	MRI	CT	Core	Mixed	None	12	14			26
Cebrián Parra et al[30]	2012	MRI	NR	NR	Mixed	NR	10	14			24
Heyer et al[31]	2012	Histopathology	CT	Core	Mixed	Mixed	10	20			30
Nam et al[32]	2011	Mixed	Mixed	NR	Mixed	Mixed	28	28			56
Marschall et al[13]	2011	MRI	Mixed	NR	Pyogenic	Mixed	40	87			127
Shibayama et al[33]	2010	NR	Fluoroscopy	FNA	Pyogenic	NR	32	28			60
de Lucas et al[34]	2009	Mixed	CT	FNA	Mixed	Mixed	11	1			12
Yang et al[12]	2008	Histopathology	CT	Core	Mixed	NR	20	26			46
Michel et al[35]	2006	MRI	CT	Core	Mixed	None	15	17			32
Colmenero et al[36]	2004	Mixed	Mixed	Core	Tuberculosis/mycobacterial	NR	11	7			18
Ben Taarit et al[37]	2002	Mixed	Mixed	NR	Pyogenic	NR	12	13			25
Nolla et al[17]	2002	Mixed	CT	NR	Pyogenic	Mixed	25	16			41
Pertuiset et al[39]	1999	Mixed	Fluoroscopy	NR	Tuberculosis/mycobacterial	NR	11	10			21
Jiménez-Mejías et al[11]	1999	Mixed	NR	NR	Pyogenic	NR	4	2			6
Vinicoff et al[40]	1998	NR	CT	Core	Pyogenic	NR	38	12			50
Fouquet et al[41]	1996	NR	NR	Core	Mixed	NR	4	2			6
Bateman et al[42]	1995	Mixed	NR	NR	NR	Mixed	12	6			18
Al Soub et al[43]	1994	Mixed	CT	NR	Mixed	NR	52	31			83
Cotty et al[44]	1988	NR	Fluoroscopy	Core	Mixed	Mixed	19	9			28
Ernst[45]	1984	NR	Fluoroscopy	NR	Pyogenic	NR	36	25			61
Seignon et al[46]	1980	NR	NR	FNA	Mixed	NR	16	4			20
Duquennoy et al[47]	1979	NR	NR	FNA	Mixed	NR	16	14			30

Note:—FN indicates false-negative; FNA, fine needle aspiration; FP, false-positive; NR, not recorded in original study; TN, true-negative; TP, true-positive.
[a] All studies used clinical characteristics in addition to the reference standards listed.

Data Collection Process

Data were collected from the full text of the eligible studies by 1 reviewer. Extracted data included the publication year and number of patients, true-positives, true-negatives, false-positives, and false-negatives. Where possible, values were also recorded for the following factors potentially contributing to study heterogeneity: biopsy performed with a large-bore cutting or core needle versus fine needle aspiration, use of CT or fluoroscopic guidance for biopsy, antibiotic use before biopsy, type of pathogen responsible for discitis (pyogenic versus mycobacterial pathogen), and use of surgical biopsy when reported in the same paper. In cases of overlapping patient sets between separate publications, the most recent series was selected and included in the systematic review and meta-analysis.

Risk of Bias in Individual Studies

The risk of bias of each study was assessed by using the Quality Assessment of Diagnostic Accuracy Studies 2, or QUADAS-2, tool independently by 2 authors with disagreements resolved by discussion. QUADAS-2 is a tool composed of 4 domains: patient selection, index test, reference standard, and flow and timing. These domains are assessed in terms of risk of bias, and the first 3 domains are also assessed in terms of concerns regarding applicability.[16]

Statistical Analysis

Statistical analysis was performed in R 3.3.0 (http://www.r-project.org/) by using the "metaprop" and "forest" functions of the "meta" package,[17] which generated confidence intervals of the proportion of true-positives (yield) as well as hypothesis testing with an inverse variance method after logit transformation. Results reported in this paper represent random-effects models of meta-analysis. Estimates of yield were produced with 95% confidence intervals. Values of $P < .05$ were regarded as significant.

RESULTS

Study Selection

The search results are shown in Fig 1. The literature search identified 1814 articles. An initial screen of the titles and abstracts identified 88 potentially relevant articles. Eighty-six of the relevant articles were obtainable, and 2 articles were unobtainable through our institution's resources or interlibrary loan. The 86 full-text relevant articles were reviewed for eligibility, and 33 articles satisfied all of the inclusion criteria. Reasons for exclusion of the 53 references are included in Fig 1. Data were extracted for 33 articles found to be eligible for inclusion in the systematic review and meta-analysis.

Study Characteristics

The individual study characteristics are presented in the Table. In total, there were 1763 image-guided biopsies with attempted culture for inclusion within the systematic review. The reference test for the diagnosis of discitis was established by a variety of methods across the studies: as an adjunct to clinical characteristics (which was used in all included studies); 13/33 (39%) used a mix of CT

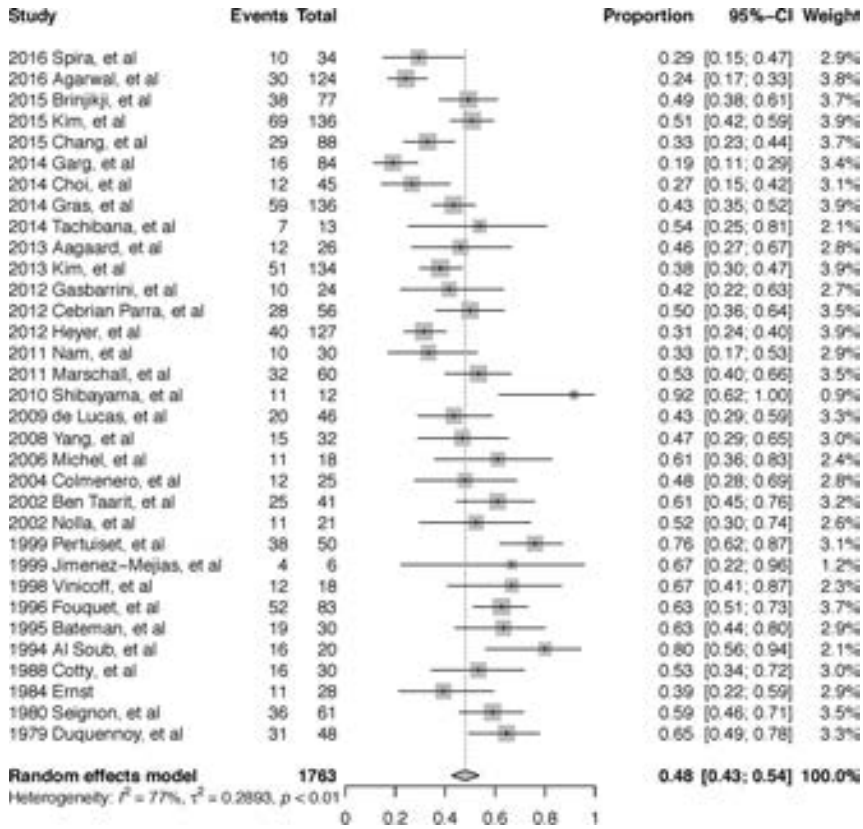

FIG 2. Forest plot of overall yield of image-guided biopsy.

and MR imaging; 8/33 (24%) used MR imaging; 3/33 (9%) used histopathology; and 9/33 (27%) did not clearly define the specific imaging or other diagnostic tests. Few studies confirmed the use of coaxial guidance (8/33 [24%]), whereas most did not report specifically on coaxial versus noncoaxial technique.

Quality and Applicability Assessment

The QUADAS-2 results of each individual study is represented in On-line Fig 1. The assessment showed that most studies had a low risk of bias with regard to flow and timing, index test, and patient selection, as shown in On-line Fig 2. Studies that required or included a positive biopsy culture, the index test, as a criterion for the diagnosis of discitis were considered to have a high risk of bias with respect to the reference standard. Studies that did not thoroughly describe the factors contributing to the diagnosis of discitis were considered to have an uncertain risk of bias regarding the reference standard. With regard to the selection of patients, studies that excluded postoperative discitis or patients with epidural abscesses were considered to have a high risk of bias. Studies that did not fully describe the methods of patient selection were considered to have an uncertain risk of bias with regard to patient selection.

Meta-Analysis

Yield was calculated by using the true-positive data and false-negative data from each study. All but 2 studies did not report data for true-negatives and false-positives.[18,19] In each of those studies, false-positive results were classified based on the growth of common contaminants without concurrent growth in blood cultures.

The pooled yield of the 33 studies included in the meta-analysis was 48% (793/1763 patients; 95% CI, 0.43–0.54 [Fig 2]). There were multiple sources of heterogeneity within the studies, including surgical biopsy, antibiotic exposure, CT or fluoroscopic guidance, large-bore and/or cutting needle biopsy versus fine needle aspiration, pyogenic versus mycobacterium tuberculosis, and polymerase chain reaction versus culture.

Eight studies included data from open surgical biopsy specimens, and the yield within this subgroup was significantly higher than image guided biopsy at 76% (152/201; 95% CI, 0.65–0.85; $P < .01$ [Fig 3]).

Twelve studies included patients with confirmed antibiotic exposure before image-guided biopsy, and 17 studies included patients with confirmed absence of antibiotic exposure before image-guided biopsy. Image-guided biopsy in patients without prior antibiotic exposure produced a higher yield at 43% (336/813; 95% CI, 0.37–0.48; $P = .08$) compared with 32% (106/346; 95% CI, 0.22–0.43) in the group with prior antibiotic exposure, though this was not statistically significant (On-line Fig 3).

Fourteen studies specified the number of biopsies performed under CT guidance, and 6 studies specified the number of biopsies performed under fluoroscopic guidance. All other studies either did not break down results by method or did not specify the method of image guidance. Fluoroscopic guidance was associated with a higher yield at 55% (158/316; 95% CI 0.40–0.69) compared with CT guidance at 44% (275/693; 95% CI, 0.36–0.53; $P = .22$), though this was not statistically significant (On-line Fig 4).

Seventeen studies specified the use of cutting or core needle biopsy (large bore) or fine needle aspiration, with 13 studies using large-bore biopsy and 4 studies using fine needle aspiration. Fine needle aspiration was associated with a significantly higher yield at 60% (98/167; 95% CI, 0.45–0.73) compared with large-bore needle biopsy at 41% (304/821; 95% CI, 0.33–0.49; $P = .03$ [On-line Fig 5]).

Seventeen studies reported data specific for pyogenic pathogen detection, and 7 studies reported data specific for mycobacterium tuberculosis detection. Image-guided biopsy had a significantly higher yield in the detection of mycobacterium tuberculosis at 71% (97/132; 95% CI, 0.54–0.84) compared with detection of pyogenic organisms at 48% (331/738; 95% CI, 0.41–0.56; $P = .02$ [On-line Fig 6]).

Two studies reported results for polymerase chain reaction detection of pathogen. There was no significant difference between the yield of polymerase chain reaction at 50% (30/60; 95% CI, 0.38–0.63) and culture at 48% (793/1763; 95% CI, 0.43–0.54; $P = .46$ [On-line Fig 7]).

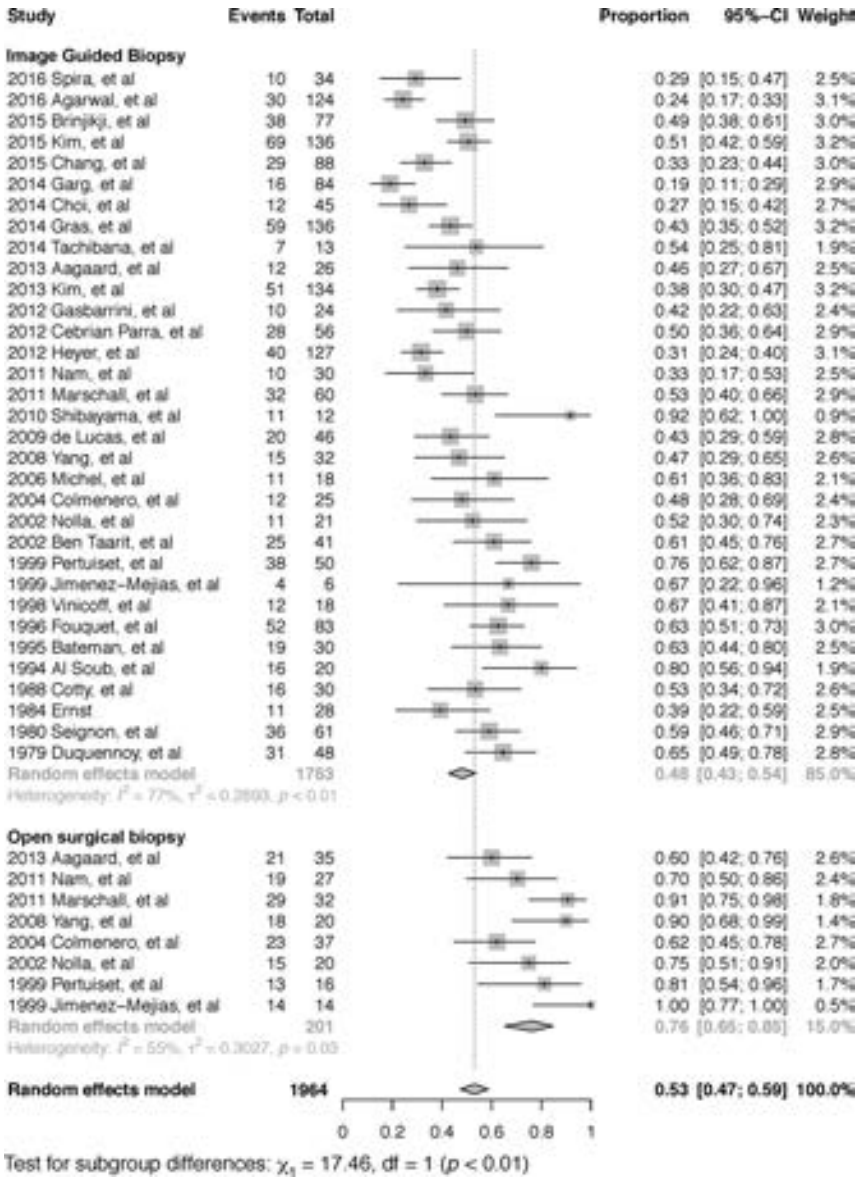

FIG 3. Forest plot of subgroup analysis of the yield of image-guided biopsy versus open surgical biopsy.

DISCUSSION

At most institutions, image-guided biopsy is routinely conducted in patients with suspected discitis because it is considered important to identify the target microorganism before appropriate therapy can be administered. We undertook this meta-analysis to estimate the yield of image-guided biopsy and to better understand the factors that influence the yield of image-guided biopsy.

Our comprehensive meta-analysis demonstrates that image guided biopsy has a moderate yield of 48% (95% CI, 0.43–0.54) for the diagnosis of infectious discitis, providing a more useful assessment of this diagnostic tool than the broad range of 31% to 91% that has been reported in the literature.[8,9] This yield is lower than open surgical biopsy (yield of 76%), consistent with other reports in the literature.[11,12] Prior antibiotic treatment causes a decrease in the yield of image-guided biopsy (43% without prior antibiotics versus 32% with prior antibiotic exposure), though this effect was statistically insignificant in this study. The decision to provide antibiotics before obtaining a positive culture result is a complex clinical decision that must weigh diagnostic certainty and decisive antibiotic selection against the benefits of early therapy.

Although this meta-analysis suggests fluoroscopy-guided biopsy had a higher yield of 55% compared with 44% for CT-guided biopsy, this difference did not reach statistical significance. The reasons for this are not clear. Intuitively, CT should provide better identification of the exact biopsy location compared with fluoroscopy. Most of the studies did not provide information regarding the location of biopsy (central versus peripheral) in all of the patients. This result may reflect the heterogeneity of confounding factors in the source studies (changing use of CT versus fluoroscopic guidance, etc). Alternatively, fluoroscopically guided biopsies may have had the needle placed more centrally than CT-guided biopsies; this could have provided more reassurance to the fluoroscopic operators that the needle was indeed within the disc compared with the CT operators, who may have stopped when the needle entered the peripheral disc because they were certain of the needle position.

There were several other sources of heterogeneity within the studies, suggesting other predictors of yield. Fine needle aspiration was associated with a higher yield of 60% compared with large-bore needle biopsy at 41%. This is also counterintuitive, though fine needle aspiration may be used more frequently in cases of abscesses, which may yield a sample more likely to grow in culture. There were many studies that examined the detection of mycobacterium tuberculosis through culture, which was associated with a higher yield of 71%, compared with the detection of pyogenic organisms with a yield of 48%. Lastly, there was no significant difference in the yield of polymerase chain reaction at 50% compared with culture, but this may be as a result of only a small number of cases with polymerase chain reaction (n = 60) being assessed.

Most (31/33) of the examined studies considered all positive culture results from image-guided biopsies to be true-positives, essentially ignoring the possibility of false-positive results caused by factors such as surface or laboratory contamination. Two assessed studies acknowledged false-positive biopsy results. This assumption reflects the difficulty of demonstrating the responsible microorganism through reference diagnostic tests aside from direct biopsy, but may reflect a substantial error in research assess-

ments of the performance of image-guided biopsy and many other scenarios of ongoing infectious disease research.

There is 1 other meta-analysis on the yield of image-guided biopsy in discitis, performed by Pupaibool et al,[15] which demonstrated a yield of 52.2%. We performed this meta-analysis because the study by Pupaibool et al[15] had several limitations. Pupaibool et al[15] excluded all studies of nonspontaneous discitis and included data from only 5 studies. Because spinal instrumentation and surgery are major contributors to cases of discitis and a high proportion of requests for image-guided biopsies involve patients post-instrumentation, we felt it was important to include these studies in our review and have evaluated the data from a much larger cohort of studies ($n = 33$).[20] In addition, our study provides further diagnostic information through the subgroup analyses on the sources of heterogeneity, including open surgical biopsy, antibiotic therapy, and CT versus fluoroscopic guidance. From a methodology standpoint, our search strategy identified a higher number of potentially applicable abstracts (1814 versus 358).

There are some limitations to our analysis. Like all meta-analyses, the conclusions of this meta-analysis are primarily limited by the heterogeneity of the included studies. Specifically, the studies varied in the extent to which they described their methods, including coaxial needle, prior antibiotic exposure, first or repeat biopsy, number of samples collected, and prior imaging studies. The methodology of the meta-analysis itself was limited by the inability to obtain 2 potentially relevant references for full-text review.

CONCLUSIONS

This study indicates that image-guided biopsy in suspected discitis has a yield for detection of the infectious organism of 48%, toward the lower end of the frequently reported range of 31%–91%.[3,8] Open surgical biopsy has a higher yield at 76%, and antibiotic treatment had an insignificant effect on the yield.

ACKNOWLEDGMENTS

The authors thank Mark MacEachern, who provided guidance in designing the literature search strategy. We also thank Dr. Bin Nan for assistance with statistical analysis.

REFERENCES

1. Gouliouris T, Aliyu SH, Brown NM. **Spondylodiscitis: update on diagnosis and management.** *J Antimicrob Chemother* 2010;65(Suppl 3):iii11–24 CrossRef Medline
2. Mylona E, Samarkos M, Kakalou E, et al. **Pyogenic vertebral osteomyelitis: a systematic review of clinical characteristics.** *Semin Arthritis Rheum* 2009;39:10–17 CrossRef Medline
3. Berbari EF, Kanj SS, Kowalski TJ, et al. **2015 Infectious Diseases Society of America (IDSA) clinical practice guidelines for the diagnosis and treatment of native vertebral osteomyelitis in adults.** *Clin Infect Dis* 2015;61:e26–46 CrossRef Medline
4. Rutges JP, Kempen DH, van Dijk M, et al. **Outcome of conservative and surgical treatment of pyogenic spondylodiscitis: a systematic literature review.** *Eur Spine J* 2016;25:983–99 CrossRef Medline
5. Agarwal V, Wo S, Lagemann GM, et al. **Image-guided percutaneous disc sampling: impact of antecedent antibiotics on yield.** *Clin Radiol* 2016;71:228–34 CrossRef Medline
6. Modic MT, Feiglin DH, Piraino DW, et al. **Vertebral osteomyelitis: assessment using MR.** *Radiology* 1985;157:157–66 CrossRef Medline
7. Cheung WY, Luk KD. **Pyogenic spondylitis.** *Int Orthop* 2012;36:397–404 CrossRef Medline
8. Sehn JK, Gilula LA. **Percutaneous needle biopsy in diagnosis and identification of causative organisms in cases of suspected vertebral osteomyelitis.** *Eur J Radiol* 2012;81:940–46 CrossRef Medline
9. Chew FS, Kline MJ. **Diagnostic yield of CT-guided percutaneous aspiration procedures in suspected spontaneous infectious diskitis.** *Radiology* 2001;218:211–14 CrossRef Medline
10. Grados F, Lescure FX, Senneville E, et al. **Suggestions for managing pyogenic (non-tuberculous) discitis in adults.** *Joint Bone Spine* 2007;74:133–39 CrossRef Medline
11. Jiménez-Mejías ME, de Dios Colmenero J, Sánchez-Lora FJ, et al. **Postoperative spondylodiskitis: etiology, clinical findings, prognosis, and comparison with nonoperative pyogenic spondylodiskitis.** *Clin Infect Dis* 1999;29:339–45 CrossRef Medline
12. Yang SC, Fu TS, Chen LH, et al. **Identifying pathogens of spondylodiscitis: percutaneous endoscopy or CT-guided biopsy.** *Clin Orthop Relat Res* 2008;466:3086–92 CrossRef Medline
13. Marschall J, Bhavan KP, Olsen MA, et al. **The impact of prebiopsy antibiotics on pathogen recovery in hematogenous vertebral osteomyelitis.** *Clin Infect Dis* 2011;52:867–72 CrossRef Medline
14. Rankine JJ. **Therapeutic impact of percutaneous spinal biopsy in spinal infection.** *Postgrad Med J* 2004;80:607–09 CrossRef Medline
15. Pupaibool J, Vasoo S, Erwin PJ, et al. **The utility of image-guided percutaneous needle aspiration biopsy for the diagnosis of spontaneous vertebral osteomyelitis: a systematic review and meta-analysis.** *Spine J* 2015;15:122–31 CrossRef Medline
16. Whiting PF, Rutjes AW, Westwood ME, et al. **QUADAS-2: a revised tool for the quality assessment of diagnostic accuracy studies.** *Ann Intern Med* 2011;155:529–36 CrossRef Medline
17. Schwarzer G. General Package for Meta-Analysis. 2015
18. Chang CY, Simeone FJ, Nelson SB, et al. **Is biopsying the paravertebral soft tissue as effective as biopsying the disk or vertebral endplate? 10-year retrospective review of CT-guided biopsy of diskitis-osteomyelitis.** *AJR Am J Roentgenol* 2015;205:123–29 CrossRef Medline
19. Choi SH, Sung H, Kim SH, et al. **Usefulness of a direct 16S rRNA gene PCR assay of percutaneous biopsies or aspirates for etiological diagnosis of vertebral osteomyelitis.** *Diagn Microbiol Infect Dis* 2014;78:75–78 CrossRef Medline
20. Gasbarrini A, Bertoldi E, Mazzetti M, et al. **Clinical features, diagnostic and therapeutic approaches to haematogenous vertebral osteomyelitis.** *Eur Rev Med Pharmacol Sci* 2005;9:53–66 Medline
21. Spira D, Germann T, Lehner B, et al. **CT-guided biopsy in suspected spondylodiscitis–the association of paravertebral inflammation with microbial pathogen detection.** *PLoS One* 2016;11:e0146399 CrossRef Medline
22. Brinjikji W, Everist B, Wald J, et al. **Association between imaging findings and microbiological findings for image-guided biopsies for spine infections.** *J Neurosurg Sci* 2015 Sep 9. [Epub ahead of print] Medline
23. Kim CJ, Kang SJ, Choe PG, et al. **Which tissues are best for microbiological diagnosis in patients with pyogenic vertebral osteomyelitis undergoing needle biopsy?** *Clin Microbiol Infect* 2015;21:931–35 CrossRef Medline
24. Garg V, Kosmas C, Young PC, et al. **Computed tomography-guided percutaneous biopsy for vertebral osteomyelitis: a department's experience.** *Neurosurg Focus* 2014;37:E10 CrossRef Medline
25. Tachibana T, Moriyama T, Maruo K, et al. **Therapeutic impact of organism isolation in management of patients with pyogenic vertebral osteomyelitis.** *Springerplus* 2014;3:62 CrossRef Medline
26. Gras G, Buzele R, Parienti JJ, et al. **Microbiological diagnosis of vertebral osteomyelitis: relevance of second percutaneous biopsy following initial negative biopsy and limited yield of post-biopsy blood cultures.** *Eur J Clin Microbiol Infect Dis* 2014;33:371–75 CrossRef Medline
27. Aagaard T, Roed C, Dragsted C, et al. **Microbiological and therapeutic challenges in infectious spondylodiscitis: a cohort study of 100**

cases, 2006–2011. *Scand J Infect Dis* 2013;45:417–24 CrossRef Medline
28. Kim BJ, Lee JW, Kim SJ, et al. **Diagnostic yield of fluoroscopy-guided biopsy for infectious spondylitis.** *AJNR Am J Neuroradiol* 2013;34:233–38 CrossRef Medline
29. Gasbarrini A, Boriani L, Salvadori C, et al. **Biopsy for suspected spondylodiscitis.** *Eur Rev Med Pharmacol Sci* 2012;16 Suppl 2:26–34 Medline
30. Cebrián Parra JL, Saez-Arenillas Martín A, Urda Martínez-Aedo AL, et al. **Management of infectious discitis. Outcome in one hundred and eight patients in a university hospital.** *Int Orthop* 2012;36:239–44 CrossRef Medline
31. Heyer CM, Brus LJ, Peters SA, et al. **Efficacy of CT-guided biopsies of the spine in patients with spondylitis–an analysis of 164 procedures.** *Eur J Radiol* 2012;81:e244–49 CrossRef Medline
32. Nam KH, Song GS, Han IH, et al. **Diagnostic value of biopsy techniques in lumbar spondylodiscitis: percutaneous needle biopsy and open biopsy.** *Korean J Spine* 2011;8:267–71 CrossRef Medline
33. Shibayama M, Nagahara M, Kawase G, et al. **New needle biopsy technique for lumbar pyogenic spondylodiscitis.** *Spine (Phila Pa 1976)* 2010;35:E1347–49 CrossRef Medline
34. de Lucas EM, González Mandly A, Gutiérrez A, et al. **CT-guided fine-needle aspiration in vertebral osteomyelitis: true usefulness of a common practice.** *Clin Rheumatol* 2009;28:315–20 CrossRef Medline
35. Michel SC, Pfirrmann CW, Boos N, et al. **CT-guided core biopsy of subchondral bone and intervertebral space in suspected spondylodiskitis.** *AJR Am J Roentgenol* 2006;186:977–80 CrossRef Medline
36. Colmenero JD, Jiménez-Mejías ME, Reguera JM, et al. **Tuberculous vertebral osteomyelitis in the new millennium: still a diagnostic and therapeutic challenge.** *Eur J Clin Microbiol Infect Dis* 2004;23:477–83 CrossRef Medline
37. Ben Taarit Ch, Turki S, Maiz H. **Infectious spondylitis. Study of a series of 151 cases.** [**Article in French**] *Acta Orthop Belg* 2002;68:381–87 Medline
38. Nolla JM, Ariza J, Gómez-Vaquero C, et al. **Spontaneous pyogenic vertebral osteomyelitis in nondrug users.** *Semin Arthritis Rheum* 2002;31:271–78 CrossRef Medline
39. Pertuiset E, Beaudreuil J, Lioté F, et al. **Spinal tuberculosis in adults. A study of 103 cases in a developed country, 1980–1994.** *Medicine* 1999;78:309–20 CrossRef Medline
40. Vinicoff P, Gutschik E, Hansen S, et al. **CT-guided biopsy in spondylodiscitis.** [**Article in Danish**] *Ugeskr Laeger* 1998;160:5931–34 Medline
41. Fouquet B, Goupille P, Gobert F, et al. **Infectious discitis diagnostic contribution of laboratory tests and percutaneous discovertebral biopsy.** *Rev Rhum Engl Ed* 1996;63:24–29 Medline
42. Bateman JL, Pevzner MM. **Spinal osteomyelitis: a review of 10 years' experience.** *Orthopedics* 1995;18:561–65 Medline
43. Al Soub H, Uwaydah AK, Hussain AH. **Vertebral osteomyelitis in Qatar.** *Br J Clin Pract* 1994;48:130–32 Medline
44. Cotty PH, Fouquet B, Pleskof L, et al. **Vertebral osteomyelitis: value of percutaneous biopsy: 30 cases.** *J Neuroradiol* 1988;15:13–21
45. Ernst H. **Der diagnostische wer der wirbel-korperpunktion bei der spondylitis.** *Orthopadie* 1984;34:443–47
46. Seignon B, Weilbacher H, Thorel J, et al. **Spinal puncture in the bacteriological diagnosis of bacterial spondylitis. Experience in the rheumatology departments of Reims, Clermont-Ferrand and Rouen.** [**Article in French**] *Rev Rhum Mal Osteoartic* 1980;47:45–47 Medline
47. Duquennoy A, Delcambre B, Duquesnoy B, et al. **Value of disk puncture in the diagnosis of infectious spondylodiskitis. Apropos of 48 punctures.** [**Article in French**] *Rev Rhum Mal Osteoartic* 1979;46:615–17 Medline

[^{18}F]-Sodium Fluoride PET MR–Based Localization and Quantification of Bone Turnover as a Biomarker for Facet Joint–Induced Disability

N.W. Jenkins, J.F. Talbott, V. Shah, P. Pandit, Y. Seo, W.P. Dillon, and S. Majumdar

ABSTRACT

SUMMARY: Our aim was to prospectively evaluate the relationship between low back pain–related disability and quantitative measures from [^{18}F]-sodium fluoride ([^{18}F]-NaF) MR imaging. Six patients with facetogenic low back pain underwent dynamic [^{18}F]-NaF PET/MR imaging. PET metrics were correlated with clinical measures and MR imaging grading of lumbar facet arthropathy. A significant positive correlation was observed between maximum facet joint uptake rate and clinical disability ($P < .05$). These data suggest that dynamic [^{18}F]-NaF PET may serve as a useful biomarker for facetogenic disability.

ABBREVIATIONS: FJ = facet joint; IPAQ = International Physical Activity Questionnaire; max = maximum; min = minimum; mL/ccm/min = milliliters/cubic centimeter/minute; ODI = Oswestry Disability Index; SUV = standard uptake value

Clinical assessment for facetogenic low back pain is often hampered by overlapping and nonspecific symptoms and physical examination findings.[1] Conventional imaging techniques limited to evaluation of structural changes in the spine may identify morphologic abnormalities in asymptomatic spinal structures that are indistinguishable from degenerative structural alterations that produce severe pain and disability.[2] Objective and quantitative biomarkers that are more specific for active generators of low back pain would greatly aid in the effective, targeted treatment of patients with low back pain.

[18F]-sodium fluoride ([^{18}F]-NaF) is a positron-emission tomography radiotracer, which is chemically absorbed into hydroxyapatite in the bone matrix by osteoblasts and can noninvasively detect osteoblastic activity. [^{18}F]-NaF has been increasingly used for evaluating bone diseases, particularly for identification of bone metastases and primary tumors.[3-5] The utility of [^{18}F]-NaF PET for evaluating degenerative disease of the lumbar spine remains largely unexplored.[6]

Received April 20, 2017; accepted after revision June 6.

From the Department of Radiology and Biomedical Imaging (N.W.J., J.F.T., V.S., P.P., Y.S., W.P.D., S.M.), University of California, San Francisco, San Francisco, California; and Department of Radiology and Biomedical Imaging (J.F.T.), Zuckerberg San Francisco General Hospital, San Francisco, California.

Research support was provided by National Institutes of Health P50AR060752 and GE Healthcare.

Please address correspondence to Jason F. Talbott, MD, Department of Radiology and Biomedical Imaging, Zuckerberg San Francisco General Hospital, 1001 Potrero Ave, Room 1X57C, San Francisco, CA 94110; e-mail: Jason.talbott@ucsf.edu

Indicates open access to non-subscribers at www.ajnr.org

Indicates article with supplemental on-line photos.

http://dx.doi.org/10.3174/ajnr.A5348

The goal of this prospective pilot study was to examine the potential correlation between facetogenic low back pain measures of disability with quantitative and semiquantitative [^{18}F]-NaF PET/MR imaging measures of bone turnover and structural MR imaging changes in lumbar facet joints.

MATERIALS AND METHODS

Patient Population

This prospective feasibility study recruited patients after obtaining human study institutional review board approval and complying with Health Insurance Portability and Accountability Act regulations. Patients served as internal controls with diseased and healthy subregions. Patients with a history of suspected lower lumbar facetogenic syndrome were recruited from UCSF Radiology Spine Clinic. Written informed consent was acquired before entry into the study. The study began in November 2014 and concluded in August 2015.

Inclusion and Exclusion Criteria

Inclusion criteria were as follows: 1) at least 18 years of age with the capacity for informed consent, 2) a reported history of axial nonradicular low back pain, and 3) recommended by the spine interventional radiologists. Exclusion criteria were as follows: 1) a history of fracture or tumor of the spine, including osteoblastic metastases, 2) women who were pregnant or breastfeeding, 3) contraindications to MR imaging or administration of tracer or contrast, and 4) prior lumbar surgery or instrumentation.

Immediately before PET/MR imaging, subjects completed questionnaires measuring pain (numeric rating scale, from 0 to 10 with 0 equal to no pain and 10, the most severe intensity of pain),

quality of life (Oswestry Disability Index Low Back Pain Disability Questionnaire [ODI]), and activity (International Physical Activity Questionnaire [IPAQ]).[7,8]

PET/MR Protocol and Image Review

A 3T Signa PET/MR imaging scanner (GE Healthcare, Milwaukee, Wisconsin) was used for a simultaneous PET and MR image acquisition. Dynamic PET was initiated as 0.08 mCi/Kg of [^{18}F]-NaF (mean dose, 4.6 ± 0.8 mCi) injected intravenously.

Acquisition Parameters

Clinical MR imaging sequences included the following: sagittal T1 (TR/TE = 510/8.6 ms), sagittal T2 fat-saturated (TR/TE = 4208/86.2 ms), axial T2 fast recovery fast spin-echo with and without fat saturation (TR/TE = 750/9.2 ms), axial T1 fast spin-echo (TR/TE = 575/8.9 ms), and axial T1 fast spin-echo postgadolinium (TR/TE = 562/8.6 ms) imaging. The MR imaging attenuation correction for the lumbar spine region was calculated with the accepted standard 2-point Dixon method.[9] Sixty minutes of dynamic PET data were acquired across 3 temporal phases (phase 1 = 12 frames of 10 seconds each, phase 2 = 4 frames of 30 seconds each, phase 3 = 14 frames of 4 minutes each). PET reconstruction included postprocessing to correct for decay, attenuation, scatter, and dead time.

MR Imaging Facet Joint Grading

Two board-certified neuroradiologists with 3 (J.F.T.) and >30 (W.P.D.) years' postfellowship experience were blinded to the clinical data and interpreted clinical MR imaging sequences on a reprocessing workstation. Facet synovitis was graded as previously described by Czervionke and Fenton (On-line Fig 1).[10]

Data Analysis

Quantitative and semiquantitative PET analysis included all facet joints from the L1–L2 to L5–S1 levels. Volumes of interest were selected using anatomic T2 MR images. A spheric VOI (7.5-mm diameter) was constructed around the center of each facet joint. A 5-mm-diameter VOI was placed in the right iliac crest in the central marrow cavity as a reference region. All PET analysis was performed with PMOD licensed software (PMOD Technologies, Zurich, Switzerland). This software facilitates model-based analysis of dynamic PET data. PMOD allows only validated kinetic models that have been extensively studied, and the output of the results is highly reproducible.

Standard Uptake Value Calculations and Kinetic Data

Placement of facet joint (FJ) VOIs is shown in On-line Fig 2*A*. A cylindric VOI covering 2 axial sections was placed on the abdominal aorta, and the partial volume correction coefficient was calculated. Maximum standard uptake value (SUV_{max}) and SUV_{mean} values (Equation 1) for each subsite were calculated using the 60-minute time point.

The 3-compartment model used for kinetic modeling is shown in On-line Fig 2*B*. In Equation 2, C_i represents the bone tissue activity concentration and is the sum of C_e (extravascular compartment) and C_t (target tissue bound compartment); C_p is the concentration of tracer in the blood; V is the effective distribution volume of the tracer.[11] A 3-compartment irreversible linear model was used for the Patlak linear model.[11] The 2-tissue irreversible compartment model was used to calculate the region-specific influx rate constants (in minute^{-1}) for [^{18}F]-NaF.[12] Uptake was normalized by using the iliac crest as the reference region. The tracer influx rate from the blood pool to the bone matrix was calculated with Equation 2 for K_{i_Patlak}. K_{i_Patlak} represents the rate at which [^{18}F]-NaF leaves the arterial blood pool and irreversibly binds to a subsite bone matrix. The kinetic analysis was performed by using PMOD. For each subject, FJs with maximum uptake were identified, henceforth referred to as FJ_{max}.

$$1)\quad SUV = \frac{\text{Radioactivity Concentration}\left|\frac{\text{kBq}}{\text{mL}}\right|}{\text{Decay-Corrected Amount of Injected Tracer}\,|\text{kBq}|} \times \text{Lean Body Mass (g)}.$$

Equation 2 is the Patlak graphical kinetic model:

$$2)\quad \frac{C_i(T)}{C_p(T)} = K_{PL}\frac{\int_0^T C_p(t)\,dt}{C_p(T)} + \text{Intercept}.$$

Statistical Analyses

The statistical significance of the correlations between PET/MR imaging and clinical disability metrics was tested with the Pearson correlation. A 2-samples *t* test was used ($P < .05$) to assess the significance of differences in the K_{i_Patlak} influx rate between the mean FJ_{max} and mean $FJ_{minimum\ (min)}$ K_{i_Patlak} and among FJ MR imaging grades.

Profile of patients with facetogenic low back pain

Profile	
No. of patients	6
Age (mean) (range) (yr)	68 (45–80)
Sex (M/F)	5:1
ODI score (mean) (SD)	18 (5.5)
Pain score (mean) (SD)	5.2 (1.5)
IPAQ (mean)	
Vigorous MET (SD)	1728 (1721)
Moderate MET (SD)	1872 (2310)
Walking MET (SD)	2376 (1454)
Categoric score (SD)	0.8 (1.09)

Note:—MET indicates metabolic equivalent task.

RESULTS

Patient Profile

Patient demographic and clinical disability scores are summarized in the Table.

[^{18}F]-NaF Uptake Measurements and MR Imaging Grading

Uptake values were measured in bilateral facet joints across 5 levels in all subjects for a total of 60 measurements. For all 60 sampled regions, the relationship between semiquantitative SUV_{max} and K_{i_Patlak} produced a linear correlation ($r = 0.58$, $P < .001$; On-line Fig 3*A*). A similar statistically significant linear correlation was observed between K_{i_Patlak} and SUV_{mean} ($r = 0.7$, $P < .001$; On-line Fig 3*B*).

For each patient, the single facet joint with the highest K_{i_Patlak} (FJ_{max} K_{i_Patlak}) was identified. When FJ_{max} K_{i_Patlak} was plotted

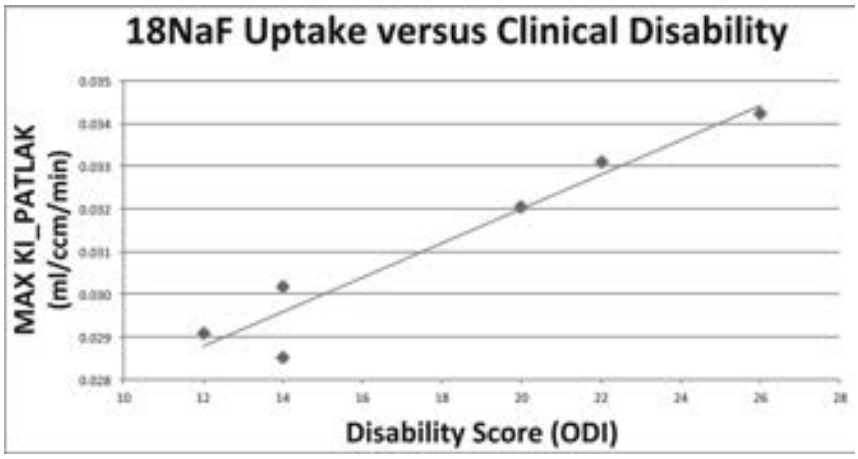

FIG 1. Maximum K_{i_Patlak} significantly correlates with clinical disability as measured by the Oswestry Disability Index. Facet joints with maximum K_{i_Patlak} (FJ_{max} K_{i_Patlak}) plotted against the corresponding patient ODI scores reveal a strong, statistically significant linear correlation ($r = 0.96$, $P = .0013$).

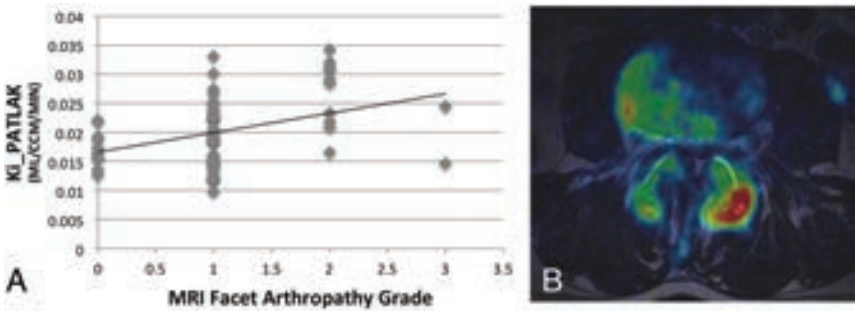

FIG 2. [^{18}F]-NaF PET uptake and MR imaging arthropathy grade are weakly correlated. *A*, [^{18}F]-NaF uptake (K_{i_Patlak}) plotted against the facet arthropathy grade on MR imaging shows a weak-to-moderate but statistically significant ($r = 0.37$, $P = .03$) correlation. *B*, Sample PET/MR imaging–fused axial image at the L3–L4 level in a 61-year-old man with suspected facetogenic pain shows differential FJ uptake with noticeably higher uptake on the left. On MR imaging, both facets were grade 2 facet synovitis.

against the ODI score, a strong, statistically significant positive correlation was observed ($r = 0.96$, $P = .0013$; Fig 1).

The FJ SUV_{max} and SUV_{mean} for each subject ($n = 6$) were plotted against the ODI score, and no significant correlations were observed ($r = -0.55$, $P = .35$, and $r = -0.47$, $P = .35$). The correlation between the maximum MR imaging grade and ODI ($n = 6$) was not significant ($r = 0.38$, $P = .44$). FJ_{max} K_{i_Patlak} plotted against corresponding patient maximum pain scores showed no correlation ($r = 0.06$, $P = .91$). FJ_{max} K_{i_Patlak} plotted against corresponding patient IPAQ categoric scores showed no correlation ($r = 0.15$, $P = .77$).

A weak-to-moderate, but statistically significant, correlation was observed between the MR imaging grade of facet arthropathy and K_{i_Patlak} ($r = 0.37$, $P = .03$; Fig 2*A*). The average uptake rate as measured by K_{i_Patlak} for FJ_{min} (0.019 milliliter/cubic centimeter/min [mL/ccm/min]) and FJ_{max} (0.032 mL/ccm/min) showed that FJ_{max} was significantly higher with close to twice the uptake rate ($P < .001$).

DISCUSSION

In this prospective pilot study of patients with suspected facetogenic low back pain, we show a strong positive linear correlation between a kinetic measure of dynamic NaF uptake by the FJ with maximum uptake (FJ_{max} K_{i_Patlak}) and disability as measured with ODI. These data suggest that FJ_{max} K_{i_Patlak} may be a useful metric for quantifying and localizing lumbar facetogenic–related disability. Thus, [^{18}F]-NaF PET may aid in treatment planning and longitudinal monitoring of degenerative lumbar facet disease. With our small sample size of 6 subjects with relatively mild disability and the lack of a healthy control cohort, these data are preliminary. However, our observed strong correlation between [^{18}F]-NaF uptake as measured with FJ_{max} K_{i_Patlak} and clinical disability, even in this small cohort of patients with facet syndrome, is reassuring that FJ_{max} K_{i_Patlak} may serve as a useful biomarker for facet joint–related disability. Further larger scale studies are warranted to validate these preliminary data, and a cost-benefit analysis will need to be performed. Most important, our average measurement for FJ_{max} K_{i_Patlak} across all subjects (0.32 ± 0.003, $n = 6$) is like that of Brenner et al[13] in areas of high bone turnover, including bone grafts, supporting the validity of our quantitative PET measurements.

Neither SUV_{max} nor SUV_{mean} showed a statistically significant correlation with the ODI score or any other clinical measure of low back pain and disability. While larger studies are needed to confirm this result, the primary finding of this study is that the kinetic variable K_{i_Patlak} may be useful for evaluating facetogenic pathology by providing a quantitative value that more accurately reflects the dynamic process of bone turnover and osteoblastic activity. SUV values assume that radiotracer is evenly distributed throughout the entire body and base the measurement off a lean body mass coefficient. K_{i_Patlak} measures specific concentrations of radiotracer reaching the target via the arterial system during the scan. This added information may reveal subtle changes in the flow of the tracer to ROIs that would otherwise be missed.

It is also of interest that a weak, but statistically significant, correlation was observed between the MR imaging morphologic grade of facet arthropathy and quantitative PET measures or ODI. This finding is consistent with a previous study in which a similarly weak correlation was found between NaF-PET uptake and CT measures of facet arthropathy, further supporting the hypothesis that physiologic information afforded by NaF uptake may supplement conventional structural imaging for identifying symptomatic facet joints.[6]

As a pilot study, the small number of patients and relatively

mild disability represent a primary limitation of this study. Despite this limitation, the observed strong and statistically significant correlation between FJ_{max} K_{i_Patlak} and ODI in this small, inclusive cohort suggests that [^{18}F]-NaF may serve as a robust biomarker for facet syndrome, and future larger studies are warranted to confirm these data. Also, we provide only correlative evidence that FJ_{max} K_{i_Patlak} and clinical disability are related. Future studies involving targeted facet joint injections based on dynamic PET/MR imaging data are planned and will be needed to validate the present results.

CONCLUSIONS

In the lumbar spine, [^{18}F]-NaF uptake rates in facet joints as measured with K_{i_Patlak} strongly correlate with patient-reported ODI scores. These pilot data suggest that kinetic measurements of [^{18}F]-NaF facet joint uptake may serve as sensitive, quantitative, and noninvasive biomarkers of facetogenic low back pain.

ACKNOWLEDGMENTS

We would like to acknowledge the support by Vahid Ravanfar, Emily Verdin, and Stephanie Murphy.

Disclosures: Nathaniel W. Jenkins—*RELATED*: *Grant*: National Institutes of Health, *Comments*: National Institutes of Health P50AR060752*; *Other*: GE Healthcare, *Comments*: PET/MR imaging research support grant.* Jason F. Talbott—*UNRELATED*: *Consultancy:* StemCells Inc, *Comments*: member of data-monitoring committee; *Expert Testimony*: Tindall Bennett and Shoup, *Comments*: expert witness. Sharmila Majumdar—*RELATED*: *Grant*: GE Healthcare*; *UNRELATED*: *Grants/Grants Pending*: GE Healthcare.* *Money paid to the institution.

REFERENCES

1. Hart LG, Deyo RA, Cherkin DC. **Physician office visits for low back pain: frequency, clinical evaluation, and treatment patterns from a U.S. national survey.** *Spine (Phila Pa 1976)* 1995;20:11–19 Medline
2. Brinjikji W, Luetmer PH, Comstock B, et al. **Systematic literature review of imaging features of spinal degeneration in asymptomatic populations.** *AJNR Am J Neuroradiol* 2015;36:811–16 CrossRef Medline
3. Spick C, Polanec SH, Mitterhauser M, et al. **Detection of bone metastases using 11C-acetate PET in patients with prostate cancer with biochemical recurrence.** *Anticancer Res* 2015;35:6787–91 Medline
4. Brans B, Weijers R, Halders S, et al. **Assessment of bone graft incorporation by 18 F-fluoride positron-emission tomography/computed tomography in patients with persisting symptoms after posterior lumbar interbody fusion.** *EJNMMI Res* 2012;2:42 CrossRef Medline
5. Quon A, Dodd R, Iagaru A, et al. **Initial investigation of ^{18}F-NaF PET/CT for identification of vertebral sites amenable to surgical revision after spinal fusion surgery.** *Eur J Nucl Med Mol Imaging* 2012;39:1737–44 CrossRef Medline
6. Mabray MC, Brus-Ramer M, Behr SC, et al. **(18)F-sodium fluoride PET-CT hybrid imaging of the lumbar facet joints: tracer uptake and degree of correlation to CT-graded arthropathy.** *World J Nucl Med* 2016;15:85–90 CrossRef Medline
7. Fairbank JC, Pynsent PB. **The Oswestry Disability Index.** *Spine* 2000; 25:2940–52, discussion 2952 Medline
8. Craig CL, Marshall AL, Sjöström M, et al. **International Physical Activity Questionnaire: 12-country reliability and validity.** *Med Sci Sports Exerc* 2003;35:1381–95 CrossRef Medline
9. Anazodo UC, Thiessen JD, Ssali T, et al. **Feasibility of simultaneous whole-brain imaging on an integrated PET-MRI system using an enhanced 2-point Dixon attenuation correction method.** *Front Neurosci* 2014;8:434 CrossRef Medline
10. Czervionke LF, Fenton DS. **Fat-saturated MR imaging in the detection of inflammatory facet arthropathy (facet synovitis) in the lumbar spine.** *Pain Med* 2008;9:400–06 CrossRef Medline
11. Hawkins RA, Choi Y, Huang SC, et al. **Evaluation of the skeletal kinetics of fluorine-18-fluoride ion with PET.** *J Nucl Med* 1992;33: 633–42 Medline
12. Phelps ME, Huang SC, Hoffman EJ, et al. **Tomographic measurement of local cerebral glucose metabolic rate in humans with (F-18)2-fluoro-2-deoxy-D-glucose: validation of method.** *Ann Neurol* 1979;6:371–88 CrossRef Medline
13. Brenner W, Vernon C, Muzi M, et al. **Comparison of different quantitative approaches to 18F-fluoride PET scans.** *J Nucl Med* 2004;45: 1493–500 Medline

American Society of Functional Neuroradiology–Recommended fMRI Paradigm Algorithms for Presurgical Language Assessment

D.F. Black, B. Vachha, A. Mian, S.H. Faro, M. Maheshwari, H.I. Sair, J.R. Petrella, J.J. Pillai, and K. Welker

ABSTRACT

INTRODUCTION: Functional MR imaging is increasingly being used for presurgical language assessment in the treatment of patients with brain tumors, epilepsy, vascular malformations, and other conditions. The inherent complexity of fMRI, which includes numerous processing steps and selective analyses, is compounded by institution-unique approaches to patient training, paradigm choice, and an eclectic array of postprocessing options from various vendors. Consequently, institutions perform fMRI in such markedly different manners that data sharing, comparison, and generalization of results are difficult. The American Society of Functional Neuroradiology proposes widespread adoption of common fMRI language paradigms as the first step in countering this lost opportunity to advance our knowledge and improve patient care.

LANGUAGE PARADIGM REVIEW PROCESS: A taskforce of American Society of Functional Neuroradiology members from multiple institutions used a broad literature review, member polls, and expert opinion to converge on 2 sets of standard language paradigms that strike a balance between ease of application and clinical usefulness.

ASFNR RECOMMENDATIONS: The taskforce generated an adult language paradigm algorithm for presurgical language assessment including the following tasks: Sentence Completion, Silent Word Generation, Rhyming, Object Naming, and/or Passive Story Listening. The pediatric algorithm includes the following tasks: Sentence Completion, Rhyming, Antonym Generation, or Passive Story Listening.

DISCUSSION: Convergence of fMRI language paradigms across institutions offers the first step in providing a "Rosetta Stone" that provides a common reference point with which to compare and contrast the usefulness and reliability of fMRI data. From this common language task battery, future refinements and improvements are anticipated, particularly as objective measures of reliability become available. Some commonality of practice is a necessary first step to develop a foundation on which to improve the clinical utility of this field.

ABBREVIATIONS: AG = Antonym Generation; ASFNR = American Society of Functional Neuroradiology; BOLD = blood oxygen level–dependent; CVR = cerebrovascular reactivity; ECS = electrocortical stimulation; NVU = neurovascular uncoupling; ON = Object Naming; LI = laterality index; PSL = Passive Story Listening; SC = Sentence Completion; SWG = Silent Word Generation

The use of fMRI in the presurgical assessment of language function, especially in patients with brain tumors, vascular malformations, or epilepsy, has become standard throughout numerous institutions in North America, Europe, and other parts of the world, and the reliance on this technology is increasing.[1] fMRI offers a valuable noninvasive means of assessing language function lateralization and localization, which complements, or in some cases, obviates intraoperative electrocortical stimulation (ECS) mapping.[2,3] The Organization of Human Brain Mapping Committee on Best Practice in Data Analysis and Sharing has recently published a white paper that addresses fMRI research reproducibility through transparency of trial design, tools used for data manipulation, and reporting.[4]

Beyond research reporting standards, the American Society of Functional Neuroradiology (ASFNR) perceives the need for increased standardization in clinical practice in an attempt to enhance the communicability of how we assess our patients and the meaningfulness of our imaging findings and reports. Functional MR imaging involves numerous processing steps, which vary among manufacturers of fMRI systems, and this complexity is

From the Mayo Clinic (D.F.B., K.W.), Rochester Minnesota; Memorial Sloan Kettering Cancer Center (B.V.), New York, New York; Boston University School of Medicine (A.M.), Boston, Massachusetts; Johns Hopkins University School of Medicine and the Johns Hopkins Hospital (S.H.F., H.I.S., J.J.P.), Baltimore, Maryland; Children's Hospital of Wisconsin (M.M.), Milwaukee, Wisconsin; and Duke University School of Medicine, (J.R.P.) Durham, North Carolina.

J.J. Pillai and K. Welker are co-senior authors.

Please address correspondence to David F. Black, MD, Mayo Clinic Radiology, 200 First St SW, Rochester, MN 55905; e-mail: black.david@mayo.edu

Indicates open access to non-subscribers at www.ajnr.org

http://dx.doi.org/10.3174/ajnr.A5345

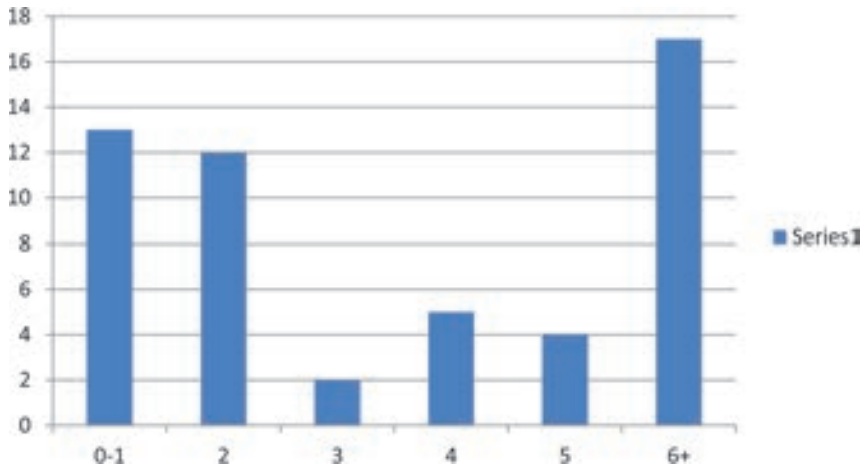

FIG 1. fMRIs performed per month for language assessment at different institutions (about one-third of responders do 6+ per month).

compounded by institution-unique methods for patient training, paradigm choice, and postprocessing. Data sharing is necessary for research integrity and scientific transparency, but current practice variability obscures reproducibility and hinders adequate interinstitutional sharing of information. This widespread variability thereby limits collective progression, particularly in the presurgical assessment of language function—one of the most important applications of fMRI in clinical practice.

Since April 2013, the ASFNR has hosted a monthly teleconference in which clinical fMRI practitioners from across North America have presented presurgical mapping cases from their various practices for educational purposes. This recurring teleconference has highlighted the existing practice variability between institutions. However, it has also offered a regularly occurring, accessible line of communication that has provided impetus for converging practice parameters with a view toward enhanced validation of imaging methodologies, data sharing, and knowledge growth. Consequently, the ASFNR Clinical Practice Committee decided that to strengthen the value of preoperative fMRI language assessment, an ASFNR-approved set of standardized language paradigms should be developed.

Because language can be represented across phonologic, orthographic, semantic, pragmatic, and discourse dimensions and 1 task cannot simultaneously activate all of these aspects, multiple tasks are recommended to provide a more sensitive and specific map of language function that will aid in surgical planning.[5,6] There are a number of desirable features for a standardized fMRI task battery: 1) The ideal fMRI language task paradigm set needs to be appropriately challenging for the patient to produce ample activation without being so difficult as to overwhelm a neurologically compromised or otherwise challenged individual; 2) the tasks need to provide an appropriate balance of sensitivity and specificity for language-related activation; and 3) there needs to be the ability to provide both reliable interhemispheric language lateralization as well as intrahemispheric localization of both expressive and receptive language sites, such as the Broca or Wernicke area, with respect to intracerebral lesions.

Language Paradigm Review Process

Members of an ASFNR Language Paradigm Taskforce were invited to join this project following discussions with the ASFNR Clinical Practice Committee and Executive Committee in an attempt to form a group of interested participants with expertise in the field, a historical perspective of how fMRI has evolved to its current state, and insight into how fMRI must continue to change to further the field.

As a first step, the members of the taskforce discussed their own institution's paradigm choices, practice parameters, and the value of combining results from multiple paradigms. From these discussions, project goals and scope were distilled, including the concept of deriving standardized recommendations that all institutions would hopefully adopt. Initially, the group decided to limit the first iteration of standard paradigms to visually presented paradigms for adult patients with a seventh-grade-equivalent or greater reading ability. Subsequently, it became clear that there was a clinical need to address the pediatric population and adults with limited reading ability, and recommendations for these populations were assessed and developed.

The entire ASFNR membership was polled as to how many language-assessment fMRIs per month were performed at their various institutions to determine the most commonly used language paradigms. The poll attempted to gauge the willingness of ASFNR members to adopt a common set of language paradigms. Poll results were assessed by the taskforce, and an attempt was made to balance current practice preferences across the nation with evidence-based data regarding the variable strengths and weaknesses of various language paradigms. The goal was to choose complementary paradigms that would be reasonably applicable to the greatest number of patients. By balancing current practice and scientific evidence, we hoped to motivate adoption of the standardized task battery by making the required change as simple as possible for the practicing members of the society while at the same time being guided by the scientific evidence. This goal necessitated a literature review for each of the most commonly used language paradigms.

Two-hundred fifty-nine requests for surveys were sent out with 6 e-mail addresses failing. Fifty-three of 253 responded (21%). Figure 1 depicts the number of fMRIs performed per month for language assessment at different institutions. Fifty-seven percent (30/53) of the responders reported being very likely to adopt language paradigm algorithms, and only 8% (4/53) reported being unlikely to adopt ASFNR recommendations (Fig 2).

Results of the ASFNR poll produced 3 tiers of commonly used paradigms across the nation (Fig 3). In the poll, Silent Word Generation (SWG) and Sentence Completion (SC) stood out as the most frequently employed tasks while Verb Generation, Object Naming, Rhyming, and Reading Comprehension seemed to coalesce in a second-tier group. Because SWG and SC were the most

commonly used paradigms and also had support in the literature for being reliable and useful, these tasks were favored to form the core of the standard language task battery. However, because a combination of language paradigms has been shown to increase sensitivity and specificity, a third task was considered desirable.[7,8] Nevertheless, converging on a single choice for that third task proved to be more difficult because the taskforce wanted to maintain flexibility for the radiologist to tailor an examination to the patient's specific clinical scenario.[9,10]

Once the paradigm recommendations were decided upon, the taskforce then converged on the specific scanning parameters and stimuli for the paradigms such that the tasks would be vendor-neutral.

ASFNR Recommendations

Following an analysis of the poll results as well as literature review regarding each of the paradigm tasks mentioned in the poll, the ASFNR taskforce developed language algorithms for both adults and pediatric subjects (Figs 4 and 5).

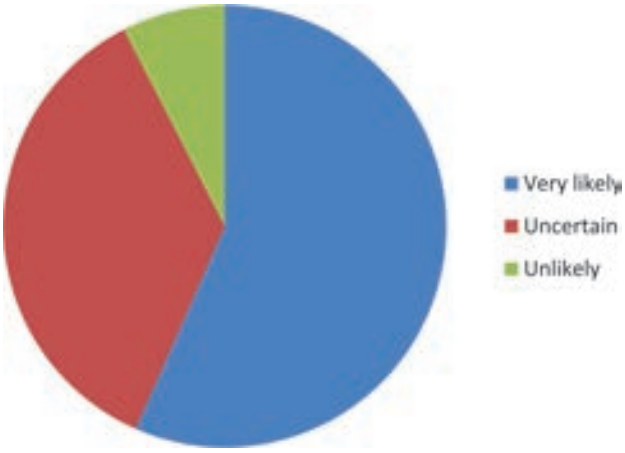

FIG 2. Fifty-seven percent (30/53) of responders reported being very likely to adopt language paradigm algorithms, and only 8% (4/53) reported being unlikely to adopt ASFNR recommendations.

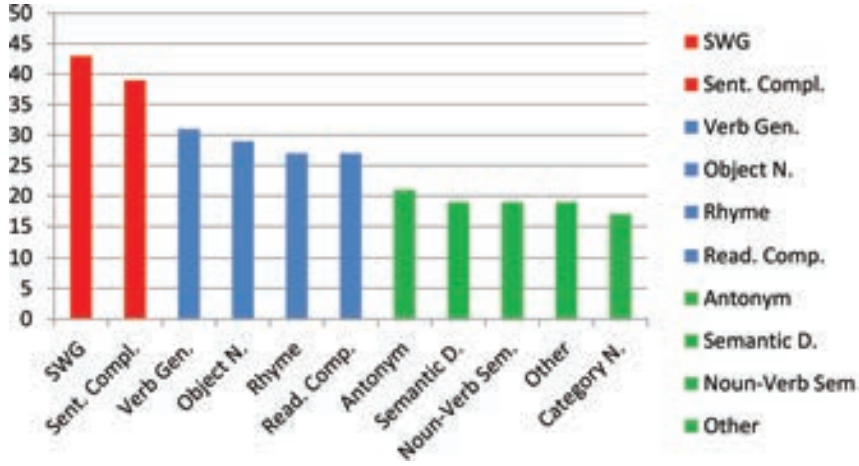

FIG 3. The most commonly used language paradigms were sorted into 3 tiers with the total number of imagers by using the paradigms represented on the y-axis. The first tier included SWG and Sentence Completion. The second tier included Verb Generation, Object Naming, Rhyming, and Reading Comprehension. The third tier included Antonym Generation, Semantic Decision, Noun-Verb Semantic Association, Category Naming, and other.

The default adult algorithm includes SC, SWG, and Rhyming. However, to satisfy the need to customize the analysis to the specific clinical scenario, the radiologist may choose to drop Rhyming and repeat the SC or SWG task as a means of confirming and correlating activations between time courses. SC most often offers more robust language area activation than SWG; thus, it would be the most appropriate task to repeat. In patients who may have difficulty adequately performing the SC or SWG tasks, the radiologist may choose either the Object Naming (ON) or Passive Story Listening (PSL) tasks. This also allows customization in that ON is primarily an expressive task and PSL is primarily receptive.

The default pediatric algorithm includes SC, Rhyming, and Antonym Generation (AG), but for those patients unable to adequately perform Rhyming, the PSL task should be used instead. In general, this pediatric algorithm should apply to most patients 5–11 years of age, but each patient's ability to adequately perform tasks should be assessed before the scan.

In addition to the language-specific tasks, breath hold fMRI may enhance the fMRI language task battery by identifying areas of potentially false-negative activation. By elevating blood carbon dioxide levels, a breath hold task measures cerebrovascular reactivity throughout the brain. It can therefore help demonstrate potential neurovascular uncoupling or confounding susceptibility artifacts as regions of absent or reduced blood oxygen level–dependent (BOLD) signal in response to breath holding, thereby clarifying regions of false-negative language activation. Due to atypical postprocessing requirements for this task, inclusion of the breath holding task is not considered to be a required component of the language task battery but is nonetheless recommended if available at an institution, to assess potential loss of sensitivity to the BOLD signal, which would influence the confidence level of the interpretation.

DISCUSSION

We have generated an adult and a pediatric algorithm to be used as the standard paradigms for presurgical language fMRI assessment (Figs 4 and 5). The scanning parameters for each of these tasks are listed in the Appendix. The ASFNR contends that all institutions should be performing the same paradigms because disparity of practice limits progress in the field and converging clinical practice is necessary to ensure that we all provide the best possible care to our patients. The following sections provide a brief review of each of these tasks, and the Table summarizes individual task utilities.

Sentence Completion Task

The Sentence Completion language task is one of the many language paradigms that can be used for language localization and hemispheric lateralization for identifying the primary language cortex. SC is a semantic language paradigm that is effective in activating the superior temporal gyrus in the Wernicke area.[11]

SC can also activate the Broca area in the dominant hemisphere because the task requires both receptive and expressive language processing, though activation of Broca is slightly less robust than in Wernicke.[11] Additionally, the pattern of activation with SC is less lateralized to Broca compared with SWG because of involvement of the homologous right hemisphere in speech-comprehension tasks, which invoke executive processing.[7,12] Since verbal comprehension tasks such as SC involve visual processing, activation of the ventral language stream, including the visual word form area, can also be seen.[13,14] SC has been found to produce increased activation in both temporal and frontal regions compared with a word generation task, suggesting more robust activation of language networks because it combines language comprehension as well as production in a naturalistic fashion.[15]

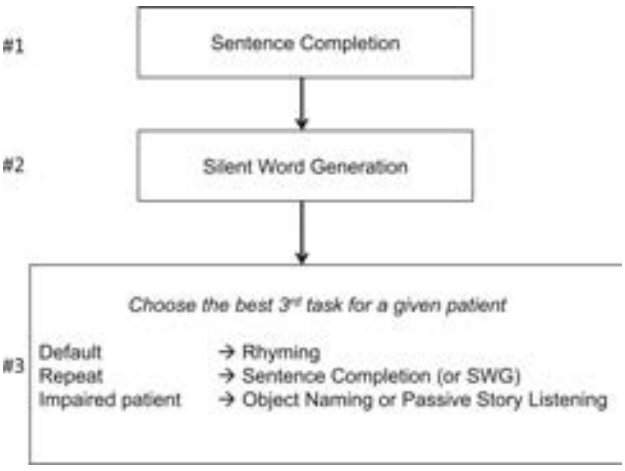

FIG 4. Adult algorithm for presurgical language fMRI.

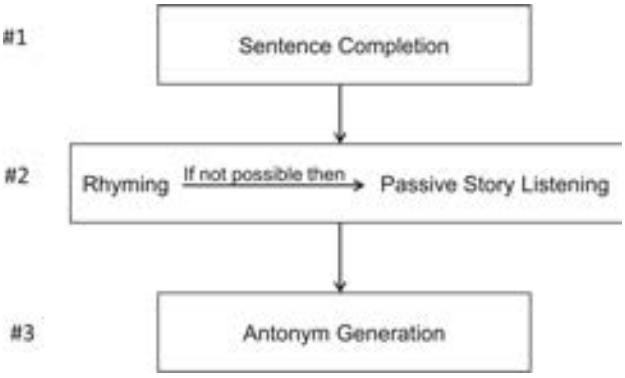

FIG 5. Pediatric algorithm for presurgical language fMRI.

Summary of individual task usefulness

Paradigm	Areas Activated	Pertinent Notes
Sentence Completion	Temporal > frontal	Robust overall
	Ventral language stream	May repeat
Silent Word Generation	Frontal > temporal	More lateralizing than SC
	Middle frontal gyrus	No patient performance metric
Rhyming	Frontal > temporal	More lateralizing than SC
	Middle frontal gyrus	
Object Naming	Frontal > temporal	Most patients can perform
Antonym Generation	Frontal > temporal	Good for pediatric patients
	Middle frontal gyrus	No patient performance metric
	Geschwind	
Passive Story Listening	Temporal > frontal	Easy task for pediatrics or impaired adults

The control task for SC uses gibberish sentences devoid of the semantic, syntactic, and lexicalization demands that are present in the active task.

Silent Word Generation Task

Silent Word Generation is a commonly applied clinical language fMRI paradigm for presurgical mapping with extensive comparisons with Wada testing.[11,14,16-19]

Like most word generation paradigms, SWG tasks activate mainly frontal lobe language and cognitive support areas but are less consistent activators of temporal language regions.[11,14,19,20] Specifically, SWG tasks yield reliable activation of the inferior frontal gyrus, dorsolateral prefrontal cortex, and superior frontal gyrus, with variable activation in the anterior cingulate gyrus, presupplementary motor area, and inferior, middle, and superior temporal gyri.[14,16,17,21,22]

Several studies have validated the SWG paradigm for both language lateralization and localization.[21-26] For example, Yetkin et al[23] reported 100% sensitivity of fMRI by using a SWG task for activation within 20 mm of the electrically stimulated cortical site during ECS and 86% sensitivity within 10 mm in a mixed series of 28 patients with predominantly epilepsy ($n = 22$) and cerebral lesions. Brannen et al[24] studied the reliability, precision, and accuracy of word generation tasks in mapping the Broca area in 34 patients with cerebral lesions by comparing regions of activation with awake (ECS) mapping of speech function during craniotomy. They noted that SWG tasks activated Brodmann areas 44 or 46 either individually or both unilaterally or bilaterally in most patients in the series with variable activation of Brodmann areas 9 and 45. Activation was noted in the same gyri when the patient performed a second iteration of the SWG task, and speech areas located with ECS coincided with areas of the brain activated with the SWG task. Comparing hemispheric language dominance by using an SWG task with results of Wada testing in a large series of 100 patients with epilepsy, Woerman et al[27] found 91% concordance between both tests. Similarly, Sabbah et al[21] demonstrated that fMRI language lateralization based on the SWG was concordant with the Wada test in 19 of 20 patients with intractable partial epilepsy.

Pillai's group compared the localization (as locally detectable statistically significant percentage signal change) and lateralization among 5 language paradigms: SWG, Sentence Completion, Visual Antonym Pair, Auditory Antonym Pair, and Noun-Verb Association in 5 ROIs: inferior frontal gyrus, middle frontal gyrus, and superior frontal gyrus for expressive language activation; and middle temporal gyrus and superior temporal gyrus for receptive language activation in a group of 12 healthy volunteers.[14] The results of this study found that SWG was the most robust paradigm for language localization and the most effective for determining language lateralization in the expressive ROIs of the dominant language hemisphere. In contrast, the analysis of patterns of activation in the receptive ROIs in the temporal gyri demonstrated a weaker BOLD percentage signal change for SWG tasks

in both hemispheres when compared with the other 4 paradigms that include some form of language comprehension in the active blocks of the paradigm, which are localized in the angular and middle temporal gyri.[28]

A typical control used for the SWG task employs nonsense symbols without the phonemic fluency-processing demands of the active task.

Rhyming Task

Rhyming is considered a phonologic task that has been shown to robustly activate the Broca area in the dominant hemisphere.[17] Rhyming also activates the Wernicke area though not as strongly as seen in Broca.[11] In addition to the above regions, Rhyming has been shown to activate the inferior parietal lobule, the dorsolateral prefrontal cortex, and posterior lateral gyrus.[29] Rhyming and SWG are the 2 paradigms found to be most helpful for language lateralization compared with Sentence Completion and Noun-Verb Association.[11] As with Sentence Completion, there is activation of the posterior temporo-occipital regions due to involvement of the visual processing pathways.[13]

Studies comparing the relative effectiveness of different commonly used expressive and receptive language paradigms by using both threshold-independent and threshold-dependent methods in patients with brain tumors demonstrated that SWG and Rhyming were more helpful for language lateralization than SC or Noun-Verb Association.[11,19] The Rhyming task has several advantages over the SWG task: It results in more specific activation of language areas than SWG, has a higher mean laterality index (LI) value, and is less threshold-dependent than SWG for determining the LI.[11,17,19] Nevertheless, both SWG and Rhyming demonstrate adequate language lateralization, even in a subgroup of patients with brain tumors located in the left hemisphere and in the frontal or parietal lobes.[19] This has clinical implications since the presence of susceptibility artifacts or neurovascular uncoupling associated with tumors in the dominant hemisphere could affect the strength of the BOLD signal.

The control task most often employs nonsense symbols wherein the patient is asked whether 2 sets of symbols are oriented in the same fashion, which allows monitoring of the patient's attention and task engagement without stimulating phonologic processing like the active task.

Object Naming Task

Simple Object Naming is an expressive language paradigm in which the subject is shown an object and is asked to silently name the presented object.[30-32] The control block consists of a nonsense symbol to exclude the visual component from the activation maps. The objects are presented in black and white.

ON tasks yield activation in the inferior frontal gyrus, middle frontal gyrus, and ventral occipitotemporal cortex, with variable activation in the posterior temporoparietal cortex.[30,31,33,34] Several studies have validated the ON paradigm for both language lateralization and localization.[8,19,31,34-36] For example, Rutten et al[8] reported that a combination of 3 different fMRI language tasks (ON, Verb Generation, and Sentence Processing) were able to localize critical language areas with 100% sensitivity and 61% specificity when compared with ECS mapping in a group of patients with epilepsy. Similarly, Hirsch et al[31] demonstrated 100% concordance of localization between fMRI and ECS when using ON and word-listening tasks in neurosurgical candidates, most of whom had brain tumors,[36] and Pouratian et al[35] demonstrated 100% sensitivity and 67% specificity for frontal language regions when correlating ECS mapping and fMRI in patients with vascular malformations who performed Object Naming, Word Generation, and auditory-response naming tasks.

Although ON provides relatively good localization predominantly of frontal language regions, the general consensus is that the activation pattern associated with ON does not allow as effective hemispheric language lateralization as with other expressive language paradigms such as SWG, Verb Generation, and Rhyming.[19,34] Moreover, like other covert paradigms, the ON task does not allow monitoring of patient responses. Despite these limitations, the ON task is easy for most patients to perform and is therefore often utilized in patients with cognitive impairment or pediatric patients, and it is frequently used during intraoperative cortical stimulation.

Antonym Generation Task

This word generation paradigm typically presents the patient with 1 word at a time, and the patient is asked to silently think of the word that means the opposite. Typically, during each activity period, 5–10 words are sequentially presented on the screen, and during the rest period, a black blank screen is presented with a white crosshair in the center for visual fixation.

This paradigm stimulates phonologic, working memory, lexical search, semantic, and orthographic processes of the speech and language system. Functional maps typically demonstrate activation in the inferior frontal gyrus, middle frontal gyrus, premotor cortex, and frequently posterior peri-Sylvian speech areas (posterior aspect of the superior temporal lobe, supramarginal and angular gyri). Frequent weak activation is also seen in the posterior aspect of the inferior temporal lobe, possibly due to engagement of the visual word form systems.[37-40] Because there is no control for visual sensory processing during the resting phase, frequently, bilateral primary visual cortex activation is also seen.

The Antonym Generation task is reported to provide a higher percentage BOLD signal change in the Broca area (versus baseline) compared with the Antonym Decision task (versus baseline).[41] It is reported that activation of the speech areas and speech lateralization in the various Word Generation tasks (letter, category, antonym word generation) is comparable.[42] However, in our experience with pediatric patients, the Antonym Generation paradigm does much better in terms of the extent of activation in the speech areas and patient compliance versus letter Word Generation tasks; thus, SWG was not included in the pediatric algorithm. One of the limitations of this paradigm is that given the design, it is difficult to assess patient performance.

Passive Story Listening Task

Passively listening to an aurally presented story involves multiple aspects of language function, including syntactic processing and word recognition. This task offers the advantage of being relatively easy to accomplish for young children or adults whose func-

tional impairments limit their ability to adequately partake in more complex language paradigms.

Passive Story Listening has been shown in pediatric populations to produce activation in the bilateral superior temporal gyrus, bilateral superior frontal gyrus, and left posterior superior temporal gyrus.[43-46] The ease of performing PSL in young or impaired adult patients must be balanced with the lack of a task performance metric and its relatively weak language activation. There is no way to know if the patient is actually listening and attending to the story during the scan, but patients may be asked to recount the stories they heard following the scan as an indirect means of assessing compliance.

Scanner noise can impede the quality and magnitude of language activation during aurally presented tasks.[47] Vannest et al[48] compared similar PSL and active-response tasks and found that both produced language activation in similar patterns of the frontal and temporal lobes but the active-response task produced more dorsolateral prefrontal activation, likely due to engagement of working memory and attention during the comprehension questions. No significant difference in hemispheric lateralization was observed. Although adding an active-response component increased memory and attention engagement as well as effect size in the left inferior frontal gyrus, we chose the simpler version of this task because it still provides adequate activation and lateralization of language function while applying to the greatest range of children and/or impaired adult patients. The control task typically involves reversed playback of the same story to remove semantic processing from the sounds presented or simply playing tones.

Breath Hold Task

One task that may be performed for quality control purposes as part of standard clinical presurgical mapping fMRI examinations is the breath hold task. Using such a task, one can alternate brief breath hold periods with periods of normal self-paced respiration in a standard block design paradigm. A general linear model analysis can be performed to evaluate percentage BOLD signal change occurring during the hypercapnia state relative to the normocapnia condition. Although one may utilize either end-inspiratory or end-expiratory breath holds to induce the transient hypercapnia, and both approaches have relative strengths and weaknesses (eg, some studies have shown greater reproducibility with the latter approach), we have found that in general, the end-inspiratory technique is easier for patients to perform and can be performed even by neurologically debilitated patients.[49-51] The purpose of this task is to evaluate cerebrovascular reactivity (CVR) in a relatively quick, easy, and effective manner without the need for exogenous controlled gas administration as is frequently used for quantitative CVR research studies.[52-55] Although emerging resting-state BOLD imaging approaches have been suggested as well for assessment of CVR, there remains some controversy regarding the reliability of such methods such as resting-state fluctuation of amplitude, and thus they cannot be recommended currently.[56-58]

The main value of this method is its utility in detecting neurovascular uncoupling potential in patients with focal resectable brain lesions such as tumors, vascular malformations, or cortical developmental abnormalities. Neurovascular uncoupling (NVU) refers to the breakdown of the normal neurovascular coupling cascade related to factors such as tumor angiogenesis, astrocytic dysfunction, neurotransmitter, or other biochemical dysfunction or abnormalities of intralesional or perilesional hemodynamics. Generally, the final step in the cascade involves the vascular response related to regional neuronal activation, and thus most cases of NVU manifest as abnormally decreased or absent regional vascular reactivity within or immediately adjacent to the brain lesion of interest.[49,59-63] Determining potential NVU increases the clinical utility of fMRI by uncovering false-negative language activations in the eloquent cortex.

CONCLUSIONS

The ASFNR proposes that institutions performing presurgical language fMRI consider adopting these recommended paradigm algorithms as standard clinical practice. The algorithms were created with an attempt to balance paradigms that primarily activate frontal/expressive regions (SWG, AG, ON) and those that primarily activate temporal/receptive areas (SC, PSL). Paradigms were also chosen to balance varying levels of sensitivity and specificity as well as strengths in lateralization and localization. The algorithms are meant to provide easily adopted, clinically useful paradigms that would apply to the greatest number of clinical scenarios. The tasks can be downloaded for free at https://www.asfnr.org/paradigms/.

Using common paradigms is only the first necessary step in practice convergence in an effort to reduce the widespread variability in clinical fMRI. By design, it is expected that these recommendations will change with time. The commonality that they provide will allow interinstitutional comparisons that will eventually provide insights into the best methodologies, enhance the value of every institution's fMRI program, and provide a common frame of reference from which the field can advance.

Radiologists, especially those who have innovated and created fMRI tasks that are used on a daily basis in their respective practices, may be hesitant to discard their favorite, personally developed language tasks in the name of standardization and convergence. Moreover, interinstitutional standardization runs against the normal business model of attempting to differentiate one's practice from one's competitors. However, adopting standard paradigms is the natural evolution of a technology that is initially replete with locally derived, often ingenious methods that because of their uniqueness, unfortunately limit meaningful communication with other professionals as well as the ability to generalize clinical and research contributions beyond one's own walls.

Converging language paradigms are only a small component of fMRI practice. Ongoing variability in terms of MR imaging scanner models, patient training sessions, and postprocessing techniques will continue to impact the generalizability of fMRI results. Institutions will still be able to differentiate themselves through interpretation quality and other patient care metrics. While there are varying degrees of support for these language paradigms in the literature, the most compelling aspect in favor of adopting this set of tasks is that they are already widely used in clinical practice.

APPENDIX: MINIMUM ACCEPTABLE SCANNER PARAMETERS FOR PERFORMING ASFNR-RECOMMENDED LANGUAGE PARADIGMS

The actual content of each paradigm will be available for download on the ASFNR Web site (https://www.asfnr.org/paradigms/).

Task list

1) Sentence Completion
2) Silent Word Generation
3) Rhyming
4) Antonym Generation
5) Passive Story Listening
6) Object Naming

*1) Sentence Completion Task Parameters**

Gradient-echo EPI sequence

Field strength: 3T
TR: 2000 ms
TE: 30 ms
Matrix: 64 × 64
FOV: 24 cm
Section thickness: 4 mm
Parallel factor: 2
Scan length: 4 minutes
Font: 42-point Times New Roman font (on a standard PowerPoint slide) in white with a black background.

Stimuli: The patient is shown incomplete sentences and is instructed to subvocally think of a word or words to complete the sentence. If there is time, the patient should continue to think of alternate words that complete the sentence before the next incomplete sentence being presented. Four sentences per 20 seconds. This stimulus timeframe is repeated 6 times.

Control: Patient views nonsense sentences. Four nonsense sentences per 20 seconds.

*From Faro et al multicenter ongoing trial.

*2) Silent Word Generation Task Parameters**

Gradient-echo EPI sequence

Field strength: 3T
TR: 2000 ms
TE: 30 ms
Matrix: 64 × 64
FOV: 24 cm
Section thickness: 4 mm
Parallel factor: 2
Scan length: 4 minutes
Font: Times New Roman font size 117 (on a standard PowerPoint slide), white font on black background.

Stimuli: A test of phonemic fluency wherein a patient is shown a single letter and asked to subvocally think of as many words that start with that letter as they possibly can before the image changes to either the control or the next letter. Ten seconds per letter. The patient can be instructed to press a button with each word they think of as a means of monitoring their active engagement with the task.

Control: Patient views nonsense symbols (10 seconds per nonsense symbol).

Six cycles = 4 minutes

*From Faro et al multicenter ongoing trial.

3) Rhyming Task Parameters

Gradient-echo EPI sequence

Field strength: 3T
TR: 2000 ms
TE: 30 ms
Matrix: 64 × 64
FOV: 24 cm
Section thickness: 4 mm
Parallel factor: 2
Scan length: 4 minutes
Font: Times New Roman font size 200 (on a standard PowerPoint slide), white font on black background.

Stimuli: The patient is shown 2 words, one on top of the other, and asked to respond with a button press if the 2 words rhyme. If the words do not rhyme, no button press should occur. Five word pairs per 20 seconds.

Control: Two sets of 5 differently oriented lines (one set on top of the other) are shown to the patient, who is asked to respond with a button press if the 2 sets are oriented in an identical fashion. If not, no button press is needed.

4) Antonym Generation Task Parameters

Gradient-echo EPI sequence

Field strength: 3T
TR: 2000 ms
TE: 30 ms
Matrix: 64 × 64
FOV: 24 cm
Section thickness: 4 mm
Parallel factor: 2
Scan length: 2 minutes 40 seconds
Font: Times New Roman font size 44 (on a standard PowerPoint slide), white font on black background.

Stimuli: The patient is shown single words and asked to generate an opposite-meaning word in his or her mind. Ten words per block and a total of 4 blocks. Each word remains on the screen for 2 seconds.

Control: Simple crosshair in the center of the screen lasts for 20 seconds for each block.

5) Passive Story Listening Task Parameters

Gradient-echo EPI sequence

Field strength: 3T
TR: 2000 ms
TE: 30 ms
Matrix: 64 × 64
FOV: 24 cm
Section thickness: 4 mm
Parallel factor: 2
Scan length: 4 minutes
Font: This is an aurally presented paradigm.

Stimuli: The patient listens to 20 seconds of a story (selected passages from "The Tale of Peter Rabbit," by Beatrix Potter). Alternates with control for a total of 4 minutes.

Control: The patient listens to 20 seconds of the same story played backwards.

(Reading performed by Ann Marie Rydberg)

6) Object Naming Task Parameters

Gradient-echo EPI sequence

Field strength: 3T

TR: 2000 ms

TE: 30 ms

Matrix: 64 × 64

FOV: 24 cm

Section thickness: 4 mm

Parallel factor: 2

Scan length: 4 minutes

Font: Similarly sized images and symbols will be shown (no text).

Stimuli: White outline images of objects on a black background will be shown to the patient who will be asked to covertly/silently name the object. One object is presented approximately every 3 seconds.

Control: Nonsense symbols are shown to the patient, and he or she does nothing other than attend to what is being shown. One symbol is presented approximately every 3 seconds.

Breath Hold Task Parameters

(Recommended but not part of the specified algorithms)

Gradient-echo EPI sequence

Field strength: 3T

TR: 2000 ms

TE: 30 ms

Matrix: 64 × 64

FOV: 24 cm

Section thickness: 4 mm

Parallel factor: 2

Scan length: 4 minutes 20 seconds

Font: Times New Roman font size 44 (on a standard PowerPoint slide), white font on black background.

Technique: Slow controlled 4-second inspiration followed by a 16-second breath hold. This is then followed by a 40-second block of self-paced normal breathing. This cycle is repeated 4 times with an additional 20-second period of normal breathing for a total task duration of 4 minutes 20 seconds.

From: Pillai JJ, Mikulis DJ. Cerebrovascular reactivity mapping: an evolving standard for clinical functional imaging. *AJNR Am J Neuroradiol* 2015;36:7-13.

REFERENCES

1. Stippich C, Rapps N, Dreyhaupt J, et al. **Localizing and lateralizing language in patients with brain tumors: feasibility of routine preoperative functional MR imaging in 81 consecutive patients.** *Radiology* 2007;243:828-36 CrossRef Medline
2. FitzGerald DB, Cosgrove GR, Ronner S, et al. **Location of language in the cortex: a comparison between functional MR imaging and electrocortical stimulation.** *AJNR Am J Neuroradiol* 1997;18:1529-39 Medline
3. Haag A, Bonelli S. **Clinical application of language and memory fMRI in epilepsy.** *Epileptologie* 2013;30:101-08
4. Nichols T, Das S, Eickhoff S, et al. **Best practices in data analysis and sharing in neuroimaging using MRI.** *Nat Neurosci* 2017;20:299-303 CrossRef Medline
5. Deblaere K, Backes WH, Hofman P, et al. **Developing a comprehensive presurgical functional MRI protocol for patients with intractable temporal lobe epilepsy: a pilot study.** *Neuroradiology* 2002;44:667-73 CrossRef Medline
6. Ojemann JG, Buckner RL, Akbudak E, et al. **Functional MRI studies of word-stem completion: reliability across laboratories and comparison to blood flow imaging with PET.** *Hum Brain Mapp* 1998;6:203-15 Medline
7. Niskanen E, Kononen M, Villberg V, et al. **The effect of fMRI task combinations on determining the hemispheric dominance of language functions.** *Neuroradiology* 2012;54:393-405 CrossRef Medline
8. Rutten GJ, Ramsey NF, van Rijen PC, et al. **Development of a functional magnetic resonance imaging protocol for intraoperative localization of critical temporoparietal language areas.** *Ann Neurol* 2002;51:350-60 CrossRef Medline
9. Gaillard WD, Balsamo L, Xu B, et al. **fMRI language task panel improves determination of language dominance.** *Neurology* 2004;63:1403-08 CrossRef Medline
10. Rutten GJ, Ramsey NF, van Rijen PC, et al. **FMRI-determined language lateralization in patients with unilateral or mixed language dominance according to the Wada test.** *Neuroimage* 2002;17:447-60 CrossRef Medline
11. Zacà D, Nickerson JP, Deib G, et al. **Effectiveness of four different clinical fMRI paradigms for preoperative regional determination of language lateralization in patients with brain tumors.** *Neuroradiology* 2012;54:1015-25 CrossRef Medline
12. Vigneau M, Beaucousin V, Herve PY, et al. **What is right-hemisphere contribution to phonological, lexico-semantic, and sentence processing? Insights from a meta-analysis.** *Neuroimage* 2011;54:577-93 CrossRef Medline
13. Ischebeck A, Indefrey P, Usui N, et al. **Reading in a regular orthography: an FMRI study investigating the role of visual familiarity.** *J Cogn Neurosci* 2004;16:727-41 CrossRef Medline
14. Zaca D, Jarso S, Pillai JJ. **Role of semantic paradigms for optimization of language mapping in clinical FMRI studies.** *AJNR Am J Neuroradiol* 2013;34:1966-71 CrossRef Medline
15. Barnett A, Marty-Dugas J, McAndrews MP. **Advantages of sentence-level fMRI language tasks in presurgical language mapping for temporal lobe epilepsy.** *Epilepsy Behav* 2014;32:114-20 CrossRef Medline
16. Cuenod CA, Bookheimer SY, Hertz-Pannier L, et al. **Functional MRI during word generation, using conventional equipment: a potential tool for language localization in the clinical environment.** *Neurology* 1995;45:1821-27 CrossRef Medline
17. Lurito JT, Kareken DA, Lowe MJ, et al. **Comparison of rhyming and word generation with FMRI.** *Hum Brain Mapp* 2000;10:99-106 Medline
18. Yetkin FZ, Hammeke TA, Swanson SJ, et al. **A comparison of functional MR activation patterns during silent and audible language tasks.** *AJNR Am J Neuroradiol* 1995;16:1087-92 Medline
19. Pillai JJ, Zaca D. **Relative utility for hemispheric lateralization of different clinical fMRI activation tasks within a comprehensive language paradigm battery in brain tumor patients as assessed by both threshold-dependent and threshold-independent analysis methods.** *Neuroimage* 2011;54(suppl 1):S136–45 CrossRef Medline
20. Stippich C, Blatow M, Krakow K. **Presurgical functional MRI in patients with brain tumors.** In: Stippich C, ed. *Clinical Functional MRI: Presurgical Functional Neuroimaging.* Berlin: Springer-Verlag; 2015:87-135
21. Sabbah P, Chassoux F, Leveque C, et al. **Functional MR imaging in assessment of language dominance in epileptic patients.** *Neuroimage* 2003;18:460-67 CrossRef Medline
22. Friedman L, Kenny JT, Wise AL, et al. **Brain activation during silent word generation evaluated with functional MRI.** *Brain Lang* 1998;64:231-56 CrossRef Medline
23. Yetkin FZ, Mueller WM, Morris GL, et al. **Functional MR activation**

correlated with intraoperative cortical mapping. *AJNR Am J Neuroradiol* 1997;18:1311-15 Medline
24. Brannen JH, Badie B, Moritz CH, et al. **Reliability of functional MR imaging with word-generation tasks for mapping Broca's area.** *AJNR Am J Neuroradiol* 2001;22:1711-18 Medline
25. Hertz-Pannier L, Gaillard WD, Mott SH, et al. **Noninvasive assessment of language dominance in children and adolescents with functional MRI: a preliminary study.** *Neurology* 1997;48:1003-12 CrossRef Medline
26. Yetkin FZ, Swanson S, Fischer M, et al. **Functional MR of frontal lobe activation: comparison with Wada language results.** *AJNR Am J Neuroradiol* 1998;19:1095-98 Medline
27. Woermann FG, Jokeit H, Luerding R, et al. **Language lateralization by Wada test and fMRI in 100 patients with epilepsy.** *Neurology* 2003;61:699-701 CrossRef Medline
28. Vandenberghe R, Price C, Wise R, et al. **Functional anatomy of a common semantic system for words and pictures.** *Nature* 1996;383:254-56 CrossRef Medline
29. Cousin E, Peyrin C, Pichat C, et al. **Functional MRI approach for assessing hemispheric predominance of regions activated by a phonological and a semantic task.** *Eur J Radiol* 2007;63:274-85 CrossRef Medline
30. Hirsch J, Moreno DR, Kim KH. **Interconnected large-scale systems for three fundamental cognitive tasks revealed by functional MRI.** *J Cogn Neurosci* 2001;13:389-405 CrossRef Medline
31. Hirsch J, Ruge MI, Kim KH, et al. **An integrated functional magnetic resonance imaging procedure for preoperative mapping of cortical areas associated with tactile, motor, language, and visual functions.** *Neurosurgery* 2000;47:711-21; discussion 721-22 Medline
32. Lurito JT, Kareken DA, Dzemidzic M, et al. **Functional MRI of covert object naming.** *Neuroimage* 2000;11:S285 CrossRef
33. Baldo JV, Arévalo A, Patterson JP, et al. **Grey and white matter correlates of picture naming: evidence from a voxel-based lesion analysis of the Boston Naming Test.** *Cortex* 2013;49:658-67 CrossRef Medline
34. Zaca D, Pillai JJ. **Bold fMRI for Presurgical Planning, Part I.** In: Pillai JJ, ed. *Functional Brain Tumor Imaging.* New York: Springer-Verlag; 2014:59-78
35. Pouratian N, Bookheimer SY, Rex DE, et al. **Utility of preoperative functional magnetic resonance imaging for identifying language cortices in patients with vascular malformations.** *J Neurosurg* 2002;97:21-32 CrossRef Medline
36. Ruge MI, Victor J, Hosain S, et al. **Concordance between functional magnetic resonance imaging and intraoperative language mapping.** *Stereotact Funct Neurosurg* 1999;72:95-102 Medline
37. Binder J. **fMRI of language systems: methods and applications.** In: Faro SA, Mohamed FB, eds. *Functional Neuroradiology Principles and Clinical Applications.* 2nd ed. Boston: Springer-Verlag; 2012:398-401
38. Liégeois F, Connelly A, Salmond CH, et al. **A direct test for lateralization of language activation using fMRI: comparison with invasive assessments in children with epilepsy.** *Neuroimage* 2002;17:1861-67 CrossRef Medline
39. Warburton E, Wise RJ, Price CJ, et al. **Noun and verb retrieval by normal subjects: studies with PET.** *Brain* 1996;119(pt 1):159-79 CrossRef Medline
40. Wise R, Chollet F, Hadar U, et al. **Distribution of cortical neural networks involved in word comprehension and word retrieval.** *Brain* 1991;114(pt 4):1803-17 CrossRef Medline
41. Dodoo-Schittko F, Rosengarth K, Doenitz C, et al. **Assessing language dominance with functional MRI: the role of control tasks and statistical analysis.** *Neuropsychologia* 2012;50:2684-91 CrossRef Medline
42. Rutten GJ, Ramsey NF, van Rijen PC, et al. **Reproducibility of fMRI-determined language lateralization in individual subjects.** *Brain Lang* 2002;80:421-37 CrossRef Medline
43. Karunanayaka PR, Holland SK, Schmithorst VJ, et al. **Age-related connectivity changes in fMRI data from children listening to stories.** *Neuroimage* 2007;34:349-60 CrossRef Medline
44. Schmithorst VJ, Holland SK, Plante E. **Cognitive modules utilized for narrative comprehension in children: a functional magnetic resonance imaging study.** *Neuroimage* 2006;29:254-66 CrossRef Medline
45. Schmithorst VJ, Holland SK, Plante E. **Development of effective connectivity for narrative comprehension in children.** *Neuroreport* 2007;18:1411-15 CrossRef Medline
46. Ahmad Z, Balsamo LM, Sachs BC, et al. **Auditory comprehension of language in young children: neural networks identified with fMRI.** *Neurology* 2003;60:1598-605 CrossRef Medline
47. Schmidt CF, Zaehle T, Meyer M, et al. **Silent and continuous fMRI scanning differentially modulate activation in an auditory language comprehension task.** *Hum Brain Mapp* 2008;29:46-56 CrossRef Medline
48. Vannest JJ, Karunanayaka PR, Altaye M, et al. **Comparison of fMRI data from passive listening and active-response story processing tasks in children.** *J Magn Reson Imaging* 2009;29:971-76 CrossRef Medline
49. Pillai JJ, Mikulis DJ. **Cerebrovascular reactivity mapping: an evolving standard for clinical functional imaging.** *AJNR Am J Neuroradiol* 2015;36:7-13 CrossRef Medline
50. Scouten A, Schwarzbauer C. **Paced respiration with end-expiration technique offers superior BOLD signal repeatability for breath-hold studies.** *Neuroimage* 2008;43:250-57 CrossRef Medline
51. Thomason ME, Glover GH. **Controlled inspiration depth reduces variance in breath-holding-induced BOLD signal.** *Neuroimage* 2008;39:206-14 CrossRef Medline
52. Bright MG, Murphy K. **Reliable quantification of BOLD fMRI cerebrovascular reactivity despite poor breath-hold performance.** *Neuroimage* 2013;83:559-68 CrossRef Medline
53. Kastrup A, Krüger G, Neumann-Haefelin T, et al. **Assessment of cerebrovascular reactivity with functional magnetic resonance imaging: comparison of CO(2) and breath holding.** *Magn Reson Imaging* 2001;19:13-20 CrossRef Medline
54. Magon S, Basso G, Farace P, et al. **Reproducibility of BOLD signal change induced by breath holding.** *Neuroimage* 2009;45:702-12 CrossRef Medline
55. Tancredi FB, Hoge RD. **Comparison of cerebral vascular reactivity measures obtained using breath-holding and CO2 inhalation.** *J Cereb Blood Flow Metab* 2013;33:1066-74 CrossRef Medline
56. Jahanian H, Christen T, Moseley ME, et al; SPRINT Study Research Group. **Measuring vascular reactivity with resting-state blood oxygenation level-dependent (BOLD) signal fluctuations: a potential alternative to the breath-holding challenge?** *J Cereb Blood Flow Metab* 2017;37:2526-38 CrossRef Medline
57. Kannurpatti SS, Motes MA, Biswal BB, et al. **Assessment of unconstrained cerebrovascular reactivity marker for large age-range FMRI studies.** *PLoS One* 2014;9:e88751 CrossRef Medline
58. Lipp I, Murphy K, Caseras X, et al. **Agreement and repeatability of vascular reactivity estimates based on a breath-hold task and a resting state scan.** *Neuroimage* 2015;113:387-96 CrossRef Medline
59. Hsu YY, Chang CN, Jung SM, et al. **Blood oxygenation level-dependent MRI of cerebral gliomas during breath holding.** *J Magn Reson Imaging* 2004;19:160-67 CrossRef Medline
60. Iranmahboob A, Peck KK, Brennan NP, et al. **Vascular reactivity maps in patients with gliomas using breath-holding BOLD fMRI.** *J Neuroimaging* 2016;26:232-39 CrossRef Medline
61. Pillai JJ, Zacá D. **Clinical utility of cerebrovascular reactivity mapping in patients with low grade gliomas.** *World J Clin Oncol* 2011;2:397-403 CrossRef Medline
62. Pillai JJ, Zacà D. **Comparison of BOLD cerebrovascular reactivity mapping and DSC MR perfusion imaging for prediction of neurovascular uncoupling potential in brain tumors.** *Technol Cancer Res Treat* 2012;11:361-74 CrossRef Medline
63. Zaca D, Hua J, Pillai JJ. **Cerebrovascular reactivity mapping for brain tumor presurgical planning.** *World J Clin Oncol* 2011;2:289-98 CrossRef Medline

Torgny Greitz, MD, PhD, FACR, Professor of Neuroradiology, Emeritus

Torgny Vilhelm Bernhard Greitz, MD, Professor at the Karolinska Institutet, distinguished leader and innovator of neuroradiology, died August 1, 2016. He was trained in the Stockholm School of Neuroradiology at the Serafimer Hospital, where neurosurgery, headed by Herbert Olivecrona, and neuroradiology at the helm of Erik Lysholm were developed in close cooperation during the 1930s and 1940s. In his capacity as chief of the Department of Neuroradiology at the Karolinska Hospital, he has conveyed to new generations the know-how of those days with great astuteness. In the early digital era, he was a front figure in the development of clinical applications of CT and positron-emission tomography.

Torgny Greitz's influence on North American neuroradiology was considerable. On September 25, 1956, he arrived at Washington University in St. Louis to spend a year practicing and teaching neuroradiology at the Mallinckrodt Institute of Radiology. His visit had been arranged by Lysholm's successor Erik Lindgren, Torgny's teacher at the Serafimer Hospital, who, the year before, had made a lecturing tour to many of the important radiology institutions in the United States. Torgny Greitz's time at the Mallinckrodt Institute of Radiology would make a lasting impression. He introduced the daily routine used at the Serafimer Hospital, which imposed a much more active role for the radiologist than what was the practice in the United States. The radiologist should not merely order a set of x-ray exposures from a radiographer, all according to a fixed program, and afterward file a report but should rather decide the method and the imaging protocol to be used in each case and be busy in the x-ray room; make punctures of arteries or the spinal theca if so needed with the overall objective to establish the anatomic and physiologic state of the patient; and suggest the most probable diagnosis. Torgny proved for anyone to see, including skeptical neurosurgeons, that a trained neuroradiologist was able to perform the then often invasive procedures safely and interpret them accurately. Hugh Wilson, head of radiology in MR imaging, was impressed by Torgny's achievements and encouraged by him; Dr Wilson established a neuroradiology section at the Mallinckrodt Institute of Radiology, which quickly became a role model in the subspecialty. This would inspire other centers to follow. Juan Taveras at the Neuroradiological Institute and Manny Schechter at the Albert Einstein Medical Center, both in New York, started training programs in neuroradiology the same year (1956). At the Silver Jubilee of the American Society of Neuroradiology in 1987, Torgny Greitz from the Stockholm School got recognition for his contributions during the early days of North American neuroradiology.

Torgny Greitz was born in Stockholm on August 13, 1921, the eldest of 3 brothers. His father, Bernhard Greitz, was a media personality, busy, in turn, as a journalist at a daily radical newspaper, as editor of a cultural magazine dedicated to modern literature and poetry, and as culture attaché in Copenhagen. Torgny's mother, Vivi Ramberg, was a bank official, who met her future husband when breaking a leg skiing in Bernhard's company.

School

The family's home was welcoming to a broad circle of friends, many of whom had cultural aspirations. In his memoirs, left unpublished to posterity, Torgny paints a vivid picture of his early life. At 3 years of age, he was so absent-minded that his parents gave him the nickname "the professor." At school, he was soon appreciated and encouraged by his teachers. He became competitive and aspired eagerly to get the better of his classmates. He had an almost uncanny gift for memorizing. He learned his lessons in minimal time and developed an appetite for practical jokes. He describes himself as a mischievous little rascal. In the upper grades at school and continuing during his university years, he devoted himself to a wealth of activities: fine arts like drawing, painting, sculpting, but also athletics like track and field sports, even wrestling and swimming. With his competitive mind, he usually proved to be much above average in most of these activities. He once won the student championship in the decathlon when he managed 3.30 m in the pole vault, at a time when the pole still was made of bamboo (in 1940, the Swedish record was 4.18 m).

Although a talented amateur painter and sculptor, he gave up early thoughts of devoting himself to the arts for a living. A decisive moment was when he read a book, *Microbe Hunters* by Paul de Kruif, about the great pioneers in medicine, among others Paul Ehrlich, Robert Koch, and Louis Pasteur. He was fascinated by the stories about how these researchers with their ingenuity and primitive tools made their revolutionary discoveries. Encouraged by his uncle, Johannes Ramberg, a medical doctor, and last but not least by Erik Lysholm, who was a friend of his parents, he decided to become a physician and devote his life to medical research.

University

He entered medical school at the Karolinska Institutet in 1940, incidentally in the same class as a future life-long friend of his, Sven-Ivar Seldinger, another Swede to become a great innovator of radiology. With cheerful temper, Torgny participated enthusiastically in the amusements of happy student life. An episode that made him and his study companion Lars Gyllensten already renowned when medical students is worth recalling. During a binge on beer and sandwiches, Torgny, on command from his friend, pronounced single words he picked at random from his imagina-

tion or from objects in the room around him. His friend put them together in unrhymed and rather, but not altogether, unintelligible poems. One short example in translation (by his friend Giovanni Ruggiero, a neuroradiologist) reads, "The greatest sin/is that of the orphans/the snotty ones/who never had a nickel marble/the greatest sin/is to be nobody's darling." They managed to have their "oeuvre" published as written by an unknown debutant, Jan Victor, a pen-name. The reviews were benevolent. After a couple of days, the "authors" disclosed the truth. The news was soon on the first page in the daily papers all over Sweden. With a practical joke, 2 medical students had challenged the genuineness of the flourishing modern lyrics of the 1940s—or had they? A debate followed on the culture pages but soon calmed down. Torgny's accomplice, Lars Gyllensten, later had a brilliant career as an author, and Torgny Greitz, endowed with a linguistic vein and a sharp pen, would, late in his life, be awarded a prize for "his efforts to promote good medical language" by the Swedish Medical Society.

Torgny married Greta Schölin, a physiotherapist, the year before he finished medical school in 1948. Soon the family also included 3 sons.

Clinical Career

After medical school, Torgny did 2 years' residency in surgery (Stockholm South Hospital and the Serafimer Hospital). His career in radiology was straight as an arrow and started at Stockholm South Hospital as a resident in 1950–53, followed by a position as radiologist at the Serafimer Hospital in 1954–58. After a feat of great strength and persistence during the summer of 1956, he was able to defend his seminal thesis, "A Radiologic Study of the Brain Circulation by Rapid Serial Angiography of the Carotid Artery." This happened only 3 days before he left for St. Louis.

In 1960, at 38 years of age, Torgny accepted a position as professor of general radiology at the Medical College of Umeå in the North of Sweden, where a new university was being established. He maintained this position until the neuroscience departments at the Serafimer Hospital were moved to a modern building at the Karolinska Hospital in 1963. Torgny Greitz was the indisputable choice for the position as head of an independent Department of Neuroradiology. He would stay in this position until his retirement in 1987. The same year as the digital image revolution was about to start, 1973, Torgny was appointed Professor of Neuroradiology, which rendered academic recognition to the discipline of neuroradiology. He reached the height of his career as President of the XIII Symposium Neuroradiologicum in Stockholm in 1986.

Tutoring

When Torgny set out to work at the Karolinska Hospital in 1963, his reputation as a dynamic innovator was recognized far and wide. Despite scarce staffing, he very soon managed to transform the department into a cutting-edge research center. Students from both North America (Hans Newton among others) and European countries and some from other continents came to learn and write papers. Three of them acquired PhD degrees (Mario Corrales, Ahmad Hatam, Xhemail Barratry). A further 28 Swedish students wrote their PhD theses supervised by Torgny. He was an inventive and diligent tutor. In a stimulating spirit of comradeship, he offered ample time for counseling and discussing manuscripts. This often had to take place late in the evenings since his days were filled with routine work, lecturing, planning for research and up-to-date equipment, administration, and so forth. Many times, he characterized the everyday situation in the department as "chaotic," but a fertile chaos it was and for the most part we had great fun and accepted long working days. A typical question from a PhD student late at night was, "May I leave now? I have a relationship with a woman who is still my spouse, you see."

Research and Professional Matters

Torgny's list of publications includes a wide field of research. Early works dealt with phlebography of the lower extremity and pelvis; others described cerebral vascular anatomy and pathology. In an article from 1954, he and his coauthor Stig Löfstedt, for the first time, suggested that arterial ectasia be defined as a disease entity in its own right, separate from arteriosclerosis, later generally accepted. His interest in contrast media is manifested by several publications—most notably those investigating intrathecal use of metrizamide (Amipaque), the first nonionic contrast medium on the market, synthesized by Nyegaard & Co in Oslo, Norway. Tests of new products from the x-ray industry (AOT film changer, Mimer III, and the rotating chair) and interventional radiology (nerve root blockade, puncture of spinal cord cysts) were the focus of yet another set of publications.

He excelled in improving established methods as well as inventing new ones: a good example of the latter being his seminal thesis, already mentioned. In this pioneering work, he laid down the principles for determination of regional and global cerebral circulation time that are still followed. Using a rapid film changer (AOT), the circulation time was measured from the angiograms and compared with an isotope method (using iodine 131) devised by himself. The thesis was one of the very first radiologic studies to bring a physiologic dimension into radiology. For the first time, it pointed to the potential of localizing mass lesions by the demonstration of local circulatory disturbances, occasionally even providing improved means for the characterization of lesions. In a series of articles, he further widened the scope of studying cerebral circulation using angiography and the xenon 133 clearance method. He proved that normal pressure hydrocephalus, another special interest to him, was accompanied by a reduced cerebral blood flow and, furthermore, that shunting of the CSF restored the blood flow to a degree that correlated with the clinical improvement. In later years, in cooperation with his disciple and nephew Dan Greitz, Torgny launched an alternative theory for the development of normal pressure hydrocephalus, challenging the bulk-flow theory of CSF. It is based on the assumption that the major cause of this disorder is of vascular origin, more specifically arteriosclerosis of the arteries on the surface of the brain. Although not yet generally accepted, the theory is steadily gaining ground.

In 1976, Torgny Greitz et al published the very first method for stereotactic CT. This work was closely linked to the construction of an all-purpose head-fixation system allowing for exact transfer of positions between imaging modalities, also between imaging and therapeutic modalities (namely, stereotactic surgery and radiation therapy). In 1977, a multidisciplinary PET research project was initiated by Torgny Greitz in cooperation with the Department of Physics at Stockholm University and the Department of

Neurophysiology at the Karolinska Hospital. A great number of institutions joined in to establish the Stockholm Positron Camera Group, which, before being split up in smaller groups, had its heyday in the 1980s. Torgny's enthusiasm and creativity laid down a fertile ground for cooperation among the many members of the group representing a variety of expertise: neurology, neurosurgery, psychiatry, pharmacology, radio-pharmacy, and so forth. Between 1979 and 1990, Torgny, together with group members, published 47 articles related to PET research; among those, a series of studies focused on metabolic changes in intracranial tumors using various tracers such as glucose and amino acids as well as studies of the use of specific ligands for various neuroreceptors.

Dedicated to studies with PET, Torgny Greitz and coworkers developed a computerized, individually adjustable stereotaxic 3D brain atlas, based on 0.2-mm-thick histologic cuts. The atlas defined more than 400 structures. It enabled much improved accuracy in defining ROIs in the PET material. It also laid the basis for statistical evaluation at a group level when every single brain in a study had been fitted into a standard anatomy by a set of mathematic transformations. It was a magnificent pioneering work, starting in the early 1980s. Image analysis, according to similar principles, is incorporated in several freeware programs used today.

Torgny shared generously his profound knowledge with the rest of the world by contributing chapters to many books, among those Herbert Abrahams' classic standard work *Angiography* (first and second editions 1961 and 1971) and the well-known textbooks *Radiology of the Skull and Brain* and *Modern Neuroradiology*, both edited by Thomas Newton and Gordon Potts (1981 and 1983). Among his own editorships, *The Metabolism of the Human Brain Studied with Positron Emission Tomography* stands out as a comprehensive state-of-the-art volume containing the works presented at the 7th Nobel Conference of Karolinska Institutet in 1983.

The Swedish Society of Neuroradiology was founded by Torgny Greitz, Ingmar Wickbom, Erik Lindgren, and Bengt Liliequist in 1971. Torgny took command as acting chairman, 1975–1979, and later contributed regularly in policy discussions related to the advancement of our discipline. As president of the Stockholm Symposium Neuroradiologicum in 1986, he became a prominent profile at the Past Presidents Board. Torgny's generous lecturing as an invited speaker all over the world, though mostly in North America, has been returned when distinguished colleagues have accepted invitations to honor him by coming to Stockholm and giving the "Torgny Greitz Lecture" (instituted by the Swedish Society of Neuroradiology at the time of his retirement); among them were George du Boulay, Giovanni di Chiro, Derek Harwood-Nash, James Barkowich, and Anne Osborne, to just mention a few "giants" in neuroradiology.

Honors

Torgny Greitz was honored with membership in the Swedish Academy of Science and many radiologic societies, among them the American Society of Neuroradiology, European Society of Neuroradiology, American College of Radiology, International Society of Radiology, Swedish Society of Neuroradiology, Swedish Society of Radiology, Association Francaise de Neuroradiologie, and Nordic Society of Neuroradiology. Among the many prizes he was awarded, he particularly cherished the Ziedses des Plantes Medaille (1988). In 1985, Torgny was invited by the British Institute of Radiology to give the Mackenzie Davidsson Memorial Lecture.

Personality

Being head of Sweden's only radiology department exclusively dedicated to neuroradiology, Torgny Greitz was the undisputed leader in our country; the discipline personified. We sometimes called him the "figurehead," of which he disapproved, but, in a way, appropriate considering his tall figure and sharp profile. Torgny had a dynamic leader's capacity to get things done. A telling story is how he managed to acquire the first CT scanner in Europe outside the United Kingdom. In a situation when austerity was proclaimed by the hospital administration, he ordered a scanner from EMI (London, UK), without a cent in his pocket and invited the neuroradiology sections at the other 6 university hospitals in Sweden to join him in writing applications for funding and to participate in the evaluation and development of the CT technique. In October 1973, the scanner was installed in his department, which started a spurt of activity around our country, resulting in a thick supplement of *Acta Radiologica (*1975), presenting a preliminary assessment of the value of the technique in a number of clinical applications. On December 10, 1979, a triumphant Torgny Greitz would introduce Geoffrey Hounsfield and Allan McCormack at the Nobel Prize ceremony. It was an achievement of masterly rhetoric to convince half the Nobel Assembly at Karolinska Institutet to vote for an engineer and a physicist as laureates of that year's Nobel Prize in Physiology or Medicine. Decided by lot (vote being 50 versus 50), the prize was awarded for the invention of Computer-Assisted Tomography, a revolutionary diagnostic tool, certainly a worthy winner, bringing something very useful to mankind and in good agreement with the wording in Alfred Nobel's Will.

Torgny Greitz reached his unique position not only from ambition but essentially by hard work. He was uncompromising in his quest for truth and progress. With his idealistic mind and exceptional persistence, he worked with dedication, addiction as some would say, to improve the methods, the hardware, and software alike, to expand our discipline and to drive it to ever increasing perfection. At the time of presentation, Torgny Greitz's research was foresighted and at the cutting edge, often at the center of discussion in the neuroradiology community even on a broader scale in allied disciplines. Much of his research has been incorporated in the body of today's knowledge of neuroradiology.

His authority was absolute, though his leadership, nonauthoritarian. He got followers by setting a good example for others. With his wit, his boyishness, his humanity, and warm heart, he made friends wherever he set foot. By being a good doctor, an outstanding scientist, and a great innovator, Torgny Greitz is a worthy role model for generations to come.

T. Hindmarsh
O. Flodmark
Department of Clinical Neurosciences
Division of Neuroradiology
Karolinska Institutet
Stockholm, Sweden

http://dx.doi.org/10.3174/ajnr.A5365

Spinal Cord, Spinal Root, and Brain MRI Abnormalities in Congenital Zika Syndrome

The recent article "Spectrum of Spinal Cord, Spinal Root, and Brain MRI Abnormalities in Congenital Zika Syndrome with and without Arthrogryposis" is very interesting.[1] Aragao et al[1] concluded that "Most infants had some degree of spinal cord thickness reduction, predominant in the thoracic segment (without arthrogryposis) or in the entire spinal cord (with arthrogryposis)." We would like to share ideas and observations from tropical Asia, where the Zika virus infection is also endemic. Although the neurologic defect is common in the affected infants in tropical America, it is rarely seen among the affected infants in tropical Asia.[2] Most affected cases in Southeast Asia are asymptomatic, and there is no abnormality in spinal or brain MR imaging.[3]

http://dx.doi.org/10.3174/ajnr.A5268

REFERENCES

1. Aragao MFVV, Brainer-Lima AM, Holanda AC, et al. **Spectrum of spinal cord, spinal root, and brain MRI abnormalities in congenital Zika syndrome with and without arthrogryposis.** *AJNR Am J Neuroradiol* 2017 Mar 31. [Epub ahead of print] CrossRef Medline
2. Wiwanitkit S, Wiwanitkit V. **Afebrile, asymptomatic and non-thrombocytopenic Zika virus infection: don't miss it!** *Asian Pac J Trop Med* 2016;9:513 CrossRef Medline
3. Joob B, Wiwanitkit V. **Fetal magnetic resonance imaging of fetus with Zika virus infection.** *Pediatr Neurol* 2017;68:e1 CrossRef Medline

B. Joob
Sanitation 1 Medical Academic Center
Bangkok, Thailand
V. Wiwanitkit
Hainan Medical University
China

High-Resolution Hybrid Imaging Could Improve Cordotomy Lesions and Outcomes

We have read with great interest the paper by Vedantam et al[1] concerning the postoperative evaluation of cordotomy with MR imaging. We agree that this is a very important step to assess treatment efficacy. Indeed, lesion localization is of prime importance; this underlines another potential of multimodal hybrid rooms. We believe that, given the proper tools, perioperative visualization of the electrode could be performed under MR guidance. Although the electrode itself may generate artifacts, it should be possible to perform improved navigation because of the superior differentiation between gray matter and the spinothalamic tracts on MR imaging compared with CT. In addition, diffusion tensor imaging performed before implantation, and even during the procedure, could also help to improve the precision of electrode placement as well as to allow better visualization and delineation of the tracts. Thus, the use of a combined MR and operating table should allow this to be performed safely. At the moment, these techniques can be applied only at the level of the cervical spine. On the other hand, by using combined MR operative techniques as well as eventually moving to higher fields, it should be possible to improve lesion delineation. A higher field, in addition to a higher resolution, should allow improved acquisition of gradient-echo images, which have been shown to provide the best gray-white matter differentiation.[2,3] Finally, this should allow cordotomy, resulting in smaller and better-localized post-procedure lesions that would correspond to the 20% of cord area that is necessary for an acceptable clinical outcome.[4]

http://dx.doi.org/10.3174/ajnr.A5269

REFERENCES

1. Vedantam A, Hou P, Chi TL, et al. **Postoperative MRI evaluation of a radiofrequency cordotomy lesion for intractable cancer pain**. *AJNR Am J Neuroradiol* 2017;38:835–39 CrossRef Medline
2. Zhao W, Cohen-Adad J, Polimeni JR, et al. **Nineteen-channel receive array and four-channel transmit array coil for cervical spinal cord imaging at 7T.** *Magn Reson Med* 2014;72:291–300 CrossRef Medline
3. Massire A, Taso M, Besson P, et al. **High-resolution multi-parametric quantitative magnetic resonance imaging of the human cervical spinal cord at 7T.** *Neuroimage* 2016;143:58–69 CrossRef Medline
4. Lahuerta J, Bowsher D, Lipton S, et al. **Percutaneous cervical cordotomy: a review of 181 operations on 146 patients with a study on the location of "pain fibers" in the C-2 spinal cord segment of 29 cases.** *J Neurosurg* 1994;80:975–85 CrossRef Medline

M.I. Vargas
J. Boto
Division of Neuroradiology, DISIM
P. Dammann
Division of Neurosurgery
K.-O. Lovblad
Division of Neuroradiology, DISIM
Geneva University Hospital
Geneva, Switzerland

The Concept of "Number Needed to Image"

In medicine, it is a common reaction for referring physicians to ask for the less expensive imaging technique if the a priori suspicion of finding abnormalities is low. For example, in a case with a mild traumatic brain injury (MTBI) and low suspicion of finding trauma-related brain abnormalities, the referring physician oftentimes asks for the cheaper, yet less sensitive, CT rather than the more expensive, but also more sensitive, MR imaging to detect, for example, diffuse axonal injuries.[1] This reaction is intuitively understandable, notably in times of increasing economic pressure.

However, when considering the situation in more depth, this reaction might be questionable. If a test with a low sensitivity is performed in the setting of a low clinical suspicion (ie, a low pretest probability), this will result in a high proportion of false-negative cases.

From the perspective of optimal patient care, a test with a low sensitivity in the setting of a low pretest probability is not suited to rule out pathology because of the high likelihood of false-negative results.

From the perspective of cost effectiveness, the less expensive yet less sensitive test will result in a high proportion of false-negative examinations. Consequently, many imaging tests must be performed to have 1 positive imaging finding. The accumulated cost for 1 positive imaging test might therefore be high despite the relative low cost of each individual imaging test. In contrast, a more expensive yet more sensitive imaging test will have fewer false-negative cases; consequently, fewer cases are needed to have 1 positive imaging finding. The resulting accumulating cost for 1 positive test might therefore be lower compared with a less expensive yet less sensitive test. This concept might be called "number needed to image" (NNI [ie, the number of imaging examinations needed to have 1 positive imaging test]).

Moreover, there are additional indirect costs that should be considered. A more expensive and more sensitive test might avoid repeated false-negative imaging and repetitive medical consultations for the patient. The earlier and more specific diagnosis might allow for earlier treatment and, consequently, faster and earlier recovery.

http://dx.doi.org/10.3174/ajnr.A5276

In fact, to have a cost-effective imaging assessment, physicians should ask for the less expensive and less sensitive imaging test in the setting of a high clinical suspicion of abnormal findings. In this setting, the less sensitive test might be very cost-efficient and, at the same time, will result in only a low rate of false-negative imaging results.

In medicine, the equivalent concept of number needed to treat (NNT) is well established.[2,3] Physicians treat patients (eg, with antiaggregation or antihypertensive medication to prevent stroke) knowing that only 1 of *n* patients will actually benefit from the treatment. For example, in patients with relatively nonsevere hypertension (diastolic blood pressure, 90–110 mm Hg), the NNT to prevent 1 stroke is 118, whereas this number is 29 in patients with more severe hypertension (diastolic blood pressure >115 mm Hg).[4] This creates not only a cost related to the medication, which is oftentimes prescribed for years or even decades, but also medication-related side effects.

Concerning imaging, the corresponding concept of NNI is not yet well established. If, in the current example of MTBI, only 1 of 29 MR imagings would demonstrate subtle posttraumatic findings not visible on CT, this would probably generally be considered as too expensive to justify imaging, though MR imaging has no relevant side effects in contrast to the medical treatment discussed above. Moreover, considering the additional effect on associated costs, such as medicolegal and insurance-related costs, imaging would probably still be highly cost-efficient even if a substantial number of cases have negative MR imaging results.

This principle of NNI applies not only to MTBI. Other examples might be cervical spine radiography instead of CT or MR imaging for low impact cervical spine trauma, or wrist radiography instead of CT or MR imaging for low suspicion of scaphoid fracture, etc.

In conclusion, it is an intuitively understandable reaction to ask for a less expensive and less sensitive imaging test in the setting of a low clinical suspicion of finding abnormalities. However, this intuitive reaction might be neither suitable to reliably rule out pathology nor cost-efficient. The concept of NNI should be further developed to define how many negative imaging tests can be allowed for 1 positive finding, both from the perspective of opti-

mal patient care as well as from the perspective of cost-effective imaging.

REFERENCES

1. Provenzale JM. **Imaging of traumatic brain injury: a review of the recent medical literature.** *AJR Am J Roentgenol* 2010;194:16–19 CrossRef Medline
2. Laupacis A, Sackett DL, Roberts RS. **An assessment of clinically useful measures of the consequences of treatment.** *N Engl J Med* 1988;318:1728–33 CrossRef Medline
3. Nuovo J, Melnikow J, Chang D. **Reporting number needed to treat and absolute risk reduction in randomized controlled trials.** *JAMA* 2002;287:2813–14 CrossRef Medline
4. Kaplan RC. **Treatment of hypertension to prevent stroke: translating evidence into clinical practice.** *J Clin Hypertens* 2001;3:153–56 CrossRef Medline

S. Haller
Affidea Centre de Diagnostic Radiologique de Carouge CDRC
Geneva, Switzerland
Department of Surgical Sciences, Radiology
Uppsala University
Uppsala, Sweden
Department of Neuroradiology
University Hospital Freiburg
Freiburg, Germany
Faculty of Medicine
University of Geneva
Geneva, Switzerland

Coregistration and Fusion: An Easy and Reliable Method for Identifying Cranial Nerve IV on MRI

We read with much interest the article by Bunch et al[1] in the March 2017 issue of the *American Journal of Neuroradiology*, in which they described the trochlear groove and trochlear cistern as reliable anatomic landmarks when searching for the tentorial segment of cranial nerve IV on MR imaging. The authors provided useful indications to recognize these 2 structures with a T2-weighted driven equilibrium radiofrequency reset pulse sequence. Confirming these 2 landmarks was significantly associated with correctly identifying the trochlear nerve.

We agree that short sequences are more practical for routine clinical use as opposed to those previously reported in the literature using high-resolution motion-sensitized driven equilibrium sequences with a 26-minute acquisition time.[2] This sequence use is particularly true for cranial nerve IV imaging because a substantial number of patients being evaluated for suspected trochlear nerve pathology, including congenital palsy, are children, who are more prone to movements than adults. Therefore, a long scanning time may exacerbate motion artifacts on MR images.

However, we believe that this study has a few limitations that may impair its scope. The trochlear nerve remains the thinnest of all cranial nerves, with a mean diameter of approximately 0.5 mm (range, 0.3–0.9 mm). It has a complex course around the midbrain and is in close proximity to many arteries and veins with similar courses and calibers. The voxel size acquired in this study ranged from $0.3 \times 0.35 \times 3.0$ to $0.4 \times 0.44 \times 3.0$; thus, the section thickness (resolution of the z-axis) provided was 3.0 mm, which is too large to identify the trochlear nerve consistently. Moreover, the gap ranged from 0.3 to 1 mm, which is too high to observe a 0.5-mm structure.[3] Much thinner sections are required to visualize the trochlear nerve, with a maximum of 0.25-mm section thickness and no gap.

The imaging findings of this study remain subjective and are not supported by surgical or pathologic correlations. Additionally, significant discrepancies between the MR imaging and anatomic findings were reported in cadaveric studies. Our colleagues' images are somewhat noisy, with CSF flow-related artifacts and are therefore not very convincing, even with annotations.

An interesting option for reliably identifying cranial nerve IV on MR imaging within a reasonable acquisition time may be the use of coregistration and fusion[4] of an MR angiography sequence and of a "routine" T2-weighted driven equilibrium radiofrequency reset pulse sequence. Regrettably, even a very high resolution may still be insufficient due to the very complex course of the nerve and its close proximity to adjacent vessels. MRA enables the reader to clearly and reliably identify both arteries and veins, despite their highly variable anatomy. Therefore, this technique supports correct identification of the closely related trochlear nerve (Figure). This method is easy and is available in various software packages. A long posttreatment process is not necessary, and it can be performed during routine clinical practice in many institutions without involving highly specialized providers. With this method, all segments of the trochlear nerve are visible, especially its tentorial segment where the nerve is parallel to the vessels and runs along the tentorial edge. This approach may also be used successfully on larger cranial nerves such as the oculomotor or the abducens nerves.

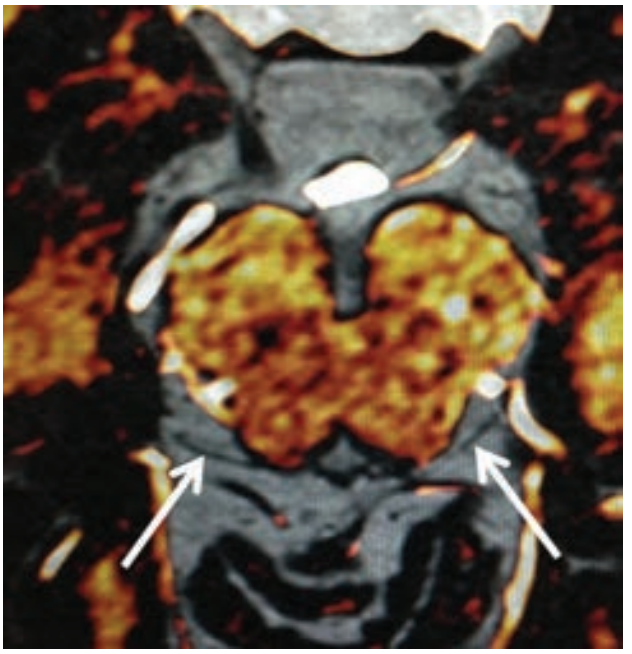

FIGURE. Coregistration-fusion of an MR angiography and a T2-weighted driven equilibrium radiofrequency reset pulse sequence allowing to distinguish cisternal vessels colored in white from the trochlear nerves in black (*arrows*).

http://dx.doi.org/10.3174/ajnr.A5286

Finally, it is possible that the key for reliable and accurate identification of the trochlear nerve may be the use of a simple coregistration and fusion instead of long and complex high-resolution MR imaging acquisitions.

Disclosures: Julien Savatovsky—*UNRELATED*: *Consultancy*: Servier International Research Institute (IRIS), Madday Pharmaceutical, Bristol-Myers Squibb, GlaxoSmithKline, *Comments*: All except IRIS paid me around $5000 2 years ago*; *Expert Testimony*: Philips Healthcare, Bayer Pharmaceutical; *Grants/Grants Pending*: Association de la Recherche Sur le Syndrome Immuno-Déficitaire Acqui*; *Payment for Lectures Including Service on Speakers Bureaus*: Philips Healthcare, IRIS, Biogen; *Travel/Accommodations/Meeting Expenses Unrelated to Activities Listed*: GE Healthcare, Philips, Bayer. *Money paid to the institution.

REFERENCES

1. Bunch PM, Kelly HR, Zander DA, et al. **Trochlear groove and trochlear cistern: useful anatomic landmarks for identifying the tentorial segment of cranial nerve IV on MRI.** *AJNR Am J Neuroradiol* 2017;38:1026–30 CrossRef Medline
2. Kanoto M, Toyoguchi Y, Hosoya T, et al. **Visualization of the trochlear nerve in the cistern with use of high-resolution turbo spin-echo multisection motion-sensitized driven equilibrium.** *AJNR Am J Neuroradiol* 2013;34:1434–37 CrossRef Medline
3. Choi BS, Kim JH, Jung C, et al. **High-resolution 3D MR imaging of the trochlear nerve.** *AJNR Am J Neuroradiol* 2010;31:1076–79 CrossRef Medline
4. Liu P, Eberhardt B, Wybranski C, et al. **Nonrigid 3D medical image registration and fusion based on deformable models.** *Comput Math Methods Med* 2013;2013:902470 CrossRef Medline

A. Lecler
J. Savatovsky
Department of Radiology
F. Audren
Department of Ophthalmology
Fondation Ophtalmologique Adolphe de Rothschild
Paris, France

REPLY:

We greatly appreciate the interest that Drs Lecler, Savatovsky, and Audren have shown in our recent article entitled "Trochlear Groove and Trochlear Cistern: Useful Anatomic Landmarks for Identifying the Tentorial Segment of Cranial Nerve IV on MRI,"[1] and we are grateful for their thoughtful comments.

Multiple anatomic studies have independently documented the existence of the trochlear groove and trochlear cistern.[2-6] We observed these structures in our clinical practice on coronally acquired fluid-sensitive MR imaging performed routinely as a component of sinus MR imaging examinations at our institution. It has been our experience interpreting these clinical studies that the trochlear groove and trochlear cistern facilitate identification of the adjacent tentorial segment of cranial nerve IV.

This observation and subsequent clinical experience provided the motivation for our recently published study, which involved the retrospective review of 25 consecutive sinus MR imaging examinations containing the fluid-sensitive sequence of interest.[1]

Our primary interest was the anatomy. We did not mean to suggest that we had developed a novel MR sequence or that this routine clinical sequence represents the best possible one for identifying cranial nerve IV in its entirety. Rather, we hoped to share an imaging observation based on anatomic facts that we believed others may find useful in the assessment of cranial nerve IV pathology.

We would like to clarify the voxel size reported in our initial article because we now realize it to be a source of confusion that could have been stated more clearly. We intended for the reported voxel size range to indicate that the in-plane resolution of the coronally acquired sequence ranged from 0.3×0.35 to 0.4×0.44 mm and that the out-of-plane section thickness (in the anteroposterior dimension rather than the superior-inferior or z-axis dimension) was 3.0 mm. Because the tentorial segment of cranial nerve IV travels nearly perpendicular to coronally acquired sections through the trochlear groove and trochlear cistern, these acquisition parameters are in fact sufficient to identify cranial nerve IV in many (but not all) cases, as was shown in our study. Moreover, the tentorial segment of cranial nerve IV was often seen on multiple contiguous sections in our study, and we considered seeing the nerve on a single image to be insufficient for nerve identification.

Additionally, we would like to reiterate that we did not identify the entire intracranial course of cranial nerve IV but only the tentorial segment—the portion of the nerve that passes beneath the tentorium before entering the cavernous sinus. It has been our experience that this particular segment of cranial nerve IV is especially difficult to identify on axial images, including high-resolution cisternographic sequences (CISS, FIESTA, and so forth), and we consider this difficulty likely to be related to volume averaging of the overlying tentorium. Thus, we remain convinced that it is advantageous to leverage in-plane resolution and scan this particular segment of cranial nerve IV in the coronal plane perpendicular to its course.

Identifying the intracranial segments of cranial nerve IV in routine clinical practice remains difficult, and we are appreciative of the coregistration-fusion technique suggested by our colleagues. Indeed, we welcome any solution to the difficult problem of identifying cranial nerve IV throughout its course using clinically practical MR imaging, and we agree that the more proximal cisternal segment of cranial nerve IV is very nicely demonstrated in our colleagues' figure.

We look forward to further discussion and exchange of ideas.

http://dx.doi.org/10.3174/ajnr.A5294

REFERENCES

1. Bunch PM, Kelly HR, Zander DA, et al. **Trochlear groove and trochlear cistern: useful anatomic landmarks for identifying the tentorial segment of cranial nerve IV on MRI.** *AJNR Am J Neuroradiol* 2017;38:1026–30 CrossRef Medline
2. Ammirati M, Musumeci A, Bernardo A, et al. **The microsurgical anatomy of the cisternal segment of the trochlear nerve, as seen through different neurosurgical operative windows.** *Acta Neurochir (Wien)* 2002;144:1323–27 CrossRef Medline
3. Rhoton AL. **The sellar region.** *Neurosurgery* 2002;51:S335–74 Medline
4. Iaconetta G, de Notaris M, Benet A, et al. **The trochlear nerve: microanatomic and endoscopic study.** *Neurosurg Rev* 2013;36:227–37; discussion 237–38 CrossRef Medline
5. Herlan S, Hirt B, Tatagiba M, et al. **Focus on the lateral incisural space: where is the trochlear nerve?** *J Neurol Surg Part B Skull Base* 2013;74:271–73 CrossRef Medline
6. Joo W, Rhoton AL Jr. **Microsurgical anatomy of the trochlear nerve.** *Clin Anat* 2015;28:857–64 CrossRef Medline

P. Bunch
Department of Radiology, Division of Neuroradiology
Massachusetts General Hospital
Boston, Massachusetts

H. Kelly
Department of Radiology, Division of Neuroradiology
Massachusetts General Hospital
Boston, Massachusetts
Department of Radiology
Massachusetts Eye and Ear
Boston, Massachusetts

D. Zander
Radiology Imaging Associates
Denver, Colorado

H. Curtin
Department of Radiology
Massachusetts Eye and Ear
Boston, Massachusetts

Minor Stroke and Thrombolysis: What Is in the Pipeline?

We read with interest the article by Messer et al[1] regarding the clinical outcome after IV thrombolysis and/or mechanical thrombectomy in patients with acute ischemic stroke due to large-vessel occlusion, presenting as minor stroke syndrome (MSS) (NIHSS score < 5). The authors retrospectively analyzed a group of 378 patients with MSS involving the anterior circulation, finding that 12% of these had large-vessel occlusion. In this subgroup, they noted that patients with immediate mechanical thrombectomy had a better outcome than patients with delayed thrombectomy (performed after neurologic deterioration) or with IV thrombolysis only. Most interesting, a recent study has shown that almost 30% of patients not treated with IV thrombolysis because they were initially considered "to-good-to-treat" (NIHSS score < 5) could suddenly worsen during the first hours following the stroke onset. This finding suggests possibly including this subgroup of patients in the IV thrombolysis decision-making algorithms.[2] Mechanical thrombectomy has become the standard of care for patients presenting with severe ischemic stroke due to large-vessel occlusion; however, it is unclear whether patients presenting with MSS would benefit from this treatment.

We have retrospectively analyzed a group of 104 patients admitted to our institution (Misericordia Hospital, Grosseto) for acute ischemic stroke during 2015–2016 who received standard IV thrombolysis. We identified 21 patients (22%) with MSS. Thirteen of those 21 patients (62%) had a good outcome at discharge (mRS < 2). No symptomatic intracranial hemorrhage occurred. All patients underwent CTA. Eleven of those 21 patients had large-vessel occlusion. Specifically, 8 patients (38%) had large-vessel occlusion in the anterior circulation (respectively, 2 patients with ICA extracranial occlusion, and 2 patients with MCA–M1 and 4 patients with MCA–M2 occlusion) and 3 patients (14%) had a posterior circulation stroke (1 patient with basilar artery apex occlusion and 2 patients with extracranial vertebral artery occlusion). One patient had an extracranial ICA dissecting pseudoaneurysm without large-vessel occlusion. Four of these 11 patients were initially treated with mechanical thrombectomy according to the model of "drip and ship," with good outcome at discharge (mRS < 2). Seven of these 11 patients were treated with IV thrombolysis only. Among this latter subgroup, 4 patients had early neurologic deterioration, and no mechanical thrombectomy was performed later because too much time had elapsed. Moreover, the patient with an ICA dissecting pseudoaneurysm had an early relapse due to an embolism.

Although our case series is too small to clarify the potential benefit of mechanical thrombectomy in MSS, this retrospective observation caused some reflection. First, we confirm that a relevant percentage of large-vessel occlusion in MSS involves not only the anterior but also the posterior circulation (52% of our observed cases). The management of MSS is currently unclear, and we would like to stress that the NIHSS alone does not represent a valid outcome predictor or an indicator of large-vessel occlusion in this subgroup of patients. In fact, a posterior circulation stroke might initially present with a low NIHSS score, as previously stated.[2,3] Again, a low NIHSS score at stroke onset might possibly reflect an anterior circulation stroke due to large-vessel occlusion in the presence of valid collateral circulation. These conditions might worsen in the immediate hours following.

We agree with Messer et al[1] that an advanced neuroimaging diagnostic work-up, including CTA, is suggested in MSS to correctly address the treatment. Second, in case of large-vessel occlusion (involving the anterior or posterior circulation), an immediate evaluation to the "hub" center for mechanical thrombectomy should be considered, given that this condition is the most common cause of early neurologic deterioration after IV thrombolysis in MSS. We believe that "spoke" centers cannot wait for neurologic deterioration to transfer the patient to the referring "hub"; in this case, the patient cannot undergo mechanical thrombectomy because of elapsed time. Third, an early severe stroke relapse may erase the benefit of IV thrombolysis when a high-risk embolic condition is present (eg, a severe ICA stenosis/dissection) as previously reported for TIAs. Thus, we recently admitted a man 63 years of age presenting with MSS due to an ICA dissecting pseudoaneurysm that relapsed a few hours after IV thrombolysis into a more disabling stroke. In this case, as suggested by Behme et al,[4] a patient having undergone thrombolysis with a high-grade extracranial ICA stenosis should be considered for ICA stent placement immediately after mechanical thrombectomy. On the other hand, the best management for patients without tandem lesions is

http://dx.doi.org/10.3174/ajnr.A5298

still unclear. Do we need to transfer the patient, according to the drip and ship model, to the referring ring hub for acute stent placement? Alternatively, is it preferable to perform mechanical thrombectomy only after the occurrence of an early relapse?

In conclusion, the correct management of MSS is unclear. While one waits for the results of ongoing clinical trials in this subgroup of patients (PRISMS, NCT02072226; clinicaltrials.gov), the experience of single-center studies might help clinicians to better define the correct therapeutic algorithms.

REFERENCES

1. Messer MP, Schönenberger S, Möhlenbruck MA, et al. **Minor stroke syndromes in large-vessel occlusions: mechanical thrombectomy or thrombolysis only?** *AJNR Am J Neuroradiol* 2017;38:1177–79 CrossRef Medline
2. Ali SF, Siddiqui K, Ay H, et al. **Baseline predictors of poor outcome in patients too good to treat with intravenous thrombolysis.** *Stroke* 2016;47:2986–92 CrossRef Medline
3. Kim JT, Park MS, Choi KH, et al. **Clinical outcomes of posterior versus anterior circulation infarction with low National Institutes of Health Stroke Scale scores.** *Stroke* 2017;48:55–62 CrossRef Medline
4. Behme D, Knauth M, Psychogios MN. **Retriever wire supported carotid artery revascularization (ReWiSed CARe) in acute ischemic stroke with underlying tandem occlusion caused by an internal carotid artery dissection: technical note.** *Interv Neuroradiol* 2017;23:289–92 CrossRef Medline

S. Gallerini
Unit of Neurology
Misericordia Hospital
Grosseto, Italy
L. Marsili
Unit of Neurology
Misericordia Hospital
Grosseto, Italy
Department of Neurology and Psychiatry
"Sapienza" University of Rome
Rome, Italy
M. Bartalucci
C. Marotti
R. Marconi
Unit of Neurology
Misericordia Hospital
Grosseto, Italy

REPLY:

We appreciate the comments by Gallerini et al regarding our recently published Clinical Report on patients with minor acute ischemic stroke syndromes and underlying large-vessel occlusion (LVO) in the anterior circulation.

We agree that in most stroke centers today, there is equipoise as to whether to transfer these patients to immediate mechanical thrombectomy (MT) or to offer thrombolysis (if possible) only, monitor the clinical course, and perform MT in case of clinical deterioration. Evidence from the recent randomized MT trials is lacking, and the nonrandomized evidence is scarce. In our experience, rescue MT, compared with immediate MT, may not be optimal in these patients. Haussen et al[1] also compared the impact of immediate MT ($n = 10$) versus initial medical treatment ($n = 22$), including rescue thrombectomy if there was clinical deterioration based on the NIHSS difference from admission to discharge. They found that patients with immediate MT had more NIHSS improvement (-2.5 versus 0; $P < .01$) and a nonsignificantly better clinical outcome at 90 days (mRS 0–2: 100% versus 77%; $P = .15$). We showed the same trend favoring immediate MT; good outcomes (mRS 0–2) were higher in patients with immediate MT (75%, $n = 8$) compared with patients with rescue MT (33%, $n = 6$).[2] However, there are also reports that immediate MT might not be superior to initial best medical management, including rescue MT, or that immediate MT might be associated with an increased risk of symptomatic intracerebral hemorrhage.[3,4]

With regard to the results of their own cohort we would like to comment, that we believe that patients with isolated proximal carotid or vertebral occlusions and patent intracranial vessels are of a different kind. Emergency stent placement, rather than MT, might be necessary in some cases if insufficient collateral flow is present. Hence, their observed LVO rate of 11/21 (52%) is much higher than that expected for MT candidates. LVO rates for patients with acute ischemic stroke vary according to clinical severity but are present in around 10%–20% of all patients with mild symptoms.[5] Furthermore, it has been estimated that 1 ICA or M1 occlusion can be detected for every 11.5 patients screened if the NIHSS score is 0–5.[6] Of those, conditions in 20%–40% of patients may deteriorate rapidly.[1,7] However, because current guidelines only recommend MT in patients with an NIHSS score of ≤ 6,[8] acute vessel imaging in patients with milder symptoms is not routinely performed; hence, many of these cases are missed by only screening patients presenting with an NIHSS score of >5.[9] We absolutely agree with Gallerini et al that the NIHSS should not be a defining criterion for performing CTA.

Unfortunately, as mentioned by Gallerini et al, PRISMS (NCT02072226; clinicaltrials.gov) will not be able to answer the question of how to proceed with the target population (ie, intracranial anterior or posterior LVO and mild symptoms) because participants will be randomized in a 1:1 ratio to receive, within 3 hours of last-known-well time, either of the following: 1) one dose of IV alteplase and 1 dose of oral aspirin placebo, or 2) one dose of IV alteplase placebo and 1 dose of oral aspirin, 325 mg). MT is not part of the protocol, and most the patients with LVO will present beyond 3 hours due to their mild symptoms.[5]

To summarize, given the lack of evidence and the conflicting reports of nonrandomized cohorts, a randomized controlled trial in the target population is warranted. Until then, in our opinion, individual treatment decisions, based on local experience, the availability of MT, and individual clinical and radiologic findings, are recommended.

http://dx.doi.org/10.3174/ajnr.A5319

REFERENCES

1. Haussen DC, Bouslama M, Grossberg JA, et al. **Too good to intervene? Thrombectomy for large vessel occlusion strokes with minimal symptoms: an intention-to-treat analysis.** *J Neurointerv Surg* 2016 Sep 2. [Epub ahead of print] CrossRef Medline
2. Messer MP, Schönenberger S, Möhlenbruch MA, et al. **Minor stroke syndromes in large-vessel occlusions: mechanical thrombectomy or thrombolysis only?** *AJNR Am J Neuroradiol* 2017;38:1177–79 CrossRef Medline
3. Dargazanil CA, Consoli A, Gory B, et al. **Mechanical thrombectomy for minor and mild stroke patients harboring large vessel occlusion in the anterior circulation: a multicenter case control study.** *J Neuroradiol* 2017;44:70–72 CrossRef
4. Urra X, San Román L, Gil F, et al; Catalan Stroke Code and Reperfusion Consortium (Cat-SCR). **Medical and endovascular treatment of patients with large vessel occlusion presenting with mild symptoms: an observational multicenter study.** *Cerebrovasc Dis* 2014;38:418–24 CrossRef Medline
5. Heldner MR, Zubler C, Mattle HP, et al. **National Institutes of Health Stroke Scale score and vessel occlusion in 2152 patients with acute ischemic stroke.** *Stroke* 2013;44:1153–57 CrossRef Medline
6. Scheitz JF, Abdul-Rahim AH, MacIsaac RL, et al; SITS Scientific Committee. **Clinical selection strategies to identify ischemic stroke patients with large anterior vessel occlusion: results from SITS-ISTR (Safe Implementation of Thrombolysis in Stroke International Stroke Thrombolysis Registry).** *Stroke* 2017;48:290–97 CrossRef Medline
7. Heldner MR, Jung S, Zubler C, et al. **Outcome of patients with occlusions of the internal carotid artery or the main stem of the middle cerebral artery with NIHSS score of less than 5: comparison between thrombolysed and non-thrombolysed patients.** *J Neurol Neurosurg Psychiatry* 2015;86:755–60 CrossRef Medline
8. Powers WJ, Derdeyn CP, Biller J, et al; American Heart Association Stroke Council. **2015 American Heart Association/American Stroke Association Focused Update of the 2013 Guidelines for the Early Management of Patients With Acute Ischemic Stroke Regarding Endovascular Treatment: A Guideline for Healthcare Professionals From the American Heart Association/American Stroke Association.** *Stroke* 2015;46:3020–35 CrossRef Medline
9. Maas MB, Furie KL, Lev MH, et al. **National Institutes of Health Stroke Scale score is poorly predictive of proximal occlusion in acute cerebral ischemia.** *Stroke* 2009;40:2988–93 CrossRef Medline

M. Messer
P.A. Ringleb
S. Nagel
Department of Neurology
University Hospital Heidelberg
Heidelberg, Germany

The authors of "Distinguishing Neuroimaging Features in Patients Presenting with Visual Hallucinations" (T.T. Winton-Brown, A. Ting, R. Mocellin, D. Velakoulis, and F. Gaillard, *AJNR Am J Neuroradiol* 2016;37:774–81) neglected to include an author who contributed materially to the paper. M. Walterfang should have been listed fourth in the author order between R. Mocellin and D. Velakoulis.

http://dx.doi.org/10.3174/ajnr.A5389

stryker

NEW

Indication for Trevo® Retrievers

A New Standard of Care in Stroke

FIRST
mechanical thrombectomy device indicated to reduce disability in stroke.*

FIRST
new treatment indication for stroke in 20 years.

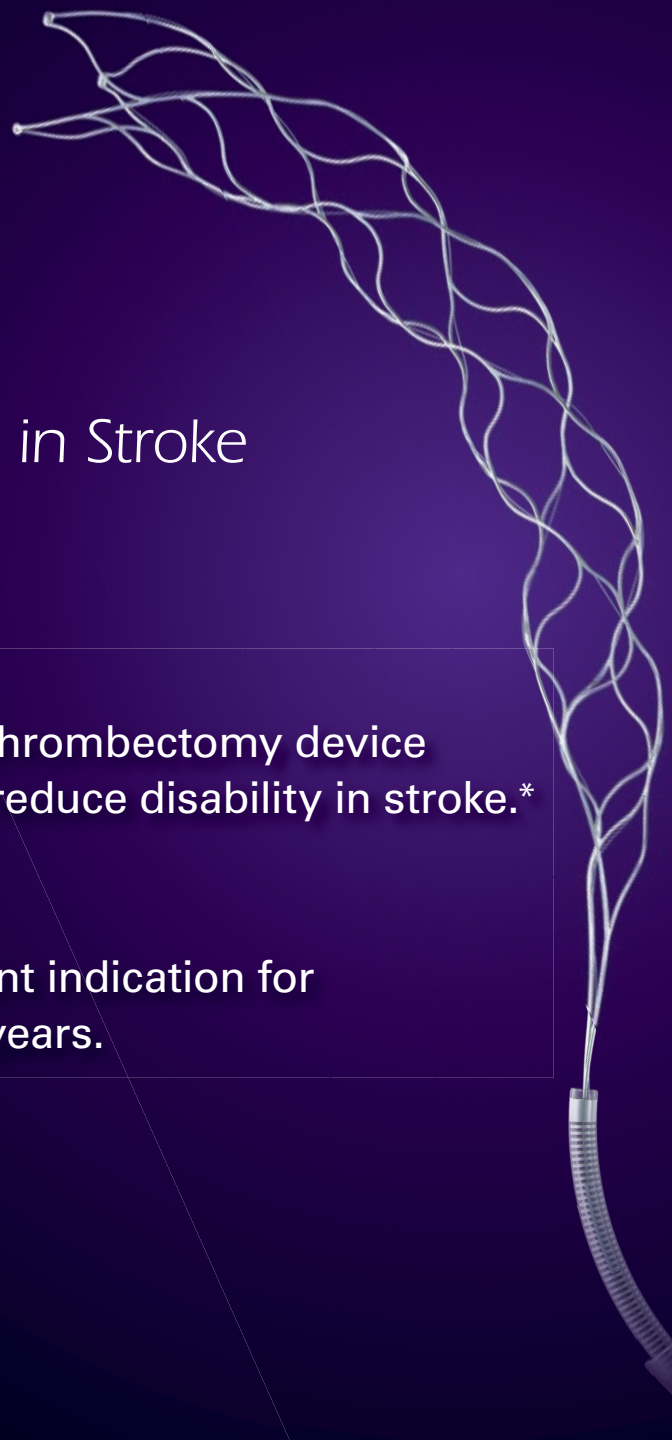

Trevo XP

PROVUE RETRIEVER

Success accelerated.

*The Trevo Retriever is indicated for use to restore blood flow in the neurovasculature by removing thrombus for the treatment of acute ischemic stroke to reduce disability in patients with a persistent, proximal anterior circulation, large vessel occlusion, and smaller core infarcts who have first received intravenous tissue plasminogen activator (IV t-PA). Endovascular therapy with the device should start within 6 hours of symptom onset.

Copyright © 2016 Stryker
NV00018973.AB

SWIFT

NINJA

STEERABLE MICROCATHETER

BY DR. YASUAKI ARAI

MERIT MEDICAL®

merit.com/ninja

#ninjafirst

403363001/B